
**Mechanistic Insights into Controlling the Molecular
Transformations of Oxygenates**

A DISSERTATION
SUBMITTED TO THE FACULTY OF THE
UNIVERSITY OF MINNESOTA
BY

Ashwin Chemburkar

IN PARTIAL FULFILLMENT OF THE REQUIREMENTS
FOR THE DEGREE OF
DOCTOR OF PHILOSOPHY

Advised by Prof. Matthew Neurock

July 2019

© 2019 Ashwin Chemburkar. **All rights reserved.**

Acknowledgements

I wish to thank my advisor, Prof. Matt Neurock for accepting me into his group as well as for facilitating multiple collaborations that culminated in various concepts presented in this dissertation. I came to the Neurock group with very little background in density functional theory methods and Prof. Stuart Winikoff was very instrumental in getting me started; I want to take this opportunity to thank him. Other group members such as Dr. Erin Fitzharris and Prof. Peng Bai were a constant source of help throughout their time in the Neurock group. Further, I want to acknowledge the current group members; Tommy, Cho, Sagar, Vineet, Rocky, Sahithi, and Roshan for maintaining a healthy working environment. I want to especially thank Sagar, Vineet, and Tommy for critiquing my dissertation. I am also very grateful to Prof. Paul Dauenhauer, Prof. Alon McCormick, and Prof. Jason Goodpaster for serving on my dissertation committee and critically reviewing my work.

I wish to express gratitude towards all my collaborators and their students that I had the privilege to work with. Experiments presented in Chapters 1-3 were performed by Dr. Toni Pfennig under the supervision of Prof. Brent Shanks. Dr. James Kammert performed the experiments reported in Chapter 5 under the guidance of Prof. Bob Davis. Ms. Bengi Demir did the experimental analysis presented in Chapter 6 under the supervision of Prof. Jim Dumesic. Prof. Dave Flaherty and Mr. James Adams were instrumental in performing experiments presented in Chapter 7. This experience of working in a collaborative setting, I believe, will go a long way as I begin my career in the industry.

My experience in graduate school was made more enjoyable due to the close friendship I developed with Pedro Constantino and Hwanhui Yun. I will miss our group lunches, intriguing conversations, and group studies. I wish you both great success in everything you pursue.

Many thanks to the CEMS department moms- Ms. Julie Prince and Ms. Teresa Bredahl for assisting me with various administrative matters.

The initial motivation to pursue graduate studies was instilled in me by my undergraduate professors- Prof. Ashwin Patwardhan, Prof. Anand Patwardhan, and Prof. Sunil Bhagwat. I am extremely grateful to all of them for teaching me the basics of chemical engineering as well as for believing in and supporting me.

Finally, I wish to express gratitude towards people closest to me for their constant support and love. Michael, my partner, has been incredibly patient and supportive during the most stressful phase of graduate school. My parents, in addition to their love and support, taught me humility, patience, honesty, and hard work, and I am forever indebted to them.

Dedicated to my parents

Veena and Madhav Chemburkar

Abstract

The detrimental environmental impact of excessive use of petroleum and fossil-fuel has motivated efforts to manufacture chemicals and fuels from biomass, a renewable feedstock. In addition, a large emphasis has been placed on developing chemistries that are not only atom-efficient, but also involve one-pot synthesis, green solvents, and easy separations, thereby, driving next generation technologies towards sustainability and green manufacturing. To that effect, this dissertation elucidates reaction mechanisms of such new chemistries, identifies catalytic features that enable fast, yet selective chemical transformations, as well as explores the complex role of greener solvents in mediating reactions, in a series of collaborative studies involving density functional theory (DFT) simulations and experiments. Biomass-derived precursors are shown to possess chemical and structural flexibility to generate a novel slate of structurally diverse intermediates that can be used as scaffolds in the synthesis of current chemical feedstocks as well as new molecules with advanced functionality for the design of new chemical and materials intermediates. Chemical diversification is demonstrated by using heterogeneous catalysts together with solvents to achieve high reactivity and selectivity. The results presented in this dissertation aim to guide the design of more active, selective, stable and cheaper catalytic materials, as well as synthesis of new molecules and establish new strategies to control the specific products that are formed.

A significant part of this dissertation focusses on chemically diversifying coumalic acid (CMA)- a bio-privileged molecule, using a selective, one-pot Diels-Alder-decarboxylation-dehydrogenation domino sequence to generate a library of aromatic compounds. Not only petroleum-derived aromatics, but also a host of novel structures can be synthesized using this approach. These new aromatics have functionalities and structures inaccessible via petroleum and have applications as pharmaceuticals, insecticides, and antimicrobials. Here, we combine in-situ NMR, DFT, and solid-state NMR to guide one-pot synthesis of aromatics from biomass, thus, providing a sustainable means to access these compounds. Our efforts lie at engineering the reactivity by identifying the rate-limiting step in the domino sequence and then subsequently catalyzing it using a heterogeneous catalyst. Selectivity is fine-tuned by esterification of CMA as well as by screening different solvents. Finally, during synthesis of more complex aromatics, structure-reactivity relationships are developed to guide stereo-selective synthesis.

This dissertation also discusses aldol condensation and esterification, reactions that can be utilized to make longer molecules from bio-derived oxygenates to synthesize fuel-grade precursors and additives respectively. Previous studies have shown that these reactions can be catalyzed when pre-equilibrated mixture of alcohol-aldehyde- H_2 is fed over metallic Cu catalysts. Here, we reveal the nature of active sites on metallic Cu that enable C-C and C-O bond formation reactions that traditionally been thought to require explicit base or acid assistance. DFT simulations, together with kinetic analyses show the prevalence of Lewis-basic alkoxide sites as well as Lewis-acidic aldehyde sites that cooperatively carry out proton and hydride transfer reactions that enable C-C and C-O bond formation reactions. The studies not only demonstrate the use of greener, earth-abundant transition metals such as Cu in biomass processing, but also opens opportunities to utilize active sites unique to Cu, and possibly other coinage metals, in reduction reactions that selectively require hydrides (for example, C-H formation).

Reactions that allow for selective C-O bond hydrogenolysis are central to biomass upgradation. This dissertation also reports hydrogenolysis of fatty acid over bimetallic rhenium oxide catalysts promoted by Pd. Such bimetallic catalysts allow for near-atmospheric pressure operations, contrary to commercial processes. The role of the constituent metals is elucidated here through DFT and multiple experimental probes including steady state and transient rate measurements, extensive characterization, and kinetic isotope effects. The results demonstrate a synergistic role of Pd and Re; while Pd directly provides hydrides (electrons) for C-H formation, Re catalyzes dehydration reactions by providing protons via Brønsted acid sites (ReOH). These results can be extended to over oxophilic metals to screen more selective, cheap and durable materials in the processing of fatty acids and other oxygenates.

The last part of this dissertation highlights the role of protic solvents in mediating reduction reactions of oxygenates. Reduction reactions are not only at the heart of biomass upgradation, but also are involved in a host of important applications such as organic and pharmaceutical synthesis. The use of greener solvents such as water, methanol or their mixtures instead of organic solvents is of critical importance from an environmental viewpoint. Here we combine DFT, kinetic isotope effects, flow reactor measurements, and in operando X-ray spectroscopy to show that protic solvents directly participate in hydrogenation reactions over transition metal surfaces. Protic solvents are shown to activate characteristically different routes that can enable transfer of hydrogens as protons

and electrons in proton coupled electron transfer (PCET) reactions that favor the formation of O-H bonds on oxygenates. In such reactions, solvent molecules react with co-adsorbed hydrogen atoms on the metal catalyst as well as enable proton-shuttling, while the metal catalyst is found to conduct electrons. In addition, we present evidence for the prevalence of heterogeneous mediator-based chemistry that governs reduction reactions when the protic solvent can decompose on the host catalyst. The structure and reactivity of these heterogeneous surface mediators are found to resemble well-known solution-phase mediators such as TEMPOH (in organic synthesis) and NADPH (in biology). These results demonstrate the ability to impact selectivity during hydrogenation of oxygenates and perhaps other unsaturated compounds by tuning the metal and the protic solvent.

Table of Contents

Acknowledgements	i
Abstract	iv
List of Figures	x
List of Tables	xviii
List of Schemes	xviii
Preface	1
1 A New Selective Route towards Benzoic Acid and Derivatives from Biomass-Derived Coumalic Acid	7
1.1 Conspectus.....	7
1.2 Introduction.....	8
1.3 Results and discussion.....	10
1.4 Conclusions.....	22
1.5 Experimental.....	23
1.6 Acknowledgements.....	25
1.7 Supporting information.....	26
2 Modulating Reactivity and Selectivity of 2-Pyrone-Derived Bicyclic Lactones through Choice of Catalyst and Solvent	39
2.1 Conspectus.....	39
2.2 Introduction.....	40
2.3 Results and Discussion.....	42
2.4 Conclusions.....	61
2.5 Methods and Materials.....	62
2.6 Acknowledgments.....	67
2.7 Supporting Information.....	68
3 Improving Selectivity of Toluic Acid from Biomass-Derived Coumalic Acid	85
3.1 Conspectus.....	85
3.2 Introduction.....	86
3.3 Results and Discussion.....	89
3.4 Conclusions.....	100
3.5 METHODS AND MATERIALS.....	101
3.6 Supplementary Information.....	104

4	Theoretical Insights into the Sites and Mechanisms for Base Catalyzed Esterification and Aldol Condensation Reactions over Cu.....	114
4.1	Conspectus	114
4.1	Introduction	115
4.2	Computational Methods.....	118
4.3	Results and Discussion	120
4.4	Conclusions.....	150
4.5	Acknowledgments	151
4.6	Supporting Information	152
5	Mechanistic Insights into the Hydrogenolysis of Fatty Acids over Supported Pd-ReO_x Catalysts	153
5.1	Introduction	153
5.2	Results and discussion.....	155
5.3	Concluding remarks	176
5.4	Computational methods.....	177
5.5	Supporting information	178
6	The Nature of Protic Solvents on Transition Metal Surfaces and Its Impact on Hydrogenation Reactivity	182
6.1	Introduction	182
6.2	Mechanistic insights into formaldehyde hydrogenation over Pd in water	184
6.3	Mechanistic insights into the hydrogenation of acetone over ruthenium and platinum.....	194
6.4	Concluding remarks	205
6.5	Computational methods.....	206
6.6	Experimental methods.....	207
6.7	Acknowledgements	208
6.8	Supporting information	209
7	Solvent Effects during Direct Synthesis of Hydrogen Peroxide over Palladium Catalysts.....	220
7.1	Introduction	220
7.2	Oxygen reduction reactions in methanol.....	221
7.3	Oxygen reduction reactions in water.....	237
7.4	Solvents control formation of PdH _x	241
7.5	Hydrogen peroxide formation in methanol vs water	243
7.6	Concluding remarks	245

7.7	Computational methodology	245
7.8	Supporting Information	247
8	Future Recommendations	249
9	References	251

List of Figures

- Figure 1.1. Plot of k_{obs} as a function of $[\text{D}_2\text{O}]$. Experimentally determined k_{obs} are represented as points and the line is a simulated fit to $k_{\text{obs}} = k_1 + k_2 \times [\text{D}_2\text{O}]^2$ where $k_1 = 1.03 \times 10^{-4} \text{ min}^{-1}$ and $k_2 = 1.51 \times 10^{-4} \text{ M}^{-2} \text{ min}^{-1}$ 16
- Figure 1.2 NMR trace of the Diels-Alder and decarboxylation reaction..... 18
- Figure 1.3 Network kinetic analysis of coumalic acid reaction with ethylene. (A) Diels-Alder reaction followed by thermal CO_2 extrusion. (B) Measured activation energy of the Diels-Alder reaction of CMA and ethylene in 1,4-dioxane at temperatures between 90-120 °C. (C) DFT-calculated reaction energy profile diagram for the CMA reaction with ethylene to the Diels-Alder adduct followed by decarboxylation to cyclohexa-1,5-diene carboxylic acid intermediate and CO_2 . (D) Measured activation energy of the thermal decarboxylation reaction of CMA-DAP in 1,4-dioxane at temperatures between 140-150 °C. 20
- Figure 1.4 Bicyclic lactone decarboxylation. (A) Bond length (Å) of the cycloadduct of CMA and ethylene. (B) The asynchronous thermal decarboxylation mechanism of the CMA/ethylene Diels-Alder adduct to cyclohexa-1,5-diene carboxylic acid. (C) Bond length (Å) of the transition state of the cycloadduct CO_2 extrusion towards the cyclohexa-1,5-diene carboxylic acid with a more advanced C-O bond cleavage. 21
- Figure 2.1(A) The individual Gibbs free energy changes for the elementary steps in the mechanism proposed in Scheme 2.3 (filled rectangles represent stationary states and unfilled rectangles represent transition states). (B) Decarboxylation reactant (1*), transition (≠) and product ((2)- CO_2^*) states 110 surface. (C) Decarboxylation reactant (1*), transition (≠) and product states ((2)- CO_2^*) on * on the 100 surface. (D) Concentration of (1) as a function of time: experiments vs the microkinetic model. (E) $\ln(k)$ vs time, where k is the intrinsic rate constant, k_2 , associated with the scission of the C-C bond and elimination of CO_2 47
- Figure 2.2 MAS ^1H solid-state NMR spectra of $\gamma\text{-Al}_2\text{O}_3$ impregnated with dioxane- d_8 solutions with different concentrations of (1). The sample is indicated next to each spectrum. (A-C) ^1H spin echo solid-state NMR spectra. (D) and (E) ^{27}Al filtered ^1H NMR spectra obtained from the positive projection of a 2D $^{27}\text{Al} \rightarrow ^1\text{H}$ D-RINEPT HETCOR spectra obtained with short and long dipolar recoupling times, respectively. (F) ^{13}C filtered ^1H NMR spectrum obtained from the positive projection of the 2D $^1\text{H}\{^{13}\text{C}\}$ HETCOR spectrum shown below. The ^{13}C chemical shifts expected for (1) are indicated with red dashed lines. The blue dashed lines illustrate the similarity of the solution and solid-state 51
- Figure 2.3(A) Reaction scheme of the proposed acid catalyzed ring-opening/dehydration reaction sequence. (B) Concentration profile of the conversion of bicyclic lactone (1) to (4) followed by conversion of (4) to (5). (S-1) and (S-2) are formed throughout the reaction and are of unknown origin..... 54
- Figure 2.4 Selectivity trend of intermediates and products from acid catalyzed ring-opening/dehydration of bicyclic lactone (1). 55
- Figure 2.5(A) DFT calculated enthalpy diagram for the bicyclic lactone decarboxylation reaction using polar protic and aprotic solvents. (B) Experimental Arrhenius plot for the water mediated catalyst-free decarboxylation of the bicyclic lactone sodium salt (1). (C) In situ ^1H -NMR concentration profile of the consumption of sodium salt of (1) and the formation of (2) as a function of time. (D) Bicyclic lactone diversification in the absence of catalyst using the polar protic solvents

water for decarboxylation and methanol for ring-opening. (E) DFT calculated enthalpy diagram for the methanol mediated ring-opening of (1). (F) Experimental Arrhenius plot for the methanol mediated catalyst-free ring-opening of (1). (G) In situ ¹H-NMR concentration profile of the consumption of (1) and the formation of (7) as a function of time. 57

Figure 2.6 Selected ¹H-NMR spectra of the bicyclic lactone (1) ring-opening in methanol-d₄. 59

Figure 3.1 NMR trace of the DA reaction products 2, 3, 4, and 5 after cycloaddition of MeCMA and propylene (left figure). NMR trace of the in-situ decarboxylation of bicyclic lactone intermediates 2, 3, 4, and 5 to 6 and 7 (right figure)..... 93

Figure 3.2(A) Reaction network of the Diels-Alder/decarboxylation reaction sequence of MeCMA 1 and propylene. (B) DFT calculated reaction energy profile diagram for the MeCMA reaction with propylene to bicyclic lactones 2, 3, 4, and 5 followed by decarboxylation to cyclohexa-1,5-diene carboxylate species 6 and 7. (C) Experimentally measured activation energies of the DA reaction of 1 with propylene to a single para species consisting of endo/exo isomers 2 and 3 and a single meta species consisting of endo/exo isomer 4 and 5. (D) Experimentally measured activation energies of the decarboxylation of the combined endo/exo para species (2+3) to 6 and endo/exo meta species (4+5) to 7. Endo/exo isomers 2, 3 and 4, 5 are combined to a single para and meta species to simplify the kinetic analysis and to obtain an average..... 96

Figure 3.3 Reactivity trend of MeCMA cycloaddition with electron donating and withdrawing dienophiles. □ Experimental p-/m- ratios, calculated FMO energy gap and ΔH_{act} values were obtained in the present study, whereas ΔH_{act} for ethylene was reported in a previous study (ref. 5). ◇ Experimental p-/m-ratio and calculated ΔH_{act} values were reported in literature,³⁰ whereas the FMO energy gap values were calculated in the present study. The p-/m- ratios are reported on the experimentally observed aromatic product except for ethyl vinyl ether and methyl propiolate. The p-/m- ratio of the reaction of MeCMA and ethyl vinyl ether is based on the cycloadduct and methyl propiolate is based on DFT.³⁰ 100

Figure 4.1 DFT-calculated pathways for the hydrogenation propanal to propanol and the reverse reaction involving the dehydrogenation of propanol to propanal and hydrogen. The propoxide path (shown with the unfilled rectangular symbols) involves the initial addition of hydrogen to the C₁ of the carbonyl to form the propoxide intermediate and the subsequent hydrogenation of the propoxide and the desorption of the propanol product. The hydroxypropyl path (shown with filled black rectangular symbols) proceeds instead by the initial addition of hydrogen to the O of the carbonyl to form the hydroxypropyl intermediate and subsequent addition of hydrogen to the C of the hydroxypropyl to form propanol which desorbs. 122

Figure 4.2.(A) The adsorption structure for propoxide bound to a 3-fold fcc site on the Cu (111) surface; (B) Charge density difference map between the adsorbed alkoxide and the alkoxide in the gas phase. The red isosurface depicts an increase of charge density whereas the blue isosurface reveals a decrease of charge density. 125

Figure 4.3 DFT-calculated reactant, transition and product states along with the intrinsic activation barriers and the overall reaction energies for elementary steps in the aldol condensation of adsorbed propoxide and propanal over Cu(111) to form the 3-hydroxy-2-methylpentanal and 2-formyl-3-pentanone intermediates. These include: A) activation of the weakly acidic C_α-H of propanal by a surface propoxide to form a surface enolate, B) enolate attack on the C=O bond of a neighboring propanal to form β-alkoxide alkanal, C) protonation of the β-alkoxide alkanal to form the aldol, and D) C-H activation of β-alkoxide alkanal to form 2-formyl-3-pentanone. 133

Figure 4.4 DFT-calculated reactant, transition and product states along with the intrinsic activation barriers and the overall reaction energies for elementary steps in the conversion of the dehydrogenated aldol intermediate, β -alkoxy-2-methyl pentanal, to 3-pentanone over Cu(111). The steps include: A) intermolecular hydride transfer from β -alkoxide alkanal to adsorbed propanal to form the 2-formyl-3-pentanone intermediate, B) C₁-H scission of the 2-formyl-3-pentanone to 2-acyl-3-pentanone, C) decarbonylation of 2-acyl-3-pentanone to form 3-penten-2-olate and CO and d) hydrogenation of 2-acyl-3-pentanone to form 3-pentanone. 135

Figure 4.5 DFT-calculated pathways for the aldol condensation reactions of propanol-propanal on Cu(111). A) The upper path (shown with black filled rectangular symbols) proceeds via the initial activation of the propyl to form an acyl intermediate which is high in energy. The middle path (shown with lighter filled oval symbols) proceeds via the coupling of the enolate and propanal followed by C₁-H activation by the Cu, whereas the lowest energy path (unfilled rectangular symbols) proceeds by the coupling of the enolate and propanal to form the β -alkoxide alkanal which subsequently hydrogenates to form the aldol. B) The two lowest energy paths shown here proceed via the coupling of the enolate and propanal to form the β -alkoxide alkanal which can: i) hydrogenate (shown with unfilled rectangular symbols) to form the aldol or ii) dehydrogenate via hydride transfer to an adsorbed propanal to form 2-formyl-3-pentanone (shown with filled black rectangular symbols). 137

Figure 4.6 DFT-computed pathways for the decarbonylation of 1-propoxy-1-propoxide intermediate to form 3-pentanone on Cu(111). Activation barriers for each step are shown larger font and in italic. 138

Figure 4.7 DFT-calculated reactant, transition state and product state structures and the corresponding activation barriers and overall reaction energies for different elementary steps in the esterification of propanal and propanol over Cu(111) surface to form propyl propionate. The steps include: A) the nucleophilic attack of the adsorbed propoxide on the adsorbed propanal (C-O bond formation), B) C₁-H activation by a surface Cu site, C) intermolecular hydride transfer from the C₁-H of the 1-propoxy-1-propoxide intermediate to a vicinal bound propanal, D) hydrogenation of the 1-propoxy-1-propoxide to form the 1-propoxy-1-propanol hemiacetal, and E) concerted S_N2-type nucleophilic attack of the adsorbed propoxide on the adsorbed propanal and C₁-H hydrogen elimination to Cu. 141

Figure 4.8 DFT-calculated reaction paths for the esterification of propanol-propanol on Cu(111). (A). The E₃ path (light unfilled symbols) which is highest energy proceeds via the C-H activation of propanal to form a surface acyl intermediate that subsequently couples with a bound propanal to form propyl propionate. The E_{1b} path (filled black symbols) which is lower in energy than the E₃ path, proceeds by the coupling of the alkoxide and the alkanal to form the 1-propoxy-1-propoxide hemiacetal intermediate that subsequently undergoes C₁-H activation over Cu to form propyl propionate. The lowest energy paths (E_{1a}, E_{1c} and E₂) are shown in (B). In the E_{1c} path (light unfilled rectangular symbols) the reaction proceeds via the coupling of the alkoxide and the alkanal followed by a hydrogen addition to the hemiacetal to form the hemiacetal product. The E_{1c} and E₃ paths are somewhat lower in energy than the E₃ path. The E_{1c} path which is shown with filled black rectangular symbols proceed via the coupling of propoxide and propanal to form the hemiacetal intermediate that subsequently reacts with a vicinal propanal to eliminate H to form the propyl propionate. The E₃ path proceeds via a concerted coupling of the surface propyl and propanal intermediates together with the C₁-H activation by Cu. 145

Figure 4.9 Formation rates versus propanal pressure for esterification (□) and aldol condensation (●) reactions from propanol-propanal-H₂ mixtures on 10 % wt. Cu/SiO₂ (5.5% dispersion) in left

axis. Aldol/ester ratio (\blacktriangle) vs propanal pressure in right axis. Reprinted with permission from Sad, M. E., Neurock, M., Iglesia, E. Formation of C–C and C–O Bonds and Oxygen Removal in Reactions of Alkanediols, Alkanols, and Alkanals on Copper Catalysts. *J. Am. Chem. Soc.* 2011, 133, 50, 20384-20398. Copyright 2011. American Chemical Society 147

Figure 4.10 A comparison between the energies for the elementary steps involved in aldol condensation and esterification reactions over Cu. The aldol condensation is shown in top curve denoted by dark filled rectangular symbols. Esterification can proceed either via the E_{1c} path involving sequential C-O formation and intermolecular hydride transfer which is shown in the light unfilled rectangular symbols or via the E_2 concerted C-O formation H-elimination path shown in the green elliptical symbols. 148

Figure 5.1 (A) Optimized structure for the 101 surface of anatase. (B) The optimized structure for single Re atom deposited on the 101 surface of anatase. The Re atom is seen to bond to 4 neighboring oxygen atoms, resulting in surface oxygen vacancies and unpaired electrons. (C) The optimized structure of the Re-substituted TiO_2 surface after adding an additional oxygen atom to pair electrons and surface oxygen vacancy in structure B. Re is now seen to bond with 5 oxygen atoms..... 155

Figure 5.2 Optimized structures showing the reactant, transition state, and product during heterolytic activation of H_2 over ReO_x 156

Figure 5.3 Optimized structures showing the reactant, transition state, and product during Brønsted acid catalyzed acyl formation and acyl hydrogenation over ReO_x 157

Figure 5.4 (A) Optimized structure showing a Pd_3 cluster next to ReO_x . (B) Optimized structure showing the Pd_3 cluster saturated with reactive intermediates- hydrogen atoms and carboxylate. 157

Figure 5.5 Reactant, transition state, and product structures during hydrogen spillover from Pd to ReO_x . The hydrogen atom that spills over is marked in orange. 158

Figure 5.6 Reactant, transition state, and product structures for: (A) the acid-catalyzed dehydration of the bound propionic acid to form the acyl intermediate and (B) the subsequent structures for the hydrogen addition to the C_1 carbon to form propionaldehyde in the acyl mechanism over $Pd-ReO_x/TiO_2$ 160

Figure 5.7 Reactant, transition state, and product structures for A) the hydrogen addition to the C_1 carbon of the bound propionic acid to form propane diol, and B) the acid-catalyzed dehydration of the diol intermediate to form propionaldehyde in the diol mechanism over $Pd-ReO_x/TiO_2$ 161

Figure 5.8 Optimized structures for reactant, transition state and product for the heterolytic dissociation of propionic acid to form the Pd-bound propionate and surface $ReOH$ intermediate on $Pd-ReO_x$ 162

Figure 5.9 The reaction energy diagram for the hydrogenation of propionic acid to 1-propanal over $Pd-ReO_x$. The energies are shown with respect to adsorbed bidentate propionate seen experimentally. The elementary steps shown here include: 1) an initial hydrogen adsorption on Pd, 2) carboxylic acid formation, 3) a second hydrogen adsorption, 4) diol formation and 5) Brønsted acid catalyzed dehydration. It is assumed that Brønsted acid sites are readily generated since the intrinsic activation barrier for spillover was found to be just 30 kJ/mol. 162

Figure 5.10 The reactant, transition state, and product structures for A) the initial addition of H to the O of propionaldehyde to form the hydroxypropyl intermediate, B) the subsequent addition of H to C₁ carbon of the hydroxypropyl intermediate to form propanal, C) the initial addition of H to the C₁ carbon of propionaldehyde to form the propoxide surface intermediate, and D) the subsequent hydrogen addition to the O of the propoxide surface intermediate to form propanol during hydrogenation of propionaldehyde over Pd-ReO_x/TiO₂. 167

Figure 5.11 The overall reaction energy diagram for hydrogenation of propionaldehyde over Pd-ReO_x (with respect to adsorbed propionate from Figure 5.9). The alkoxy route is shown in blue while the hydroxyalkyl route is shown in red. Since oxygen sites on ReO_x are assumed to be covered in protons due to rapid, favorable spillover, the energy of formation of the Brønsted acid site will not affect the apparent barriers and is not shown here. 168

Figure 5.12 The reactant, transition state, and product structures formed during hydrogenation of propionaldehyde over Pd(111) via A) and B) the hydroxyalkyl path and C) and D) the alkoxy path to form propanol. 169

Figure 5.13 Reaction energy diagram for hydrogenation of propionaldehyde over Pd-111. The alkoxy route is shown in blue, while the hydroxyalkyl route is shown in red. 170

Figure 5.14 Structures for elementary reactions for the hydrogenolysis of propionic acid to propionaldehyde over the Re(0001) surface covered with 5/8 ML of carboxylates, via the diol mechanism- (A) formation of propionic acid from the most abundant propionate intermediate, (B) diol formation from propionic acid, (C) C-OH activation of the diol to form propionaldehyde, (D) hydroxyl removal as water. 172

Figure 5.15 Structures for elementary reactions for the hydrogenolysis of propionic acid to propionaldehyde over the Re(0001) surface via the acyl mechanism- (A) formation of propionic acid from the most abundant propionate intermediate, (B) acyl formation from propionic acid, (C) acyl hydrogenation to form propionaldehyde, (D) hydroxyl removal as water. 173

Figure 5.16 Reaction energy diagram for hydrogenolysis of propionic acid to propionaldehyde over the Re(0001) surface via diol and acyl intermediate pathways. Energies are shown with respect to propionate intermediates that presumably exist on the surface at high coverage. Shown in blue is the diol mechanism, while the acyl mechanism is shown in red. 174

Figure 6.1 Reaction energy diagram for the vapor phase hydrogenation of formaldehyde to methanol via alkoxy and hydroxyalkyl routes. All of the structures are reported in Figures S 5.1 and S 5.2. Intrinsic activation barriers for both the hydrogenation steps in the kinetically faster hydroxyalkyl route are marked in grey. 186

Figure 6.2 DFT-calculated reactant (R), transition (TS), and product (P) state structures for the hydrogenation of formaldehyde to (A) hydroxymethyl and (B) methoxy formation over Pd(111) in water. The hydrogen that is added to formaldehyde is highlighted in yellow. (C) Reaction profile diagram for the metal-mediated hydrogenation of formaldehyde to methanol via alkoxy and hydroxymethyl routes in water. The intrinsic activation barriers on the kinetically faster hydroxyalkyl route are marked in grey. 188

Figure 6.3 Water-mediated pathway catalyzing the formation of hydroxymethyl from formaldehyde. (A) Reactant state consisting of adsorbed formaldehyde and hydrogen (marked with an orange circle). (B) Transition state for the formation of protons and electrons (the orange arrow shows the movement of hydrogen atom from the surface into the solution). (C) Intermediate state showing a

hydronium ion (highlighted in yellow) (D) Transfer of proton via shuttling (the path is highlighted in yellow) (E) Product state consisting of adsorbed hydroxymethyl group. 190

Figure 6.4 Water-mediated pathway catalyzing the formation of methanol from hydroxymethyl. (A) Reactant state consisting of adsorbed formaldehyde and hydrogen (marked with an orange circle). (B) Transition state for the formation of protons and electrons (the orange arrow shows the movement of hydrogen atom from the surface into the solution). (C) Intermediate state showing a hydronium ion (highlighted in yellow) (D) Transfer of proton via shuttling to adsorbed formaldehyde (the path is highlighted in yellow) (E) Product state consisting of adsorbed the methoxy group. 192

Figure 6.5 The impact of water on the kinetically faster hydroxymethyl route during hydrogenation of formaldehyde. Shown in dark blue is the gas-phase reaction and the corresponding barriers are marked in grey. Shown in red is the water-mediated pathway and the barriers are marked in light blue. Dotted curves show the formation of protons and electrons. O-H formation barrier is shown with respect to adsorbed CH_2O^* and H^* for the gas-phase and the solution-phase reaction. C-H formation barrier is shown with respect to CH_2OH^* and H^* for the gas-phase reaction and CH_2OH^* and H_3O^+ for the solution-phase reaction. 193

Figure 6.6 (A) Turnover frequency for acetone hydrogenation over Pt for different conditions in the vapor phase. Catalysts: 3% Pt/SiO₂ and 250mg Pt/SiO₂/2000mg $\alpha\text{-Al}_2\text{O}_3$. Reaction conditions: T = 80 °C, P = 1 atm, Feed: Acetone = 0.1 ml/min, H₂ = 80 cc/min. (B) Turn over frequency for acetone hydrogenation over Ru/C under different conditions in the vapor phase. Catalysts: 5% Ru/C and 200mg RuC/2000mg $\alpha\text{-Al}_2\text{O}_3$. Reaction conditions: T = 80 °C, P = 1 atm, Feed: Acetone = 0.2 ml/min, H₂ = 27 cc/min. 195

Figure 6.7 Reaction profile diagram for the vapor phase hydrogenation of acetone on Pt(111). Shown in red is the hydroxyalkyl pathway and shown in dark blue is the alkoxy pathway. The intrinsic activation barrier (with respect to CH_2OH^* and H^* as most abundant surface intermediates) is shown in grey for the hydroxyalkyl route and in light blue for the alkoxy route. The relevant structures are reported in the supporting information Figure S 6.11. 196

Figure 6.8 Reaction profile diagram for the vapor phase hydrogenation of acetone on Ru(001). Shown in red is the hydroxyalkyl pathway and shown in blue is the alkoxy pathway. The apparent activation barrier (with respect to CH_3O^* and H^* as most abundant surface intermediates) is shown in grey for the hydroxyalkyl route and in light blue for the alkoxy route. The relevant structures are reported in the supporting information Figure S 6.12. 197

Figure 6.9 Reaction energy diagram for the water-mediated hydrogenation of acetone on Pt-111. Dotted lines indicate formation of protons and electrons. Shown in red is the hydroxyalkyl pathway that undergoes initial O-H formation via PCET to form the hydroxyisopropyl intermediate, which subsequently undergoes a hydride attack from the metal surface forming isopropanol. The activation barrier for this mechanism is shown in grey. Shown in blue is the alkoxy pathway that undergoes initial C-H formation via hydride attack from the surface to form the isopropoxy intermediate, which undergoes a PCET reaction forming isopropanol. The activation barrier for this route is shown in light blue. Activation barriers shown here are with respect to lowest energy state consisting of hydroxyisopropyl intermediate on the surface and protons in the solution. 199

Figure 6.10 Structures for the water-mediated acetone hydrogenation on Pt(111) via the hydroxyalkyl route. (A1) Reactant state showing adsorbed acetone and hydrogen (marked by an orange circle). (A2) Transition state for the reaction between water and hydrogen to form a hydronium ion and an electron (the orange arrow shows the movement of hydrogen atom from the surface into the solution). (A3) Product state for hydronium complex in water (highlighted in yellow).

(A4) Transition state for proton and electron transfer to form the hydroxyisopropyl intermediate (the path highlighted in yellow). (A5) Product state for adsorbed hydroxyisopropyl. (B1) Reactant state showing adsorbed hydroxyisopropyl and hydrogen (marked in orange). (B2) Transition state for the formation of isopropanol from hydroxyisopropyl via hydride attack. (B3) Product state showing adsorbed isopropanol..... 200

Figure 6.11 Reaction profile diagrams for water mediated acetone hydrogenation over Ru-001. (A) Direct mediation of acetone hydrogenation via the PCET mechanism. Water molecules co-react with surface hydrogen atoms to form protons and electrons that are delivered to oxygen (dotted lines) on acetone and alkoxy intermediates. Shown in red is the hydroxyalkyl mechanism and the corresponding apparent barrier is marked in grey. Shown in blue is the alkoxy mechanism and the corresponding apparent barrier is marked in light blue. Barriers are shown with respect to the lowest energy state consisting of isopropoxy and hydrogen on the surface of Ru. (B) Energy diagram for the activation of kinetically faster alkoxy mechanism on Ru using Brønsted acid sites. The apparent barrier is marked in light blue. Dotted line shows the formation (regeneration) of Brønsted acids prior to hydrogenation via PCET..... 202

Figure 6.12 Structures for the water-mediated acetone hydrogenation on Ru(001) via the alkoxy route. (A1) Reactant state showing adsorbed acetone and hydrogen (marked in orange). (A2) Transition state for the formation of isopropoxy intermediate via hydride attack. (A3) Product state showing adsorbed isopropyl. (B1) Reactant state showing adsorbed isopropoxy and hydrogen (marked in orange). (B2) Transition state for the reaction between water and hydrogen to form hydronium and electrons (the orange arrow shows the movement of hydrogen atom from the surface into the solution). (B3) A structure along the reaction coordinate showing transfer of electrons and protons (highlighted in yellow) to isopropoxy (over Ru, an isolated hydronium was not captured by DFT). (B4) Product state showing adsorbed isopropanol. 203

Figure 6.13 Structures for Brønsted acid catalyzed hydrogenation of the isopropoxy intermediate on Ru to isopropanol. (A1) Reactant state for Brønsted acid site regeneration consisting of adsorbed H*(orange circle) and O*(red circle). (A2) Transition state for proton and electron formation ((the orange arrow shows the movement of hydrogen atom from the surface into the solution). (A3) A structure along the reaction coordinate showing transfer (highlighted in yellow) of electrons and protons to O* (over Ru, an isolated hydronium was not captured by DFT). (A4) Product state consisting of regenerated Brønsted acid site (red circle). (B1) Reactant state for hydrogenation of isopropoxy using a Brønsted acid site (red circle). (B2) Transition state for hydrogenation of isopropoxy using a Brønsted acid site. (B3) Product for hydrogenation of isopropoxy using a Brønsted acid site (red circle). 205

Figure 7.1 Transient H₂O₂ turnover rates (at 60 kPa H₂ and O₂) in pure methanol (black), pure water (red), and 70 % vol. methanol (blue). The rate in water reaches a steady value over time, while the rate in pure and 70 % vol. methanol exponentially decreases over time presumably via deposition of organic residue..... 222

Figure 7.2 Reaction energy diagram for methanol activation in condensed phase over Pd-111 surface covered with 1/3 monolayer of atomic oxygen and 1/3 monolayer of sub-surface hydride. 224

Figure 7.3 Methanol activation via the hydroxyalkyl pathway. (A) C-H activation on methanol to form the hydroxymethyl intermediate (B) O-H activation on the hydroxymethyl intermediate to form formaldehyde using the proton-coupled-electron transfer mechanism. The methoxonium ion (CH₃OH₂⁺) is highlighted in yellow, and hydrogen atom on the surface is marked in orange. 225

Figure 7.4 Methanol activation via the alkoxy pathway. (A) O-H activation on the methanol to form the methoxy intermediate using the proton-coupled-electron transfer mechanism. The methoxonium ion (CH_3OH_2^+) is highlighted in yellow. (B) C-H activation on methoxy to form formaldehyde. Hydrogen atom on the surface is marked in orange.	226
Figure 7.5 Optimized structures for CH_2OH^* catalyzed formation of (A) HOO^* and CH_2O^* , (B) HOOH^* and CH_2O^* , (C) HOH^* , O^* and CH_2O^*	227
Figure 7.6 Energetics for formaldehyde formation using different routes. Shown in blue is the conventional route examined directly over Pd sites. Shown in red is the MPV mechanism forming HOOH^* and CH_2O^* (Scheme 7.2(B)). Shown in green is the MPV mechanism forming HOH^* , O^* and CH_2O^* (Scheme 7.2(C)).....	228
Figure 7.7 Structures for hydrogenation of oxygen to hydrogen peroxide with the Langmuir-Hinshelwood surface mediated mechanism (A1 and A2) and proton coupled electron transfer using a methanol molecule (B1 and B2).....	230
Figure 7.8 Bader charge analysis of the reaction coordinate for hydrogen transfer between (A) CH_2OH^* and O_2^* (B) CH_2OH^* and HOO^*	231
Figure 7.9 Structures of (A1) NADPH (A2) NADP (B1) TEMPOH (B2) TEMPO.	232
Figure 7.10 H_2O_2 (blue) and H_2O (black) formation rates as function of H_2 pressure (5-1000 kPa) in (a) methanol and (b) water at 60 kPa O_2 . Complementary EXAFS spectra were conducted in operando at comparable H_2 and O_2 pressures in both (c) methanol and (d) water. All measurements were performed on silica-supported Pd catalysts (278 K, $35 \text{ cm}^3 \text{ min}^{-1}$ solvent).....	234
Figure 7.11 H_2O_2 concentration as a function of time in DI water in the presence and absence of formaldehyde.	236
Figure 7.12 HOO^* formation pathway via (A) Surface-mediated route (B) Proton-coupled-electron-transfer route; B1 shows proton/electron generation, while B2 shows proton/electron transfer to O_2^* . Surface conditions of $1/3 \text{ O}^* \text{ ML}$ and $1/3 \text{ H}^* \text{ s}$ were simulated. Surface hydrogen atom that is transferred is marked in orange. Hydronium ion is highlighted in yellow.....	238
Figure 7.13 HOOH^* formation pathway via (A) Surface-mediated route (B) Proton-coupled-electron-transfer route; B1 shows proton/electron generation, while B2 shows proton/electron transfer to HO_2^* . Surface conditions of $1/3 \text{ O}^* \text{ ML}$ and $1/3 \text{ H}^* \text{ s}$ were simulated. Surface hydrogen atom that is transferred is marked in orange. Hydronium ion is highlighted in yellow.	240
Figure 7.14 Structures and energies for the HOO^* decomposition pathway ($\text{H}^* + \text{HOO}^* \rightarrow \text{H}_2\text{O} + \text{O}^*$) using the proton couple electron transfer route at surface coverage of $1/3 \text{ ML O}^*$ and $1/3 \text{ ML H}^* \text{ s}$. The surface hydrogen is marked in orange. The surface O^* in the product state is marked in green.	241
Figure 7.15 Hydride formation Reactant state (R) and Product state (P) structures for (1) $5/9 \text{ ML of O}^*$ (2) $1/3 \text{ ML of O}^*$ (3) $4/9 \text{ ML of CH}_2\text{OH}^*$ (4) $1/3 \text{ ML of CH}_2\text{OH}^*$ (5) $1/3 \text{ ML of O}^*$ and $2/9 \text{ ML of CH}_2\text{OH}^*$	242
Figure 7.16 Reaction profile diagram for H_2O_2 formation in methanol over Pd at surface coverage of O^* of $1/3 \text{ ML}$ and $\text{H}^* \text{ s}$ of $2/3 \text{ ML}$	243

Figure 7.17 Reaction profile diagram for H ₂ O ₂ formation in water over Pd at surface coverage of O* of 1/3 ML and H*s of 2/3 ML.	244
Figure 7.18 Rate and selectivity of hydrogen peroxide synthesis in mixtures of methanol and water.....	244

List of Tables

Table 1.1 Conversion of CMA/MeCMA with ethylene to BA/MeBA.	11
Table 1.2 Degradation of CMA and MeCMA in 1,4-dioxane.....	14
Table 2.1 Bicyclic lactone (1) conversion in the presence of Lewis acids	43
Table 2.2 Bicyclic lactone (1) conversion in the presence of Brønsted acids.....	53
Table 2.3 CMA conversion to benzoic acid.....	59
Table 3.1 Conversion of CMA/MeCMA with propylene to TA/MeTA.	90
Table 4.1 Charge density differences on the oxygen of the alkoxide and alcohol before and after adsorption on the Cu(111) surface. ^a	126
<i>Table 4.2 Summary of the charge accumulated on O atom for adsorbed HO* and CH₃O* groups bound to different transition metal (111) surfaces.</i>	127
Table 4.3 DFT calculated gas phase deprotonation energies and charges on different H atoms in propanal.	128
<i>Table 4.4 Reaction and Activation energies of C-H bond activation for propanal and propanol.</i>	129
Table 4.5 Reaction and activation energies for the □C ₂ -H bond activation of propanal with different RO* species on Cu(111).	130
Table 4.6 The apparent rate constants and activation energies for the E ₁ ,E ₂ and E ₃ esterification paths.....	144
<i>Table 4.7 Comparison of the activation enthalpies, entropies and free energies for the condensation and esterification of propanal and propoxide species on the Cu (111) surface.....</i>	146
Table 5.1 Change in the adsorption energy of hydrogen gas (0.5H ₂ + * → H*) at different coverage of hydrogen and carboxylate over Pd (ML = monolayer).....	158
Table 5.2 Value of constants that appear in microkinetic analysis (Equations 5.2-5.6). The temperature dependent contributions are based on the energy diagram presented in Figure 5.9.	164
Table 5.3 Kinetic isotope effect contributions 400 K and 1 atm for individual steps that appear in Equation 5.6. Overall kinetic isotope effect for 1 st order in H ₂ can be estimated by evaluated the product K1HK1D . K2HK2D . k3H k3D.	165

Table 5.4 DFT-calculated values for the constants that appear in microkinetic analysis (Equation 5.7). The temperature dependent contributions are based on the energy diagram presented in Figure 5.16.	175
Table 5.5 Kinetic isotope effect contributions at 400 K and 1 atm for individual steps that appear in Equation 5.7. Overall kinetic isotope effect for 1 st order in H ₂ can be estimated by evaluated the product K1HK1D . K2HK2D . k3H k3D.	176
Table 6.1 . Partial charges on the structures during hydrogenation of formaldehyde to form the hydroxymethyl intermediate via the proton coupled electron transfer pathway.	190
Table 7.1 Dehydrogenation energies of different mediators.	231
Table 7.2 Influence of the dissolved hydride on dehydrogenation energy of CH ₂ OH* intermediate on Pd. The surface coverage of O* is kept constant at 1/3 monolayer.	232
<i>Table 7.3 Influence of the dissolve hydrogen sublayer on the energetics of HOO* and HOOH* formation in methanol as solvent (surface coverage of O* was constant at 1/3 ML),</i>	<i>233</i>
<i>Table 7.4 Activation barriers and reaction energies for HOO* decomposition HOO* + CH₂OH* → HOH* + O* at different concentrations of the dissolved hydrogen sublayer.</i>	<i>233</i>
Table 7.5 Influence of the dissolve hydrogen sublayer on the energetics of HOO* and HOOH* formation in water as solvent (surface coverage of O* was constant at 1/3 ML).	240
Table 7.6 Influence of catalyst structure the decomposition of HOO* in water as solvent via the proton-coupled-electron-transfer route	241
Table 7.7 Subsurface hydrogen formation energy at different surface conditions	242

List of Schemes

Scheme 1 Diels-Alder/Decarboxylation/Dehydrogenation domino sequence yielding aromatics from Coumalic acid.	2
Scheme 1.1 The formation of benzoic acid starting from glucose fermentation to malic acid using acid catalysed dimerization to coumalic acid followed by a Diels-Alder/decarboxylation/dehydrogenation reaction sequence to yield the desired aromatics.	9
Scheme 1.2 Network for the reaction of CMA/MeCMA with ethylene.	13
Scheme 1.3 General degradation of coumalic acid in the absence and presence of water.	16
Scheme 1.4 CMA breakdown mechanism to 2-butenal in the presence of water (Units in kJ/mol).	17
Scheme 2.1 Diels-Alder conversion of 2-pyrones to form bicyclic lactones followed by decarboxylation to dihydrobenzenes.	41
Scheme 2.2 γ -Al ₂ O ₃ catalyzed decarboxylation.	42

Scheme 2.3 Proposed elementary steps and mechanism for the decarboxylation of (1)	48
Scheme 3.1 The formation of toluic acid starting from glucose fermentation to malic acid using acid catalysed dimerization to coumalic acid followed by a Diels-Alder/decarboxylation/dehydrogenation reaction sequence to yield the desired aromatics.....	89
Scheme 3.2 The reaction cascade from CMA (or MeCMA) to 2 (para exo), 3 (para endo), 4 (meta exo) and 5 (meta endo) to 6 (para) and 7 (meta) to 8 (para) and 9 (endo) (R = H, CH ₃).....	90
Scheme 3.3 Hydrogenation of 6(para) and 7(meta) to 10 (para) and 11(meta) with R = H, CH ₃ ..	91
Scheme 4.1 Reaction paths for the conversion of propanol/propanal/H ₂ over Cu/SiO ₂ , Reprinted with permission from Sad, M. E., Neurock, M., Iglesia, E. Formation of C–C and C–O Bonds and Oxygen Removal in Reactions of Alkanediols, Alkanols, and Alkanals on Copper Catalysts. J. Am. Chem. Soc. 2011, 133, 50, 20384-20398. Copyright 2011. American Chemical Society. Selectivities for six major products are given based on the following conditions: 5 wt.% Cu/SiO ₂ , 5.6% dispersion, 503 K, 2160 g cat.-ks (mol propanol) ⁻¹ , 0.64 kPa propanol, 80 kPa H ₂ , balance He, 3% conversion.	117
<i>Scheme 4.2 Routes for the dehydrogenation of propanol to form propanal.</i>	121
Scheme 4.3 Mechanism of base-catalyzed A) aldol condensation and B) esterification.	124
Scheme 4.4 Illustration of the electron-withdrawing inductive effect of the hydroxyl group in propanol. The amount of charge relative to the original charge of C: $\delta^{+++} > \delta^{++} > \delta^{+}$. The arrow shows the direction the charges flows.	129
Scheme 4.5 Possible reaction pathways following aldol condensation.	132
Scheme 4.6 Three possible reaction paths for the esterification paths involving C-O bond formation via the coupling of propanal and propoxide intermediates over Cu. E ₁ paths proceed by sequential C-O formation followed by hydrogen addition (E _{1a}) or hydrogen elimination via Cu (E _{1b}) or via an adsorbed alkanal (E _{1c}). The E ₂ path follows simultaneous C-O formation and H-elimination. The E ₃ proceeds via the initial activation of the propoxide to form an acyl intermediate.	140
Scheme 5.1 Reaction scheme showing the diol and acyl pathways on Pd-ReO _x . Activation barriers shown here are intrinsic barriers and are calculated below.	159
<i>Scheme 5.2 Elementary steps leading to alcohol production from carboxylic acids over Pd-ReO_x catalysts.</i>	163
Scheme 5.3 Hydrogenation of propionaldehyde via the alkoxy and hydroxyalkyl route over Pd-ReO _x . C-H formation reactions are catalyzed by hydride transfer from Pd, while O-H formation reactions are catalyzed by the Brønsted acid site Re-OH. The reported intrinsic activation barriers for each step are calculated and discussed below.	166
Scheme 5.4 The hydrogenation of propionaldehyde via the alkoxy and hydroxyalkyl route over Pd(111) to form 1-propanol. The activation barriers are intrinsic and are calculated in Figure 5.12 below.	169
Scheme 5.5 Elementary steps for the hydrogenolysis of carboxylic acids over Re catalysts to form corresponding aldehyde and water. Sites marked by (*) are active sites on the surface of Re	

accessible to only hydrogen atoms due their relatively small van der Waals radii. Sites marked by (**) are active sites on the surface of Re where all intermediates except hydrogen atoms are adsorbed or chemisorbed. The inclusion of different types of sites allow for modeling of coverage effects, which are typically not captured in single site Langmuir-Hinshelwood microkinetics. 175

Scheme 6.1 Pathways during hydrogenation of C=O bonds, the hydroxyalkyl pathway involves initial O-H formation followed by C-H formation, and the alkoxy pathway involves initial C-H formation followed by O-H formation. 185

Scheme 6.2 Hydrogenation of formaldehyde to hydroxymethyl via the PCET pathway. 189

Scheme 7.1 Methanol activation on Pd surface via alkoxy and hydroxyalkyl pathways. 224

Scheme 7.2 MPV type bimolecular routes leading to activation of hydroxymethyl (CH_2OH^*) to (A) CH_2O^* and HOO^* (B) CH_2O^* and HOOH^* (C) CH_2O^* , HOH and O^* . The arrow shows movement of hydrogen from CH_2OH^* to the reacting substrate..... 226

Scheme 7.3 Formation of hydrogen peroxide via surface-mediated mechanism (A1 and A2) and via proton-coupled electron transfer (B1 and B2). 229

Scheme 7.4 Proposed mechanism for oxygen reduction over Pd in methanol. Hydrogens shown in red are utilized in O-H formation reactions consistent with KIE measurements..... 237

Scheme 7.5 Hydrogenation of dioxygen to hydrogen peroxide in water via Langmuir-Hinshelwood surface mediated mechanism (A1) and (A2) and via proton-coupled-electron-transfer mechanism (B1) and (B2)..... 237

Preface

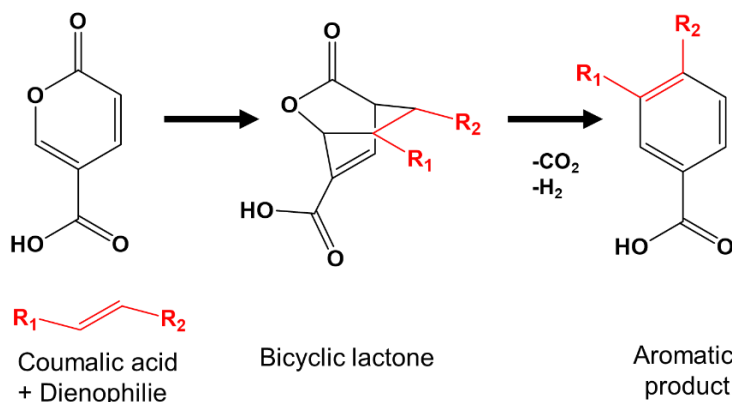
The ever-increasing demand for chemicals and fossil-fuels, together with the non-replenishable nature of petroleum feedstocks necessitates investigation of alternative, renewable feedstocks for sustainable and green manufacturing of everyday-chemicals and fuels. Further, green-house emissions due to fossil-fuel consumption have been on the rise, raising significant environmental concerns, thereby encouraging the use of cleaner sources of energy. In recent times, the potential of biomass as a sustainable source of both carbon and energy has become evident through many studies that demonstrate alternative routes to access many chemicals and fuels of interest.¹⁻⁵ Consequently, experts predict that about 20 % of transportation fuel and 25 % of chemicals could be biomass-based by 2030.¹

The petrochemical industry benefits from the use of price-advantaged feedstocks, as a result, biomass-based *drop-in* products may not be able to directly outcompete petrochemical products. However, the recent shale gas revolution has evidently led to a shortage of several building blocks including propylene, butadiene, and aromatics (BTX),^{6,7} motivating efforts to synthesize these chemicals from biomass. Propylene has been synthesized from bio-isopropanol and bio-n-propanol via dehydration,⁸ from propane (produced by glycerol hydrodeoxygenation),⁹ as well as via bio-methanol to propylene technologies.^{10,11} Butadiene, similarly, has been accessed via dehydration of bio-n-butanol and bio-1,4-butanediol.¹² Many different ways to access aromatics have been reported including thermochemical fast-pyrolysis;¹³⁻¹⁵ formic acid mediated deoxygenation of glucose-based quinic and shikimic acid;¹⁶ Diels-Alder chemistry on furans,¹⁷⁻²⁵ 2-pyrones,²⁶⁻³¹ isoprene,^{32,33} trans-trans muconic acid,^{34,35} and sorbic acid.^{36,37} These studies demonstrate versatility of biomass in accessing different petrochemical building blocks via combined fermentation and chemo-catalytic technologies.

While the petrochemical industry also benefits from decades of process engineering and optimization, its highly established infrastructure ultimately discourages manufacturing of newer products within the petrochemical industry. Biomass, on the other hand, as an emerging feedstock, could offer ample opportunities for the manufacturing of new products, thereby, catering to the new market needs of next-generation consumer goods, pharmaceuticals, specialty chemicals, and materials.³⁸ For economic sustenance and competitive manufacturing, biorefineries need platform chemicals that demonstrate

molecular and chemical flexibility allowing for the production of not only petrochemical building blocks, but also a host of new structures inaccessible via petroleum that can be used in next-generation applications. This has driven efforts into the identification of bio-privileged structures that allow for facile generation of a library of compounds including drop-in replacements and novel structures.

The discovery and diversification of bio-privileged molecules has been at the core mission of the NSF Engineering Center for Biorenewable Chemicals (CBiRC) that the author of this dissertation was a part of. The center has extensively worked on the diversification of 2-pyrone and has found success with two molecules and their derivatives- triacetic acid lactone (TAL) and Coumalic acid (CMA). TAL can be biologically synthesized from glucose³⁹ and can be converted to important drop-in replacements⁴⁰ such as acetyl acetone, 1-pentene, sorbic acid, substituted pentanones as well as high value compounds such as pogostone, styrenylpyrones, 4-amino-2-pyrines and 4-hydroxy-2-pyridones.^{41–43} CMA, on the other hand, can provide access to a range of aromatics via Diels-Alder/elimination chemistry in a one-pot reaction. Glucose fermentation can yield malic acid, which can be subsequently dimerized to CMA.²⁶ CMA can then undergo a Diels-Alder/elimination domino sequence to yield desired aromatics as depicted in Scheme 1. Scheme 1 shows the molecular flexibility of CMA and its esters in the synthesis of aromatics; by tuning the dienophile, different drop-in compounds as well as novel structures can be synthesized in an atom-efficient and possibly one-pot synthesis.



Scheme 1 *Diels-Alder/Decarboxylation/Dehydrogenation domino sequence yielding aromatics from Coumalic acid.*

Previous efforts by the Kraus group have demonstrated the utility of this sequence in the synthesis of terephthalic acid,²⁷ carbazoles,⁴⁴ alkyl benzoates as well as more complex

aromatics.²⁶ In this dissertation, we seek to understand the elementary steps that drive these reactions as well as catalyze these reactions, if necessary to improve the overall process yield and reactivity. **Chapters 1-3** of this document are standalone published manuscripts highlighting our efforts in systematically engineering diversification of CMA.

Chapter 1 highlights a scalable, selective route (> 95% at ~100% conversions) in the synthesis of benzoic acid, a large-scale commodity chemical. We study the formation of benzoic acid or methyl benzoate from CMA or methyl coumalate (MeCMA) respectively in a sequence that involves Diels-Alder-decarboxylation-dehydration domino sequence carried out in different solvents over supported Pd/C catalysts. Reaction steps are elucidated using a combination of in-situ NMR and density functional theory (DFT) calculations with an intention to identify the rate-limiting step. We find that the rate limiting step involves decarboxylation of the bicyclic lactone that forms in the initial Diels-Alder reactions (see Scheme 1). In addition, we explore the underlying mechanism for CMA degradation in different solvents that is essentially found to be mediated by water impurity in these solvents, suggesting the use of dry solvents when performing these transformations.

Chapter 2 highlights our efforts in accelerating the rate-limiting decarboxylation of bicyclic lactone using heterogeneous Lewis-acid catalysts and solvents. All the tested heterogeneous Lewis acid catalysts were found to be active in catalyzing decarboxylation of bicyclic lactone, γ -alumina in particular, was found to be very active and selective. DFT and solid-state NMR results revealed that only weakly Lewis acidic penta-coordinate Al sites were active for decarboxylation consistent with observed selectivity, while the more Lewis acidic sites were blocked by OH groups due to “wetness” of alumina surfaces. Solvent-mediated decarboxylation resulted in unexpected results, while polar protic solvent such as water was able to lower the activation barrier for decarboxylation, methanol, instead resulted in a nucleophilic ring opening of bicyclic lactone revealing a new route to access isophthalate intermediates. Methanol assisted ring-opening further motivated testing of ring opening reactions using Brønsted acids providing access to isophthalic acid. These studies demonstrated the influence of different catalysts- Lewis vs Brønsted, different solvents- protic vs aprotic in activating different reactions on bicyclic lactone molecules, providing access to a range of different compounds.

Chapter 3 is focused on utilizing more complex dienophiles and the regiochemical implications that follow. Methods to improving overall selectivity to aromatics as well as regioselectivity to a desired stereoisomer are discussed. Overall selectivity can be improved by the use of MeCMA instead of CMA. Regio-selectivity is found to be a function of the electronics of the Diels-Alder reaction and can be influenced to obtain higher para-substituted aromatic through the use of electron rich dienophiles.

With biorefineries presumably making profit via high-demand building blocks as well as new high-value products, break-even manufacturing of biomass-derived fuels could be a reality. Besides, the growing environmental concerns may encourage subsidies on the manufacturing of biofuels, which will further positively impact the cost of manufacturing. A critical strategy in the synthesis of fuels from biomass is the formation of C-C bonds to control the molecular weight as well as complete deoxygenation of fuel precursors.⁴⁵

Chapters 4 and 5 highlight our efforts at aldol condensation and hydrogenolysis reactions, which can be used to form C-C bonds and cleave C-O bonds respectively.

Chapter 4 is a published manuscript dealing with aldol condensation over metallic Cu and aims at understanding the nature of active sites and the mechanism that lead to C-C formation. Previous experimental results show that 1,3-propanediol readily equilibrates on metallic Cu to form a mixture of H₂-propanol-propanal, that undergoes C-C formation at long residence time.⁴⁶ In addition to the condensation reaction, esterification was also observed. While the condensation products can be used as fuel precursors, ester can directly be used as fuel additives.⁴⁷⁻⁴⁹ Our studies demonstrate the unique role of Cu that allows for in-situ generation of Lewis basic propoxide sites and Lewis acidic propanal sites that co-operatively result C-C and C-O bond formation reactions respectively.

Chapter 5 presents results on hydrogenolysis of fatty acid, which can be extended to other oxygenates. Selective C-O bond hydrogenolysis is an atom efficient, green process that activates C-O bonds with the help of hydrogen gas, thereby, preserving C-C bonds and forming water as a byproduct. Hydrogenolysis over commercial catalysts such as CuO/CuCr₂O₄ not only require high H₂ pressures, but these processes are environmentally undesirable due to the use of Cr.⁵⁰ Heterogeneous bimetallic catalysts consisting of a reducible metal such as Pd and Pt in conjunction with oxophilic metals such as Re have been successful at carrying out these reactions at much lower H₂ pressures. However, the mechanistic studies on the nature of active sites and reaction mechanisms are still very

speculative and the role of the individual constituent metals remains unexplored. Here we report a combination of DFT, steady-state and transient flow reactor measurements, steady-state kinetic isotope effects to elucidate the reaction mechanism and the involvement of both the metals in driving hydrogenolysis of propanoic acid. We show that hydrogenolysis proceeds via initial C-H formation reaction on adsorbed propanoic acid to form a diol intermediate. The hydride that is required for this step comes from metallic Pd sites adjacent to ReO_x sites, where the carboxylic acid is adsorbed. Further, dehydration of the diol intermediate happens on Brønsted acid sites on ReO_x . DFT simulations show that ReO_x sites cannot independently carry out hydrogenolysis since Brønsted acid sites cannot catalyze C-H formation reactions. Such reactions more readily happen with hydride when Pd is present in close proximity.

Reduction reactions are at the heart of biomass upgradation, organic and pharmaceutical synthesis. Due to the polar nature of bio-derived reactive substrates, these reactions are typically carried out in the liquid phase in the presence of protic solvents such as water. Methanol or mixtures of methanol-water are also preferred greener solvents over many commonly used organic solvents.⁵¹ **Chapters 6-7** highlight the use of protic solvents in hydrogenation reactions over reducible transition metal surfaces, specifically how these solvents considerably change the reaction mechanisms where they act as co-catalysts and co-reactants.

Chapter 6 covers hydrogenation of C=O bonds in the presence of water over common hydrogenation catalysts- Palladium, Platinum, and Ruthenium. The results suggest that water over these metals can react with co-adsorbed hydrogen atoms to form protons and electrons that then catalyze O-H formation reactions similar to proton coupled electron transfer reactions that drive enzymatic and organic transformations.⁵²⁻⁵⁷ These solution-mediated pathways are kinetically faster than direct hydride transfer from the catalyst surface to oxygen. C-H formation, on the other hand, is found to be faster when catalyzed by direct hydride transfer from the metal surface, instead of the solution-mediated route. Further, generation of protons and electron from surface hydrides tends to affect the energetics of C-H formation reactions. For instance, over Pd and Pt, where hydrogen is more stable as proton in the solution than as hydride on the surface, C-H formation apparent activation barriers are referenced with respect to protons in the solution since proton and electron formation may be quasi-equilibrated. This results in activation barriers that are similar across the gas phase and the condensed phase. C-H formation reactions,

therefore, may not benefit kinetically by the presence of protic solvents. The results demonstrate that protic solvents may not always promote hydrogenation rates and the choice of solvent must also consider 1) metal-adsorbate interactions, that dictate whether the rate-determining step involves C-H or O-H formation and 2) electron affinity of the metal and proton solvation energy of the protic solvent that dictate the ease of formation of electrons and protons respectively.

Chapter 7 extends mechanistic framework described in chapter 6 to selective production of hydrogen peroxide, directly from hydrogen and oxygen gas over supported Pd catalysts. Using DFT simulations and multiple experimental probes, new insights into the role of alcoholic solvents and water during oxygen reduction reactions are presented. In water, oxygen reduction happens in the same manner as C=O bond hydrogenation via proton coupled electron transfer mechanism that is enabled by water molecules. Water molecules promote heterolytic activation of Pd-H bonds, generating protons and electrons that are delivered to oxygen via solvent molecules and the metal respectively. Methanol on the other hand, decomposes on the surface to form hydroxymethyl intermediates. These hydroxymethyl intermediates mediate formation of O-H bonds by transferring protons and electrons to oxygen, similar to mediator-based reactions reported in biology and organic synthesis.⁵⁸⁻⁶² Although the mechanism in both water and methanol involves proton coupled electron transfer, activation barriers are much lower in methanol consistent with high turnover numbers in methanol. Methanol, however, leads to catalyst deactivation over time due to condensation of decomposed products. Mixtures of methanol and water are found to slow down catalyst deactivation as well as result in high rate and selectivity. The results demonstrate the involved role these solvents play at an atomic level that activates distinct mechanisms enabling control over rate and selectivity during hydrogen peroxide synthesis.

1 A New Selective Route towards Benzoic Acid and Derivatives from Biomass-Derived Coumalic Acid

Adapted from Pfennig, T., Carraher, J. M., Chemburkar, A., Johnson, R. L., Anderson, A. T., Tessonnier, J-P., Neurock, M., Shanks, B. H. *A New Selective Route towards Benzoic Acid and Derivatives from Biomass-Derived Coumalic Acid*. *Green Chem.* **2017**, 19, 4879-4888. Reproduced by permission of The Royal Society of Chemistry.

DFT calculations were performed by AC under the supervision of MN.

1.1 Conspectus

The selective production of aromatics from bio-based sources is an area of interest to expand the potential for greener alternatives to petroleum-derived chemicals. A scalable, efficient route to produce bio-based benzoates is demonstrated in up to 100 mol% yield by carrying out heterogeneous catalytic reactions in non-toxic bio-based solvents at 180 °C. This approach extends the 2-pyrone (coumalic acid/methyl coumalate) Diels-Alder platform by utilizing a bioavailable co-reactant ethylene. A detailed investigation using a combination of kinetic experiments, DFT calculations, and multi-dimensional NMR was carried out to determine the detailed reaction network, and corresponding activation energies for critical steps. Additionally, a series of experiments were conducted to maximize yields by comparing different solvents, for both coumalic acid and methyl coumalate. Our results show that the choice of solvent was a significant factor when coumalic acid was the reactant (yields 71-92 mol%), while methyl coumalate was only minimally affected by the solvent (yields 95-100 mol%). Interestingly, the reaction network and kinetic analysis showed that the Diels-Alder reactions were not significantly different between coumalic acid and methyl coumalate, with the rate limiting step for both being decarboxylation with an activation barrier of 141 kJ/mol compared to 77 kJ/mol for the formation of the bicyclic adduct. Lastly, the reaction cascade was found to be highly susceptible to by-product formation when as little as 5 vol% water was present in the solvent, which demonstrates that the absence of water is essential for high yielding benzoate production.

1.2 Introduction

The search for alternatives to fossil-based feedstocks has led to rapid technological advances in the field of bio-renewable chemicals creating many potential opportunities for materials based on renewable carbon sources.^{16,63–67} Technologies to produce aromatics from biomass-derived sources have become targets of interest due to the expansion of shale gas extraction, which has led to a relatively reduced availability of >C4 building blocks, including aromatics.^{16,20,67} Aromatics are among the most important building blocks used by the chemical industry for the production of a wide array of products, so there is an incentive for the development of selective processes to produce aromatics from bio-based feedstocks.^{16,67,20}

Benzoic acid (BA) is a large scale commodity chemical with an annual production of 638 kt⁶⁸ currently produced by the partial oxidation of toluene using a cobalt-manganese catalyst. BA is used in a wide variety of applications including plasticizers, preservatives, dyes/perfumes and as a feed to produce other chemicals including phenol, caprolactam, and benzaldehyde. Hence, a renewable pathway to produce BA would have broad ranging impacts throughout the chemical value chain.

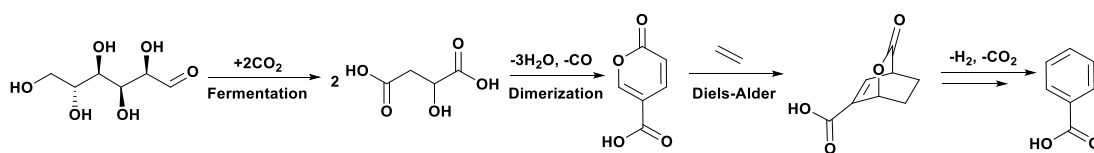
One route to make bio-based BA is through a formic acid mediated dehydration of quinic or shikimic acid produced via fermentation. This process has several desirable features including high yields for the chemical transformation of quinic and shikimic acids into benzoic acid (up to 90%)¹⁶ and high titers up to 60 g/L for quinic acid and 71 g/L shikimic acid starting from the substrate glucose and using *metabolically engineered E. coli*.^{69,70} Although, the primary drawback of this approach is the intrinsically low maximum theoretical yield of the shikimic/quinic acid fermentation of 43 %, and to date the highest yields reported correspond to an overall mol/mol yield of 23, and 27 %.⁷⁰ This fermentation bottleneck creates a significant problem for efficient utilization of the glucose feedstock. As a major fraction of the total cost of the fermentation step is the glucose feedstock, its inefficient utilization would have a significant negative impact on the cost required to produce BA.

An alternative pathway to bio-based BA and its methyl ester (MeBA) is through a furanic based platform utilizing a Diels-Alder reaction sequence of furan with methyl acrylate (or acrylic acid) showing moderate yields up to 51 mol%.²⁰ Additionally Diels-Alder reactions

of methyl furan with ethylene provides a viable pathway to produce bio-based toluene, which could be utilized as a drop-in replacement for production of BA. Toluene selectivities, however, never exceeded 46 mol% due to by-product formation.²¹ Improvement to this selectivity would require approaches to improve the stability of the bio-based starting materials thereby minimizing by-product formation.

Another approach utilizing biological and chemical catalysis to produce partially biomass-derived methyl benzoate (MeBA) is based on the bio-based cyclic lactone methyl coumalate (MeCMA). The formation of bio-based MeBA is accomplished using a one-pot Diels-Alder/decarboxylation/dehydrogenation reaction sequence between MeCMA and butyl vinyl ether with excellent yields up to 89 mol%.²⁶

Bio-based 2-pyrone coumalic acid (CMA) can be produced by the fermentation of glucose to form malic acid^{71,72} followed by acid catalyzed dimerization of malic acid to coumalic acid (Scheme 1.1).²⁶ The synthesis of 2-pyrone coumalic acid (CMA) via this route has several attractive features. First, the atom efficiency of the malic acid fermentation is highly favorable, with the capability to even utilize a CO₂ fixing pathway allowing for a theoretical yield of 2 moles of malate per mole of glucose (Scheme 1.1).⁷² Second, efficient fermentation technology is already developed for this route. For example, Novozymes currently uses a metabolically engineered *Aspergillus oryzae* capable of producing 1.38 mol malate per mol glucose at a theoretical yield of 69 % and with high titers of 154 g/L, which could be implemented on an industrial scale.⁷¹



Scheme 1.1 The formation of benzoic acid starting from glucose fermentation to malic acid using acid catalysed dimerization to coumalic acid followed by a Diels-Alder/decarboxylation/dehydrogenation reaction sequence to yield the desired aromatics.

An approach to improve the viability of the 2-pyrone CMA/MeCMA platform is to utilize a less expensive dienophile as the co-reactant. In theory ethylene should work in an analogous fashion as butyl vinyl ether, but at a substantially lower cost with nearly perfect atom efficiency. Additionally, as the production of ethylene from bio-ethanol is commercially demonstrated, a potential exists for 100 % bio-based process.⁶⁴

As part of the development of new biomass-derived and renewable processes, we report herein report on the synthesis of BA or MeBA from CMA or MeCMA, respectively, and ethylene with very high yields of >91 mol-% utilizing a one-pot sequential Diels-Alder/decarboxylation/dehydrogenation reaction path. Considering the industrial importance of renewable BA, and the lack of available comprehensive information about this alternative route in the literature, the focus of this work is to provide detailed information of the reaction network, and intrinsic kinetics of individual reaction steps, which can be used to improve the overall process.

1.3 Results and discussion

1.3.1 The formation of benzoic acid from coumalic acid

Experiments were conducted to examine the BA and MeBA yields obtained in several solvents using either CMA or MeCMA, respectfully. The reaction between CMA and ethylene in a nonpolar solvent, toluene, resulted in 71 mol% yield of BA at 100 mol% CMA conversion (Table 1.1, Entry 1). This outcome was similar to reported yields (76 %) for the Diels-Alder reaction of CMA with propylene in toluene,^{31,73} which was thought to be due to CMA being sparingly soluble in toluene leading to a substantial amount of CMA being converted to unidentified by-products. Therefore, a solvent was used to increase the solubility of CMA in order to improve the overall reaction yield. We have previously shown that γ -valerolactone (GVL) is a good polar aprotic solvent for this reaction system due to structural similarities.³¹ The use of GVL resulted in only a slightly higher BA yield of 76 mol% (Table 1.1, Entry 2 and Figure S 1.1). Still, a considerable amount (~24 mol%) of the initial CMA was lost to by-product formation. Results from previous studies suggested that CMA stability was limited in GVL under reaction conditions due to the presence of residual water in GVL.³¹ This hypothesis was tested by using the polar aprotic solvents, 1,4-dioxane or acetone, resulting in a significant improvement in the BA yield (Table 1.1, Entry 3 and 7). The reaction profile of the CMA consumption over time is displayed in Figure S 1.2. At 100 mol% CMA conversion the BA selectivity was 91 mol% after a 4 hr reaction at 180 °C for both solvents. From UPLC-PDA/QDa analysis, it was evident that small amounts of (4) and (6) (see Scheme 1.2) were present. Additionally, the formation of (4) was verified with NMR analysis showing that roughly 6 mol% of (4) was formed (Table 1.1, Entry 3). At this reaction temperature, the dehydrogenation reaction was extremely rapid as evident from the lack of an observable amount of the diene intermediate

(3). This result was consistent with previous studies³¹ in which we have shown that the dehydrogenation of the diene species proceeded significantly faster than the decarboxylation of the bicyclic intermediate, thereby suggesting that the decarboxylation of the cycloadduct was the limiting step in the reaction network.³¹ Kinetic studies and DFT calculations corroborate that decarboxylation is the rate limiting step, which will be discussed in the subsequent sections.

Table 1.1 Conversion of CMA/MeCMA with ethylene to BA/MeBA.

Entry	Reactant	Solvent	Conv.		Selectivity		
			(1) [mol%]	(5) [mol%]	(3) [mol%]	(4) [mol%]	(6) [mol%]
1	CMA	Toluene	100	71	[a]	[a]	[a]
2	CMA	GVL	100	76	[a]	[a]	[a]
3	CMA	1,4-Dioxane	100	91±1.5	[a]	5.8 [d]	[a]
4	MeCMA	Toluene	100	100±2	[b]	[b]	7±2 [c]
5	MeCMA	GVL	100	99±1	[b]	[b]	2±10 [c]
6	MeCMA	1,4-Dioxane	100	95±1	2±7 [c]	2±3 [c]	5±8 [c]
7	CMA	Acetone	100	91	[a]	[a]	[a]

Reaction conditions: Temperature: 180 °C; reaction time: 4 h, starting concentration: 10 mg ml⁻¹ MeCMA/CMA (1) in 1,4-dioxane, reaction volume: 30 ml, pressure: 500 psig ethylene, agitation: 400 rpm, Pd/C catalyst: 100 mg, [a] unable to quantify by-products with UPLC-PDA/QDa, [b] by-products not detected with GC-FID/MS, [c] cyclohexadiene (3) and cyclohexene (6) intermediates were quantified based on methyl benzoate (5) as reference due to the similar FID response factor. Double Diels-Alder by-product (4) was approximated using methyl benzoate (5) as reference material, [d] quantified via ¹H-NMR.

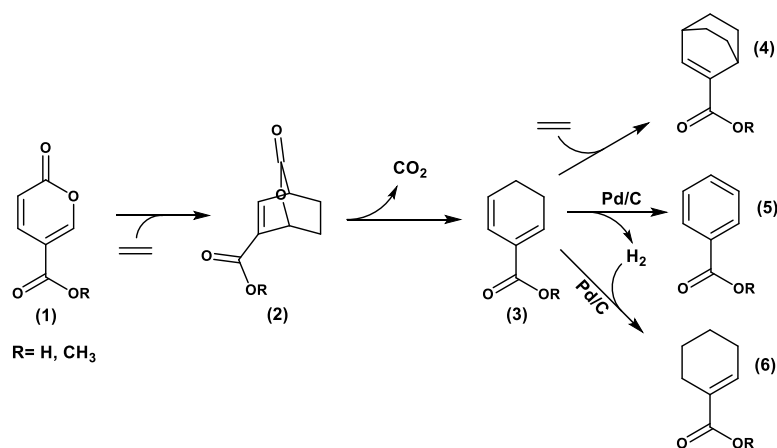
Literature reports suggest that changing the functional group on the starting substrate could significantly influence the stability and reactivity towards Diels-Alder reactions.^{19,37,73} This effect was demonstrated by Pacheco et al. using furanic dienes showing different product selectivities when various oxidized versions of HMF were reacted with ethylene, which was purported to be the outcome of different functionalities of the oxygenated furans.¹⁹ Furthermore, Bérard et al. observed that the reaction of sorbic acid with ethylene resulted in only low conversion (3 %), while using the ethyl ester of sorbic acid instead, afforded a ~5 fold increase in conversion (14 %).³⁷ A similar phenomena was also observed with 2-pyrones showing improved yields when reacting MeCMA instead of CMA with propylene.⁷³

Therefore, reactions were also run using MeCMA as the reactant to determine if starting with the methyl ester of CMA (MeCMA) would alter the reaction. Interestingly, the reaction in toluene showed tremendous improvement in yield with 100 mol% selectivity after complete conversion (Table 1.1, Entry 4 and Figure S 1.3). The higher selectivity with MeCMA was also consistent with the hypothesis of the importance of the solubility of the starting substrate in the 2-pyrone conversion. Similarly, when the polar aprotic solvent GVL was used to mediate the MeCMA and ethylene reaction, a conversion of 100 mol% with nearly 100 mol% MeBA selectivity (Table 1.1, Entry 5 and Figure S 1.4) was achieved. As the CMA conversion in GVL only resulted in a selectivity of 76 mol% (Table 1.1, Entry 2 and Figure S 1.1), the esterification of the carboxylate moiety likely played a significant role in improving the selectivity. Since CMA conversion to BA achieved the highest selectivity in 1,4-dioxane, we also performed the MeCMA conversion in 1,4-dioxane. As shown in Table 1.1, Entry 6 reported only a slightly better product selectivity (95 mol%) compared to CMA (91 mol%). GC-MS analysis suggested that the remaining five percent was attributed to the unreacted methyl cyclohexa-1,5-diene carboxylate intermediate (3), the formation of methyl cyclohex-1-ene carboxylate (6), and the double Diels-Alder (DDA) by-product (4), which was believed to be the outcome of a consecutive Diels-Alder reaction of (3) with ethylene (Scheme 1.2). The concentration profile of (1), (2), (3), (4), (5) and (6) over time is displayed in Figure S17. The formation of (2), (3), and (6) were validated via 2D-NMR COSY and HSQC experiments (see Figure S 1.1-S 1.11) and will be explained in detail in the following section.

1.3.2 Elucidating the reaction network

To elucidate where by-product formation was occurring, experiments were performed to determine the reaction network. Given the extensive work on Diels-Alder reactions of 2-pyrones^{26, 27-30,74-80} a reaction network was postulated, which is depicted in (Scheme 1.2). The reaction of CMA/MeCMA with ethylene follows a series of reactions that include Diels-Alder adduct formation (2), decarboxylation of the adduct to yield (3) and a Pd/C catalysed dehydrogenation reaction to form the desired aromatics (5). In the presence of the Pd/C catalyst additional minor products (4) and (6) were observed (Table 1.1, Entry 6). The formation of (6) is likely the result of a Pd catalysed hydrogenation of (3). The hydrogen needed for this step was likely formed through dehydrogenation of (3) to (5). Data shown in Figure S 1.5 support the proposed reaction network which is evident via the clear trend

showing how the conversion of (1) resulted in the formation of intermediates (2) and (3) and small amounts (<8 mol%) of (4) and (6) while (5) was formed. Structural identification of the intermediates (2), (3) and by-products (4) were determined by performing 1D and 2D NMR experiments of the reaction products from the MeCMA reaction with ethylene in the absence of catalyst to examine the Diels-Alder/decarboxylation sequence (see Figure S 1.6-S 1.16 and Table S 1.1-S 1.3). These analyses confirmed the formation of (2), (3) and (4). Without the catalyst, the by-product (6) was not observed. Therefore, it appeared that the formation of (6) was only realized when there was formation of hydrogen from dehydrogenation of (4) to (5). Similar observations were made when CMA was used as the starting substrate.



Scheme 1.2 Network for the reaction of CMA/MeCMA with ethylene.

1.3.3 2-Pyrone degradation studies

Loss in selectivity due to MeCMA and CMA degradation was examined. These reactions were performed in the absence of ethylene or catalyst and the results are given in Table 1.2 and Figures S 1.17-S 1.18. The results are consistent with a previous study³¹ showing that CMA stability is compromised in GVL as 25 mol% of the starting material is degraded after 8 h at 180 °C (Table 1.2, Entry 1). Identical tests in 1,4-dioxane showed that both CMA and MeCMA were significantly more stable with only 3 mol% of MeCMA and 10 mol% of CMA being converted (Table 1.2, Entry 3 and 4). This observation demonstrated that not only the solvent, but also the state of the starting substrate (acid vs ester) impacts the stability of the 2-pyrone. Given the observed selectivity loss (Table 1.1, Entry 2, 3 and

6) it appears that CMA breakdown occurs concomitantly while forming (2), thus, impacting the global yield of the desired aromatic product.

In a previous study, it was shown that the presence of small amounts of water accelerated CMA degradation.³¹ A similar water mediated breakdown was observed by Chia et al. when the 2-pyrone, triacetic acid lactone (TAL), was exposed to water and heat.⁸¹ They report that TAL undergoes ring-opening in the presence of water but is stable in aprotic polar solvents. To determine if the esterified 2-pyrone was more resistant to breakdown due to water, MeCMA stability experiments were also performed in 1,4-dioxane with 5 vol% of water. (Table 1.2, Entry 6). These results show that esterification did little to prevent breakdown in the presence of water, since both CMA and MeCMA were entirely consumed. Based on these observations, it is evident that the presence of water in the solvent has to be minimized to maximize yields of the Diels-Alder reaction products.

Table 1.2 Degradation of CMA and MeCMA in 1,4-dioxane.

Entry	Reactant	Solvent	CMA Conv. (mol-%)
1	CMA	GVL	25 ¹⁶
2	CMA	GVL + 5 vol% water	100 ¹⁶
3	CMA	1,4-dioxane	10
4	MeCMA	1,4-dioxane	3
5	CMA	1,4-dioxane + 5 vol% water	100
6	MeCMA	1,4-dioxane + 5 vol% water	100

Reaction conditions: Temperature: 180 °C, reaction time: 8 h, starting concentration: 10 mg ml⁻¹ MeCMA/CMA (1) in 1,4-dioxane, reaction volume: 30 ml, pressure: 500 psig N₂, agitation: 400 rpm.

Overall, GVL is an environmentally friendly renewable solvent with many positive characteristics such as low toxicity and biodegradability⁸²⁻⁸⁴ and, as such, is a desirable solvent for the conversion of MeCMA to MeBA. However, when BA formation was targeted, the effect of GVL on CMA stability was not as high since 25 mol% of the starting material was lost most likely through a concomitant degradation pathway (Table 1.1, Entry 2). Moreover, the high boiling point of GVL would make the product separation difficult. As

such, a low boiling bio-based acetone solvent could be utilized for increased BA selectivity of 91 mol% and would be an environmentally-advantaged substitute.

1.3.4 Reaction kinetics of water mediated coumalic acid breakdown

The reaction kinetics and products from the water-mediated breakdown of CMA were determined using NMR analysis with deuterated dioxane- d_8 . Dioxane, an aprotic polar solvent, was chosen as the ideal model system due to minimal by-product formation and CMA/MeCMA degradation. Moreover, fully deuterated dioxane- d_8 was commercially available allowing the kinetic studies to be performed in a closed system (high pressure NMR tube from Wildmad-Labglass), which simplified the product identification and quantification without further sample workup.

Different D_2O concentration (1-5 vol%) were added to the reaction mixture to identify the CMA breakdown dependence with respect to the water concentration. The main product identified via 1H NMR after a 6.4 h reaction at 171 °C with 3 vol% D_2O was 2-butenal yielding 14.5 mol% at 25.3 mol% conversion (Figure S 1.19). Minimal 2-butenal was observed with 1 vol% D_2O and virtually none with 0 vol% D_2O . The rate constant for the CMA breakdown reaction, was obtained from initial conversion data (no more than 20 mol% conversion). For each D_2O concentration experiment, a pseudo-first order reaction in CMA was fit to the data. The changes with respect to water in this regime were considered negligible as the reactions were carried out in excess D_2O (e.g. $[D_2O]$ was about 4 times $[CMA]_0$ at 1 vol% D_2O). Fits of $\ln([CMA]_t/[CMA]_0)$ vs time were linear and the observed rate constant (k_{obs}) was obtained from the slope. Interestingly, the plot of the pseudo-first order rate constants k_{obs} as a function of $[D_2O]$ revealed a second order dependence on $[D_2O]$ with an independent degradation pathway when no D_2O was added (Figure 1.1). Therefore, an overall rate law for CMA degradation was expressed as:

$$r_{CMA} = -k_{obs}[CMA] = -(k_1 + k_2 [D_2O]^2)[CMA] \quad (1.1)$$

The degradation of coumalic acid with and without the presence of water can be captured by the paths shown in Scheme 1.3. Further insights into the steps and mechanisms responsible for the degradation of CMA to 2-butenal were established by carrying out density functional theory calculations (Scheme 1.4). The results suggest that water-initiated degradation of CMA proceeds via a nucleophilic attack of water on the double bonds in CMA. The intermediate formed (1a) subsequently undergoes ring-opening via

keto-enol tautomerization to form a keto intermediate (1b). The presence of water molecules facilitates this ring-opening by providing a hydrogen bonding network to enable rapid proton shuttling and a low energy paths for keto-enol tautomerization and ring-opening. The intermediate (1b) has two carboxylic groups, which can then undergo decarboxylation yielding 2-butenal. This is very similar to a previously reported mechanism for water catalysed ring-opening and decarboxylation of triacetic acid lactone.⁸¹

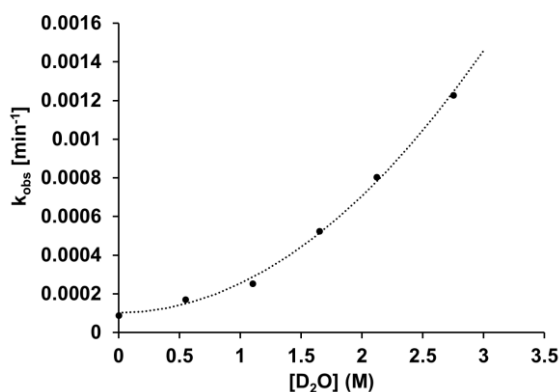
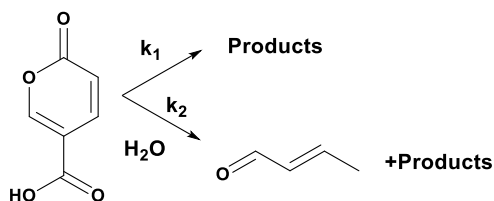


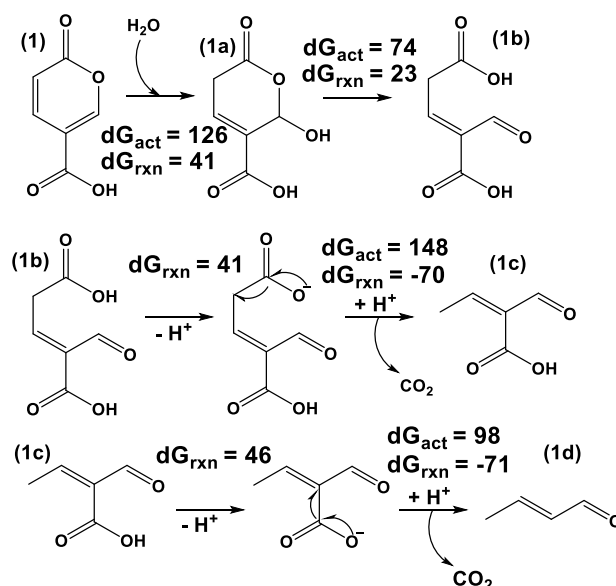
Figure 1.1. Plot of k_{obs} as a function of $[D_2O]$. Experimentally determined k_{obs} are represented as points and the line is a simulated fit to $k_{obs} = k_1 + k_2 \times [D_2O]^2$ where $k_1 = 1.03 \times 10^{-4} \text{ min}^{-1}$ and $k_2 = 1.51 \times 10^{-4} \text{ M}^2 \text{ min}^{-1}$.



Scheme 1.3 General degradation of coumalic acid in the absence and presence of water.

To further validate whether CMA breakdown is solely responsible for the observed selectivity loss (Table 1.1, Entry 2, 3 and 6) or is a result of by-product formation on the pathway to BA, the rate constants of CMA breakdown and CMA Diels-Alder addition with ethylene were compared. Based on the rate constants provided in Figure 1.1 and calculated from the Diels-Alder reaction step (Table S 1.4), it is evident that the CMA degradation proceeds significantly slower (>100 times) than the Diels-Alder addition step. Therefore, the observed loss in product selectivity less likely originates from 2-pyrone breakdown as opposed to by-product formation from intermediates on the pathway to BA. This was further supported by DFT calculations which predicted that the Gibbs free energy

of activation barrier for water addition (126 kJ/mol) was ~15 kJ/mol higher than ethylene addition (111 kJ/mol). The increase in the barrier is likely due to hydrogen bonding stabilization of the reactant by water. Moreover, the Gibbs free energy of reaction for ethylene addition (-79 kJ/mol) was calculated to be much more exothermic than that for water addition (41 kJ/mol) suggesting that the Diels-Alder adduct is thermodynamically favoured over CMA decomposition. Therefore, it appears that the selectivity loss of 24 mol% originates from intermediates (2) or (3) on the pathway to BA when reacting CMA with ethylene in GVL (Table 1.1, Entry 2).



Scheme 1.4 CMA breakdown mechanism to 2-butenal in the presence of water (Units in kJ/mol).

Given that reactions performed in dry polar aprotic solvents resulted in selectivities >90 mol% (with <10 mol% known by-products (4) and (6)), it appears that residual water in GVL is responsible for the selectivity loss likely from intermediate (2) or (3). To test this hypothesis, reactions of (2) were performed *in situ* (NMR tubes) in dioxane-*d*8 at 180 °C for 4 h in the presence of 5 vol% D₂O and without a catalyst. The results from these experiments suggest that species in the ¹H-NMR spectra are primarily attributed to unidentified by-products that originate from either (2) or (3) on pathway to (5) when water is present. From this observation, it is clearly critical to avoid water in the system to maximize product yield by minimizing by-product formation from the reactive intermediates.

1.3.5 Reaction kinetics in the absence of catalyst

Kinetic measurements were performed in 1,4-dioxane which is an excellent model solvent for detailed kinetic analyses as it has a low boiling point, results in minimal by-product formation during reaction and is readily available commercially in the fully deuterated dioxane-*d*8 form to perform complementary *in situ* NMR analysis. Choosing a solvent with a low boiling point (compared to GVL) was critical for isolation, identification and quantification (via NMR) of the temperature sensitive reactant CMA (1) and intermediates (2) and (3) for both the Diels-Alder and decarboxylation reactions. Fully resolved spectra of the formation of (2) and (3) are depicted in Figure 1.2 showing that the peak assignments and the method of quantification via NMR was unambiguous with carbon balances of >96 mol%.

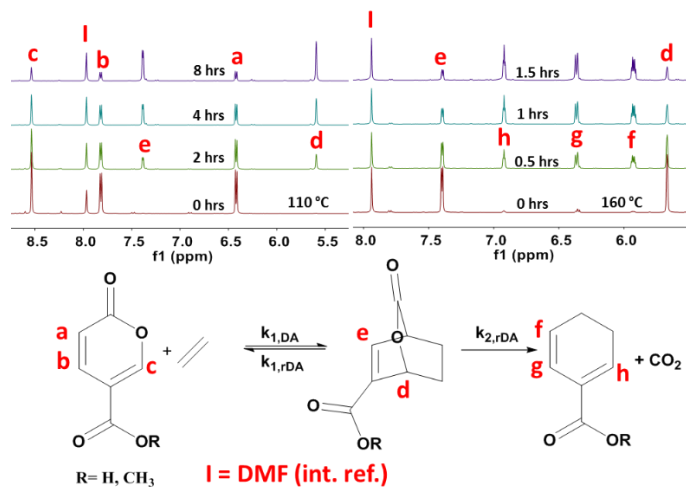


Figure 1.2 NMR trace of the Diels-Alder and decarboxylation reaction.

1.3.5.1 Diels-Alder reaction step

The activation barrier associated with the formation of the Diels-Alder (DA) adduct (2) was investigated by comparing the rate of consumption of CMA at temperatures ranging from 90-120 °C. Under these conditions, the cycloadduct was formed in high yields without breakdown of CMA simplifying the examination of the kinetics of this single step. The net rate of cycloadduct formation can be written as the forward rate of cycloaddition formation via Diels Alder reaction between CMA and ethylene minus the rate of the back reaction involving the retro Diels-Alder (rDA) of the cycloadduct. Assuming both of these reactions

are elementary, the net rate can be written as that in equation 1.2. This equation can be simplified (Equation 1.3) based on the experimental conditions since ethylene was in ~10x excess, which was validated by plots of $\ln([CMA]_t/[CMA]_0)$ versus time all giving linear relationships (Figure S 1.20 and S 1.21 (MeCMA)). The experimental results and spectra (Figure 1.2) suggested that the rDA reaction had only a minimal contribution as (2) can be obtained with yields of 98 mol%, which further showed that $k_{1,DA} \gg k_{1,rDA}$ and justified the simplification of equation (3) into (4). DFT calculations also fully support this since ethylene addition is predicted to be highly exothermic (-127 kJ/mol).

$$-r_{CMA} = k_{1,DA}[CMA][Ethylene] - k_{1,rDA}[DAP] \quad (1.2)$$

$$-r_{CMA} = k'_{1,DA}[CMA] - k_{1,rDA}[DAP] \quad (1.3)$$

$$-r_{CMA} = k'_{1,DA}[CMA] \quad (1.4)$$

The observed rate constants at temperatures in the range of 90-120 °C are given in Table S 1.4. The activation energy (E_A) for the Diels-Alder reaction of CMA (or MeCMA) (depicted in Figure 1.3(A)) was calculated based on the slope of the Arrhenius plot shown in Figure 1.3(B) and Figure S 1.21. The reaction of CMA and MeCMA with ethylene, resulted in a similar activation barrier of 77 kJ/mol. The experimental values were compared to the DFT-calculated barriers, which showed excellent agreement as the calculated enthalpic activation barriers were 67 and 68 kJ/mol, respectively. Therefore, the functionality (acid or ester) had negligible influence on the 2-pyrone reactivity (Table S 1.4). Literature reports for the cycloaddition of CMA derivatives and dienophiles with donating or withdrawing substituents report activation barriers that range from 28⁸⁵ to 118³⁰ kJ/mol when using butyl vinyl ether or methyl acrylate, respectively. Given the nature of an inverse electron demand Diels-Alder cycloaddition, dienophiles with higher electron density from donating substituents should react more readily than dienophiles with electron withdrawing substituents.^{85,86} With an activation barrier of 77 kJ/mol, the reaction of CMA (MeCMA) and ethylene showed that the unactivated dienophile resulted in intermediate Diels-Alder reactivity.

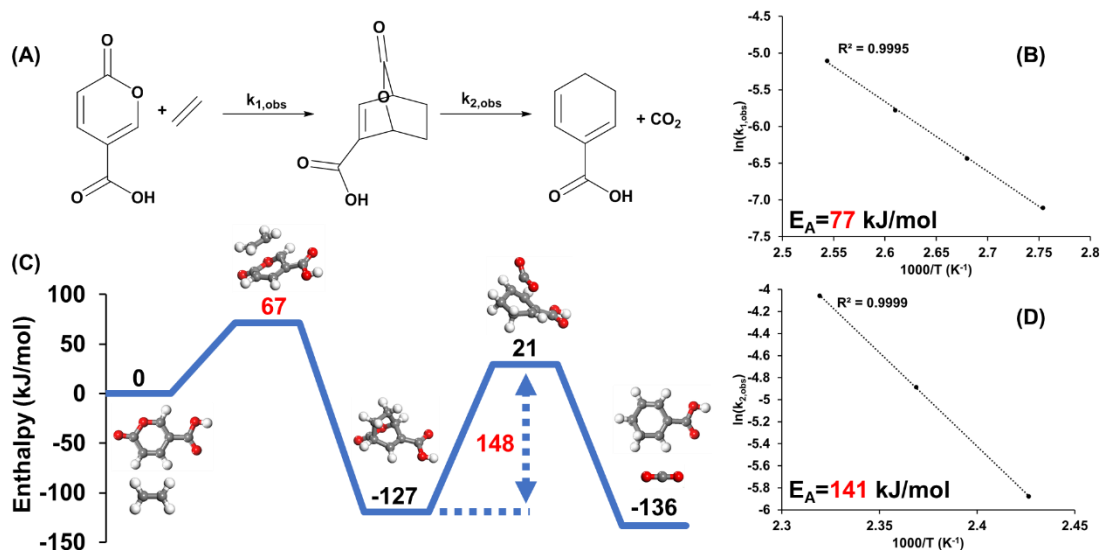


Figure 1.3 Network kinetic analysis of coumalic acid reaction with ethylene. (A) Diels-Alder reaction followed by thermal CO₂ extrusion. (B) Measured activation energy of the Diels-Alder reaction of CMA and ethylene in 1,4-dioxane at temperatures between 90-120 °C. (C) DFT-calculated reaction energy profile diagram for the CMA reaction with ethylene to the Diels-Alder adduct followed by decarboxylation to cyclohexa-1,5-diene carboxylic acid intermediate and CO₂. (D) Measured activation energy of the thermal decarboxylation reaction of CMA-DAP in 1,4-dioxane at temperatures between 140-150 °C.

1.3.6 Decarboxylation reaction step

Examination of the bicyclic lactone (DAP) intermediate decarboxylation was carried out at temperatures ranging from 140-160 °C. The reactant, intermediate (2), was prepared using a 16 h reaction at 110 °C in 1,4-dioxane, which yielded almost pure DAP (2) with only trace amounts of intermediate (3) and unreacted (1). Decarboxylation reactions were performed using high pressure Wilmad-Labglass NMR tubes. The synthesized DAP (2) was dissolved in dioxane-*d*8 within the tubes and the decarboxylation reactions as a function of time was measured via NMR (Figure 1.2). The rate law for the decarboxylation step was assumed to follow unimolecular first order kinetics (Equation 1.5).

$$-r_{DAP} = k_{2,rDA}[DAP] \quad (1.5)$$

During the decarboxylation reactions, no accumulation of CMA (or MeCMA) was observed at any of the temperatures tested, which provided additional support that $k_{1,DA} \gg k_{1,rDA}$ and helped to validate the assumption that the equilibrium between CMA (or MeCMA) and

DAP (2) was strongly shifted towards DAP formation. Plots of $\ln([DAP]_t/[DAP]_0)$ vs time resulted in linear trends for all temperatures tested (Figure S 1.22-23).

The activation barriers for the decarboxylation of CMA/MeCMA-derived (2) (142/133 kJ/mol) were calculated based on the slope of the Arrhenius plots (Figure 1.3(D) and Figure S 1.22) using the observed rate constants (Table S 1.5). DFT calculations predicted an enthalpic activation barrier of 148 kJ/mol for both bicyclic lactones (CMA-DAP and MeCMA-DAP) as shown in Figure 1.3(C). The DFT barriers agree well with those from experiment. Abdullahi et al. reported that the decarboxylation of the bicyclic lactone formed from ethyl coumalate and butyl vinyl ether also result in a high activation barrier of 111 kJ/mol which is also in close agreement with the DFT results that give a CO₂ extrusion barrier of 120 kJ/mol.⁸⁷ By comparing these results with our experimental activation energy, it is evident that the decarboxylation step is significantly influenced by the degree of functionalization of the bicyclic lactone intermediate. DFT energy mapping calculations (Figure 1.4) further suggested a mechanism where the CO₂-bridge leaves in an asynchronous fashion with a significantly elongated C-O bond in the transition state. As such, the C-O bond cleavage occurs prior to C-C bond cleavage, which is in agreement with observations from the literature.⁸⁷

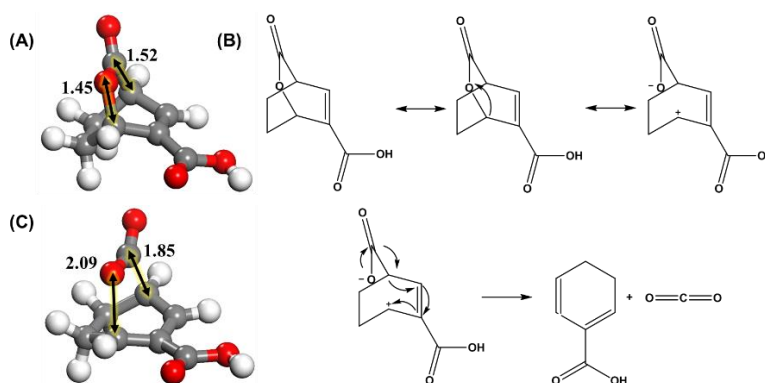


Figure 1.4 Bicyclic lactone decarboxylation. (A) Bond length (Å) of the cycloadduct of CMA and ethylene. (B) The asynchronous thermal decarboxylation mechanism of the CMA/ethylene Diels-Alder adduct to cyclohexa-1,5-diene carboxylic acid. (C) Bond length (Å) of the transition state of the cycloadduct CO₂ extrusion towards the cyclohexa-1,5-diene carboxylic acid with a more advanced C-O bond cleavage.

From this analysis we conclude that the rate-limiting step in this reaction network is the decarboxylation reaction of (2). We observed that all reactions run with catalyst led to only

minimal accumulation of (3), suggesting that the rate of (3) dehydrogenation is much more rapid than the rate of (3) formation. These results provide critical insight for what should be targeted to further enhance the overall process. Clearly, finding a catalyst to reduce the activation barrier of the rate-limiting decarboxylation would allow for this reaction to be carried out under milder reaction conditions, which would improve overall yields by reducing the extent to which by-products were formed.

1.4 Conclusions

In this work, we have shown that the Diels-Alder chemistry between CMA (or MeCMA) and ethylene can yield high conversion and selectivity towards BA (or MeBA), which provides a renewable alternative to current benzoate production. We were able to effectively elucidate the reaction network and revealed kinetic information such as activation energies for the Diels-Alder and the decarboxylation step. Although CMA stability studies revealed two independent break down pathways as a function of water concentration resulting in 2-butenal as the main by-product, the CMA decomposition rate was significantly slower than the Diels-Alder cycloaddition indicating that CMA stability is not a contributing factor. Instead, we have shown that the selectivity loss is a result of the formation of (4) and (6) and that in the presence of water intermediates on the pathway to BA led to by-product generation. Thus, the avoidance of water is critical to improve overall selectivity. Utilizing MeCMA gave diminished by-product formation, consequently improving benzoate selectivity.

Kinetic studies revealed that the activation barrier of the decarboxylation reaction was considerably higher than for the Diels-Alder reaction, giving evidence that the extrusion of CO₂ is the rate limiting step, which is in agreement with DFT results. The high activation barrier of the CO₂ extrusion afforded the successful isolation of (2), granting access to bicyclic molecules in high yield and selectivity that could be utilized as synthetic starting substrates to synthesize a broad array of new compounds. For instance, we have shown that diene intermediates (3) can be obtained from bicyclic lactones (2) through controlled thermal extrusion of CO₂, providing access to novel molecules with dual-functionality. These insights can be leveraged to produce a plethora of products based on the coumalate conversion platform.

1.5 Experimental

1.5.1 Reagents and Materials

Coumalic acid (>97 %), γ -valerolactone (98 %), and 10 wt% Pd on activated carbon were obtained from Sigma Aldrich. Toluene (99.9 %), methanol (MS grade), water (MS grade), acetic acid (MS grade) were obtained from Fischer Scientific. Methyl coumalate (98 %) and ethylene (99.5 %) were obtained from Acros Organics and Matheson, respectively. The deuterated solvents benzene-*d*6 (99.5 %), dioxane-*d*8 (99.5 %) were obtained from Cambridge Isotope Laboratories Inc. All chemicals were used without further purification.

1.5.2 Apparatus and general procedure

Reaction kinetic measurements for the overall reaction of CMA (or MeCMA) and ethylene were performed using a 50 ml micro reactor system from Parr (4590 Series). Catalytic reactions were carried out using a 10 wt% Pd/C catalyst, which was added to the CMA (or MeCMA) containing solution before the reactor was sealed and purged five times with nitrogen to remove residual air. The reactor was then charged with ethylene for approximately 30 min until saturation of ethylene in the solvent was achieved. Subsequently, the system temperature was increased to the desired reaction condition with a heating rate of 10 K min⁻¹. Samples were periodically withdrawn from the reactor through a high pressure sampling tip tube to follow the reaction progress over time. Samples were withdrawn once the reactor reached the desired reaction temperature as the starting point reference. After the liquid phase reaction products were collected, the samples were filtered through a 0.2 micron syringe filter and analysed via NMR, UPLC-PDA/QDa and GC-FID/MS.

The Diels-Alder reaction evaluation of CMA or MeCMA with ethylene were performed at a temperature range between 90-120 °C without the presence of catalyst following the reaction procedure described above. The solvent 1,4-dioxane was used due to its superior solubility of both CMA and MeCMA.

The decarboxylation reaction studies of the Diels-Alder product (DAP) decarboxylation were performed at a temperature range between 140-160 °C, using high pressure NMR tubes from Wilmad-Labglass. The reactant (2) for this study was synthesized via Diels-Alder reaction of CMA (or MeCMA) and ethylene in 1,4-dioxane at 110 °C for 16 h giving

high yield (>98 %). Through evaporation (using a stream of dry air) of the solvent, the reaction product (2) was obtained and subsequently dissolved in dioxane-*d*8. The solution was then transferred into the high-pressure NMR tubes. Before the tube was sealed, 2.5 μ l of an internal standard (dimethyl formamid, DMF) was added to perform quantitative analysis. Subsequently, the tubes were placed into a heated oil bath to initiate the decarboxylation reaction. The tubes were periodically taken out of the oil bath cooled to room temperature and the reaction products were analysed via ^1H -NMR. Running the reaction in a deuterated solvent allowed for direct NMR sample analysis of the reaction products without further sample workup.

Reaction kinetics measurements of water mediated CMA breakdown was performed using different amounts of D_2O added to the solution comprising the deuterated solvent dioxane-*d*8 and the reactant CMA. This reaction was conducted using high pressure NMR tubes from Wilmad-LabGlass that were loaded with the reaction solution, sealed and heated without exposing the reaction solution to the gaseous reactant ethylene to exclusively investigate the stability of CMA under reaction conditions. Here, a 0.15 M stock solution of coumalic acid and 0.025 M solution of DMSO_2 (internal standard) was prepared in deuterated dioxane-*d*8. A total volume of 300 μ L of stock solution were added to the high pressure NMR tubes (Wilmad-Labglass) and H_2O or D_2O were added to yield 0-5 vol%. NMR tubes were sealed and heated to 171 $^\circ\text{C}$. Samples were removed and allowed to cool to room temperature prior to collection of ^1H NMR spectra.

To elucidate the reaction network of the MeCMA reaction with ethylene, 2D-NMR structural assignments were carried out using different NMR techniques such as ^1H -NMR, ^1H - ^1H COSY, ^{13}C - ^1H HSQC. The products analysed via 2D-NMR were obtained from the reaction of MeCMA and ethylene following a 48 h reaction at 90 $^\circ\text{C}$ in the absence of the Pd/C catalyst.

1.5.3 Sample analysis

NMR sample analysis of the reaction mixtures obtained from the batch reactions were carried out using a Bruker spectrometer equipped with a 14.1 Tesla superconducting magnet. The data were acquired and processed using TOPSPIN (version 3.0) and MestReNova (version 10.0.1-14719), respectfully. These samples were prepared using fully deuterated benzene-*d*6 or dioxane-*d*8, to both reduce the solvent background and as

a species to use for field calibration. ^1H spectra were acquired using a recycle delay of 1.0 sec. and 30° ^1H excitation pulse lengths. ^1H - ^1H 2D plots were acquired using a COSY pulse sequence, and ^{13}C - ^1H 2D plots were acquired using a HSQC pulse sequence.

Reaction products were also analyzed with ultra-pressure liquid chromatography (UPLC) using a Waters Acquity H-Class System equipped with a Photodiode Array (PDA) and a QDa mass detector. UPLC separation was carried out on a Waters BEH Phenyl column (2.1x100 mm, 1.7 μm particles). Additionally, samples were analyzed by GC using an Agilent 7890B gas chromatograph equipped with an Agilent DB-1701 column (60 m x 0.25 mm), a flame ionization detector (FID), and an Agilent 5977A mass spectrometer (MS). The methyl ester version of (1), (3), (4), (5), and (6) were verified with NIST MS spectral library.

1.5.4 Computational

All of the calculations reported herein were performed using density functional theory with the M062X^{88,89} hybrid functional as implemented in Gaussian 09.⁹⁰ Optimizations were performed with a 6-311G+(d,p)⁹¹ basis set on an ultrafine grid and tight convergence criterion for force. Solvation was modeled implicitly using the SMD model.⁹² Thermal corrections and partition functions were calculated within Gaussian at 298.15 K and subsequently used to calculate enthalpy and Gibbs free energies of all species. A factor of $RT \ln(24.46)$ was added to the free energies of all species to account for change of reference state from 1 atm to 1 M in solution. For degradation in water, additional corrections were applied corresponding to 55.56 M concentration of the bulk solvent.

1.6 Acknowledgements

We gratefully acknowledge funding from the National Science Foundation under Award EEC-0813570, the Iowa State University Chemical Instrument Facility staff members, and the Minnesota Supercomputing Institute (MSI) at the University of Minnesota. Furthermore, we would like to acknowledge all co-workers at CBiRC for their support.

1.7 Supporting information

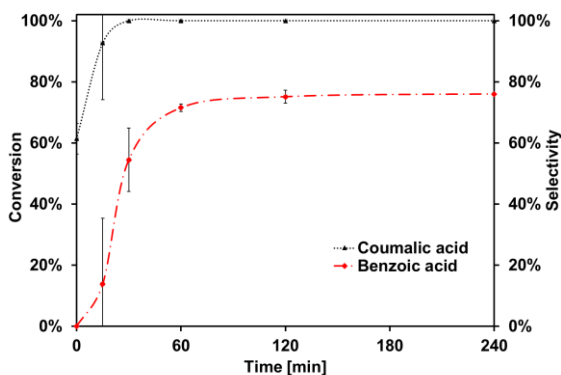


Figure S 1.1 The conversion of coumalic acid to benzoic acid at 180 °C using 10 wt.-% Pd/C and the solvent GVL.

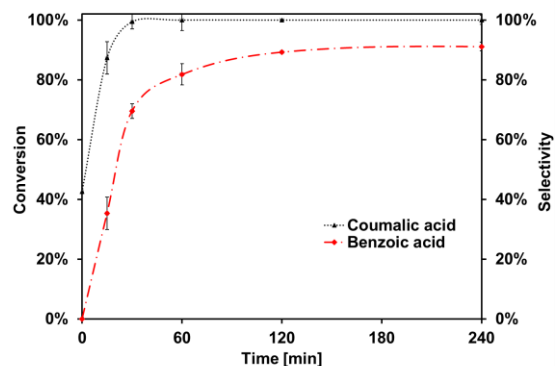


Figure S 1.2 The conversion of coumalic acid to benzoic acid at 180 °C using 10 wt.-% Pd/C and the solvent 1,4-dioxane.

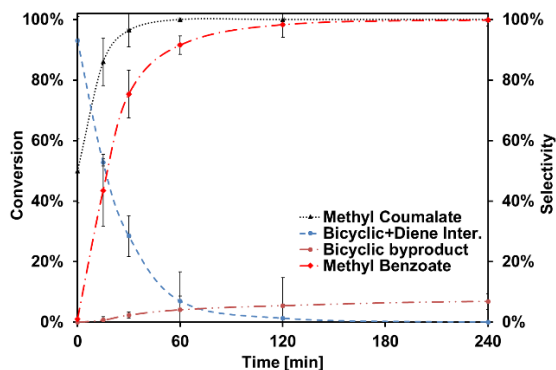


Figure S 1.3 The conversion of methyl coumalate to methyl benzoate at 180 °C using 10 wt.-% Pd/C and the solvent toluene.

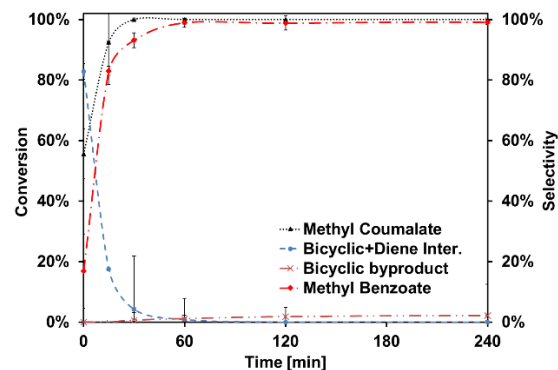


Figure S 1.4 The conversion of methyl coumalate to methyl benzoate at 180 °C using 10 wt.-% Pd/C and the solvent GVL.

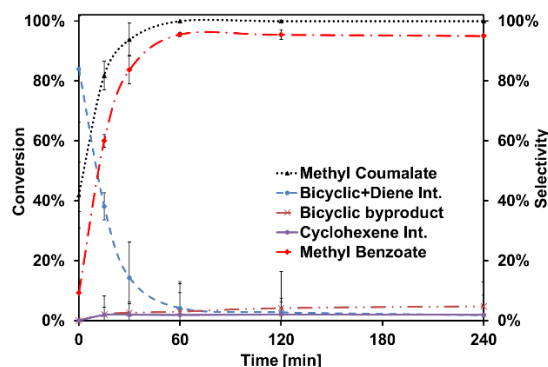


Figure S 1.5 The conversion of methyl coumalate to methyl benzoate at 180 °C using 10 wt.-% Pd/C and the solvent 1,4-dioxane.

1.7.1 Structural assignment of intermediates and by-products

The structural assignment of intermediates, products and by-products were identified via 2D-NMR experiments of the reaction products obtained from a 48 h reaction of MeCMA and ethylene in benzene-d₆ (Figure S 1.1). Fully deuterated benzene-d₆ was used due to its cheapness (compared to dioxane-d₈) and as a result of identical findings when compared to dioxane-d₈. We identified the bicyclic lactone intermediate and cyclohexa-1,5-diene intermediate as well as the double Diels-Alder by-product from cycloaddition of the diene intermediate and ethylene (Figure S 1.1-11). Additionally, GC-MS and UPLC-QDa analysis provided the mass of the identified compounds. The toluene peak in Figure S 1.1-S 1.11 was the result of residual toluene (solvent used to mediate reactions) in the reactor head space and can thus, be neglected.

Methyl -3-oxo-2-oxabicyclo[2.2.2]oct-5-ene-6-carboxylate intermediate (DAP): ¹H NMR (600 MHz, Benzene-d₆) δ 6.81 (dd, J = 6.5, 2.3 Hz, 1H), 5.47 (dt, J = 4.0, 1.9 Hz, 1H), 3.36 (s, 3H), 1.66 – 1.55 (m, 1H), 1.40 – 1.31 (m, 1H), 0.98 – 0.87 (m, 1H), 0.80 – 0.69 (m, 1H), m/z: 180.1.

Table S 1.1 Tabulated NMR assignment of methyl -3-oxo-2-oxabicyclo[2.2.2]oct-5-ene-6-carboxylate intermediate (DAP).

¹ H-label	δ ¹ H, ppm, (mult)	δ ¹³ C	¹ H Int.	¹ H- ¹ H-COSY	rel. mol-%
1	0.74 (m)	19.24	1.00	1-3, 1-7, 1-8, 1-14	73.01
3	0.94 (m)	24.82	1.04	3-1, 3-7, 3-8, 3-20	
7	1.36 (m)	19.08	1.06	7-1, 7-3, 7-8, 7-14	
8	1.60 (m)	24.33	1.03	8-1, 8-3, 8-7, 8-20	
15	3.36 (m)	51.49	2.99	-	

20	5.47 (s)	73.08	0.94	20-2, 20-8, 20-2
23	6.81 (dd)	140.86	1.08	23-14, 23-20

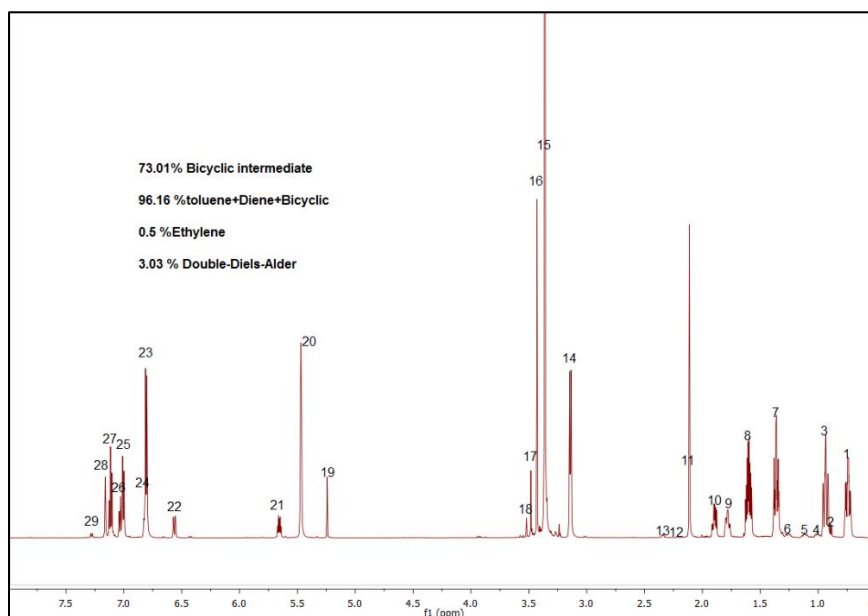


Figure S 1.6 $^1\text{H-NMR}$ of the reaction of MeCMA and ethylene at 90 °C for 48 hrs (600 MHz, benzene- d_6).

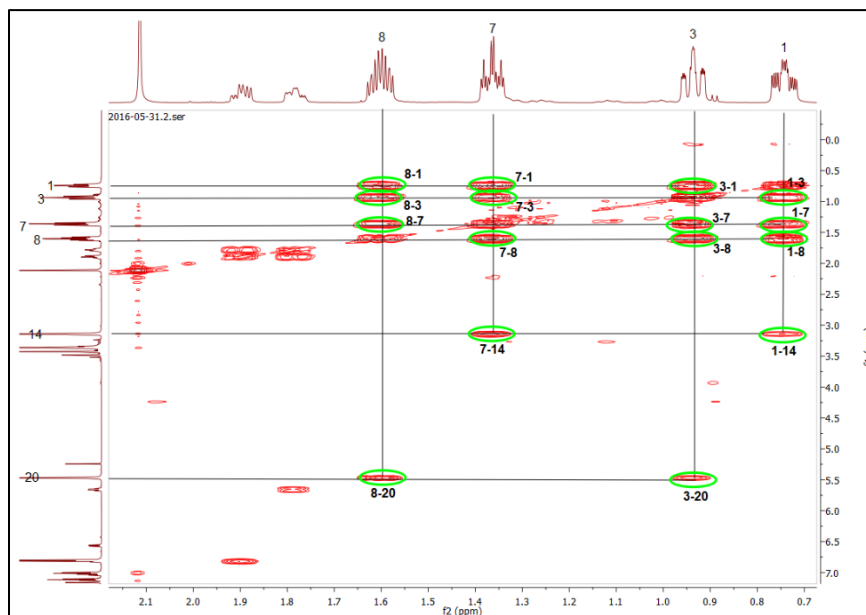


Figure S 1.7 $^1\text{H-}^1\text{H-COSY}$ of the methyl -3-oxo-2-oxabicyclo[2.2.2]oct-5-ene-6-carboxylate intermediate from the reaction of MeCMA with ethylene (600 MHz, benzene- d_6).

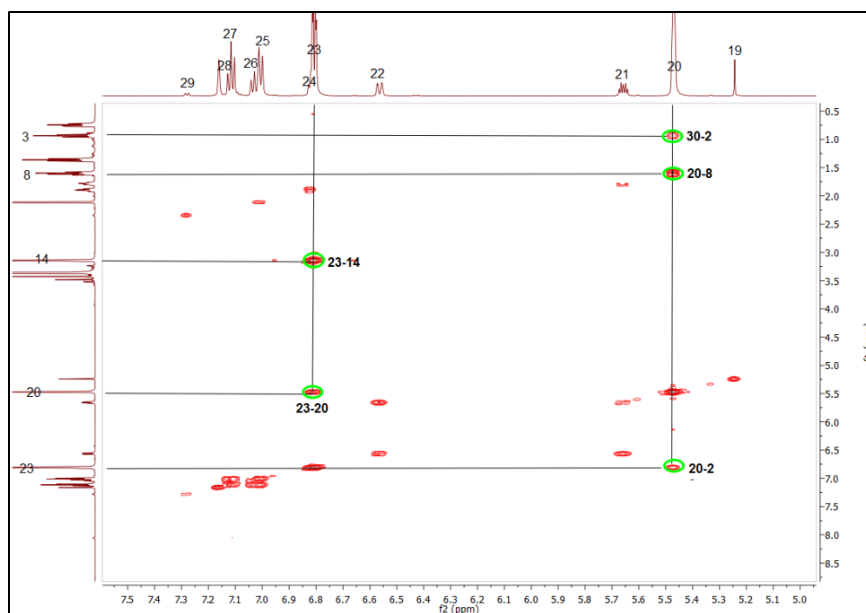


Figure S 1.8 ^1H - ^1H - COSY of the methyl -3-oxo-2-oxabicyclo[2.2.2]oct-5-ene-6-carboxylate intermediate from the reaction of MeCMA with ethylene (600 MHz, benzene- d_6).

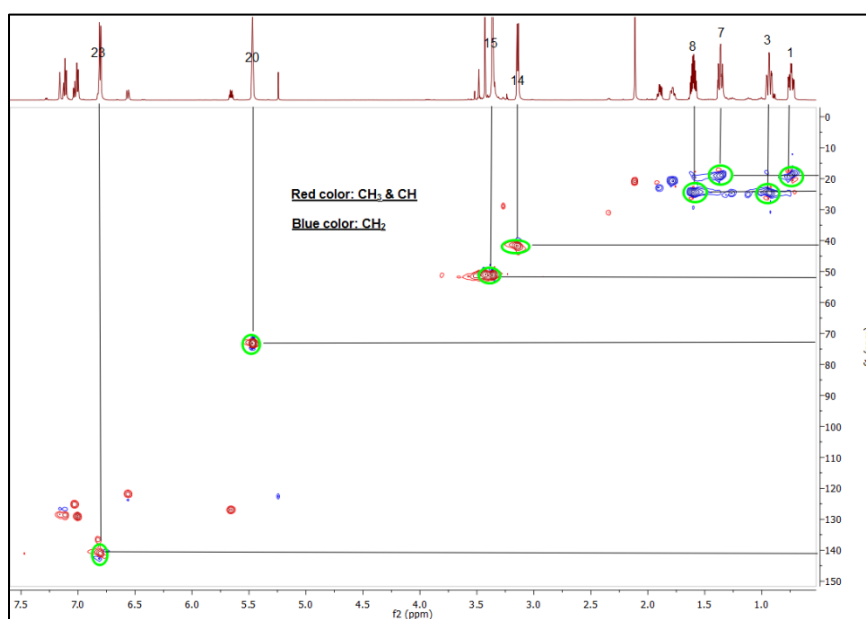


Figure S 1.9 ^{13}C - ^1H - HSQC of the methyl -3-oxo-2-oxabicyclo[2.2.2]oct-5-ene-6-carboxylate intermediate from the reaction of MeCMA with ethylene (600 MHz, benzene- d_6).

Methyl cyclohexa-1,5-diene carboxylate (Diene): ^1H NMR (600 MHz, Benzene- d_6) δ 6.56 (dq, $J = 9.9, 1.9$ Hz, 1H), 5.68 – 5.64 (m, 1H), 8.45 – 0.52 (m, 102H), 3.43 (s, 3H), 1.93 – 1.86 (m, 2H), 1.81 – 1.75 (m, 2H), m/z : 138.1.

Table S 1.2 Tabulated NMR assignment of the methyl cyclohexa-1,5-diene carboxylate intermediate.

^1H -label	δ ^1H , ppm, (mult)	$\delta^{13}\text{C}$	^1H Int.	^1H - ^1H -COSY	rel. mol-%
9	1.79	20.60	2.40	9-10, 9-21, 9-24	11.10
10	1.90	22.71	2.40	10-9, 10-24	
16	3.43	50.64	3.16	-	
21	5.66	126.98	1.13	21-9, 21-22	
22	6.56	121.66	1.04	22-10, 22-21	
24	6.82*	136.45	1.04	24-10	

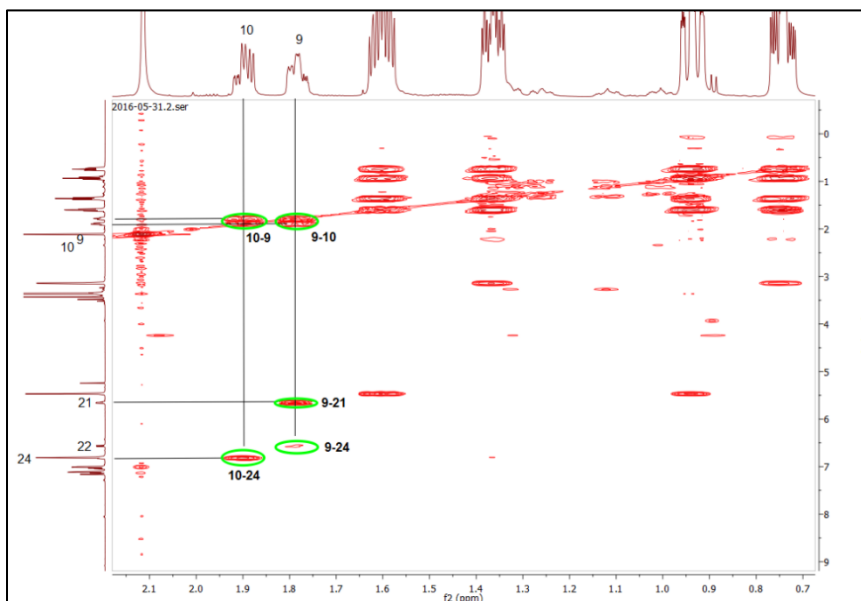


Figure S 1.10 ^1H - ^1H - COSY of the methyl cyclohexa-1,5-diene carboxylate intermediate from the reaction of MeCMA with ethylene (600 MHz, benzene- d_6).

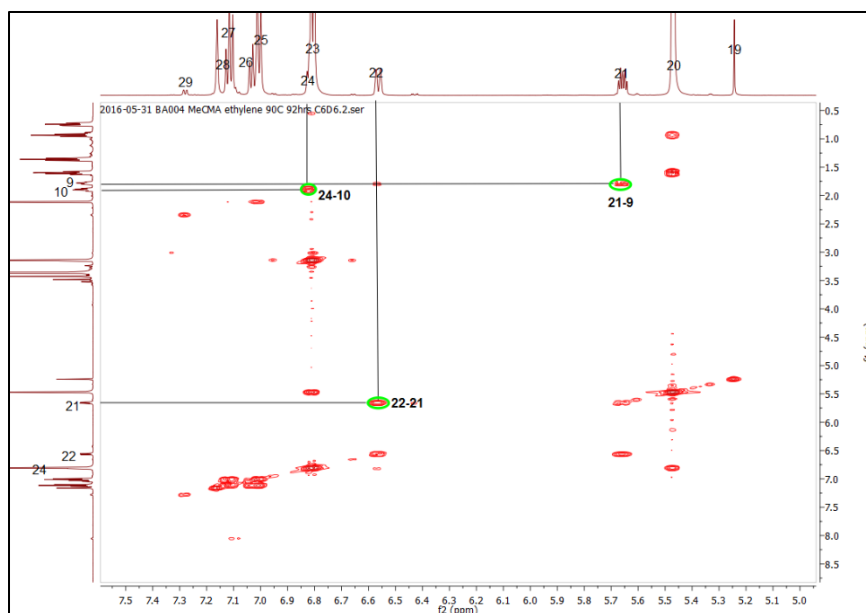


Figure S 1.11 ^1H - ^1H - COSY of the methyl cyclohexa-1,5-diene carboxylate intermediate from the reaction of MeCMA with ethylene (600 MHz, benzene- d_6).

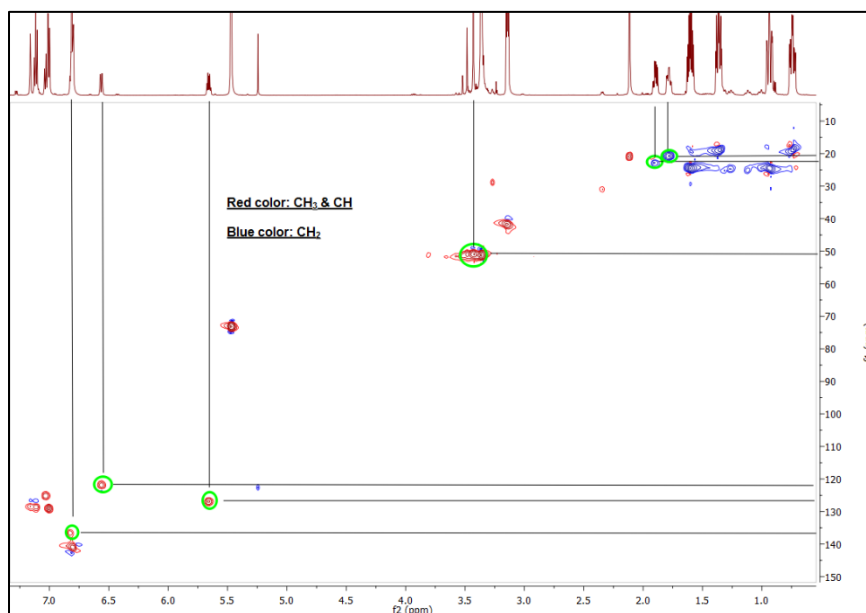


Figure S 1.12 ^{13}C - ^1H - HSQC of the methyl cyclohexa-1,5-diene carboxylate intermediate from the reaction of MeCMA with ethylene (600 MHz, benzene- d_6).

Methyl bicyclo[2.2.2]oct-2-ene-2-carboxylate: ^1H NMR (600 MHz, Benzene- d_6) δ 7.28 (dd, $J = 6.9, 1.7$ Hz, 1H), 3.48 (s, 3H), 3.28 – 3.25 (m, 1H), 2.36 – 2.32 (m, 1H), 1.33 – 1.29 (m, 2H), 1.29 – 1.23 (m, 2H), 1.16 – 1.08 (m, 2H), 1.05 – 0.97 (m, 2H), m/z : 166.1.

Table S 1.3 Tabulated NMR assignment of methyl bicyclo[2.2.2]oct-2-ene-2-carboxylate.

¹ H-label	δ ¹ H, ppm, (mult)	δ ¹³ C	¹ H Int.	¹ H- ¹ H-COSY	rel. mol-%
4	1.01 (m)	24.36	1.62	4-5, 4-6, 4-6a, 4-13	3.03
5	1.12 (m)	24.88	1.92	5-4, 5-6, 5-6a, 5-14a	
6	1.26 (m)	24.57	2.11	6-4,6-5, 6-6a, 6-13	
6a	1.31 (m)	25.08	1.78	6a-4, 6a-5, 6a-6, 6a-14a	
13	2.34 (m)	31.01	0.84	13-4, 13-6, 13-29	
14a	3.27 (m)	28.74	1.21	14a-5, 14a-6a, 14a-29	
17	3.48 (s)	51.63	2.92	-	
29	7.28 (dd)	144.33	0.88	29-13, 29-14a	

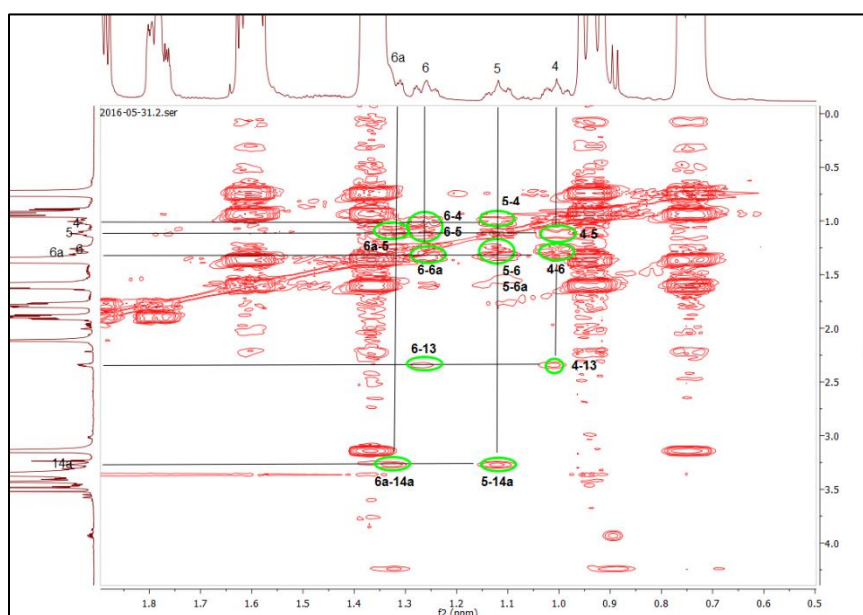


Figure S 1.13 ¹H-¹H- COSY of the methyl bicyclo[2.2.2]oct-2-ene-2-carboxylate from the reaction of MeCMA with ethylene (600 MHz, benzene-d₆).

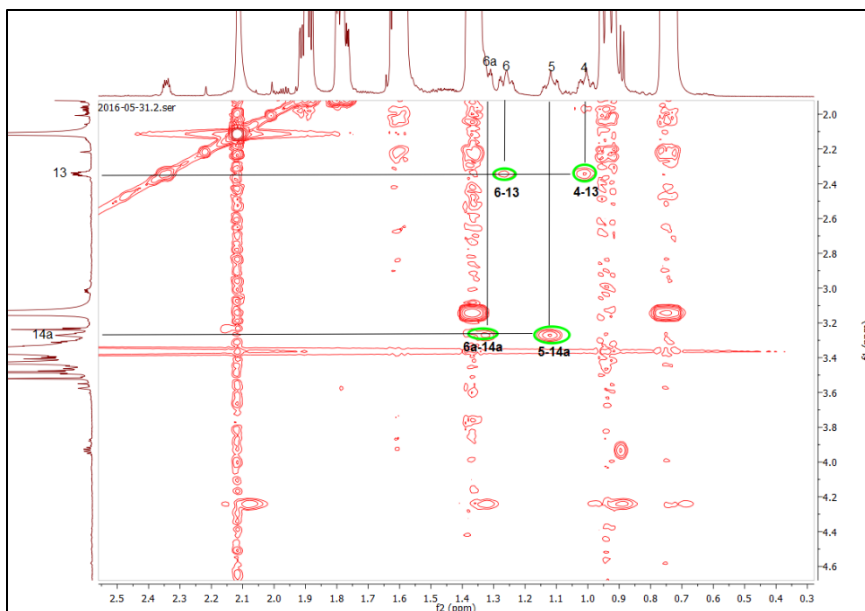


Figure S 1.14 ^1H - ^1H - COSY of the methyl bicyclo[2.2.2]oct-2-ene-2-carboxylate from the reaction of MeCMA with ethylene (600 MHz, benzene- d_6).

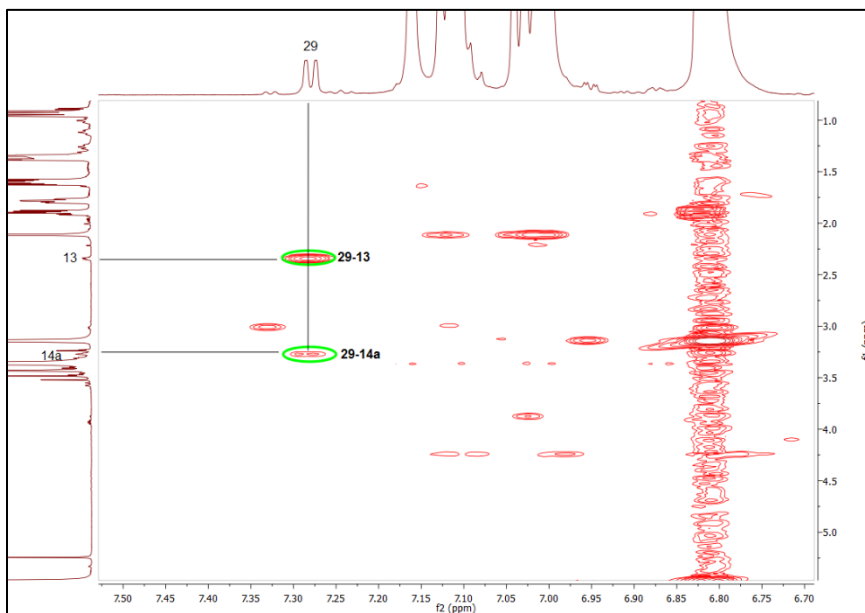


Figure S 1.15 ^1H - ^1H - COSY of the methyl bicyclo[2.2.2]oct-2-ene-2-carboxylate from the reaction of MeCMA with ethylene (600 MHz, benzene- d_6).

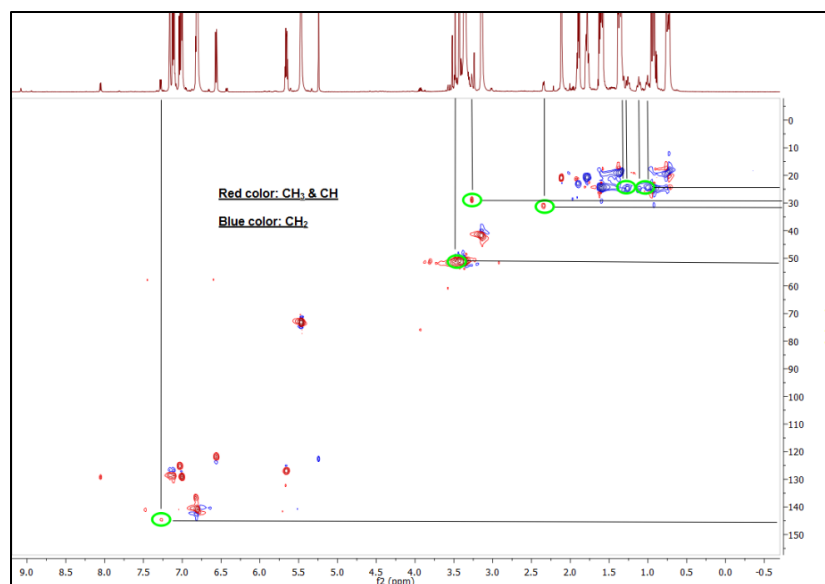


Figure S 1.16 ^{13}C - ^1H - HSQC of the methyl bicyclo[2.2.2]oct-2-ene-2-carboxylate from the reaction of MeCMA with ethylene (600 MHz, benzene- d_6).

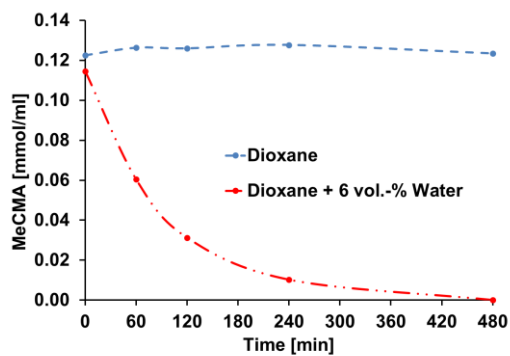


Figure S 1.17 Stability test of coumalic acid in 1,4-dioxane in the presence and absence of water at 180 °C.

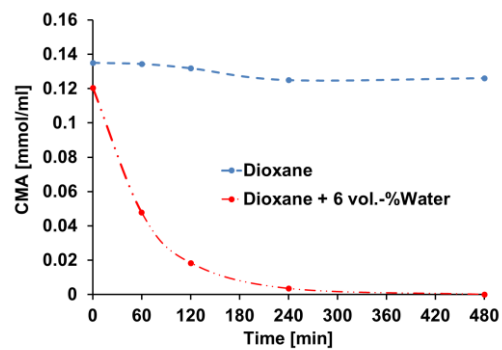


Figure S 1.18 Stability test of methyl coumalate in 1,4-dioxane in the presence and absence of water at 180 °C.

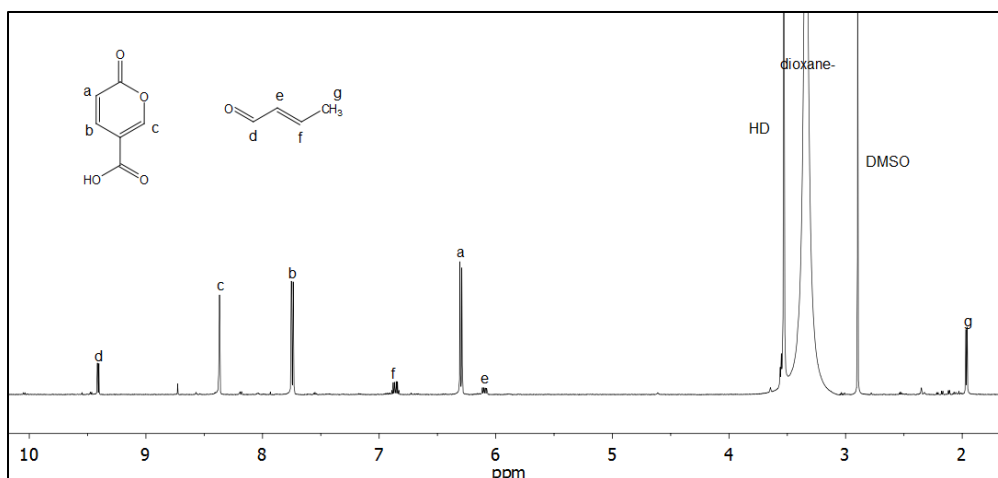


Figure S 1.19 ^1H NMR (600 MHz, dioxane- d_8) of 0.15M coumalic acid and 3 vol.-% H_2O after 386 min at 171 °C.

Table S 1.4 Rate constants and activation energy of the Diels-Alder reaction of coumalates with ethylene.

Entry	Substrate	Temp. [°C]	$10^3 1/T$ [K $^{-1}$]	$10^{-3} k_{\text{obs}}$ [min $^{-1}$]	Ink	E_A [kJ/mol]
1	MeCMA	90	2.75	0.99	-6.92	76.74
2	MeCMA	100	2.68	2.03	-6.20	
3	MeCMA	110	2.61	4.15	-5.49	
4	MeCMA	120	2.54	6.72	-5.00	
5	CMA	90	2.75	0.82	-7.11	77.06
6	CMA	100	2.68	1.61	-6.43	
7	CMA	110	2.61	3.10	-5.77	
8	CMA	120	2.54	6.07	-5.10	

Table S 1.5 Rate constants and activation energy of the decarboxylation reaction of the bicyclic intermediate DAP from coumalate reaction with ethylene.

Entry	Substrate	Temp. [°C]	$10^3 1/T$ [K $^{-1}$]	$10^{-3} k_{\text{obs}}$ [min $^{-1}$]	Ink	E_A [kJ/mol]
1	MeCMA-DAP	140	2.42	2.56	-5.97	132.79
2	MeCMA-DAP	149	2.36	5.65	-5.18	
3	MeCMA-DAP	160	2.31	15.24	-4.18	
4	CMA-DAP	139	2.42	2.81	-5.88	141.56
5	CMA-DAP	149	2.36	7.56	-4.88	
6	CMA-DAP	158	2.32	17.31	-4.06	

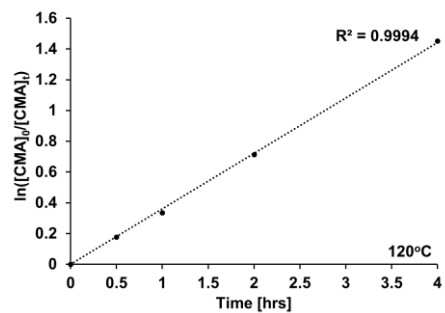
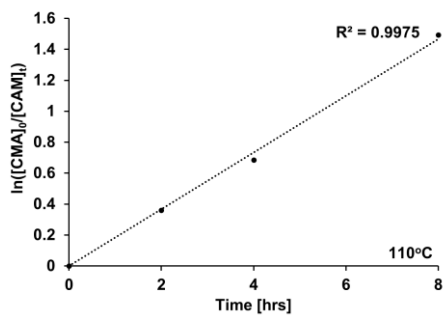
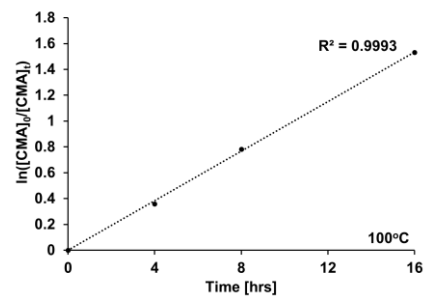
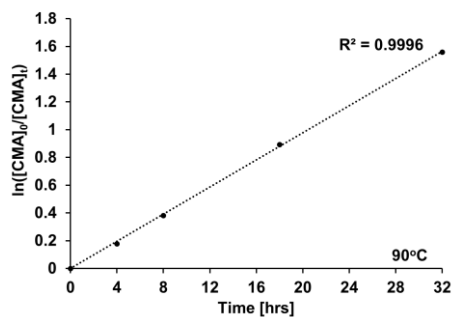
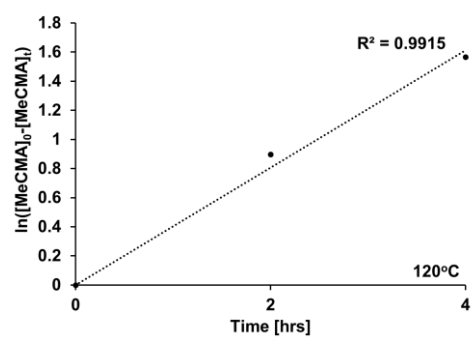
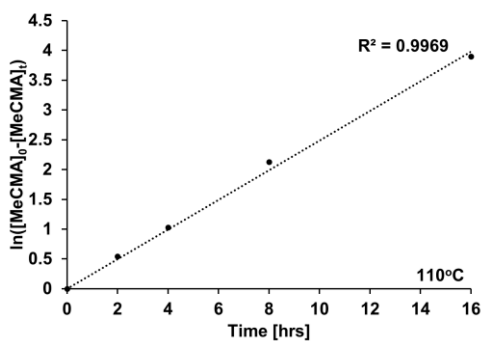
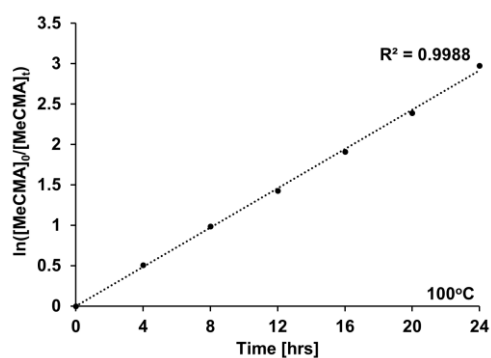
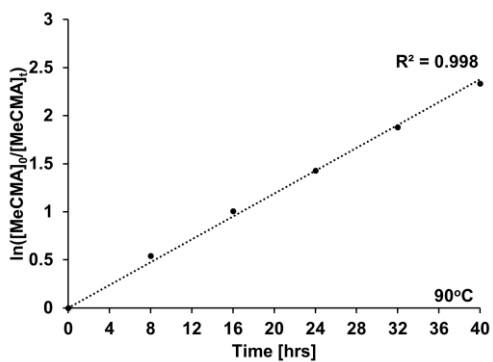


Figure S 1.20 Diels-Alder reactions kinetics of coumalic acid and ethylene at different temperatures.



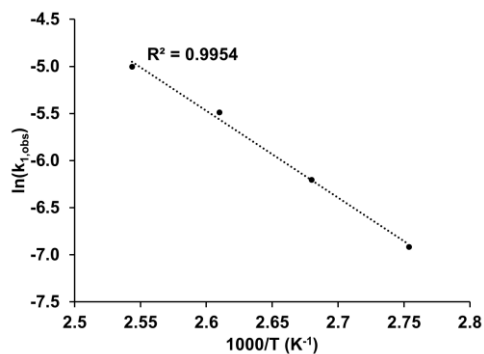


Figure S 1.21 Diels-Alder reaction kinetics of methyl coumalate and ethylene at different temperatures.

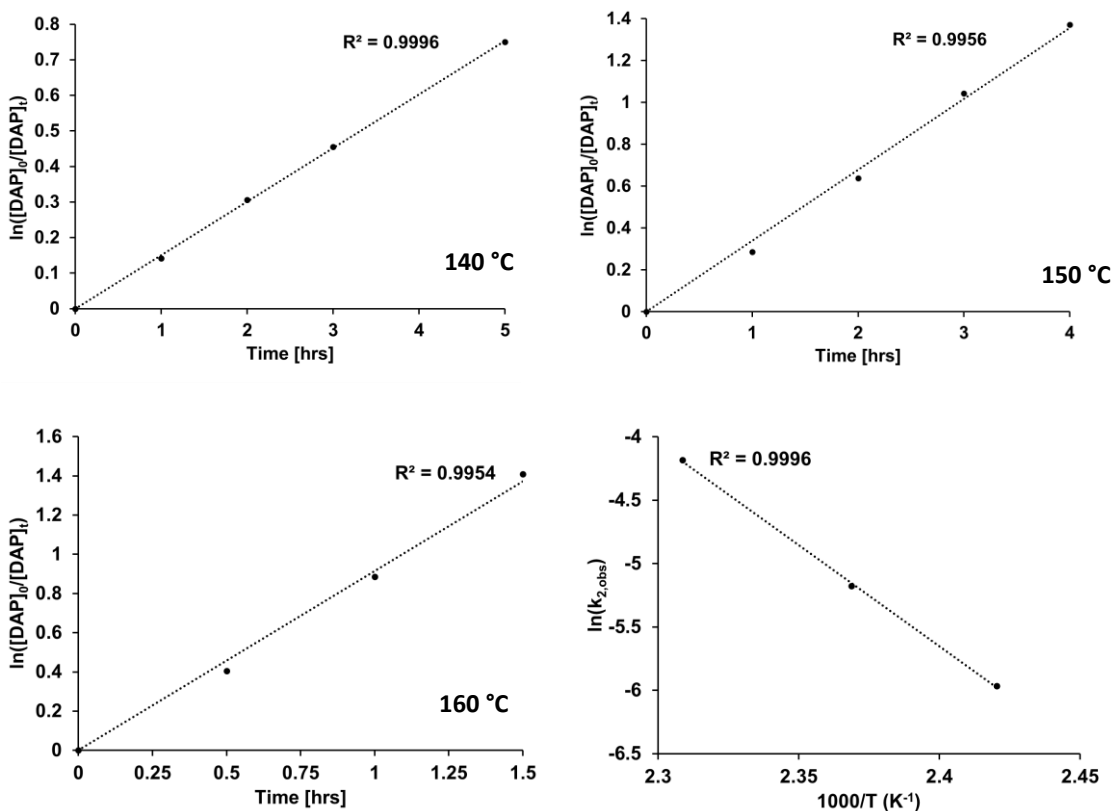


Figure S 1.22 Decarboxylation reaction kinetics of the Diels-Alder product of methyl coumalate and ethylene at different temperatures and the corresponding Arrhenius plot.

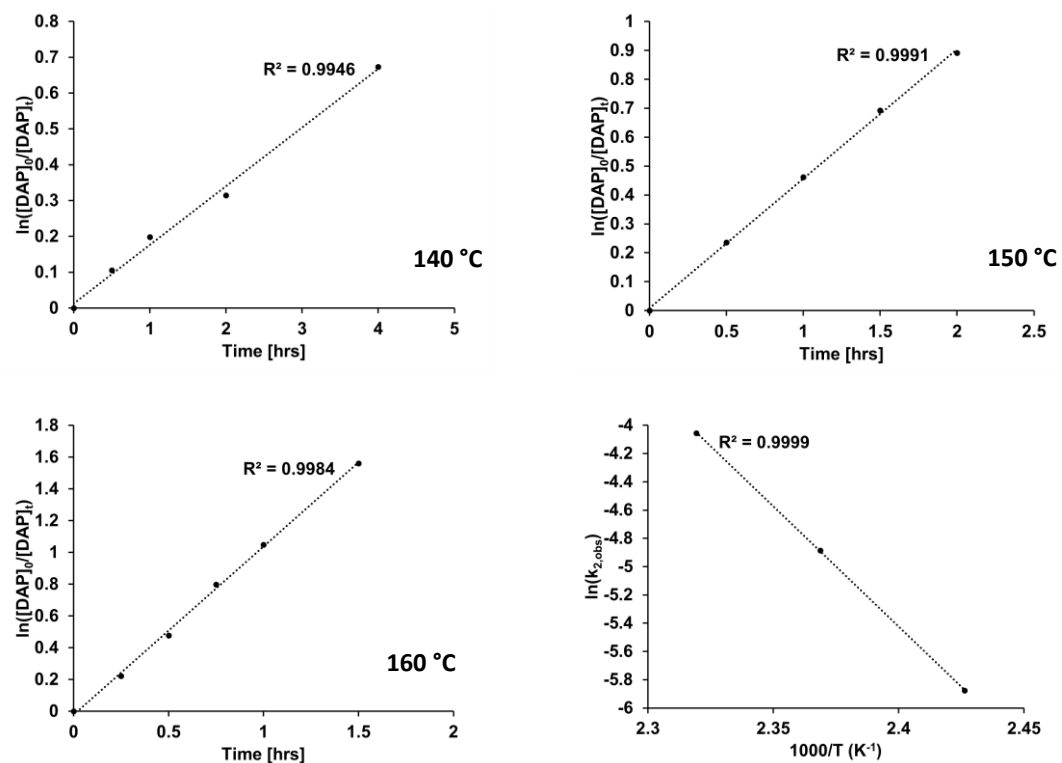


Figure S 1.23. Decarboxylation reaction kinetics of the Diels-Alder product of coumalic acid and ethylene at different temperatures and the corresponding Arrhenius plot

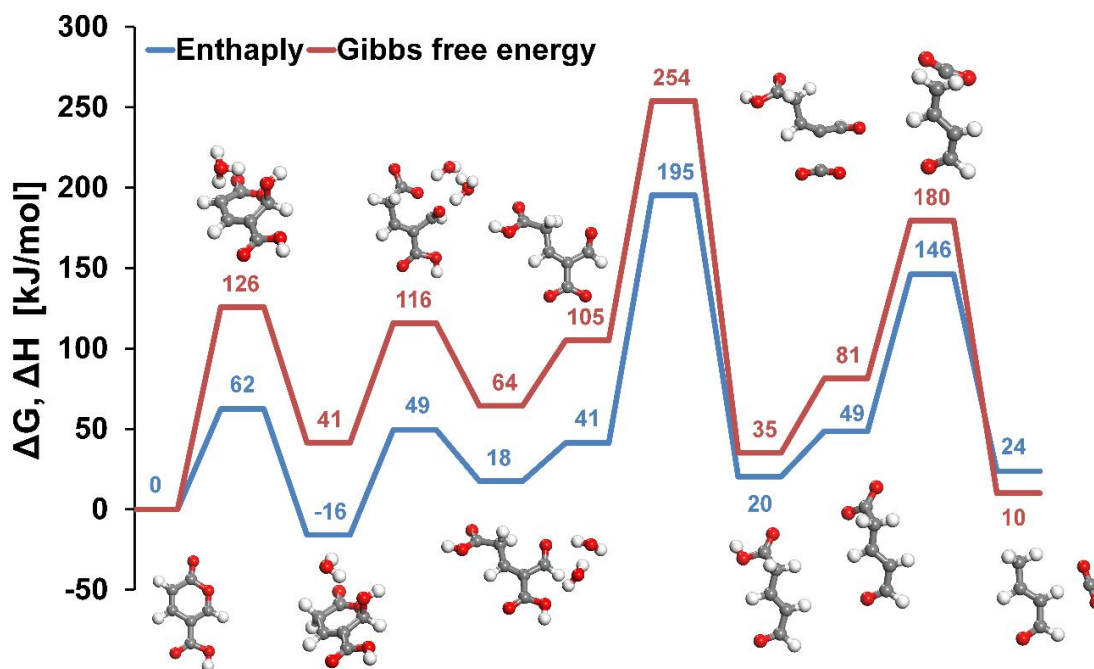


Figure S 1.24 Reaction profile diagram of the coumalic acid breakdown in water

2 Modulating Reactivity and Selectivity of 2-Pyrone-Derived Bicyclic Lactones through Choice of Catalyst and Solvent

Reprinted with permission from Pfennig, T., Chemburkar, A., Johnson, R. L., Ryan, M. J., Rossini, A. J., Neurock, M., Shanks, B. H. *Modulating Reactivity and Selectivity of 2-Pyrone-Derived Bicyclic Lactones through Choice of Catalyst and Solvent*. ACS Catal. **2018**, 8, 3, 2450-2463. Copyright 2018 American Chemical Society.

Theoretical calculations were performed by AC under the supervision of MN

2.1 Conspectus

2-Pyrones, such as coumalic acid, are promising bio-based molecules that through Diels-Alder reactions can provide access to a wide range of bio-based chemicals, including molecules with functionality that are not easily accessible via conventional petrochemical routes. A complete reaction network and kinetic parameters for three individual diversification routes that start from a single bicyclic lactone produced via the Diels-Alder cycloaddition of coumalic acid and ethylene were examined experimentally and probed through complementary first-principle density functional theory (DFT) calculations, in situ nuclear magnetic resonance (NMR) spectroscopy and thin film solid-state NMR spectroscopy. These experiments provide insights into the routes for several molecular structures from bicyclic lactones by leveraging Lewis or Brønsted acid catalysts to selectively alter the reaction pathway. The bicyclic lactone bridge can be decarboxylated to access dihydrobenzenes at a substantially reduced activation barrier using γ -Al₂O₃ as the catalyst or selectively ring-opened via Brønsted acids to yield 1,3-diacid six membered rings. DFT computations and microkinetic modeling in combination with experimental results provide molecular insights into the catalytically active sites on γ -Al₂O₃ and provide a general mechanism for the catalyzed bicyclic lactone decarboxylation in polar aprotic solvents, which involves CO₂ extrusion as the kinetically relevant step. Solid-state NMR spectroscopy provides direct evidence of strong binding of the bicyclic lactone to the γ -Al₂O₃ surface, fully consistent with DFT simulation results and experimental reaction

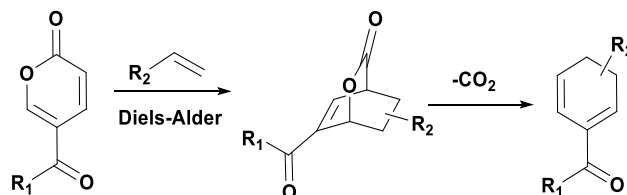
kinetics. In addition, the role of the solvent was examined and found to be an additional means to improve reaction rates and selectively produce new structures from the bicyclic intermediate. The rate of the decarboxylation reaction was increased dramatically by using water as the solvent whereas methanol acted as a nucleophile and selectively induced ring-opening, showing that both pathways are operative in the absence of catalyst. Taken together, the results demonstrate an approach for selective diversification of the coumalate platform to a range of molecules.

2.2 Introduction

New technologies to extract non-renewable carbon feedstocks, such as shale gas, exert significant economic pressure on the potential to manufacture bio-based commodity chemicals. This challenge creates the need to develop flexible chemical conversion platforms that can be used to pivot from biomass-derived bulk chemicals to higher value chemicals. Leveraging novel transformation pathways from biomass feedstocks via bioprivileged molecules provides an attractive means to access higher value chemicals such as next-generation nutraceuticals, antimicrobials, pharmaceuticals, consumer goods, specialty chemicals, *etc.*, in a manner that is cost competitive compared to traditional petrochemical routes.³⁸

As a potential bioprivileged molecule platform, Diels-Alder conversion of 2-pyrone coumalic acid (CMA) provides a highly versatile pathway to the synthesis of a wide range of bio-based chemicals through the utilization of a variety of dienophiles.²⁶⁻³⁰ Particularly important are those dienophiles that are less expensive and lead to more efficient downstream separations. Renewable CMA can be synthesized from malic acid via acid catalyzed dimerization,²⁶ with malic acid being readily produced from biomass via fermentation with genetically modified microorganisms.^{71,72,93} Given that malic acid has been cited as one of the 12 most promising bio-based platform chemicals,⁹⁴ considerable effort has already been invested into the biochemical conversion of glucose to malate. A particularly interesting feature of 2-pyrone Diels-Alder reactions is the formation of stable bicyclic lactones that are highly functionalized, stereochemically rich building blocks which can be used as versatile synthetic intermediates.^{74-78,80,95-100} Decarboxylation of these structures leads to synthetically valuable dihydrobenzenes^{78,87,101,102} (DIH) with potential applications in the manufacture of medically useful products (Scheme 2.1). DIH can then be utilized for chemical diversification, granting access to polycyclic

systems^{92,100,102,105,107,108} and aromatics^{26–30,76,80,100,102,103} with wide-ranging applications. Although bicyclic compounds can be accessed from 2-pyrones in high yield, their selective transformation via thermal decarboxylation can be challenging due to degradation⁸⁷ or in situ aromatization,^{26–28,76,80,102} which limit the selective access of interesting and potentially value-added diene structures in high purity.

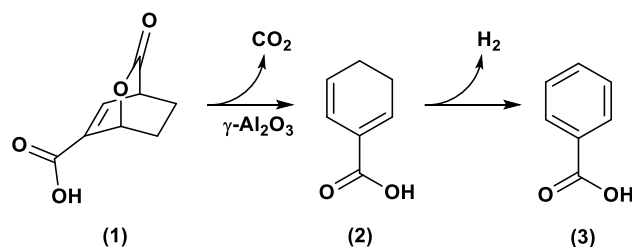


Scheme 2.1 Diels-Alder conversion of 2-pyrones to form bicyclic lactones followed by decarboxylation to dihydrobenzenes.

In-situ aromatization of these conjugated diene species is especially favored when the desired diene contains a leaving group (e.g. alkoxy), demonstrated by reactions of methyl coumalate in combination with ketals, acetals, captodative dienophiles or vinyl ethers, which lead to high aromatic yields without the requirement of a dehydrogenation catalyst.^{26–28} We recently demonstrated that the catalytic production of benzoic acid from CMA and ethylene proceeds via a sequence of reactions including Diels-Alder, decarboxylation, and palladium catalyzed dehydrogenation. The rate for this reaction is limited by the decarboxylation of the bicyclic lactone intermediate to the respective DIH resulting in an activation energy of 142 kJ/mol.¹⁰⁴ Given the high activation barrier of decarboxylation of the bicyclic lactone molecules, an effective catalyst that activates the decarboxylation step is of great interest to allow for CO₂ extrusion under milder reaction conditions. This could preserve the diene functionality and prevent in situ aromatization and formation of other decomposition products.

Herein, we report a highly selective technology platform to synthesize DIHs through the use of Lewis and Brønsted acid catalysts that alter the reaction path of the bicyclic intermediate that forms. This approach can be applied to other bicyclic lactone systems, opening the door to the production of many different specialty chemicals without the requirement of numerous dienophiles. We demonstrate this approach using a bicyclic lactone (1) derived from CMA in conjunction with inexpensive and easily separable ethylene (Scheme 2.2). Detailed kinetic experiments, density functional theory calculations, and thin layer solid-state high resolution magic angle spinning (HR-MAS)

NMR spectroscopy which were carried out show that bicyclic intermediate (1) derived from the Diels-Alder addition of 2-pyrone and ethylene undergoes a direct decarboxylation on the surface of $\gamma\text{-Al}_2\text{O}_3$ to form cyclohexa-1,5-diene-1-carboxylic acid (2) and show that the coordinatively saturated Al-species selectively drives the decarboxylation reaction to completion.



Scheme 2.2 $\gamma\text{-Al}_2\text{O}_3$ catalyzed decarboxylation.

Through in situ $^1\text{H-NMR}$ spectroscopy experiments, we further demonstrate that the presence of Brønsted acids result in the ring-opening of the bicyclic intermediate followed by an acid catalyzed dehydration leading to cyclohexa-1,3-diene-1,3-dicarboxylic acid in high selectivity.

The impact of solvents in steering the reaction was also explored. Using solvents that can serve as weak nucleophiles (e.g. methanol) provides an alternative path for transforming (1) to (5)-(methoxycarbonyl)cyclohexa-1,5-diene-1-carboxylic acid with high selectivity (>99 mol%). Conversely, polar protic water leads to enhanced decarboxylation of (1) to (2) as compared to the polar aprotic 1,4-dioxane. These routes offer catalyst-free pathways with the potential to be broadly applied to bicyclic lactone molecules. Lastly, we applied these findings to synthesize benzoic acid (3) by using a bifunctional 1 wt% Pd/ $\gamma\text{-Al}_2\text{O}_3$ catalyst to activate the rate limiting decarboxylation step, reduce the reaction temperature, and show the full conversion of (2) to (3) with a selectivity > 99 mol%.

2.3 Results and Discussion

2.3.1 Decarboxylation in the presence of catalyst

To overcome the high activation barrier required to decarboxylate (1) to form the DIH (2), a catalyst that can selectively activate the decarboxylation step is required. Given that Brønsted acids and Lewis acids facilitate Diels-Alder reactions,^{74,77–80,105–107} we

hypothesized that these acid catalysts could also enable retro-Diels-Alder extrusion of CO₂ from bicyclic lactones to generate DIH.

Starting with γ -Al₂O₃ as a Lewis acid catalyst,¹⁰⁸ we found that (1) can be effectively decarboxylated to (2) at 120 °C (Table 2.1, Entry 2). The 47 mol% conversion of (1) resulted in a yield of 43 mol% of (2) and small amounts of (3) (Scheme 2.2). This is a significant improvement over the control experiment which gave only 9 mol% conversion of (1) at identical reaction conditions but in the absence of a catalyst (Table 2.1, Entry 1). It is evident from these experiments that γ -Al₂O₃ can be effectively used as a highly active decarboxylation catalyst for bicyclic lactones. Additional experiments were performed with Lewis acid metals supported on γ -Al₂O₃ including 5 wt.-% Zn/ γ -Al₂O₃, Cu/ γ -Al₂O₃, Fe/ γ -Al₂O₃ and Ce/ γ -Al₂O₃. The Cu/ γ -Al₂O₃ showed a slight improvement in the decarboxylation activity with a 58 mol% yield at 59 mol% conversion (Table 2.1, Entry 2). Zn, Fe, and Ce on γ -Al₂O₃ showed either similar or lower decarboxylation activity (Table 2.1, Entry 3-5). Cu, Zn, and Ce were chosen due to their known Lewis acid activities.¹⁰⁵⁻¹⁰⁷ A more comprehensive correlation between Lewis acidity of the synthesized catalysts and the decarboxylation activity will be subject of future experimental investigation.

Table 2.1 Bicyclic lactone (1) conversion in the presence of Lewis acids

Entry	Catalyst	(1) Conv. [mol%]	(2) Yield [mol%]	(3) Yield [mol%]	By-products [mol%]
Control	-	9	7	<2	-
1	γ -Al ₂ O ₃	47	43	< 4	-
2	5 wt% CuO/ γ -Al ₂ O ₃	59	58	< 2	<1
3	5 wt% ZnO/ γ -Al ₂ O ₃	49	36	< 3	<11
4	5 wt% Ce ₂ O ₃ / γ -Al ₂ O ₃	47	45	< 3	-
5	5 wt% Fe ₂ O ₃ / γ -Al ₂ O ₃	47	34	< 3	<11

Conditions: Reaction time 2 h, temperature 120 °C, stirring rate 500 rpm, initial concentration 71.38 μ mol/mL, reaction volume 4 mL, 1,4-dioxane, 25 mg catalyst.

Through this approach, we showed that γ -Al₂O₃ is an excellent decarboxylation catalyst for bicyclic lactones to access novel diene species (e.g. (2)) in high selectivity at

significantly reduced temperatures. Given that some bicyclic lactones and diene species are susceptible to degradation and in situ aromatization at elevated temperatures, γ -Al₂O₃ can be generally applied to overcome this challenge.

2.3.2 Reaction kinetics for γ -Al₂O₃ catalyzed decarboxylation

To gain a more detailed understanding of the role of the γ -Al₂O₃ in catalyzing decarboxylation, an in-depth kinetic investigation of the conversion of (1) to (2) over γ -Al₂O₃ was performed using temperatures between 130-160 °C in 1,4-dioxane. The Weisz-Prater number was calculated to be < 1 for the reaction conditions used which verified the absence of mass transfer limitations (see Supporting Information). Assuming a first-order reaction with respect to (1), we obtained linear trends of $\ln([1]_0/[1]_t)$ with respect to time (Table S 2.1) from which the rate constants (Table S 2.1) were calculated to generate the Arrhenius plot shown in Figure S 2.1. The resulting activation barrier was found to be 108 kJ/mol, which is significantly lower than non-catalyzed decarboxylation (142 kJ/mol¹⁰⁴) and provides evidence that γ -Al₂O₃ strongly impacts the decarboxylation step.

2.3.3 Computational analysis of the γ -Al₂O₃ catalyzed decarboxylation

DFT calculations and microkinetic analyses were carried out to gain further insights into the nature of the active sites on γ -Al₂O₃ and the surface-catalyzed decarboxylation mechanism. As discussed below, HR-MAS NMR spectroscopy provides experimental evidence of a strongly adsorbed bicyclic lactone species (1) on the γ -Al₂O₃ surface as well as high surface hydroxylation. This information was used to guide DFT computations.

DFT calculations and microkinetic analyses were carried out to gain further insights into the nature of the active sites on γ -Al₂O₃ and the surface-catalyzed decarboxylation mechanism. As discussed below, HR-MAS NMR spectroscopy provides experimental evidence of a strongly adsorbed bicyclic lactone species (1) on the γ -Al₂O₃ surface as well as high surface hydroxylation. This information was used to guide DFT computations.

Different surfaces such as 110, 100 and 111 faces can exist on γ -Al₂O₃ particles under reaction conditions. The 111 surface typically exposes only oxygen atoms and is extremely difficult to dehydrate under realistic conditions, while the other surfaces tend to exist with an appropriate OH coverage and exposed Al sites that can be catalytically active.¹⁰⁹ Therefore, in the present work, we explored different Al sites on the 110 and 100 surfaces with different levels of hydroxylation.

The fully dehydrated 110 surface exposes Al_{III} and Al_{IV} sites while the dehydrated 100 surface exposes different types of Al_V sites.¹¹⁰ However, all of these sites are typically covered by OH groups, leading to stabilization of these terminations. OH groups preferentially occupy the sites with high Lewis acidity ($Al_{III} > Al_{IV} > Al_V$). On the 110 surface, the Al_{III} sites are converted to tetragonal Al_{IV} sites and are potentially blocked by OH groups. Alternatively, the Al_{IV} sites are converted to Al_V sites that are still catalytically active. However, Al_V sites can further be hydroxylated to Al_{VI} sites, rendering them fully saturated and possibly catalytically inactive. This is predicted to occur at the Al_V sites on the 100 surface, generating saturated Al_{VI} sites. Results by Digne et al. suggest that under reacting temperatures (120 °C – 150 °C), the OH coverage can be as high as 15 OH/nm² and 13 OH/nm² on the 110 and 100 surfaces respectively, which can expose both catalytically active Al_V sites and catalytically inactive tetrahedral Al_{IV} and octahedral Al_{VI} sites.¹¹⁰ At OH coverage of 15 OH/nm², all Al sites on the 110 surface are covered by hydroxyls and water molecules. We find that the coverage of H_2O^* is 40% and that of OH^* is 60%. On the other hand, on the 100 surface, the OH coverage of 13 OH/nm² results in an OH^* coverage of 25%, H_2O^* coverage of 50% and empty Al site (*) coverage of 25%. Given that the γ - Al_2O_3 catalyst was not heat treated (dehydroxylated) prior to the decarboxylation experiments and that the solvent used in our experiments contained residual water (0.028 mol%), the Al_2O_3 surface was likely highly hydroxylated. Therefore, in order to determine appropriate hydroxyl surface coverage and to assess its impact on the adsorption behavior of species (1), we first calculated the Gibbs free energy of adsorption of water and (1) on the various sites on surfaces with different levels of OH coverage. An ab-initio thermodynamic analysis was then performed to predict the OH coverage of the most abundant surface under these conditions. Further, detailed energetics were calculated to deduce activation barriers of the surface catalyzed decarboxylation which were then compared to results obtained from microkinetic modeling.

2.3.3.1 Adsorption of water and (1) on different γ - Al_2O_3 surfaces

The standard gas phase Gibbs free energy of adsorption for the bicyclic lactone (1) and water were carried out at 140 °C for the 110 and 100 Al_2O_3 surfaces at different surface coverages of Al^* , H_2O^* and OH^* . The results are reported in Tables S 2.2 and S 2.4 and the relevant structures are given in Figure S 2.2. The adsorption of (1) was found to be more favorable than water on the 110 surfaces with high OH coverages (Table S 2.2,

entries 2 and 3). This is likely the result of the relatively weak molecular adsorption of water at high OH coverages and the strong adsorption of (1) on Lewis acidic surface Al-sites promoted by hydrogen bonding interactions between (1) and surface OH groups. The high coverage of the strongly bound bicyclic lactone species (1) on the hydroxylated Al₂O₃ surface was confirmed via HR-MAS NMR (*vide infra*). At lower OH coverages (Table S 2.2, Entry 4), water was found to adsorb dissociatively, making water adsorption very strong and more favorable than the adsorption of (1). On the 100 surface, the limited hydrogen bonding interactions between surface OH groups and (1) result in slightly less favorable adsorption of (1) compared to water at different surface coverages examined in this work (Table S 2.4). Therefore, on the 110 surface, we find that the most energetically favorable configuration has an OH* coverage of 60%, H₂O* coverage of 20% and (1*) coverage of 20% (Table S 2.3, Entry 3), while on the 100 surface, the most energetically favorable surface has an OH* coverage of 25%, H₂O* coverage of 50% and Al(*) coverage of 25% (Table S 2.5, Entry 1). Now, assuming adsorption and desorption of (1) and water is quasi-equilibrated and that different configurations in Tables S 2.3 and S 2.4 are also in equilibrium with each other, we can calculate the most favorable surface configuration under reaction conditions wherein we have 0.028% water and the balance of (1) (Table S 2.3-S 2.5 with calculations in Supporting Information). We predict that the most abundant 110 configuration has an 60%, H₂O* coverage of 20% and (1*) coverage of 20% (relative abundance of this configuration = 1). The most abundant 100 configuration was found to have an OH* coverage of 25%, H₂O* coverage of 50% and Al(*) coverage of 25%. Such high abundance (94%) of a slightly energetically unfavorable configuration was likely due to the very high concentration of (1) compared to water. The active sites on both of these surfaces are penta-coordinate as discussed previously.

2.3.3.2 Decarboxylation on γ -Al₂O₃: mechanism and microkinetic modeling

The decarboxylation of (1) on the 110 and 100 surfaces obtained from thermodynamic analysis was examined by carrying out DFT calculations. Figure 2.1 shows the Gibbs free energy change for the proposed mechanism (Scheme 2.3) with relevant structures on both surfaces. All of the reported energies are reference to an empty active site (*) and (1) in the gas phase. After adsorption, (1*) undergoes decarboxylation, forming the product diene (2), which is weakly physisorbed to the bound CO₂ ((2)—CO₂*). The surface bound CO₂* then desorbs, allowing (2) to adsorb on the surface. The bound surface species (2*) then desorbs regenerating the active site and completing the catalytic cycle.

The free energy diagram reported in Figure 2.1(A) indicate that it is much more favorable for the products that form as result of decarboxylation to desorb from surface than to react back and form (1), as the barrier for the microscopic reverse of decarboxylation is significantly higher than the energy for desorption. Therefore, the products preferentially desorb, making the decarboxylation of (1) irreversible and very likely the kinetically relevant step.

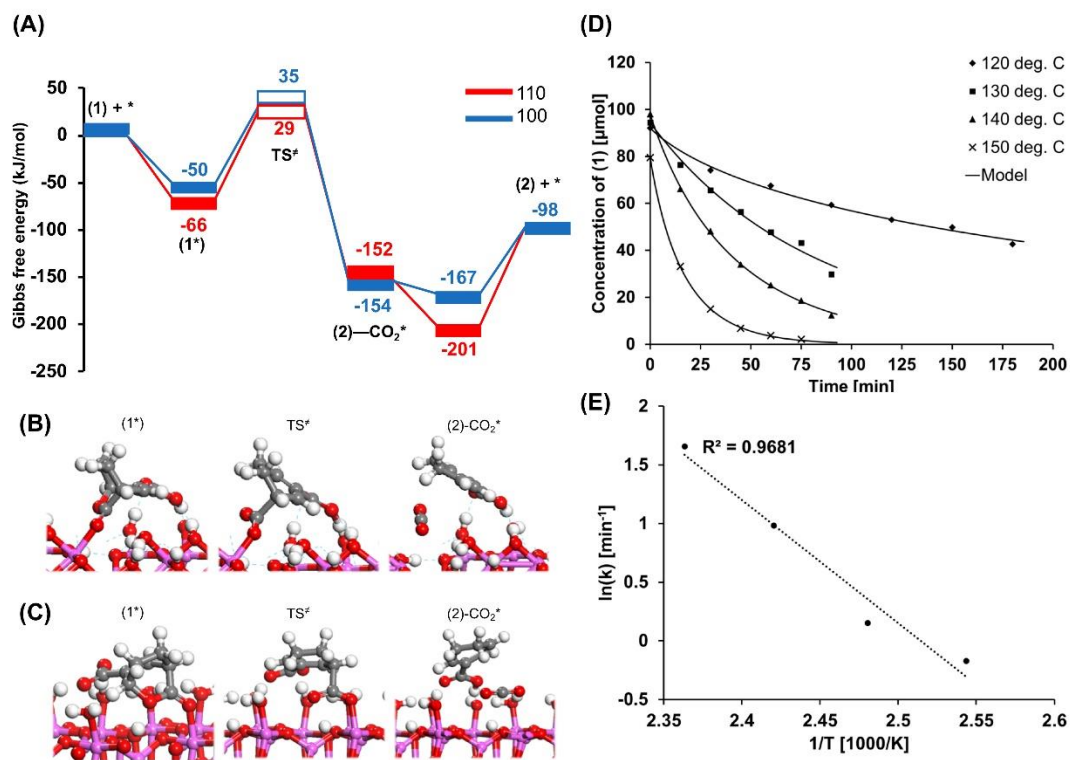


Figure 2.1(A) The individual Gibbs free energy changes for the elementary steps in the mechanism proposed in Scheme 2.3 (filled rectangles represent stationary states and unfilled rectangles represent transition states). **(B)** Decarboxylation reactant (1*), transition (#) and product ((2)-CO₂*) states 110 surface. **(C)** Decarboxylation reactant (1*), transition (#) and product states ((2)-CO₂*) on * on the 100 surface. **(D)** Concentration of (1) as a function of time: experiments vs the microkinetic model. **(E)** ln(k) vs time, where k is the intrinsic rate constant, k₂, associated with the scission of the C-C bond and elimination of CO₂

Assuming that the decarboxylation of (1*) is rate determining step and all others are quasi-equilibrated, we can derive Equation 2.1 (see Supporting Information):

$$r = \frac{K_1 k_2 [(1)]}{1 + K_1 [(1)] + \frac{[(2)][CO_2]}{K_4 K_3} + \frac{[(2)]}{K_4}} \quad (2.1)$$

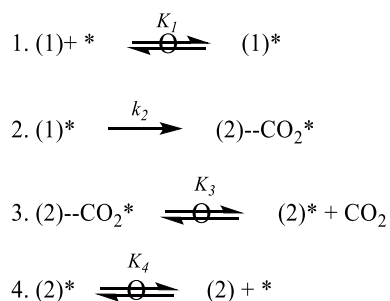
where k_2 , K_1 , K_3 and K_4 refer to the intrinsic rate constant for decarboxylation, the adsorption equilibrium constant for (1*), the equilibrium between the weakly physisorbed product diene (2*) and CO_2 and the equilibrium desorption constant for (2*)

Based on the free energy diagram (Figure 2.1), high surface coverages of (1*) and (2*) are expected due to the high Gibbs free energies of adsorption. Therefore, Equation 2.1 can be simplified as follows:

$$r = \frac{A[(1)]}{1 + B[(1)] + C[(2)]} \quad (2.2)$$

where, $A = K_1 k_2$, $B = K_1$ and $C = K_4^{-1}$. This rate expression was used to model the concentration profiles at different temperatures and resulted in a nearly perfect fit as shown in Figure 2.1(D). The values of parameters A, B and C are reported in the Table S 2.6

The initial activation barrier was calculated by assuming a high concentration of (1). As such the observed rate constant, $k_2 K_1 [(1)] / K_1 [A(1)]$, is equivalent to the intrinsic rate constant for decarboxylation, k_2 . An Arrhenius plot (Figure 2.1(E)) yields an initial activation barrier of 87 kJ/mol, which is in good agreement with the activation barrier determined from experimental data (108 kJ/mol, see Table S 2.1). On the free energy diagram, this barrier corresponds to the intrinsic barrier for the decarboxylation of (1*).



Scheme 2.3 Proposed elementary steps and mechanism for the decarboxylation of (1)

However, since only temperature was varied, this barrier needs to be compared with the enthalpy of activation. The enthalpic barriers for (1*) decarboxylation were calculated to be 96 kJ/mol and 85 kJ/mol on the 110 and 100 surfaces respectively, which are in good

agreement with the initial barrier resulting from microkinetic modeling (87 kJ/mol). Therefore, decarboxylation of (1) can be catalyzed via the retro Diels-Alder mechanism on Al_v sites on both 110 and 100 surfaces with the reaction being limited by the decarboxylation of surface bound (1*).

The experimental and theoretical results presented here on the thermal and Lewis acid catalyzed decarboxylation of 2 are very similar to those reported for the ring opening of triacetic acid lactone (TAL)⁸¹ and γ -valerolactone (GVL)¹¹¹ that readily undergo acid catalyzed decarboxylation as a result of the unsaturated bond at the C3-C4 position similar to the unsaturated C3=C4 bond in 2 which facilitates a direct retro Diels-Alder elimination of the CO₂ dienophile.

2.3.4 Characterization of (1) immobilized on γ -Al₂O₃ by HR-MAS NMR spectroscopy

To probe for interactions between the bicyclic lactone with the γ -Al₂O₃ surface in the condensed phase, ¹H, ¹³C and ²⁷Al HR-MAS NMR spectroscopy of γ -Al₂O₃ impregnated with a thin film (2 nm) of a solution of (1) in 1,4-dioxane-*d*₈ was performed. This new and unique NMR technique¹¹² allows the study of the interactions of probe molecules on solid catalyst surfaces (i.e. (1) on alumina) at the liquid-surface interface which provides additional information to guide DFT computations. As described below, the NMR experiments provide direct evidence that the surface is highly hydroxylated and that (1) is strongly adsorbed on the surface of γ -Al₂O₃.

Samples were prepared by first drying γ -Al₂O₃ at 120 °C to remove excess water. The dry γ -Al₂O₃ was then impregnated in a glovebox with liquid loadings of 1 μ L of solution per mg of γ -Al₂O₃ and the concentrations of (1) were 200 or 132 mg/mL in dioxane-*d*₈. A control sample impregnated with pure dioxane-*d*₈ was also prepared. All samples were packed into 2.5 mm zirconia rotors under the inert atmosphere. The results of the HR-MAS NMR spectroscopy experiments on the various impregnated alumina samples are summarized in Figure 2.2.

Rotor-synchronized ¹H spin echo solid-state NMR spectra of the different impregnated alumina samples are shown in Figure 2.2(A-C). The ¹H solid-state NMR spectrum of the alumina impregnated with dioxane-*d*₈ shows a broad underlying signal that covers a shift range of ca. 0 ppm to 10 ppm and three sharp ¹H NMR signals (Figure 2.2(C)). The sharp

signals are attributed to the residual protons of dioxane- d_8 ($\delta = 3.6$ ppm) and to mobile or dissolved water molecules and/or isolated/mobile alumina hydroxyl groups ($\delta = 1.3$ ppm and 0.9 ppm). Proton detected 2D ^{27}Al - ^1H D-RINEPT HETCOR spectra confirm that the broad NMR signal arises from the hydroxyl groups and/or water molecules that are immobilized on the surface of the alumina (see below).

The ^1H NMR spectrum of alumina impregnated with the 200 mg/mL solution of (1) in dioxane- d_8 shows several additional sharp ^1H NMR signals at the expected ^1H chemical shifts for (1) (Figure 2.2(A)). These narrow signals are attributed to (1) which is either dissolved in the dioxane- d_8 or is very weakly bound to the alumina surface and remains highly mobile. The narrow ^1H NMR signals arising from (1) are absent from the ^1H NMR spectrum of alumina impregnated with the solution of (1) at 132 mg/mL in dioxane- d_8 . Comparison of the ^1H NMR spectra of the alumina impregnated with the 132 mg/mL solution to the ^1H NMR spectrum of alumina impregnated with dioxane- d_8 alone shows that there are additional signals at higher chemical shifts of ca. 7.4 ppm and 5.6 ppm. The additional signals at higher chemical shifts and the absence of sharp ^1H NMR signals suggests that in the sample impregnated with the 132 mg/mL solution, all of the molecules of (1) are immobilized on the alumina surface.

To confirm that (1) was immobilized on alumina, proton detected $^1\text{H}\{^{13}\text{C}\}$ cross-polarization CP-HETCOR spectra were obtained. In this case, proton detection was employed to boost sensitivity and obtain the ^{13}C solid-state NMR spectra in a reasonable experimental time (less than 16 hours).^{113,114} A 2D $^1\text{H}\{^{13}\text{C}\}$ CP-HETCOR spectrum of alumina impregnated with a 200 mg/mL solution is shown in Figure 2.2(F). The ^{13}C dimension shows NMR signals at all of the chemical shifts expected for (1) and the ^1H dimension shows broad signals between 8 ppm and 3 ppm, consistent with the expected ^1H chemical shifts of (1). A CP experiment acts as a mobility filter since an NMR signal is only observable if the molecules are rigid. Additionally, broad ^1H NMR signals observed in the CP-HETCOR spectrum imply that the molecules of (1) are immobilized. Therefore, the 2D $^1\text{H}\{^{13}\text{C}\}$ CP-HETCOR spectrum confirms that a large fraction of (1) is bound to the alumina surface, which is consistent with the DFT results. Additional 2D $^1\text{H}\{^{13}\text{C}\}$ CP-HETCOR spectra are shown in Figure S 2.3.

Finally, proton detected 2D $^{27}\text{Al} \rightarrow ^1\text{H}$ D-RINEPT HETCOR experiments^{115,116} were used to obtain surface selective ^{27}Al solid-state NMR spectra (Figure S 2.4). ^1H chemical shifts associated with (1). All experiments were performed with a 25 kHz MAS frequency.

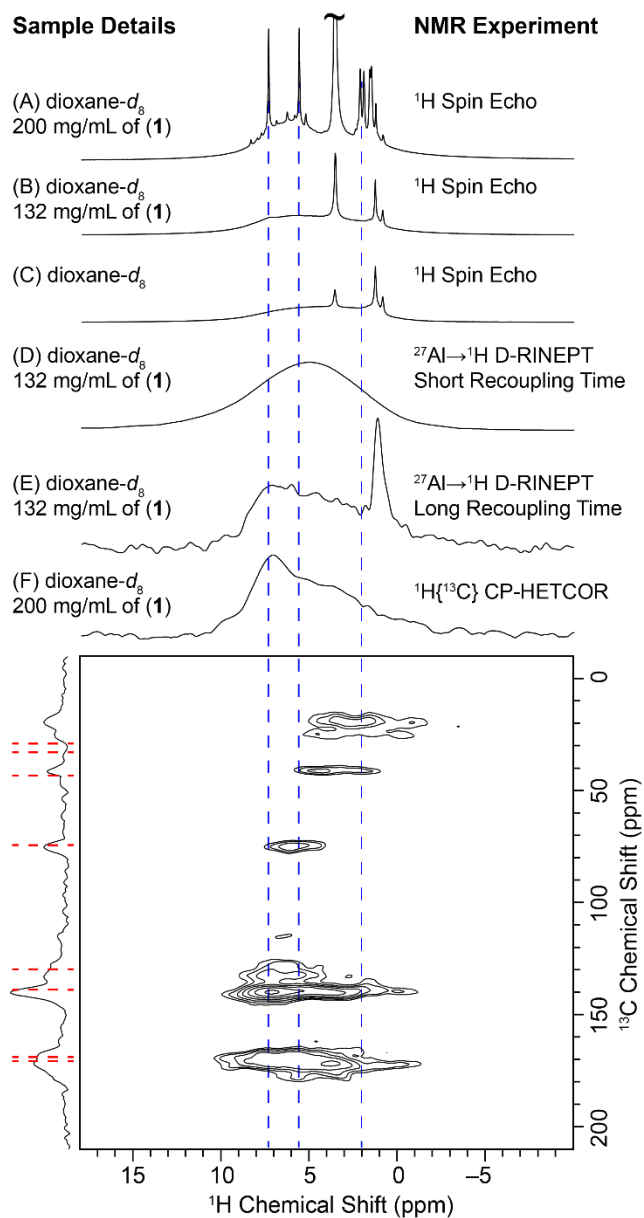


Figure 2.2 MAS ^1H solid-state NMR spectra of $\gamma\text{-Al}_2\text{O}_3$ impregnated with dioxane- d_8 solutions with different concentrations of (1). The sample is indicated next to each spectrum. (A-C) ^1H spin echo solid-state NMR spectra. (D) and (E) ^{27}Al filtered ^1H NMR spectra obtained from the positive projection of a 2D $^{27}\text{Al} \rightarrow ^1\text{H}$ D-RINEPT HETCOR spectra obtained with short and long dipolar recoupling times, respectively. (F) ^{13}C filtered ^1H NMR spectrum obtained from the positive projection of the 2D $^1\text{H}\{^{13}\text{C}\}$ HETCOR spectrum shown below. The ^{13}C chemical

shifts expected for (1) are indicated with red dashed lines. The blue dashed lines illustrate the similarity of the solution and solid-state

The ^1H NMR spectra obtained from 2D $^{27}\text{Al} \rightarrow ^1\text{H}$ D-RINEPT experiments acquired with long and short dipolar recoupling times are shown in Figure 2.2(D) and 2.2(E), respectively. The ^{27}Al filtered ^1H NMR spectrum obtained with a short recoupling time selectively probes the ^1H spins that are in close proximity to aluminum. This spectrum shows a very broad signal, which must represent the ^1H nuclei of the surface hydroxyl and adsorbed water molecules, consistent with previous surface selective ^{27}Al NMR experiments on hydrated alumina.^{123,124} This information of a highly hydroxylated $\gamma\text{-Al}_2\text{O}_3$ surface provide important insights to help guide the DFT calculations and benchmark their results. The ^{27}Al filtered ^1H NMR spectrum obtained with a longer recoupling time shows similar intensities and chemical shifts to those observed in the ^{13}C filtered ^1H NMR spectrum. Therefore, the spectrum obtained with a longer dipolar recoupling time suggests that the ^1H nuclei of (1) are proximate to ^{27}Al spins, consistent with adsorption of (1) to the alumina surface. At longer recoupling times, the surface bound species (1) strongly correlates to Al_{IV} and Al_{VI} sites of the alumina surface, while $^1\text{H}\text{-}^{27}\text{Al}$ correlation to Al_{V} sites is suppressed (see full 2D spectra in Figure S 2.4). The key knowledge of a strong surface bound species (1) existing is important to further support the DFT results. Additional solid-state NMR experiments are summarized in the Supporting Information.

In summary, HR-MAS and solid-state NMR spectroscopy is an excellent technique to investigate the $\gamma\text{-Al}_2\text{O}_3$ catalyst surface in the presence of probe molecules (e.g. bicyclic lactone (1)) and small amounts of water in the condensed phase (e.g. 1,4-dioxane- d_8). This unique technique provides key information about the degree of surface hydroxylation, the molecule-surface interaction and information about the catalytically active Al-species on the alumina surface. The results provide additional means to guide and compare computational studies with high level experimental detail of reactant/product molecules behavior at the solvent-catalyst interphase.

2.3.5 The impact of Brønsted acids on conversion

The impact of Brønsted acidity on the bicyclic lactone (1) was examined through reactions using a variety of Brønsted acid-containing catalytic materials. The use of Davisil silica gel (150 Å), a weakly acidic material,¹¹⁷ at 120 °C for 2 h, gave 16 mol% conversion of (1) to

(2) (Table 2.2, Entry 1) which was roughly a twofold increase in conversion compared to the control experiment without catalyst (Table 2.1, Control). The use of the more acidic ZSM-5 zeolite with a Si:Al ratio of 50:1 gave similar results with only minimal decarboxylation activity (Table 2.2, Entry 2). In fact, increasing the acid strength of ZSM-5 (Si:Al, 23:1) showed no improvement in the decarboxylation yield (Table 2.2, Entry 3). Interestingly, the mesoporous Y-zeolite (Si:Al, 30:1), demonstrated enhanced reactivity and consumed all the bicyclic lactone (1) yielding 53 mol% DIH (2), 35 mol% isophthalic acid intermediate (5) and 13mol% isophthalic acid (6) (Table 2.2, Entry 4). Given this result, it appeared that the larger pores of the Y-zeolite structure provide enhanced accessibility of the bulky lactone (1). Since Y-zeolite contains both Lewis¹¹⁸ and Brønsted acid¹¹⁹ sites, it was unclear as to which site was responsible for ring-opening or if a synergistic effect was operative.

Table 2.2 Bicyclic lactone (1) conversion in the presence of Brønsted acids

Entry	Catalyst	(1) Conv. [mol%]	(2) Yield [mol%]	(3) Yield [mol%]	(4) Yield [mol%]	(5) Yield [mol%]	(6) Yield [mol%]	By- products [mol%]
1	Davisil (150 Å)	16	15	<2	-	-	-	-
2	ZSM-5 (CBV5524G)	12	8	<3	-	-	-	<2
3	ZSM-5 (CBV2314)	7	5	<2	-	-	-	<1
4	Y-Zeolite (CBV720)	100	53	<2	-	35	13	-
5	Amberlyst 45	51	13	<2	12	13	-	<11
6	Amberlyst 45 ^a	90	14	<2	32	39	<4	<2

Conditions: Reaction time 2 h, reaction temperature 120 °C, stirring rate 500 rpm, starting concentration 71.38 μmol/mL, reaction volume 4 mL, solvent 1,4-dioxane, 25 mg catalyst. ^a 50 mg catalyst+40 uL D₂O.

To decouple the roles of Lewis and Brønsted acid sites, a series of experiments were performed using the heterogeneous Brønsted acid-only catalyst, Amberlyst 45.¹²⁰ The experimental results shown in Table 2.2, Entries 5 and 6 demonstrate that Brønsted acid sites promote ring-opening of the lactone bridge forming the intermediate 6-hydroxycyclohex-1-ene-1,3- dicarboxylic acid (4) followed by acid catalyzed dehydration to an isophthalic acid intermediate (5) (Figure 2.3(A)). Doubling the amount of catalyst and

adding small amounts of water to the polar aprotic solvent 1,4-dioxane dramatically enhanced the acid catalyzed ring-opening with increased conversion and yield towards intermediate (4) and product (5) (Table 2.2, Entry 6). This is consistent with results reported by Chia et al.⁸¹ which show that the addition of Brønsted acids and water facilitate the ring opening, hydrolysis and dehydration of triacetic acid lactone.

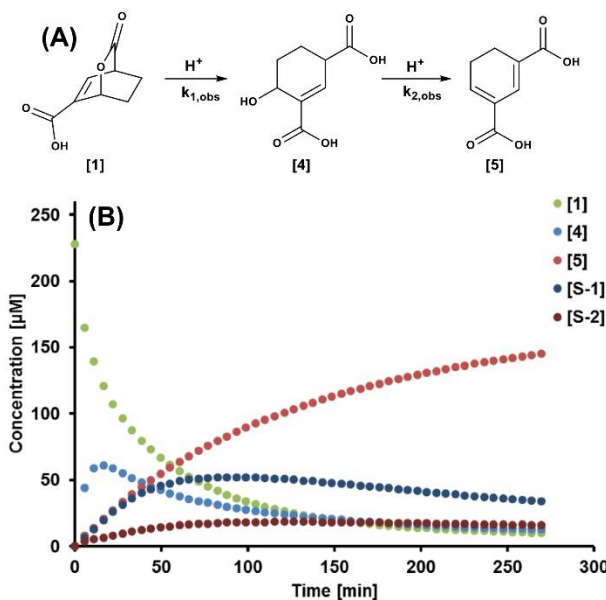


Figure 2.3(A) Reaction scheme of the proposed acid catalyzed ring-opening/dehydration reaction sequence. **(B)** Concentration profile of the conversion of bicyclic lactone (1) to (4) followed by conversion of (4) to (5). (S-1) and (S-2) are formed throughout the reaction and are of unknown origin.

A series of in situ ¹H solution NMR experiments were performed to gain a better understanding as to why Brønsted acid sites led to the formation of (4) and (5). In the experiments, the bicyclic lactone (1) was exposed to the fully deuterated sulfuric acid-*d*₂ and heat using dioxane-*d*₈ to mediate the reaction. These experiments serve as an ideal model to understand the reaction mechanism of the Brønsted acid catalyzed ring-opening reaction that can be potentially further applied to other bicyclic lactone systems. In this set of experiments, 5 μL (0.089 μmol) of D₂SO₄ was added to 300 μL of a 71.38 μmol/mL solution of (1) in fully deuterated dioxane-*d*₈, transferred to high pressure NMR tubes and heated to the desired reaction temperature (80-110 °C) inside the NMR spectrometer (Figure S 2.7).

The experimental results revealed that the rate of consumption of (1) did not match the rate of formation of (5) at all temperatures tested. The reason for this observation was the formation of the reactive intermediate (4) and species (S-1) and (S-2) on the pathway to (5). Species (4) is likely formed through acid-catalyzed hydrolysis of the lactone bridge of (1) (Figure 2.3(A)). The concentration profile in Figure 2.3(B) further suggests that the initial formation of (4) was then followed by acid-catalyzed dehydration of (4) to (5) as evident from the increasing concentration of (5) accompanied with a decrease in (4). Clearly, the mechanism involved in the formation of (5) from (1) is more complicated given the formation of unknowns (S-1) and (S-2).

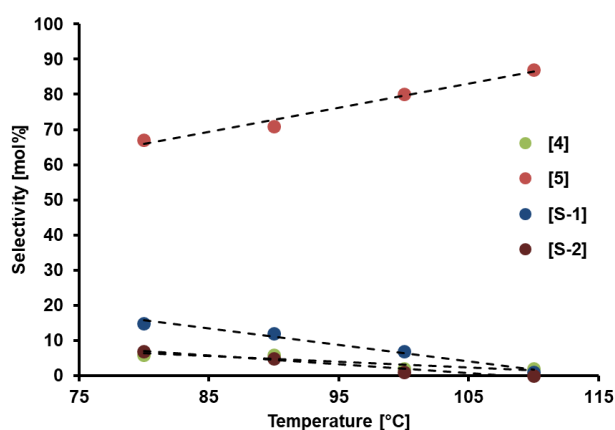


Figure 2.4 Selectivity trend of intermediates and products from acid catalyzed ring-opening/dehydration of bicyclic lactone (1).

With increased reaction temperature (4), (S-1) and (S-2) vanished while the concentration of (5) increased, so it appears that (S-1) and (S-2) are intermediates on the pathway from (1) to (5). This selectivity relationship is apparent in Figure 2.4 since the formation of (5) increases linearly as a function of reaction temperature, whereas a linear downward trend is seen for (4), (S-1), and (S-2). After reaction for 4 h and 35 min at 110 °C there was a significant amount of (5) (87 mol%), with only 2 mol% of intermediate (4) and less than 5 mol% of (S-1) and (S-2) remaining (Table S 2.8). From NMR analysis of the product solution, (S-1) and (S-2) are likely isomers of (4) given the similar proton shifts and NMR correlations. It is known that lactones are able to undergo different hydrolysis pathways (e.g., unimolecular and bimolecular) in acidic media,¹²¹ which could explain the observation of species (S-1) and (S-2). Structural identification of (S-1) and (S-2), however, is beyond the scope of this work and will be a subject of further investigation.

The Brønsted acid catalyzed ring-opening/dehydration sequence provides general guidance for the conversion of (1) and can potentially be applied to similar bicyclic lactone systems. In this particular case, we were able to access the isophthalic acid intermediate (5) in high selectivity, which cannot be easily obtained via conventional petroleum routes. Catalytic dehydrogenation of this molecule provides isophthalic acid, a bulk chemical currently manufactured in the petrochemical industry and used in applications ranging from unsaturated polyester and specialty resins¹²² to metal organic polyhedral crystals (MOPs) which are potentially useful for drug-delivery, catalysts, sensing and gas storage.¹²³

2.3.6 Solvent impact on the conversion of (1)

Lactones such as CMA degrade in the presence of water due to nucleophilic attack and consequent ring-opening, which renders the diene ineffective for Diels-Alder chemistry.^{31,104} This degradation was also observed by Chia et al. showing that the molecular integrity of the 2-pyrone triacetic acid lactone (TAL) was significantly compromised in the presence of water but was stable in polar aprotic solvents such as tetrahydrofuran (THF).⁸¹

To investigate whether the bicyclic lactone (1) can be ring-opened to (5) via catalyst-free, water-mediated hydrolysis of the lactone bridge, experiments were performed in D₂O. For the reactions, the sodium salt of the bicyclic intermediate (1) was heated in D₂O, and the reaction progress monitored via in situ ¹H-NMR. The sodium salt of (1) was required to overcome solubility limitations in D₂O and to improve the resolution of the ¹H-NMR spectra for subsequent analysis.

Surprisingly, when the consumption of (1) was monitored over time, decarboxylation occurred rather than ring-opening. Additional kinetic experiments were carried out at temperatures in the range of 50 to 90 °C along with DFT calculations to obtain further insights into the water-mediated decarboxylation mechanism.

Figure 2.5(C) shows an example of the concentration profiles for the water-mediated decarboxylation of (1) to (2). Plots of $\ln([1]_0/[1]_t)$ over time for all temperatures tested displayed linear relationships, (Figure S 2.8) indicating a first order reaction with respect to (1). Since (2) was obtained in high yield and selectivity with no formation of CMA, the retro Diels-Alder reaction of (1) to CMA was absent, meaning the observed

decarboxylation rate constants k_{obs} (Table S 2.10) are solely for the conversion of (1) to (2). The activation energy of the water-mediated decarboxylation was calculated using the Arrhenius plot shown in Figure 2.5(B). The experimentally obtained activation barrier was 107.2 kJ/mol. This value is significantly lower than for decarboxylation in the polar aprotic solvent dioxane- d_6 (142 kJ/mol),¹⁰⁴ which explains the enhanced decarboxylation activity at moderate temperatures.

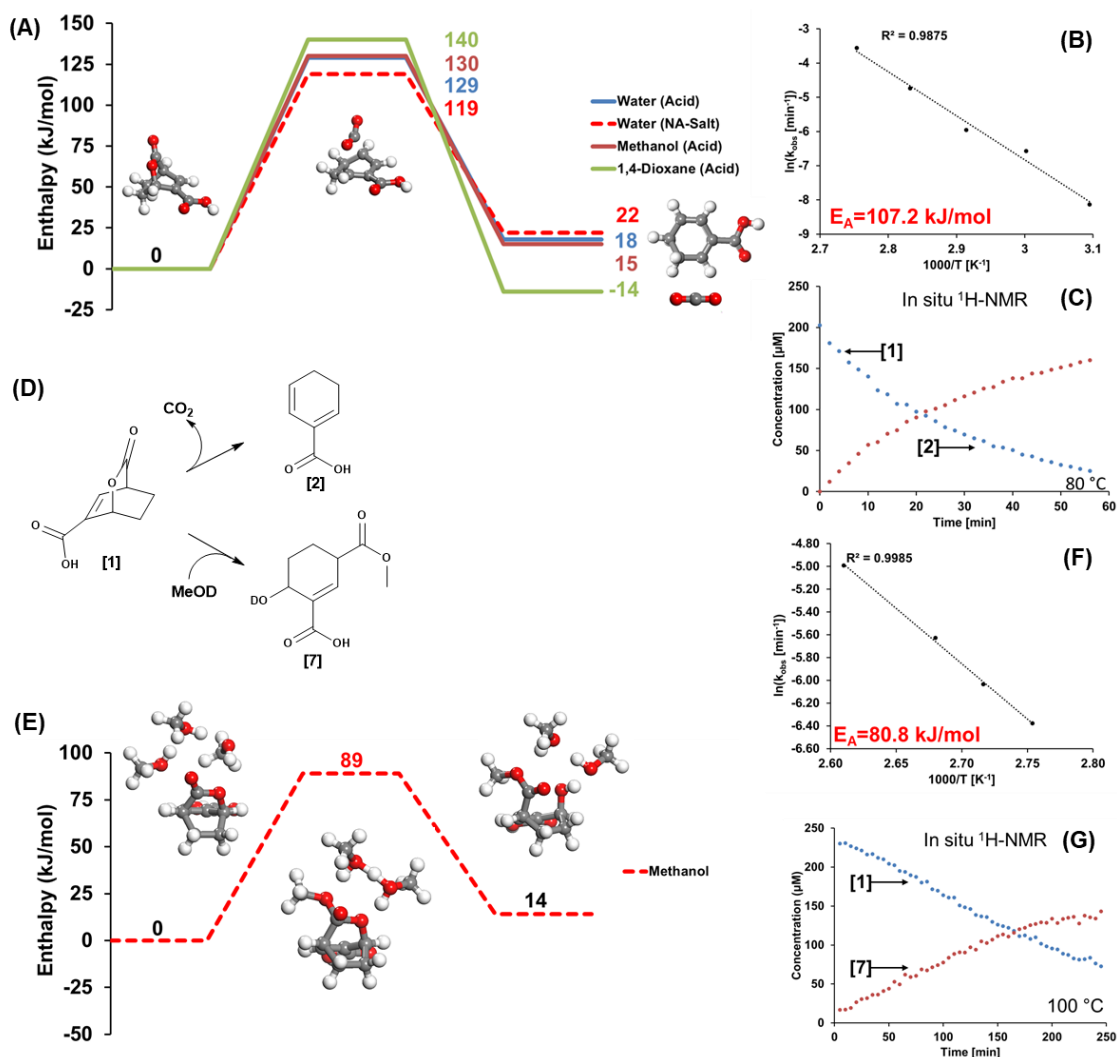


Figure 2.5(A) DFT calculated enthalpy diagram for the bicyclic lactone decarboxylation reaction using polar protic and aprotic solvents. **(B)** Experimental Arrhenius plot for the water mediated catalyst-free decarboxylation of the bicyclic lactone sodium salt (1). **(C)** In situ $^1\text{H-NMR}$ concentration profile of the consumption of sodium salt of (1) and the formation of (2) as a function of time. **(D)** Bicyclic lactone diversification in the absence of catalyst using the polar protic solvents water for decarboxylation and methanol for ring-opening. **(E)**

DFT calculated enthalpy diagram for the methanol mediated ring-opening of (1). (F) Experimental Arrhenius plot for the methanol mediated catalyst-free ring-opening of (1). (G) In situ ¹H-NMR concentration profile of the consumption of (1) and the formation of (7) as a function of time.

DFT predicts an enthalpic decarboxylation barrier of the bicyclic lactone (1) sodium salt of 119 kJ/mol in close agreement with experimental results. Additionally, the Gibbs free energy barrier for decarboxylation was calculated to be 116 kJ/mol, which is favored over the water mediated ring-opening of the lactone bridge which has a barrier of 121 kJ/mol. Moreover, the decarboxylation product was found to be thermodynamically favored over the ring-opened product because the system gains entropy through the loss of CO₂ in the former case. This makes decarboxylation both thermodynamically and kinetically favored over ring-opening in water, which explains the experimental results in water (see Figure S 2.9 for the Gibbs free energy profiles). The strong hydrogen bonding with water molecules in the bulk makes water a weak nucleophile, limiting the addition of water to the lactone which prevents ring opening. Although the acid form of (1) resulted in a slightly higher calculated enthalpic activation barrier of 130 kJ/mol, the decarboxylation of (1) to (2) remains favored in water as compared to the polar aprotic solvent 1,4-dioxane in the absence of catalyst (Figure 2.5(A)). This rate enhancement in water is due to stabilization of the charge separated transition state on the pathway from (1) to (2), which is preferentially stabilized by polar protic solvents such as water.

Anticipating broad applicability of polar protic solvents to enhance bicyclic lactone decarboxylation, we also performed reactions of (1) in methanol. Methanol is an ideal model solvent as it provides excellent solubility of (1) through which the neutralization step of (1) to the sodium salt can be prevented. Experimental results showed that (1) in the presence of methanol afforded ring-opening of the lactone bridge to give the novel species (7) in high selectivity as confirmed by 2D NMR experiments in combination with UPLC-QDa mass analysis (see Supporting Information). Several selected ¹H-NMR spectra of the in-situ conversion of (1) to (7) are displayed in Figure 2.6. These fully resolved spectra make the identification and quantification of the reactant and product unambiguous with carbon balances >99 mol%. This interesting and unexpected result was further investigated through in situ NMR kinetic investigation and DFT calculations to obtain kinetic parameters and mechanistic insight as to why methanol caused (1) to enter this new pathway.

NMR kinetics were carried out within the temperature range of 90-110 °C. The reactions were conducted in neat methanol- d_4 . The consumption of (1) followed a pseudo-first order reaction. A typical concentration profile of (1) in methanol- d_4 is displayed in Figure 2.5(G). Plots of $\ln([1]_0/[1]_t)$ with respect to time show linear relationships for all temperatures tested (Figure S 2.10), validating our assumption of a pseudo-first order reaction. These plots were then used to extract the observed rate constants (Table S 2.11) and calculate the apparent activation barrier for the methanol induced ring-opening (Figure 2.5(F)).

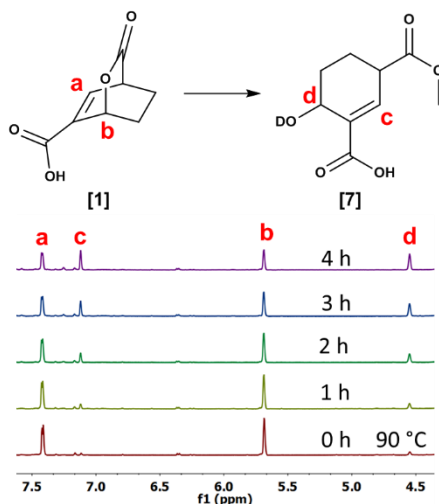


Figure 2.6 Selected $^1\text{H-NMR}$ spectra of the bicyclic lactone (1) ring-opening in methanol- d_4 .

An activation barrier of 80.8 kJ/mol was calculated using the Arrhenius plot in Figure 2.5(F). The experimental data and structures were used to compare with DFT results for the methanolysis of the lactone bridge of (1). The DFT-calculated enthalpic activation barrier of 89 kJ/mol agrees rather well with the experimentally measured activation barrier of 80.8 kJ/mol. The barrier for the ring-opening and methanolysis of (1) is approximately 40 kJ/mol lower than that for direct decarboxylation of (1) (129 kJ/mol) which explains the preference for ring-opening and methanolysis over decarboxylation for reactions carried out in methanol (Figure 2.5(A)).

Table 2.3 CMA conversion to benzoic acid

Entry	CMA conv. [mol%]	(1) Sel. [mol%]	(2) Sel. [mol%]	(3) Sel. [mol%]
1 ^a	89.6	-	-	99.7 ^d
2 ^b	100	53.9 ^c	-	46.1 ^d

Conditions: CMA 300 mg, 1,4-dioxane 30 mL, temperature 140 °C, time 4 h, catalyst ^a200 mg 1wt% Pd/ γ -Al₂O₃, ^b20 mg 10wt% Pd/C. ^cNo other by-products detected via UPLC-QDa (ESI). ^dQuantified via UPLC-QDa (ESI).

The computational results further suggest that methanol is a better nucleophile than water, likely because water forms a strong hydrogen bonding network and results in decarboxylation rather than hydrolysis of (1). Similar to water, methanol stabilizes the transition state and promotes proton shuttling, providing a low energy path from (1) to (7). This pathway grants access to the selective formation of the new novel species (7) (> 95 mol%) using low temperatures and a low boiling solvent in the absence of a catalyst, which provides an attractive and environmentally benign diversification path of the renewable coumalate platform.

2.3.7 Broader Implications

DIH (2) is a precursor of the bulk chemical benzoic acid which is currently manufactured via conventional petroleum routes based on toluene. We recently presented a new route to benzoic acid with ~90 mol% selectivity at 100 mol% CMA conversion.¹⁰⁴ The 10 mol% loss in selectivity was attributed to by-product formation from the high reaction temperature (180 °C) needed to overcome the rate limiting decarboxylation step. The catalyst used to convert (2) to (3) was a commercial 10 wt% Pd/C catalyst. With the goal of further increasing the selectivity and improving the overall process, we utilized a bifunctional 1 wt% Pd/ γ -Al₂O₃ catalyst to perform the reaction of CMA and ethylene to benzoic acid (BA) at milder reaction conditions. This lower temperature was possible because of the increased decarboxylation activity of bicyclic lactones in the presence of γ -Al₂O₃.

Experimental results are provided in Table 2.3, with Entry 1 showing that the benzoic acid selectivity was further increased to > 99 mol% at reduced temperatures (140 °C) with a reaction time of 4 h. The base Pd/C catalyst, on the contrary, only gave a selectivity of 46.1 mol% towards (3) at 100 mol% conversion (Table 2.3, Entry 2). The remaining 53.9 mol% were attributed to (1) as no other by-products were detected via UPLC-QDa analysis. Given the high selectivity of BA, this concept might be broadly applicable when aromatics from 2-pyrone in conjunction with an array of dienophiles are envisioned.

2.4 Conclusions

The combination of experimental kinetic analyses, DFT calculations and MAS solid-state NMR provided mechanistic insights into the decarboxylation of the 2-pyrone derived bicyclic molecule (1). Lewis acid sites on the γ -Al₂O₃ act as catalytically active sites that significantly lower the decarboxylation activation barrier, providing access to DIH (2) in high selectivity. The strong adsorption of the bicyclic lactone species on the surface provides a driving force for its catalytic decarboxylation. The immobilization of (1) was predicted with DFT computations and experimentally confirmed with MAS solid-state NMR experiments.

The in-depth catalytic investigation presented here provides guidance to tailor a bifunctional 1 wt% Pd/ γ -Al₂O₃ catalyst that enables access to the aromatic drop-in replacement benzoic acid (BA) with significantly improved selectivity starting from the 2-pyrone coumalic acid reaction with ethylene. Given previous literature reports of aromatics synthesized from 2-pyrones in an analogous fashion, we believe that this catalyst can be broadly applied to these systems allowing the production of aromatics at optimized reaction conditions.

We further investigated the impact of Brønsted acid catalysts on the conversion of (1) and showed through kinetic studies that a ring-opening/dehydrogenation sequence yielded a novel isophthalic acid precursor (5) in high selectivity. Since isophthalic acid is a bulk chemical in the chemical industry, this route provides a renewable alternative.

Finally, the impact of polar protic solvents on the conversion of (1) was explored, through which highly selective, catalyst free pathways of (1) to novel species (2) and (5) were identified. The decarboxylation of the sodium salt of species (1) was mediated in the polar protic solvent, revealing a significantly reduced decarboxylation barrier compared to that of 1,4-dioxane. The nucleophilic solvent methanol induced ring-opening of the lactone bridge through methanolysis providing an additional diversification path of (1) to a new novel species (7) in high selectivity.

The results presented herein outline a diversification platform starting from renewable coumalic acid in conjunction with a single dienophile (ethylene) that allows highly selective access to a variety of novel molecules with unique functionality which are of potential interest for new materials. As such, this technological approach can be leveraged to other

bicyclic lactones to form a plethora of new and interesting molecules that cannot be easily accessed via conventional petroleum-based routes.

2.5 Methods and Materials

2.5.1 Reagents and Materials

Pd(II)-, Cu(II)-, Ce(III)-, Zn(II)-acetate (>99.9 %), coumalic acid (>97 %), 10 wt% Pd/C, sulfuric acid- d_2 (96-98 wt%, 99.5 atom % D), D_2O (99.9 atom % D) and Davisil (Silica Gel, 150 Å, >99 %) were obtained from Sigma Aldrich. DMSO- d_6 (99.9 %), dioxane- d_8 (99 %), methanol- d_4 (99.8 %) were obtained from Cambridge Isotope Laboratories Inc. Dimethylformamid (99.9 %), 1,4-dioxane (99.9 %) and sodium bicarbonate (> 99.7 %) were obtained from Fisher Scientific. Methyl coumalate (Acros Organics, 98 %). Ethylene (99.5 %, Matheson). Zeolites ZSM-5 (CBV5524G), Y-Zeolite (CBV 720), and ZSM-5 (CBV2314), were obtained from Zeolyst International in very high purity (100 wt%), $\gamma-Al_2O_3$ (Strem Chemicals, Inc., >99.8 %), Amberlyst 45 (Dow >98%). All chemicals were used without further purification.

2.5.2 Catalyst Preparation

The 5 wt% metal catalysts were prepared via incipient wetness impregnation using $\gamma-Al_2O_3$, and the respective metal acetate salts of Cu, Fe, Zn, and Ce, dried at 65 °C (24 h) and calcined at 450 °C (6 h) in a steady flow (200 mL/min) of air.

2.5.3 Batch Reaction Experiments

The Diels-Alder product (1) was obtained from batch reactions at 110 °C for 16 h using a 50 mL 4590 Parr reactor setup. Mechanical agitation was maintained at 400 rpm using a magnet-driven stirrer. 300 mg of CMA was placed into the reactor vessel and 30 mL of 1,4-dioxane was added to mediate the reaction, resulting in a starting concentration of 71.38 $\mu\text{mol/mL}$. After the reactor was sealed, the reactor was purged five times to replace residual air with nitrogen. Next, the reactor was charged for 30 min with 500 psig ethylene to ensure saturation of ethylene in the solvent. Under these conditions the reactions were performed in large excess of ethylene. After charging the vessel with ethylene, the reactor was heated to the desired reaction temperature using a controlled heating ramp of 10 K/min. After completion of the reaction, the reactor vessel was purged to replace

unreacted ethylene with nitrogen. A sample was withdrawn, and the solvent was carefully evaporated with dry air before 600 μL fully deuterated solvent ($\text{DMSO-}d_6$) and 2.5 μL internal standard (DMF) were added. Finally, the samples were analyzed via $^1\text{H-NMR}$.

Batch reactions for the catalyst screening experiments were performed in 10 mL thick-walled glass vial reactors (Alltech) equipped with magnetic stir bars. Agitation and heat were provided using a temperature-controlled oil-bath that was regulated with an Isotemp Digital Plate Stirrer from Fisher Scientific. The glass vial reactor was loaded with 4 mL of a 71.38 $\mu\text{mol/mL}$ solution of (1) in 1,4-dioxane. 25 mg of catalyst was added before the vial was sealed and placed into the hot oil bath to initiate the reaction. After the reaction was completed, the product was filtered through a 0.2 micron syringe filter to remove the catalyst from the products. A sample was then taken and the solvent was removed via careful evaporation. Fully deuterated $\text{DMSO-}d_6$ (600 μL) and 2.5 μL of internal standard DMF (Dimethylformamid) were added to the crude material for quantification via $^1\text{H-NMR}$.

The $\gamma\text{-Al}_2\text{O}_3$ catalyzed decarboxylation reactions were carried out in a 50 ml 4590 Parr reactor. The vessel was charged with 30 mL of a 71.36 $\mu\text{mol/mL}$ solution containing (1). 200 mg of the $\gamma\text{-Al}_2\text{O}_3$ catalyst ($\sim 53 \mu\text{m}$ particle size) was added before the reactor was sealed and purged 5 times with nitrogen to remove residual air while agitation was applied (400 rpm). Next, the respective reaction temperature was obtained using a controlled heat ramp of 10 K/min. After the reactor reached the desired temperature a sample was withdrawn as a reference using a high-pressure sampling dip tube. Further samples were withdrawn periodically to obtain a concentration profile over time. After the reaction was completed, all samples were filtered via a 0.2 micron syringe filter and the solvent was carefully evaporated with dry air before 600 μL deuterated solvent ($\text{DMSO-}d_6$) and 2.5 μL internal standard DMF were administered. The samples were then analyzed via $^1\text{H-NMR}$.

2.5.4 In situ NMR Experiments

The general procedure for the in situ kinetic measurements was performed using high-pressure NMR tubes from Wilmad-Labglass. The solvents used for the decarboxylation and ring-opening experiments were D_2O , dioxane- d_8 , and methanol- d_4 , respectively. As aforementioned, reactant (1) for this study was synthesized via Diels-Alder reaction of CMA and ethylene in 1,4-dioxane at 110 $^\circ\text{C}$ and 16 h, with a high yield ($>98\%$). Through careful evaporation of the solvent using dry air, the reaction product (1) was obtained and

subsequently dissolved in the respective deuterated solvent. The solution was then transferred into the high-pressure NMR tubes. The tubes were placed into the Bruker Avance III 600 MHz spectrometer and heated to the respective temperature to initiate the reaction. The progress of the reaction was subsequently monitored over time.

The water-mediated decarboxylation of the sodium salt of the bicyclic lactone (1) was performed in D₂O at temperatures in the range of 50-90 °C. 50 mg of the reactant (1) was dissolved in 1 mL of D₂O (263.16 μmol/mL). The sodium salt of (1) was synthesized via neutralization using sodium bicarbonate.

The methanol-*d*₄-mediated reactions were performed in a temperature range of 90-110 °C using 71.38 μmol of (1) that was dissolved in 300 μL (237.93 μmol/mL) of methanol-*d*₄.

The ring-opening reactions in 1,4-dioxane using D₂SO₄ as a catalyst were performed in a temperature range of 70-110 °C. 71.38 μmol of (1) was dissolved in 300 μL (237.93 μmol/mL) dioxane-*d*₈ and 5 μL of D₂SO₄ were added to catalyze the reaction.

To elucidate the reaction network, all compounds were verified via NMR structural assignments performed using different techniques including ¹H-NMR, ¹H-¹H COSY, ¹³C-¹H HSQC and validated using UPLC-QDa (ESI) mass analysis.

2.5.5 Analytical methods

The batch reaction solution products were analyzed via NMR using a Bruker spectrometer equipped with a 14.1 Tesla superconducting magnet. The data were acquired and processed using TOPSPIN (version 3.0) and Mestre Nova (version 10.0.1-14719), respectively. NMR samples were prepared using fully deuterated solvents, to both reduce the solvent background and to perform field calibration. Additionally, a 2.5 uL DMF internal standard was added for quantification. All ¹H spectra were acquired using a recycle delay of 3.0 sec. and 30° ¹H excitation pulse lengths. ¹H-¹H 2D NMR spectra were acquired using a COSY pulse sequence, and ¹³C-¹H 2D NMR spectra were acquired using a HSQC pulse sequence.

Ultra-pressure liquid chromatography (UPLC) was also applied to analyze known species in the reaction products and to obtain the amount of each compound. A Waters Acquity H-Class System equipped with a Photodiode Array (PDA) and a QDa mass detector was

used to perform the analysis. UPLC separation was carried out on a Waters BEH Phenyl column (2.1x100 mm, 1.7 μm particles).

The samples for HR-MAS/solid-state NMR experiments were prepared by first drying $\gamma\text{-Al}_2\text{O}_3$ overnight at 120 $^\circ\text{C}$ in a convection oven to remove residual adsorbed water. Next, 30 mg $\gamma\text{-Al}_2\text{O}_3$ was weighed into a 2 mL polypropylene screwcap vial and then transferred into the glovebox. The vials were allowed to sit with the cap removed in the glovebox for 48 h prior to impregnation. Samples were impregnated with a liquid loading of 1 $\mu\text{L}/\text{mg}$ and allowed to equilibrate overnight with the cap on. Following impregnation, the samples were then packed into 2.5 mm rotors inside the glove box to prevent excess moisture from being introduced.

All solid-state NMR experiments were performed on a 9.4 T (400 MHz) Bruker Avance III HD NMR spectrometer with a 2.5 mm HXY triple resonance probe. A 25 kHz MAS frequency was used for all experiments. ^1H solid-state NMR spectra were obtained with a rotor synchronized spin echo pulse sequence. Proton detected 2D $^{27}\text{Al}\rightarrow^1\text{H}$ D-RINEPT HETCOR spectra were obtained using the previously described D-RINEPT pulse sequence.^{115,116} The symmetry based recoupling sequence supercycled (S) $R4_1^2$ was used for dipolar recoupling.¹²⁴ Proton detected 2D $^1\text{H}\{^{13}\text{C}\}$ CP-HETCOR spectra were obtained with the previously described pulse sequence.^{113,114} The contact time for the $^1\text{H}\rightarrow^{13}\text{C}$ forwards CP transfer was 2000 μs and different 2D spectra were obtained with contact times of 200 μs , 500 μs and 2000 μs for the $^{13}\text{C}\rightarrow^1\text{H}$ backwards CP transfer. CP was performed with a ^{13}C spin lock pulse with an RF field of ca. 91 kHz and a ^1H spin lock pulse with a nominal RF field of ca. 68 kHz. The amplitude of the ^1H spin lock pulses was linearly ramped from 85% to 100% RF field to broaden the CP match conditions.¹²⁵ In both the ^{13}C and ^{27}Al NMR experiments SPINAL-64 ^1H heteronuclear decoupling¹²⁶ was performed during the indirect dimension evolution period with a 100 kHz RF field. Details on acquisition parameters for the 2D spectra (number of scans, indirect dimension points, etc.) are described in the Figure captions.

2.5.6 Computational

2.5.6.1 Periodic density functional theory

All of the calculations carried out on model γ -Al₂O₃ surfaces were carried out using periodic plane-wave density functional theory methods as implemented in the Vienna ab initio simulation package (VASP).^{127–130} The PBE functional¹³¹ was used to calculate exchange and correlation energies. The D3 method¹³² was used to estimate the dispersive interactions. A plane-wave energy cutoff of 396 eV was used for all periodic calculations reported herein. Optimizations were performed in two steps. First, wave-functions were converged to within 10⁻⁴ eV, until the maximum force upon each atom was less than 0.1 eV/Å. In step two, wave-functions were converged to within 10⁻⁶ eV, with maximum allowable force upon each atom less than 0.05 eV/Å. Step two calculations were carried out spin-polarized and monopole/dipole moments were calculated to correct for energies. Transition states were obtained using the nudged elastic band method^{133,134} and the dimer method.¹³⁵ Calculations were performed on 1x1 unit cells of 110 and 2x1 unit cells of 100 surfaces of γ - Al₂O₃. The bulk structure of γ - Al₂O₃ reported elsewhere was used.¹³⁶ For hydroxylated surfaces, structures found by Sautet and co-workers were used.^{109,136} For 110 surfaces, the periodic slab models consisted of 8 layers (Al:O = 3:2) separated by vacuum with bottom two layers frozen to bulk position. While for the 100 surfaces, 4 layers (Al:O = 3:2) were modeled with the bottom two layers frozen to bulk positions. Optimizations on the 1x1 unit cells of 110 surfaces were performed on a 3x3x1 k¹³⁷ point mesh while a k point mesh of 2x2x1 was used for the 2x1 unit cells of 100 surfaces.

The entropies of adsorbed molecules were estimated by equations 2.3 and 2.4, where S_{ad}^o(T) is the entropy of adsorbed molecule and S_{gas}^o(T) is the ideal gas entropy of that molecule. These values roughly correspond to the loss of 1/3rd entropy of the molecules in the gas phase.¹³⁸

$$S_{ad}^o(T) = 0.70 \times S_{gas}^o(T) - 3.3R, \text{ for } S_{gas}^o(T) < 60 R \quad (2.3)$$

$$S_{ad}^o(T) = 0.99 \times S_{gas}^o(T) - 20.7R, \text{ for } S_{gas}^o(T) > 60 R \quad (2.4)$$

As an approximation, the entropy of a weakly physisorbed molecule was estimated by subtracting just the 1/3rd transitional component. Since, the transition state for

decarboxylation was in close resemblance to the reactant state, the entropy of activation was assumed to be negligible.

2.5.6.2 Molecular density functional theory

Molecular density functional theory calculations were performed using the M062X⁸⁸ hybrid functional as implemented in Gaussian 09.⁹⁰ 6-311G+(d,p) basis set⁹¹ on an ultrafine grid and tight convergence criterion for force (RMS force within 10^{-5} Hartree/Å, maximum force within 1.5×10^{-5} Hartree/Å, and maximum displacement within 6×10^{-5} Å) was used for all stationary and saddle point calculations. The SMD solvation model⁹² was used to implicitly model the effect of solvation. In cases where the solvent directly participated in reaction, explicit solvent molecules were used in conjunction with implicit solvation. Enthalpies and Gibbs free energies were calculated at standard state and 298.15 K within Gaussian 09. A correction factor of $RT \ln(24.46)$ was added to the free energies of species having standard concentration of 1 M. While for bulk solvents, (water and methanol), corrections corresponding to 55.5 M for water and 24.9 M for methanol were applied.

2.6 Acknowledgments

We gratefully acknowledge funding from the National Science Foundation under Award EEC-0813570, the Iowa State University Chemical Instrument Facility staff members, computational support from the Minnesota Supercomputing Institute (MSI) at the University of Minnesota and the Molecular Science Computing Facility (MSCF) in the William R. Wiley Environmental Molecular Sciences Laboratory, a national scientific user facility sponsored by the U.S. Department of Energy, Office of Biological and Environmental Research at the Pacific Northwest National Laboratory. Furthermore, we would like to acknowledge co-workers in CBiRC for their support.

2.7 Supporting Information

2.7.1 Reaction kinetics of the γ - Al_2O_3 catalyzed decarboxylation

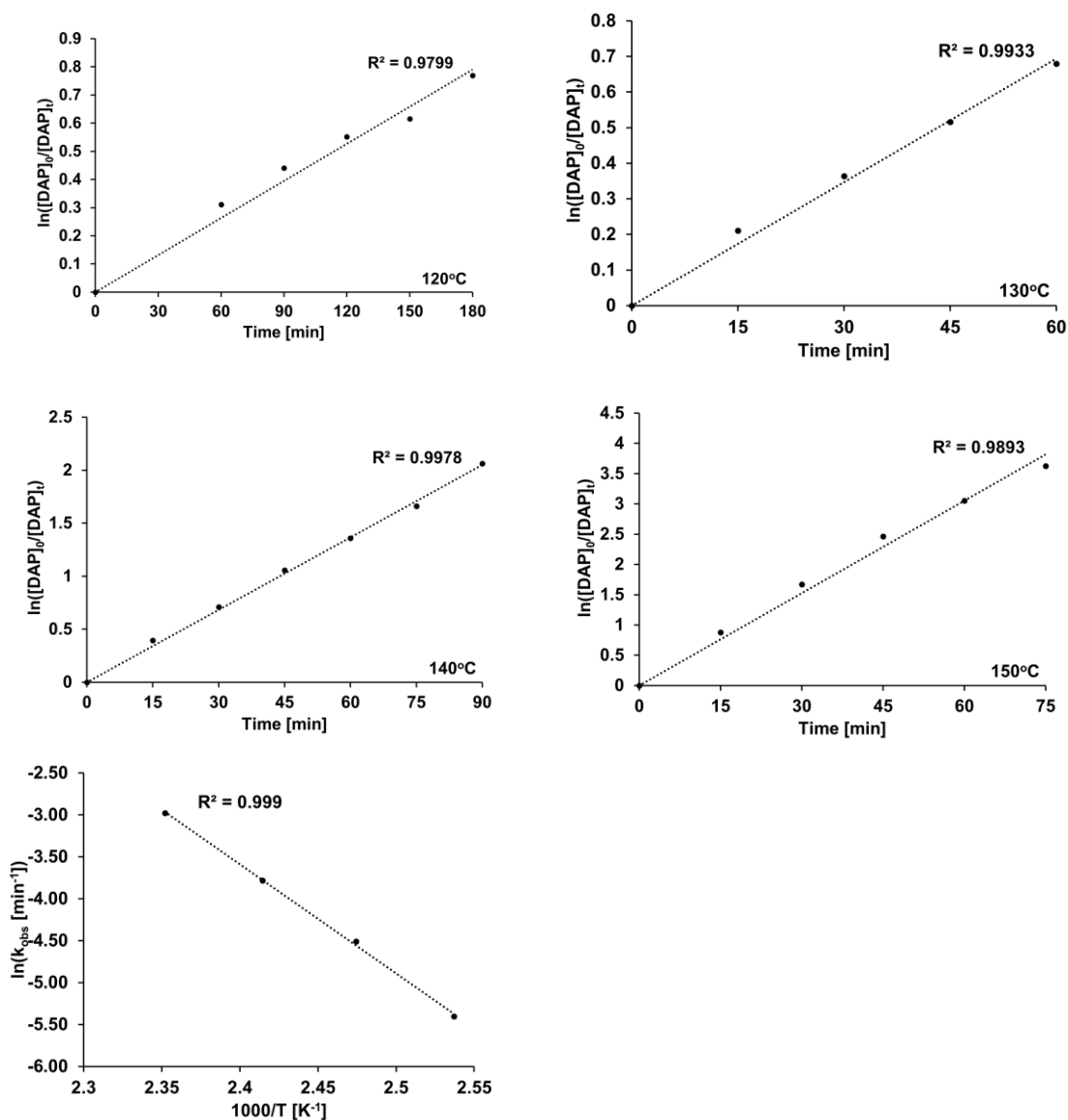


Figure S 2.1 Kinetic data of the conversion of DAP (1) with gamma alumina

Table S 2.1 Rate constants of the γ - Al_2O_3 catalyzed conversion of (1) in 1,4-dioxane

Temp. [°C]	Temp. [K]	k [min ⁻¹]
121	394.15	4.50E-03
131	404.15	1.10E-02
141	414.15	2.28E-02

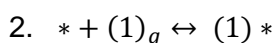
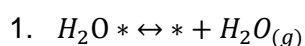
152	425.15	5.09E-02
-----	--------	----------

2.7.2 Computational analysis and microkinetic modeling

2.7.3 Ab-initio thermodynamics

2.7.3.1 For the 110 surface

We start with fully hydroxylated 110 surface wherein all Al sites are covered with water and OH groups (water coverage = 40% and OH coverage = 60%) and desorb water molecules and adsorb bicyclic (1) molecules as per the following equations.



We calculate the water desorption and (1) adsorption energies for different OH and H₂O coverage. We then compare energies of resulting different surfaces. Under reacting conditions, we will likely have surface coverage of (1), H₂O and OH corresponding to the lowest energy surface. The water desorption and (1) adsorption energies at 140 °C are as follows:

Table S 2.2 Desorption energies of water and adsorption energies of (1) at different coverage of Al, OH and H₂O on the 110 surface at 140 °C

Entry	%Al	%OH	%H ₂ O	%(1)	Gibbs free energy of water desorption (kJ/mol)	Gibbs free energy of water adsorption (kJ/mol)	Gibbs free energy of (1) adsorption (kJ/mol)
1	0	60	40	0	$\Delta G_1^{\text{desp}} = 61$	-	-
2	20	60	20	0	$\Delta G_3^{\text{desp}} = 110$	-61	$\Delta G_2^{\text{ads}} = -66$
3	40	60	0	0	$\Delta G_5^{\text{desp}} = 177$	-110	$\Delta G_4^{\text{ads}} = -123$
4	60	20	20	0	NA	-177	$\Delta G_6^{\text{ads}} = -107$

Now, with respect to the fully hydroxylated surface (40% H₂O and 60 % OH), the relative energies of 110 surface with different coverage of Al, (1), H₂O and OH are as follows:

Table S 2.3 Relative energy and abundance of the 110 surface at different coverage of Al, OH, H₂O and (1) at 140 °C and H₂O mole fraction of 0.00028 and balance (1)

Entry	%Al	%OH	%H ₂ O	%(1)	Relative energy (kJ/mol)	Relative abundance of each configuration
1	0	60	40	0	0	2.059 x 10 ⁻⁵
2	20	60	20	0	61	9.607 x 10 ⁻¹⁰
3	0	60	20	20	-5	0.9989
4	40	60	0	0	171	2.059 x 10 ⁻²⁰
5	20	60	0	20	48	1.060 x 10 ⁻³
6	60	20	20	0	348	1.6139 x 10 ⁻³⁹
7	40	20	20	20	241	1.8385 x 10 ⁻²⁵

The 110 surface has the lowest energy when the coverage of Al, OH, H₂O and (1) is 0, 60%, 20% and 20% respectively making it the most favorable configuration from the configurations examined herein. In addition, concentration effects can be estimated by assuming the reactions at different surface coverage of OH, Al, H₂O and (1) are quasi-equilibrated. The relative abundance of each surface configuration can be estimated by assuming a Langmuir-Hinshelwood surface and from equilibrium constants K_i corresponding to ΔG_i from Table S 2.2. The relative abundance of different configurations in Table S 2.3 are as follows:

$$1. \text{ [Table S 2.3, Entry 2]} = \frac{1}{1 + \frac{[H_2O]}{K_1} + K_2[(1)] + \frac{K_3}{[H_2O]} + \frac{K_3K_4}{[H_2O]}[(1)] + \frac{K_5K_3}{[H_2O]^2} + \frac{K_6K_5K_3}{[H_2O]^2}[(1)]}$$

$$2. \text{ [Table S 2.3, Entry 1]} = \frac{\frac{[H_2O]}{K_1}}{1 + \frac{[H_2O]}{K_1} + K_2[(1)] + \frac{K_3}{[H_2O]} + \frac{K_3K_4}{[H_2O]}[(1)] + \frac{K_5K_3}{[H_2O]^2} + \frac{K_6K_5K_3}{[H_2O]^2}[(1)]}$$

$$3. \text{ [Table S 2.3, Entry 3]} = \frac{K_2[(1)]}{1 + \frac{[H_2O]}{K_1} + K_2[(1)] + \frac{K_3}{[H_2O]} + \frac{K_3K_4}{[H_2O]}[(1)] + \frac{K_5K_3}{[H_2O]^2} + \frac{K_6K_5K_3}{[H_2O]^2}[(1)]}$$

$$4. \text{ [Table S 2.3, Entry 4]} = \frac{\frac{K_3}{[H_2O]}}{1 + \frac{[H_2O]}{K_1} + K_2[(1)] + \frac{K_3}{[H_2O]} + \frac{K_3K_4}{[H_2O]}[(1)] + \frac{K_5K_3}{[H_2O]^2} + \frac{K_6K_5K_3}{[H_2O]^2}[(1)]}$$

$$5. \text{ [Table S 2.3, Entry 5]} = \frac{\frac{K_3K_4}{[H_2O]}[(1)]}{1 + \frac{[H_2O]}{K_1} + K_2[(1)] + \frac{K_3}{[H_2O]} + \frac{K_3K_4}{[H_2O]}[(1)] + \frac{K_5K_3}{[H_2O]^2} + \frac{K_6K_5K_3}{[H_2O]^2}[(1)]}$$

$$6. \text{ [Table S 2.3, Entry 6]} = \frac{\frac{K_5K_3}{[H_2O]^2}}{1 + \frac{[H_2O]}{K_1} + K_2[(1)] + \frac{K_3}{[H_2O]} + \frac{K_3K_4}{[H_2O]}[(1)] + \frac{K_5K_3}{[H_2O]^2} + \frac{K_6K_5K_3}{[H_2O]^2}[(1)]}$$

$$7. [Table S 2.3, Entry 7] = \frac{\frac{K_6 K_5 K_3}{[H_2O]^2} [(1)]}{1 + \frac{[H_2O]}{K_1} + K_2 [(1)] + \frac{K_3}{[H_2O]} + \frac{K_3 K_4}{[H_2O]} [(1)] + \frac{K_5 K_3}{[H_2O]^2} + \frac{K_6 K_5 K_3}{[H_2O]^2} [(1)]}$$

We find that under reacting conditions, the 110 surface will have coverage of Al, OH, H₂O and (1) as 0, 60%, 20% and 20% respectively since the relative abundance of this configuration is very close to 1. We therefore, examine this surface for decarboxylation reactivity.

2.7.3.2 For 100 surface

For the 100 surface as well, we calculate water desorption and (1) adsorption energies at different surface coverage of Al, H₂O and OH. The results are reported in Table S 2.4.

Table S 2.4 Desorption energies of water and adsorption energies of (1) at different coverage of Al, OH and H₂O on the 100 surface at 140 °C

Entry	%Al	%OH	%H ₂ O	%(1)	Gibbs free energy of water desorption (kJ/mol)	Gibbs free energy of water adsorption (kJ/mol)	Gibbs free energy of (1) adsorption (kJ/mol)
1	25	25	50	0	$\Delta G_1^{desp} = 71$	-	-
2	37.5	25	37.5	0	$\Delta G_3^{desp} = 86$	-71	$\Delta G_2^{ads} = -50$
3	50	25	25	0	NA	-86	$\Delta G_4^{ads} = -43$

The above free energies result in the following relative surface energies and surface abundance at 140 °C and water mole fraction of 0.00028.

Table S 2.5 Relative energy and abundance of the 110 surface at different coverage of Al, OH, H₂O and (1) at 140 °C and H₂O mole fraction of 0.00028 and balance (1)

Entry	%Al	%OH	%H ₂ O	%(1)	Relative energy (kJ/mol)	Relative abundance of each configuration
1	25	25	50	0	0	5.0551×10^{-2}
2	37.5	25	37.5	0	71	1.2380×10^{-7}
3	25	25	37.5	12.5	21	0.9449
4	50	25	25	0	157	3.7439×10^{-15}
5	37.5	25	25	12.5	114	3.4825×10^{-9}

The relative abundance of each configuration reported in Table S 2.5 can be estimated by assuming a Langmuir-Hinshelwood surface and by assuming adsorption-desorption equations at different coverage of Al, H₂O, OH and (1) are quasi-equilibrated resulting in the following equations.

$$1. [Table S 2.5, Entry 2] = \frac{1}{1 + \frac{[H_2O]}{K_1} + K_2[(1)] + \frac{K_3}{[H_2O]} + \frac{K_3 K_4}{[H_2O]}[(1)]}$$

$$2. [Table S 2.5, Entry 1] = \frac{\frac{[H_2O]}{K_1}}{1 + \frac{[H_2O]}{K_1} + K_2[(1)] + \frac{K_3}{[H_2O]} + \frac{K_3 K_4}{[H_2O]}[(1)]}$$

$$3. [Table S 2.5, Entry 3] = \frac{K_2[(1)]}{1 + \frac{[H_2O]}{K_1} + K_2[(1)] + \frac{K_3}{[H_2O]} + \frac{K_3 K_4}{[H_2O]}[(1)]}$$

$$4. [Table S 2.5, Entry 4] = \frac{\frac{K_3}{[H_2O]}}{1 + \frac{[H_2O]}{K_1} + K_2[(1)] + \frac{K_3}{[H_2O]} + \frac{K_3 K_4}{[H_2O]}[(1)]}$$

$$5. [Table S 2.5, Entry 5] = \frac{\frac{K_3 K_4}{[H_2O]}[(1)]}{1 + \frac{[H_2O]}{K_1} + K_2[(1)] + \frac{K_3}{[H_2O]} + \frac{K_3 K_4}{[H_2O]}[(1)]}$$

Although the lowest energy configuration was Entry 1, the very low concentration of water makes the slightly less favorable configuration of Entry 3 the most abundant configuration. Therefore, on the 100 surface we will likely have Al, OH, H₂O and (1) coverage of 25%, 25%, 37.5% and 12.5% respectively.

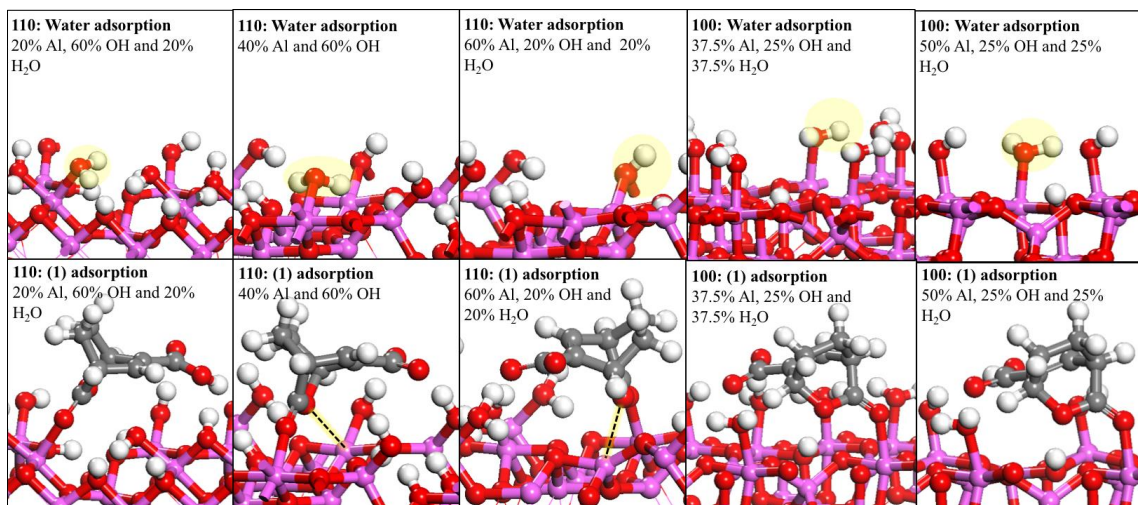
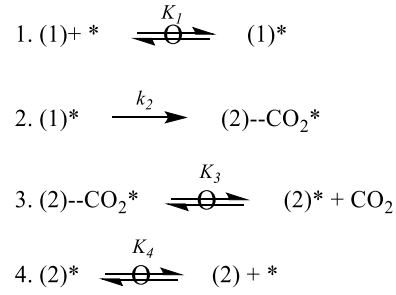


Figure S 2.2 Structures for adsorbed water and adsorbed (1) on different surfaces of γ -Al₂O₃ at different coverage of Al, OH and H₂O

2.7.4 Rate expression derivation



Step 2 rate determining

$$r = K_1 k_2 [(1)][*]$$

$$[(2)^*] = \frac{[(2)][*]}{K_4}$$

$$[(2) - \text{CO}_2] = \frac{[(2)][\text{CO}_2][*]}{K_4 K_3}$$

$$[\text{DAP}^*] = K_1 [(1)][*]$$

$$r = \frac{K_1 k_2 [(1)]}{1 + K_1 [(1)] + \frac{[(2)][\text{CO}_2]}{K_4 K_3} + \frac{[(2)]}{K_4}}$$

DFT predicted free energy diagram suggests that adsorption of (1) and (2) is very strong. Therefore, we expect the surface to be predominantly covered by (1*) and (2*). Therefore, the coverage of (2)—CO₂ can be neglected which then gives us:

$$r = \frac{K_1 k_2 [(1)]}{1 + K_1 [(1)] + \frac{[(2)]}{K_4}}$$

Define $K_1 k_2 = A$, $K_1 = B$ and $1/K_4 = C$, we have

$$r = \frac{A[(1)]}{1 + B[(1)] + C[(2)]}$$

2.7.5 Results of regression analysis

The rate expressions were solved by assuming that rate of consumption of (1) is equal to the rate of formation of (2).

This results in the following coupled differential equations:

$$\frac{d[(1)]}{dt} = -\frac{A[(1)]}{1 + B[(1)] + C[(2)]}$$

$$\frac{d[(2)]}{dt} = \frac{A[(1)]}{1 + B[(1)] + C[(2)]}$$

These equations were solved by discretizing using explicit Euler method for given initial conditions. The resulting profiles were solved for different values of A, B and C such that the root mean square error was minimized. The values of these constants at different temperatures are as followed:

Table S 2.6 Values of regression parameters A, B and C

T [°C]	A [min ⁻¹]	B	C
120	1.59411881	1.88800885	10.0421926
130	3.99776346	3.43062155	4.106534
140	5.79053195	2.16686937	3.05424603
150	8.2482893	1.57044347	2.16034609

2.7.6 Derivation of initial activation barrier

$$r = \frac{A[(1)]}{1 + B[(1)] + C[(2)]}$$

Assuming [(1)] >> 1 and [(2)]

$$r = \frac{A[(1)]}{B[(1)]}$$

Therefore, $k_{\text{obs}} = A/B = k_2$ which corresponds to intrinsic forward rate constant of decarboxylation of (1*).

Table S 2.7 Ideal gas entropies of different molecules at standard state and 140 °C

Chemical species	S _{Gas} [kJ/mol*K]
Bicyclic (1)	0.463432392
Diene (2)	0.417132248
CO ₂	0.226002944
Water	0.199593536

On metal oxides, the entropy loss following adsorption is estimated to be 1/3rd ideal gas entropy.¹³⁸ Accordingly, the Gibbs free energy was calculated by adding appropriate contribution to the enthalpy.

2.7.7 1D and 2D NMR product and intermediate identification

6-hydroxy-3-((methoxy-d₃)carbonyl)cyclohex-1-ene-1-carboxylic acid: ¹H NMR (600 MHz, Methanol-d₄) δ 7.14 (d, *J* = 2.7 Hz, 1H), 4.54 – 4.52 (m, 1H), 3.30 – 3.28 (m, 1H), 1.96 – 1.92 (m, 3H), 1.72 – 1.66 (m, 1H). ¹H-¹³C-HSQC: δ 7.14 – 138.63, δ 4.54 – 61.22, δ 3.30 – 42.89, δ 1.96 – 19.25, δ 1.96 – 30.05, δ 1.72 – 30.05 (600 MHz, Methanol-d₄): Exact mass: 203.09. Found m/z: 203.02 (UPLC-MS-ESI).

cyclohexa-1,3-diene-1,3-dicarboxylic acid: ¹H NMR (600 MHz, DMSO-d₆) δ 7.22 (t, *J* = 1.7 Hz, 1H), 7.13 (td, *J* = 4.6, 1.3 Hz, 1H), 2.42 – 2.38 (m, 2H), 2.33 (dd, *J* = 9.9, 1.8 Hz, 2H). ¹H-¹³C-HSQC (600 MHz, DMSO-d₆): δ 7.22-130.47, δ 7.13-143.37, δ 2.42-23.66, δ 2.33-20.08. Exact mass: 168.04. Found m/z: 168.04 (UPLC-MS-ESI).

Isophthalic acid: ¹H NMR (600 MHz, DMSO-d₆) δ 7.95 – 7.92 (m, 2H), 7.64 – 7.59 (m, 1H), 7.48 (t, *J* = 7.6 Hz, 1H). ¹H-¹³C-HSQC (600 MHz, DMSO-d₆): δ 7.95 – 129.82, δ 7.62 – 133.30, δ 7.48 – 129.12. Exact mass: 166.03. Found m/z: 166.05 (UPLC-MS-ESI)

6-hydroxycyclohex-1-ene-1,3-dicarboxylic acid: ¹H NMR (600 MHz, DMSO-d₆) δ 6.89 (d, *J* = 2.6 Hz, 1H), 4.33 (d, *J* = 2.9 Hz, 1H), 3.17 (ddd, *J* = 9.4, 6.5, 2.8 Hz, 1H), 1.80 – 1.73 (m, 3H), 1.51 (ddq, *J* = 12.6, 8.9, 4.0 Hz, 1H). ¹H-¹³C-HSQC (600 MHz, DMSO-d₆): δ 6.89 – 138.82, δ 4.33 – 60.27, δ 3.17 – 42.56, δ 1.78 – 20.17, δ 1.53 – 30.65. Exact mass: 186.05. Found m/z: 186.14 (UPLC-MS-ESI).

2.7.8 Mass transfer effect calculations of γ-Al₂O₃ catalyzed decarboxylation

Catalyst: γ-Al₂O₃ (Strem Chemicals)

Mass of catalyst: 200 mg

Particle size (dp) of γ -Al₂O₃: 53 μ m

Particle size (R) of γ -Al₂O₃: $2.65 \cdot 10^{-3}$ cm

Tortuosity (τ) of γ -Al₂O₃: 4 (conservative estimation based on Davis, M. E. and Davis, R. J.)¹³⁹

Porosity (ϵ) of γ -Al₂O₃: 0.872 (provided by Strem Chemicals)

True density (ρ_c) of γ -Al₂O₃: 3.9 g/cm¹⁴⁰ (provided by Strem Chemicals)

2.7.8.1 Calculation of the diffusion coefficient

To calculate the diffusion coefficient D_{AB} (based on Wilke, C. R. and Chang, P.),¹⁴¹ we first have to determine the molal volume (V_m) of the model compound benzoic acid.

$$D_{AB} = \frac{7.4 * 10^{-8} (X * M_s)^{0.5} T}{\eta * V_m^{0.6}}$$

Molal volume (V_m) of benzoic acid (model compound): 134.8 cm³/mol (based on Wilke, C. R. and Chang, P.)¹⁴¹

Association factor (X) of 1,4-dioxane: 1 (based on Wilke, C. R. and Chang, P.)¹⁴¹

Molar mass (M) of the solvent 1,4-dioxane: 88.1 g/mol

Calculated molar diffusivity (D_{AB}) of benzoic acid in 1,4-dioxane at 25 °C: 9.2526E-06 cm²/s

$$D_{AB} = \frac{7.4 * 10^{-8} (X * M_s)^{0.5} T}{\eta * V_m^{0.6}}$$

Calculated molar diffusivity (D_{AB}) of benzoic acid in 1,4-dioxane at 140 °C: 1.35E-05 cm²/s

Calculated effective diffusivity (D_{eff}) of benzoic acid in 1,4-dioxane at 140 °C: 2.96E-05 cm²/s (D_{eff} calculated based on Fogler, H. S.)¹⁴⁰

$$D_{eff} = \frac{\epsilon}{\tau} D_{AB}$$

Calculated Weisz-Prater number (N_{WP}) (Calculation based on Fogler, H. S.)¹⁴⁰

$$N_{WP} = \frac{r_{obs}^{mass\ cat} * \rho_c * R^2}{C_{Bulk} * D_{eff}}$$

Initial observed rate r_{obs} of the consumption of (1) at 140 °C: 2.13 $\mu\text{mol}/\text{min} * \text{ml}$ (volume)

Initial observed rate r_{obs} of the consumption of (1) at 140 °C: 7.1E-06 $\text{mmol}/\text{s} * \text{mg}(\text{cat})$

$$N_{WP} = \frac{7.1 * 10^{-6} \frac{\text{mmol}}{\text{s mg}(\text{cat})} * \frac{3.9 * 10^3 \text{ mg}}{\text{cm}^3} * (2.65 * 10^{-03} \text{ cm})^2}{\frac{7.14 * 10^{-2} \text{ mmol}}{\text{cm}^3} * 2.96 * 10^{-6} \frac{\text{cm}^2}{\text{s}}} = 0.92$$

For $N_{WP} < 1$ the absence of internal mass transfer limitations is confirmed. Additionally, the calculations of internal mass transfer limitations at a temperature of 120 °C yielded a value of $N_{WP} = 0.27$. Given that a linear trend of the Arrhenius plot at temperatures in the range of 120-150 °C was observed (Figure S 2.1) is further proof of the absence of transport effects.

In a previous study, we have shown that the absence of external transport effect for the 4590 Parr reactor system was given at an agitation speed of 400 rpm using the same $\gamma\text{-Al}_2\text{O}_3$ support material that was used in this study. Therefore we assume that a 400 rpm agitation rate is sufficient to eliminate external mass transfer effects.

Given the linear relationship of the Arrhenius plot (Figure S 2.1) in the temperature range of 120-150 °C, it is evident that reaction was performed in the absence of internal or external transport effects. Additionally, we have performed reactions with 5 times less catalyst (40 mg) which resulted in a ~ 5 times lower conversion rate of (1) further suggesting the absence of mass transfer limitations.

2.7.9 HR-MAS NMR investigation of immobilized (1) on γ -Al₂O₃

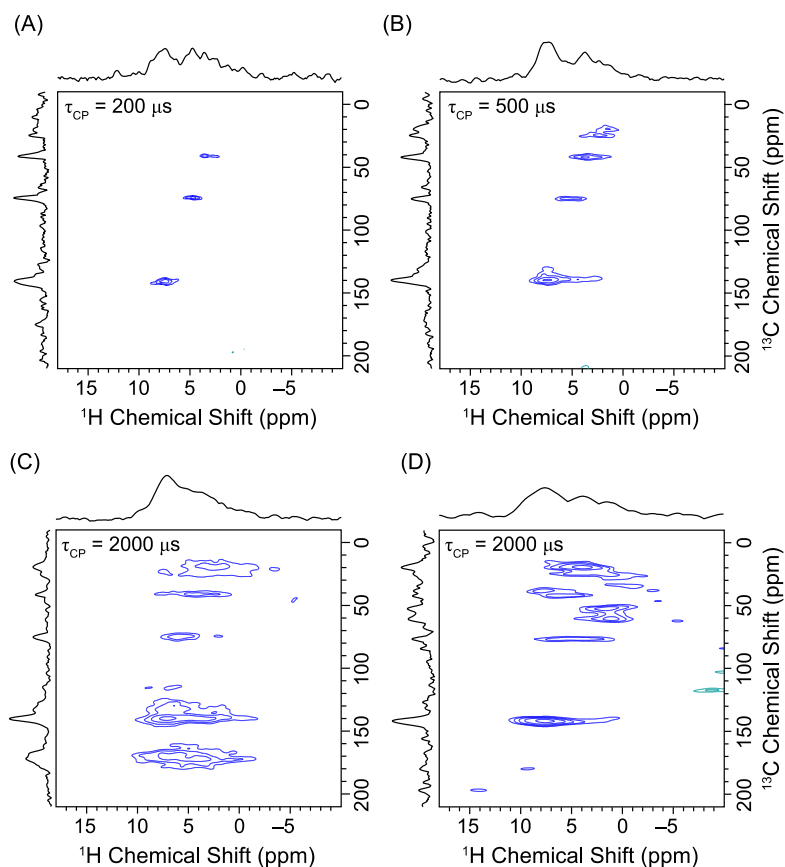


Figure S 2.3 Proton detected 2D $^1\text{H}\{^{13}\text{C}\}$ CP-HETCOR NMR spectra of alumina impregnated with 1,4-dioxane- d_8 solutions of bicyclic (1) with concentrations of 200 mg/mL (A-C) and 132 mg/mL (D). All spectra were obtained with a 25 kHz MAS frequency and forwards CP contact time (τ_{CP}) of 2.0 ms. The contact time used for the backwards $^{13}\text{C}\rightarrow^1\text{H}$ CP transfer is indicated on the 2D spectrum. The 2D spectra were acquired with a 1.3 s recycle delay, 224 to 320 scans per increment, 128 t_1 increments and t_1 was incremented in steps of 40 μs . Total experiment times were between 10.3 hours and 14.8 hours.

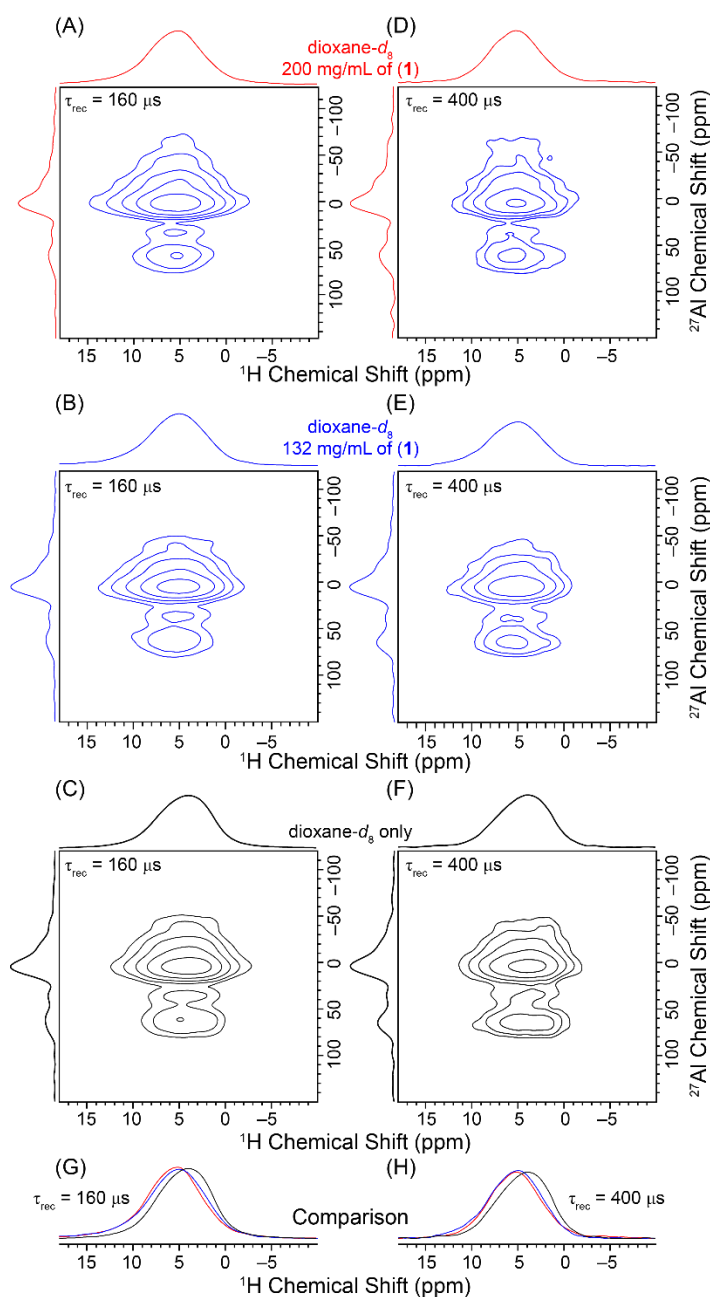


Figure S 2.4 Proton detected 2D $^{27}\text{Al} \rightarrow ^1\text{H}$ D-RINEPT HETCOR spectra of alumina impregnated with 1,4-dioxane- d_8 solutions of bicyclic (1) with concentrations of 200 mg/mL (A, D) and 132 mg/mL (B, E) and pure dioxane (C, F). The spectra were obtained with dipolar recoupling times (τ_{rec}) of 160 μs (left column) or 400 μs (right column). ^1H solid-state NMR spectra obtained from the positive projections of the direct dimension of each sample are compared in (G) and (H). The 2D spectra were typically acquired with recycle delays between 50 ms and 100 ms, between 1024 to 2400 scans per increment, 80 t_1 increments and t_1 was

incremented in steps of 11.0 μs (1.1 hours to 5.3 hours total experiment time). The spectra obtained with $\tau_{\text{rec}} = 160 \mu\text{s}$ have the best sensitivity, however, the relative intensity of signals from 4- and 5-coordinate aluminum are enhanced in the spectra recorded with $\tau_{\text{rec}} = 400 \mu\text{s}$. The ^{27}Al solid-state NMR spectra are compared in Figure S 2.5.

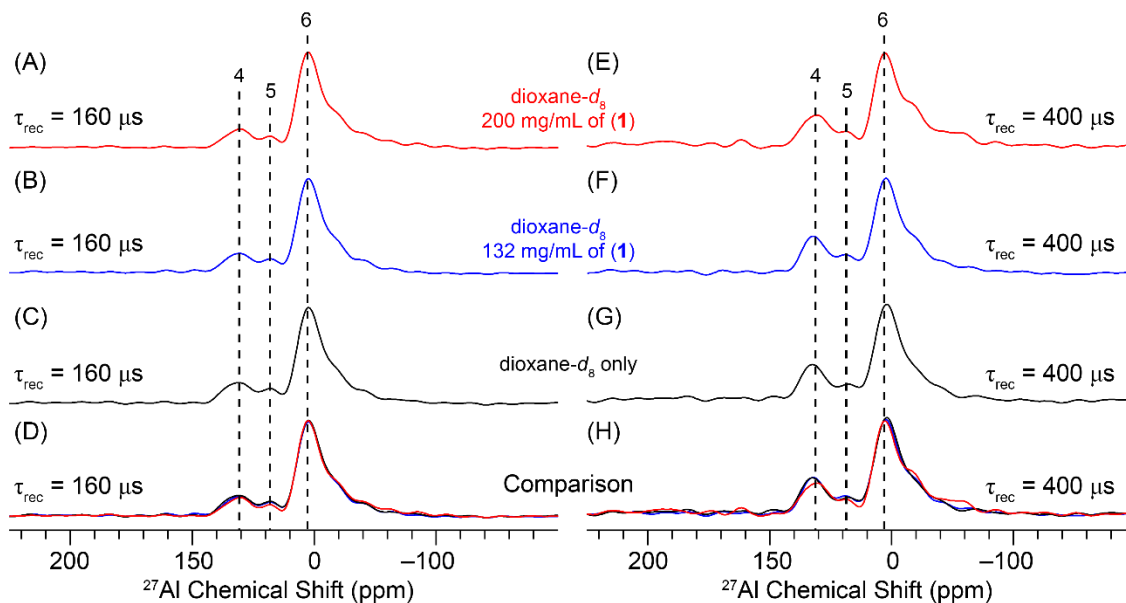


Figure S 2.5 Comparison of surface selective ^{27}Al solid-state NMR spectra of alumina impregnated with 1,4-dioxane- d_8 solutions of bicyclic (1) with concentrations of 200 mg/mL (A, E) and 132 mg/mL (B, F) and pure dioxane (C, G). The ^{27}Al solid-state NMR spectra were obtained from the sum of the indirect dimension of the proton detected 2D $^{27}\text{Al} \rightarrow ^1\text{H}$ D-RINEPT HETCOR spectra. The spectra were obtained with dipolar recoupling times (τ_{rec}) of 160 μs (left column) or 400 μs (right column). Signals from 4-, 5- and 6-coordinate aluminum are clearly visible. The ^{27}Al solid-state NMR spectra of the different samples are compared in (D) and (H) and show that there is not a substantial variation in the relative intensity of the different aluminum sites with loading level.

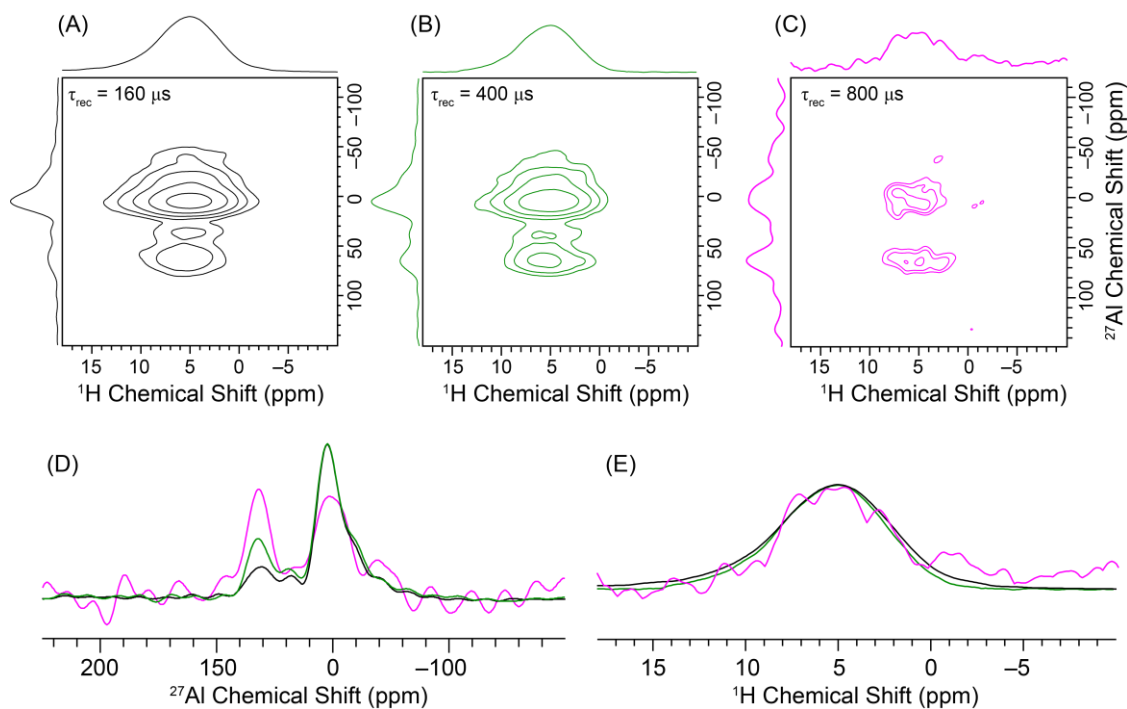
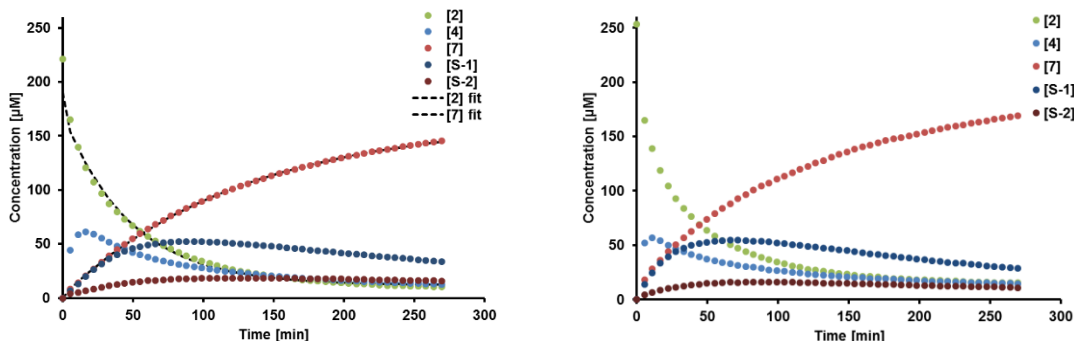


Figure S 2.6 Proton detected 2D $^{27}\text{Al} \rightarrow ^1\text{H}$ D-RINEPT HETCOR spectra of alumina impregnated with a 1,4-dioxane- d_8 solution with a 200 mg/mL concentration of bicyclic (1). The spectra were obtained with dipolar recoupling times (τ_{rec}) of 160 μs (A), 400 μs (B) and 800 μs (C). (D) Comparison of the ^{27}Al solid-state NMR spectra obtained from the sum of the indirect dimension of each 2D spectrum shows that with longer recoupling times there is a substantial increase in the relative intensity of the 4-coordinate aluminum site. (E) Comparison of the ^1H solid-state NMR spectra obtained from the positive projections of the direct dimension of each 2D spectrum. The 2D spectrum obtained with $\tau_{\text{rec}} = 800 \mu\text{s}$ was acquired with a recycle delay of 50 ms, 4096 scans per increment, 80 t_1 increments and t_1 was incremented in steps of 11.0 μs (4.6 hours total experiment time).

2.7.10 Reaction kinetic investigation of the acid catalyzed ring-opening of (1)



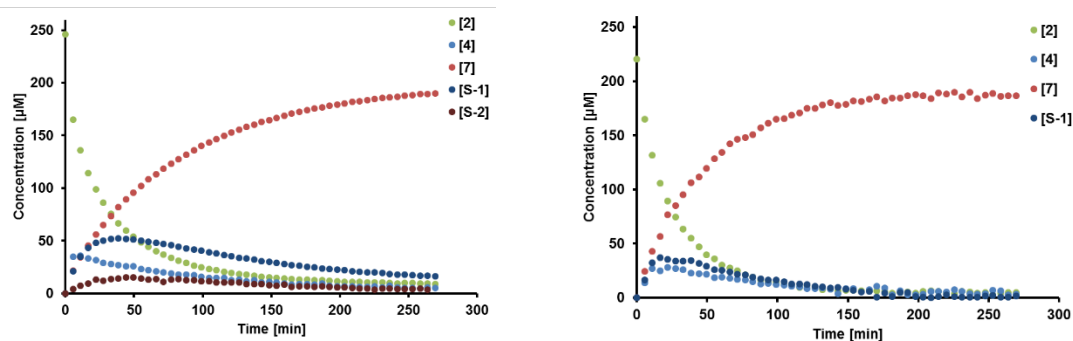


Figure S 2.7 The acid catalyzed ring-opening of (1) in 1,4-dioxane-d₈

Table S 2.8 Conversion and selectivity of the acid catalyzed conversion of (1) to (4) and (5)

Temp. [°C]	(1) conv. [mol%]	(4) Sel. [mol%]	(5) Sel. [mol%]	[S-1] Sel. [mol%]	[S-2] Sel. [mol%]
80	96	6	67	15	7
90	94	6	71	12	5
100	96	2	80	7	1
110	98	2	87	1	-

Condition: starting concentration: ~237.93 µmol/mL reaction volume: 300 µl, NMR acquisition time: 269.5 min, solvent: 1,4-dioxane-d₈, catalyst: 5 µL D₂SO₄

Table S 2.9 First order rate constants of the acid catalyzed ring-opening step of (1) to intermediate (4)

Temp. [°C]	Temp. [K]	k [min ⁻¹]
80	353.15	0.031
90	363.15	0.033
100	373.15	0.036
110	383.15	0.040

Table S 2.10 First order rate constants of the acid catalyzed dehydration step of intermediate (4) to (5)

Temp. [°C]	Temp. [K]	k [min ⁻¹]
80	353.15	0.010
90	363.15	0.013

100	373.15	0.016
110	383.15	0.023

Table S 2.11 First order rate constants of the Na-(1) decarboxylation in D₂O

Temp. [°C]	Temp. [K]	k [min ⁻¹]
60	333.15	1.40E-03
70	343.15	2.60E-03
80	353.15	8.80E-03
90	363.15	2.85E-02

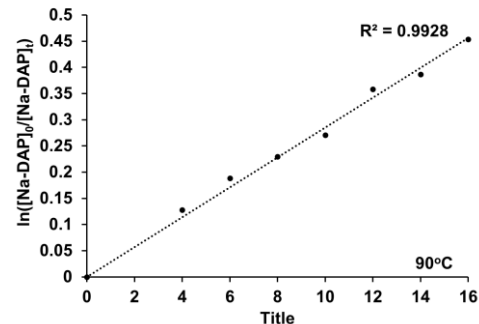
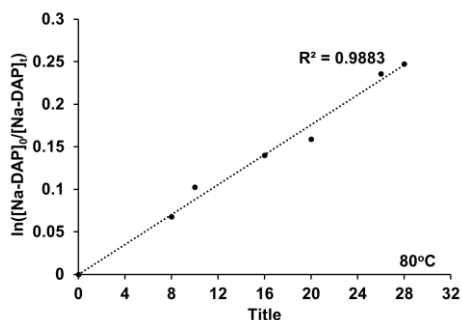
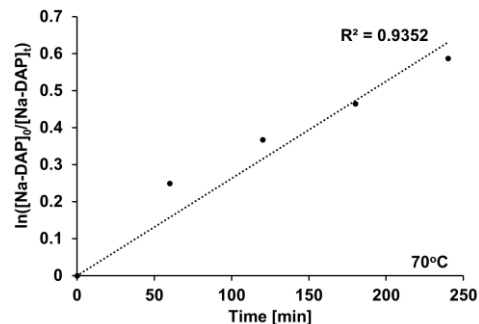
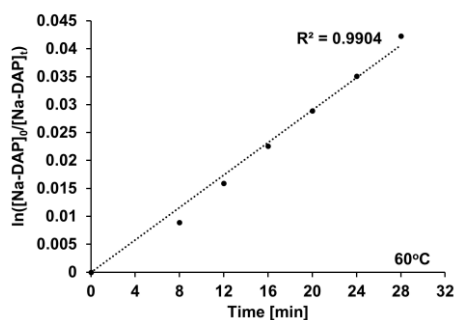


Figure S 2.8 Kinetic data of the conversion of Na-(1) in D₂O

Table S 2.12 Pseudo first order rate constants of (1) ring-opening step in methanol-d₄

Temp. [°C]	Temp. [K]	k [min ⁻¹]
90	363.15	1.70E-03
95	368.15	2.40E-03
100	373.15	3.60E-03

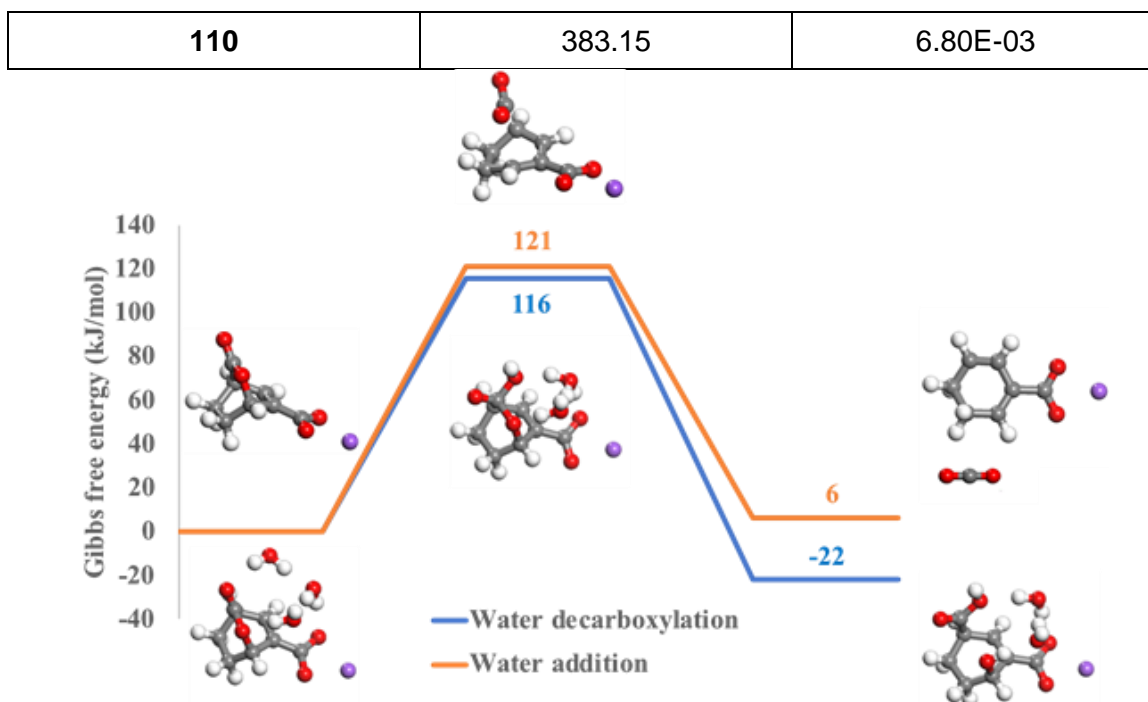


Figure S 2.9 Gibbs free energy profiles of the water addition and water-initiated decarboxylation of (1)

2.7.11 Reaction kinetics of the ring-opening of (1) in methanol- d_4

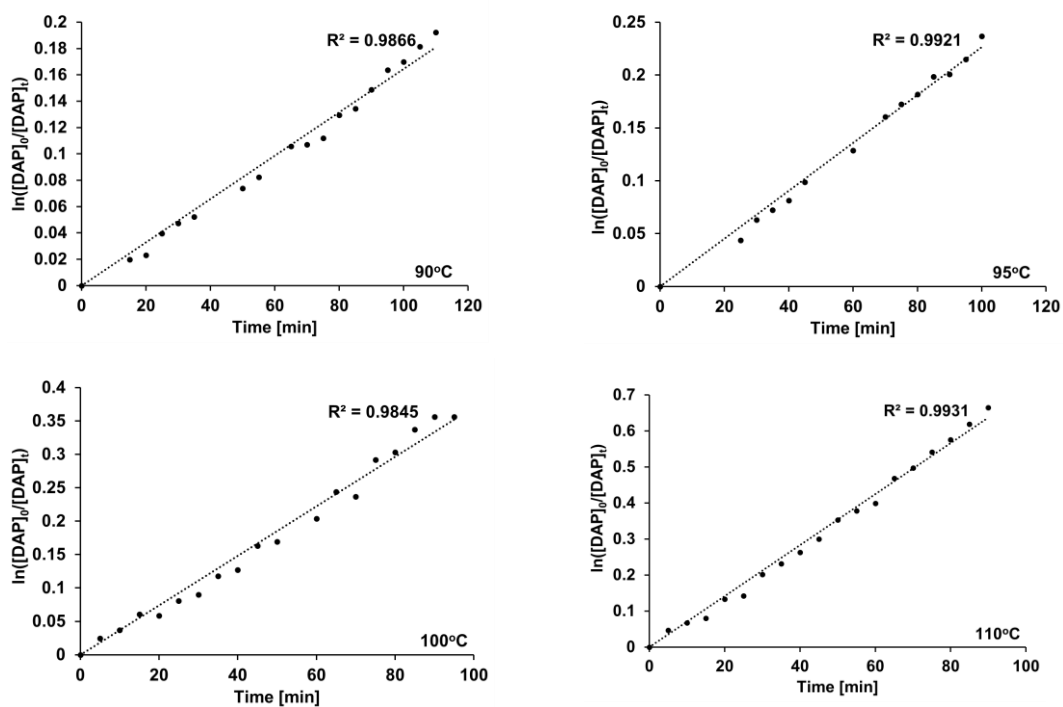


Figure S 2.10 Kinetic data of the conversion of DAP (1) in methanol- d_4

3 Improving Selectivity of Toluic Acid from Biomass-Derived Coumalic Acid

Reprinted with permission from Pfennig, T., Chemburkar, A., Cakolli, S., Neurock, M., Shanks, B. H. *Improving Selectivity of Toluic Acid from Biomass-Derived Coumalic Acid*. ACS Sustain. Chem. Eng. **2018**, 6, 12855–12864. Copyright 2018 American Chemical Society.

Theoretical calculations were performed by AC under the supervision of MN.

3.1 Conspectus

The selective formation of bio-aromatics from renewable sources to access greener alternatives to petroleum-derived aromatics is of great interest in development of sustainable chemicals. An innovative and efficient bio-based route towards the formation of toluic acid is demonstrated with selectivities of >99 mol% utilizing a Diels-Alder/decarboxylation/dehydrogenation domino sequence in conjunction with a heterogeneous catalyst. 2-Pyrone coumalic acid (or methyl coumalate) cycloaddition with bioavailable propylene extends the chemical diversity of the coumalate platform. Additionally, an inexpensive as well as easy to separate dienophile such as propylene offers an attractive alternative to access bio-aromatics with high atom efficiency. Herein, we report an in-depth kinetic investigation to evaluate the activation energies of individual reaction steps and identify the rate limiting step to guide the development of an improved overall process. The kinetic analysis is complemented by first principle density functional theory calculations, which corroborate the experimental results. We further explore the influence of solvents on the production of aromatics from both coumalic acid as well as methyl coumalate. We show that toluic acid formation is highly susceptible to the solvent used to mediate the reaction with yields ranging from 51-88 mol% at 100 mol% coumalic acid conversion. In addition, we provide evidence that the chemical moiety (ester vs acid) of the starting substrate plays a critical role in the yield. While the maximum toluic acid yields are 88 mol%, methyl coumalate reactions with propylene afforded increased methyl toluate yields (up to 98 mol%). Kinetic analyses of methyl coumalate cycloaddition with propylene and the subsequent decarboxylation reactions indicate that decarboxylation is

likely the rate limiting step. The Diels-Alder reaction step has activation barriers of 80 kJ/mol (para) and 85 kJ/mol (meta), respectively, whereas decarboxylation barriers are 142 kJ/mol (para) and 152 kJ/mol (meta), respectively. We combine our results with propylene and different dienophiles reported previously to show that activation barriers as well as regioselectivity of the cycloaddition depends on the nature of the dienophile. Electron rich dienophiles appear to have lower activation barriers and higher para to meta ratio, while electron deficient dienophiles result in high activation barriers and lower para to meta ratio.

3.2 Introduction

Through technological advances in extraction processes (e.g. hydraulic fracturing), the economic exploration of non-renewable carbon sources (e.g. shale gas) became a target of interest in the U.S. energy sector.^{6,20,37,104,142,143} The utilization of this inexpensive alternative as raw material supply in the petrochemical industry, however, causes a reduced availability of >C4 building blocks and negatively affects the carbon footprint.^{20,104,143} Given that aromatics are heavily utilized as chemical building blocks in the manufacture of consumer products such as cosmetics, plastics, preservatives, and pharmaceuticals, the development of environmentally benign and economically feasible alternatives are therefore of interest.^{16,18–23,26–31,37,104,142,144–150}

Aromatic synthesis from biomass often starts with microbial fermentation or hydrolysis of sugars that provide direct or indirect access to furanics (furfural,¹⁵¹ furan,^{151,152} methyl furan,^{151,153} DMF,^{154,155} 5-HMF,¹⁵⁶ as well as oxidized analogs of HMF^{19,157}), malic acid,^{71,72} lactic acid,¹⁵⁸ quinic/shikimic acid,^{69,70,159} muconic acid^{150,160–162}, sorbic acid,³⁷ etc. These substrates are examples of a relatively diverse slate of bioavailable feedstocks that can be used for selectively producing a plethora of functionalized aromatics via chemocatalytic conversion.^{16,18–23,26–31,37,104,142,144–148,163} The commercial opportunity for many of these alternative technologies, however, is still problematic as they lack economic feasibility due to low yield and selectivity. This fosters the need to develop new innovative processes to access biomass-derived aromatics. In recent years, the manufacture of a terephthalic acid (TPA) bio-substitute gained significant attention due to the immense TPA utilization as a precursor for one of the largest volume industrial polymer polyethylene terephthalate (PET). PET annual global production exceeds 50 million tonnes,¹⁶⁴ which translates to a \$58 billion market²⁷ that is projected to grow to nearly 67 million tonnes¹⁴⁴

by 2018. Despite the promising development of the bio-advantaged TPA substitute 2,5-furandicarboxylic acid (FDCA), which could potentially reduce the future TPA need, renewable alternatives are still of interest for the manufacture of TPA-based pharmaceuticals, dyes, pesticides, and other chemicals.³¹

A promising pathway to access a biomass-derived TPA precursor involves Diels-Alder/acid-catalyzed dehydration (via modified BEA zeolite) sequence of dimethyl furan (DMF) and ethylene to *p*-xylene, a reaction that affords high aromatic yield (up to 97%).^{23,146,163} DMF can be obtained from hydrogenolysis of 5-hydroxymethyl furfural (HMF) in yields of up to 96%,¹⁵⁵ while HMF can be synthesized via acid-catalyzed dehydration of fructose with reported selectivities as high as 89%¹⁵⁴ resulting in an overall aromatic yield of 83%. Unfortunately, this yield is negatively impacted when glucose is used as the starting sugar. Alternatively, biomass derived *p*-xylene can be synthesized from DMF and acrolein in a sequence of reactions which include Diels-Alder (DA) addition, oxidation, and dehydration followed by decarboxylation.²² This reaction, however, suffers from low overall *p*-xylene yield of <48% and is therefore economically less relevant.

Recently, an ethanol mediated two-step process was introduced starting with the cycloaddition of *trans, trans*-muconic acid (ttMA) and ethylene in the presence of silico-tungstic acid followed by palladium-catalyzed dehydrogenation, which resulted in an overall diethyl terephthalate yield of 81%.¹⁴⁹ ttMA was synthesized via isomerization of bio-derived *cis, cis*-muconic acid (ccMA). Further developments in the isomerization of ccMA to ttMA led to an improved overall process with ttMA yields up to 88%.¹⁵⁰ The current bottleneck in the manufacture of bio-derived TPA from ttMA, lies in the glucose fermentation step with a maximum reported titer of 59.2 g/L and a yield of 30% ($\text{mol}_{\text{ccMA}}/\text{mol}_{\text{glucose}}$).¹⁶² Since the maximum theoretical carbon yield is 86% for this metabolic pathway,¹⁶⁰ further enhancements are needed for the advancement of this technology.

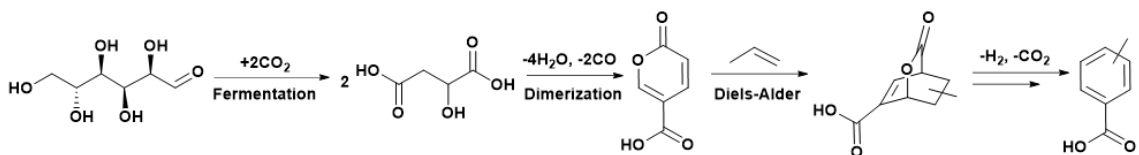
Miller *et al.* showed that the TPA precursor *p*-toluic acid (pTA) can be synthesized from bio-derived acrylic acid and isoprene in yields up to 77 % using homogeneous Lewis acids such as TiCl_4 .³³ A slightly different pTA synthesis approach with isoprene and acrylic acid utilized BH_3 -THF to give a Diels-Alder cycloadduct yield of 80% followed by a 91% yield dehydro-aromatization step in concentrated H_2SO_4 .³² Taken together the overall yield of pTA was about 73%. Harsh reaction conditions (e.g., concentrated H_2SO_4 , TiCl_4 , anhydrous solvents, etc.), however, limits the attractiveness of the reaction system.

Another approach to bio-derived TPA is based on 2-pyrone (e.g., coumalic acid) and proceeds through a reaction sequence involving Diels-Alder/ decarboxylation/ dehydrogenation reactions. Different dienophiles used in the Diels Alder reaction result in formation of different products.^{26–31,104,143} Coumalic acid (CMA) is accessible in high yield (86%) via dimerization of malic acid,²⁶ which has been identified by the US Department of Energy as a bio-based platform molecule.^{165,166} There are known organisms that provide very high titer (159 g/L) and yield (69%) of malic acid from glucose fermentation,^{71,72} which is an important attribute for the overall route to be economically competitive with the existing petroleum-derived technology.

Various CMA or methyl coumalate (MeCMA) reaction routes in combination with functionalized dienophiles (acrylates, vinyl ethers, ketals, ortho esters, etc.) have been demonstrated in literature.^{26–30} Many of them, however, suffer from low (regio) selectivity and/or atom efficiency on the pathway to the final aromatic. For instance, Lee *et al.*²⁷ reported an interesting approach to directly access the TPA analog dimethyl terephthalate (DMT) from MeCMA and captodative dienophiles in high selectivity (up to 95%). This reaction was achieved via a Diels-Alder/decarboxylation/in situ elimination sequence in the absence of a solvent and catalyst. Despite exceptional DMT yields, one of the limitations of this route is the in-situ aromatization/elimination of intermediates on the pathway to DMT that leads to loss of carbon fragments, which is problematic from an atom economy perspective. Additional oxidation is needed to transform DMT into TPA thus resulting in further carbon loss. Despite the success of recent developments in the manufacture of TPA and TPA analogs from 2-pyrone, the high dienophile substrate cost, low selectivity and poor atom economy limits the ultimate viability of this alternative technology. A potential solution for this dilemma is the reaction of CMA with propylene, which provides a route to manufacture TA in high selectivity and yield (84 mol%)³¹ as shown in Scheme 3.1. This route is of relevance since propylene is inexpensive, easy to separate/recycle and results in nearly perfect atom efficiency. Additionally, as the production of propylene from biomass has been demonstrated,^{8,10} a potential alternative for a 100% bio-based process exists.

As part of the development of biomass-derived TPA technology, we herein report an improved TA synthesis pathway using a one-pot sequential process affording high TA selectivities (up to 99 mol%). Given the industrial importance of TA as precursor for TPA,

the focus of this work is to provide detailed information of intrinsic kinetics of individual reaction steps to guide the development of an improved overall process to biomass-derived TA. More broadly, we present a general Diels-Alder reactivity trend for 2-pyrone coumalates with different dienophiles. A clear trend is revealed when MeCMA is reacted with electron withdrawing and donating dienophiles as dienophiles with electron withdrawing groups resulted in high activation barriers and low p-/m- ratio and electron donating groups resulted in low activation barriers and high p-/m- ratio.



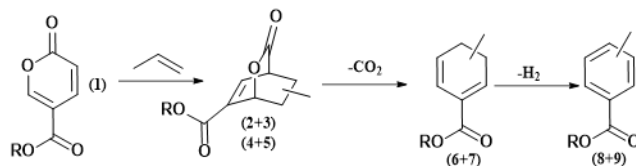
Scheme 3.1 The formation of toluic acid starting from glucose fermentation to malic acid using acid catalysed dimerization to coumalic acid followed by a Diels-Alder/decarboxylation/dehydrogenation reaction sequence to yield the desired aromatics.

3.3 Results and Discussion

3.3.1 The formation of toluic acid from coumalic acid

To identify the impact of the solvent on toluic acid (TA) formation, we conducted a series of experiments in which CMA and MeCMA were reacted with propylene using polar and non-polar solvents (Scheme 3.2). As shown in Table 3.1, Entry 1 mediating the reaction in non-polar toluene showed significant limitations in the formation of TA (8(para)+9(meta)). A large amount of the starting substrate CMA was lost due to by-product formation, which was likely due to the poor solubility of CMA in toluene. Substantial CMA by-product formation was also observed in previous studies in which CMA was reacted with ethylene or propylene using the non-polar solvent toluene to form benzoic acid (BA) or TA.^{31,104} Mediating the CMA reaction in a polar aprotic solvent such as γ -valerolactone (GVL), however, considerably improved aromatic yield and selectivity. Therefore, CMA and propylene reactions were performed in GVL to obtain concentration-time profiles to elucidate and improve the formation of TA from CMA. The experimental concentration-time profile in Figure S 3.1 shows that maximum selectivity was achieved after 1 h at 180 °C in GVL. Performing the reaction in GVL resulted in a yield increase from 51 mol% to 84 mol% (Table 3.1, Entry 1 and 2). The concentration-time profile,

displayed in Figure S 3.1, further shows that a significant fraction of the initial CMA is transformed into by-products of unknown origin which has also been reported in the literature.^{31,104}



Scheme 3.2 The reaction cascade from CMA (or MeCMA) to 2 (para exo), 3 (para endo), 4 (meta exo) and 5 (meta endo) to 6 (para) and 7 (meta) to 8 (para) and 9 (endo) ($R = H, CH_3$).

Table 3.1 Conversion of CMA/MeCMA with propylene to TA/MeTA.

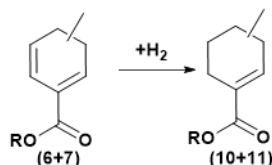
Entry	Reactant	Solvent	Conv. (1) [mol%]	Selectivity			
				(8+9) [mol%]	(6+7) [mol%]	(10+11) [mol%]	8/9 [p-/m- ratio]
1	CMA	Toluene	100	51	[a]	[a]	4.8
2	CMA	GVL	99±4	84±2	[a]	[a]	4.8
3	CMA	1,4-Dioxane	100±10	88±1	[a]	[a]	4.4
4	MeCMA	Toluene	100±0	97±4	<2 [b]	<7 [b]	4.2
5	MeCMA	GVL	100±0	91±1	<2 [b]	<7 [b]	4.7
6	MeCMA	1,4-Dioxane	100±4	98±1	<3 [b]	<5 [b]	4.6

Reaction conditions: Temperature: 180 °C; reaction time: 4 h, starting concentration: 10 mg ml⁻¹ MeCMA/CMA (1) in solvent (1,4-dioxane), reaction volume: 30 ml, pressure: 130 psig propylene, agitation: 400 rpm, Pd/C catalyst: 100 mg, [a] unable to quantify by-products with UPLC-PDA/QDa, [b] by-products detected with GC-FID/MS and quantified based on methyl toluate as reference due to the similar FID response factor.

Aromatic selectivity improvements of up to 100 mol% were also seen when MeCMA was used as the reactant in conjunction with ethylene to form methyl benzoate (MeBA).¹⁰⁴

Therefore, experiments were performed starting with MeCMA and propylene using various solvents (e.g. toluene, GVL, and 1,4-dioxane) to further improve aromatic selectivity and to examine the solvent impact on methyl toluate (MeTA) formation.

As shown in Table 3.1, Entry 4, a dramatic improvement in MeTA yield and selectivity was observed when toluene was the solvent used, which is further demonstrated in Figure S 3.3. The high aromatic selectivity of 97 mol% was unambiguous evidence that the solubility of the starting substrate (1) played a critical role in the coumalate transformation to toluates. Lack of hydrogen bonding in toluene limits the solubility of CMA resulting in its degradation to unidentified products. On the other hand, due to high solubility of MeCMA, only small amounts <2 mol% of the diene intermediates 6 and 7 remained after the reaction period was completed. Less than 7 mol% was attributed to methyl 3-/4-methylcyclohex-1-ene-1-carboxylate by-products (10 and 11 in Scheme 3.3), which resulted from hydrogenation of 6 and 7 in the presence of the Pd/C catalyst (Table 3.1, Entry 4). The hydrogen required for this reaction was likely formed by the concomitant dehydrogenation of 6 and 7 to 8 and 9. This interplay can be seen in the concentration-time data in Figure S 3.3. Similar observations of methyl cyclohex-1-ene-1-carboxylate by-product formation were made in the reaction network analysis of MeCMA conversion to MeBA.¹⁰⁴



Scheme 3.3 Hydrogenation of 6(*para*) and 7(*meta*) to 10 (*para*) and 11(*meta*) with $R = H, CH_3$

Species identification of combined 10 and 11 was based on GC-FID/MS data suggesting that hydrogenation of species 6 and 7 (m/z 152) was operative. Structural identification of diene species 6 and 7 was performed in a previous study³¹ in which intermediates and by-products of the CMA to TA were analysed via ¹H-¹H COSY, ¹³C-¹H HSQC, GC-FID/MS and UPLC-PDA/MS.

Reactions of MeCMA with propylene in GVL gave a 7 mol% selectivity improvement from 84 mol% (CMA) to 91 mol% (MeCMA) (Table 3.1, Entry 2 and Entry 5). Similar to the reactions in toluene, <2 mol% of the reaction products were unreacted diene species 6

and 7 and <7 mol% of 10 and 11 were detected via GC-FID/MS (Figure S 3.4). MeCMA reactions with propylene in 1,4-dioxane (Figure S 3.5) further increased the aromatic selectivity of MeTA (8+9) to 98 mol% at 100% MeCMA conversion with only minor by-product formation (Table 3.1, Entry 6). This 10 mol% increase compared to TA formation from CMA was likely due to the functional group (ester vs acid) of the starting substrate 1. This hypothesis was reinforced by CMA and MeCMA stability tests reported previously showing that the molecular integrity of CMA is slightly inferior compared to MeCMA.¹⁰⁴ After an 8 h duration at 180 °C, a 10 mol% CMA degradation was observed while MeCMA degradation to unidentified by-products was only 3 mol%. In addition, mechanistic insights into CMA breakdown showed that CMA reacts in the presence of water via nucleophilic attack that initiates ring-opening,¹⁰⁴ since small water amounts were needed to facilitate CMA ring-opening via rapid proton shuttling. GVL used in our experiments had a water content of 3.3 vol%, while toluene and dioxane had very low water contents at ~ 300 ppm. As a result, the observed selectivity to aromatics in GVL was lower by ~ 7% as compared to toluene and dioxane. Therefore, performing the reaction in the absence of water would increase aromatic yield and selectivity.

Overall, the presence of an additional methyl group on MeCMA improves its solubility in non-polar solvents, as a result, the DA reaction and subsequent decarboxylation and dehydrogenation reactions can be carried out in a range of different solvents, both polar and non-polar with high selectivity to MeTA. On the other hand, poor hydrogen bonding offered by non-polar solvents, makes CMA poorly soluble in such solvents and prone to degradation, decreasing the selectivity to aromatics. In addition, the presence of water can degrade CMA, but the presence of the additional methyl group makes MeCMA slightly more stable.

3.3.2 Reaction kinetics in the absence of a catalyst

The kinetic investigation for DA cycloaddition of MeCMA and propylene followed by decarboxylation of the bicyclic intermediates were performed in 1,4-dioxane, which was an ideal model solvent for kinetic investigation as shown previously.¹⁰⁴ Using the polar aprotic low boiling solvent 1,4-dioxane (compared to GVL) provided high substrate solubility and stability, which was essential to minimize by-product formation and to isolate temperature sensitive intermediates in high yield and selectivity. This attribute was of paramount importance for subsequent NMR identification and quantification. Additionally,

fully deuterated 1,4-dioxane- d_8 is commercially available through which kinetic investigation of the bicyclic lactone (DAP(2,3,4 and 5)) decarboxylation can be performed in-situ in high pressure NMR tubes to minimize sample workup and to increase sample throughput. Fully resolved spectra are shown in Figure 3.1, which provides clear evidence that this methodology enables clear species quantification while maintaining high carbon balances of >92 mol%. Species identification of 2,3, 4, 5, 6, and 7 was corroborated via 2D NMR ^1H - ^1H -COSY and ^{13}C - ^1H -HSQC analysis in combination with UPLC-PDA/QDA and GC-FID/MS analysis from our previous CMA to TA reaction network analysis.³¹ Quantification of species 2, 3, 4, 5, 6, and 7 was based on ^1H NMR.

3.3.3 Diels-Alder reaction step

An in-depth kinetic investigation of the DA reaction of MeCMA and propylene was conducted to identify kinetic parameters (e.g. activation barrier) and to gain critical information as to how selectivity and the para to meta TA ratio could be further improved. Given the industrial importance of pTA in the production of the large-scale commodity TPA, pTA would be preferred.

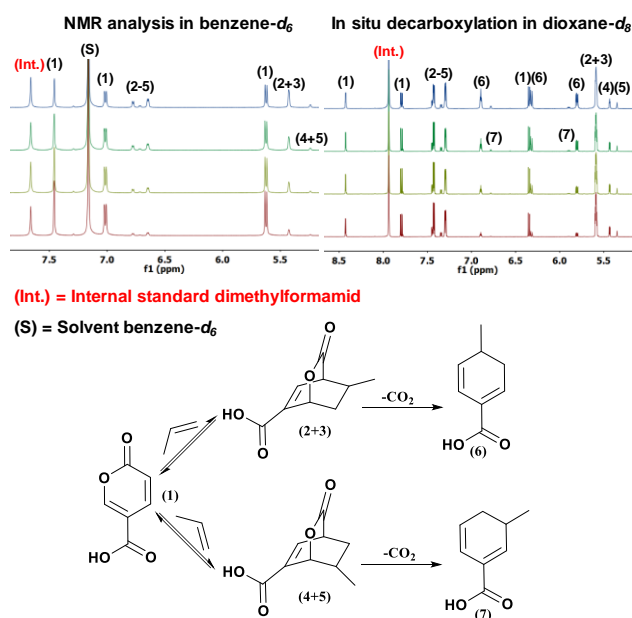


Figure 3.1 NMR trace of the DA reaction products 2, 3, 4, and 5 after cycloaddition of MeCMA and propylene (left figure). NMR trace of the in-situ decarboxylation of bicyclic lactone intermediates 2, 3, 4, and 5 to 6 and 7 (right figure).

Batch reactor kinetics of MeCMA and propylene in 1,4-dioxane were performed within a temperature range of 90-120 °C to screen the concentration-time dependency of the CMA consumption and concomitant formation of the bicyclic lactone intermediates (Figure 3.2 (A)). Based on a previous reaction network analysis,³¹ the reaction of MeCMA with propylene forms four DAP isomers (para (endo/exo) and meta (endo/exo)) resulting in a complex rate equation (Eqn. (3.1)) where [P] is the concentration of propylene and [2], [3], [4], [5] are the concentration of the individual bicyclic lactones.

$$-r_{MeCMA} = k_{1,exo}[1][P] + k_{1,endo}[1][P] - k_{2,exo}[2] - k_{2,endo}[3] + k_{3,exo}[1][P] + k_{3,endo}[1][P] - k_{4,exo}[4] - k_{4,endo}[5] \quad (3.1)$$

$$-r_{MeCMA} = k_1[1][P] - k_2[S_{2-3}] + k_3[1][P] - k_4[S_{4-5}] \quad (3.2)$$

$$-r'_{MeCMA} = k_1[1] - k_2[S_{2-3}] + k_3[1] - k_4[S_{4-5}] \quad (3.3)$$

$$-r'_{MeCMA} = k_1[1] + k_3[1] \quad (3.4)$$

$$-r'_{MeCMA} = (k_1 + k_3)[1] \quad (3.5)$$

To simplify the kinetic analysis, we assumed that kinetic difference in the end/exo isomer formation were negligible so 2 and 3 were lumped into a single species S_{2-3} as were 4 and 5 into S_{4-5} . Based on this assumption, we used a simplified rate law that only accounted for the DA reaction of MeCMA and propylene to the combined DAP species S_{2-3} and S_{4-5} and included the reverse reaction (rDA) (Eqn. 3.2). Since propylene was in large excess ~10 times, Eqn. (3.2) was further simplified to a pseudo-first order rate law as shown in Eqn. (3.3). The kinetic and DFT computational results presented herein indicate that the formation of 2, 3, 4 and 5 proceed in the absence of the retro DA (rDA) reaction. A least square regression analysis of the experimental concentration-time profiles (Figure S 3.6) clearly show that $k_2 \ll k_1$ and $k_4 \ll k_3$. This is consistent with DFT results that show that the reverse reaction (rDA) has a very high barrier (> 180 kJ/mol) (Figure 3.2 (B)) as compared to the forward reaction (~147 kJ/mol). This further suggests the absence of the rDA reaction. These results allowed the rate expression reported in Eqn. (3.3) to be simplified to Eqn. (3.4) and subsequently to Eqn. (3.5).

The rate constants k_1 and k_3 obtained at different temperatures (Table S 3.1-S 3.2) were used to calculate the apparent activation barrier (E_A) from an Arrhenius plot for the

combined formation of the endo/exo DAP species S_{2-3} and S_{4-5} , respectively (Figure 3.2 (C)). The calculated barriers of formation for S_{2-3} and S_{4-5} were 80 kJ/mol and 85 kJ/mol, respectively, and were in close agreement to the DFT calculated gas phase barriers (Figure 3.2 (B)). Both species 2 and 3 resulted in theoretical enthalpic barriers of 74 kJ/mol, while species 5 and 4 had slightly different barriers of 76 and 81 kJ/mol, respectively. The structures for all of the different isomers are reported in Figure S 3.7-S 3.8. We calculated the barriers for lumped S_{2-3} and S_{4-5} species by taking a Boltzmann average of individual activation barriers between 90 °C- 120 °C. This resulted in a DFT activation barrier of 74 kJ/mol for the formation of S_{2-3} and 77 kJ/mol for the formation of S_{4-5} . In a similar manner, we calculated the Boltzmann averaged Gibbs free energy barrier for cycloaddition to form the lumped para species was 130 kJ/mol and that for the lumped meta species was 134 kJ/mol. The detailed Gibbs free energy diagram is reported in the SI (Figure S 3.9).

From the rate constant analysis (Table S 3.1-S 3.2), it is evident that the formation of Species S_{2-3} is roughly 5 times faster than S_{4-5} , which explains the observed 8/9 product composition shown in Table 3.1, Entry 6. Given the absence of an rDA reaction step, the p/m ratio can be obtained from the ratio of the rate constants k_1/k_3 . At temperatures in the range of 90 °C and 110 °C, the ratios of k_1/k_3 were only slightly affected by temperature and ranged from 4.6 to 4.8. This implied that the p/m product ratio can only be slightly influenced by temperature and is effectively predetermined by the DA reaction step. Based on the DFT calculated Gibbs free energy barriers, we obtain p/m values in the range 3.4 to 3.8 for temperatures of 90 to 120 °C, which is in close agreement to the experimental values of p/m.

Interestingly, in comparing the activation barrier for propylene addition to MeCMA with activation barriers of 2-pyrones in combination with various dienophiles, it is evident that not only degree of functionalization but also position of the functional group on the 2-pyrone considerably contributes to the success of the Diels-Alder junction. While ethyl coumalate cycloaddition with butyl vinyl ether results in an activation barrier of 27.6 kJ/mol, a noticeable change in the barrier was observed when changing the functional group position of the 2-pyrone from the C5 to the C6 carbon position that results in a barrier of 36.4 kJ/mol.⁸⁷ Evidently, changing the position of the functional group influences the charge distribution in the 2-pyrone conjugated C=C bonds of the pyrone that results in

altered reactivity. When MeCMA is reacted with deactivated dienophiles such as acrolein, methyl acrylate and acrylonitrile, it resulted in activation barriers that were in the range of 106.7- 125.1 kJ/mol,³⁰ providing clear evidence that that degree of functionalization of the dienophile is another contributing factor that dictates the cycloaddition.

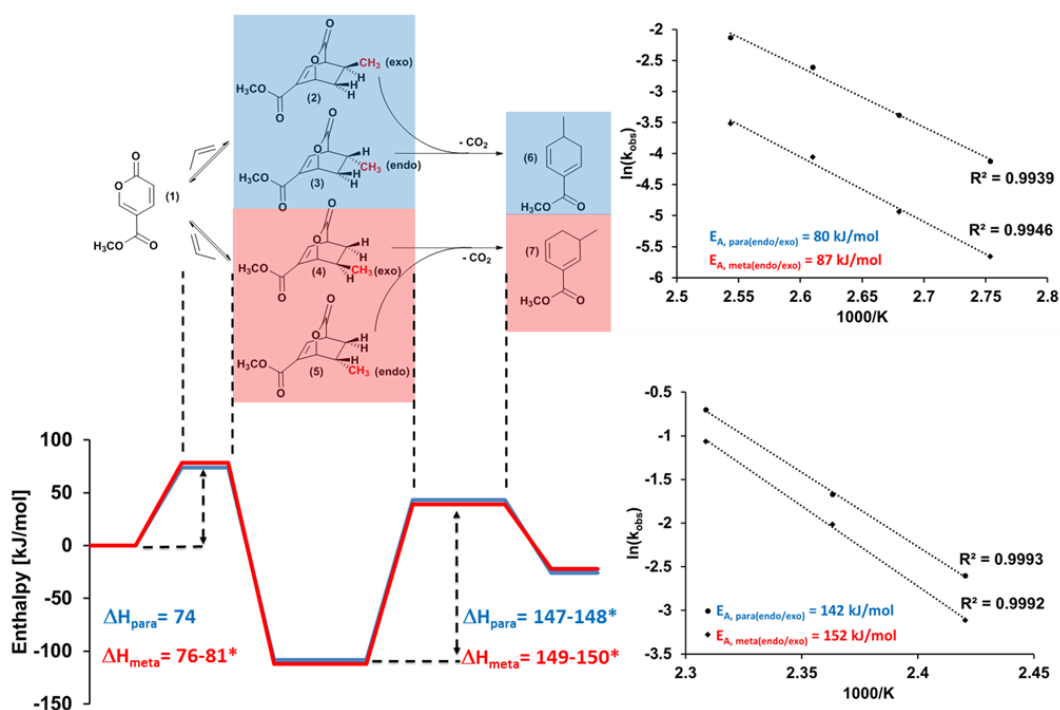


Figure 3.2(A) Reaction network of the Diels-Alder/decarboxylation reaction sequence of MeCMA 1 and propylene. (B) DFT calculated reaction energy profile diagram for the MeCMA reaction with propylene to bicyclic lactones 2, 3, 4, and 5 followed by decarboxylation to cyclohexa-1,5-diene carboxylate species 6 and 7. (C) Experimentally measured activation energies of the DA reaction of 1 with propylene to a single para species consisting of endo/exo isomers 2 and 3 and a single meta species consisting of endo/exo isomer 4 and 5. (D) Experimentally measured activation energies of the decarboxylation of the combined endo/exo para species (2+3) to 6 and endo/exo meta species (4+5) to 7. Endo/exo isomers 2, 3 and 4, 5 are combined to a single para and meta species to simplify the kinetic analysis and to obtain an average

Gas phase calculations for ethylene addition to MeCMA resulted in an enthalpic barrier of 74 kJ/mol and a Gibbs free energy barrier of 127 kJ/mol. Propylene addition to MeCMA

on the contrary exhibited enthalpic and Gibbs free energy barriers of 74/77 kJ/mol (para/meta) and 130/134 kJ/mol (para/meta), respectively. Comparing the Gibbs free energy barriers for the two cases, we expect ethylene to react faster than propylene, which was observed experimentally. However, the presence of the additional $-\text{CH}_3$ group should make propylene more electron donating compared to ethylene, and in principle accelerate the rate of the propylene cycloaddition. We found that the energy difference between interacting molecular orbitals $\text{LUMO}_{\text{diene}} - \text{HOMO}_{\text{dienophile}}$ for the inverse electron demand Diels-Alder addition was equal to 656 kJ/mol for propylene addition and 709 kJ/mol for ethylene, suggesting that propylene reacts slightly faster than ethylene just based on the Frontier Molecular Orbital theory. However, the presence of the additional methyl group on propylene makes it slightly bulkier possibly increasing steric hindrance during addition which could explain why ethylene addition is ~ 3 fold faster than propylene addition. The calculation results show that steric repulsion during propylene addition resulted in a longer C-C bond by $\sim 0.1 \text{ \AA}$ and slightly larger angles with MeCMA as the dienophile approaches (Figure S 3.12). The similar enthalpic barriers calculated for propylene and ethylene addition are likely due to a balance between electronic effects that favour propylene and steric effects that favour ethylene. The entropic differences between ethylene and propylene addition are also important as the calculated Gibbs free energy of activation for ethylene 177 J/(mol K) is $> 11 \text{ J/(mol K)}$ lower than that of propylene 188-193 J/(mol K), depending on regioselectivity of addition. Therefore, it seems that while electronics slightly favour propylene addition, sterics and entropic contributions render cycloaddition between ethylene and MeCMA to be a slightly faster reaction than propylene and MeCMA.

3.3.4 Decarboxylation reaction step

In situ decarboxylation of the bicyclic lactones 2, 3, 4 and 5 to 6 and 7 were performed in a temperature range of 140 °C to 160 °C using Wilmad-Labglass high pressure NMR tubes. The bicyclic lactones for the experiments were synthesized at 110 °C for 40 h using a batch reactor and resulted in 86 mol% combined yield at $\sim 98 \text{ mol\%}$ selectivity. The crude material was subsequently dissolved in dioxane- d_6 , transferred into NMR tubes and heated to the respective temperature to initiate decarboxylation.

In previous decarboxylation studies of bicyclic lactones from MeCMA and ethylene cycloaddition, we purported that the decarboxylation of the cycloadduct of MeCMA and propylene followed unimolecular first order kinetics with respect to the bicyclic lactones

(Eqn. (3.6)). To further simplify the decarboxylation kinetic analysis, we assumed that the activation barriers for the decarboxylation of the endo and exo isomers were similar and lumped the endo/exo species 2, 3 and 4, 5 into single species, S_{2-3} and S_{4-5} . Hence, the rate equation (Eqn. (3.6)) was simplified to Eqn. (3.7).

$$-r_{DAP} = k_5[2] + k_6[3] + k_7[4] + k_8[5] \quad (3.6)$$

$$-r_{DAP} = k_{10}[S_{2-3}] + k_{11}[S_{4-5}] \quad (3.7)$$

Based on Eqn. (3.7), plots of $\ln(DAP_o/DAP_t)$ vs time resulted in linear relationships (Figure S 3.13), validating our assumption of a first order reaction with respect to the bicyclic lactones. From these plots we obtained the rate constants k_{10} and k_{11} (Table S 3.1-S 3.4), through which the decarboxylation activation barrier was determined via the Arrhenius plot in Figure 3.2 (D). The activation barrier for the combined species S_{2-3} was 142 kJ/mol, while that for species S_{4-5} was 152 kJ/mol. These values were in close agreement with DFT results, which predicted decarboxylation activation barriers of 147 kJ/mol for 2 and 148 kJ/mol for 3, while the barriers for decarboxylation of 4 and 5 were 149 and 150 kJ/mol, respectively. The structures are shown in the SI (Figure S 3.7-S 3.8). We further calculated the barriers for the lumped S_{2-3} and S_{4-5} species by taking a Boltzmann average of individual activation barriers between 140 °C- 160 °C. This resulted in activation barriers from DFT of 147 kJ/mol for S_{2-3} decarboxylation and 150 kJ/mol for S_{4-5} decarboxylation fully consistent with the barriers resulting from the lumped experimental kinetic model.

The decarboxylation activation barrier of the bicyclic lactones of MeCMA and propylene were in close agreement to the decarboxylation barrier of the bicyclic lactone DAP from MeCMA and ethylene (148 kJ/mol).¹⁰⁴ Evidently, the methyl group of propylene has no significant influence on the DAP decarboxylation as compared to the ethylene based bicyclic lactone.

In contrast, decarboxylation of the cycloadduct from activated dienophile butyl vinyl ether in conjunction with ethyl coumalate revealed significant lower barriers (111 kJ/mol experimental and 120 kJ/mol computational) than those for ethylene and propylene with MeCMA.⁸⁷ The decarboxylation of the cycloadduct of 3-carbomethoxy-2(H)-pyran-2-on and butyl vinyl ether on the other hand results in a decarboxylation barrier of 90 kJ/mol experimentally and 108 kJ/mol computationally. Apparently, the degree of dienophile

functionalization and position of the functional group on the 2-pyrone plays an important role in DAP decarboxylation.

DFT energy mapping calculations reported in literature,¹⁰⁴ provides evidence that the CO₂ bridge of the bicyclic lactone of CMA and ethylene leaves in an asynchronous mechanism with a significantly elongated C-O bond in the transition state which was also reported in the literature.⁸⁷ Based on literature data and from our observations, it appears that thermal decarboxylation of 2-pyrone derived DAP species first induces C-O followed by C-C bond cleavage. These findings provide a better understanding about the CO₂ extrusion mechanism and can potentially be applied to similar 2-pyrone based bicyclic systems. Lastly, our kinetic analysis showed that decarboxylation was the rate-determining step in the Diels-Alder/decarboxylation/ dehydrogenation sequence as only minimal accumulation of the diene species 6 and 7 was observed when the reaction was carried out in the presence of catalyst. Additionally, decarboxylation is significantly slower than the DA reaction step, which renders the CO₂ extrusion as the bottle neck in this sequence of reactions, which was also reported.¹⁰⁴ This information is of critical importance as it provides evidence that enhancements on the decarboxylation step could significantly improve the overall reaction process. A recent study with the ethylene-derived bicyclic lactone with MeCMA showed, that the decarboxylation reaction could be considerably enhanced via use of a solid Lewis acid catalysts.⁸⁷ The Lewis acid catalyst, γ -Al₂O₃, was found to significantly lower the decarboxylation barrier allowing a lower reaction temperature and minimized by-product formation resulting in a nearly 100 mol% aromatic yield.

3.3.5 Diels-Alder reactivity trend of coumalates

Based on our research findings combined with literature data, it appears that 2-pyrone coumalates follow a general reactivity trend of ethyl vinyl ether > ethylene > propylene > acrolein > methyl acrylate > acrylonitrile > methyl propiolate (Figure 3.3) in which the DA activation barrier increases with increasing the frontier molecular energy gap of the dienophiles and diene MeCMA. As expected, the reactivity trend appears to follow that of an inverse electron demand DA reaction in which the coumalate cycloaddition is enhanced with activated (electron donating) dienophiles. In contrast, deactivated (electron withdrawing) dienophiles have a considerable HOMO-LUMO mismatch, which translates to lower reactivity. Interestingly, the regioselectivity towards the para substituted product

follows the opposite trend. With increasing activation barrier and FMO gap, the para to meta ratio decreases from electron donating to withdrawing dienophiles (ethyl vinyl ether > propylene > acrolein > methyl acrylate > acrylonitrile > methyl propiolate). This drop-in selectivity towards para adduct likely results from localization of electron density away from the terminal sp^2 carbon atom (C6) due to electron withdrawing groups (Figure S 3.10). This result is evident from the charge analysis of the dienophiles and resonance structures (Figure S 3.14). Since the enthalpic activation barrier ΔH_{act} accounts for both electronic and steric effects and the FMO gap only accounts for electronic effects, it appears that steric effects play a role in the DA reaction of coumalates and activated and deactivated dienophiles. Sterics effects likely result in the observed scatter in Figure 3.3.

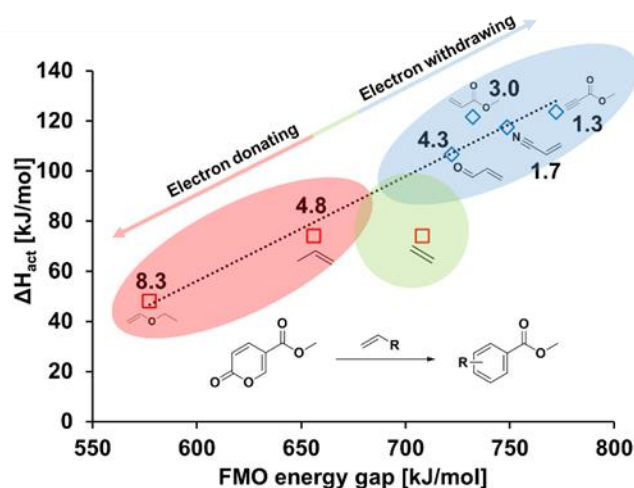


Figure 3.3 Reactivity trend of MeCMA cycloaddition with electron donating and withdrawing dienophiles. □ Experimental *p*-/*m*-ratios, calculated FMO energy gap and ΔH_{act} values were obtained in the present study, whereas ΔH_{act} for ethylene was reported in a previous study (ref. 5). ◇ Experimental *p*-/*m*-ratio and calculated ΔH_{act} values were reported in literature,³⁰ whereas the FMO energy gap values were calculated in the present study. The *p*-/*m*-ratios are reported on the experimentally observed aromatic product except for ethyl vinyl ether and methyl propiolate. The *p*-/*m*-ratio of the reaction of MeCMA and ethyl vinyl ether is based on the cycloadduct and methyl propiolate is based on DFT.³⁰

3.4 Conclusions

Herein, we demonstrate that the DA chemistry between CMA or MeCMA and propylene can yield high conversion and selectivity towards TA and MeTA, which provides a

renewable alternative to current petroleum based toluate production. Detailed kinetic analyses provided important kinetic information including rate constants and activation energies for DA cycloaddition and decarboxylation showing that DA was considerably faster than decarboxylation within the tested temperature range. The decarboxylation activation barrier was considerably higher than the barrier for DA cycloaddition which was corroborated via DFT computational analysis. Experimental investigation further revealed that methyl 3-/4-methylcyclohexa-1,5-diene-1-carboxylate species accumulation was minimal throughout the reaction procedure and was the result of immediate dehydrogenation to the final aromatic indicating that CO₂ extrusion was rate limiting.

We show, that the high decarboxylation activation barrier allowed for the successful isolation of DAP species from CMA (or MeCMA) conversion in conjunction with propylene, providing access to novel bicyclic lactone molecules in high selectivity. These species could be exploited as substrates to further expand the 2-pyrone platform with new and novel biomass-derived compounds that are challenging to access via conventional petroleum routes. Moreover, the controlled decarboxylation of the DAP yielded dihydrobenzenes with dual functionality that are potentially interesting for various applications (e.g., pharmaceuticals, antimicrobials, surfactants, etc.). Lastly, we provided a general reactivity trend of 2-pyrone coumalate cycloaddition with various electron donating and withdrawing dienophiles, which can be used to predict the feasibility of the Diels-Alder reaction step.

3.5 METHODS AND MATERIALS

3.5.1 Reagents and Materials

Coumalic acid (>97 %), γ -Valerolactone (98 %), and 10 wt% Pd on activated carbon were obtained from Sigma Aldrich. Methyl coumalate (> 98 %) and methyl *m*-toluate (98 %) were obtained from Alfa Aesar. *p*-Toluic acid (98 %), *m*-toluic acid (99 %), and methyl *p*-toluate (99 %) were obtained from Acros Organics. 1,4-Dioxane (> 99%), toluene (99.9 %), methanol (MS grade), water (MS grade), acetic acid (MS grade) were obtained from Fisher Scientific. Propylene (>99.9 %) was obtained from Matheson. The deuterated solvents DMSO-*d*₆ (99.5 %), dioxane-*d*₈ (99.5 %) were obtained from Cambridge Isotope Laboratories Inc. All chemicals were used without further purification.

3.5.2 Apparatus and general procedure

Kinetic measurements of the overall reaction sequence (Diels-Alder/decarboxylation/dehydrogenation) of CMA or MeCMA in with propylene were conducted using a 50 mL microreactor system from Parr Instruments (4590 Series). Reactions in the presence of catalyst were performed using a 10 wt% Pd/C catalyst, which was added to the reaction solution before the reactor was sealed and purged with nitrogen to remove residual air from the system. Subsequently, the batch reactor was charged with 130 psig propylene for 30 min to ensure saturation of propylene in the solvent so that the concentration of propylene was at all times in large excess (~10 times) compared to the starting substrate MeCMA or CMA. Next, the reactor temperature of the system was increased to the desired reaction condition with a heating rate of 10 K min⁻¹. Samples were periodically withdrawn from the reactor through a high-pressure sampling tip tube to obtain the concentration-time profile. Once the reactor reached the desired reaction temperature, a sample was withdrawn as the starting point reference. After sample collection, the liquid phase products were filtered through a 0.2 micron syringe filter to retain the catalyst and analyzed via ¹H-NMR, UPLC-PDA/QDa and GC-FID/MS.

Reaction kinetics for the DA reaction of MeCMA and propylene were performed at a temperature range between 90-120 °C in the absence of the 10 wt% Pd/C catalyst following the reaction procedure described above. 1,4-Dioxane was used as the solvent due to its superior solubility and stability of both CMA and MeCMA.

Reaction kinetics of the DA product (DAP) decarboxylation were performed at a temperature range between 140-160 °C, using high pressure NMR tubes from Wilmad-Labglass to minimize sample workup and improve the carbon balance. The DAP for this study was synthesized via DA reaction of MeCMA and propylene in 1,4-dioxane at 110 °C for 40 h giving high yield (> 86 mol%) and selectivity (>98 mol%). The DAP was separated from the solvent through careful evaporation using a stream of dry air and subsequently dissolved in fully deuterated dioxane-d₈. The reactant solution was then transferred into the high-pressure NMR tubes. Before the tube was sealed, 2.5 µL of an internal standard (dimethylformamid, DMF) was added to perform quantitative analysis. Next, the tubes were placed into a heated oil bath to initiate the decarboxylation reaction. The tubes were periodically taken out of the oil bath cooled to room temperature and the reaction products analyzed via ¹H-NMR.

3.5.3 Sample analysis

¹H-NMR sample analysis of the reaction products obtained from the batch reactions were carried out using a Bruker spectrometer equipped with a 14.1 Tesla superconducting magnet. TOPSPIN (version 3.0) and MestReNova (version 10.0.1-14719), were used to process the acquired data from NMR analysis. The NMR samples were prepared using fully deuterated DMSO-*d*₆ or dioxane-*d*₈, to reduce the solvent background and as a species to use for field calibration. ¹H spectra were acquired using a recycle delay of 3.0 sec. and 30° ¹H excitation pulse lengths.

The liquid reaction products were also analyzed with ultra-pressure liquid chromatography (UPLC) using a Waters Acquity H-Class System. The UPLC was equipped with a Photodiode Array (PDA) and a QDa mass detector and species separation was carried out on a Waters BEH Phenyl column (2.1x100 mm, 1.7 μm particles). Additionally, samples were analyzed by GC using an Agilent 7890B gas chromatograph equipped with an Agilent DB-1701 column (60 m x 0.25 mm), a flame ionization detector (FID), and an Agilent 5977A mass spectrometer (MS).

3.5.4 Computational

The calculations reported herein were performed using density functional theory with M062X^{88,89} hybrid functional as implemented in Gaussian 09.⁹⁰ Optimizations were performed on an ultrafine grid while using a tight force convergence criterion. The 6-311+G(d,p) basis set was utilized for all optimizations including saddle point calculations. Transition states were isolated using the QST2 algorithm within Gaussian. Frequency calculations were performed to confirm stationary and saddle points. Thermal corrections and partition functions were used to estimate values of enthalpy and Gibbs free energy for all species in the gas phase under harmonic approximation at 298.15 K. All the values reported for enthalpy and Gibbs free energy of reaction as well as activation barriers correspond to reactions in the gas phase.

3.6 Supplementary Information

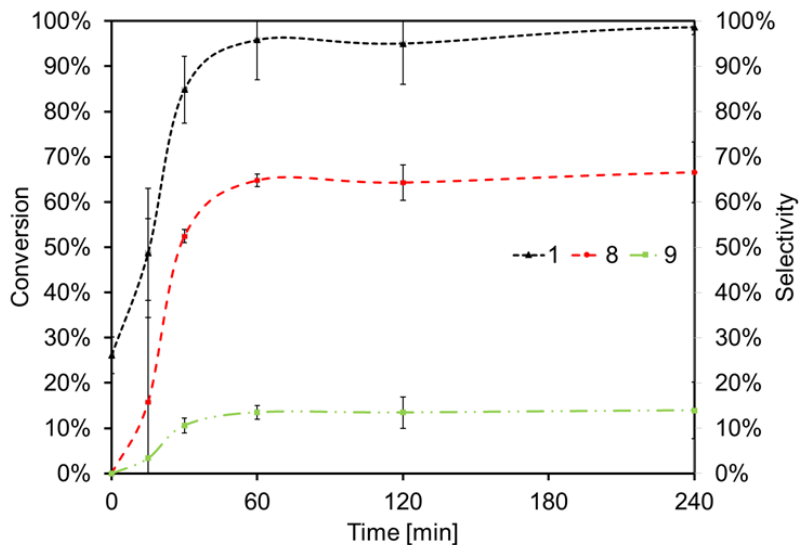


Figure S 3.1 The formation of toluic acid from coumalic acid in GVL at 180 °C 4h.

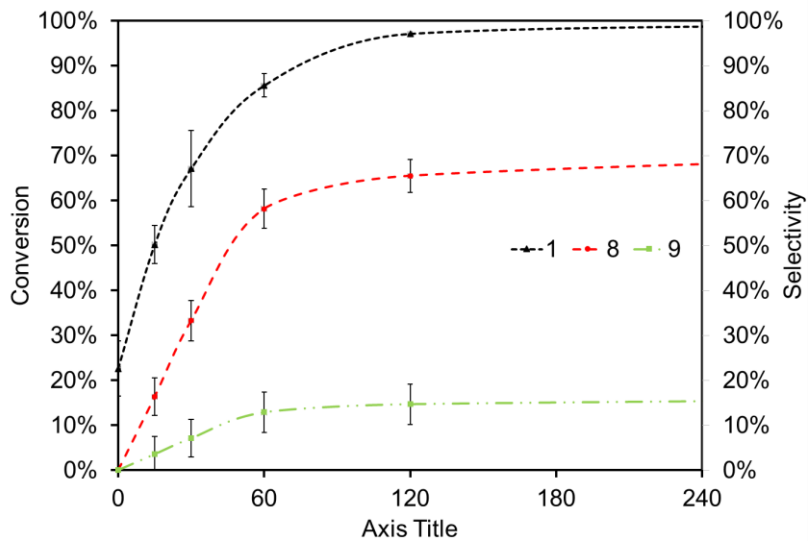


Figure S 3.2 The formation of toluic acid from coumalic acid in 1,4-dioxane at 180 °C 4h.

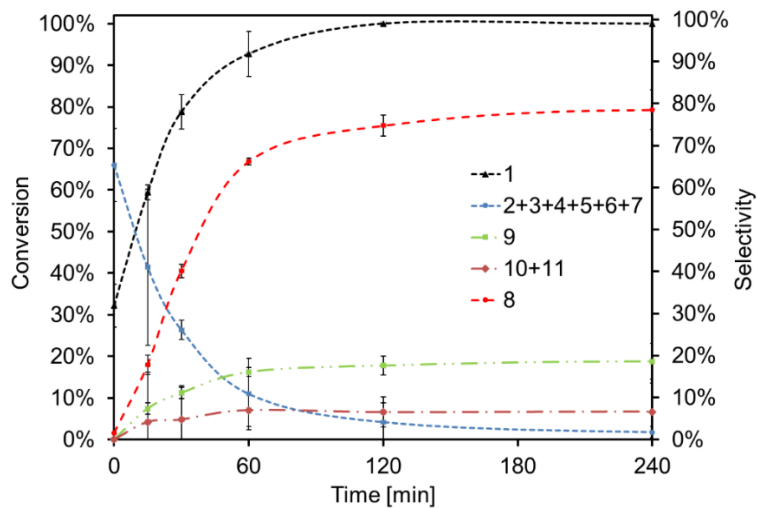


Figure S 3.3 The formation of methyl toluate from methyl coumalate in toluene at 180 °C 4h.

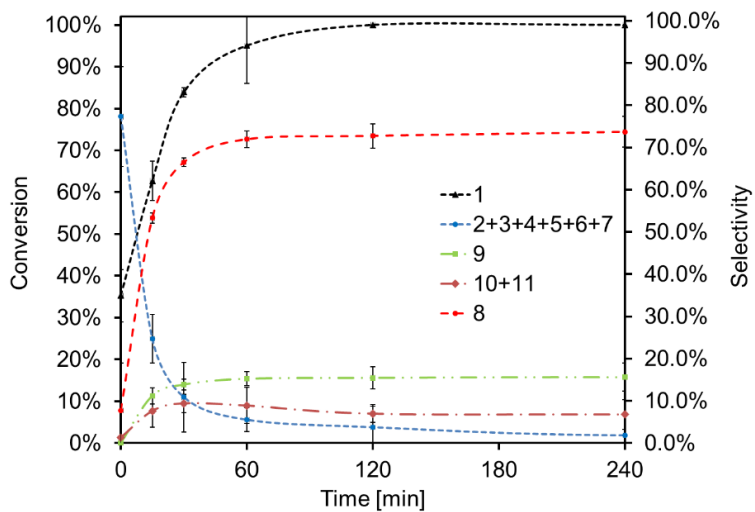


Figure S 3.4 The formation of methyl toluate from methyl coumalate in GVL at 180 °C 4h.

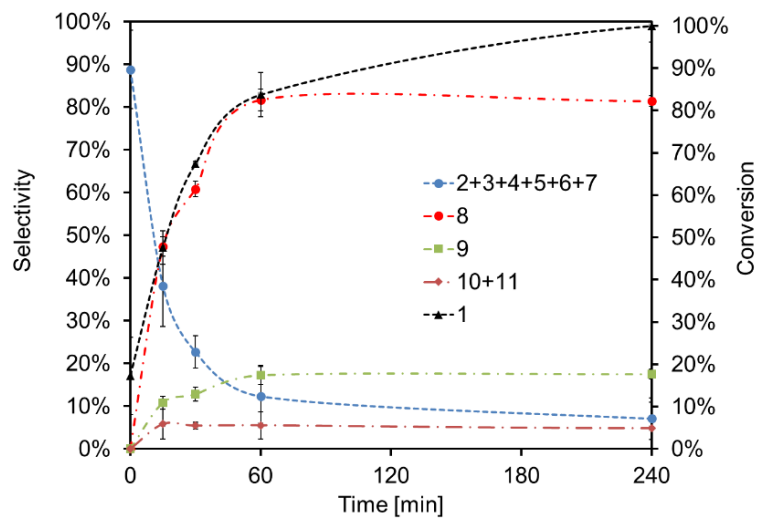


Figure S 3.5 The formation of methyl toluate from methyl coumalate in 1,4-dioxane at 180 °C 4h.

Table S 3.1 Rate constants and activation energy of the Diels-Alder reaction of coumalates with propylene to species S₂₋₃.

Entry	Substrate	Temp. [°C]	10 ³ 1/T [K ⁻¹]	10 ⁻³ k _{obs} [sec ⁻¹]	lnk	E _A [kJ/mol]
1	MeCMA	90	2.75	4.54E-06	-12.30	80
2	MeCMA	100	2.68	9.78E-06	-11.54	
3	MeCMA	110	2.61	2.18E-05	-10.73	
4	MeCMA	120	2.54	3.24E-05	-10.34	

Table S 3.2 Rate constants and activation energy of the Diels-Alder reaction of coumalates with propylene to species S₄₋₅.

Entry	Substrate	Temp. [°C]	10 ³ 1/T [K ⁻¹]	10 ⁻³ k _{obs} [sec ⁻¹]	lnk	E _A [kJ/mol]

1	MeCMA	90	2.75	9.50E-07	-13.87	82
2	MeCMA	100	2.68	2.18E-06	-13.03	
3	MeCMA	110	2.61	4.36E-06	-12.34	
4	MeCMA	120	2.54	7.46E-06	-11.81	

The rate constants in Table S 3.1 and S 3.2 were calculated based on the least square regression analysis of theoretical and experimental reaction rates (See eqn. (S1-S4)). Here, the rate constants k_1 , k_2 , k_3 , and k_4 were adjusted so that the experimental reaction rates (calculated from concentration-time profiles) are in alignment with theoretical reaction rates and the sum, S , of the squared residuals is at a minimum. From this analysis we observed best fits when the k_2 and k_4 equal zero indicating the absence of a retro Diels-Alder (rDA) reaction. This is also supported via DFT computations that show that the rDA reaction is energetically not favored (Fig. S13). To also proof the stability of our least square fit regression analysis and to proof we reached a global minimum, we used different initial k -values which all led to the same end results that are displayed in Fig. S6.

$$S = \sum (r[\text{MeCMA}]_{\text{exp}} - r[\text{MeCMA}]_{\text{theo}})^2 + (r[\text{S}_{2-3}]_{\text{exp}} - r[\text{S}_{2-3}]_{\text{theo}})^2 + \quad (\text{S } 3.1)$$

$$(r[\text{S}_{4-5}]_{\text{exp}} - r[\text{S}_{4-5}]_{\text{theo}})^2$$

$$d[\text{MeCMA}]/dt = -k_1[\text{MeCMA}] + k_2[\text{S}_{2-3}] - k_3[\text{MeCMA}] + k_4[\text{S}_{4-5}] \quad (\text{S } 3.2)$$

$$d[\text{S}_{2-3}]/dt = k_1[\text{MeCMA}] - k_2[\text{S}_{2-3}] \quad (\text{S } 3.3)$$

$$d[\text{S}_{4-5}]/dt = k_3[\text{MeCMA}] - k_4[\text{S}_{4-5}] \quad (\text{S } 3.4)$$

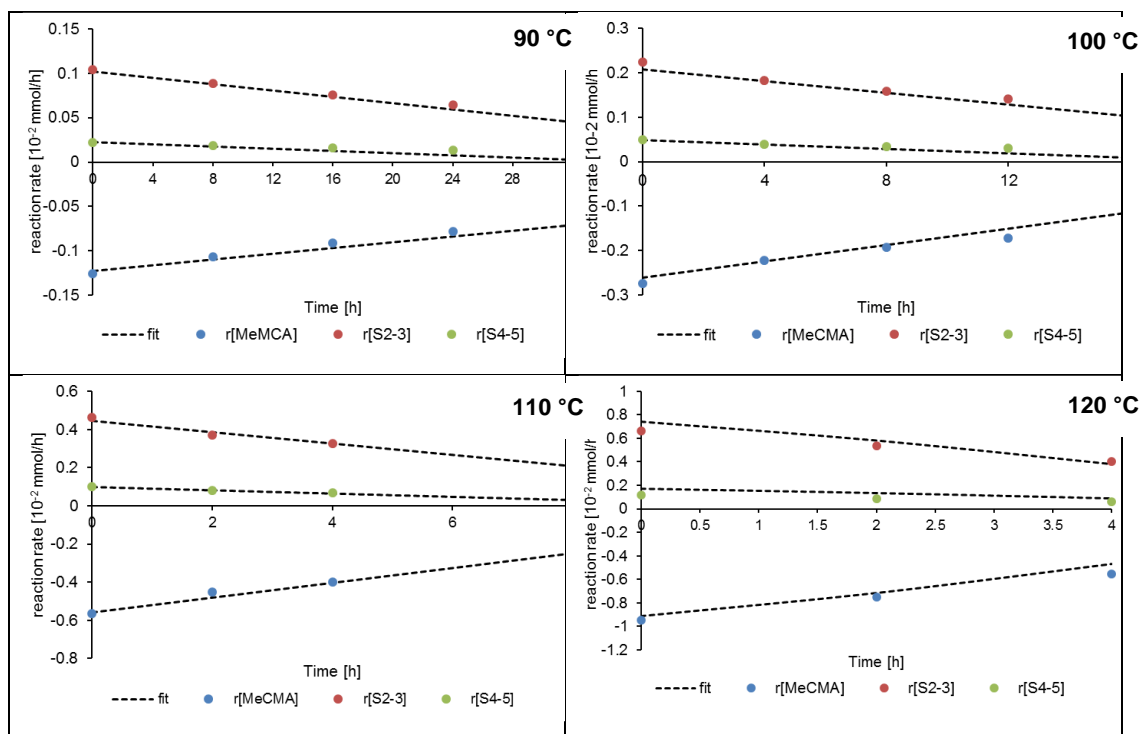


Figure S 3.6 Experimental and fitted reaction rates of the consumption of MeCMA and the formation of species S₂₋₃ and S₄₋₅.

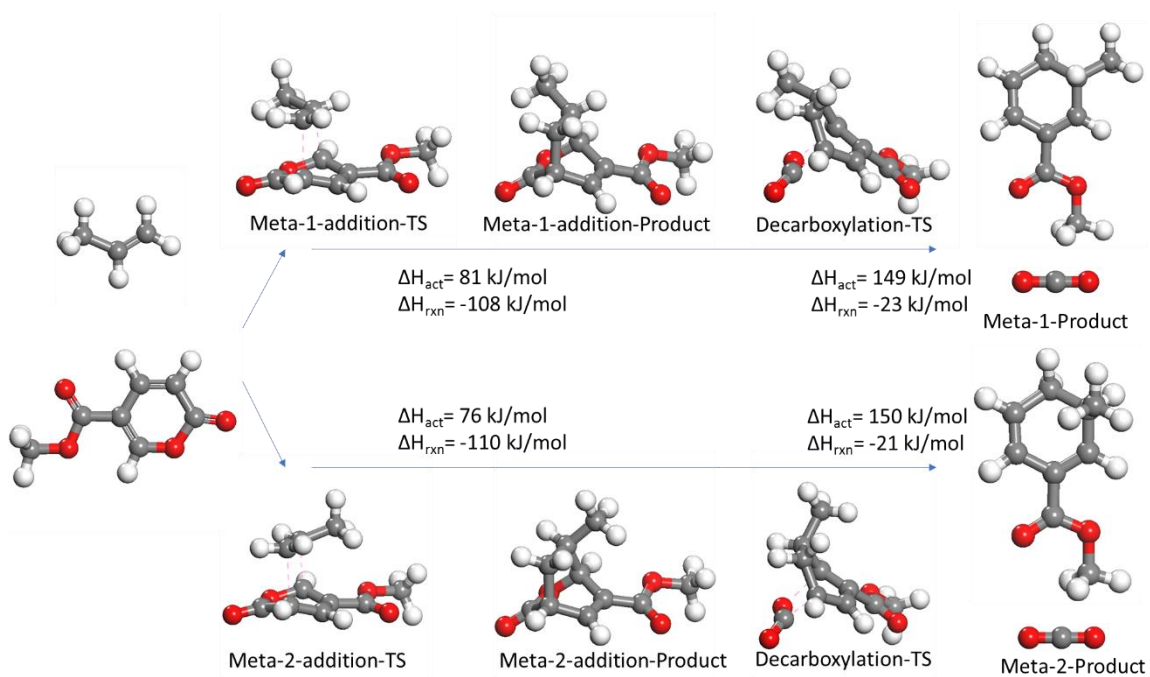


Figure S 3.7 Structures and enthalpies for meta addition and subsequent decarboxylation

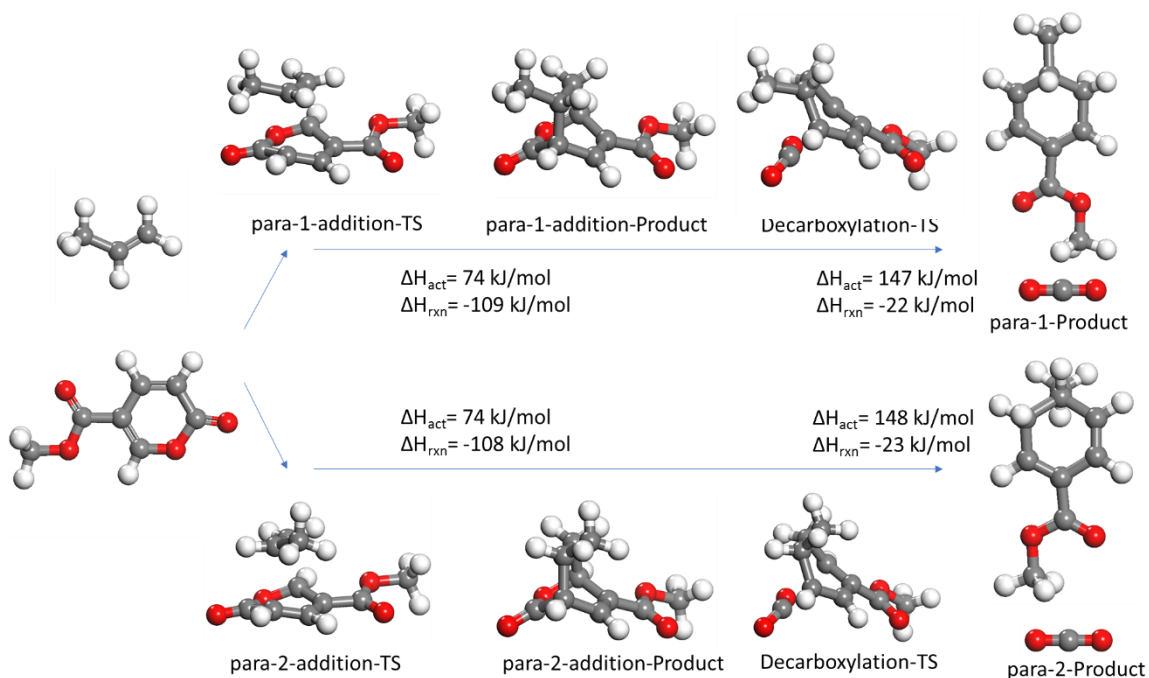


Figure S 3.8 Structures and enthalpies for para addition and subsequent decarboxylation

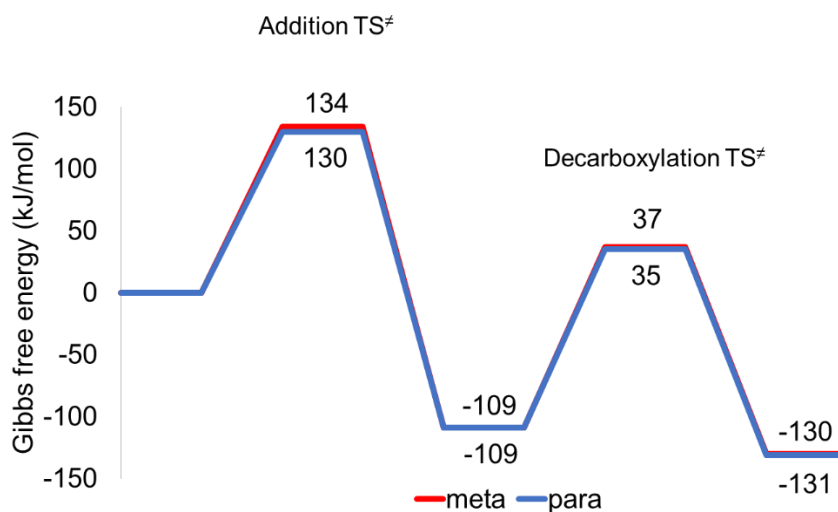


Figure S 3.9 Standard state Gibbs free energy diagram for meta and para cycloaddition of propylene and MeCMA and subsequent decarboxylation. All values are Boltzmann averaged over endo/exo structures

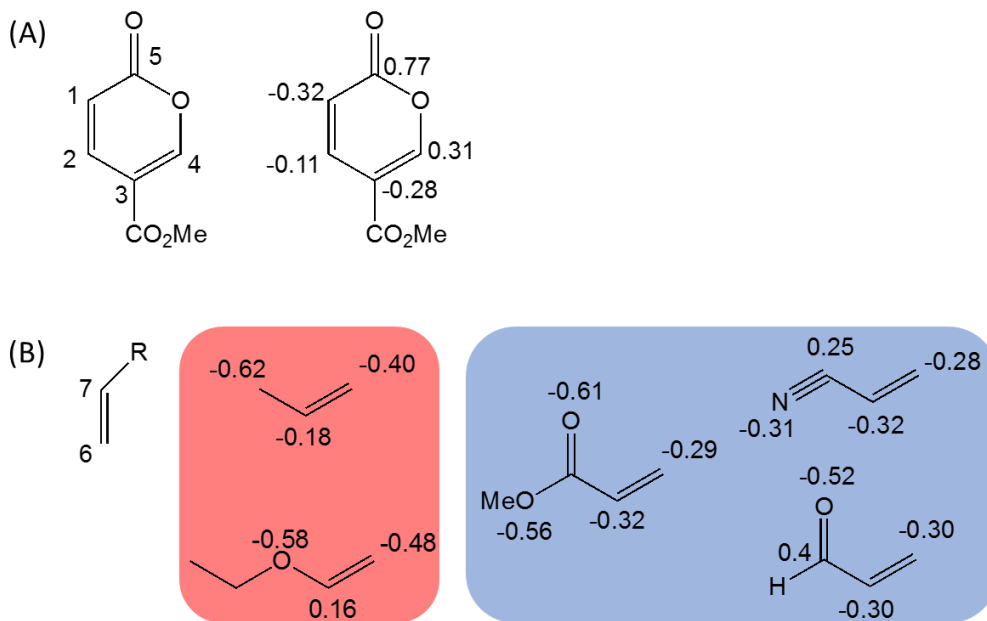


Figure S 3.10(A) Charge distribution on different carbon atoms on MeCMA. As seen, positive charge is more localized on C5 and C4 carbon atoms. **(B)** Charge distribution on different dienophiles. In all cases, para addition seems more favorable than meta purely based on electronics due to bond formation between negatively charged terminal carbon (C6) and positively charged C4 atom. Electron donating dienophiles (red) tend to localize negative charge on the terminal C6 carbon atom, while electron withdrawing dienophiles tend to withdraw electron density from the terminal C6 carbon atom. As a result, para addition is highly favorable for electron donating dienophiles. On the other hand, withdrawal of electron density from the terminal C6 position by electron withdrawing dienophiles makes para addition harder decreasing the selectivity to para.

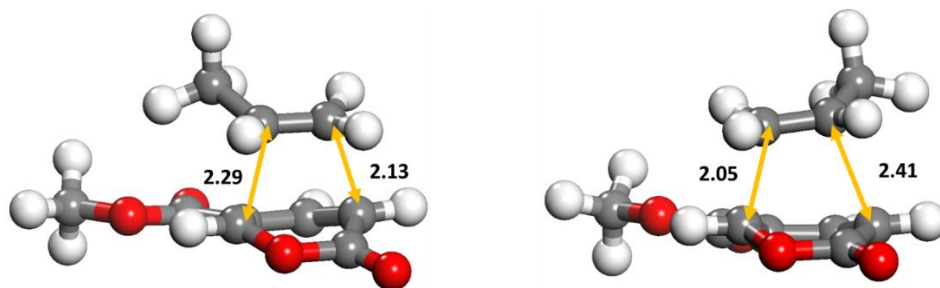


Figure S 3.11 Secondary interactions leading to shorter C-C bond distance during para cycloadduct formation compared to meta formation. Secondary molecular orbital interactions were proposed by Kraus et al. to favor para formation over meta.

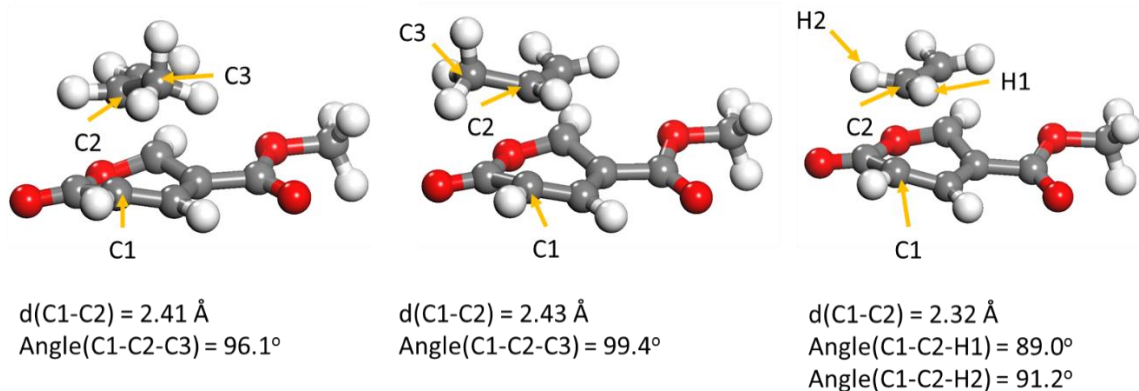


Figure S 3.12 Steric effects during addition of propylene vs ethylene to MeCMA. For the favored endo and exo para adduct formation, the C1-C2 distance is about 0.1 Å longer. In addition, the angle formed by the methyl group in propylene with the diene (C3-C2-C1) is larger than the angle formed by H in ethylene with the diene (H3/H2-C2-C1)

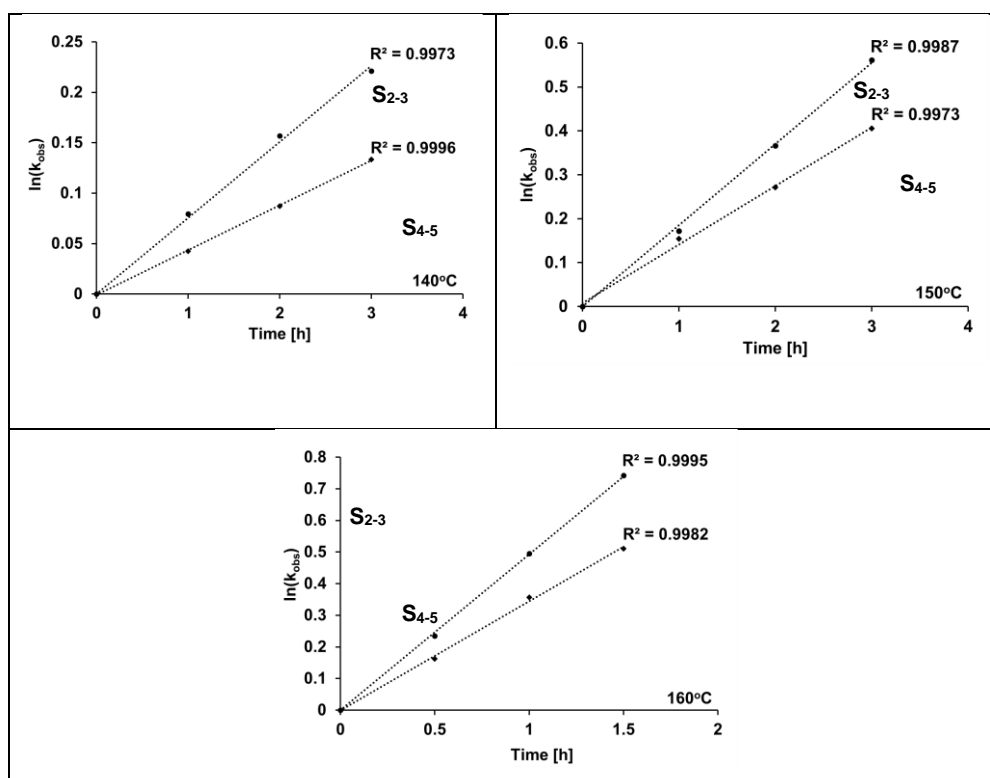


Figure S 3.13 Decarboxylation kinetics of the Diels-Alder cycloadduct species S₂₋₃ and S₄₋₅.

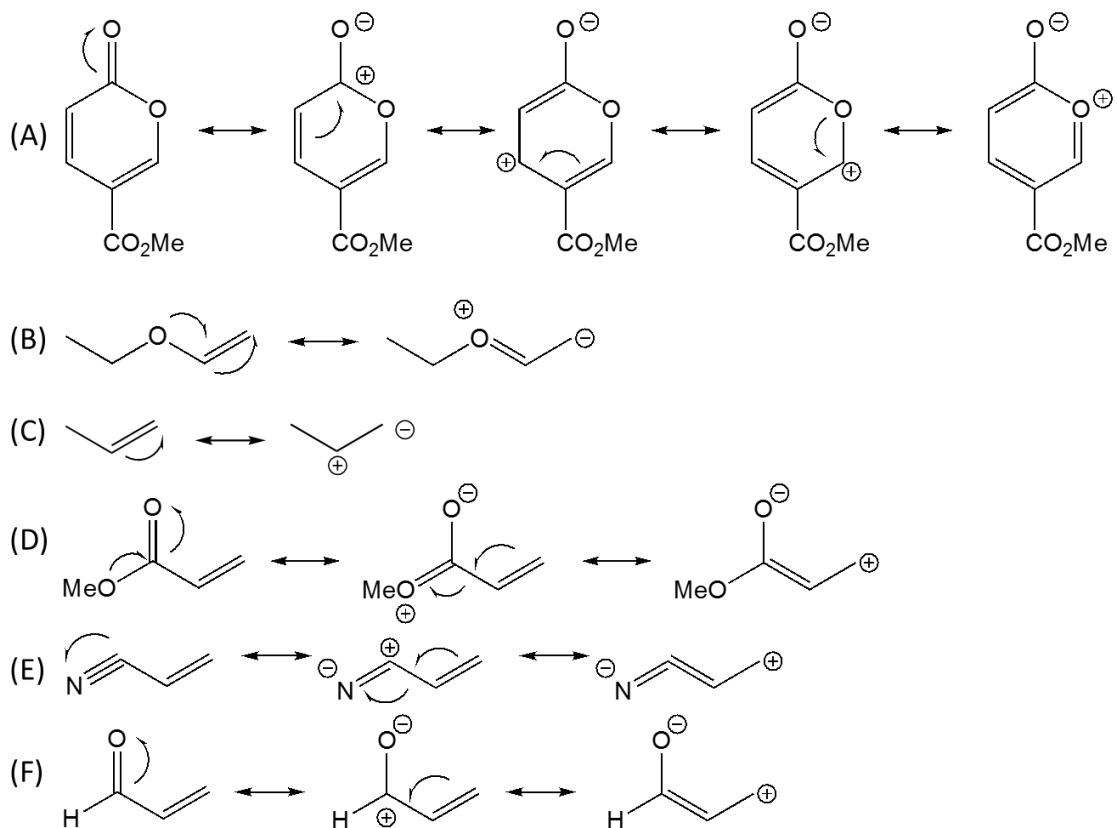


Figure S 3.14 Resonance structures for (A) MeCMA (B) Ethyl vinyl ether (C) Propylene (D) Methyl acrylate (E) Acrylonitrile (F) Acrolein

Table S 3.3 Rate constants and activation energy of the decarboxylation reaction of the para bicyclic lactones S_{4-5} form coumalate reaction with propylene.

Entry	Substrate	Temp. [°C]	$10^3 1/T$ [K ⁻¹]	$10^{-3} k_{\text{obs}}$ [h ⁻¹]	lnk	E_A [kJ/mol]
1	S_{2-3}	140	2.42	0.0741	-2.60	142
2	S_{2-3}	150	2.36	0.188	-1.67	
3	S_{2-3}	160	2.30	0.497	-0.70	

Table S 3.4 Rate constants and activation energy of the decarboxylation reaction of the meta bicyclic lactones S₄₋₅ form coumalate reaction with propylene.

Entry	Substrate	Temp. [°C]	10 ³ 1/T [K ⁻¹]	10 ⁻³ k _{obs} [h ⁻¹]	lnk	E _A [kJ/mol]
1	S ₄₋₅	140	2.42	0.0445	-3.11	152
2	S ₄₋₅	150	2.36	0.1334	-2.01	
3	S ₄₋₅	160	2.30	0.3453	-1.06	

4 Theoretical Insights into the Sites and Mechanisms for Base Catalyzed Esterification and Aldol Condensation Reactions over Cu

Adapted from Neurock, M., Tao, Z., Chemburkar, A., Hibbitts, D. D., Iglesia, E. *Theoretical Insights into the Sites and Mechanisms for Base Catalyzed Esterification and Aldol Condensation Reactions over Cu*. *Faraday Discuss.*, **2017**,197, 59-86. Reproduced by permission of The Royal Society of Chemistry.

Calculations were performed by AC and ZT under the supervision of MN.

4.1 Conspectus

Condensation and esterification are important catalytic routes in the conversion of polyols and oxygenates derived from biomass to fuels and chemical intermediates. Previous experimental studies⁴⁶ show that alkanal, alkanol and hydrogen mixtures equilibrate over Cu/SiO₂ and form surface alkoxides and alkanals that subsequently aid in catalyzing condensation and esterification reactions. First-principle density functional theory (DFT) calculations were carried out herein to elucidate the elementary paths and the corresponding reaction energetics for the interconversion of propanal + H₂ to propanol and the subsequent C-C and C-O bond formation paths involved in aldol condensation and esterification of these mixtures over model Cu surfaces. Propanal and hydrogen readily equilibrate with propanol via C-H and O-H addition steps to form surface propoxide intermediates and equilibrated propanal/propanol mixtures. Cu behaves as a Lewis acid and promotes the activation of the alkanal to an enol-like intermediate that can subsequently activate hydridic C₁-H bonds. Surface propoxides readily form via low energy paths involving a hydrogen addition to electrophilic carbon center of the carbonyl of propanal or via a proton transfer between two propanol surface intermediates. The resulting surface propoxide withdraws electron density from the surface and behaves as a base catalyzing the activation of propanal and subsequent esterification and condensation reactions. These basic propoxides readily abstract the acidic C_α-H of propanal to produce the CH₃CH⁽⁻⁾CH₂O* enolate thus initiating aldol condensation. The

enolate subsequently reacts with a second adsorbed propanal to form a C-C bond and the β -alkoxide alkanal intermediate. The β -alkoxide alkanal can subsequently undergo facile hydride transfer to form the 2-formyl-3-pentanone intermediate that decarbonylates to give the 3-pentanone product. Cu is unique in that it rapidly catalyzes the decarbonylation of the C_{2n} intermediates to form C_{2n-1} 3-pentanone as the major product with very small yields of C_{2n} products. This appears to be due to the absence of Brønsted acid sites that are present on metal oxide catalysts that rapidly catalyze protonation and dehydration of the hemiacetal or β -alkoxide alkanal species over decarbonylation. The basic surface propoxide can nucleophilically attack the carbonyl of a surface propanal to form propyl propionate. Theoretical results indicate that the rates for both aldol condensation and esterification are controlled by reactions between surface propoxide and propanal intermediates. In the condensation reaction, the alkoxide abstracts the weakly acidic hydrogen of the C_{α} -H of the adsorbed alkanal to form the surface enolate whereas in the esterification reaction the alkoxide nucleophilically attacks the carbonyl group of a vicinal bound alkanal. As both condensation and esterification involve reactions between the same two species in the rate-limiting step, they result in the same rate expression which is consistent with experimental results. The theoretical results indicate that the barriers between condensation and esterification are within 3 kJ mol^{-1} of one another with esterification being slightly more favored. Experimental results also report small differences in the activation barriers but suggest that condensation is slightly preferred.

4.1 Introduction

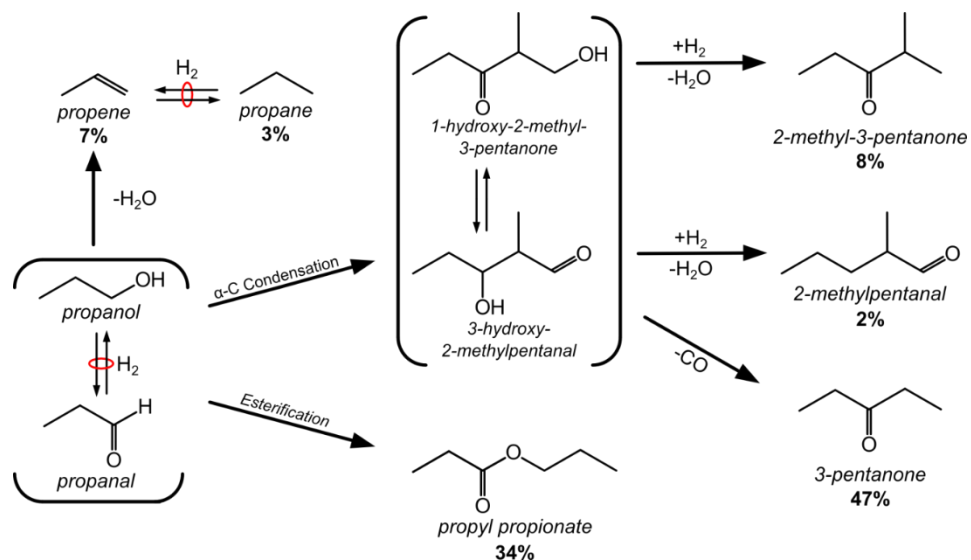
Aldol condensation, Guerbet coupling as well as other alkanal/alkanol coupling reactions provide attractive routes for the removal of oxygen and hydrocarbon chain growth, important steps in the conversion of oxygenates to fuels as well as chemicals. Aldol condensation reactions are currently used industrially in the synthesis 2-ethyl hexanal, methyl isobutyl ketone and Guerbet alcohols¹⁶⁷ and are also being considered for the conversion of bio-alcohols to fuels.^{2,168} Aldol condensation and Guerbet reactions typically proceed via coupling of aldehydes and alcohols, respectively to form β -hydroxy alkanals and alkanones that dehydrate to form α,β -unsaturated carbonyl intermediates on acid or base catalyst.¹⁶⁹ Base-catalyzed aldol condensation mechanisms are thought to proceed via the abstraction of the weakly acidic hydrogen at the α -C of an alkanal, thus resulting

in the formation of an enolate that subsequently attacks the electrophilic carbonyl group of a vicinal alkanal to form a new C-C bond. These reactions can be carried out over a range of different homogeneous catalysts including Cu(II), Co(II), Mn(II), and Zn(II)¹⁷⁰ together with base promoters (NaOH, NaOR, and Na₂CO₃) or basic ligands,¹⁷¹⁻¹⁷⁴ as well as on heterogeneous base catalysts, including MgO,¹⁷⁴⁻¹⁷⁷ Mg-AlOx, ZnO,^{167,178} phosphates,¹⁷⁹ and base-promoted mesoporous silicas, such as diamino-functionalized MCM-41¹⁸⁰ and hydrotalcites.^{181,182}

Previous kinetic studies have shown that while aldol condensation of primary C_n alcohols to C_{2n-1} alkanones proceed over CuO/ZnO/Al₂O₃ as well as Cu/ZnO,¹⁸³ the basic sites on the ZnO support are responsible for C-C bond formation. In a recent study, Sad et al.⁴⁶ demonstrated for the first time that both aldol condensation as well as esterification can proceed over non-basic catalysts, specifically monofunctional Cu/SiO₂ catalysts. Propanol (C₃H₇OH) was found to rapidly equilibrate with propanal (C₃H₆O) and H₂, to form an equilibrated propanol-propanal-H₂ reactant pool that subsequently reacts via the three predominant paths shown in Scheme 4.1: 1) dehydration of propanol to form propene and then propane through subsequent hydrogenation steps; 2) aldol condensation followed by decarbonylation and dehydrogenation to form 3-pentanone (C₅H₁₀O) or dehydration paths to form minor 2-methyl-3-pentanone and 2-methyl-pentanal (C₆H₁₂O) products; and 3) esterification to form propyl propionate (C₆H₁₂O₂). The reported selectivities to form the propene, propane, 2-methyl-3-pentanone, 2-methyl-pentanal, 3-pentanone, and propyl propionate at 3% conversion shown in Scheme 4.1 were 7%, 3%, 8%, 2%, 47%, and 34%, respectively. Detailed kinetic analyses indicated that both esterification and condensation reactions proceed via the in-situ formation of surface alkoxides on Cu that act as bases that catalyze C-C and C-O bond-forming reactions.

Detailed kinetic analyses showed that rate equations for esterification and condensation follow the exact same functional form (with the rate of condensation being ~2 times faster than the rate of esterification), suggesting that they proceed via a similar kinetically-relevant step that precedes a kinetic branch point unaffected by H₂ and alkanal/alkanol pressures or that they have distinct kinetically-relevant steps that share the same reactant precursors.⁴⁶ The experimental results were used together with simple estimates from gas phase molecular calculations to suggest that condensation proceeds by the reaction of a surface enolate with an adsorbed propanal to form a hemi-acetalate (β -alkoxide alkanal)

that ultimately decarbonylates to form 3-pentanone. In contrast, propyl propionate was proposed to proceed via a Cu-catalyzed esterification of two aldehydes similar to the classic base-catalyzed esterification routes proposed by Cannizzaro and Tishchenko.^{184,185}



Scheme 4.1 Reaction paths for the conversion of propanol/propanal/ H_2 over Cu/SiO_2 , Reprinted with permission from Sad, M. E., Neurock, M., Iglesia, E. Formation of C–C and C–O Bonds and Oxygen Removal in Reactions of Alkanediols, Alkanols, and Alkanals on Copper Catalysts. *J. Am. Chem. Soc.* 2011, *133*, 50, 20384-20398. Copyright 2011. American Chemical Society. Selectivities for six major products are given based on the following conditions: 5 wt.% Cu/SiO_2 , 5.6% dispersion, 503 K, 2160 g cat.-ks (mol propanol)⁻¹, 0.64 kPa propanol, 80 kPa H_2 , balance He, 3% conversion.

Herein we carry out a detailed series of first principle density functional theoretical (DFT) calculations to provide detailed insights into the elementary steps, elucidate the mechanisms and establish the kinetics for Cu-catalyzed alcohol dehydrogenation, esterification and condensation. The simulation results indicate that propoxide surface intermediates are readily formed on Cu via the hydrogenation and dehydrogenation of the propanal and propanol, respectively and act as a base co-catalyzing esterification and condensation pathways. Adsorbed alkanals work together with Cu to subsequently promote hydride transfer from the adsorbed alkoxide intermediates to remove condensation and esterification products from the surface and to regenerate the catalytic propoxides.

4.2 Computational Methods

All of the calculations reported herein were carried out using periodic, plane-wave density functional theory (DFT) calculations using the Vienna ab initio Simulation Program (VASP).^{127–130} The wave functions were constructed from a series of plane-wave basis functions expanded out to an energy cutoff of 396 eV using the Perdew-Wang form of the generalized-gradient approximation (PW91).¹⁸⁶ Electron-ion interactions were described through the use of Vanderbilt ultrasoft pseudopotentials.¹⁸⁷ The surface Brillouin zone was sampled with a 3x2x1 Monkhorst–Pack k-point grid. The electronic energies were converged to within 1×10^{-6} eV.

Experimental results show that both esterification and condensation rates increase with increasing particle size.⁴⁶ Large particles are comprised of high fractions of coordinatively unsaturated (111) sites which suggest that these may be active sites. The simulations were therefore predominantly carried out over Cu(111) surface to mimic the large supported Cu clusters. The Cu(111) surface was modeled using a four-layer slab comprised of 18 Cu atoms in each layer in a (3x6) surface unit cell. A vacuum region of 10 Å was included between metal slabs to prevent any interactions between the slabs. The bottom two layers of the Cu substrate were held fixed throughout the structural optimizations at their bulk positions with Cu-Cu distance of 2.55 Å. All structures were optimized until the maximum forces on all of the atoms were less than 0.05 eV Å⁻¹. The influence of edge and corner sites on the activation of C-H and O-H bonds of propanol were examined by carry out calculations on a Cu-110 surface.

The adsorption energies for all of the reactant and product molecules were calculated as:

$$\Delta E_{\text{ads}} = E_{\text{surf+ads}} - E_{\text{surf}} - E_{\text{ads}} \quad (4.1)$$

where $E_{\text{surf+ads}}$, E_{surf} , and E_{ads} are the energies of the surface-adsorbate complex, the bare metal surface, and the adsorbate in vacuum, respectively. For reactions, the activation barriers and reaction energies were calculated as:



$$\Delta E_{\text{ACT}} = E_{\text{TS}^*} + \delta E_{\text{surf}} - E_{\text{A}^*} - E_{\text{B}^*} \quad (4.3)$$

$$\Delta E_{\text{RXN}} = E_{\text{C}^*} + E_{\text{D}^*} - E_{\text{A}^*} - E_{\text{B}^*} \quad (4.4)$$

where E_i^* and E_{TS^*} refer to the energies of adsorbed intermediate i (A^* , B^* , C^* or D^*) and the transition state (TS^*), respectively. δE_{surf} refers to the change in energy required to bring the “infinitely” separated species on the surface together into the reactant state where they sit adjacent to one another thus accounting for any attractive or repulsive interactions.

Activation barriers were determined using a two-step transition state search scheme. In the first step, the nudged elastic band (NEB) method^{133,134} was used to determine the minimum energy reaction path and establish a reliable first guess of the transition state. The reaction path was divided into a sequence of 8 equally spaced images. Each of these images were optimized until the forces normal to the reaction coordinate were calculated to be less than 0.20 eV \AA^{-1} . The highest energy image along the minimum energy path was used as an initial guess of the transition state structure and used in the Dimer method¹³⁵ to isolate the transition state structure and minimize the forces on all of the atoms in the structure to below 0.03 eV \AA^{-1} . The intrinsic activation barriers for the elementary steps reported herein all refer to the direct energy difference between the transition state and the bound reactant(s) state along the elementary step reaction coordinate ($E_{TS^*} - E_{A^*} - E_{B^*}$ in Eq. 4.3). In order to compare with experimental results, we also provide apparent activation energies where the transition state energies are reference to the most abundant species present on the surface under reaction conditions rather than from the elementary step reactant state. We use adsorbed propoxide and alkanal as the zero-energy reference state to calculate apparent barriers for most of the systems discussed herein.

The enthalpy, entropy and free energies of activation were calculated for the rate controlling esterification and condensation steps. The Gibbs free energy of activation for the reaction between two surface intermediates can be calculated by:

$$G^\ddagger = -RT \ln \left(\frac{q_{vib}^{TS}}{q_{vib}^R} \right) \quad (4.5)$$

where, R is the ideal gas constant, T is the temperature, q_{vib}^{TS} and q_{vib}^R are vibrational partition functions of the transition state and the reactant state, respectively. The vibrational frequencies and the vibrational corrections to the electronic and internal energies were calculated within VASP on the optimized structure using the quasi-harmonic approximation. For frequency calculations, the electronic energies were

converged to within 10^{-8} eV and a step size of 0.015 Å was used. The reaction enthalpies and activation enthalpies were estimated by applying translational and rotational corrections to the internal energy. The vibrational frequencies were subsequently used to calculate the vibration partition functions of the reactant, transition and product states. The results were used to calculate the free energies of activation. The activation entropies were back-calculated from the free energies and enthalpies

The charges for reactant, product and transition states were calculated by using quasi-atomic minimal basis set orbitals (QUAMBO)¹⁸⁸ which recreate the electron density determined using VASP.

4.3 Results and Discussion

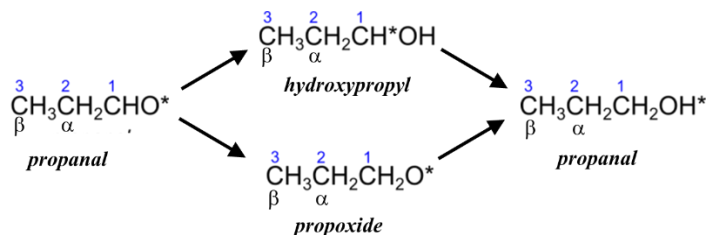
4.3.1 Conversion between Propanol to Propanal

4.3.1.1 Equilibrium of Propanal and Hydrogen to Propanol

As was discussed earlier, mixtures of propanal and hydrogen along with propanol readily react and equilibrate over Cu/SiO₂. DFT calculations were used here to examine the elementary steps in the hydrogenation of propanal to propanol over the Cu(111) as well at the reverse reactions involving the dehydrogenation of propanol to propanal and hydrogen. Propanal was calculated to preferentially adsorb atop in an η_1 configuration resulting in an adsorption energy of -28 kJ mol⁻¹ which is consistent with the adsorption site and energy reported from ultrahigh vacuum experimental studies carried out on Cu(111)^{189,190} and previous theoretical studies.^{191–193} Hydrogen readily dissociates over the Cu(111) surface to form two H* surface species with an overall energy of -32 kJ mol⁻¹ which is consistent with experimentally reported adsorption energies of ~40 kJ mol⁻¹.¹⁹⁴ The adsorbed propanal can subsequently be hydrogenated either by the initial addition of H* to the oxygen or the carbon of its carbonyl thus resulting in the formation of the hydroxypropyl (CH₃CH₂CH*OH) or propoxide (CH₃CH₂O*) intermediate, respectively as shown in Scheme 4.2. The paths which proceed via propoxide and hydroxypropyl intermediates are known more generally in the literature as the alkoxide and hydroxyalkyl paths.

The propoxide path which is shown in grey (unfilled symbols) in Figure 4.1 proceeds by the initial addition of hydrogen to the carbon of the bound carbonyl to form propoxide

resulting in a barrier of 63 kJ mol⁻¹ when taken with respect to the adsorbed propanal and a single H* (or 19 kJ mol⁻¹ if referenced to clean Cu surface and gas phase propanal and hydrogen). The surface under reaction conditions is thought to be covered by propanal and propoxide intermediates so the intrinsic barrier of +63 kJ mol⁻¹ provides a more reliable estimate of the apparent activation barrier. The overall reaction energy for this step is highly exothermic with an overall energy of -52 kJ mol⁻¹. The propoxide intermediate subsequently hydrogenates to the form adsorbed propanol. The intrinsic activation energy and the overall reaction energy to hydrogenate the propoxide to form propanol were calculated to be +99 kJ mol⁻¹ (or -21 kJ mol⁻¹ taken with respect to the clean Cu(111) surface) and -21 kJ mol⁻¹, respectively. The propanol that forms desorbs from the surface with an energy of +29 kJ mol⁻¹. The overall potential energy surface for this path shown in Figure 4.1 (unfilled symbols) suggests that propoxide forms and builds up on the surface as its rate of removal appears to be controlled by high barrier for the second hydrogen addition step.



Scheme 4.2 Routes for the dehydrogenation of propanol to form propanal.

In the hydroxypropyl path which is shown in black in Figure 4.1, the barrier to add hydrogen first to the oxygen of the carbonyl rather than the carbon was calculated to be significantly higher at +90 kJ mol⁻¹ taken with respect to the adsorbed propanal and H* as it requires the breaking a strong Cu-O bond (or +46 kJ mol⁻¹ taken with respect to gas phase propanal and hydrogen). The overall reaction energy to form the hydroxypropyl intermediates was calculated to be endothermic at +2 kJ mol⁻¹. The intrinsic activation barrier and overall reaction energy to subsequently hydrogenate hydroxypropyl intermediate to form adsorbed propanol were calculated to be 28 kJ mol⁻¹ taken with respect to the adsorbed hydroxypropyl intermediate and H* and -115 kJ mol⁻¹, respectively. The results in Figure 4.1 indicate that the rate for this path is likely limited by the initial hydrogen addition to the oxygen to form the hydroxyalkyl intermediate. A more detailed analysis of the energies for both the propoxide and the hydroxyalkyl paths shown in Figure 4.1 suggests that the propoxide path is more favorable than the hydroxypropyl path as the barrier to form the

propoxide (+63) is 27 kJ mol⁻¹ lower than that to form the hydroxypropyl (+90 kJ mol⁻¹). As such the propoxide, regardless of the path, is readily formed and likely builds up on the surface. This is consistent with previous analyses for the hydrogenation of different aldehydes and ketones over Ru.¹⁹⁵

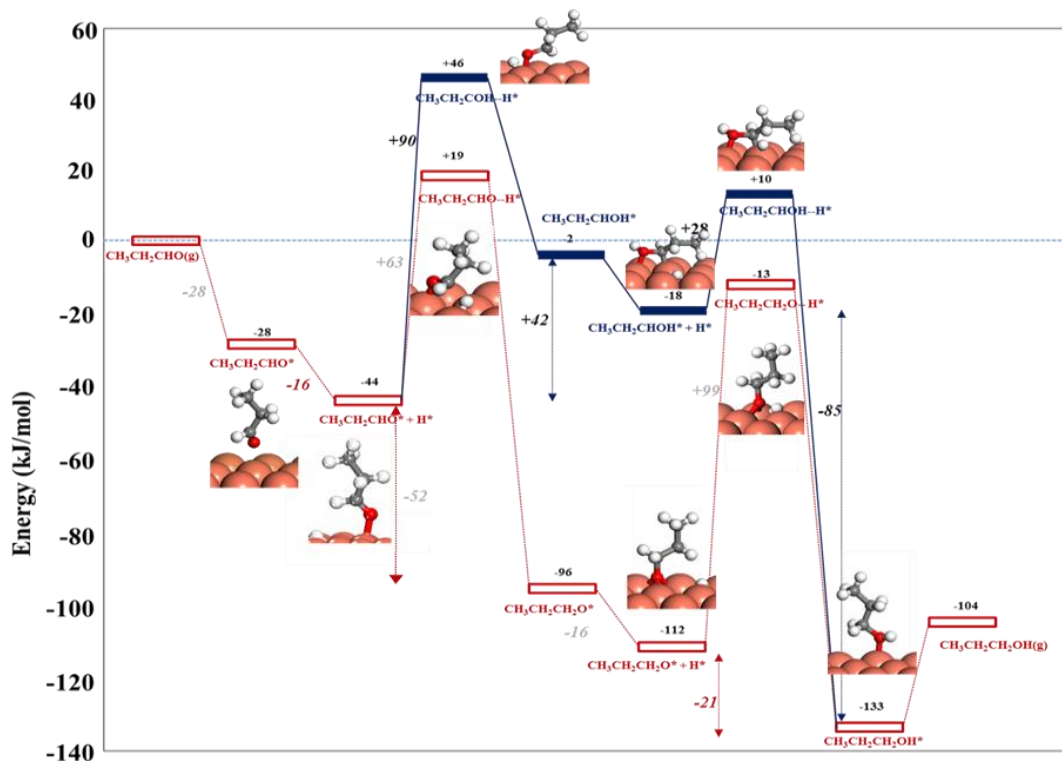


Figure 4.1 DFT-calculated pathways for the hydrogenation propanal to propanol and the reverse reaction involving the dehydrogenation of propanol to propanal and hydrogen. The propoxide path (shown with the unfilled rectangular symbols) involves the initial addition of hydrogen to the C₁ of the carbonyl to form the propoxide intermediate and the subsequent hydrogenation of the propoxide and the desorption of the propanol product. The hydroxypropyl path (shown with filled black rectangular symbols) proceeds instead by the initial addition of hydrogen to the O of the carbonyl to form the hydroxypropyl intermediate and subsequent addition of hydrogen to the C of the hydroxypropyl to form propanol which desorbs.

Propanol dehydrogenation, the microscopic reverse of propanal hydrogenation, is not likely to proceed over the Cu(111) surface as the intrinsic activation energies to activate the O-H or the C-H bond of propanol taken with respect to adsorbed propanol are 115 and 143 kJ mol⁻¹, respectively as is shown in Figure 4.1. This is consistent with ultrahigh vacuum studies which show that in the absence of oxygen, methanol as well as other light

alcohols desorb and do not dissociate over Cu(111), and other previous theoretical studies of methanol dehydration on Cu(111) [35-36]. The results by Sad et al.⁴⁶ carried out over Cu/SiO₂ at higher pressures with mixtures of propanal, hydrogen and propanol, however, show that mixtures readily equilibrate. The difference may be the result of higher propanol coverages at relevant reaction conditions which can assist O-H activation or via the presence and reactivity of coordinatively unsaturated sites that exist at edges or corner on the Cu particles. The results reported in Figure S 4.1 show that barrier to activate the O-H bond of propanol decreases to 70 kJ mol⁻¹ with increasing propanol surface coverage as higher coverages result in the formation of hydrogen bonding networks which stabilize the transition state and allow facile proton-transfer via a Grotthus-like mechanism similar to that reported for other alcohol decomposition reactions in the presence of water over different metals.¹⁹⁶⁻¹⁹⁸ While the higher coverages help to promote the formation of surface propoxide intermediates, the subsequent C-H activation would still likely be prohibitive as the barrier is 115 kJ mol⁻¹ and does not decrease at higher coverages.

Propanol dehydration may proceed more favorably at the edge and corner sites of Cu particles. Both the O-H and C-H activation barriers decrease significantly to 73 kJ mol⁻¹ when carried out at the more coordinatively unsaturated edge site on a Cu(110) (Figure S 4.2) which is consistent with experimental results for the activation of methanol, ethanol and propanol to form methoxy, ethoxy and propoxy, respectively over Cu(110) under ultrahigh vacuum conditions.¹⁹⁹⁻²⁰² As such, propanol dehydrogenation to propanal and H₂ can readily occur at the edge and corner sites. The propanal and hydrogen that form can subsequently adsorb and react on the Cu(111) terrace sites to carry out condensation and esterification. This would still be fully consistent with the results from Sad et al.⁴⁶ which show that the rates increase with Cu particle size thus indicating that the terrace sites are most active for the steps that control the rate.

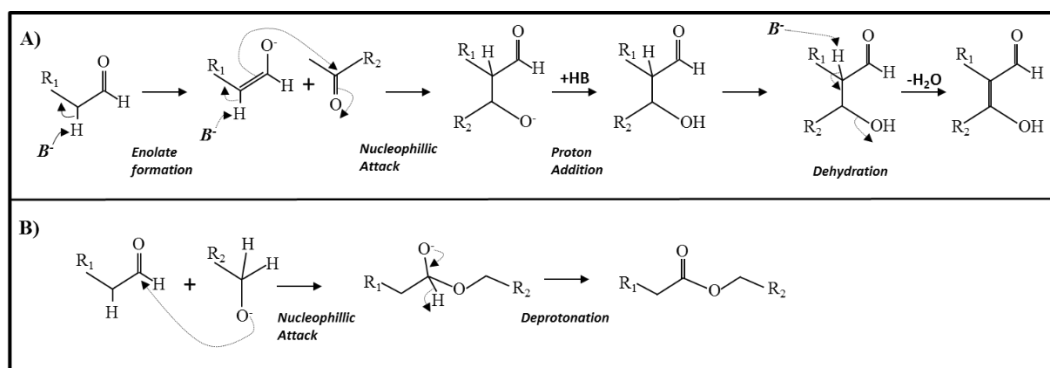
4.3.2 Reactions of Propanol and Propanal

4.3.2.1 Base-catalyzed Reactions on Cu

As discussed, esterification and aldol condensation reactions are thought to proceed over Cu via base-catalyzed reactions. The classic mechanism for a base catalyzed aldol condensation involves the base abstracting the weakly acidic proton from the C_α-H bond of an alkanal or alkanone to form an enolate intermediate that subsequently attacks the

electrophilic carbon on the carbonyl group of a vicinal alkanal or alkanone to form a β -hydroxy alkanal (aldol) as shown in Scheme 4.3(A). The base can then dehydrate the aldol to form an α,β -unsaturated alkanal. Esterification proceeds via the nucleophilic attack of an alkoxide at the electrophilic carbon of the carbonyl group on the alkanal which then deprotonates to form an ester product as shown in Scheme 4.3(B).

While base-catalyzed aldol condensation and esterification reactions are well-established, neither Cu or SiO₂ exhibit basic surfaces; yet Cu/SiO₂ catalyzes both reactions.⁴⁶ The reaction instead has been proposed to proceed via the formation of a negatively-charged and basic propoxide intermediate on Cu, derived in-situ from the interconversion of the equilibrated propanol-propanal-H₂ mixture. Alkoxides are electronically very similar to hydroxides which abstract electron density from group 11 metals to form weakly bound (HO ^{δ^- *}) intermediates.^{203–205} These weakly bound surface alkoxides can act as a base thus enabling the activation of the weakly-acidic proton at the α C position of a vicinal aldehyde to initiate aldol condensation. In addition, the basic alkoxide intermediate can also nucleophilically attack the carbonyl of a vicinal aldehyde to initiate esterification. Before describing the energetics of such reactions, we first present details on the electronic structure of these adsorbed alkoxide intermediates on transition metal surfaces.



Scheme 4.3 Mechanism of base-catalyzed A) aldol condensation and B) esterification.

4.3.2.2 Basic Nature of RO* on Cu

Bases can be characterized by their ability to donate electrons.²⁰⁶ Alkoxide anions (RO⁻) in solution are bases that can readily abstract protons and carry out nucleophilic attack. The properties and behavior of a bound alkoxide (RO*), on the other hand, are controlled by the electronic properties of the metal surface and the binding of the alkoxide to the

metal both of which are dictated by the direction and degree of charge transfer between the alkoxide and the metal. For noble metals such as Cu, Ag and Au, charge is transferred from the metal to the alkoxide. The charge transfer may be sufficient to allow for the formation of an anionic alkoxide intermediate, which would exhibit basicity comparable to solvated alkoxide anions. The electron density for propoxide adsorbed at a 3-fold fcc site on Cu(111) calculated from DFT is shown in Figure 4.2 and quantitatively summarized in Table 4.1. The structure shown on the left-hand side of Figure 4.2 (A) shows that the propoxide adsorbs via its oxygen to a three-fold fcc Cu site with its C-O axis normal to the surface resulting in a binding energy of -218 kJ mol^{-1} . The charge density differences between the adsorbed and the separated propoxide/Cu system depicted in Figure 4.2 (B) show a significant shift in the electron density from the Cu metal onto the oxygen upon adsorption.

The calculated charges on the O atoms of the alcohol and the alkoxide and the 3 Cu atoms that make up the fcc adsorption site before and after adsorption are reported in Table 4.1. The results show a charge transfer of $> 0.5 e^-$ from the Cu surface to the O-atom in the bound propoxide thus resulting in a negative $-0.83 e^-$ on the oxygen which is consistent with anionic hydroxide and alkoxide species in solution thus allowing it to behave as a base with properties similar to those of anionic alkoxides in solution. For comparison, we examined the charge transfer from the metal to the oxygen of molecularly adsorbed propanol. The results shown in Table 4.1 indicate that there is essentially no charge transfer from the metal to the propanol as the charge on the O-atom following adsorption is less than $0.009 e^-$.

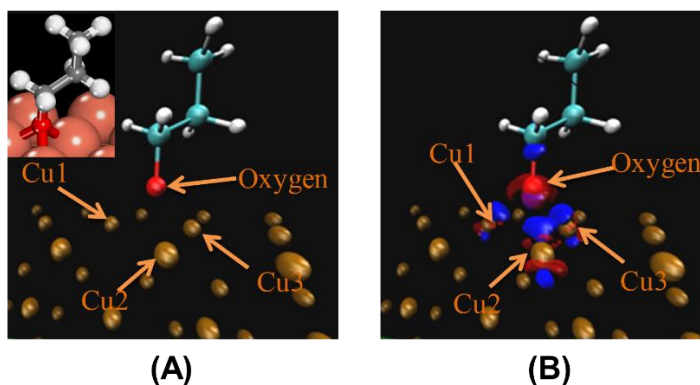


Figure 4.2.(A) The adsorption structure for propoxide bound to a 3-fold fcc site on the Cu (111) surface; (B) Charge density difference map between the adsorbed alkoxide and the

alkoxide in the gas phase. The red isosurface depicts an increase of charge density whereas the blue isosurface reveals a decrease of charge density.

Table 4.1 Charge density differences on the oxygen of the alkoxide and alcohol before and after adsorption on the Cu(111) surface.^a

Species	Before adsorption (e⁻)	After adsorption (e⁻)
Cu ₃ ^b	0.13	0.71
O of CH ₃ CH ₂ CH ₂ O*	-0.33	-0.83
O of CH ₃ CH ₂ CH ₂ OH*	-0.62	-0.62

^a The charge difference analysis is carried out using QUAMBO. ^b The total charge of the three Cu atoms of the 3-fold site.

The basicity of bound oxygen atoms and oxygen-containing intermediates on the group 11 (Cu, Ag, and Au) metals and other late transition metals including Pd, Pt, Rh and Ir has been discussed previously.^{203–205,207–209} Hydroxide species (HO*) adsorbed to Au(111), Pt(111), or Pd(111) surfaces can readily abstract protons from water or from adsorbed alcohols during the dehydrogenation of alcohols to form aldehydes.^{203–205} Adsorbed hydroxides (HO*) were also found to nucleophilically attack the carbonyl group at a vicinal alkanal to form a carboxylic acid.^{203–205} A comparison of the charges on the O atoms for HO* and RO* species bound to different metal surfaces helps to provide a more detailed understanding of the relative basicity of the two intermediates. Herein, we examine the adsorption of the methoxide species as a simple probe alkoxide intermediate.

The charge transfer to the O of HO upon its adsorption to different 3d, 4d and 5d transition metals ranges from -0.77 e⁻ on the more oxophilic metals (Pd, Rh and Ru) which bind O strongly to -1.04 to -1.07 e⁻ on the group 11 metals (Cu, Ag, Au) which bind O* weakly as shown in Table 4.2. Similarly, charge transfer from the metal to the O-atom in the adsorbed alkoxide (RO*) results in a charge on the oxygen that ranges from -0.54 on Rh and Ru to -0.83 e⁻ on Cu, Ag, and Au. A larger anionic charge leads, in turn, to more strongly basic O-atoms on the adsorbed HO* or RO*. The reactivity of HO* in activating weakly acidic O-H and C-H bonds in adsorbed alkanols and alkanals, and attacking the electrophilic carbon of carbonyl groups in selective oxidation reactions,^{203–205} also provides evidence for the basicity of the HO* adsorbed on model Au, Pt, and Pd metal surfaces.

The results presented herein show that both RO* and HO* groups bound to group 11 metals (Cu, Ag and Au) surfaces act as basic moieties because their O-atoms acquire significant anionic character through electron transfer from the metal surface (Table 4.2). The charge transferred to the RO* and HO* species from other metals is significantly less than that from group 11 metals, likely due to the high electron density in the nearly-filled d-bands of these coinage metals (Cu: 3d¹⁰; Ag: 4d¹⁰; Au: 5d¹⁰).

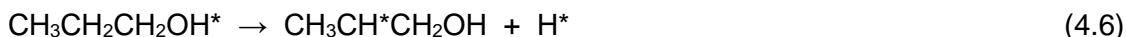
Table 4.2 Summary of the charge accumulated on O atom for adsorbed HO* and CH₃O* groups bound to different transition metal (111) surfaces.

<i>Species</i>	<i>Metal</i>	<i>Charge on O after ads.</i>	<i>Species</i>	<i>Metal</i>	<i>Charge on O after ads.</i>
	Cu	-1.05		Cu	-0.83
HO*	Au	-1.04	CH ₃ O*	Au	-0.77
-0.44 ^a	Ag	-1.07	-0.33 ^a	Ag	-0.81
	Pd	-0.79		Pd	-0.56
	Ru	-0.77		Ru	-0.54
	Rh	-0.77		Rh	-0.55

^a The number in the bracket is the charge on the O of OH/OR before

4.3.2.3 C-H Activation of Propanal and Propanol

Enolates which are key intermediates in aldol condensation form via the activation of the α-C-H bond of the aldehyde either by the metal surface or by an adsorbed alkoxide. C_α-H activation on Cu proceeds via an oxidative addition reaction where a Cu atom in the surface inserts into the C-H bond to form CH₃CH*CH=O and H* intermediates (Eq.4.6).



The weakly acidic C_α-H bond can also be activated by an adsorbed RO* intermediate which instead proceeds via proton abstraction by the alkoxide to form the corresponding alcohol and an enolate (Eq. 4.7).



The α and β carbons of the propanol and propanal refer to the carbon atoms at the C₂ and C₃ positions, respectively, as is shown in Scheme 4.2. The barrier to activate the C₁-H bond of propanal via Cu-insertion to form the adsorbed CH₃CH₂C*O* acyl and H* intermediates is 91 kJ mol⁻¹, which is 10 kJ mol⁻¹ lower than the barrier for Cu to activate

the C₂-H bond of propanal to form surface CH₃CH*CHO* and H* (101 kJ mol⁻¹) intermediates. While the C₂-H bond is weaker than the C₁-H bond, there are greater steric limitations in activating the secondary C₂-H bond than the primary C₁-H bond over metal surface sites. The steric constraints compensate for the C-H bond energies thus resulting in a lower barrier to activate the primary C₁-H bond.

The activation of the C₂-H can also proceed in a heterolytic manner, through a reaction in which a vicinal propoxide (CH₃CH₂CH₂O^{(δ-)*}) abstracts the weakly acidic αH (with a charge of +0.166) to form propanol and an adsorbed enolate (CH₃CH^{(-)*}CHO*). The barrier for the heterolytic activation of the C_α-H bond is 80 kJ mol⁻¹ which is 21 kJ mol⁻¹ lower than that for the homolytic C_α-H activation by Cu. The barrier to activate the C₁-H bond heterolytically by the adsorbed propoxide to form the acyl intermediate is 122 kJ mol⁻¹, which is 52 kJ mol⁻¹ higher than the heterolytic activation of the C_α-H as the C₁-H hydrogen is non-acidic (with a charge of +0.041). While the activation of the C₁-H bond on Cu is 10 kJ mol⁻¹ lower than that for activating the C₂-H bond, it is 11 kJ mol⁻¹ higher than the base-catalyzed C_α-H activation of the adsorbed propanal via the basic adsorbed propoxide. This is consistent with previous theoretical gas phase calculations, which show the heterolytic abstraction of the C₁-H from the propanal via a gas phase OH intermediate is 60 kJ mol⁻¹ higher than the abstraction of the acidic C_α-H of the propanal. The activation of the terminal C₃-H bond of propanal was found to be unfavorable on both the Cu surface as well as by the vicinal bound propoxide. These results are consistent with the gas phase deprotonation energies and the charges on each of the H and C atoms for propanal and propanol (reported in Table 4.3) which provide a measure and ranking of their acidity. This is also consistent with pKa values reported in the literature that show that pKa values for the C_α-H of different aldehydes range from 16-20 while that for the C₃-H hydrogen range from 40-50.²¹⁰

Table 4.3 DFT calculated gas phase deprotonation energies and charges on different H atoms in propanal.

<i>Hydrogen Atom</i>	<i>Deprotonation Energies (kJ mol⁻¹)</i>	<i>Charge on the O</i>	<i>Charge on the C</i>
C ₁ -H of propanal	1668	0.09	+0.45
C ₂ -H of propanal (αC-H)	1556	0.23	-0.50
C ₃ -H of propanal	1687	0.20	-0.59
C ₁ -H of propanol	1756	0.15	-0.02
C ₂ -H of propanol	1656	0.20	-0.41

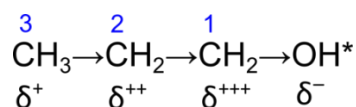
C ₃ -H of propanol	1760	0.19	-0.58
-------------------------------	------	------	-------

The preferential activation at the C_α site via basic surface species is consistent with experiments results⁴⁶ that show only the formation of 2-methyl-3-pentanone, 2-methyl-3-pentanal and 3-pentanone products which form only via the reactions between a C_α enolate and a vicinal bound propanal. The detailed elementary steps to form these products are reported in the next section. The formation of the linear 1-hexanal and 3-hexanone products which would form via the attack of C₃ enolate on a vicinally bound propanal were notably absent.

Table 4.4 Reaction and Activation energies of C-H bond activation for propanal and propanol.

C-H Bond Activation	Metal Catalyzed		Alkoxide Catalyzed	
	ΔE_{rxn} kJ mol ⁻¹	ΔE_{act} kJ mol ⁻¹	ΔE_{rxn} kJ mol ⁻¹	ΔE_{act} kJ mol ⁻¹
C ₁ -H of propanal	41	91	24	122
C ₂ -H of propanal (αC-H)	52	101	34	70
C ₃ -H of propanal	112	166	91	162
C ₁ -H of propanol	118	144	107	166
C ₂ -H of propanol	117	166	104	155
C ₃ -H of propanol	129	174	117	163

The activation of each type of C-H bond in 1-propanol was also examined. The C₁-H bond is the most reactive on Cu as the -OH group withdraws electron-density from the C-H bonds at the terminal C-atom, leading to the inductive effect sketched in Scheme 4.4.²¹⁰ A detailed charge analysis shows that the C₁ has a partial charge of -0.02 e⁻, while C₂ has a partial charge -0.41 e⁻ and the C₃ has a partial charge -0.58 e⁻. As such, the barriers for C-H activation over Cu(111) at these three carbons increase from 144, 166 and 174 kJ mol⁻¹ for C₁-H, C₂-H and C₃-H, respectively.



Scheme 4.4 Illustration of the electron-withdrawing inductive effect of the hydroxyl group in propanol. The amount of charge relative to the original charge of C: $\delta^{+++} > \delta^{++} > \delta^+$. The arrow shows the direction the charges flows.

The barriers for activating the C₁-H and C₂-H bonds of propanol by the adsorbed alkoxide were calculated to be significantly higher than those calculated for activating the C₁-H and C₂-H bonds of bound propanal. This is due to the fact that carbonyl group on the propanal offers conjugation that can stabilize the negative charge that results in abstracting a proton at the C₁ and C₂ position. Propanol, however, lacks the conjugation offered by the C=O bond and as such offers little stabilization of the negative charge. As such C₁-H and C₂-H bonds of the alcohol are non-acidic. The barriers to activate the C₃-H for both propanol and propanal are very similar as the CH=O and CH₂OH groups are now far enough removed from the C₃-H bond to influence its properties and reactivity.

The alkoxide chain length was varied to determine its effect on the barrier to activate the αC₂-H bond in propanal. The results, shown in Table 4.5, indicate that hydroxides are slightly more basic than methoxides on Cu surfaces and thus more effective in the activation of the mildly acidic αC₂-H bond. This is likely due to the fact that the O-atom in OH* is more negative than the O in CH₃O* and thus more basic. For larger alkoxides, the activation barriers increase slightly with chain length, from 65 kJ mol⁻¹ for methoxide to 72 and 70 kJ mol⁻¹ for ethoxide and propoxide, respectively. These small increases are the result in steric hindrance between the alkoxide and aldehyde on the surface and will likely disappear with the inclusion of dispersion.

Table 4.5 Reaction and activation energies for the αC₂-H bond activation of propanal with different RO* species on Cu(111).

C_α-H Bond Activation	ΔE_{rxn} kJ mol⁻¹	ΔE_{act} kJ mol⁻¹
Metal Catalyzed	52	101
HO* (R=H)	35	56
CH ₃ O* (R=CH ₃)	36	65
CH ₃ CH ₂ O* (R=CH ₃ CH ₂)	34	72
CH ₃ CH ₂ CH ₂ O* (R=CH ₂ CH ₂ CH ₂)	30	70

The theoretical analyses reported here show that C-H bond activation in propanal preferentially proceeds via proton-transfer to RO* bound at Cu surfaces. These RO* species acts as a base and abstract the most acidic hydrogen, which is located at the α-C-atom in propanal, to form enolate species that can subsequently react with a second adsorbed aldehyde via aldol condensation to form a new C-C bond. The barriers to activate the C₁-H (99 kJ mol⁻¹) and C₃-H (166 kJ mol⁻¹) bonds in the aldehydes and the

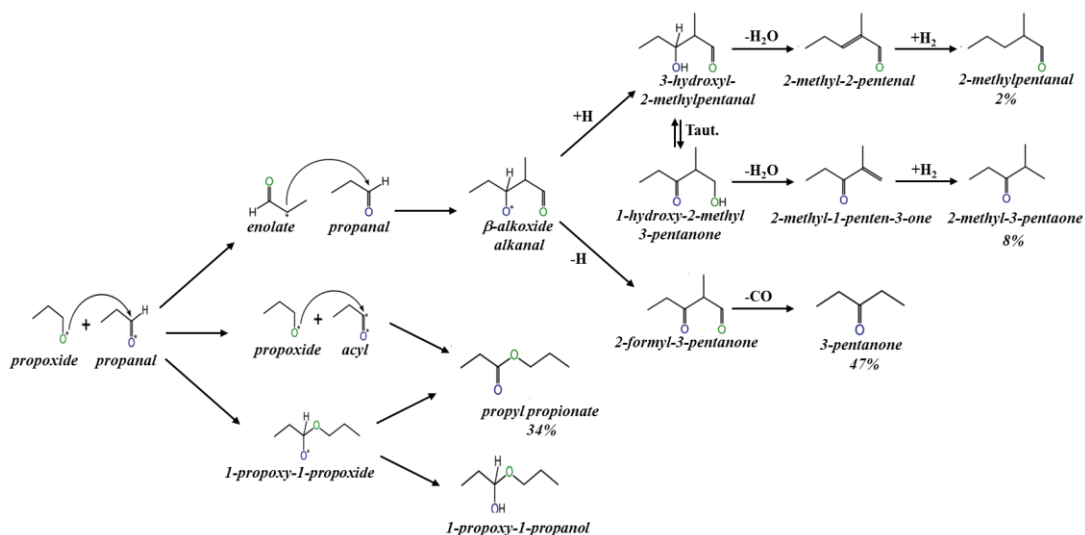
C₁-H (144 kJ mol⁻¹), C₂-H (166 kJ mol⁻¹) and C₃-H (174 kJ mol⁻¹) bonds in the alcohols with the bound propoxide were all significantly higher than the base-catalyzed activation of the C_α-H as all of the other hydrogens are non-acidic and as such will not be activated by a base.

4.3.3 Aldol Condensation Paths on Cu

Base-catalyzed aldol condensation of two C_n alkanals typically proceeds through the activation of the first alkanal to form an enolate. The enolate subsequently attacks the C-atom of the carbonyl group in vicinal bound alkanal to form a β-alkoxy-alkanal intermediate that rapidly protonates to form the C_{2n} β-hydroxy alkanal (aldol) as shown in the first step in Scheme 4.5. β-hydroxy alkanals can readily dehydrate to form α,β-unsaturated alkanal (a conjugated enone). In the propanal reactions examined here, the C_{2n} aldol (3-hydroxy-2-methyl-pentanal) dehydrates to form 2-methyl-2-pentenal (α,β-unsaturated alkanal), that can readily hydrogenate resulting in the observed 2-methyl-pentanal product as shown in the upper branch in Scheme 4.5. The 2-methyl-pentanal product, however, only accounts for 2% of the products observed and neither the aldol (3-hydroxyl-2-methyl-pentanal) or the conjugated enone (2-methyl-2-pentenal) products were observed experimentally.⁴⁶ As such, this path is only a minor route for condensation. The second condensation product observed, 2-methyl-3-pentanone (8% selectivity) forms via tautomerization or intra-molecular hydrogen transfer reactions that convert the aldol (3-hydroxy-2-methylpentanal) to the β-hydroxy ketone (1-hydroxy-2-methyl-3-pentanone) which subsequently dehydrates and then hydrogenates to form 2-methyl 3-pentanone that desorbs from the surface.⁴⁶ This is the path in the center of Scheme 4.5.

The predominant condensation product is 3-pentanone which makes up a ~82.5% of all of the condensation products formed and ~47% of the total products which include those from esterification as well as direct dehydration. The prevalence of the 3-pentanone product is consistent with previous studies that indicate that the most favorable coupling products are C_{2n-1} ketones.^{211,212} This suggests that aldol condensation is followed by rapid decarbonylation or decarboxylation where oxygen is removed as either CO or CO₂. These decarbonylation/decarboxylation reactions can proceed via an *intra* molecular or hydrogen transfer or intermolecular (with a vicinal alkanal) to form the β-diketo intermediate (2-formyl-3-pentanone) that can then react via a retro-aldol reaction to eliminate CO and form 3-pentanone (shown as the lower condensation path in Scheme 4.5).

The first step in aldol condensation as discussed earlier involves the propoxide-catalyzed activation of the weakly acidic C $_{\alpha}$ -H bond of propanal to form the enolate which was calculated to have an intrinsic activation barrier of 70 kJ mol $^{-1}$ (taken with respect to the adsorbed propoxide and propanal) (Figure 4.3(A) and Table 4.4). The enolate subsequently reacts with a vicinal bound alkanal to form the β -alkoxide alkanal surface intermediate with a barrier of only 19 kJ mol $^{-1}$ and an overall reaction energy of -26 kJ mol $^{-1}$ (Figure 4.3(B)). The structures of the reactant, transition and product states for the relevant aldol condensation are reported in Figures 4.3 and 4.4.



Scheme 4.5 Possible reaction pathways following aldol condensation.

4.3.3.1 Formation of 2-methyl-2-pentanol

The β -alkoxy-alkanal intermediate formed via the C $_3$ -enolate attack on the propanal can hydrogenate to give the 3-hydroxy-2-methyl-pentenal which can subsequently dehydrate and then hydrogenate to form the 2-methyl-2-pentanol product shown in the upper path in Scheme 4.5. This sequence proceeds by the protonation of the β -alkoxide alkanal as shown in Figure 4.3(C) and has an intrinsic activation barrier of 69 kJ mol $^{-1}$ calculated with respect to the adsorbed β -alkoxide and H*. The subsequent dehydration and hydrogenation steps to form 2-methyl-2-pentenal may occur but were not examined. The tautomerization and subsequent dehydration and hydrogenation of the 1-hydroxy-2-methyl 3-pentanone to form 2-methyl-3-pentanone product (center condensation path in scheme 4.5) were also not examined.

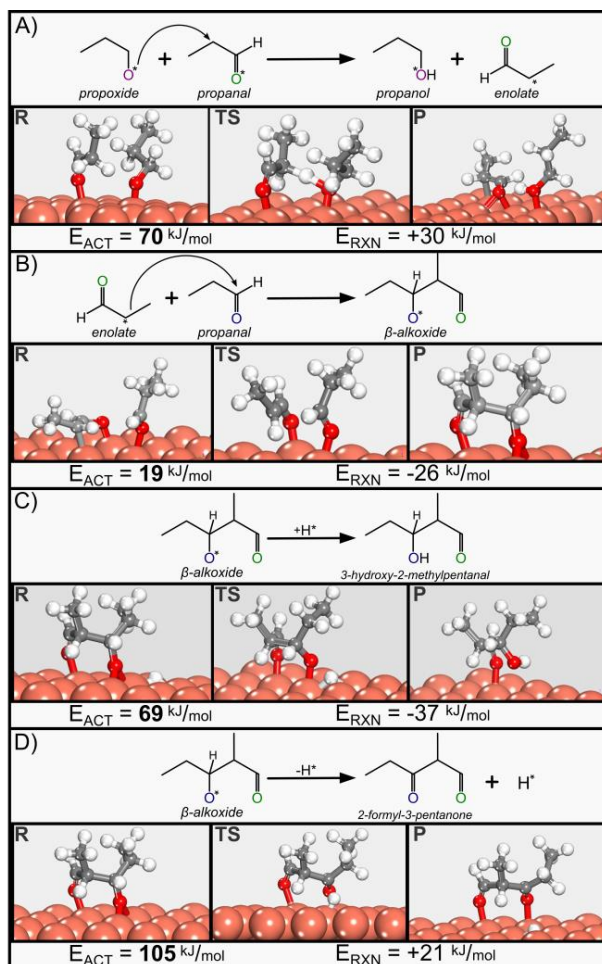


Figure 4.3 DFT-calculated reactant, transition and product states along with the intrinsic activation barriers and the overall reaction energies for elementary steps in the aldol condensation of adsorbed propoxide and propanal over Cu(111) to form the 3-hydroxy-2-methylpentanal and 2-formyl-3-pentanone intermediates. These include: A) activation of the weakly acidic C α -H of propanal by a surface propoxide to form a surface enolate, B) enolate attack on the C=O bond of a neighboring propanal to form β -alkoxide alkanal, C) protonation of the β -alkoxide alkanal to form the aldol, and D) C-H activation of β -alkoxide alkanal to form 2-formyl-3-pentanone.

4.3.3.2 Formation of 3-pentanone

The predominant aldol product as discussed above is 3-pentanone which proceeds via dehydrogenation of the β -alkoxide alkanal and its subsequent decarbonylation (bottom condensation path in Scheme 4.5). The C-H activation of the β -alkoxide alkanal over Cu (Figure 4.3(D)) was calculated to be prohibitive with an intrinsic barrier of 105 kJ mol $^{-1}$.

The reaction instead appears to proceed via *inter-molecular* hydrogen transfer. The C₁-H hydrogen of the alkoxide is hydridic in character, and as such, it can be readily abstracted by a vicinal-bound electrophile such as propanal. The barrier to activate the C₁-H bond of the β-alkoxide alkanal by a co-adsorbed propanal was calculated to be 74 kJ mol⁻¹ ($\Delta E_{\text{rxn}} = 0 \text{ kJ mol}^{-1}$) as shown in Figure 4.4(A). The intrinsic barrier for the propanal activation of the β-alkoxide alkanal is 31 kJ mol⁻¹ lower than that calculated for the Cu C₁-H activation (105 kJ mol⁻¹).

The β-alkoxide alkanal can subsequently decarbonylate via a direct retro-aldol CO elimination from the C₁-alkoxide alkanal intermediate as shown in Scheme 4.5. The barrier for this path, however, was calculated to be > 110 kJ mol⁻¹. Decarbonylation can instead proceed via the initial activation of the C₁-H bond of the 2-formyl-3-pentanone intermediate to form the surface 2-acyl-3-pentanone (CH₃CH₂C(O)CH(CH₃)CO*) intermediate with an intrinsic activation barrier of +74 kJ mol⁻¹ and an overall reaction energy of +42 kJ mol⁻¹ (see Figure 4.4(B)). This C₁-H activation subsequently weakens the C₁-C₂ bond thus allowing for direct C=C bond scission over Cu to form 3-pentene-2-olate (CH₃CH₂C(O*)CHCH₃) and CO* products with an intrinsic activation energy of only +7 kJ mol⁻¹ and an overall reaction energy of -40 kJ mol⁻¹ (Figure 4.4(C)). The resulting 3-pentene-2-olate (CH₃CH₂C(O*)CHCH₃) intermediate subsequently hydrogenates to form 3-pentanone with a barrier of +68 kJ mol⁻¹ and a reaction energy of -60 kJ mol⁻¹ (Figure 4.4(D)) which then desorbs from the surface.

The final aldol condensation path considered is rather different than the first two paths in that it proceeds via the initial C-H activation of the alkanal to form an acyl (RCO*) intermediate, that subsequently attacks a vicinal bound propanal to form the aldol product directly.¹⁹¹ This path was found to be unlikely as the intrinsic activation barriers for the initial C-H activation and subsequent C-C bond formation steps were calculated to be very high at 133 and 153 kJ mol⁻¹, respectively.

The activation barriers and reaction energies for the elementary steps presented in Figure 4.3 and 4.4 above were used to construct the overall reaction energy diagram shown in Figure 4.5, compare the three predominant condensation paths discussed, determine the rate equations for each path and establish the lowest energy route. In all three paths, we assume, based on the results above, that propanal and hydrogen are equilibrated with

propanol. For simplicity, all of the paths in Figure 4.5 are therefore referenced to the same adsorbed propanal and propoxide initial state defined as $E=0$.

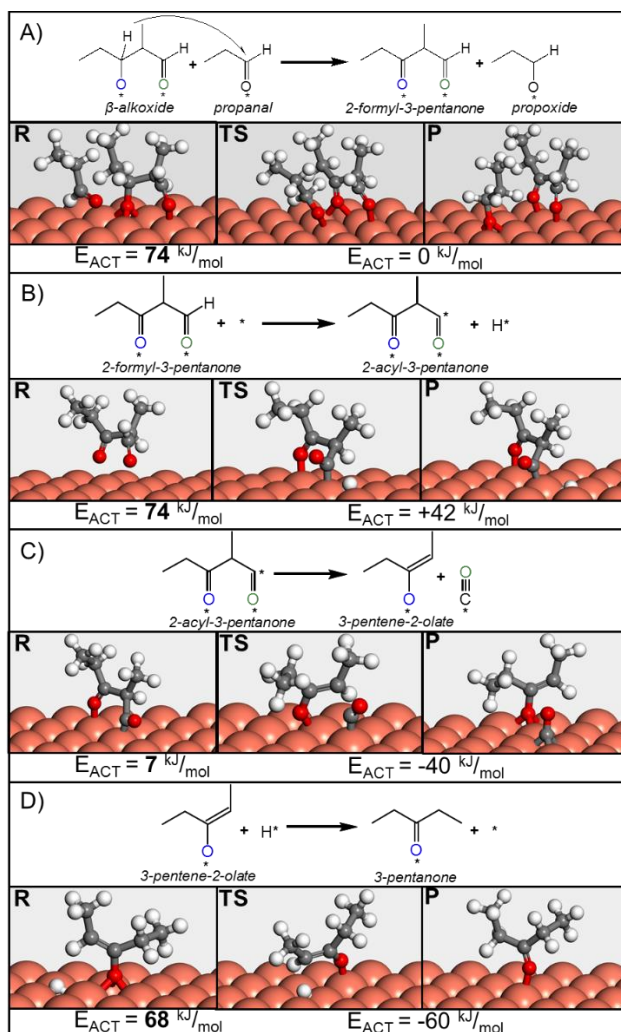


Figure 4.4 DFT-calculated reactant, transition and product states along with the intrinsic activation barriers and the overall reaction energies for elementary steps in the conversion of the dehydrogenated aldol intermediate, β -alkoxy-2-methyl pentanal, to 3-pentanone over Cu(111). The steps include: A) intermolecular hydride transfer from β -alkoxide alkanal to adsorbed propanal to form the 2-formyl-3-pentanone intermediate, B) C_1 -H scission of the 2-formyl-3-pentanone to 2-acyl-3-pentanone, C) decarbonylation of 2-acyl-3-pentanone to form 3-pentene-2-olate and CO and d) hydrogenation of 2-acyl-3-pentanone to form 3-pentanone.

The results in Figure 4.5(A) show that the reaction does not proceed through the dehydrogenation of the adsorbed propanal to an acyl intermediate as it would require an

apparent barrier of 160 kJ mol⁻¹ taken with respect to the adsorbed propoxide and propanal. The two paths which proceed via the coupling of propanal and propoxide to form the β-hydroxide alkanal are significantly lower in energy and more viable than the acyl path. The energy diagrams in Figure 4.5 show that the rates for the paths involving the coupling of propoxide and propanal are ultimately dictated by the barrier for enolate formation which involves the abstraction the weakly acidic H of C_α-H of the adsorbed alkanal. The barrier for enolate formation was calculated to be 70 kJ mol⁻¹ taken with respect to the adsorbed propoxide and propanal which are the most abundant species on the surface. The β-hydroxide alkanal that results from C-C bond formation subsequently reacts by: 1) H* addition to form the aldol which subsequently reacts to form 2-methyl-pentanal and 2-methyl-3-pentanone products or 2) hydride transfer to an adsorbed propanal that goes on to form 3-pentanone.

The rate for both propoxide and propanal coupling reactions are controlled by the initial activation of the weakly acidic C_α-H bond on the alkanal by a basic propoxide surface intermediate and can be written as:

$$r_{cond} = k_{cond}[\text{propanal}^*][\text{propoxide}^*] = k_{cond}K_{PAL}^2K_{HYD}K_{H_2}^{1/2} P_{PAL}^2P_{H_2}^{1/2}/[1 + K_{PAL}P_{PAL} + K_{POL}/(K_{HYD}K_{H_2}K_d)]^2 \quad (4.8)$$

where k_{cond} refers to the intrinsic rate constant for deprotonation of the weakly acidic C_α-H bond; K_{PAL} , K_{HYD} , K_{H_2} , K_d are the equilibrium constants for the adsorption of propanal, the hydrogenation of propanal to propanol over Cu, the dissociative adsorption of hydrogen and the gas phase hydrogenation of propanal to propanol, respectively, and P_{AL} and P_{H_2} refer to the partial pressure of propanal and hydrogen, respectively. The apparent activation barrier for this path calculated with respect to the adsorbed propanal and propoxide is simply the 70 kJ mol⁻¹ barrier for the initial C_α-H activation by the propoxide to form the enolate (Figure 4.3(A)). The theoretical results suggest that propanal and propoxide may be abundant surface intermediates. Experimentally-measured rates of reaction as a function of the pressures of propanal and hydrogen indicate that while both propanal and propoxide exist on the surface, the propanal is the most abundant surface intermediate.⁴⁶

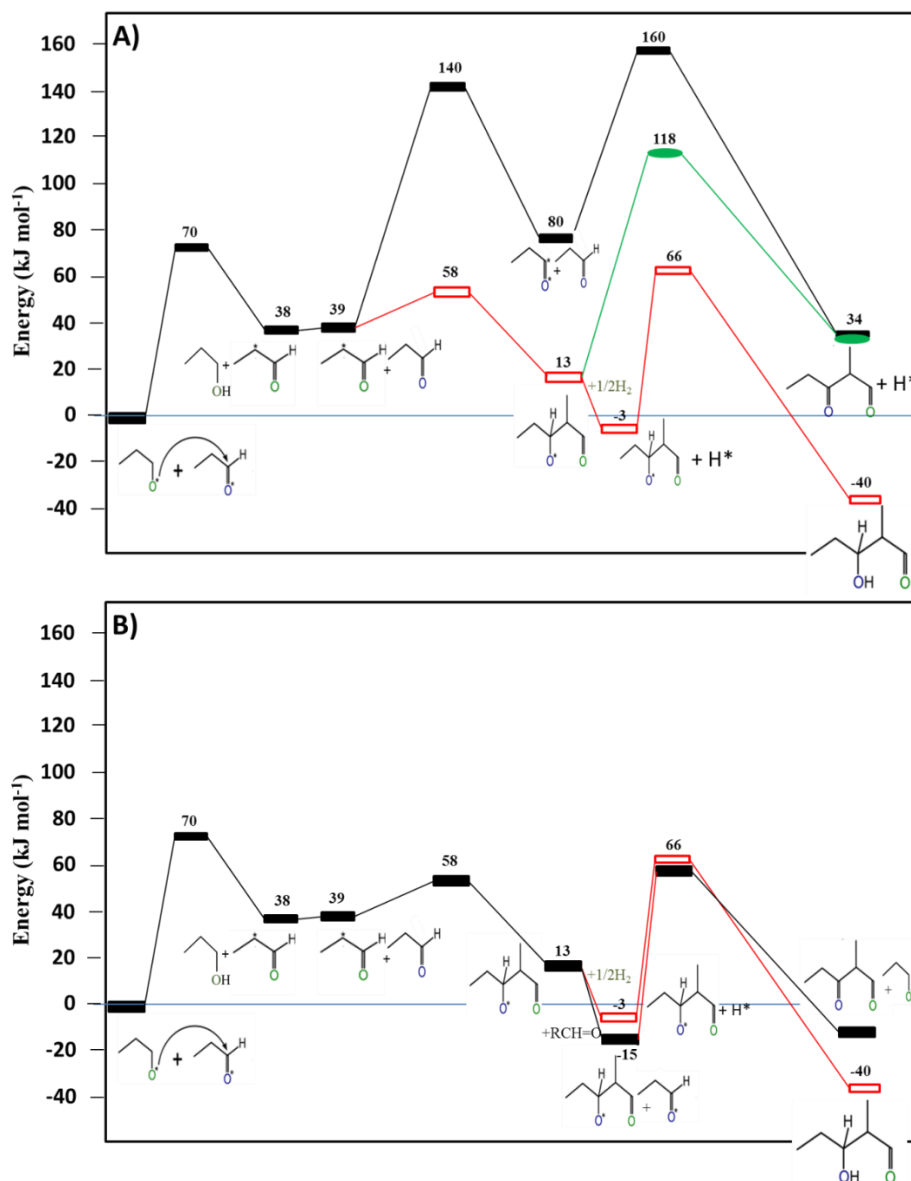


Figure 4.5 DFT-calculated pathways for the aldol condensation reactions of propanol-propanal on Cu(111). **A)** The upper path (shown with black filled rectangular symbols) proceeds via the initial activation of the propyl to form an acyl intermediate which is high in energy. The middle path (shown with lighter filled oval symbols) proceeds via the coupling of the enolate and propanal followed by C₁-H activation by the Cu, whereas the lowest energy path (unfilled rectangular symbols) proceeds by the coupling of the enolate and propanal to form the β-alkoxide alkanal which subsequently hydrogenates to form the aldol. **B)** The two lowest energy paths shown here proceed via the coupling of the enolate and propanal to form the β-alkoxide alkanal which can: i) hydrogenate (shown with unfilled

rectangular symbols) to form the aldol or ii) dehydrogenate via hydride transfer an adsorbed propanal to form 2-formyl-3-pentanone (shown with filled black rectangular symbols).

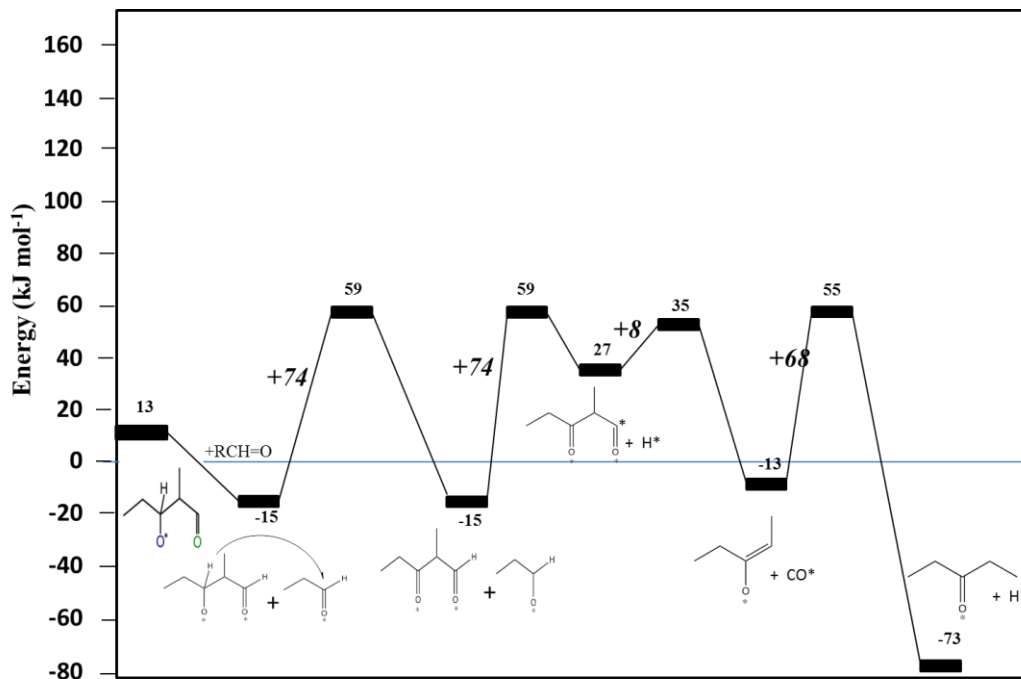


Figure 4.6 DFT-computed pathways for the decarbonylation of 1-propoxy-1-propoxide intermediate to form 3-pentanone on Cu(111). Activation barriers for each step are shown larger font and in italic.

4.3.4 Esterification Paths on Cu

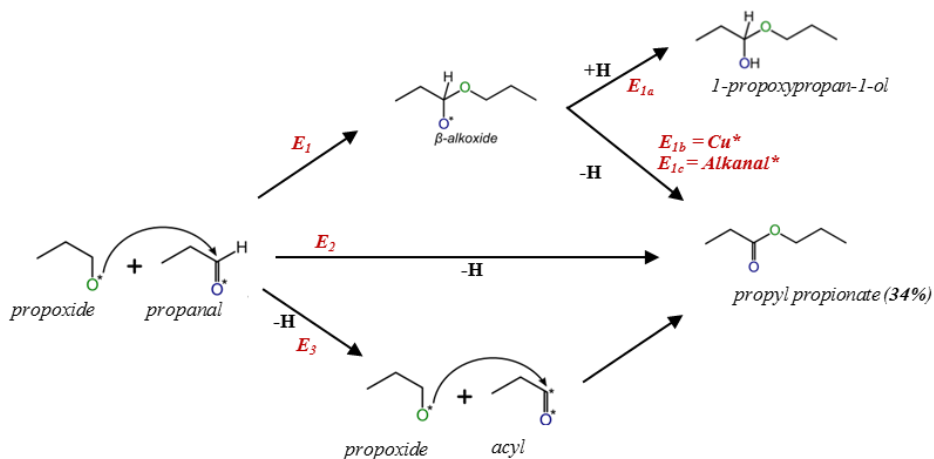
Base-catalyzed esterification reactions typically proceed via Tischenko-type pathways involving the reaction between an adsorbed alcohol and aldehyde. Three potential paths by which the surface alkoxide and alkanal species can react over Cu are shown in Scheme 4.6. The first path (E_1 in Scheme 4.6) proceeds via nucleophilic addition of the surface alkoxide to the vicinal alkanal to form a hemiacetalate (1-propoxy-1-propoxide) surface intermediate. The reaction proceeds by an initial shift of the alkoxide from its stable 3-fold adsorption site to a bridging site where it readily attacks the carbonyl C of the neighboring propanal intermediate to form the C-O bond resulting in an intrinsic barrier of 60 kJ mol⁻¹. A significant portion of the activation barrier is associated with the incipient activation of the strong Cu-OC₃H₇ bond to form the more weakly bound and reactive propoxide. The Cu-OC₃H₇ weakening is compensated by the formation of a strong O-CuC₆H₁₁O bond in the resulting 1-propoxy-1-propoxide intermediate, as shown in Figure 4.7(A). The 1-

propoxy-1-propoxide can subsequently dehydrogenate (Path E_{1a} in Scheme 4.6) either by Cu-catalyzed C₁-H bond cleavage of the 1-propoxy-1-propionate to form the propyl propionate product and a surface H* or via intermolecular hydride transfer from the C₁-H bond of the 1-propyl-1-propoxide to a vicinal propanal species (E_{1c}) thus resulting in the formation of propyl propionate and a surface propoxide. The Cu-catalyzed C₁-H activation of the hemiacetalate (1-propoxy-1-propoxide) was found to be rather difficult with a barrier of 90 kJ mol⁻¹ (as shown in Figure 4.7(B)) which is nearly identical to the barrier for propoxide C₁-H activation (91 kJ mol⁻¹) reported in Table 4.3. The propanal-catalyzed hydride transfer occurs via a Meerwein-Ponndorf-Verley (MPV) type mechanism as shown in Figure 4.7(C) resulting in a barrier of only 35 kJ mol⁻¹ which is 55 kJ mol⁻¹ lower than the barrier to activate the C₁-H bond over Cu. The adsorbed alkanal acts as a Lewis acid that readily catalyzes hydride transfer from the alkoxide. The lower barrier for propanal-catalyzed hydride transfer over that for Cu-catalyzed C-H activation is consistent with the results for the propanal-propanol equilibrium and Cu-catalyzed C₁-H activation of the β-alkoxide during aldol condensation. The hydride-transfer barrier here in the esterification path, however, is 43 kJ mol⁻¹ lower than the hydride transfer from β-alkoxide alkanal in the condensation path. The O in the ester significantly increases the hydricity of the C₁-H bond by stabilizing the charge in the transition state which results in the significantly lower hydride transfer barrier in the esterification path. In addition to dehydrogenation, the 1-propoxy-1-propoxide can also hydrogenate via protonation of the alkoxide to form the 1-propoxy-1-propanol hemiacetal (Path E_{1b} in Scheme 4.6) resulting in a barrier of 69 kJ mol⁻¹ (Figure 4.7(E)). The 1-propoxy-1-propanol can desorb from the surface or dehydrogenate to form propyl propionate product.

The surface propoxide and propanal can also react together in a second path (path E_2 shown in Scheme 4.6) that proceeds via a concerted S_N2 type reaction involving the nucleophilic attack of the surface propoxide on the carbonyl of the surface propanal (C-O bond formation) together with the simultaneous elimination of C₁ propoxyl hydrogen to the Cu surface to form propyl propionate directly (path E_2 Scheme 4.6). The transition state for this concerted path (Figure 4.7(E)) involves the elongation of the C-O and C=O bonds in the ester (1.39 Å and 1.28 Å, respectively) relative to their product state (1.34 Å and 1.24 Å), which helps to assist the activation of the propoxyl C₁-H bond. The intrinsic barrier for this reaction taken with respect to the adsorbed propanal and propoxide was calculated to be 69 kJ mol⁻¹ (Figure 4.7(D)) which is only slightly higher than that for the direct

coupling of surface propanal and propoxide thus making it a viable path for esterification and the direct formation of propyl propionate.

The third and final path to form propyl propionate is characteristically different than the first two paths in that it proceeds by initially activating the C₁-H bond of the alkanal to form an acyl intermediate. The acyl subsequently reacts with a surface alkoxide to form the ester product directly (path E₃ in Scheme 4.6). The intrinsic barrier to activate the alkanal to form the surface acyl intermediate is high at 101 kJ mol⁻¹. The acyl subsequently couples with a co-adsorbed propoxide with an intrinsic barrier of 81 kJ mol⁻¹, which is significantly higher than the coupling barrier between propanal and propoxide (53 kJ mol⁻¹). This does not appear to be viable path to esterification products that form.



Scheme 4.6 Three possible reaction paths for the esterification paths involving C-O bond formation via the coupling of propanal and propoxide intermediates over Cu. E₁ paths proceed by sequential C-O formation followed by hydrogen addition (E_{1a}) or hydrogen elimination via Cu (E_{1b}) or via an adsorbed alkanal (E_{1c}). The E₂ path follows simultaneous C-O formation and H-elimination. The E₃ proceeds via the initial activation of the propoxide to form an acyl intermediate.

The elementary steps and corresponding activation and reaction energies for the 3 esterification paths presented in Table 4.6 were used to establish the operative rate equations and determine the lowest energy paths shown in Figure 4.8 and the kinetics for esterification. For simplicity, all three paths presented in Figure 4.8 are referenced to adsorbed propanal and propoxide as these species rapidly equilibrate as was discussed previously.

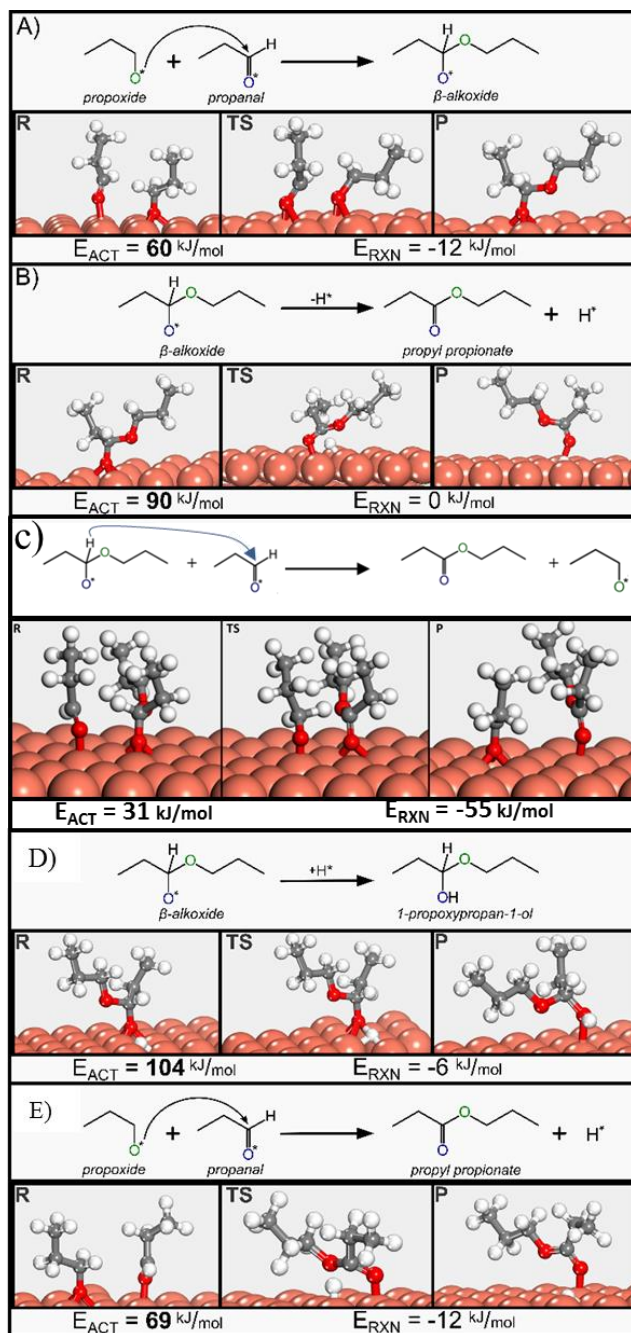


Figure 4.7 DFT-calculated reactant, transition state and product state structures and the corresponding activation barriers and overall reaction energies for different elementary steps in the esterification of propanal and propanol over Cu(111) surface to form propyl propionate. The steps include: A) the nucleophilic attack of the adsorbed propoxide on the adsorbed propanal (C-O bond formation), B) C₁-H activation by a surface Cu site, C) intermolecular hydride transfer from the C₁-H of the 1-propoxy-1-proxide intermediate to a vicinal bound propanal, D) hydrogenation of the 1-propoxy-1-proxide to form the 1-

propoxy-1-propanol hemiacetal, and E) concerted S_N2-type nucleophilic attack of the adsorbed propoxide on the adsorbed propanal and C₁-H hydrogen elimination to Cu.

The three paths presented in Scheme 4.6 (and in Figure 4.8) proceed via reactions involving surface bound propoxide and propanal intermediates. These paths are similar in nature to those reported previously for methanol and ethanol²¹³ esterification over Au. All three of the E_1 paths as well as the E_2 path proceed via coupling of the surface propoxide and propanal to form the hemiacetalate or hemiacetal directly, and as such, show similarities in their mechanisms and rate expressions. These paths differ in the subsequent reactions that lead to different products. The potential energy surfaces reported in Figures 4.8 indicate that the rates for path E_{1a} , E_{1b} , E_{1c} paths are controlled by C₁-H activation of the 1-propoxy-1-propoxide over Cu, H-addition to the 1-propoxy-1-propoxide, and coupling of surface propoxide and propanal, respectively. The rate controlling step in the E_2 path involves the simultaneous coupling of the adsorbed propoxide and propanal together with the direct activation of the C₁-H bond by Cu. Despite the differences in the rate controlling step, the rate equations for the E_1 and E_2 paths are all very similar and can be written as:

$$\begin{aligned} r_{E1a} &= k_{E1a}[1\text{-propoxy-propoxide}^*] = k_{E1a} K_{C-O}[\text{propanal}^*][\text{propoxide}^*] \\ &= k_{E1a} K_{C-O} K_{PAL}^2 K_{HYD} K_{H_2}^{1/2} P_{PAL}^2 P_{H_2}^{1/2} / [1 + K_{PAL} P_{PAL} + (K_{POL} / (K_{HYD} K_{H_2} K_d)) P_{AL} P_{H_2}] \end{aligned} \quad (4.9)$$

$$\begin{aligned} r_{E1b} &= k_{E1b}[1\text{-propoxy-propoxide}^*][H^*] = k_{E1b} K_{HYD}[\text{propanal}^*][\text{propoxide}^*][H^*] \\ &= k_{E1b} K_{Hadd} K_{PAL}^2 K_{HYD} K_{H_2} P_{PAL}^2 P_{H_2} / [1 + K_{PAL} P_{PAL} + (K_{POL} / (K_{HYD} K_{H_2} K_d)) P_{AL} P_{H_2}]^2 \end{aligned} \quad (4.10)$$

$$\begin{aligned} r_{E1c} &= k_{E1c}[\text{propanal}^*][\text{propoxide}^*] \\ &= k_{E1c} K_{PAL}^2 K_{HYD} K_{H_2}^{1/2} P_{PAL}^2 P_{H_2}^{1/2} / [1 + K_{PAL} P_{PAL} + (K_{POL} / (K_{HYD} K_{H_2} K_d)) P_{AL} P_{H_2}]^2 \end{aligned} \quad (4.11)$$

$$\begin{aligned} r_{E2} &= k_{E2}[\text{propanal}^*][\text{propoxide}^*] \\ &= k_{E2} K_{PAL}^2 K_{HYD} K_{H_2}^{1/2} P_{PAL}^2 P_{H_2}^{1/2} / [1 + K_{PAL} P_{PAL} + (K_{POL} / (K_{HYD} K_{H_2} K_d)) P_{AL} P_{H_2}]^2 \end{aligned} \quad (4.12)$$

where k_{E1a} , k_{E1b} , and k_{E1c} are the intrinsic rate constants for the rate controlling steps for paths E_{1a} (Cu-catalyzed H-elimination from the hemiacetalate intermediate), E_{1b} (H-addition to the hemiacetalate) and E_{1c} (coupling of surface propoxide and propanal); K_{C-O} , K_{PAL} , K_{Hadd} , K_{HYD} , K_{H_2} , K_d are the equilibrium constants for the for the coupling of the surface propoxide and propanal to form the C-O bond of the hemiacetalate, adsorption of

propanal, hydrogen addition to the 1-propoxy-1-propoxide, hydrogenation of propanal to propanol, the dissociative adsorption of hydrogen and the gas phase hydrogenation of propanal to propanol, respectively, and P_{AL} and P_{H_2} refer to the pressure of propanal and hydrogen, respectively.

The rate in path 3 (Figure 4.8(B)) is characteristically different than those reported in paths 1 and 2 as the reaction proceeds by first activating the C-H bond of the adsorbed propanal to form a surface acyl ($C_3H_5O^*$) intermediate that subsequently reacts with a vicinal propoxide to form the adsorbed propyl propionate. The results in Figure 4.8, indicate that the initial C-H activation step is quasi-equilibrated as the intrinsic barrier for the forward step involving the attack of the acyl on the vicinal bound propanal (85 kJ mol^{-1}) is considerably higher than the barrier for the reverse reaction (60 kJ mol^{-1}) involving the hydrogenation of the bound acyl back to propanal. The rate for this route is therefore thought to be controlled by the coupling of the bound acyl and propanal surface intermediates and can be written as:

$$r_{E3} = k_{E3}K_{acyl}[acyl^*][propanal^*] = k_{E3}K_{acyl}K_{PAL}^2K_{HYD}K_{H_2}^{1/2} P_{PAL}^2P_{H_2}^{1/2}/[1+ K_{PAL}P_{PAL} + (K_{POL}/(K_{HYD}K_{H_2} K_d))P_{AL}P_{H_2}]^2 \quad (4.13)$$

where k_{E3} , refers to the intrinsic rate constant for the coupling of the surface propanal and acyl; K_{acyl} , K_{PAL} , K_{HYD} , K_{H_2} , K_d are the equilibrium constants for the C-H activation of propanal to form the surface acyl, the adsorption of propanal, the hydrogenation of propanal to propanol over Cu, the dissociative adsorption of hydrogen and the gas phase hydrogenation of propanal to propanol, respectively, and P_{AL} and P_{H_2} refer to the pressure of propanal and hydrogen, respectively.

The results in Figure 4.8 along with the rate expression can be used to provide insights in the kinetics and the likelihood of the 3 paths. The results presented earlier concerning the propanal/propanol equilibrium suggest that the surfaces are covered with either propanal or propoxide intermediates. Experimental results indicate that the propanal is the most abundant surface intermediate. The detailed elementary step kinetics presented here are currently being used to develop microkinetic models that will aid in elucidating surface coverages and compositions and will be reported in a future communication.

For simplicity and in order to compare the different paths we make the assumption that the apparent barriers are measured with respect to adsorbed propanal and propoxide. As such, the elementary step activation and reaction energies for the different paths considered in Figures 4.8(A) and 4.8(B) are all taken with respect to adsorbed propoxide and propanal as the initial 0 energy reference state. The potential energy diagrams in Figure 4.8 along with the rate expressions derived in Equations 4.9-4.12 indicate that the rate controlling steps for the E_{1a} , E_{1b} , E_{1c} , E_2 and E_3 paths are H-addition to the hemiacetalate, the Cu-catalyzed C₁-H activation, the nucleophilic attack of propoxide on adsorbed propanal, the simultaneous nucleophilic attack of propoxide on propanal together with H-elimination to Cu, and the coupling acyl and propanal, respectively. As such the apparent activation barriers for the E_{1a} , E_{1b} , E_{1c} , E_2 and E_3 paths were calculated in Table 4.6 to be 76, 78, 60, 69 and 126 kJ mol⁻¹. The apparent barriers for the E_{1a} (76 kJ mol⁻¹), E_{1b} (78 kJ mol⁻¹) and E_3 (126 kJ mol⁻¹) paths all appear to be rather high and unlikely paths. The rates for the E_{1c} and the E_2 paths are both controlled by the initial attack on of the propoxide on the propanal and have barriers that are similar at 60 and 69 kJ mol⁻¹, respectively and as such both are viable paths for esterification.

The results reported here indicate that the ester is formed either by an E_{1c} path which involves a sequential mechanism where the rate-controlling C-O formation step, involving the coupling of a surface propoxide and propanal precedes a rapid hydride transfer from the alkoxide C-H bond to the vicinal bound propanal or by an E_2 path which proceeds via the concerted coupling of a surface propoxide with coadsorbed propanal and direct hydrogen elimination to the surface. Both of these paths result in rate expressions and propanal and hydrogen dependencies that match those reported experimentally.^{46,213,214}

Table 4.6 The apparent rate constants and activation energies for the E_1, E_2 and E_3 esterification paths.

k^{app}	ΔE_a^{App}	$\Delta E_a^{intrinsic}$ (kJ mol ⁻¹)	ΔE_{rxn} (kJ mol ⁻¹)	$\Delta E_a^{App\ calc.}$ (kJ mol ⁻¹)
$k_{1a} K_{C-O}$	$E_{a_{1a}} + \Delta E_{rxn}(C-O)$	104	-28	76
$k_{1b} K_{Hadd}$	$E_{a_{1a}} + \Delta E_{rxn}(H_{add})$	90	-12	78
k_{1c}	$E_{a_{1c}}$	60	-	60
k_2	E_{a_2}	69	-	69
$k_3 K_{acyl}$	$E_{a_3} + \Delta E_{rxn}(acyl)$	-	-	-

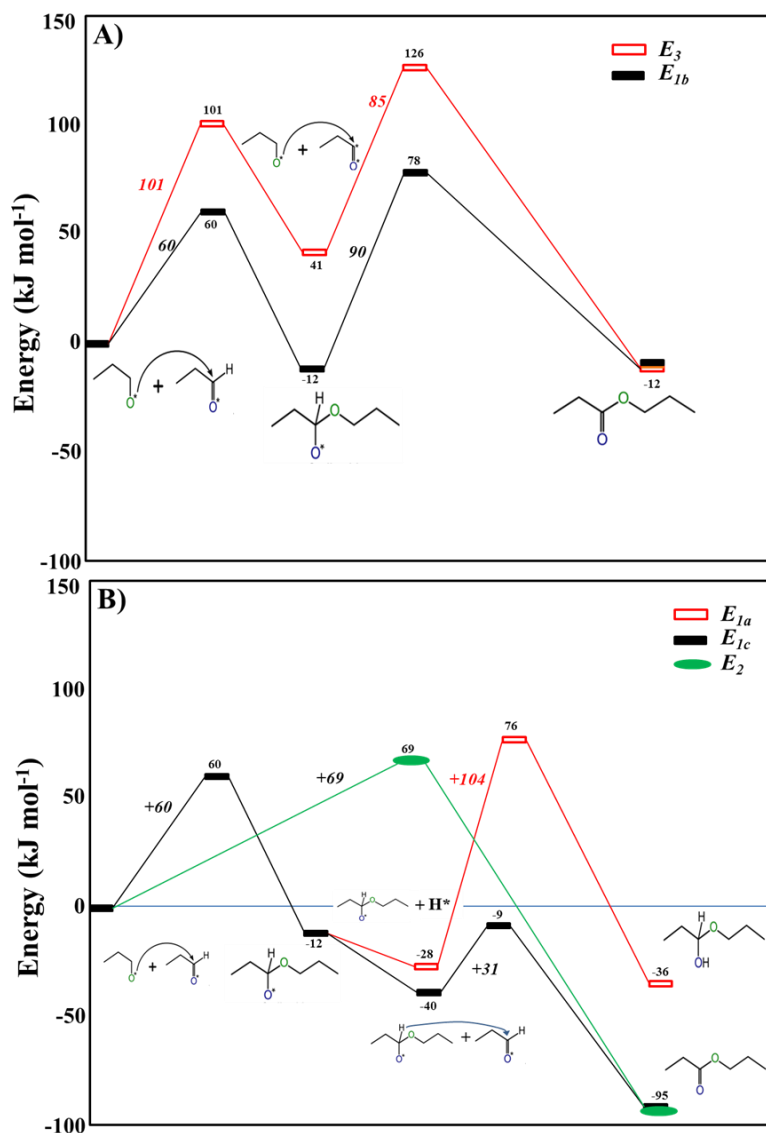


Figure 4.8 DFT-calculated reaction paths for the esterification of propanol-propanol on Cu(111). (A). The E_3 path (light unfilled symbols) which is highest energy proceeds via the C-H activation of propanal to form a surface acyl intermediate that subsequently couples with a bound propanal to form propyl propionate. The E_{1b} path (filled black symbols) which is lower in energy than the E_3 path, proceeds by the coupling of the alkoxide and the alkanal to form the 1-propoxy-1-propoxide hemiacetalate intermediate that subsequently undergoes C₁-H activation over Cu to form propyl propionate. The lowest energy paths (E_{1a} , E_{1c} and E_2) are shown in (B). In the E_{1c} path (light unfilled rectangular symbols) the reaction proceeds via the coupling of the alkoxide and the alkanal followed by a hydrogen addition to the hemiacetalate to form the hemiacetal product. The E_{1c} and E_3 paths are somewhat lower in

energy than the E_3 path. The E_{1c} path which is shown with filled black rectangular symbols proceed via the coupling of propoxide and propanal to form the hemiacetalate intermediate that subsequently reacts with a vicinal propanal to eliminate H to form the propyl propionate. The E_3 path proceeds via a concerted coupling of the surface propyl and propanal intermediates together with the C_1 -H activation by Cu.

4.3.5 Comparing Free Energies for Condensation and Esterification

In order to appropriately compare the rates of condensation and esterification we calculated the enthalpies, entropies and the free energies for the most favorable condensation and esterification paths. The activation energies reported earlier for condensation (70 kJ mol^{-1}) and esterification (60 kJ mol^{-1} for the E_{1c} and 69 kJ mol^{-1} for the E_2 paths) were calculated at 0 K. These values were subsequently corrected for zero point energies as well as changes that result in specific heats in moving from 0 to 298 K. The resulting activation enthalpies for condensation (66 kJ mol^{-1}) and esterification (62 kJ mol^{-1}) were used together with the activation entropies reported in Table 4.7 to determine free energy barriers of 69 kJ mol^{-1} and 66 kJ mol^{-1} for the condensation and esterification reactions, respectively. The difference between the condensation and esterification free energy barriers is only 3 kJ mol^{-1} with the esterification being slightly favored.

Table 4.7 Comparison of the activation enthalpies, entropies and free energies for the condensation and esterification of propanal and propoxide species on the Cu (111) surface.

	Condensation	Esterification
$\Delta H^\ddagger (\text{kJ mol}^{-1})$	66	62
$\Delta S^\ddagger (\text{kJ (mol K}^{-1})$	-0.009	-0.013
$\Delta G^\ddagger (\text{kJ mol}^{-1})$	69	66

Sad et al.¹ showed that rates of esterification and condensation follow identical dependencies on the partial pressures of the propanal as well as propanol and hydrogen. The ratio of the rate of condensation to the rate of esterification was found to be constant over a range of propanal pressures as well as propanol and hydrogen pressures as is shown in Figure 4.9. This suggests that rates of condensation and esterification obey similar rate equations but contain different rate constants,¹ indicating that their respective kinetically-relevant steps involve the same adsorbed propanal ($\text{CH}_3\text{CH}_2\text{CHO}^*$) and surface propoxide ($\text{CH}_3\text{CH}_2\text{CH}_2\text{O}^*$) intermediates. The two steps are limited by kinetically-

relevant propoxide-propanal reactions mediated by bimolecular transition states, but lead to different products. This is fully consistent with the theoretical results discussed above and summarized in Figure 4.10 that show that rate-controlling step for condensation involves the abstraction of the weakly acidic H at the α -position of propanal by basic propoxide to form the enolate intermediate whereas that for esterification involves nucleophilic addition of the basic propoxide to bound propanal.

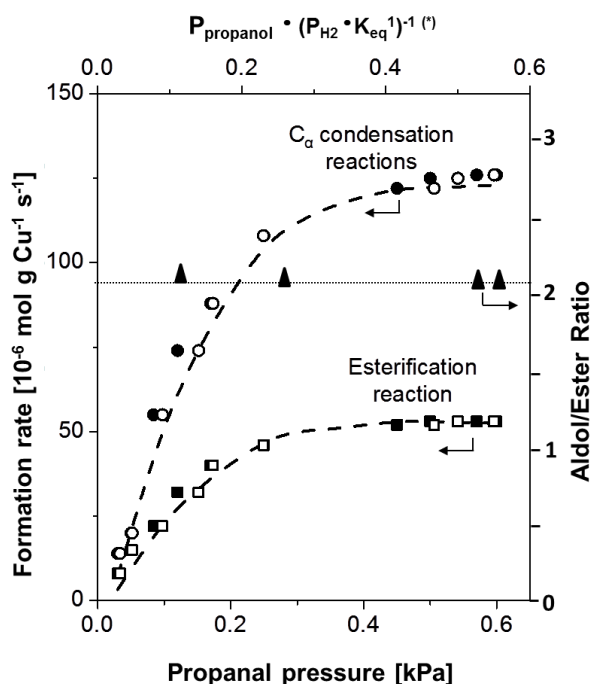


Figure 4.9 Formation rates versus propanal pressure for esterification (\square) and aldol condensation (\bullet) reactions from propanol-propanal- H_2 mixtures on 10 % wt. Cu/SiO₂ (5.5% dispersion) in left axis. Aldol/ester ratio (\blacktriangle) vs propanal pressure in right axis. Reprinted with permission from Sad, M. E., Neurock, M., Iglesia, E. Formation of C–C and C–O Bonds and Oxygen Removal in Reactions of Alkanediols, Alkanols, and Alkanals on Copper Catalysts. *J. Am. Chem. Soc.* 2011, 133, 50, 20384-20398. Copyright 2011. American Chemical Society

In condensation, the enolate species that forms in the rate-limiting step can readily attack a vicinal propanal to form a β -alkoxide alkanal which can undergo facile inter- or intramolecular hydride transfer to form the aldol species that can subsequently dehydrogenate and decarbonylate to form 3-pentanone (shown in the upper path in Figure 4.10). The 1-propoxy-1-propoxide intermediate that forms in the rate controlling step for esterification can undergo facile intermolecular hydride transfer to a surface propanal (path E_{1c} which

is the lower path in Figure 4.10) or a concerted S_N2-like mechanism (path E₂ shown with filled oval symbol) involving simultaneous C-O formation via the coupling of the surface propoxide with coadsorbed propanal and direct H-elimination to form the propyl propionate product.

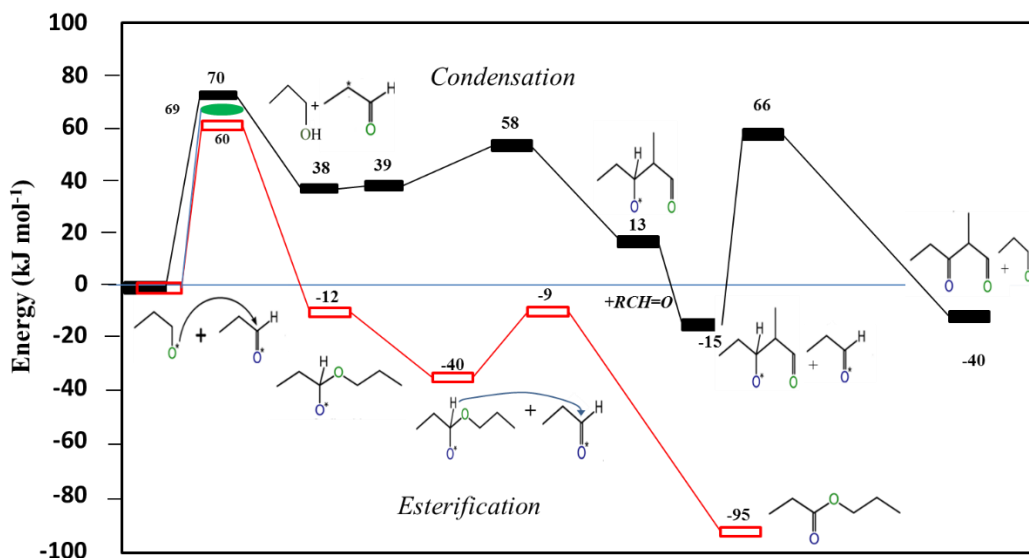


Figure 4.10 A comparison between the energies for the elementary steps involved in aldol condensation and esterification reactions over Cu. The aldol condensation is shown in top curve denoted by dark filled rectangular symbols. Esterification can proceed either via the E_{1c} path involving sequential C-O formation and intermolecular hydride transfer which is shown in the light unfilled rectangular symbols or via the E₂ concerted C-O formation H-elimination path shown in the green elliptical symbols.

The ratio of the rates shown in Figure 4.9 can be analyzed by writing out the ratio of the rate expressions for condensation (Eq. 4.8) to esterification (Eq. 4.11 or Eq. 4.12). This ratio simplifies to ratio of rate constants for the C-C bond formation (k_c) versus C-O bond formation (k_e):

$$\frac{r_C}{r_E} = \frac{k_C K_{PAL}^2 K_{HYD} K_{H_2}^2 P_{PAL}^2 P_{H_2}^2 / [1 + K_{PAL} P_{PAL} + K_{POL} / (K_{HYD} K_{H_2} K_d)]^2}{k_E K_{PAL}^2 K_{HYD} K_{H_2}^2 P_{PAL}^2 P_{H_2}^2 / [1 + K_{PAL} P_{PAL} + K_{POL} / (K_{HYD} K_{H_2} K_d)]^2} = \frac{k_C}{k_E} \quad (4.13)$$

This can be further simplified to the following expression:

$$\frac{r_C}{r_E} = \frac{k_C}{k_E} = \frac{A_C \exp(-E_{aC}/RT)}{A_E \exp(-E_{aE}/RT)} = \frac{A_C}{A_E} \exp(-(E_{aC} - E_{aE})/RT) \quad (4.14)$$

where r_C , r_E , E_{aC} , E_{aE} , A_C , and A_E are the rates, activation energies and pre-exponential factors and the subscripts C and E denote condensation and esterification routes.

The experimental rate data reported by Sad et al. (shown above in Figure 4.9) indicate that condensation rates are about two-fold larger than for esterification at all pressures at 503 K. This corresponds to an esterification barrier that is $\sim 3 \text{ kJ mol}^{-1}$ higher than that for condensation (i.e. $E_{aC} - E_{aE} = -3 \text{ kJ mol}^{-1}$), provided that both reactions have similar pre-exponential factors. Theoretical treatments (Figure 4.10) show that the barriers for aldol condensation and esterification are similar, with a condensation barrier that is 3 kJ mol^{-1} higher than that for esterification ($E_{aC} - E_{aE} = 3 \text{ kJ mol}^{-1}$). Although the sign is different between experimental and theoretical estimations, the difference between these two very close is well within the accuracy of density functional theory of $\pm 5 \text{ kJ mol}^{-1}$.²¹⁵

Previous experimental results show that Cu can uniquely catalyze condensation as well as esterification reactions. Such reactions are typically catalyzed by acids and bases for reactions that are carried out over metal oxides. The theoretical and experimental results presented here show that the exposed Cu metal surface sites act as Lewis acid sites that readily binds to the oxygen of alkanal, alkanol and alkoxide intermediates and works cooperatively with basic sites formed by the in-situ generation of propoxide intermediates to create acid-base site pairs that can rapidly equilibrate alkanal/hydrogen/alkanol mixtures and catalyze condensation and esterification reactions.

Alkoxy intermediates on Cu as well as other group 11 metals (Au and Ag) are more weakly bound to the metal than those on other transition metal surfaces as a result of significant Pauli repulsion with nearly filled d-band of Cu and other group 11 metals. They act to abstract electron density from the metal thus creating negatively charged alkoxides that behave as a base and work together with the Lewis acid sites to form acid-base site pairs that can readily activate acidic C-H and O-H bonds and carry out nucleophilic attack.

The nearly filled nature of the d-band of Cu as well as other group 11 metals, limit their ability to readily activate C-H bonds alone. The Cu surface atoms, however, can act as Lewis acid sites and bind to the O of the alkanal thus creating an enol-like surface intermediate that can undergo electrophilic additions, readily accept hydric H atoms and catalyze the activation of C-H bonds. These adsorbed alkanals are electron acceptors and thus behave as weak Lewis acids. They work closely with the basic alkoxides sites of the

surface to provide acid-base site pairs, similar to those on metal oxides such as TiO_2 ,^{216,217} and ZrO_2 ²¹⁸⁻²²⁰ that can readily catalyze aldol condensation and esterification reactions. The cooperative influence of weak Lewis acid-base pairs for these reactions and others was pioneered by Tanabe.²²⁰⁻²²² Cu is unique in that it selectively carries out decarbonylation along with C-C bond formation. This is likely due to the fact Cu does not form Brønsted acid sites upon the deprotonation of C-H or O-H bonds but instead delivers the proton to weakly held alkoxide intermediates to produce non-acidic alcohols. The Brønsted acid sites that form metal oxide catalysts, on the other hand readily promote hemiacetal formation and in addition catalyze dehydration reactions which lead to the hemiacetal and deoxygenated alkanal and alcohol products.

4.4 Conclusions

First principle density functional theory calculations demonstrate that Cu can catalyze both aldol condensation and esterification reactions without the addition of basic oxide promoters or a basic oxide support. This chemistry is facilitated by the in-situ production of adsorbed alkoxide species which act as a base as well as an active nucleophile, effectively replacing the role of the basic oxide support. In addition, the adsorbed alkanal species weakly bind to Cu to form enolic type Lewis acid sites that catalyze the activation of hydridic C₁-H bonds for various different reactive intermediates. Propanal-propanol-H₂ readily react to form an equilibrated mixture that subsequently undergoes aldol condensation and esterification reactions. The primary product from aldol condensation is 3-pentanone which is formed via C-C coupling followed by decarbonylation. The 2-methyl-pentanal and 2-methyl-3-pentanone which are the predominant products over typical acid and base catalysts as result of subsequent dehydration steps are only produced in minor amounts (< 10 %), indicating that decarbonylation is facile on these Cu/SiO₂ catalysts. Cu was also found to catalyze the C-O bond formation for the reactions between propanol and surface propionate resulting in the formation of propyl propionate as a second primary product

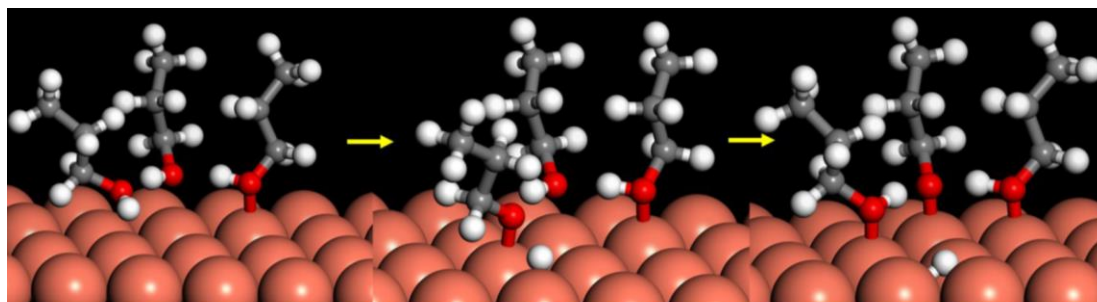
The alkoxide that forms from the interconversion of propanal+H₂ and propanol mixtures withdraws electron density from the Cu substrate thus resulting in the formation of an alkoxide anion that behaves as a base that catalyzes both aldol condensation and esterification. The alkoxide can directly abstract the acidic α-H of aldehyde to form the C₃ enolate during aldol condensation and can carry out the nucleophilic attack of the carbonyl

of the adsorbed aldehyde to form C-O bonds during esterification. Theoretical results show that these two steps have the highest activation barriers and are the kinetically-relevant steps for the condensation or esterification paths, respectively. Since the C-H activation of propanal by propoxide and the nucleophilic attack of the propoxide onto propanal are the kinetically relevant steps for aldol condensation and esterification and since both reactions proceed via identical reactants (i.e. propanal and propoxide), both aldol condensation and esterification should have the same rate equations and have the same kinetic dependencies on the partial pressures of propanal and hydrogen which is consistent with the experimental results. The calculated difference in the activation barriers for rate-limiting steps for esterification (C-O bond formation) and condensation (enolate formation) is small at 3 kJ mol⁻¹. This is consistent with the small differences in the activation barriers found experimentally but condensation is favored experimentally over esterification.

4.5 Acknowledgments

The authors gratefully acknowledge BP for the financial support of this work as part of the BP-XC2 program and the computational support and resources from Minnesota Supercomputing Institute and the Molecular Science Computing Facility (MSCF) in the William R. Wiley Environmental Molecular Sciences Laboratory, a national scientific user facility sponsored by the U.S. Department of Energy, Office of Biological and Environmental Research at the Pacific Northwest National Laboratory for computing resources. The authors also wish to thank Dr. Maria Sad, Dr. George Huff, Dr. Glenn Sunley, Dr. John Shabaker and Professor Jay Labinger and Professor John Bercaw for their helpful discussions.

4.6 Supporting Information



$$\Delta E_{\text{act}} = 80 \text{ kJ/mol (0.2 ML OR}^*) \\ (120 \text{ kJ/mol (0.05 ML OR}^*))$$

$$\Delta E_{\text{rxn}} = 17 \text{ kJ/mol (0.2 ML OR}^*) \\ (20 \text{ kJ/mol (0.05 ML OR}^*))$$

Figure S 4.1 Influence of higher coverage on the dissociation of propanal over Cu(111). Higher coverages of propanal decrease the barrier by 40 kJ/mol to activate propanol by allowing for proton-coupled electron shuttling paths.

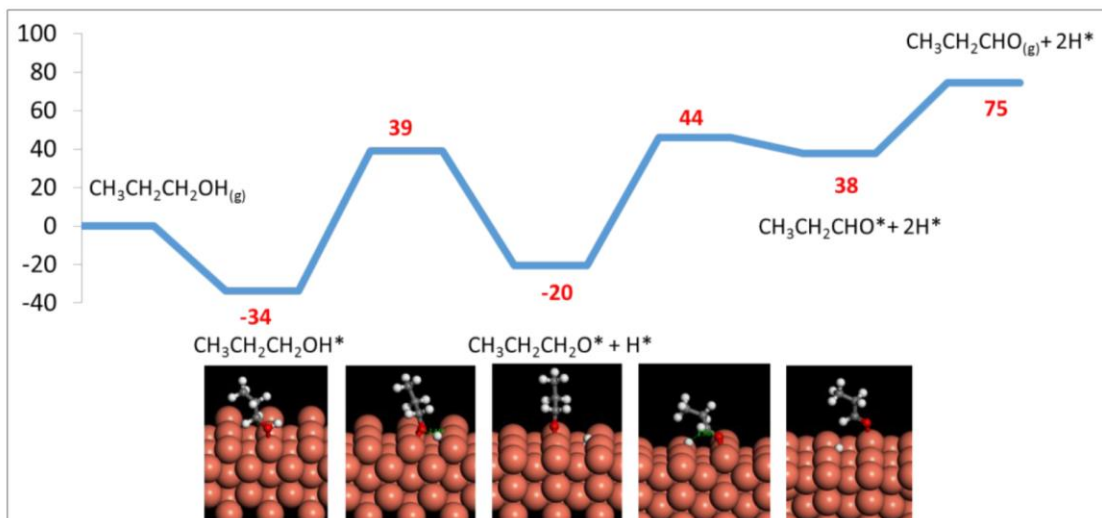


Figure S 4.2 DFT-calculated activation barriers and reaction energies for the adsorption and dissociation of propanol to propoxide and H^* and the subsequent reaction of propoxide to propanal and hydrogen over the Cu(110) surface.

5 Mechanistic Insights into the Hydrogenolysis of Fatty Acids over Supported Pd-ReO_x Catalysts

The experimental results presented in this chapter are adapted from Kammert, J. D., Chemburkar A., Miyake, N., Neurock, M., and Davis, R. J. *Reaction Kinetics and Mechanism for the Catalytic Reduction of Propionic Acid over Supported ReO_x Promoted by Pd*. Manuscript under preparation.

Experiments were performed by JDK and NM under the supervision of RJD. DFT simulations were performed by AC under the supervision of MN.

5.1 Introduction

Hydrogenolysis of fatty acids produces fatty alcohols (Equation 5.1), which are important intermediates in the synthesis of detergents, lubricants, plasticizers, biofuels, pharmaceuticals, fragrances, emulsifiers, emollients and thickeners.^{223–226} With the advancement in microbial fermentation, short to long chained carboxylic acids can be derived from biomass,^{1,227,228} allowing for renewable manufacturing of many everyday chemicals and intermediates. Hydrogenolysis of fatty acids and esters has been previously reported over copper chromite catalysts.^{50,229,230} These catalysts, however, require very high H₂ pressure (> 25 MPa) as well as raise environmental concerns due to the use of chromium. Consequently, hydrogenolysis catalysts that do not contain chromium yet operate at lower H₂ pressure are being investigated as greener and more viable catalysts. Bimetallic catalysts consisting of an oxophilic metal promoted by a non-reducible metal have demonstrated high reactivity and selectivity towards C-O bond hydrogenolysis at reduced H₂ pressures. Supported rhenium oxide catalysts (ReO_x), promoted by other metals (Ru, Rh, Pd, Ir, Pt) were shown to result in high selectivities (> 85 %) at a much lower H₂ pressure (8 MPa).²²⁵ Among these, Pd-ReO_x catalyst yielded the highest selectivity of 92 %, ²²⁵ and consequently is of interest from mechanistic and characterization perspective so as to tailor similar catalytic systems based on cheaper and perhaps more reactive as well as selective materials.



Previous computational results on model Pd-Re surfaces suggest that Re is instrumental in C-O bond activation, while Pd catalyzes hydrogenation of reactive intermediates.²³¹ The results suggest that the mechanism of acetic acid hydrogenolysis involves initial C-O bond activation on Re to generate acetyl intermediates, that undergo several C-H formation steps to form ethanol. These models, however, assume that both Pd and Re are present as reduced metals, which is inconsistent with more recent characterization studies. These newer experimental studies suggest that Re is present as well-dispersed oxide species, while Pd is present in its reduced form.^{224,232,233} Consequently, a new mechanism was proposed by Tomishige and co-workers,²²⁴ where Re promotes the dissociation of H₂ via heterolytic cleavage on ReO_x. Metallic Pd, on the other hand, was proposed to increase the interaction between the catalytic surface and the carboxylic acid. The rate determining step was thought to involve hydride attack from Re sites. The chemisorption of H₂ on Re, however, is known to be sluggish,^{234–237} suggesting that the heterolytic dissociation of H₂ over ReO_x proposed by Tomishige is unlikely. Our theoretical results also show that heterolytic activation of H₂ over ReO_x is unlikely (Figure 5.2). H₂, instead, can more readily dissociate over metallic Pd and then carry out chemistry. Hydrogen would also bind strongly on the proposed Re sites, as a result, hydride attack would more likely proceed through Pd sites, where hydrogen is known to bind relatively weakly.²³⁸ Therefore, the mechanism as well as the promotive role of Pd appears to be unclear through previous investigations. Moreover, a recent study by Murzin and co-workers²²³ shows that Pd or any other promoter is not necessary to catalyze hydrogenolysis of fatty acids, and that high-temperature-treated ReO_x catalysts alone can produce alcohols with a high selectivity further questioning the role of Pd.

Here, we report fundamental insights into the hydrogenolysis of propionic acid to propanol over Pd-ReO_x/TiO₂. The mechanism is elucidated through the use of rate order dependencies, kinetic isotope effect (KIE) experiments, density functional theory (DFT) simulations, and diffuse reflectance infrared fourier transform spectroscopy (DRIFTS). We show that both Pd and ReO_x are involved in the chemistry over the bimetallic Pd-ReO_x/TiO₂ catalyst; where Pd sites aid in the activation of hydrogen and supply surface hydrides necessary to form C-H bonds and protons on well-dispersed ReO_x sites which are necessary for dehydration. DFT results show that the close proximity between Pd and ReO_x sites is desired for direct hydride transfer from Pd sites over to intermediates on ReO_x sites. Active catalysts for hydrogenolysis of carboxylic acids are therefore shown to

require sites that not only directly provide hydrides, but also possess surface acidity to catalyze C-O bond activation.

5.2 Results and discussion

5.2.1 Theoretical analysis of propionaldehyde formation from propionic acid over Pd-ReO_x/TiO₂ catalyst

This section describes theoretical efforts examining the role of Pd during hydrogenolysis of propionic acid. Reactions were first simulated on dispersed ReO_x clusters deposited on TiO₂. Pd atoms were then deposited within close proximity of ReO_x to simulate the same reactions with direct assistance from Pd sites.

Single Re atoms were deposited on the 101 surface of anatase TiO₂ as a model for well-dispersed Re species. Structural optimization results in oxidation of the Re atom to generate four-coordinate Re species on the surface of TiO₂ (Figure 5.1(B)). The optimized structure was further capped with an additional oxygen atom to fill an oxygen vacancy that is generated on the surface of TiO₂ resulting in a penta-coordinate Re species.

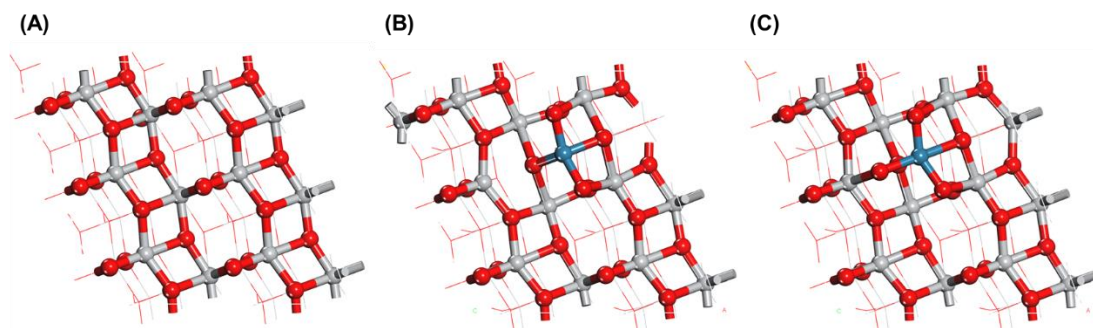


Figure 5.1 (A) Optimized structure for the 101 surface of anatase. (B) The optimized structure for single Re atom deposited on the 101 surface of anatase. The Re atom is seen to bond to 4 neighboring oxygen atoms, resulting in surface oxygen vacancies and unpaired electrons. (C) The optimized structure of the Re-substituted TiO₂ surface after adding an additional oxygen atom to pair electrons and surface oxygen vacancy in structure B. Re is now seen to bond with 5 oxygen atoms.

The penta-coordinate ReO_x species was first tested for heterolytic H₂ activation proposed by Tomishige and co-workers (Figure 5.2).²²⁴ The activation barrier for H₂ dissociation was found to be rather high (79 kJ/mol with respect to adsorbed H₂ and 44 kJ/mol with respect to gaseous H₂) consistent with previous reports showing activated H₂ dissociation over

Re.^{234–237} In contrast, H₂ activation on Pd particles has been shown to be barrierless in previous studies.^{239,240} Further, hydrogen atoms that form on a metal have been shown to spillover onto the TiO₂ support and diffuse on the support as protons.^{241–243} These protons can also diffuse on to ReO_x from the TiO₂ support and form acid sites that aid in hydrogenolysis. Hydrogenolysis on ReO_x, therefore, was simulated using protons available on neighboring oxygen sites (Brønsted acid sites), see Figure 5.3.

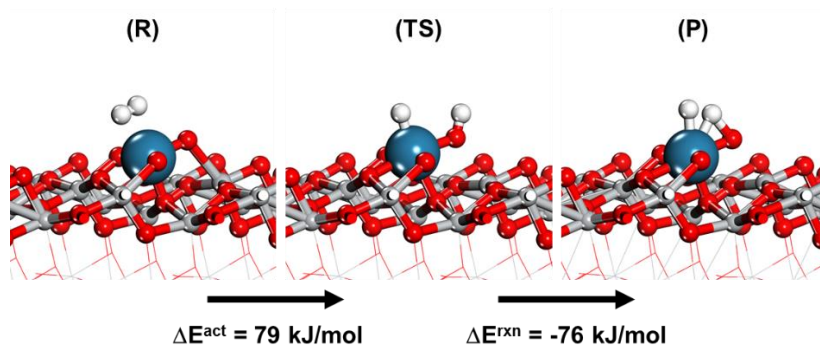


Figure 5.2 Optimized structures showing the reactant, transition state, and product during heterolytic activation of H₂ over ReO_x.

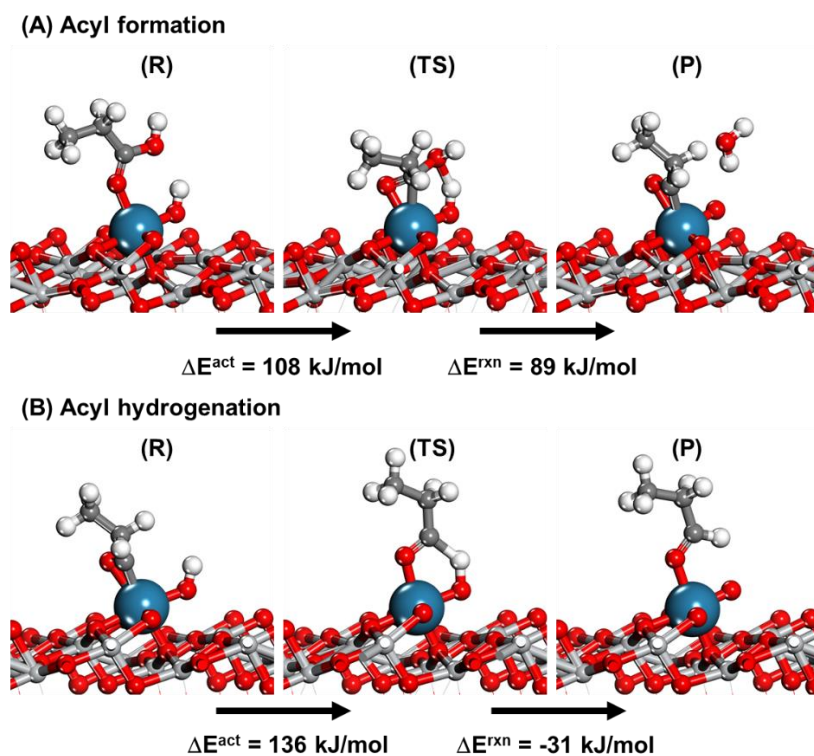


Figure 5.3 Optimized structures showing the reactant, transition state, and product during Brønsted acid catalyzed acyl formation and acyl hydrogenation over ReO_x .

The Brønsted acid catalyzed dehydration of propionic acid (Figure 5.3(A)) to produce the acyl intermediate ($\text{CH}_3\text{CH}_2\text{COOH}^* + \text{HO}^* \rightarrow \text{CH}_3\text{CH}_2\text{CO}^* + \text{O}^* + \text{H}_2\text{O}$) proceeds with an activation barrier of 108 kJ/mol, with the reaction being endothermic by 89 kJ/mol. The subsequent hydrogenation of the acyl intermediate (Figure 5.3(B)) using the Brønsted acid site ($\text{CH}_3\text{CH}_2\text{CO}^* + \text{HO}^* \rightarrow \text{CH}_3\text{CH}_2\text{CHO}^* + \text{O}^*$), however, requires a higher activation barrier of 136 kJ/mol. The higher barrier is likely due to repulsion between the positively charged proton and the positive charge that forms on the carbonyl that is adjacent to electron-withdrawing oxygen of the carbonyl.²⁴⁴ Previous theoretical results from Pallasanna and Neurock,²⁴⁵ in contrast, show that the acyl intermediate can be hydrogenated using a chemisorbed hydrogen atom which is more hydridic in character with a much lower activation barrier of 66 kJ/mol over metallic palladium. Characterization results show that Pd is present on the bimetallic catalyst in its metallic form.^{224,232} We therefore examined a new model where the Pd atoms were deposited next to the penta-coordinate ReO_x species (Figure 5.4(A)). This close proximity of Pd and ReO_x , which was missing in the previous model (Figure 5.1(C)), enables direct hydride transfer from metallic Pd sites.

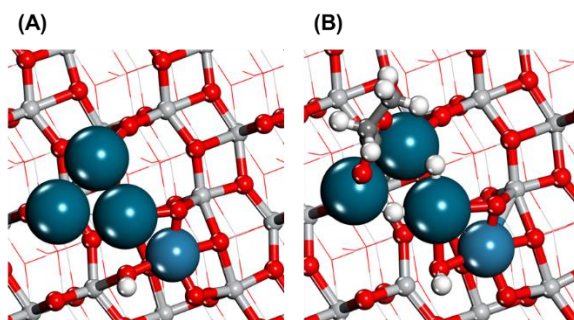


Figure 5.4 (A) Optimized structure showing a Pd_3 cluster next to ReO_x . (B) Optimized structure showing the Pd_3 cluster saturated with reactive intermediates- hydrogen atoms and carboxylate.

A Pd_3 cluster was deposited next to the ReO_x species on anatase (Figure 5.4(A)). Previous theoretical results examining hydrogen spillover from Ru to TiO_2 show that hydrogen spillover is observed only at higher coverage of hydrogen,²⁴² highlighting the importance of coverage effects in simulating such systems. Other experiments studies provide spectroscopic evidence for adsorbed H^* ²⁴⁶ and propionate ($\text{CH}_3\text{CH}_2\text{COO}^*$)²⁴⁷ on Pd in the

presence of H₂ gas and propionic acid respectively. Hydrogen chemisorption energies were, therefore, calculated at different coverages and are shown in Table 5.1. The results show that hydrogen atoms bind very strongly to the pristine supported Pd₃ cluster but becomes significantly weaker with increasing hydrogen or carboxylate coverage which is consistent with previous results on Ru.²⁴²

Table 5.1 Change in the adsorption energy of hydrogen gas ($0.5\text{H}_2 + * \rightarrow \text{H}^*$) at different coverage of hydrogen and carboxylate over Pd (ML = monolayer).

Hydrogen coverage	Carboxylate coverage	ΔE_{ads} (kJ/mol)
1/3 ML	0	-139
2/3 ML	0	-58
2/3 ML	2/3 ML	-30

Pd₃ cluster completely saturated by one propionate species (CH₃CH₂COO*) and two hydrogen atoms (Figure 5.4(B)) was further used to simulate spillover of hydrogen from Pd₃ cluster to oxygen on ReO_x (Figure 5.5). The calculations show a low activation barrier for spillover (30 kJ/mol with respect to hydrogen on Pd₃ and 13 kJ/mol with respect to H₂ in the gas-phase). The reaction energy is found to be exothermic by -29 kJ/mol. The model surfaces, therefore, predict that hydrogen can readily spillover onto ReO_x forming Brønsted acid sites. Consequently, two types of hydrogens are available over Pd-ReO_x sites, protons on Brønsted acid sites and hydrides on metallic Pd clusters. Protons can be used to catalyze O-H formation reactions, while hydrides can be used for C-H formation steps during hydrogenolysis of propionic acid.

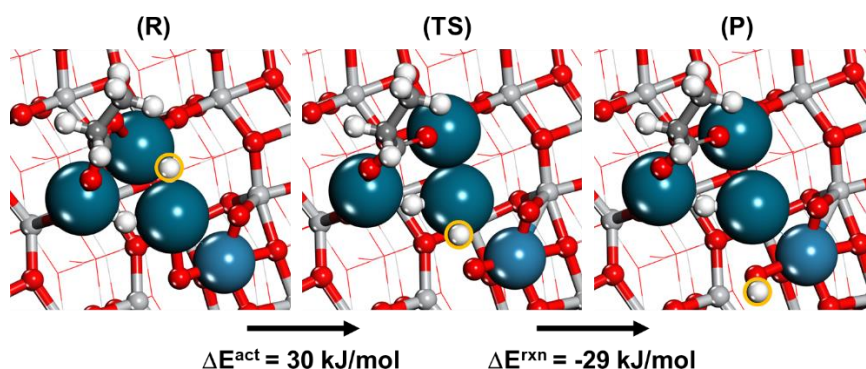
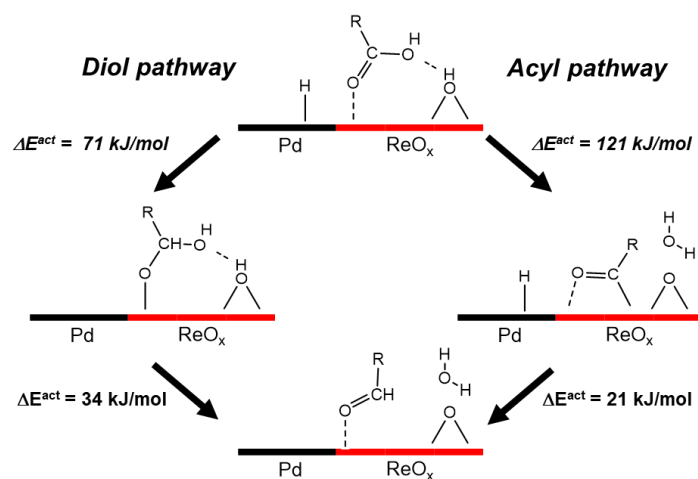


Figure 5.5 Reactant, transition state, and product structures during hydrogen spillover from Pd to ReO_x. The hydrogen atom that spills over is marked in orange.

Two different routes were considered on the Pd-ReO_x model surface due to the availability of two types of hydrogen. The first route involves initial C-O bond activation via a Brønsted acid-catalyzed dehydration of the acid to yield the acyl intermediate. The acyl intermediate then undergoes a C-H formation step forming a bound aldehyde species on the surface. This route will be termed the acyl route. In the second route termed the diol path, the elementary steps are switched. The hydrogen addition to addition to the C₁ carbon to form a diol intermediate precedes the Brønsted acid catalyzed C-O bond activation step thus yielding the surface bound aldehyde. Both these routes are highlighted in Scheme 5.1.



Scheme 5.1 Reaction scheme showing the diol and acyl pathways on Pd-ReO_x. Activation barriers shown here are intrinsic barriers and are calculated below.

The initial Brønsted acid catalyzed dehydration step to form an acyl intermediate (CH₃CH₂CO*) was found to have an activation barrier of 121 kJ/mol and an overall reaction energy of 96 kJ/mol (Figure 5.6(A)) which is similar to energies calculated for these same steps on the isolated ReO_x (Figure 5.2(A)). The energies for the hydrogenation of the acyl intermediate catalyzed by the hydride bound to Pd (Figure 5.6(B)), however, was found to be very facile ($\Delta E^{\text{act}} = 21$ kJ/mol, and $\Delta E^{\text{rxn}} = -75$ kJ/mol). The barrier is over 92 kJ/mol lower than the same hydrogenation reaction carried out over above over the isolated ReO_x site (115 kJ/mol) where this reaction was catalyzed instead by a Brønsted acid site (Figure 5.2(B)). The reduction in barrier is presumably due to the transfer of a hydride rather than a proton to the positively charged carbonyl carbon. The close proximity of Pd to the ReO_x sites helped to enable a direct hydride attack thus facilitating the acyl route. The direct dehydration of acetic acid on Pd was investigated previously²³¹ and the resulting activation barrier was found to be very high (142 kJ/mol), thus suggesting that Pd sites alone are

inactive in the direct C-O bond activation due to their low acidity. C-O bond activation reactions on Pd were therefore not considered herein.

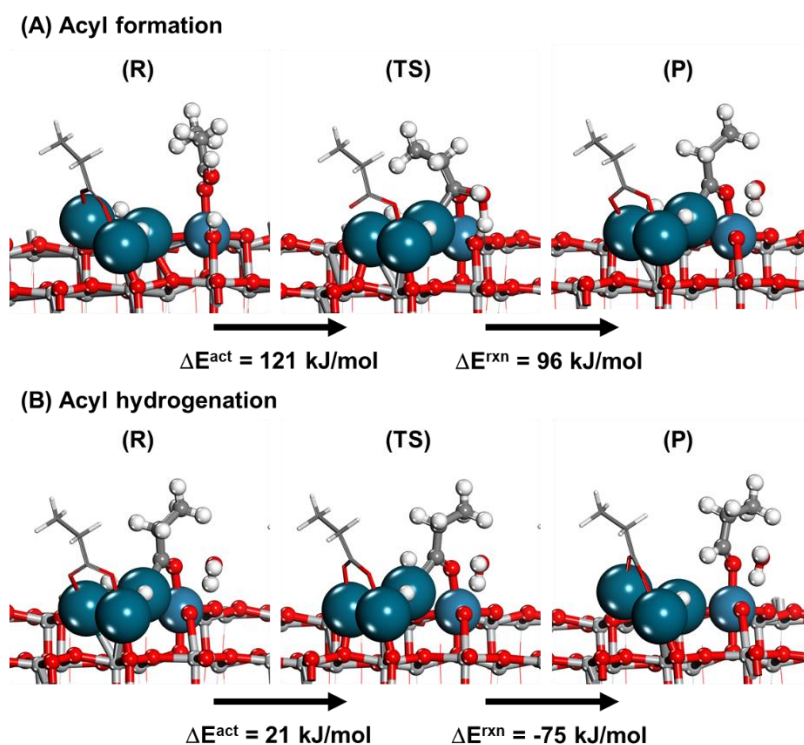


Figure 5.6 Reactant, transition state, and product structures for: (A) the acid-catalyzed dehydration of the bound propionic acid to form the acyl intermediate and (B) the subsequent structures for the hydrogen addition to the C₁ carbon to form propionaldehyde in the acyl mechanism over Pd-ReO_x/TiO₂.

The diol mechanism (see Scheme 5.1) proceeds via a hydride attack at the C₁ carbon of the bound acid ($\text{CH}_3\text{CH}_2\text{COOH}^* + \text{H}^* \rightarrow \text{CH}_3\text{CH}_2\text{CHOOH}^* + *$) to form the diol intermediate (Figure 5.7(A)). The intrinsic activation barrier and the overall reaction energy were found to be rather low at 71 kJ/mol and 8 kJ/mol, respectively. The diol intermediate can also easily dehydrate using proton on the Brønsted acid site with an activation barrier of 34 kJ/mol and an energy of reaction of 14 kJ/mol. The initial C-H formation presumably weakens the C-O bond, thus, making dehydration easier compared to the previous path involving direct C-O bond activation (Figure 5.6(A)). The hydridic nature of hydrogen on Pd sites also seems to promote the initial diol formation reaction. Comparing the intrinsic activation barriers marked on Scheme 5.1, the diol mechanism appear to be the kinetically faster reaction (due to low intrinsic activation barriers) that is enabled by the close proximity of metallic Pd sites and the Brønsted acid sites on ReO_x. Pd, in addition, also

allows for facile activation of H₂ activation and subsequent H spillover which enables the formation of acidic protons on ReO_x. These Brønsted acid ReOH sites subsequently aid in the dehydration of the diol intermediate to form propionaldehyde on Re sites.

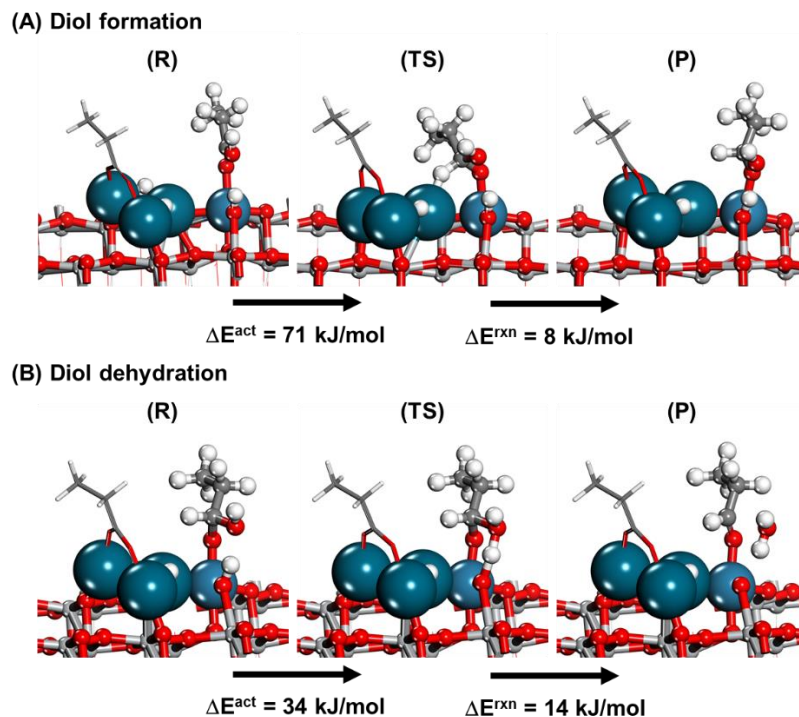


Figure 5.7 Reactant, transition state, and product structures for A) the hydrogen addition to the C1 carbon of the bound propionic acid to form propane diol, and B) the acid-catalyzed dehydration of the diol intermediate to form propionaldehyde in the diol mechanism over Pd-ReO_x/TiO₂.

The calculated reaction energies and activation barriers were subsequently used to construct an overall reaction energy diagram that will be used to predict the rate determining step, apparent activation barrier and rate orders. Before constructing the energy diagram, it is important to understand which species cover active sites at steady state reaction conditions. Previous results on Pd(111) surfaces show that Pd sites are covered by carboxylate species.^{231,247} Such intermediates could also cover exposed Re sites. DFT results show that propionic acid can deprotonate very easily over the Re-Pd site with an activation barrier of just 15 kJ/mol with the reaction being exothermic by -55 kJ/mol (Figure 5.8) to form bidentate propionate intermediates. Such intermediates are also detected experimentally over Pd-ReO_x catalysts examined herein by DRIFTS (Figure S 5.1 and Table S 5.1) which is fully consistent with the DFT results. An energy diagram

is constructed next with respect to adsorbed propionate intermediates as the reference state. The rate-determining step with respect to the reference state appears to involve the formation of the diol intermediate. Assuming hydrogenation of propionaldehyde is easier (which is shown later to be the case), a microkinetic model can be derived with the elementary steps shown in Scheme 5.2.

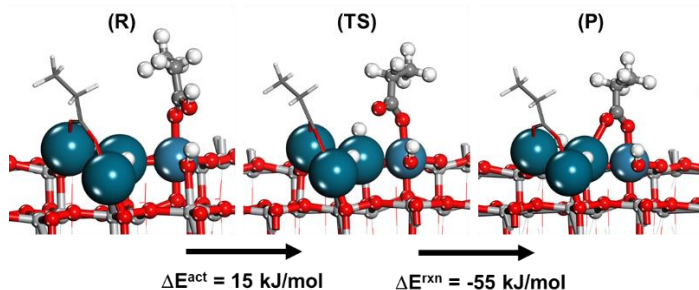


Figure 5.8 Optimized structures for reactant, transition state and product for the heterolytic dissociation of propionic acid to form the Pd-bound propionate and surface ReOH intermediate on Pd-ReO_x.

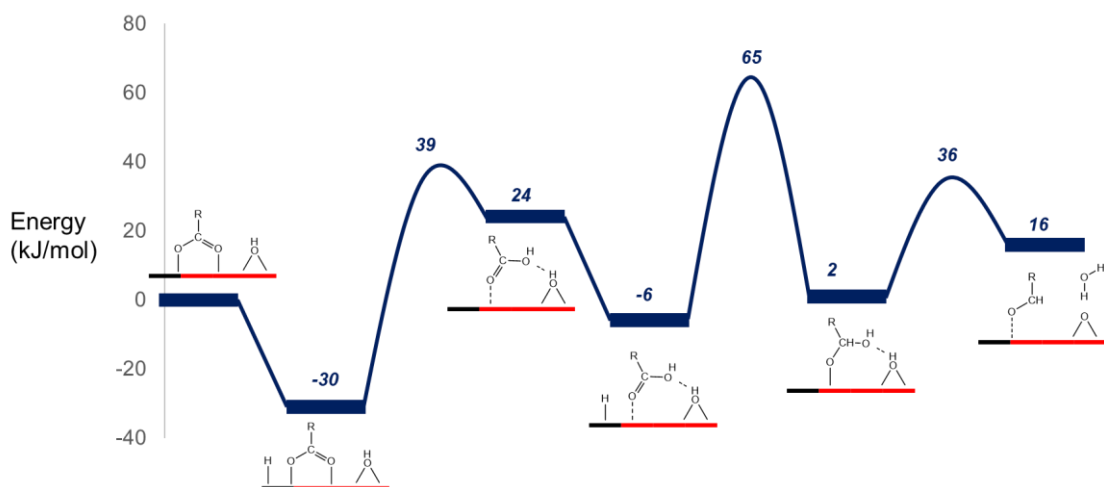
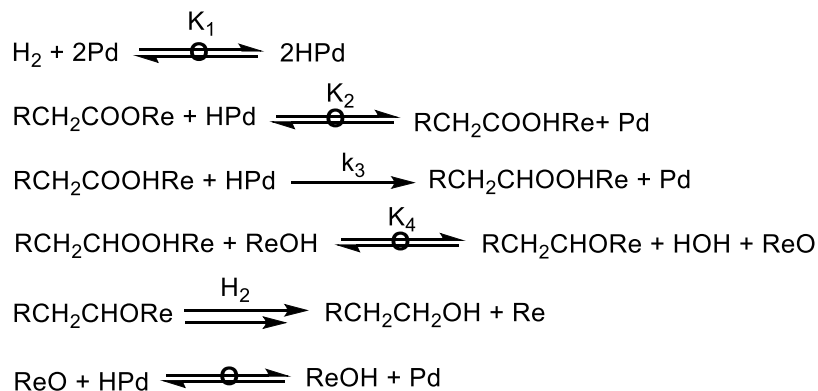


Figure 5.9 The reaction energy diagram for the hydrogenation of propionic acid to 1-propanal over Pd-ReO_x. The energies are shown with respect to adsorbed bidentate propionate seen experimentally. The elementary steps shown here include: 1) an initial hydrogen adsorption on Pd, 2) carboxylic acid formation, 3) a second hydrogen adsorption, 4) diol formation and 5) Brønsted acid catalyzed dehydration. It is assumed that Brønsted acid sites are readily generated since the intrinsic activation barrier for spillover was found to be just 30 kJ/mol.



Scheme 5.2 Elementary steps leading to alcohol production from carboxylic acids over Pd-ReO_x catalysts.

$$\text{rate} = k_3[\text{RCH}_2\text{COOHRe}][\text{HPd}] \quad (5.2)$$

$$\text{rate} = k_3K_2[\text{RCH}_2\text{COORe}][\text{HPd}]^2 \quad (5.3)$$

$$\text{rate} = k_3K_2[\text{RCH}_2\text{COORe}] \frac{K_1P_{\text{H}_2}}{(1+K_1^{0.5}P_{\text{H}_2}^{0.5})^2} \quad (5.4)$$

$$\text{rate} = k_3K_2C_1 \frac{K_1P_{\text{H}_2}}{(1+K_1^{0.5}P_{\text{H}_2}^{0.5})^2} \quad (5.5)$$

$$\text{rate} = k_3K_2C_1K_1P_{\text{H}_2} \quad (5.6)$$

The steady state rate can be written as Equation (5.2). Substituting for the concentration of RCH₂COOHRe using equilibrium constant K₂, we get Equation (5.3). Now, [HPd] can be replaced in terms of partial pressure of H₂ using equilibrium constant K₁ (Equation (5.4)). Since carboxylates cover Re sites at high coverage as shown by experiments and simulations, [RCH₂COORe] can be replaced by a constant C₁ (Equation (5.5)). Equation (5.5) suggests that at steady state, a zero-order dependence on acid is expected, while a zero to 1st order dependence on the partial pressure of H₂ can be obtained depending on the coverage of hydrogen over exposed Pd sites (K₁^{0.5}P_{H₂}^{0.5} vs 1). Equation 5.5 is consistent with previous results by Tomishige et al.²²⁴ and Davis et al.²³² that show a zero order dependence on acid and a 1st order dependence on H₂ over Pd-ReO_x/SiO₂ catalysts. Over Pd-ReO_x/TiO₂, while a zero-order dependence on acid is maintained, a slightly reduced dependence of 0.6 is observed for H₂ pressure (Figure S 5.3). These results can still be explained by the microkinetic model (Equation 5.5), however, only if hydrogen is present at sufficiently large coverage such that it results in partial reduction of the apparent dependence from 1 to 0.6. An apparent activation barrier from DFT can be estimated by

summing the temperature dependent contributions that appear in the rate and equilibrium constants of Equation 5.6 using Figure 5.9 (see Table 5.2). For a dependence of 1st order in H₂ and zero order in acid, an apparent activation barrier of 65 kJ/mol is obtained, which is consistent with the activation barrier of 60 kJ/mol and 75 kJ/mol observed experimentally over Pd-ReO_x/SiO₂ and Pd-ReO_x/TiO₂ respectively (Figure S 5.2).

The microkinetic modeling results presented herein allow us to consolidate the elementary reactions and their corresponding energetics obtained from density functional theory calculations (Figure 5.9) into the steady-state macroscopic results presented herein (Figure S 5.3). The simulations together with experimental observations suggest that hydrogenolysis of carboxylic acids over bimetallic Pd-ReO_x catalysts proceeds via the formation of a diol intermediate. The proposed mechanism is also consistent with the mechanism aldehyde oxidation to carboxylic acid (microscopic reverse of carboxylic acid to aldehyde) over gold, which is thought to proceed through the diol intermediate.²⁰³ Similarly, esterification reactions that form esters (RCOOR') instead of carboxylic acids (RCOOH) are also proposed to proceed via over coinage metals via the formation of a β-alkoxide (RCHOOR'*) intermediate that closely resembles the diol intermediate (RCHOOH*).^{248,249}

Table 5.2 Value of constants that appear in microkinetic analysis (Equations 5.2-5.6). The temperature dependent contributions are based on the energy diagram presented in Figure 5.9.

Constant	Expression from DFT simulations
K ₁	$\exp\left(\frac{\Delta S_1}{R}\right) \exp\left(\frac{-[-60]}{R^*T}\right)$
K ₂	$\exp\left(\frac{\Delta S_2}{R}\right) \exp\left(\frac{-[54]}{R^*T}\right)$
k ₃	$\frac{k_B T}{h} \exp\left(\frac{\Delta S_3}{R}\right) \exp\left(\frac{-[71]}{R^*T}\right)$
ΔE^{act} for 1st order in H₂	-60 + 54 + 71 = 65 kJ/mol

Additional support for the elementary steps proposed here comes from the agreement between kinetic isotope effects observed experiments and those determine from the simulations. Experimentally, an inverse kinetic isotope effect of 0.79 (Table S 5.2) is observed for propionic acid hydrogenolysis with H₂/D₂ over Pd-ReO_x/TiO₂. The individual

elementary step kinetic isotope effects estimated from DFT which are presented in Table 5.2 show an overall kinetic isotope effect of 0.49 for 1st order in H₂. The inverse effect that is observed experimentally is found to be dominated by pre-equilibrated steps involving hydrogen atoms that result in an overall inverse equilibrium isotope effect. Such inverse kinetic isotope effects dominated by quasi-equilibrated H₂ dissociation and hydrogenation steps are reported for the hydrogenation of CO over Co, Fe and Pd.^{250–252} Such reactions ultimately lead to C-O bond activation similar to hydrogenolysis of propionic acid.

Table 5.3 Kinetic isotope effect contributions 400 K and 1 atm for individual steps that appear in Equation 5.6. Overall kinetic isotope effect for 1st order in H₂ can be estimated by

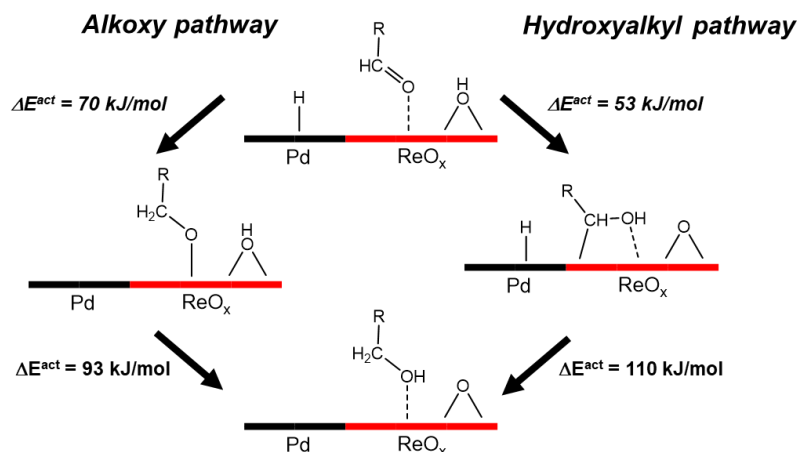
evaluated the product $\frac{K_{1H}}{K_{1D}} \cdot \frac{K_{2H}}{K_{2D}} \cdot \frac{k_{3H}}{k_{3D}}$.

Elementary step	Kinetic isotope effect
$\text{H}_2 + 2\text{Pd} \xrightleftharpoons{K_1} 2\text{HPd}$	$\frac{K_{1H}}{K_{1D}} = 0.22$
$\text{RCH}_2\text{COORe} + \text{HPd} \xrightleftharpoons{K_2} \text{RCH}_2\text{COOHRe} + \text{Pd}$	$\frac{K_{2H}}{K_{2D}} = 0.41$
$\text{RCH}_2\text{COOHRe} + \text{HPd} \xrightarrow{k_3} \text{RCH}_2\text{CHOHRe} + \text{Pd}$	$\frac{k_{3H}}{k_{3D}} = 5.62$

5.2.2 Theoretical analysis of propionaldehyde hydrogenation to propanol over Pd-ReO_x catalyst

The aldehyde that forms as a result of the dehydration of the acid can be hydrogenated over the Pd-ReO_x sites or via those on Pd to form the alcohol. We therefore examined the hydrogenation of propionaldehyde over both Pd-ReO_x sites as well as over Pd sites on Pd(111) surface which acts as a model for the larger Pd particles detected from spectroscopic measurements^{224,232}. The hydrogenation of the C=O bond of propionaldehyde can proceed via an alkoxy route which involves the addition of hydrogen to C₁ of the carbonyl bond of propionaldehyde to form the propoxy intermediate followed by a second hydrogen addition to the O of the alkoxide to form to form propanol on the surface. The hydrogenation of the C=O bond can also proceed via a hydroxyalkyl route which involves the initial addition of hydrogen to the O of the carbonyl to form the hydroxypropyl intermediate, followed by a second hydrogen addition to the C₁ carbon of

the hydroxypropyl that is bound to the catalyst to form propanol on the surface. Both the alkoxy and hydroxyalkyl routes are depicted in Schemes 5.3 and 5.4 that show these reactions over Pd-ReO_x and Pd(111) surfaces respectively.



Scheme 5.3 Hydrogenation of propionaldehyde via the alkoxy and hydroxyalkyl route over Pd-ReO_x. C-H formation reactions are catalyzed by hydride transfer from Pd, while O-H formation reactions are catalyzed by the Brønsted acid site Re-OH. The reported intrinsic activation barriers for each step are calculated and discussed below.

Propionaldehyde can hydrogenate over the Pd-ReO_x surface via an initial O-H formation, activating the hydroxyalkyl route to form the hydroxypropyl intermediate (Figure 5.10(A)) with a barrier of 52 kJ/mol and an overall endothermic reaction energy of 21 kJ/mol. The subsequent C-H formation on the hydroxypropyl intermediate is predicted to have a high activation barrier likely due to the fact that, the Re-C bond is broken in the transition state and a weaker Pd-C partial bond is formed as hydride attacks carbon (Figure 5.10(B)). Propionaldehyde can also react via the initial addition of hydrogen to the C₁ carbon of the carbonyl to form the propoxide intermediate (via the alkoxy route) (Figure 5.10(C)), with an activation barrier of 70 kJ/mol and an overall reaction energy of -41 kJ/mol. The exothermic nature of propoxy formation arises out of high oxophilicity of Re. The propoxy intermediate can subsequently undergo a Brønsted acid catalyzed O-H formation to form propanol (Figure 5.10(D)) with an activation barrier of 93 kJ/mol and a reaction energy of -6 kJ/mol. The high barrier for O-H formation on the propoxy intermediate is likely due to energy cost needed to break the strong Re-O bond forming the more weakly bound alcohol. From Figure 5.9, we see that the energy of propionaldehyde is 16 kJ/mol with respect to propionate intermediate on ReO_x. Figure 5.11 begins from adsorbed aldehyde

on the surface (at 16 kJ/mol) and shows the subsequent hydrogenation steps. The energies shown in Figure 5.11 indicate that propionaldehyde hydrogenation should be kinetically faster via the alkoxy route consistent with previous results on metallic Ru(0001).¹⁹⁵ Furthermore, if we compare the highest energy transition state in Figures 5.9 and 5.11 with respect to the dominant adsorbed propionate intermediate, the diol formation transition state (65 kJ/mol) is 8 kJ/mol higher than that for propionaldehyde hydrogenation (57 kJ/mol), indicating that the hydrogenation of propionaldehyde is equilibrated and that the rate of the overall reaction of propionic acid to propanol is controlled by the diol formation.

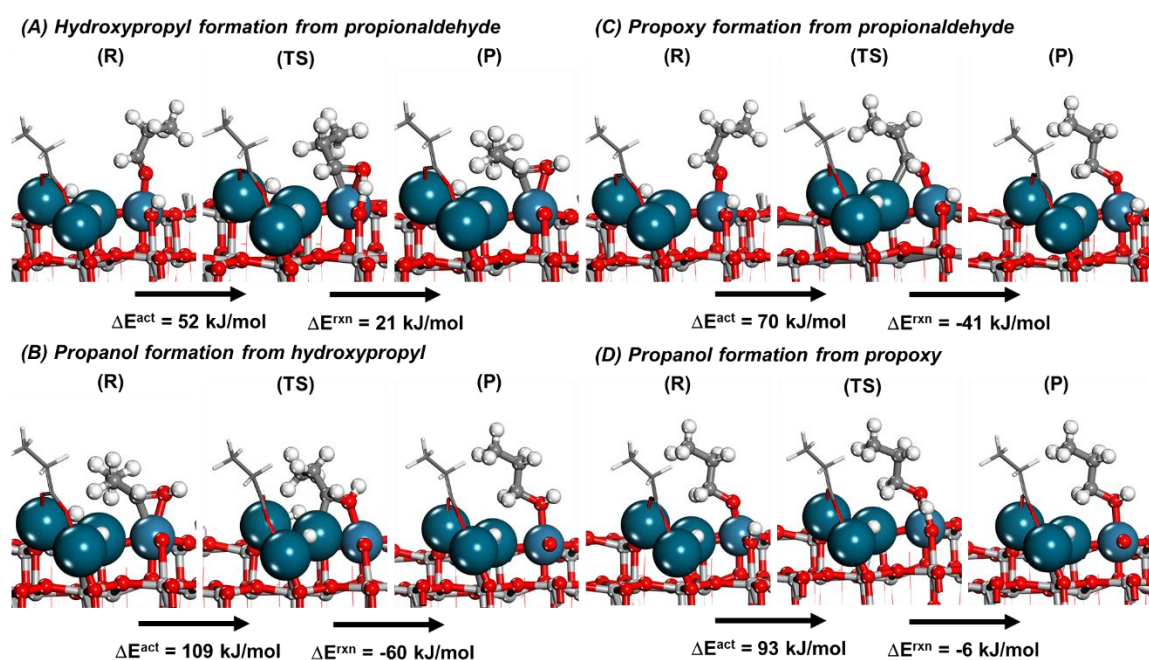


Figure 5.10 The reactant, transition state, and product structures for A) the initial addition of H to the O of propionaldehyde to form the hydroxypropyl intermediate, B) the subsequent addition of H to C₁ carbon of the hydroxypropyl intermediate to form propanal, C) the initial addition of H to the C₁ carbon of propionaldehyde to form the propoxide surface intermediate, and D) the subsequent hydrogen addition to the O of the propoxide surface intermediate to form propanol during hydrogenation of propionaldehyde over Pd-ReO_x/TiO₂.

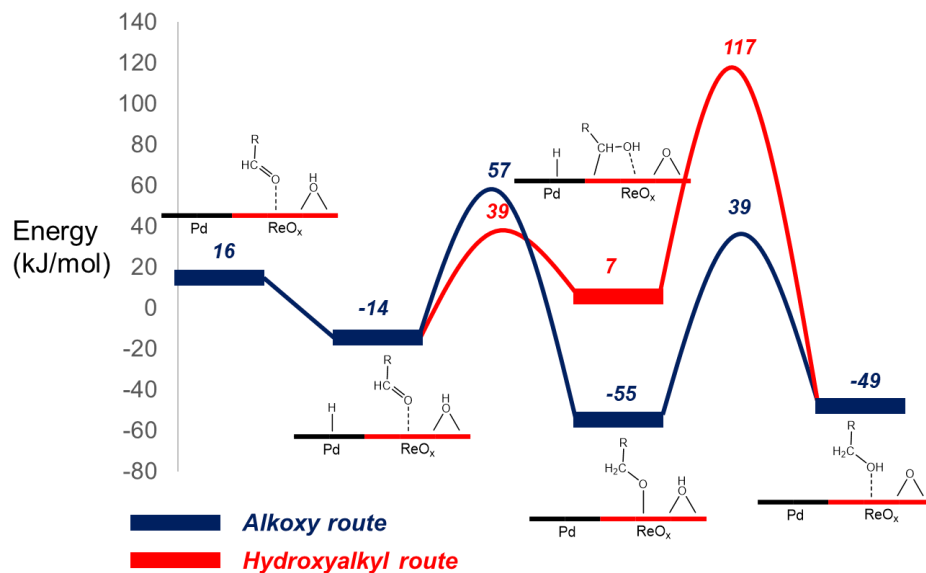
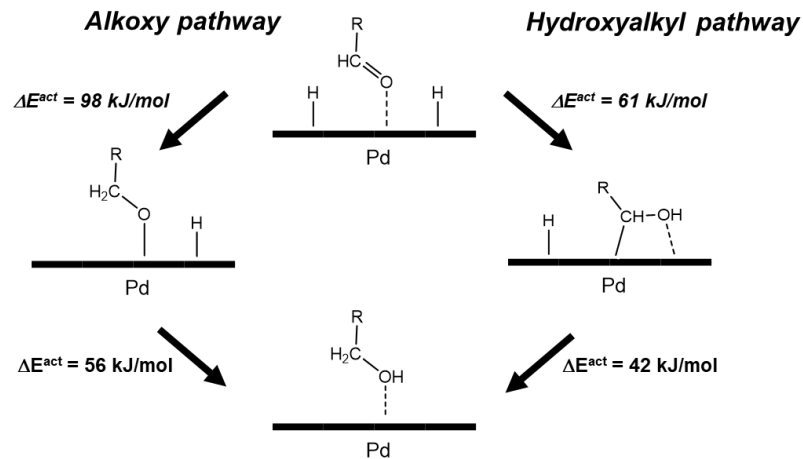


Figure 5.11 The overall reaction energy diagram for hydrogenation of propionaldehyde over Pd-ReO_x (with respect to adsorbed propionate from Figure 5.9). The alkoxy route is shown in blue while the hydroxyalkyl route is shown in red. Since oxygen sites on ReO_x are assumed to be covered in protons due to rapid, favorable spillover, the energy of formation of the Brønsted acid site will not affect the apparent barriers and is not shown here.

The hydrogenation of the propionaldehyde via the alkoxy and hydroxyalkyl paths (Scheme 5.4) was also simulated over the Pd(111) surface to model the larger Pd particles that form in the Pd-ReO_x/TiO₂ system. Previous experimental studies indicate that the Pd particles are likely covered in propionate intermediates under reaction conditions. Herein we carry out simulations on the model Pd(111) surface with up to 5/8 ML of propionate to mimic the high coverages suggested in experimental studies.²⁴⁷ Within the hydroxyalkyl route (Figure 5.12 (A) and (B)), the initial O-H formation reaction to form the hydroxypropyl intermediate from the bound propionaldehyde proceeds with a barrier of 61 kJ/mol and releases -42 kJ/mol energy. The hydroxypropyl intermediate subsequently reacts with a hydridic hydrogen on the Pd surface to form adsorbed propanol with an activation barrier of 42 kJ/mol and a reaction energy of -2 kJ/mol. Propionaldehyde can also proceed via the alkoxy path where the surface bound hydric hydrogen initial adds to the C₁ carbon of the bound propionaldehyde to form the propoxy intermediate (Figure 5.12 (C)). This reaction proceeds with an activation barrier of 98 kJ/mol, and a reaction energy of -2 kJ/mol. The subsequent hydrogenation of propoxy to form adsorbed propanol (Figure 5.12 (D)) requires an activation barrier of 56 kJ/mol and releases reaction energy of -46 kJ/mol.



Scheme 5.4 The hydrogenation of propionaldehyde via the alkoxy and hydroxyalkyl route over Pd(111) to form 1-propanol. The activation barriers are intrinsic and are calculated in Figure 5.12 below.

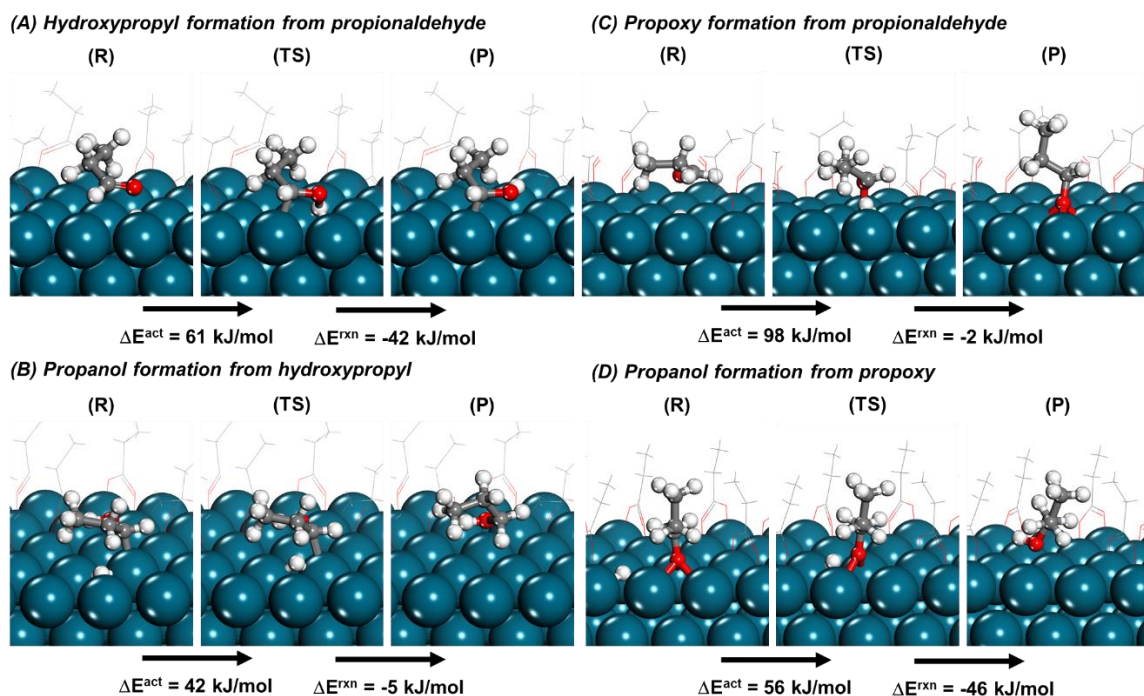


Figure 5.12 The reactant, transition state, and product structures formed during hydrogenation of propionaldehyde over Pd(111) via A) and B) the hydroxyalkyl path and C) and D) the alkoxy path to form propanol.

The energies presented in Figure 5.12 were subsequently used to construct an overall reaction energy diagram for hydrogenation of propionaldehyde on Pd(111) shown in

Figure 5.13. Propionaldehyde which is initially produced via the dehydration of propionic acids on the Re sites must desorb from Re sites and re-adsorb onto the Pd. Propionaldehyde desorb from the Re sites on ReO_x with an energy of 121 kJ/mol and a Gibbs free energy of 65 kJ/mol at 443 K. The large pre-factor of desorption ensures that propionaldehyde quickly desorbs forming a pool of gaseous propionaldehyde that is detected experimentally (Figure S 5.4). The gaseous propionaldehyde can then re-adsorb on the carboxylate covered Pd(111) with an energy of -73 kJ/mol and a Gibbs free energy of 17 kJ/mol. Hydrogen subsequently dissociately adsorbs on the Pd(111) surface to form two hydrogen atoms (2H^*) with an energy of -68 kJ/mol. The hydrogen can then hydrogenate the $\text{C}=\text{O}$ bond of the propionaldehyde via the hydroxyalkyl or the alkoxy. The energies for these paths which are shown in Figure 5.12. show that the hydroxyalkyl path is the more favored route. This is consistent with previous theoretical results that show that hydrogenation of aldehyde (or alcohol oxidation) proceed through the hydroxyalkyl intermediate over Pt(111) which is similar to that of Pd(111).^{193,253} The overall hydrogenation reaction taken with respect to gas phase propionaldehyde and H_2 is barrierless suggesting that propionaldehyde hydrogenation is much faster than propionic acid hydrogenolysis. This is consistent with experiments that show an activation barrier of 75 kJ/mol for acid hydrogenolysis, while an activation barrier of 25-29 kJ/mol for aldehyde hydrogenation alone.

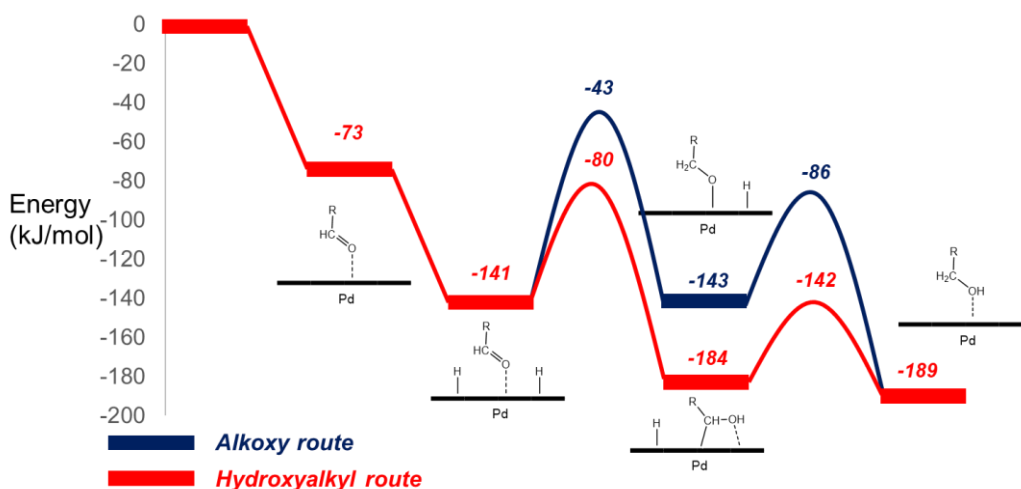


Figure 5.13 Reaction energy diagram for hydrogenation of propionaldehyde over Pd-111. The alkoxy route is shown in blue, while the hydroxyalkyl route is shown in red.

5.2.3 Theoretical analysis of propionaldehyde formation over high temperature treated Re/TiO₂

While the bimetallic Pd-ReO_x/TiO₂ effectively carries out the hydrogenolysis of different acids to alcohols, the reaction can also proceed over the supported ReO_x alone. Experimental results reveal that the pretreatment of ReO_x at 673 K results in the formation of metallic Re clusters,²³² that subsequently carry out hydrogenolysis of propionic acid. In this section, based on previous results over other metals,²⁴⁷ a Re(0001) surface with 5/8 ML coverage of propionate was used to model the reaction paths to form propionaldehyde over the high carboxylate covered Re clusters that are thought to form under reaction conditions. Microkinetic modeling, together with kinetic isotope effect results from DFT are used to compare theoretical and experimental results.

The reaction on metallic Re proceeds via the exothermic adsorption of propionic acid which releases 119 kJ/mol of energy. The adsorbed propionic acid can then deprotonate, releasing an additional 68 kJ/mol of energy (Figure 5.14(A)). While the adsorption and deprotonation energies become less exothermic at the higher propionate coverages, propionic acid can still readily deprotonate to form propionate intermediates. The highly covered propionate surface acts as the resting state during steady state catalysis on metallic Re. Following the bond order conservation principle, C-OH bond is expected to be weaker than C-O bond. We therefore investigate hydrogenolysis through the adsorbed acid species. Both the diol and the acyl pathways were considered over the Re(0001) surface to determine which path is more favorable.

The diol pathway proceeds by the hydrogenation of propionate which is the most abundant surface intermediate to form adsorbed propionic acid. This reaction is 67 kJ/mol endothermic and has a activation barrier of 103 kJ/mol (Figure 5.14(A)). The bound propionic acid intermediate can subsequently react with surface hydride to form the diol intermediate. This step which is shown in Figure 5.14 is slightly endothermic at 6 kJ/mol and has an activation barrier of 63 kJ/mol. The C-OH bond of the diol can then be activated on the Re surface to form a surface bound aldehyde and a hydroxyl group. The dehydroxylation step appears to be rather facile with an activation barrier of just 26 kJ/mol, releasing 25 kJ/mol of energy (Figure 5.14(C)). The subsequent hydroxyl removal by another adsorbed hydrogen atom to form water further releases 45 kJ/mol of energy and has an activation barrier of 47 kJ/mol (Figure 5.14(D)). The adsorbed water molecule can then desorb with an energy penalty of 105 kJ/mol (corresponding to heat of desorption).

This high energy penalty for water removal is a result of high oxophilicity of Re. While the heat of desorption is rather high, there is a significant entropic gain at the reaction temperature of 413 K. As such, the Gibbs free energy penalty is only 49 kJ/mol, thus suggesting that water removal is not likely rate limiting.

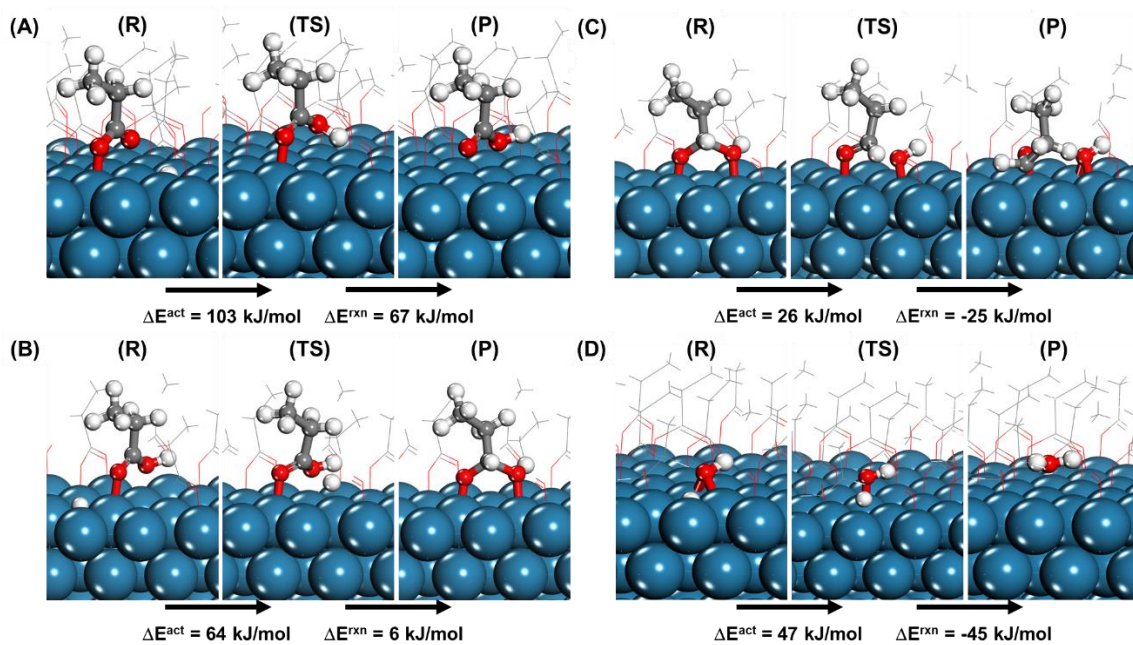


Figure 5.14 Structures for elementary reactions for the hydrogenolysis of propionic acid to propionaldehyde over the Re(0001) surface covered with 5/8 ML of carboxylates, via the diol mechanism- (A) formation of propionic acid from the most abundant propionate intermediate, (B) diol formation from propionic acid, (C) C-OH activation of the diol to form propionaldehyde, (D) hydroxyl removal as water.

In addition to the diol path, the hydrogenolysis of the acid can also proceed via the acyl path (Figure 5.15) where the C-OH bond of the acid is activated first to form the covalently bound acyl and hydroxyl intermediates (Figure 5.15(B)). The activation of the C-OH of the bound acid on Re proceeds with an activation barrier of 36 kJ/mol and an overall reaction energy of 26 kJ/mol. The acyl intermediate is subsequently hydrogenated to form propionaldehyde intermediate. This subsequent addition of hydrogen to the bound carbon has an activation barrier of 62 kJ/mol and an overall reaction energy of -45 kJ/mol. The hydroxyl intermediate can then be protonated to water which desorbs from the surface as was described earlier. The DFT results were used to construct the energy diagram shown in Figure 5.16 where the energies are referenced to the bound propionate intermediates that are thought to cover the surface. Comparing the energetics of the acyl and the diol

mechanism, it appears that the diol mechanism is kinetically preferred which is consistent with earlier results on the Pd-ReO_x model.

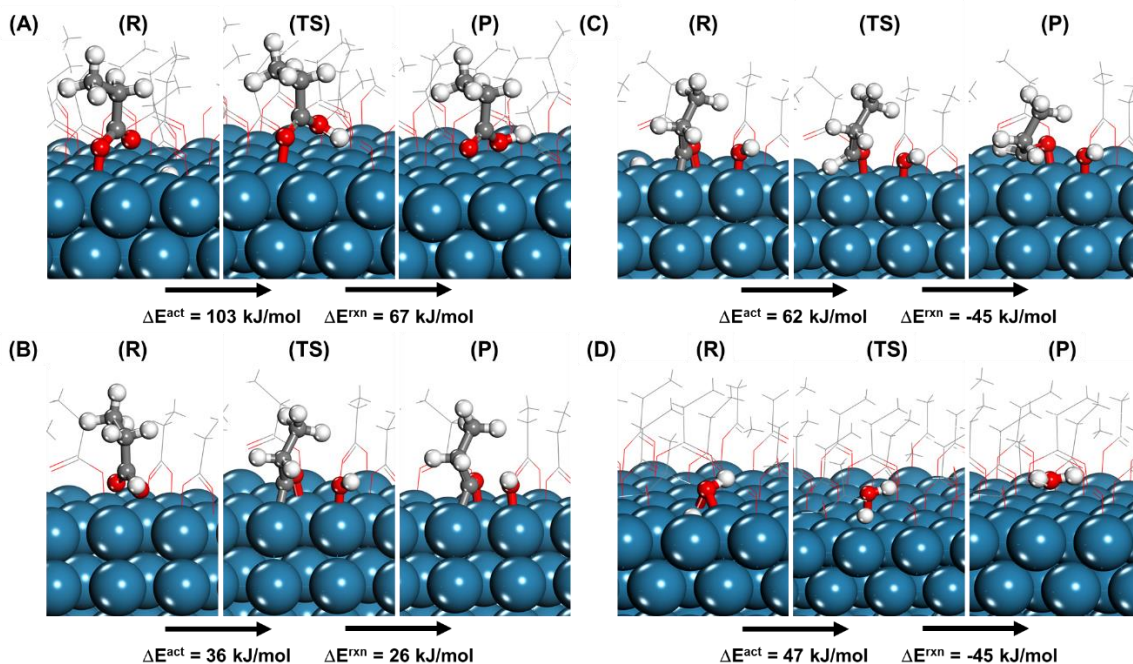


Figure 5.15 Structures for elementary reactions for the hydrogenolysis of propionic acid to propionaldehyde over the Re(0001) surface via the acyl mechanism- (A) formation of propionic acid from the most abundant propionate intermediate, (B) acyl formation from propionic acid, (C) acyl hydrogenation to form propionaldehyde, (D) hydroxyl removal as water.

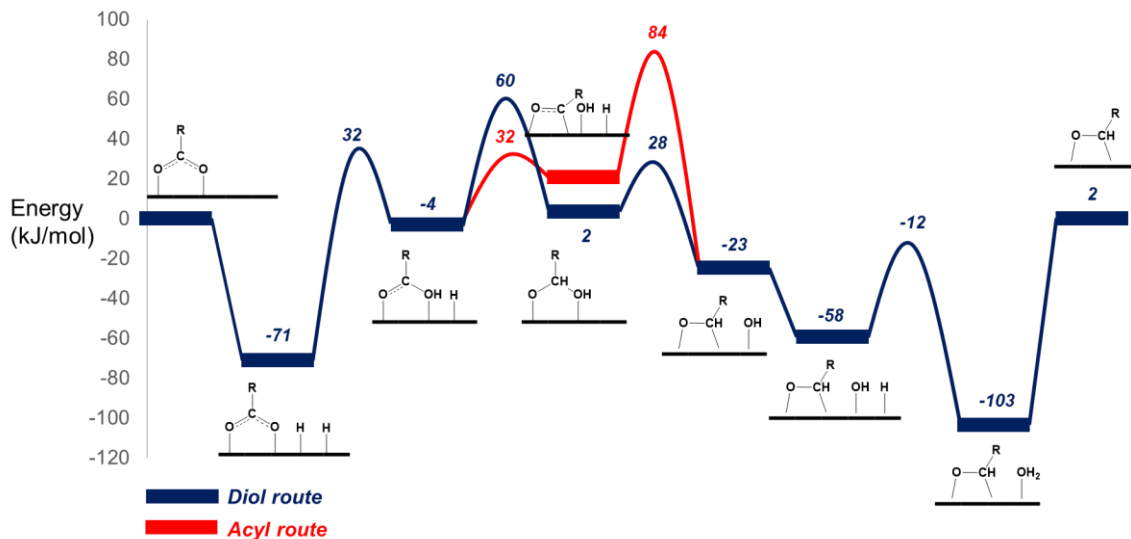
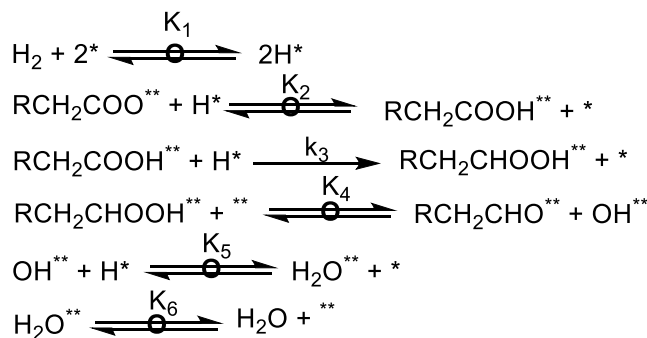


Figure 5.16 Reaction energy diagram for hydrogenolysis of propionic acid to propionaldehyde over the Re(0001) surface via diol and acyl intermediate pathways. Energies are shown with respect to propionate intermediates that presumably exist on the surface at high coverage. Shown in blue is the diol mechanism, while the acyl mechanism is shown in red.

The results presented in Figure 5.16 suggest that the diol formation step is the rate limiting step in the diol mechanism as this is the highest energy state along the reaction path. The results in the energy diagram in Figure 5.16 were subsequently used to develop a microkinetic model (Scheme 5.5) using a Langmuirian model that is similar to that which was developed above for the Pd-ReO_x system (Equations 5.2-5.6). Equation 5.7 can be derived (based on Scheme 5.5) if it is assumed that [RCH₂COO*] covers the surface of Re catalyst. The model has a zero-order dependence on acid and 1st order on H₂ which is consistent with the experiments results.^{223,224}

$$\text{rate} = k_3 K_2 K_1 P_{\text{H}_2} [\text{RCH}_2\text{COO}^*] \quad (5.7)$$

The temperature dependence for all of the constants appearing in Equation 5.7 can be estimated from Figure 5.16 and are documented in Table 5.4. The DFT calculated intrinsic activation energies and overall reaction energies were subsequently used to calculate an apparent activation barrier of 60 kJ/mol. This is consistent with our experimentally measured activation barriers of 60 and 71 kJ/mol over Re/SiO₂ and Re/TiO₂ respectively.



Scheme 5.5 Elementary steps for the hydrogenolysis of carboxylic acids over Re catalysts to form corresponding aldehyde and water. Sites marked by (*) are active sites on the surface of Re accessible to only hydrogen atoms due their relatively small van der Waals radii. Sites marked by () are active sites on the surface of Re where all intermediates except hydrogen atoms are adsorbed or chemisorbed. The inclusion of different types of sites allow for modeling of coverage effects, which are typically not captured in single site Langmuir-Hinshelwood microkinetics.**

Table 5.4 DFT-calculated values for the constants that appear in microkinetic analysis (Equation 5.7). The temperature dependent contributions are based on the energy diagram presented in Figure 5.16.

Constant	Expression from DFT simulations
K_1	$\exp\left(\frac{\Delta S_1}{R}\right) \exp\left(\frac{-[-71]}{R^*T}\right)$
K_2	$\exp\left(\frac{\Delta S_2}{R}\right) \exp\left(\frac{-[67]}{R^*T}\right)$
k_3	$\frac{k_B T}{h} \exp\left(\frac{\Delta S_3}{R}\right) \exp\left(\frac{-[64]}{R^*T}\right)$
ΔE^{act} for 1 st order in H_2	$-71 + 67 + 64 = 60 \text{ kJ/mol}$

The DFT-calculated kinetic isotope effects were compared with the experimentally measured KIE values to further test the proposed model. The DFT results were used together with the microkinetic model (Scheme 5.5, Equation 5.7 and Table 5.5), to calculate a kinetic isotope effect with H_2/D_2 of 0.18 during the hydrogenolysis of propionic acid to propanol. The results are found to be in qualitative agreement with the measured inverse kinetic isotope effect of 0.84 (Table S 5.3). Our combined analyses, therefore,

suggests that the diol mechanism also prevails on metallic Re and the rate determining step involves hydride attack to form the diol intermediate similar to that on Pd-ReO_x.

Table 5.5 Kinetic isotope effect contributions at 400 K and 1 atm for individual steps that appear in Equation 5.7. Overall kinetic isotope effect for 1st order in H₂ can be estimated by evaluated the product $\frac{K_{1H}}{K_{1D}} \cdot \frac{K_{2H}}{K_{2D}} \cdot \frac{k_{3H}}{k_{3D}}$.

Elementary step	Kinetic isotope effect
$\text{H}_2 + 2^* \xrightleftharpoons{K_1} 2\text{H}^*$	$\frac{K_{1H}}{K_{1D}} = 0.15$
$\text{RCH}_2\text{COO}^{**} + \text{H}^* \xrightleftharpoons{K_2} \text{RCH}_2\text{COOH}^{**} + ^*$	$\frac{K_{2H}}{K_{2D}} = 0.75$
$\text{RCH}_2\text{COOH}^{**} + \text{H}^* \xrightarrow{k_3} \text{RCH}_2\text{CHOOH}^{**} + ^*$	$\frac{k_{3H}}{k_{3D}} = 1.57$

5.2.4 Theoretical analysis of propionaldehyde hydrogenation over high temperature treated Re

The hydrogenation of propionaldehyde over the propionate covered Re(0001) model surfaces is not covered here in detail. Mechanistic framework discussed previously on ReO_x (Figure 5.10) may still apply on extended Re surfaces, where hydrogenation of propionaldehyde proceeds through the alkoxy route. Besides, experiments show that the direct rate of propanal hydrogenation is an order of magnitude higher than propionic acid hydrogenolysis over Re. In addition, the activation barrier was estimated to be 29 kJ/mol, which is significantly lower than the barrier for hydrogenolysis 71 kJ/mol suggesting hydrogenation of propionaldehyde will be quasi-equilibrated.

5.3 Concluding remarks

DFT simulations along with multiple experimental probes presented herein elucidate the mechanism as well as the nature of active sites that drive hydrogenolysis of propionic acid over heterogeneous Pd-ReO_x and Re catalysts. These results can be extended to other carboxylic acids as well as similar supported bimetallic and monometallic catalysts. Over Pd-ReO_x catalysts, Pd enables the activation of hydrogen and provides the hydrides necessary for hydrogenation as well as hydrogen atoms that spillover onto the support and then subsequently diffuse over to ReO_x. The hydrides that form on the Pd sites appear to be instrumental in catalyzing C-H formation reactions whereas the hydrogen atoms that

spill over and bind to the oxygens on the ReO_x support become protonic in character thus providing Brønsted acidity that catalyzes C-O bond activation steps. Close contact between Pd and ReO_x sites results in a synergistic effect that enables hydrogenolysis via formation of a diol intermediate via direct hydride attack from Pd sites over to adsorbed acid on Re sites. The diol intermediate is subsequently dehydrated using proton on the Brønsted acid site formed on ReO_x . Other bimetallic catalysts, comprised of a reduced metal along with an oxophilic metal may behave similarly with the reduced metal catalyzing H_2 dissociation and surface hydrogenation while oxophilic metal provides acid sites that promote the subsequent dehydration reactions. Over metallic Re catalyst, Re sites enable hydride transfer catalyzing C-H bond formation, as well as Lewis acid catalyzed C-O bond activation. Metallic Re sites, therefore, carry out individual roles that Pd and ReO_x play in the bimetallic catalyst likely via the same diol formation mechanism. The results show that selective and fast hydrogenolysis of fatty acids require catalytic sites that enable direct transfer of hydrides as well as sites that are Brønsted or Lewis acidic.

5.4 Computational methods

All calculations reported herein were performed using the planewave density functional theory methods as implemented in the Vienna Ab-Initio Simulation Package (VASP).^{127–130} The PBE¹³¹ form of generalized gradient approximation was used to describe exchange and correlation energies. D3 corrections were implemented to account for dispersion.¹³² For calculations over TiO_2 , PBE+U calculations were implemented using the Dudarev's approximation²⁵⁴ and the value of U_{eff} was set to 3.0 eV for Ti as suggested in the literature for catalysis over TiO_2 .²⁵⁵ For all calculations, a planewave energy cutoff of 396 eV was utilized along with the projector augmented wave [cite] (PAW) pseudopotentials. Conjugate gradient algorithms within VASP were used for optimization. Saddle points were isolated using the nudged elastic band^{133,134} and dimer methods.¹³⁵

For calculations over metallic Pd and Re, 4 x 4 unit cells consisting of 4 layers of Pd and Re were used. The 111 surface for Pd and 001 surface for Re respectively, were used as model catalytic surfaces. A vacuum layer of 18 Å was introduced between the top and the bottom layer to accommodate reacting molecules and intermediates. Bottom two layers were kept frozen at respective bulk equilibrium distances during all calculations. Calculations over both Pd and Re surfaces were simulated at a carboxylate coverage of 0.625 ML to simulate reaction environment during steady state catalysis as observed during experiments. All optimized structures over metal surfaces were obtained at a

wavefunction convergence of 10^{-6} eV , a force convergence of 0.05 eV/Å, and a k-point mesh¹³⁷ of $2 \times 2 \times 1$. All energies are evaluated as single points at a k-mesh of $5 \times 5 \times 1$ on optimized structures.

Well-dispersed ReO_x species were modeled as single Re atom ReO_x cluster. These clusters were supported on appropriate sites on the 110 surface of anatase TiO_2 given moderate temperatures and pressure in experimental setups. Placement of the Re atom on the TiO_2 surface was modeled after previous studies of Ru/TiO_2 .²⁴² The 110 surface of anatase was modeled using 2×3 unit cell consisting of 3 layers of TiO_2 . The bottom layer was capped with protons and all atoms were allowed to relax during optimizations. All optimized structures as well as energies over TiO_2 were calculated spin-polarized at a wavefunction convergence of 10^{-4} eV, a force convergence of 0.05 eV/Å, and a k-point mesh of $2 \times 2 \times 1$.

Kinetic isotope effects were estimated using the quasi-harmonic oscillator approach and ideal gas treatment as described by Iglesia and co-workers.²⁵⁰ The vibrational frequencies required for these calculations were estimated with VASP at a wavefunction convergence of 10^{-6} eV , a force convergence of 0.05 eV/Å, and a k-point mesh of $2 \times 2 \times 1$.

The entropy of desorption was estimated by following the approach described by Campbell and Sellers.¹³⁸ These values are tabulated below in Table S 5.5.

5.5 Supporting information

Table S 5.1 Vibrational modes observed by DRIFTS during in situ reduction of propionic acid over PdRe/TiO₂.

Band	Infrared wavenumber (cm ⁻¹)	Notes
$\nu_a(\text{CH}_3)$	2994	
	2978	
$\nu_a(\text{CH}_2)$	2944	
$\nu_s(\text{CH}_3)$	2930-2900 w	
$\nu_s(\text{CH}_2)$	2884	
$\nu(\text{C=O})$	1791,1772,1732	Propionic acid, (vapor, monomer and dimer)
$\nu_a(\text{O—C=O})$	1520	Propionate, bridging bidentate
$\delta(\text{C—H})$	1470	Propionic acid
$\nu_s(\text{O—C=O})$	1436	Propionate, bridging bidentate

$\delta(\text{C—H})$	1418	Propionic acid (vapor)
$\delta(\text{C—H})$	1377	

Table S 5.2 Comparison of the rate of reduction of 0.5 kPa propionic acid, in 0.1 MPa H₂ or D₂, at 433 K, flowed at 30 cm³ min⁻¹ over Pd-ReO_x/TiO₂.

H ₂ /D ₂	Conversion	Rate of reduction (mol g _{cat} ⁻¹ h ⁻¹)	Overall isotope effect (rate _H /rate _D)
H ₂	7.9%	2.8×10 ⁻⁴	0.79
D ₂	10.%	3.5×10 ⁻⁴	

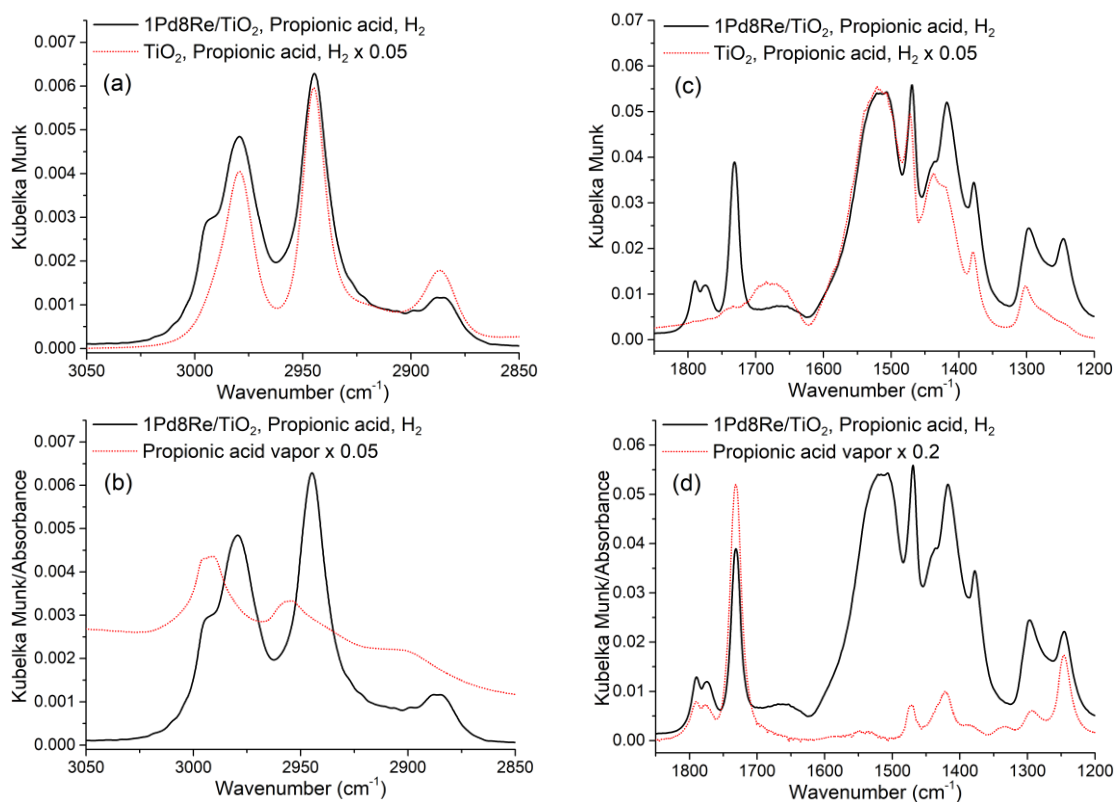


Figure S 5.1 Spectra obtained during in situ DRIFTS over PdRe/TiO₂ and TiO₂ or gas phase transmission in 0.3 kPa propionic acid, 0.1 MPa H₂ at 413 K in the (a) C-H stretching region, (b) compared to gas phase propionic acid, (c) carbonyl/backbone vibration region, (d) compared to gas phase propionic acid, collected in transmission mode.

Table S 5.3 Comparison of the rate of reduction of 0.5 kPa propionic acid, in 0.1 MPa H₂ or D₂, at 433 K, flowed at 30 cm³ min⁻¹ over Re/SiO₂.

H ₂ /D ₂	Conversion	Rate of reduction (mol g _{cat} ⁻¹ h ⁻¹)	Overall isotope effect (rate _H /rate _D)
H ₂	2.6%	9.1×10 ⁻⁵	0.84

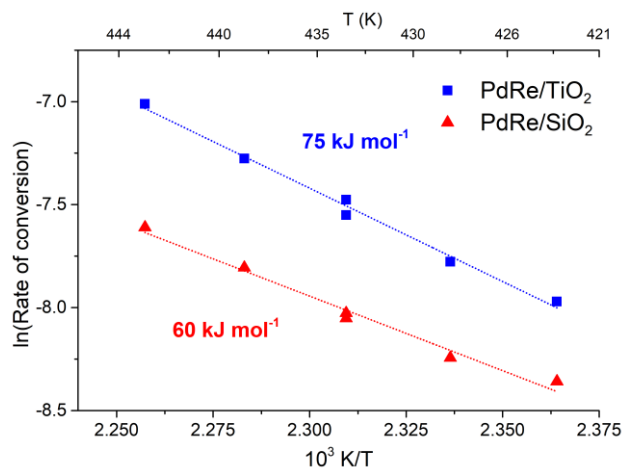


Figure S 5.2 Influence of temperature on propionic acid (0.5 kPa) reduction in 0.1 MPa H₂ over Pd-ReO_x/TiO₂. Conversion ranged between 4.5 and 18%.

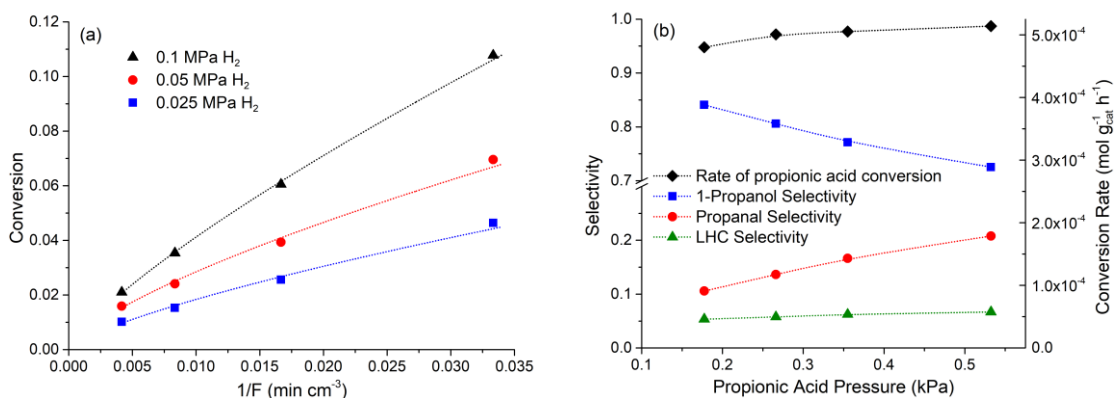


Figure S 5.3 Influence of (A) flowrate and H₂ pressure on the reduction of 0.5 kPa propionic acid at 433 K, and (B) propionic acid pressure (at constant mass of catalyst and flowrate) on rate and selectivity of propionic acid (0.5 kPa) reduction over Pd-ReO_x/TiO₂ at 433 K.

Table S 5.4 Comparison of the rate of reduction of 0.5 kPa propionic acid and 1 kPa propanal in 0.1 MPa H₂ at 433 K, flowed at 30 cm³ min⁻¹ over Re/SiO₂.

Conversion	Rate of reduction (mol g _{cat} ⁻¹ h ⁻¹)
1.4%	1.3×10 ⁻³
2.6%	9.1×10 ⁻⁵

Table S 5.5 Entropy of desorption of different molecules

Molecule	Ideal gas entropy (J/mol.K)	$T\Delta S^{\text{des}}$ (kJ/mol)
Water	202	-39
Hydrogen	142	-31
Acid	360	-60
Aldehyde	327	-56
Alcohol	343	-58

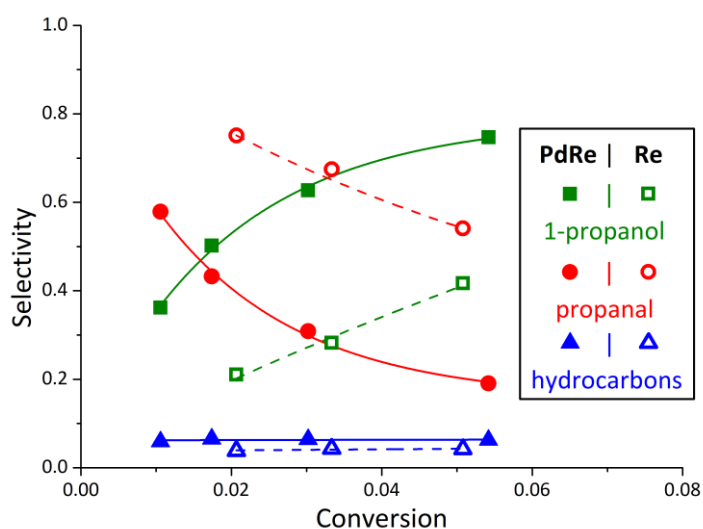


Figure S 5.4 Effect of conversion (measured by varying flowrate) on selectivity during the reduction of propionic acid to alcohols, aldehydes, and hydrocarbons over PdRe/SiO₂ (0.1 MPa H₂ and 0.5 kPa propionic acid) and Re/SiO₂ at 433 K (0.3 MPa H₂ and 1.0 kPa propionic acid). The PdRe/SiO₂ catalyst was not reduced prior to reaction, whereas the Re/SiO₂ catalyst was pretreated at 673 K in H₂ in situ for 1 hour prior to reaction. Dashed and solid lines indicate trends.

6 The Nature of Protic Solvents on Transition Metal Surfaces and Its Impact on Hydrogenation Reactivity

Results on formaldehyde hydrogenation are adapted from Chemburkar, A., Desai, S., Neurock, M. *Direct Participation of Protic Solvents in the Selective Catalytic Hydrogenation of Oxygenates. Under preparation.*

Results on acetone hydrogenation are in collaboration with Bengi Demir and Prof. Jim A. Dumesic. Theoretical calculations were performed by AC under the supervision of MN. Experiments were done by BD under the supervision of JAD.

6.1 Introduction

The selective hydrogenation of specific unsaturated bonds is used in the production of commodity and specialty chemicals, the synthesis of pharmaceuticals, as well as upgrading of oxygenates and bio-renewables.^{1,4,256–259} The mechanism for this reaction, carried out in the gas-phase, was first proposed by Horiuti-Polyani²⁶⁰ and is thought to proceed via the activation of molecular hydrogen (H_2) at the active sites of a metal catalyst (*) to form two atomic hydrogens on the surface (H^*) and is followed by a step-wise addition of hydrogen atoms across the unsaturated bond. These hydrogen atoms are directly added from the surface of the host catalyst to the unsaturated bond of a vicinal co-adsorbed reactant in a Langmuir-Hinshelwood surface-mediated fashion. Optimal hydrogenation catalysts operate at high activities and selectivities for extended lifetimes. Protic solvents are often used in as they tend to promote the reaction and lead to higher overall rates. Protic solvents such as water have been utilized in a number of reported studies and are thought to accelerate reactivity by stabilizing charges that form in the transition states, increasing the solubility of reacting molecules, and increasing mass transfer rates by decreasing viscosity. The underlying mechanism proposed for reaction in the condensed phase, is thought to follow the same mechanism operational in the gas-phase.^{261–269}

In the first part of this chapter, we report ab-initio density functional theory simulations that show the direct participation of water molecules in the hydrogenation of formaldehyde (a probe oxygenate) in water, revealing a characteristically different mechanism than the classic surface bound mechanism by Horiuti and Polanyi.²⁶⁰ Solution phase water molecules at water/metal interface are shown to readily react with co-adsorbed hydrogen atoms on Pd surface to form energetically favorable hydronium complexes ($\text{H}_{13}\text{O}_6^+$) in the solution and electrons that reside in the Pd surface that can populate low energy antibonding π^* states of the bound unsaturated reactants. The O-H formation reactions in the reduction of formaldehyde are shown to have lower activation barriers when mediated by the transfer of these protons and electrons in a PCET reaction. On the other hand, C-H formation reactions involved in the reduction of formaldehyde are shown to be unlikely via the PCET mechanism. They proceed instead via the direct nucleophilic backside attack of a surface hydride at the unsaturated carbon. Detailed charge analyses of the reaction coordinates for these reactions are carried out to show the difference in the nature of hydrogen that is delivered during both C-H and O-H formation reaction. These differences allow for rationalization of activation barriers obtained from simulations and demonstrate the consequence of non-innocent nature of vicinal water molecules that allow for faster O-H formation reactions, but, appear to have no significant effect on C-H formation reactions.

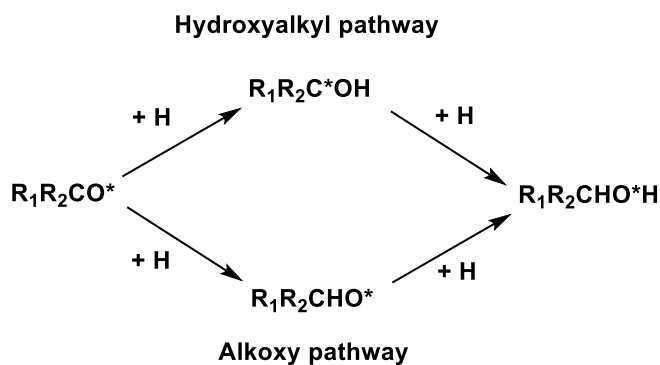
In the second half of this chapter, we extend the mechanistic framework established in hydrogenating formaldehyde on Pd to acetone hydrogenation over Pt and Ru. More detailed experimental and theoretical analyses which were carried out for these systems further support the notion that protic solvent molecules act as co-reactants and co-catalysts during hydrogenation. A systematic study of acetone hydrogenation over supported ruthenium and platinum catalysts using steady state turnover frequency (TOF) measurements and density functional theory is reported. Hydrogenation of acetone is first studied over both catalysts in the gas phase and subsequently examined in the presence of water. While experiments show that hydrogenation reactivity is higher over Ru in the presence of water, water has negligible effects on steady state hydrogenation turnover numbers over supported Pt catalysts. Theoretical results indicate that the rate determining step over Ru and Pt are different and involve O-H formation and C-H formation respectively. Consequently, water molecules are found to promote the reaction over Ru by activating a PCET route, as well as via the formation of Brønsted acid sites (by water activation). In contrast, the rate determining C-H formation step over Pt is not catalyzed

by PCET, but, instead by direct hydride attack (similar to Pd). The quasi-equilibrated favorable formation of hydronium ions and electrons from surface hydrides over Pt, however, imposes an additional energy penalty on the barrier for C-H formation via surface hydride. This results in similar activation barriers both in the presence and absence of water, consistent with no detectable changes in reactivity as shown by experiments.

6.2 Mechanistic insights into formaldehyde hydrogenation over Pd in water

6.2.1 Reactions in the gas phase

Formaldehyde hydrogenation over the model Pd(111) surface was initially examined in the gas phase to establish a reference to compare back against simulations that examine the influence of water. The hydrogenation of formaldehyde to methanol over Pd(111) proceeds first via the chemisorption of formaldehyde onto the metal surface to form the di- σ bound $\text{H}_2\text{C}=\text{O}^*$ intermediate and the dissociative adsorption of H_2 to form two surface hydrogen atoms that are partly hydridic as they withdraw electron density from the metal. The bound hydrogen can then add either to the C or the O of the adsorbed formaldehyde to form the bound methoxy (CH_3O^*) or hydroxymethyl (CH_2OH^*) intermediates, respectively, which undergo a second hydrogen addition to form methanol which subsequently desorbs. More generally, these paths are known as the alkoxy and hydroxyalkyl paths respectively (Scheme 6.1) and the gas phase mechanisms have been reported previously in the literature.^{195,270–274} The calculated structures for the elementary steps in both the alkoxy and hydroxyalkyl paths in the vapor phase are shown in Figures S 6.1-S 6.2.



Scheme 6.1 Pathways during hydrogenation of C=O bonds, the hydroxyalkyl pathway involves initial O-H formation followed by C-H formation, and the alkoxy pathway involves initial C-H formation followed by O-H formation.

The calculated reaction energy diagram for vapor phase hydrogenation of formaldehyde via the hydroxymethyl and the methoxy routes is shown in Figure 6.1. Formaldehyde was calculated to chemisorb in a di- σ η^2 configuration onto the Pd(111) surface with an energy of -75 kJ/mol. The di- σ bonding results in back-donation of electron density into the π^*_{CO} antibonding orbital of C=O. This leads to an initial activation and elongation of the C-O and results in the partial rehybridization of the carbon and oxygen atoms from sp^2 to sp^3 (Figure S 6.1(A)). Hydrogen then dissociatively adsorbs in a barrierless step that is exothermic by -121 kJ/mol resulting in the formation of two hydrogen adatoms (H^*) that bind to three-fold fcc hollow sites. The methoxy path proceeds via the oxidative addition of hydrogen to the C of the bound $H_2C=O^*$ to form the surface methoxy intermediate with an intrinsic activation barrier 91 kJ/mol and overall reaction energy of +43 kJ/mol. The methoxy subsequently hydrogenates via a hydrogen addition to the bound oxygen to form a surface bound methanol (CH_3OH^*) with an intrinsic activation energy of 64 kJ/mol and an overall reaction energy of -30 kJ/mol. The hydroxymethyl path proceeds instead via hydrogen addition to the oxygen of the bound $H_2C=O^*$ to form the hydroxymethyl (CH_2OH^*) intermediate with an intrinsic activation barrier of 84 kJ/mol and an overall reaction energy of -3 kJ/mol. The hydroxymethyl intermediate subsequently undergoes a hydrogen addition to the bound carbon to form a surface methanol (CH_3OH^*) with an activation barrier of 82 kJ/mol and a reaction energy of 16 kJ/mol. Methanol desorbs from Pd with an energy of 57 kJ/mol, which is in good agreement with the experimentally reported desorption energy of methanol on Pd (55 kJ/mol).²⁷⁵ The vapor phase reaction energy diagram shown in Figure 6.1 suggests that the hydroxyalkyl route is favored over the alkoxy route. In addition, the vapor phase hydrogenation of formaldehyde appears to follow the classical Langmuir-Hinshelwood metal-mediated mechanism consistent with previous experimental results in the vapor phase.²⁷⁶⁻²⁷⁸

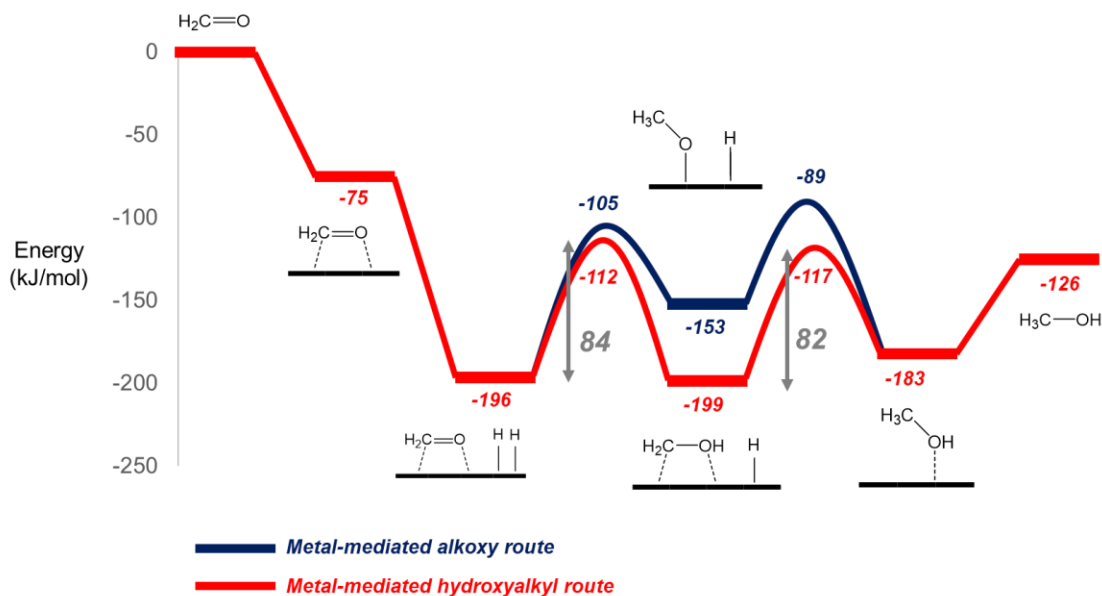


Figure 6.1 Reaction energy diagram for the vapor phase hydrogenation of formaldehyde to methanol via alkoxy and hydroxyalkyl routes. All of the structures are reported in Figures S 5.1 and S 5.2. Intrinsic activation barriers for both the hydrogenation steps in the kinetically faster hydroxyalkyl route are marked in grey.

6.2.2 Reactions in the aqueous phase

The vapor phase results were subsequently used to examine both the alkoxy and hydroxyalkyl paths in aqueous solution. Explicit water molecules were added to the unit cell such that the density of water molecules with formaldehyde was ~ 1 g/cm³. Two water molecules near the surface were then removed to accommodate formaldehyde since molar volume of formaldehyde (~ 37 cc/mol) is approximately twice that of water (~ 18 cc/mol). Ab-initio molecular dynamics simulations were carried out to equilibrate the water molecules and the adsorbed formaldehyde on the Pd surface. The lowest energy structures from the molecular dynamics simulations were subsequently used as initial structures for subsequent DFT optimizations. We first report on the dielectric effect that water has on the hydroxyalkyl and alkoxy routes and then subsequently examine paths where water and the metal substrates cooperatively mediate the hydrogen-addition via coupled proton and electron transfer analogous to the electrochemical proton-coupled electron transfer pathways that proceed in electrochemical reduction reactions.

6.2.2.1 The influence of water as a dielectric medium

The simulations show that water binds to Pd forming an intricate network of hydrogen bonds (dotted blue lines in Figure 6.2) that can stabilize charged transition states for both metal-mediated C-H and O-H formation steps by forming hydrogen bonds with the oxygen of the adsorbed carbonyl (Figure 6.2A-(R)). The intrinsic barriers for metal-mediated C-H and O-H formation steps to form the surface methoxy and hydroxymethyl intermediates, respectively in water were both calculated to be ~ 72 kJ/mol, which is lower than the gas phase barriers of 91 kJ/mol and 84 kJ/mol for C-H and O-H bond formation paths over Pd, respectively. In addition, the intrinsic barriers to form methanol from the methoxy (O-H formation) and hydroxymethyl (C-H formation) intermediates decreased from 63 kJ/mol and 82 kJ/mol in the gas phase to 54 kJ/mol and 66 kJ/mol in the aqueous phase, respectively. The 12-20 kJ/mol stabilization energies reported here roughly correspond to energies that are 2-3 times that of typical hydrogen bonding energies in pure water.²⁷⁹ Solvation effects on the addition of hydrogen to the carbon of formaldehyde to form the methoxy intermediate were calculated to be very small as the overall energy of reaction in water (41 kJ/mol) was roughly the same as in the vapor phase (43 kJ/mol). This negligible change in the reaction energy is due to the cancellation of weak H-bonding of the $\text{H}_2\text{C}=\text{O}^*$ reactant (Figure 6.2B-(R)) and the CH_3O^* product (Figure 6.2B-(P)) with water. The hydrogenation of formaldehyde to form the hydroxymethyl intermediate shown in Figure 6.2(A), on the other hand, was stabilized by water as hydrogen addition to the oxygen was calculated to be more exothermic in water (-16 kJ/mol) than in gas phase (-3 kJ/mol). The energies of formation of methanol from either the hydroxymethyl (4 kJ/mol in Figure S 6.3) or methoxy (-52 kJ/mol in Figure S 6.4) in water were calculated to be more favorable than the formation energies in the gas phase, suggesting that methanol is also stabilized over the bound methoxy intermediate via hydrogen bonding. The resulting energies for aqueous phase hydrogenation of formaldehyde by the alkoxy and hydroxyalkyl routes over Pd reported in Figure 6.2(C) indicate that the hydroxyalkyl route is kinetically favored. In addition, the intrinsic activation barriers for this route are reduced by 8 kJ/mol for O-H formation and 16 kJ/mol for C-H formation compared to the gas-phase reaction (compared barriers in grey between Figures 6.1 and 6.2(C)).

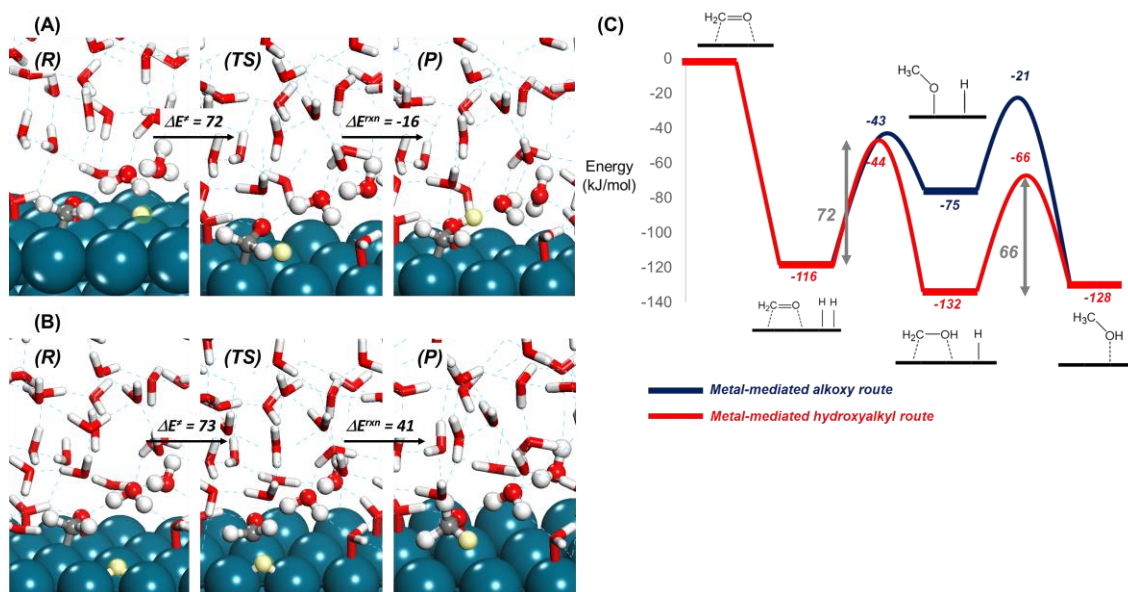


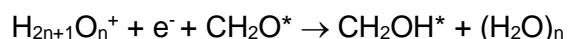
Figure 6.2 DFT-calculated reactant (R), transition (TS), and product (P) state structures for the hydrogenation of formaldehyde to (A) hydroxymethyl and (B) methoxy formation over Pd(111) in water. The hydrogen that is added to formaldehyde is highlighted in yellow. (C) Reaction profile diagram for the metal-mediated hydrogenation of formaldehyde to methanol via alkoxy and hydroxymethyl routes in water. The intrinsic activation barriers on the kinetically faster hydroxyalkyl route are marked in grey.

Bader charge analysis²⁸⁰ (Figure S 6.5 and Table S 6.1) suggests that C-H formation involves a hydride attack on carbon, while O-H formation proceeds via proton addition to oxygen. Both these transition states involve charge separation, which is stabilized by the effective dielectric of the aqueous media as well as by direct hydrogen bonding between the water molecules and the transition state, resulting in lower barriers than corresponding gas-phase reactions.

6.2.2.2 Direct participation of water molecules in hydrogenation chemistry

In the metal-mediated routes, water molecules in the solution phase stabilized the polar transition states, but, did not explicitly take part in the reaction. In addition to these paths, the simulations reveal a path in which water molecules directly participate in the reaction by enabling the formation, facile shuttling, and addition of protons to the oxygen of the bound formaldehyde intermediate (Figure 6.3 (A-C)). Herein, we report the direct participation of water in the kinetically faster hydroxyalkyl pathway, while the slower alkoxy pathway is reported in the supporting information (Figures S 6.8 and S 6.9). Previous work

has shown that adsorbed hydrogen on transition metal surfaces in the presence of water or other protic solvents can be heterolytically activated to release protons into solution provided that the metal has a high enough work function to readily accept the electron that is generated.^{281,282} The activation barrier to generate a proton from an adsorbed hydrogen at the Pd-water interface (Figures 6.3 (A-C)) was calculated to be just 46 kJ/mol, resulting in an overall reaction energy of -25 kJ/mol. The proton generated near the surface was found to exist as a hexahydrate $H_{13}O_6^+$ ion with the negatively charged surface as its counter anion (Figure S 6.6). A similar ion-pair structure was previously reported to exhibit maximum delocalization of charge, therefore, making it the thermodynamic ground state of H^+ in aqueous solutions.²⁸³ This proton can then be delivered to the carbonyl oxygen on the adsorbed formaldehyde via proton shuttling (Scheme 6.2 and Figure 6.4(D-E)) with an intrinsic barrier of just 18 kJ/mol. O-H formation via this route has an apparent activation barrier of 46 kJ/mol, which is 26 kJ/mol lower than the metal-mediated route. This pathway is characteristically different than the traditional Langmuir Hinshelwood surface hydrogenation pathway, in that, hydrogenation here takes place via proton transfer through solution concomitant with electron transfer through the metal. Facile proton shuttling is well established in aqueous phase systems. Such proton/electron transfer processes are ubiquitous in enzyme-catalyzed,⁵² electrocatalytic^{53,54} as well as homogeneous reduction and oxidation processes.⁵⁵



Scheme 6.2 Hydrogenation of formaldehyde to hydroxymethyl via the PCET pathway.

Bader charge analysis on the optimized structures (Table 6.1) and along the reaction coordinate on either side of the transition state (Figure S 6.7(A)) suggest that hydride on the surface transfers electron density into the metal surface and is released from the surface as a proton that transfers to the solution. We find that the partial charge on the bound hydrogen increases from -0.06 to +0.59 as it moves into the solution, while the partial charge on the metal slab and bound $H_2C=O^*$ decrease from +0.37 to -0.19 and -0.40 to -0.49, respectively. Electron density in the metal is then transferred into the $\pi^*_{C=O}$ antibonding state of the adsorbed formaldehyde allowing for the activation of the C=O bond along the reaction coordinate. This is reflected by the loss of electron density in the metal as its negative charge decreases from -0.19 to -0.06, while the negative charge on

the $\text{H}_2\text{C}=\text{O}^*$ increases from -0.49 to -0.61 as the proton transfers from the solution phase to form the C-OH bond of the bound hydroxymethyl intermediate. The hydrogenation of the formaldehyde, therefore, appears to proceed via a proton coupled electron transfer process, wherein the proton and electron transfer concurrently to form the hydroxymethyl intermediate. A detailed analysis of the partial charge profile along the reaction coordinate (Figure S 6.7(A)) indicates that the protonation of formaldehyde and electron density transfer from the metal slab to the formaldehyde proceed in a concerted fashion.

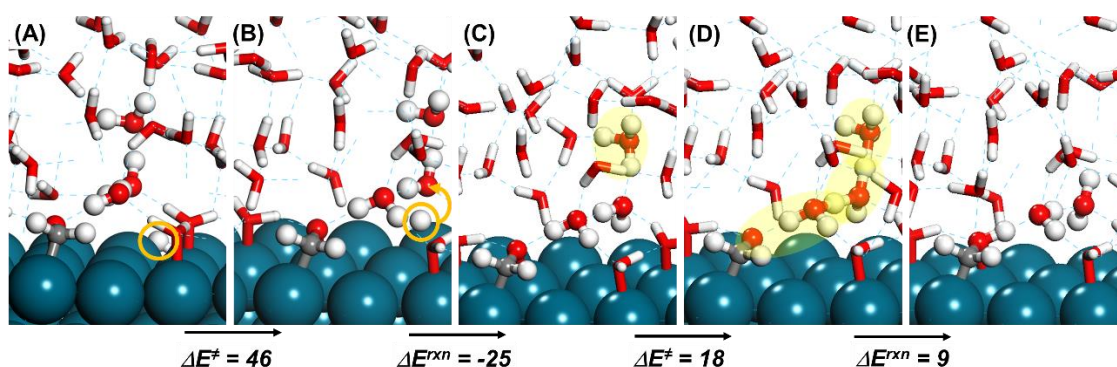


Figure 6.3 Water-mediated pathway catalyzing the formation of hydroxymethyl from formaldehyde. (A) Reactant state consisting of adsorbed formaldehyde and hydrogen (marked with an orange circle). (B) Transition state for the formation of protons and electrons (the orange arrow shows the movement of hydrogen atom from the surface into the solution). (C) Intermediate state showing a hydronium ion (highlighted in yellow) (D) Transfer of proton via shuttling (the path is highlighted in yellow) (E) Product state consisting of adsorbed hydroxymethyl group.

Table 6.1 . Partial charges on the structures during hydrogenation of formaldehyde to form the hydroxymethyl intermediate via the proton coupled electron transfer pathway.

	Reactant state (Fig. 6.3A)	Proton formation transition state (Fig. 6.3B)	Proton transfer transition state (Fig. 6.3C)	O-H formation product state (Fig. 6.3E)
Charge on attacking hydrogen	-0.06	+0.59	+0.66	+0.59
Charge on metal slab	+0.37	-0.19	-0.16	-0.06
Charge on the carbon of $\text{H}_2\text{C}=\text{O}^*$	+0.45	+0.46	+0.39	+0.32

Charge on the oxygen of H₂C=O*	-1.06	-1.07	-1.07	-1.12
Charge on H₂C=O*	-0.40	-0.49	-0.51	-0.61

Proton coupled electron transfer was also used to examine the addition of hydrogen to the carbon of the bound hydroxymethyl shown in Figure 6.4. The intrinsic barrier (with respect to proton in the solution), however, was calculated to be over 170 kJ/mol, suggesting that C-H formation via PCET is unlikely. Direct addition of a proton to carbon on hydroxymethyl is found to proceed via initial Pd-C bond activation (Figure 6.4D), which likely incurs a high energy penalty. In addition, the partial charge on carbon is positive since it is adjacent to oxygen,²⁴⁴ therefore, addition of proton from the solution leads to repulsive interactions in the transition state, resulting in a high activation barrier. In the previous section, we showed that C-H formation reaction on the hydroxymethyl intermediate occurs with a much lower intrinsic activation barrier of 66 kJ/mol (with respect to surface hydride), as the reaction is mediated by a surface hydride (H*), therefore, this reaction would preferentially proceed by a direct hydride attack, instead of water-mediated PCET. However, it seems that on the examined surface of Pd, surface hydride would readily come off into the solution, since the reaction with water molecules to form hydronium complexes has low activation barrier (~45 kJ/mol) as well as favorable energetically (~-20-25 kJ/mol). Therefore, hydrogen atoms on the surface of Pd would be in equilibrium with hydronium ions in the solution phase and electrons in the metal. Consequently, the barrier for surface-mediated C-H formation (66 kJ/mol) must be referenced to protons in the solution, instead of hydrides on the Pd surface (Figure 6.5). The corrected apparent barrier would be 66 + 25 = 91 kJ/mol for hydride attack, accounting for the equilibrium that favors hydronium and electrons over the surface hydride. The impact of the direct participation of water on the energetics of the hydrogenation of formaldehyde is shown in detail in Figure 6.5. Essentially, an evident kinetic promotion is seen for the O-H formation route compared to the reaction in the gas-phase ($\Delta E_{\text{act}}^{\text{water}} = 46 \text{ kJ/mol}$ vs $\Delta E_{\text{act}}^{\text{gas}} = 84 \text{ kJ/mol}$), while C-H formation reaction is predicted to have similar activation barriers in the presence of water and in the gas-phase ($\Delta E_{\text{act}}^{\text{water}} = 91 \text{ kJ/mol}$ vs $\Delta E_{\text{act}}^{\text{gas}} = 82 \text{ kJ/mol}$).

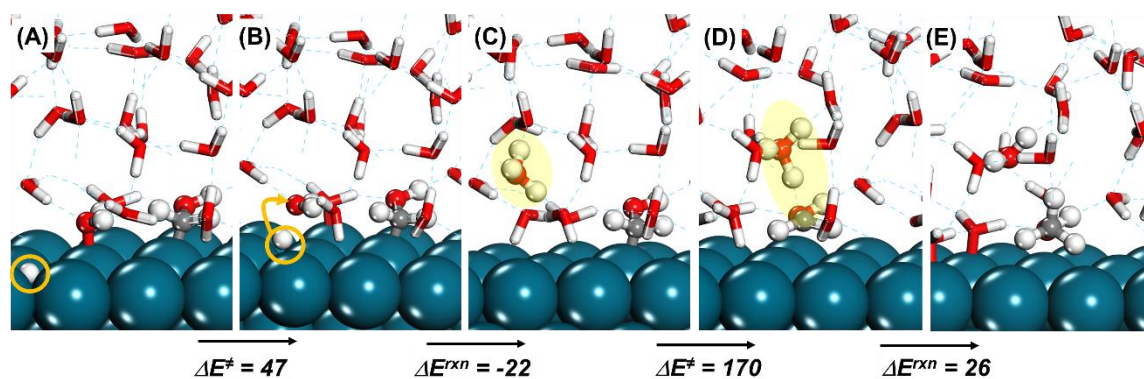


Figure 6.4 Water-mediated pathway catalyzing the formation of methanol from hydroxymethyl. (A) Reactant state consisting of adsorbed formaldehyde and hydrogen (marked with an orange circle). (B) Transition state for the formation of protons and electrons (the orange arrow shows the movement of hydrogen atom from the surface into the solution). (C) Intermediate state showing a hydronium ion (highlighted in yellow) (D) Transfer of proton via shuttling to adsorbed formaldehyde (the path is highlighted in yellow) (E) Product state consisting of adsorbed the methoxy group.

The effect of water on the less favored alkoxy route is reported in the supporting information (Figures S 6.8 - S 6.10). Essentially, water is found to activate the O-H formation reaction on the methoxy intermediate to form methanol, but not the initial C-H formation reaction to generate methoxy from formaldehyde. Further, generation of protons and electrons is found to increase the apparent barrier for C-H formation similar to the reactions in the hydroxymethyl pathway reported earlier.

A crucial step in the protic solvent-mediated hydrogenation path involves the transfer of hydrogen adatoms adsorbed on the metal surface into solution in the form of protons. Kizhakerariam and Stuve²⁸¹ showed that hydrogen adatoms on metal surfaces that can readily accept electrons such as Pt can readily release protons into solution. Thermodynamic analyses were used together with experimental data to identify the minimum work function of the metal (4.9 eV) necessary to generate solvated protons at the water-metal interface from surface bound hydrogen.²⁸¹ The clean Pd(111) surface and the hydrogen-covered Pd(111) surfaces were calculated here to have work functions of 5.31 eV and 5.32 eV, respectively which are in very good agreement with known experimental²⁸⁴ and theoretical²⁸⁵ results. In addition, the work function for the 2/3 ML hydrogen and 1/3 ML formaldehyde surface was calculated to be 5.26 eV, which satisfies the thermodynamic criterion for the generation of protons in solution from adsorbed

hydrogen. These protons and electrons can subsequently transfer through the solution and the metal surface, respectively to hydrogenate the bound oxygenate. Similar proton coupled electron transfer mechanisms may occur on other metals such as Ni, Pt, Au, Ru and Ir which have work functions of 5.2 eV,²⁸⁶ 6.1 eV,²⁸⁷ 5.26 eV,²⁸⁸ 5.00 eV,²⁸⁹ and 5.7 eV,²⁹⁰ respectively that meet the minimum work function criteria.

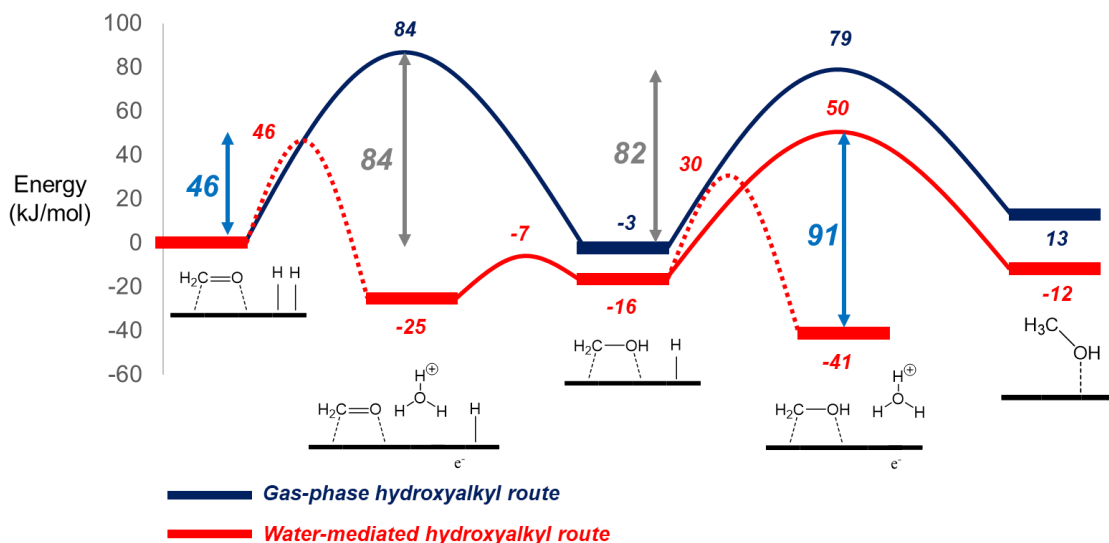


Figure 6.5 The impact of water on the kinetically faster hydroxymethyl route during hydrogenation of formaldehyde. Shown in dark blue is the gas-phase reaction and the corresponding barriers are marked in grey. Shown in red is the water-mediated pathway and the barriers are marked in light blue. Dotted curves show the formation of protons and electrons. O-H formation barrier is shown with respect to adsorbed CH₂O* and H* for the gas-phase and the solution-phase reaction. C-H formation barrier is shown with respect to CH₂OH* and H* for the gas-phase reaction and CH₂OH* and H₃O* for the solution-phase reaction.

The simulations reported herein show the direct involvement of a protic solvent (water) in the formation and transfer of protons and electrons in catalytic hydrogenation of a model carbonyl-containing oxygenate (formaldehyde) over a metal surface in the absence of an external potential. The proton coupled electron transfer path, which involves transfer of electron density into the antibonding π^* orbital of the bound C=O bond together with a proton transfer via solution was calculated to be the kinetically preferred over the metal-mediated pathway for O-H formation as the intrinsic activation barrier was found to be 26 kJ/mol lower. The results found here for the hydrogenation of formaldehyde may also be extended to the hydrogenation of other unsaturated carbonyl groups or polar C=X bonds

(such as C=S and C=N) over other metal surfaces in different protic solvents important in selective hydrogenation of other bio-renewable intermediates and the synthesis of fine chemical and pharmaceutical intermediates. This characteristically different pathway is unable to promote C-H formation reactions, instead these reactions appear to be directly catalyzed by back-side hydride attack on the electron deficient carbon. The existence of a quasi-equilibrium between surface hydrides and solution hydronium ions may affect the energetics of C-H formation reactions by favorable locking of protons in local water pockets.

In the next section, we extend these results to other transition metals that are commonly used in hydrogenation reactions- Ruthenium and Platinum. The binding energy of hydrogen²³⁸ is the lowest on Pt (2.72 eV), followed by Pd (2.88 eV) and Ru (2.97 eV). The work function of these metals follow the opposite trend ($\Phi_{\text{Pt}} = 6.1 \text{ eV} > \Phi_{\text{Pd}} = 5.6 \text{ eV} > \Phi_{\text{Ru}} = 5.0 \text{ eV}$). The favorable formation of protons and electrons in water requires high work function as well as low hydrogen binding energy, consequently, the ease of proton and electron generation for these metals can be ranked as Pt > Pd > Ru, which will have direct implications on the water-mediated PCET pathway. In addition, Ru is known to be more oxophilic than both Pt and Pd²⁹¹ and this may impact the preferred pathway for C=O hydrogenation (hydroxyalkyl vs alkoxy). Ru can also activate water to form surface hydroxyl groups are bound strongly to the Ru, thus making the H of the RuOH site Brønsted acidic²⁹² and active carrying out hydrogenation. These differences are probed using DFT along with steady state flow reactor kinetic measurements.

6.3 Mechanistic insights into the hydrogenation of acetone over ruthenium and platinum

In this section, we discuss the hydrogenation of acetone to 2-propanol is discussed over ruthenium and platinum. Reaction rates are compared for hydrogenation in the vapor phase to those determine in the presence and absence of co-fed water to understand the role of water in mediating the chemistry. The turnover rates for acetone hydrogenation over Pt and Ru catalysts measured in a constant flow reactor are presented in Figure 6.6. The results show that water has different effects on the reactivity over Pt and Ru. While the reaction rates appear to increase over Ru by about a factor of 4, the values hardly change over Pt. In this part of the chapter, experimental observations are rationalized

using DFT simulations based on the mechanistic framework discussed in the previous sections.

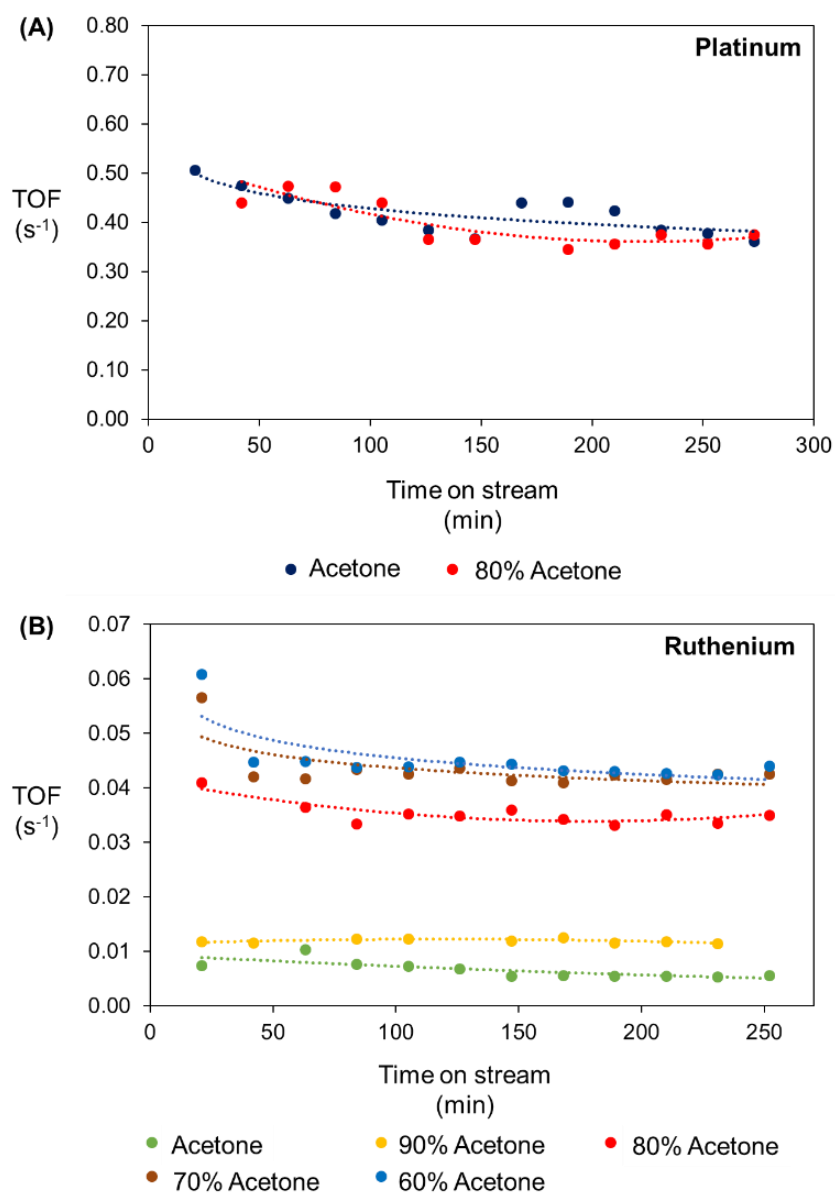


Figure 6.6 (A) Turnover frequency for acetone hydrogenation over Pt for different conditions in the vapor phase. Catalysts: 3% Pt/SiO₂ and 250mg Pt/SiO₂ /2000mg α -Al₂O₃. Reaction conditions: T = 80 °C, P = 1 atm, Feed: Acetone = 0.1 ml/min, H₂ = 80 cc/min. (B) Turn over frequency for acetone hydrogenation over Ru/C under different conditions in the vapor phase. Catalysts: 5% Ru/C and 200mg RuC/2000mg α -Al₂O₃. Reaction conditions: T = 80 °C, P = 1 atm, Feed: Acetone = 0.2 ml/min, H₂ = 27 cc/min.

6.3.1 Theoretical results for acetone hydrogenation in absence of water

6.3.1.1 Hydrogenation over Pt

Density functional theory calculations were carried out over the model Pt(111) surface to examine the gas phase hydrogenation of acetone. Both alkoxy and hydroxyalkyl pathways discussed previously were examined to determine the potential energy diagram for this reaction (Figure 6.7). The results presented in Figure 6.7 show that the hydroxyalkyl pathway is favored over the alkoxy pathway, similar to results over Pd. The hydroxyalkyl path proceeds by an initial exothermic O-H formation reaction between $(\text{CH}_3)_2\text{CO}^*$ and H^* to generate the hydroxyisopropyl intermediate $(\text{CH}_3)_2\text{C}^*\text{OH}$. The hydroxyisopropyl intermediate is the lowest energy intermediate on the Pt surface as shown in Figure 6.7 and likely covers the surface at steady state conditions. As a result, the rate of hydrogenation is likely governed by the subsequent C-H formation reaction, resulting in an apparent activation barrier of 79 kJ/mol with respect to adsorbed hydroxyisopropyl and hydrogen state. The reaction orders for acetone and hydrogen were measured in the hydrogenation of formaldehyde over Pt/SiO₂ to be zero and one half, respectively thus suggesting that the reaction occurs via the initial hydrogen addition to formaldehyde which covers the surface. The calculated apparent barrier would then be $79 - 46 = 33$ kJ/mol which is in good agreement with the measured barrier of 30-40 kJ/mol.²⁹³

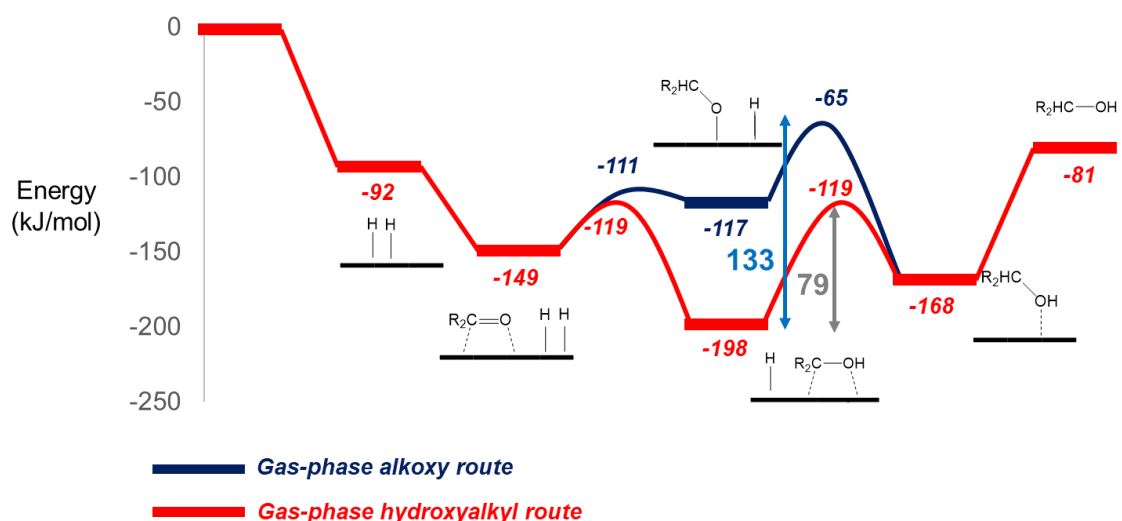


Figure 6.7 Reaction profile diagram for the vapor phase hydrogenation of acetone on Pt(111). Shown in red is the hydroxyalkyl pathway and shown in dark blue is the alkoxy pathway. The intrinsic activation barrier (with respect to CH_2OH^* and H^* as most abundant

surface intermediates) is shown in grey for the hydroxyalkyl route and in light blue for the alkoxy route. The relevant structures are reported in the supporting information Figure S 6.11.

6.3.1.2 Hydrogenation over Ru

Contrary to hydrogenation over Pt and Pd, acetone hydrogenation over Ru was found to preferentially proceed via the initial C-H formation reaction rather than the O-H reaction, thus activating the alkoxy pathway (Figure 6.8). This is likely a result of the higher oxophilicity of Ru over that of Pt and Pd. The formation of isopropoxy intermediate ($\text{CH}_3)_2\text{CHO}^*$ is found to be energetically favorable, suggesting these intermediates would be present on the surface at high coverage consistent with previous reports.¹⁹⁵ The energy diagram in Figure 6.8 suggests that the alkoxy mechanism would be kinetically faster over Ru. Within the alkoxy mechanism, the rate limiting step will involve O-H formation on the isopropoxy intermediate, resulting in an intrinsic activation barrier of 131 kJ/mol with respect to adsorbed isopropoxy and hydrogen. With respect to adsorbed isopropoxy and H_2 gas, the activation barrier becomes $131 - 61 = 70$ kJ/mol, which is slightly higher than the measured barrier of 50 kJ/mol but consistent with rate orders of zero and half with respect to acetone and H_2 gas respectively over Ru/SiO_2 .²⁹⁴

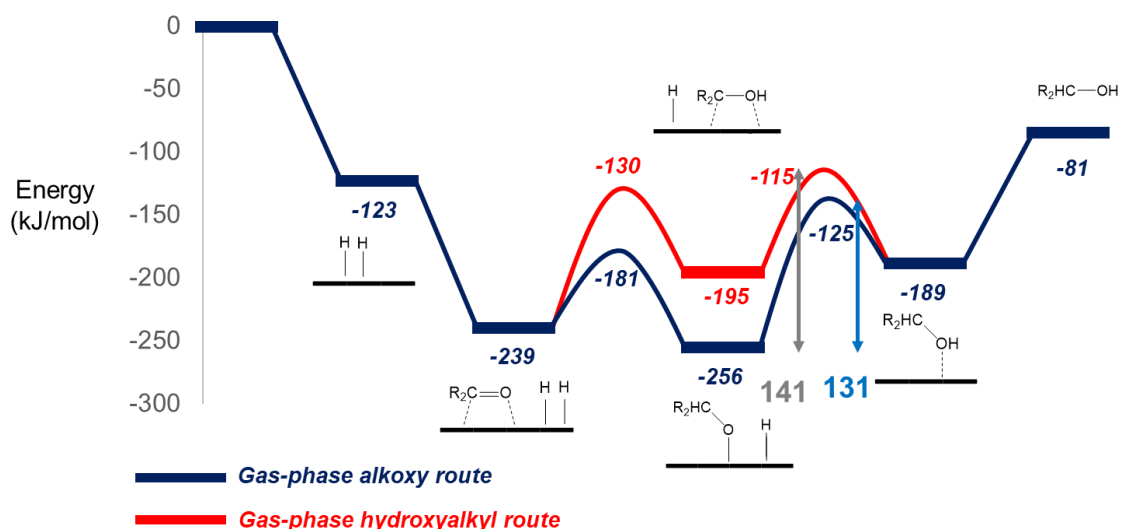


Figure 6.8 Reaction profile diagram for the vapor phase hydrogenation of acetone on Ru(001). Shown in red is the hydroxyalkyl pathway and shown in blue is the alkoxy pathway. The apparent activation barrier (with respect to CH_3O^* and H^* as most abundant surface intermediates) is shown in grey for the hydroxyalkyl route and in light blue for the alkoxy route. The relevant structures are reported in the supporting information Figure S 6.12.

Comparing the predicted activation barriers over Ru and Pt, we find that hydrogenation barrier over Pt is lower than that on Ru by 52 kJ/mol. These predictions are qualitatively consistent with vapor phase turnover numbers obtained experimentally, where TOF on Pt is an order of magnitude higher than on Ru.

The gas-phase calculations presented herein highlight the differences between hydrogenation mechanisms on Pt and Ru. Over Pt, the reaction is predicted to proceed via the hydroxyalkyl mechanism with C-H formation as the likely rate limiting step. If the theoretical results presented earlier on Pd apply to Pt, the rate limiting C-H formation will likely not be promoted in the presence of water, since water will not directly mediate C-H formation with PCET, but, will favorably react with hydrogen atoms to form protons and electrons. This would lead to locking of protons in the local reaction environment and may result in similar reaction rates in the presence and absence of water consistent with experiments on Pt. On the other hand, we find that the reaction over Ru proceeds via the alkoxy mechanism with O-H formation as the rate determining step. Water, as such, will be able to promote O-H formation via PCET and may result in higher reaction rates observed experimentally over Ru. Next, we test these ideas by performing DFT calculations in the presence of water molecules.

6.3.2 Theoretical results for acetone hydrogenation in the presence of water

6.3.2.1 Hydrogenation over Pt

The influence of water was simulated by adding explicit water molecules such that density of water in the unit cell is ~ 1 g/cm³. Ab-initio molecular dynamics simulations were used to relax water molecules around the adsorbed acetone molecule for 5000 steps of 1 fs each. Low energy structures along the trajectory were further optimized using DFT and lowest energy structure was chosen to perform detailed quantum mechanical simulations.

Both the hydroxyalkyl and the alkoxy pathways were simulated in water over Pt. The O-H formation reactions in both of these routes ($(\text{CH}_3)_2\text{CO}^* + \text{H}^* \rightarrow (\text{CH}_3)_2\text{C}^*\text{OH} + *$ in hydroxyalkyl and $(\text{CH}_3)_2\text{CHO}^* + \text{H}^* \rightarrow (\text{CH}_3)_2\text{CHO}^*\text{H} + *$ in alkoxy) were simulated via the PCET mechanism, directly mediated by water molecules as discussed in Section 6.3.2.2. The simulations were used to construct energy diagram shown in Figure 6.9 and the corresponding structures are reported in Figure 6.10 (for hydroxyalkyl pathway) and Figure S 6.13 (for alkoxy pathway). Hydroxyalkyl pathway in the presence of water as well,

is found to be more favorable over the alkoxy mechanism. This is again related to the stability of the hydroxyisopropyl intermediate vs the isopropoxy intermediate on Pt; the former is more stable by 65 kJ/mol. These results are consistent with previous experimental and theoretical reports that show methanol decomposition to formaldehyde proceeds via the hydroxymethyl intermediate.^{193,196,295}

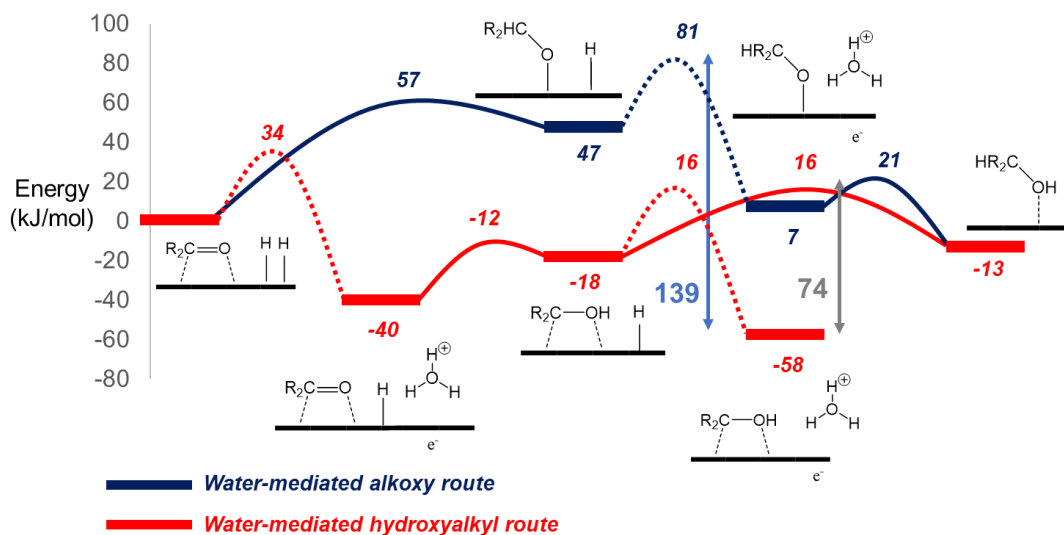
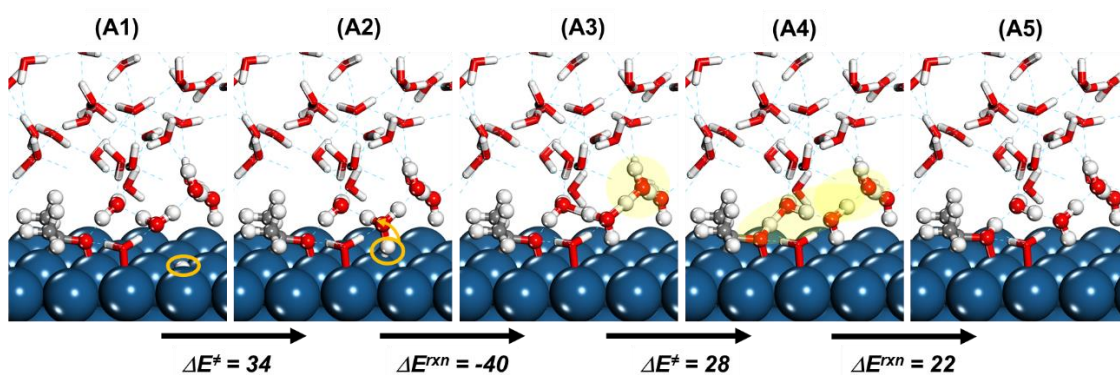


Figure 6.9 Reaction energy diagram for the water-mediated hydrogenation of acetone on Pt-111. Dotted lines indicate formation of protons and electrons. Shown in red is the hydroxyalkyl pathway that undergoes initial O-H formation via PCET to form the hydroxyisopropyl intermediate, which subsequently undergoes a hydride attack from the metal surface forming isopropanol. The activation barrier for this mechanism is shown in grey. Shown in blue is the alkoxy pathway that undergoes initial C-H formation via hydride attack from the surface to form the isopropoxy intermediate, which undergoes a PCET reaction forming isopropanol. The activation barrier for this route is shown in light blue. Activation barriers shown here are with respect to lowest energy state consisting of hydroxyisopropyl intermediate on the surface and protons in the solution.

Similar to reactions over Pd, water molecules were found to react favorably with co-adsorbed hydrogen atoms to form protons in the solution and electrons in the metal (dotted lines in Figure 6.9). These reactions were found to be easier and more favorable over Pt compared to Pd due to higher work function and weaker hydrogen binding energy over Pt ($\Delta E_{\text{act}}^{\text{Pt}} = 34 \text{ kJ/mol}$ vs $\Delta E_{\text{act}}^{\text{Pd}} = 46 \text{ kJ/mol}$, $\Delta E_{\text{rxn}}^{\text{Pt}} = -40 \text{ kJ/mol}$ vs $\Delta E_{\text{rxn}}^{\text{Pd}} = -25 \text{ kJ/mol}$). These electrons and protons can be subsequently used to catalyze O-H formation reactions with very low intrinsic barriers (15-30 kJ/mol). On the other hand, since these

protons and electrons cannot directly catalyze C-H formation reactions in the hydroxyalkyl ($(\text{CH}_3)_2\text{C}^*\text{OH} + \text{H}^* \rightarrow (\text{CH}_3)_2\text{CHO}^*\text{H} + *$) and the alkoxy ($(\text{CH}_3)_2\text{CO}^* + \text{H}^* \rightarrow (\text{CH}_3)_2\text{CHO}^* + *$) pathways, these reaction proceed instead via direct hydride attack. The favorable quasi-equilibrated formation of protons and electrons, however, affects the overall barrier as seen previously. This results in an apparent activation barrier of 74 kJ/mol with respect to adsorbed hydroxyisopropyl and protons in solution as the most abundant intermediates. This activation barrier is within numerical errors of gas-phase activation barrier of 79 kJ/mol and suggests hydrogenation rates would be similar in the presence and absence of water consistent with experimental findings. Over Pt, the direct participation of water in hydrogenation reactions of C=O bonds, therefore, does not promote the reaction. While Pt has a high enough work function to convert H^* to protons and electrons, the protons preferentially localize in water pockets near the surface and do not co-catalyze the rate-limiting C-H formation reaction.

Hydroxyisopropyl formation via PCET



Isopropanol formation from hydroxyisopropyl via hydride attack

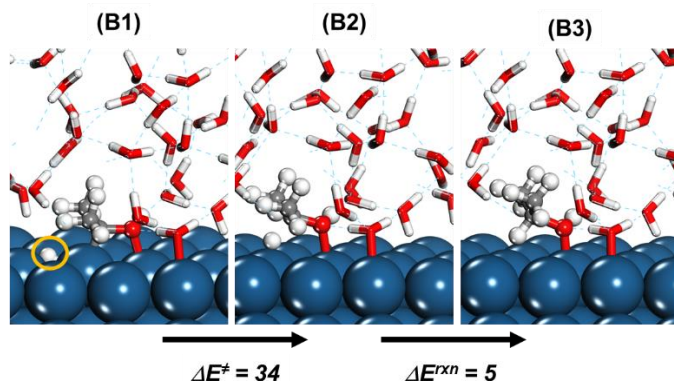


Figure 6.10 Structures for the water-mediated acetone hydrogenation on Pt(111) via the hydroxyalkyl route. (A1) Reactant state showing adsorbed acetone and hydrogen (marked

by an orange circle). (A2) Transition state for the reaction between water and hydrogen to form a hydronium ion and an electron (the orange arrow shows the movement of hydrogen atom from the surface into the solution). (A3) Product state for hydronium complex in water (highlighted in yellow). (A4) Transition state for proton and electron transfer to form the hydroxyisopropyl intermediate (the path highlighted in yellow). (A5) Product state for adsorbed hydroxyisopropyl. (B1) Reactant state showing adsorbed hydroxyisopropyl and hydrogen (marked in orange). (B2) Transition state for the formation of isopropanol from hydroxyisopropyl via hydride attack. (B3) Product state showing adsorbed isopropanol.

6.3.2.2 Hydrogenation over Ru

In this section, we report the explicit role of water in mediating acetone hydrogenation over Ru. The initial starting structures for DFT calculations over Ru were generated using ab initio molecular dynamics simulations similar to those carried out to generate the water structures on Pt and Pd. Simulations were performed to understand the water-activated PCET chemistry on Ru to elucidate the promotional effect that is observed experimentally, where TOF was found to increase in the presence of water. Water activation to form Brønsted acid sites on Ruthenium has been proposed previously,²⁹² therefore, in addition to generation of hydronium ions and electrons, the participation of Brønsted acid sites was also probed.

Figure 6.11(A) reports the energy diagram for the PCET route explored in the previous sections for Pd and Pt, where water molecules react with co-adsorbed hydrogen atoms to form protons and electrons (Scheme 6.2, reaction 1), that subsequently catalyzed O-H formation reaction in a separate elementary step. Over Ru, these reactions are instead found to occur in a concerted fashion, wherein protons and electrons are generated along the reaction coordinate and transferred directly to the oxygen of the bound formaldehyde in a single elementary step $((\text{CH}_3)_2\text{CHO}^* + \text{H}^* + (\text{H}_2\text{O})_n \rightarrow [(\text{CH}_3)_2\text{CHO}^* \cdots \text{H}(\text{H}_2\text{O})_n]^\ddagger \rightarrow (\text{CH}_3)_2\text{CHOH}^* + *)$. This is a result of lower work function and high hydrogen binding energy over Ru that makes direct proton-electron formation harder, such that a favorable state with isolated hydronium ions in water is not captured by DFT simulations. Instead the protons and electrons that form are quickly delivered to oxygen of formaldehyde. Figure 6.11(A) shows both the hydroxyalkyl pathway and the alkoxy pathway and the relevant structures are reported in Figure 6.12 (for alkoxy pathway) and Figure S 6.14 (for hydroxyalkyl pathway). Similar to gas-phase reactions over Ru (Figure 6.8), the alkoxy route is found to be favorable over the hydroxyalkyl route. This is likely a result on initial

exothermic C-H formation that forms a strongly bound isopropoxy intermediate on Ru due to higher oxophilicity of Ru. In the rate determining step, these intermediates undergo O-H formation reaction co-catalyzed by water molecules forming isopropanol alcohol on the surface. The apparent barrier with respect to isopropoxy intermediates and adsorbed hydrogen atoms on the surface is calculated to be 107 kJ/mol, which is 24 kJ/mol less than the gas-phase apparent activation barrier of 131 kJ/mol, consistent with increase in the reactivity seen experimentally.

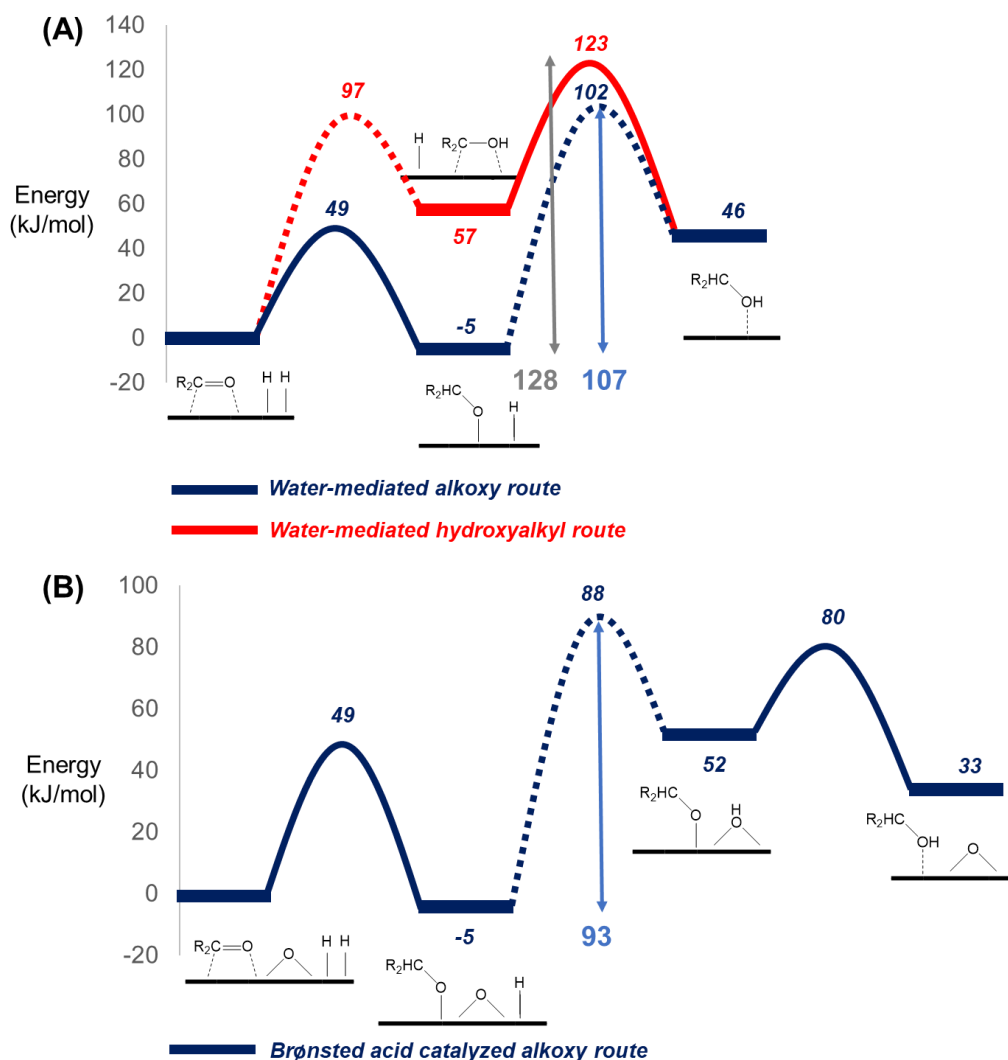


Figure 6.11 Reaction profile diagrams for water mediated acetone hydrogenation over Ru-001. (A) Direct mediation of acetone hydrogenation via the PCET mechanism. Water molecules co-react with surface hydrogen atoms to form protons and electrons that are delivered to oxygen (dotted lines) on acetone and alkoxy intermediates. Shown in red is the hydroxyalkyl mechanism and the corresponding apparent barrier is marked in grey. Shown

in blue is the alkoxy mechanism and the corresponding apparent barrier is marked in light blue. Barriers are shown with respect to the lowest energy state consisting of isopropoxy and hydrogen on the surface of Ru. (B) Energy diagram for the activation of kinetically faster alkoxy mechanism on Ru using Brønsted acid sites. The apparent barrier is marked in light blue. Dotted line shows the formation (regeneration) of Brønsted acids prior to hydrogenation via PCET.

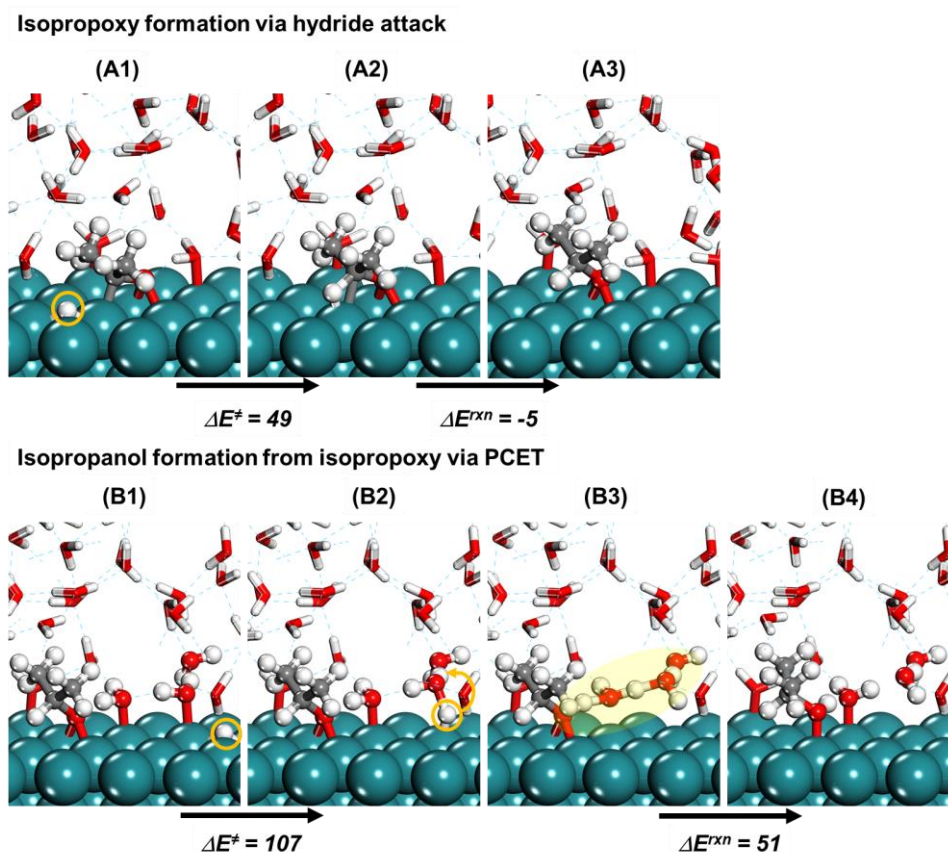


Figure 6.12 Structures for the water-mediated acetone hydrogenation on Ru(001) via the alkoxy route. (A1) Reactant state showing adsorbed acetone and hydrogen (marked in orange). (A2) Transition state for the formation of isopropoxy intermediate via hydride attack. (A3) Product state showing adsorbed isopropyl. (B1) Reactant state showing adsorbed isopropoxy and hydrogen (marked in orange). (B2) Transition state for the reaction between water and hydrogen to form hydronium and electrons (the orange arrow shows the movement of hydrogen atom from the surface into the solution). (B3) A structure along the reaction coordinate showing transfer of electrons and protons (highlighted in yellow) to isopropoxy (over Ru, an isolated hydronium was not captured by DFT). (B4) Product state showing adsorbed isopropanol.

Water activation to form Brønsted acid sites ($\text{H}_2\text{O}^* + * \rightarrow \text{HO}^* + \text{H}^*$) on Ru has been proposed previously.²⁹² We find that water can activate with an activation barrier of 72 kJ/mol and a reaction energy of 15 kJ/mol (Figure S 6.15). These Brønsted acid sites can then catalyze the rate determining O-H formation reaction on the isopropoxy intermediate ($\text{HO}^* + (\text{CH}_3)_2\text{CHO}^* \rightarrow \text{O}^* + (\text{CH}_3)_2\text{CHOH}^*$) to form O^* and isopropanol, similar to Brønsted acid dehydration reported over oxophilic Re supported on Rh.²⁹⁶

The transfer of hydrogen from the Brønsted acid site leaves oxygen on the surface of Ru (O^*). Consequently, at steady state, the catalytic cycle must involve regeneration of these Brønsted acid sites ($\text{O}^* + \text{H}^* \rightarrow \text{HO}^* + *$) for sustenance of hydrogenation chemistry via such sites. The reaction energy diagram depicting this route is shown in Figure 6.11(B) and the structures are shown in Figure 6.13. The harder step seems to be regeneration of the Brønsted acid sites ($\Delta E^{\text{act}} = 93$ kJ/mol) that can subsequently transfer protons (and electron from the metal) over to the isopropoxy intermediates with an intrinsic activation barrier of 28 kJ/mol. Figure 6.11(B) suggests that the rate-determining step for such a mechanism will involve formation of Brønsted acid sites and the apparent barrier is estimated to be 93 kJ/mol with respect to adsorbed isopropoxy, O^* and H^* . Between the Brønsted acid route and the direct PCET route, the Brønsted acid route appears to have a lower activation barrier suggesting it could be a viable mechanism that leads to the observed promotion of reaction rates over Ru. As such, both these routes could result in the observed promotion and experimental studies to distinguish both these mechanisms are a part of future efforts. A more detailed analysis of the impact of O^* during acetone hydrogenation is also a subject of future investigation.

Overall, in the presence of water, theoretical calculations predict an apparent barrier of 74 kJ/mol for acetone hydrogenation over Pt, while a barrier of 93 kJ/mol is predicted on the model Ru surface. These results are found to be consistent with the reactivity trend seen experimentally in that TOF over Pt is an order of magnitude higher.

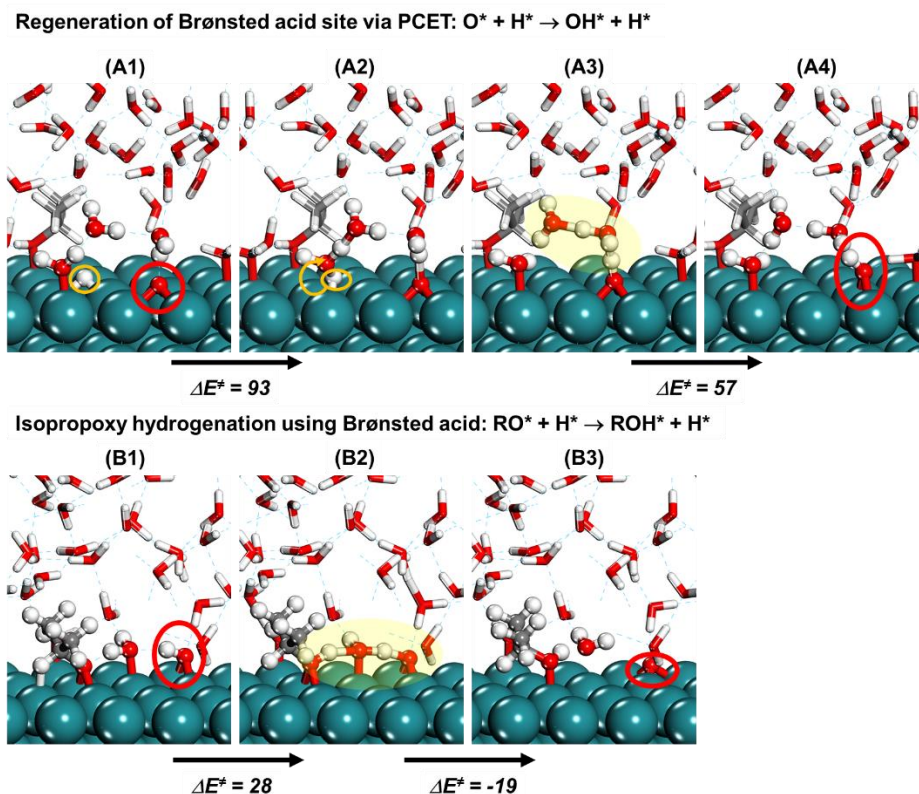


Figure 6.13 Structures for Brønsted acid catalyzed hydrogenation of the isopropoxy intermediate on Ru to isopropanol. (A1) Reactant state for Brønsted acid site regeneration consisting of adsorbed H^* (orange circle) and O^* (red circle). (A2) Transition state for proton and electron formation ((the orange arrow shows the movement of hydrogen atom from the surface into the solution). (A3) A structure along the reaction coordinate showing transfer (highlighted in yellow) of electrons and protons to O^* (over Ru, an isolated hydronium was not captured by DFT). (A4) Product state consisting of regenerated Brønsted acid site (red circle). (B1) Reactant state for hydrogenation of isopropoxy using a Brønsted acid site (red circle). (B2) Transition state for hydrogenation of isopropoxy using a Brønsted acid site. (B3) Product for hydrogenation of isopropoxy using a Brønsted acid site (red circle).

6.4 Concluding remarks

The calculations presented herein demonstrate how metals as well as the presence of protic media can influence the C=O hydrogenation pathways. Metals with higher affinity for oxygen (such as Ru) likely result in favorable initial C-H formation reactions, and the rate will be governed by the second O-H formation reaction as it involves activating the strong M-O bond. On other metals that have lower affinity for oxygen (Pt and Pd), the initial O-H formation will likely be more facile than C-H formation, and the rate will be

dictated by the second C-H formation step. Similar ideas perhaps hold true for hydrogenation of other unsaturated bonds and the chemistry will be a function of the relative stability of partially hydrogenated intermediates that are generated initially and may populate the catalyst surface.

Protic solvents can act as dielectric screening medias, co-reactants or co-catalyst thus aiding in lowering the activation barriers for the rate controlling steps. Protic solvents result in an effective dielectric field around the transition states, thus stabilizing the partial charges that form in the transition state. Protic solvents can also act as co-reactants and favorably react with co-adsorbed hydrogen atoms forming protons and electrons. The stability of protons and electrons is dictated by the work function of the metal, hydrogen binding energy on the metal as well as proton solvation energy of the solvent. While protons are readily transferred to oxygen via shuttling to form O-H bonds, the stability of these protons and electrons will hinder the formation of C-H bonds. Therefore, over transition metals where C-H formation is rate-determining, it is advisable to use polar aprotic solvents. Over transition metals that result in O-H formation rate determining steps, protic solvents that can readily shuttle protons and electrons can promote hydrogenation rates. In addition, over transition metals that involve O-H formation reactions, but cannot readily generate protons and electrons, it is advisable to use protic solvents in conjunction with basic solvents such as dimethyl sulfoxide (DMSO) and γ -valero lactone (GVL) that can aid in metal-hydrogen cleavage by stabilizing protons in the condensed phase.²⁹⁷

6.5 Computational methods

All of the calculations reported herein were carried out using periodic density functional theory (DFT) methods as implemented in the Vienna ab-initio simulation program.¹²⁷⁻¹³⁰ The exchange and correlation energies were calculated using the PBE form of generalized gradient approximation.¹³¹ Dispersive interactions were modeled using the D3-method of Grimme et al.¹³² The Pd(111) surface was modeled in all of the calculations by using a periodic slab consisting of four layers of 3 x 3 unit cell. The Pt(111) and Ru(001) surfaces were modeled using 4 layers of 4 x 4 unit cells. The bottom two layers were fixed to bulk positions during all optimizations. A vacuum of 20 Å was introduced to separate the bottom and the top layers of the metal slab. A plane wave energy cutoff of 396 eV was used. All of the structures and their corresponding energies reported herein were converged using a two-step process. In the first step, a 3 x 3 x 1 k-point¹³⁷ mesh for Pd and 2 x 2 x 1 k-point

mesh for Pt and Ru was used to model the wave functions and converge the electronic structure to within 10^{-4} eV. The geometric structures were converged to within a maximum force cutoff on each atom of $0.1 \text{ eV}/\text{\AA}$. In the second step, the wavefunctions were converged to within 10^{-6} eV, until the maximum force acting upon each atom was less than $0.05 \text{ eV}/\text{\AA}$. All of the energies reported herein were subsequently calculated by doing single point energy calculations on the converged structures on a $6 \times 6 \times 1$ k-point mesh for Pd and $5 \times 5 \times 1$ k-point mesh for Pt and Ru.

A minimum energy pathway from the reactant state to the product state was determined using the nudged elastic band^{133,134} (NEB) method, where the wavefunctions were converged to within 10^{-4} eV with maximum allowable force acting upon each atom to be $0.1 \text{ eV}/\text{\AA}$. Transition state structures were subsequently isolated using the dimer method¹³⁵ and the images near the saddle point predicted by NEB.

For the solution phase calculations, explicit water molecules were introduced such that the density of water molecules in the unit cell was $\sim 1 \text{ g/cm}^3$. A few water molecules near the metal surface were then replaced with the formaldehyde reactant. The system was then allowed to relax using ab-initio thermodynamics for 5 ps at 500 K. The lowest energy structure along the molecular dynamics trajectory was chosen for static DFT calculations. Stationary and saddle points were obtained as described earlier.

Charge analysis was performed using the Bader charge analysis.²⁸⁰ Following FFT mesh was used for charge calculations: NGXF = 160, NGYF = 160 and NGZF = 432. Work function was calculated as a difference of the vacuum potential and the Fermi level. These calculations were performed on a $6 \times 6 \times 1$ k-point mesh.

6.6 Experimental methods

Pt/SiO₂ catalyst was synthesized using the method described by Gerceker et al.²⁹⁸ 5 wt% Ru/C was purchased from Sigma-Aldrich. The metal surface site density was estimated using CO chemisorption at 307 K (Micromeritics, ASAP, 2020C Analyzer). The number of catalytically active Pt and Ru sites are calculated from irreversible CO uptake. Acetone (Fisher Scientific; HPLC Grade) and 2-propanol (Sigma Aldrich; 99.9%) were used as purchased. A flow reactor system was used to study acetone hydrogenation. Catalyst was mixed with $\alpha\text{-Al}_2\text{O}_3$ ($\alpha\text{-Al}_2\text{O}_3/\text{catalyst} = 10$) and loaded on top of a bed containing silica

chips in a 0.25" stainless steel tube reactor. Quartz wool was used to immobilize the catalyst bed.

In a typical experiment, 0.2 g of the catalyst is packed with 2 g α -Al₂O₃. The effect of water on reaction kinetics is measured by varying the concentration of water in the feed solution between. An HPLC pump (Lab Alliance Series I) was used to pump the solution from the bottom of the flow system at the flow rate of 0.1-0.2 mL/min [STP] and preheated in the lines before combining with H₂ flow (30-80 cm³/min [STP]). The reaction occurred at 353 K and 1 atm. The reactor effluent was passed through the heat-traced stainless steel lines at 353 K until the inlet of GC sampling loop to prevent product condensation.

An online gas chromatograph (Shimadzu GC-2010 Plus) equipped with a barrier discharge ionization detector (BID) and a Zebron ZB-BAC2 GC column (Phenomenex; L = 30 mm; ID = 0.53 mm; FT = 2.0 μ m) was used to monitor concentration of acetone and isopropanol. External calibrations with known standards were used to quantify the concentrations of reactant and product. Conversions of acetone and the yield of 2-propanol were estimated using Equations 5.1 and 5.2 respectively, where C_{AC}^o is the initial concentration of acetone in the feed, and C_{AC} and C_{IPA} are the concentrations of acetone and 2-propanol in the product, respectively. Reaction rates and turnover frequencies (TOF) of 2-propanol production are calculated using Equations 5.3 and 5.4, where F_{IPA} is the flow rate of 2-propanol in the effluent.

$$\text{acetone conversion (\%)} = \frac{C_{AC}^o - C_{AC}}{C_{AC}^o} \times 100 \quad (5.1)$$

$$\text{isopropanol yield (\%)} = \frac{C_{IPA}}{C_{AC}^o} \times 100 \quad (5.2)$$

$$\text{rate}_{IPA} = \frac{F_{IPA}}{\text{catalyst weight}} \quad (5.3)$$

$$\text{TOF} = \frac{\text{rate}_{IPA}}{\text{site density}} \quad (5.4)$$

6.7 Acknowledgements

The authors would like to thank the National Science Foundation for the support of this work through the NSF Engineering Research Center for Biorenewable Chemicals (CBiRC; <https://www.cbirc.iastate.edu>) under Award No. EEC-0813570. Computational support

from the Minnesota Supercomputing Institute (MSI) and the Molecular Science Computing Facility (MSCF) in the William R. Wiley Environmental Molecular Sciences Laboratory, a national scientific user facility sponsored by the U.S. Department of Energy, Office of Biological and Environmental Research at the Pacific Northwest National Laboratory are highly acknowledged. The authors would also like to thank Professor R. J. Davis from the University of Virginia for helpful discussions.

6.8 Supporting information

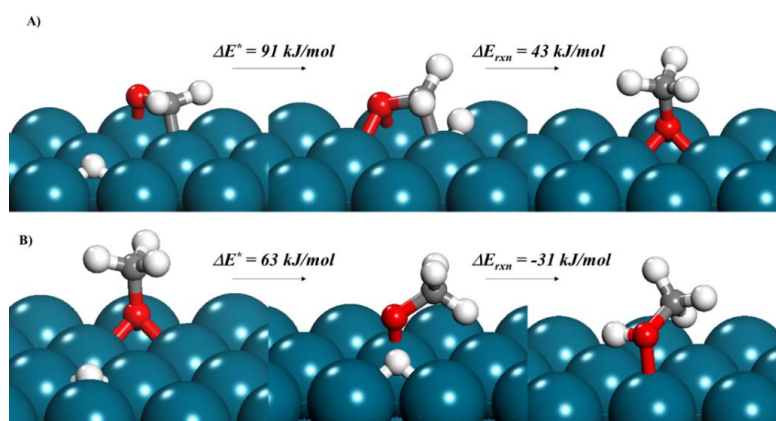


Figure S 6.1 Structures for hydrogenation of formaldehyde to methanol via the alkoxy route in the gas phase over the Pd(111) surface. (A) Reactant, transition and product states for the hydrogenation of a surface bound formaldehyde to methoxy, (B) Reactant, transition and product states for the subsequent hydrogenation of the surface bound methoxy to methanol over Pd.

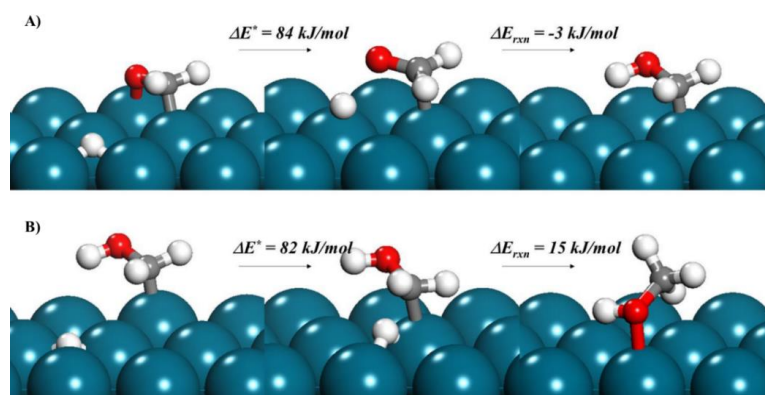


Figure S 6.2 Structures for hydrogenation of formaldehyde to methanol via the hydroxyalkyl route in the gas phase over the Pd(111) surface. (A) Reactant, transition and product states for the hydrogenation of formaldehyde to hydroxyalkyl, (B) Reactant, transition and product states for the subsequent hydrogenation of hydroxyalkyl to methanol.

for the hydrogenation of surface formaldehyde to hydroxymethyl, (B) Reactant, transition and product states for the hydrogenation of bound hydroxymethyl to methanol over Pd.

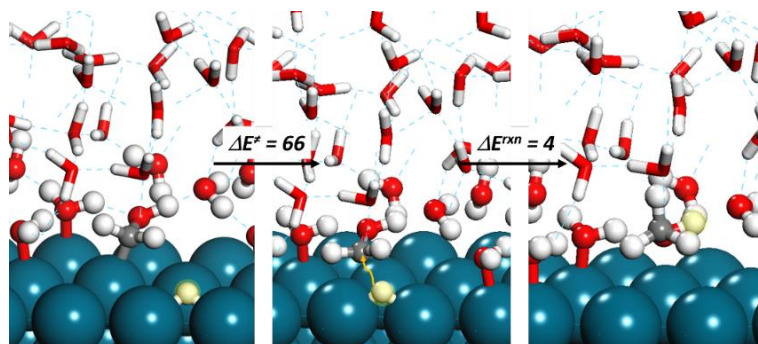


Figure S 6.3 Structures of reactant, transition, and product states for the metal-mediated hydrogenation of hydroxymethyl to methanol in water over the Pd(111) surface.

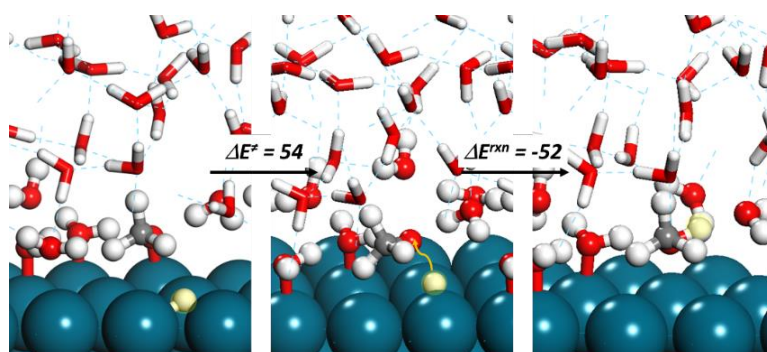


Figure S 6.4 Structures of reactant, transition and product states for the metal-mediated hydrogenation of methoxy to methanol in water over Pd(111).

Table S 6.1 Partial charges on structures during metal-mediated C-H and O-H formation in water

	Reactant state (Figure 6.2A- (R))	C-H formation transition state (Figure 6.2B-(TS))	O-H formation transition state (Figure 6.2A-(TS))
Charge on attacking hydrogen	-0.06	-0.02	+0.64
Charge on metal slab	+0.37	+0.34	+0.08
Charge on the carbon of H ₂ C=O*	+0.45	+0.51	+0.48

Charge on the oxygen of $\text{H}_2\text{C}=\text{O}^*$	-1.06	-1.09	-1.04
Charge on $\text{H}_2\text{C}=\text{O}^*$	-0.40	-0.37	-0.56

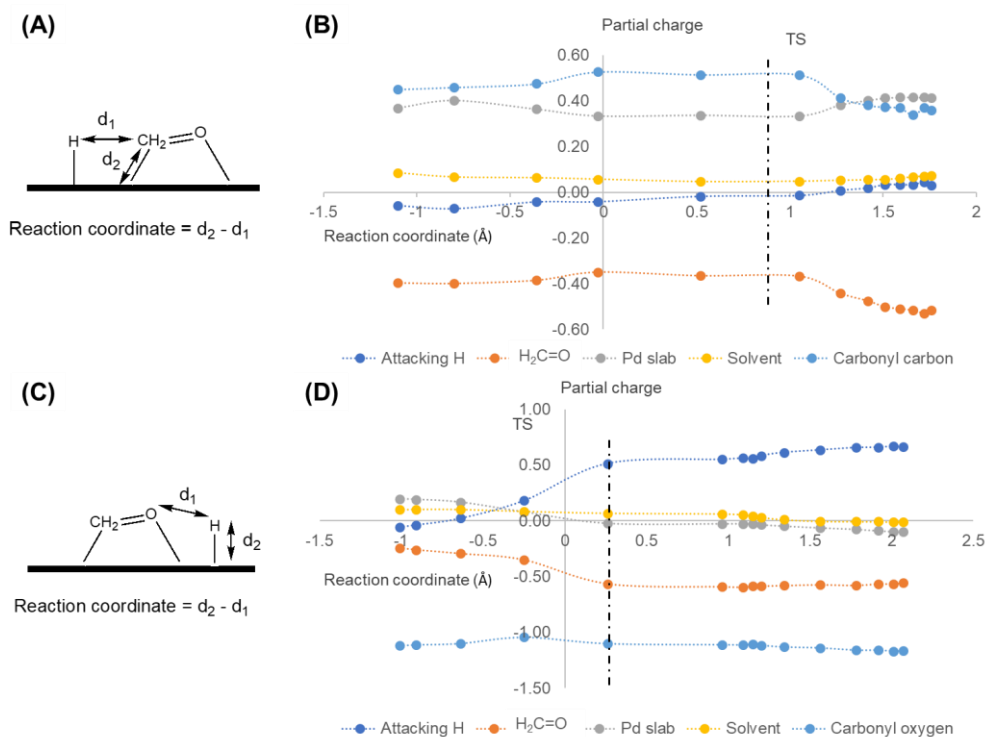


Figure S 6.5 (A) Reaction coordinate for the metal-mediated hydrogenation of formaldehyde to methoxy in water over Pd. (B) Partial charge profile for the metal mediated conversion of formaldehyde to methoxy in water. (C) Reaction coordinate for the metal-mediated hydrogenation of formaldehyde to hydroxymethyl in water. (D) Partial charge profile for the metal-mediated conversion of formaldehyde to hydroxymethyl in water. (Note that the nudged elastic band paths were converged using a weaker convergence criteria than that for the dimer isolated transition states and the optimized reactants and products thus resulting in subtle differences in the charge profiles here and those reported in Table S 5.1).

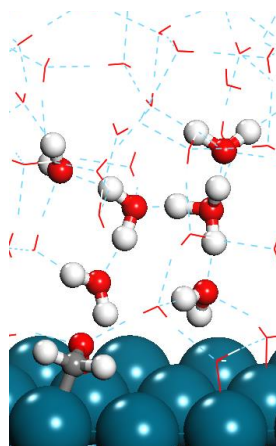


Figure S 6.6 Hexahydrate hydronium complex formed near the water-Pd metal interface

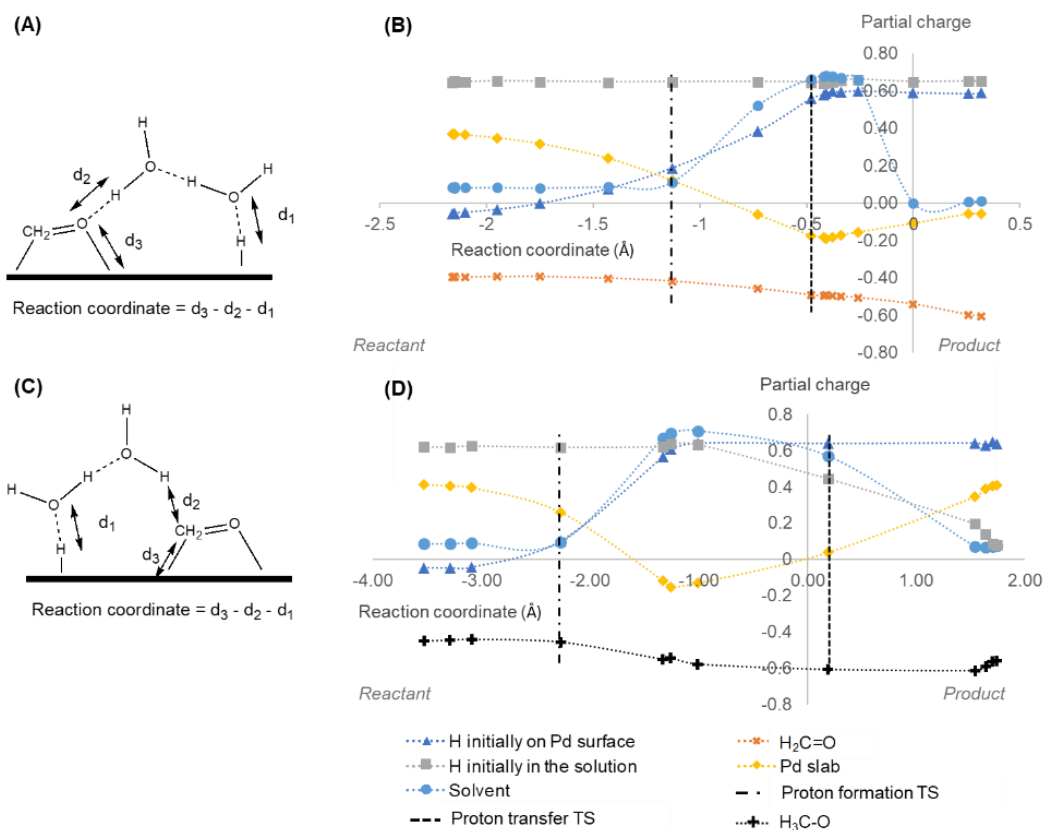


Figure S 6.7 (A) Reaction coordinate for the hydrogenation of formaldehyde to hydroxymethyl via proton coupled electron transfer. (B) Partial charge profile during hydrogenation of formaldehyde to hydroxymethyl via proton coupled electron transfer. (C) Reaction coordinate for the hydrogenation of formaldehyde to methoxy via proton coupled electron transfer. (D) Partial charge profile during hydrogenation of formaldehyde to methoxy via proton coupled electron transfer. (Note that these charge profiles were generated on a converged nudged elastic band pathway, which was set to a less strict

convergence criteria than the optimized structures, resulting in subtle differences in charges between the profiles here and those reported in Table 6.1)

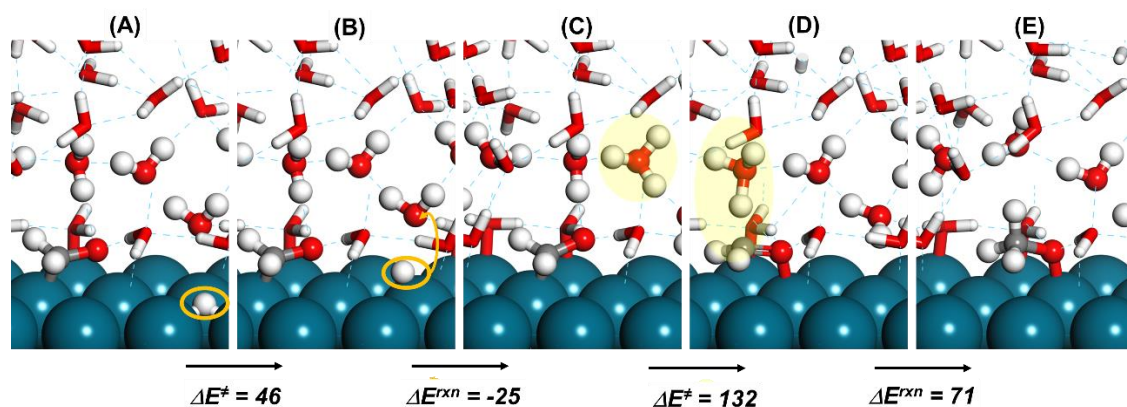


Figure S 6.8 Structures during the formation of methoxy intermediate from formaldehyde over Pd(111) in water via the proton coupled electron transfer pathway. (A) Reactant state showing adsorbed formaldehyde and hydrogen (orange circle). (B) Transition state to generate a hydronium ion near the surface (the orange arrow shows the movement of the surface hydrogen into the solution). (C) Product state for the hydronium ion near the surface. (D) Transition state during proton transfer to formaldehyde. (E) Product state for the methoxy intermediate.

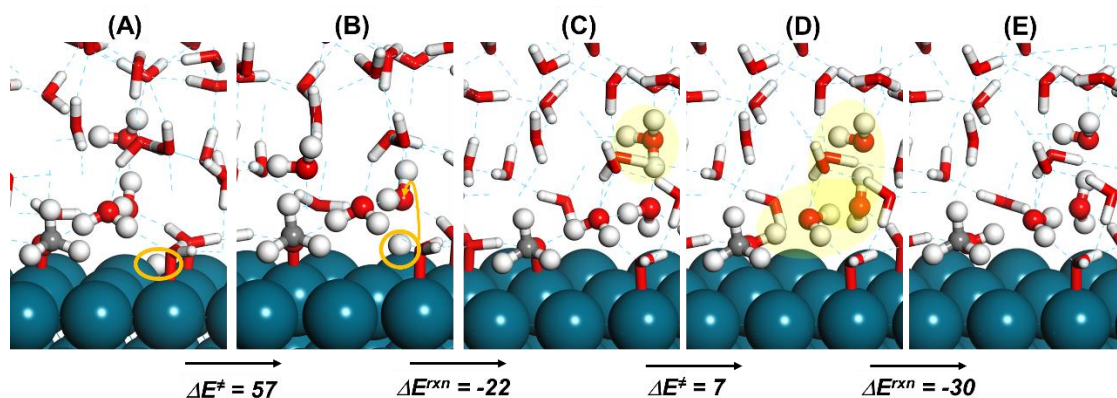


Figure S 6.9 Structures during the formation of methanol from the methoxy intermediate via the proton coupled electron transfer pathway over the Pd(111) surface in water. (A) Reactant state (surface hydrogen is circled in orange). (B) Transition state to generate a hydronium ion near the surface (the orange arrow shows the movement of the surface hydrogen into the solution). (C) Product state for the hydronium ion near the surface (highlighted in yellow). (D) Transition state during proton transfer to methoxy (path highlighted in yellow). (E) Product state for showing adsorbed methanol.

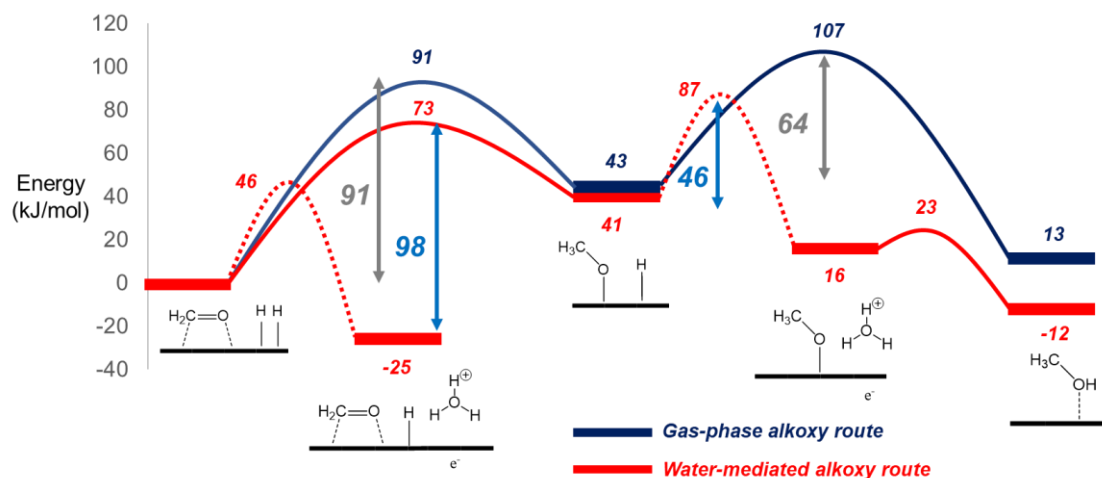


Figure S 6.10 The impact of water on the kinetically slower alkoxy route during hydrogenation of formaldehyde. Shown in dark blue is the gas-phase reaction and the corresponding barriers are marked in grey. C-H formation barrier in the gas phase is shown with respect to H^* and CH_2O^* (91 kJ/mol), while O-H formation barrier is shown with respect to H^* and CH_3O^* (64 kJ/mol). Shown in red is the water-mediated pathway and the barriers are marked in light blue. Dotted lines show the formation of protons and electrons. C-H formation barrier in the solution phase is shown with respect to H_3O^+ and CH_2O^* (98 kJ/mol). O-H formation reaction is benefitted by direct participation of water, while C-H formation reaction does not display a significant promotion.

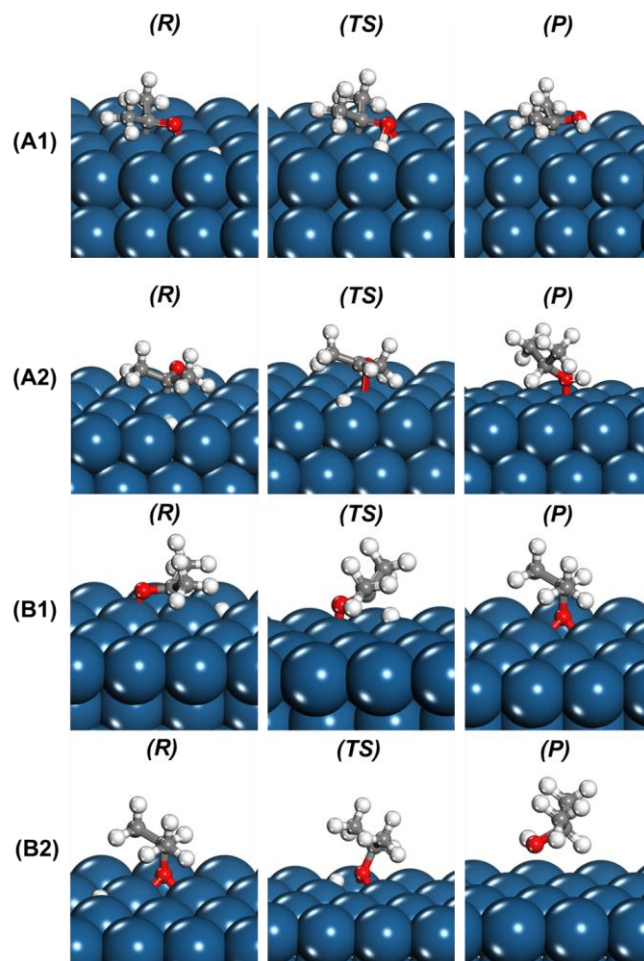


Figure S 6.11 Structures for gas-phase acetone hydrogenation over Pt(111). (R), (TS), and (P) stand for reactant, transition, product state respectively. A1 shows formation of hydroxyisopropyl from acetone. A2 shows hydrogenation of hydroxyisopropyl to isopropanol. B1 shows formation of isopropoxy from acetone. B2 shows hydrogenation of isopropoxy to isopropanol.

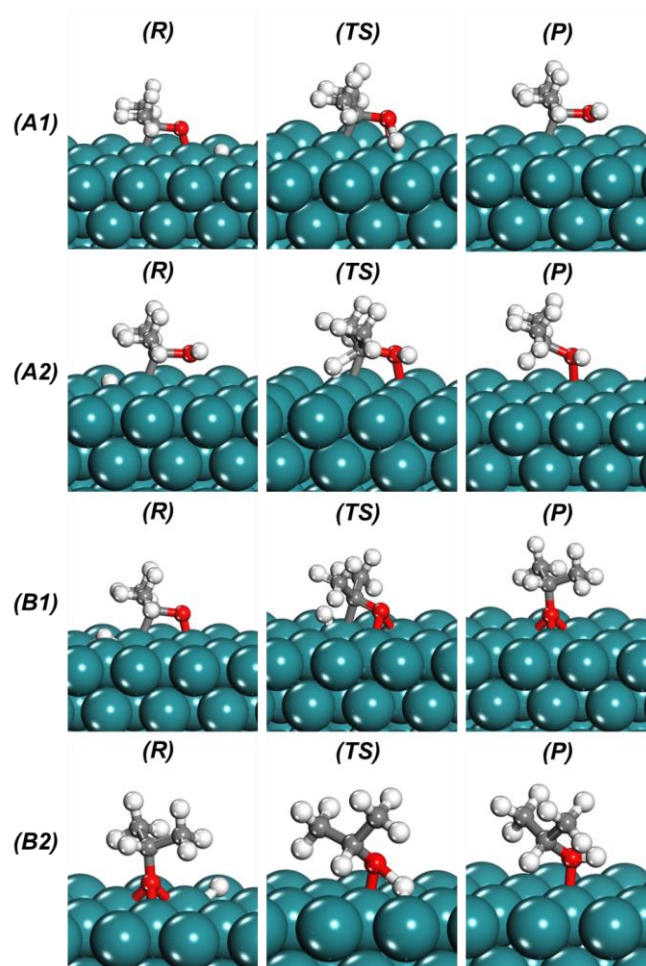


Figure S 6.12 Structures for gas-phase acetone hydrogenation over Ru(001). (R), (TS), and (P) stand for reactant, transition, product state respectively. A1 shows formation of hydroxyisopropyl from acetone. A2 shows hydrogenation of hydroxyisopropyl to isopropanol. B1 shows formation of isopropoxy from acetone. B2 shows hydrogenation of isopropoxy to isopropanol.

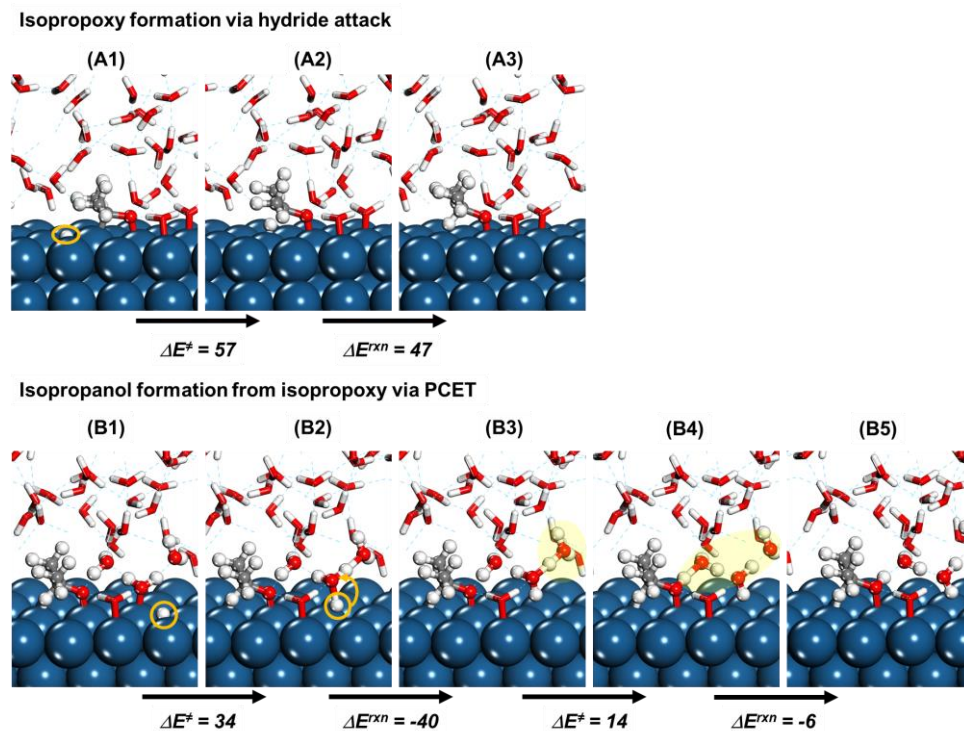
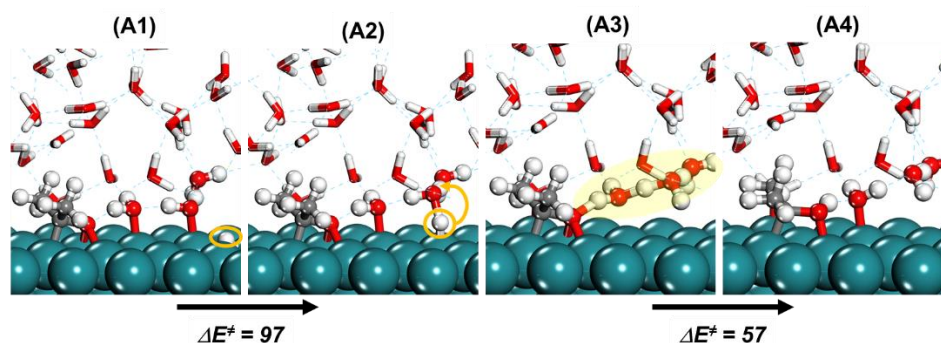


Figure S 6.13 Structures for the water-mediated acetone hydrogenation on Pt(111) via the alkoxy route. (A1) Reactant state showing adsorbed acetone and hydrogen (marked in orange). (A2) Transition state for the formation of isopropoxy via hydride attack. (A3) Product state showing adsorbed isopropyl. (B1) Reactant state showing adsorbed isopropoxy and hydrogen (marked in orange). (B2) Transition state for the reaction between water and hydrogen to form hydronium and electrons (the orange arrow shows the movement of the surface hydrogen into the solution). (B3) Product state for hydronium complex in water (highlighted in yellow). (B4) Transition state for proton and electron transfer to form the isopropanol (path shown in yellow). (B5) Product state for adsorbed isopropanol.

Hydroxyisopropyl formation via PCET



Isopropanol formation from hydroxyisopropyl via hydride attack

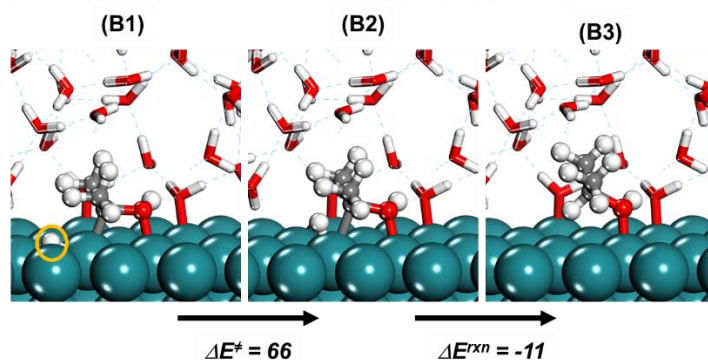


Figure S 6.14 Structures for the water-mediated acetone hydrogenation on Ru(001) via the hydroxyalkyl route. (A1) Reactant state showing adsorbed acetone and hydrogen (marked in orange). (A2) Transition state for the reaction between water and hydrogen to form hydronium and electrons (the orange arrow shows the movement of the surface hydrogen into the solution). (A3) A structure along the reaction coordinate showing transfer of electrons and protons (path highlighted in yellow) to acetone (over Ru, an isolated hydronium was not captured by DFT). (A4) Product state for adsorbed hydroxyisopropyl. (B1) Reactant state showing adsorbed hydroxyisopropyl and hydrogen (marked in orange). (B2) Transition state for the formation of isopropanol from hydroxyisopropyl via hydride attack. (B3) Product state showing adsorbed isopropanol.

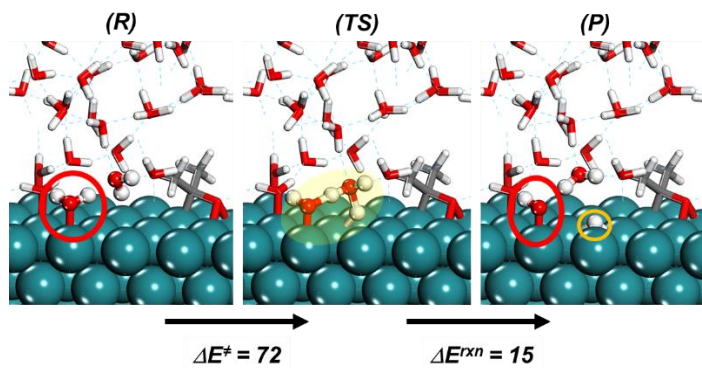


Figure S 6.15 Structures for Brønsted acid formation ($H_2O^* + * \rightarrow HO^* + H^*$) on Ru via water activation in a PCET reaction. Shown in red is the water molecule that activates to form OH^* .

7 Solvent Effects during Direct Synthesis of Hydrogen Peroxide over Palladium Catalysts

This chapter is adapted from Adams, J. S., Chemburkar, A., Priyadarshini, P., Riccuirdulli, T., Kulkarni, G., Lu, Y., Karim, A. M., Neurock, M., Flaherty, D. W. *Solvents Control Catalyst Phase and Reaction Mechanism During the Direct Synthesis of H₂O₂*. Under preparation.

Theoretical results presented herein were performed by AC under the supervision of MN.

7.1 Introduction

Direct synthesis of hydrogen peroxide from hydrogen and oxygen gases is an environmentally as well as economically attractive route to the commercial anthraquinone process.^{299–304} The commercial process uses anthraquinone, an organic substrate, and the downstream processing involves several, energy-intensive separation and concentration steps.³⁰¹ The direct route, on the other hand, not only employs greener solvents (such as water or methanol),⁵¹ but also involves few, low-energy separation units, providing an alternative economical, yet, greener route to substitute popular chlorinated oxidizers with H₂O₂.^{299,300,302–304} Direct synthesis, however, suffers from low selectivity towards H₂O₂, and therefore, seems less attractive from a commercial point of view. Low selectivity arises from irreversible O-O cleavage reactions that produce H₂O instead of H₂O₂.^{304,305} Selectivity towards H₂O₂ on supported catalysts has been shown to depend on a variety of factors including the choice of solvent,^{299,304,306} the presence of halide salts and mineral acids,^{307–310} as well as the presence and identity of a diluent gas.^{299,304} Further, little changes in these disparate factors has led to significant changes in the rate and selectivity of H₂O₂.^{299,302,303,306} Although several important insights have been revealed from previous studies, the explicit role of these factors in influencing the selective chemistry is still not well-understood.²⁹⁹ Rational design of catalysts requires systematic, fundamental studies of these factors, one at a time (herein, we look at the influence of solvents only). Such studies allow one to understand the nature of the metal-solution interface that drives the chemistry and aid in establishing explicit structure-reactivity rules that can be used to improve reactivity and selectivity to H₂O₂.

Herein, we examine the effects of different solvents- water and methanol, that are commonly utilized²⁹⁹ by many researchers during direct synthesis of H₂O₂. We combine kinetic isotope effects (KIE) measurements, density functional theory (DFT) simulations, steady-state rate measurements, and operando X-ray absorption spectroscopy (XAS) to understand fundamental similarities and differences that arise in these solvents and how these features result in significantly different H₂O₂ formation rates and selectivities observed herein on supported Pd catalysts as well as reported previously.²⁹⁹ The results show evidence for characteristically different pathways that involve direct participation from water and methanol molecules in proton coupled electron transfer (PCET) reactions. Water molecules co-catalyze formation of proton and electrons by heterolytic activation of Pd-H bonds, that are subsequently used to reduce oxygen gas, similar to biological hydrogenation reactions^{56,57} and proton-electron-exchange fuel-cells.³¹¹ Methanol molecules demonstrate more complex involvement by decomposing on the surface of metallic Pd forming surface-bound hydroxymethyl intermediates that co-catalyze oxygen reduction reactions in a bimolecular redox step, akin to mediator-based hydrogenation in biology,⁵⁸⁻⁶⁰ organic⁶¹ and electrochemical synthesis.^{62,311} These solvents are also found to induce phase transitions in the host Pd catalyst by forming subsurface hydrides (PdH_x). In methanol, subsurface hydride is detected during the entire range of examined H₂ pressure range and increases with H₂ pressure. On the contrary, PdH_x is detected in water only at high H₂ pressures. The results reveal a direct connection between H₂O₂ production rate and selectivity and PdH_x; the presence of PdH_x favors electron transfer reactions, but also disfavors O-O rupture, increasing both hydrogenation rates and selectivity to H₂O₂. Overall, we provide new molecular insights into the nature of Pd-solvent interfaces that drives O₂ reduction in water and alcoholic solvents. We demonstrate the deceptively complex role of solvents that can be engineered to improve reactivity and selectivity of O₂ reduction and extended to other metals and hydrogenation of other oxygenates.

7.2 Oxygen reduction reactions in methanol

7.2.1 Evidence for the presence and direct participation of organic residue during oxygen reduction reaction in methanol

Transient rate behavior of hydrogen peroxide production in pure methanol, pure water and a mixture of 70 % vol. of methanol over 0.05 % wt. Pd is reported in Figure 7.1. While, the turnover of H₂O₂ in water reaches a steady value, the turnover in the presence of methanol

is found to decrease over time, possibly due to site blocking caused by deposition of organic residue derived from methanol. However, the initial turnover in pure methanol can be recovered by externally adding H_2O_2 (see Figure S 7.1), that likely removes organic residue from the Pd surface. It is also worth noting that the turnover rate, remains higher in methanol (up to ~ 200 min) and methanol-water mixture (> 1200 min) compared to pure water suggesting differences in the way these solvents impact dioxygen reduction.

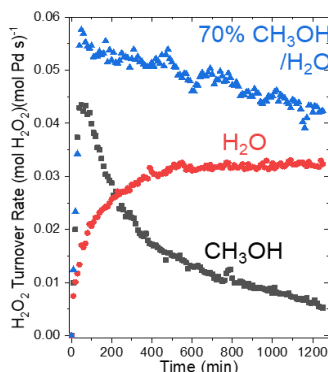
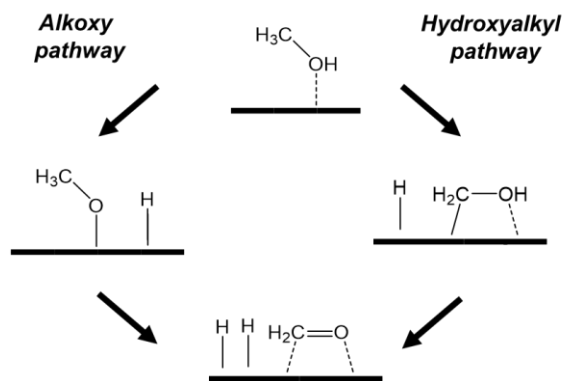


Figure 7.1 Transient H_2O_2 turnover rates (at 60 kPa H_2 and O_2) in pure methanol (black), pure water (red), and 70 % vol. methanol (blue). The rate in water reaches a steady value over time, while the rate in pure and 70 % vol. methanol exponentially decreases over time presumably via deposition of organic residue.

The composition of these organic residues was further analyzed via infrared spectroscopy revealing features consistent with decomposed CH_3OH , CH_2O , as well as other higher molecular weight organics possibly formed by condensation reactions of CH_2O (Figure S 7.2). Decomposition of methanol was also probed by transient ^1H NMR spectra in CD_3OD (Figure S 7.3) revealing scrambling between deuterons and hydrogen atoms (i.e. $\text{CD}_3\text{OD} \leftrightarrow \text{CD}_3\text{OH}$). The deuterated methyl group, however, did not scramble with hydrogen atoms. Given that considerable amount of formaldehyde is detected during direct synthesis (Figure S 7.4), activation of methanol appears to be irreversible in nature. It is evident that these organic species cause deactivation of the catalyst over a long time, but, some of these species could also participate in oxygen reduction reactions, resulting in higher initial turnover in pure methanol and 70 % vol. methanol (compared to pure water). Such transfer hydrogenation pathways between alcohols and carbonyl compounds via the Meerwein-Ponndorf-Verley mechanism³¹² have been proposed previously over metal

surfaces,²⁴⁹ zeolites,^{313–315} metal oxides,^{316–319} and homogeneous metal complexes.^{320,321} Similar pathways could lead to hydrogenation of O=O, instead of C=O.

Previous theoretical and experimental studies examining activation of methanol on Pt^{193,196,253,295,322} suggest that methanol activation proceeds via an initial C-H activation step to form the hydroxymethyl intermediate (CH₂OH*) that further undergoes a rate limiting O-H activation step to form formaldehyde CH₂O*. Previous studies on Pd-111 (Chapters 5 and 6) have revealed similar results, in that methanol activated via C-H bond cleavage followed by O-H bond activation. However, the Pd surface during O₂ reduction is not pristine, but covered with oxygen (O*) and subsurface hydride (H*s) as revealed by operando X-ray spectroscopy in a recent study.³²³ Therefore, methanol oxidation was modeled on Pd-111 having an oxygen coverage of 1/3 monolayer and a dissolved hydride of 1/3 monolayer. Similar to earlier chapters (5 and 6), both the hydroxyalkyl and alkoxy routes for methanol oxidation were examined (Scheme 7.1) and corresponding energetics and structures are reported in Figures 7.2-7.4). Adsorption of methanol on the model Pd surface is estimated to occur by releasing -59 kJ/mol of energy. Subsequent C-H activation on methanol to generate the hydroxymethyl intermediate (CH₂OH*) is found to be slightly faster compared to O-H activation to form the methoxy intermediate (CH₃O*) by 5 kJ/mol. Both these reactions appear to be endothermic, however, methoxy formation is found to be less favored by 31 kJ/mol. Subsequent activation of the hydroxymethyl intermediate occurs with a lower intrinsic barrier (91 kJ/mol) compared to activation of methoxy (101 kJ/mol). The 2H* and CH₂O* intermediates that result from methanol activation can subsequently desorb with 22 and 42 kJ/mol of energy respectively. (Note that O-H activation reactions in both these pathways were simulated using the proton-coupled-electron-transfer mechanism (Figures 7.3(B) and 7.4(A)) studied in Chapter 6. A neighboring methanol molecule was used in these routes to activate the O-H bond on adsorbed methanol, forming methoxonium ions (CH₃OH₂*) in the transition state. These methoxonium ions quickly deposit protons back on the surface of Pd, which then combine with electrons from the metal and from hydrogen atoms (H*). Studies by Masel and co-workers³²⁴ provide an experimental evidence for the formation of methoxonium cations during methanol dehydration on Pt-110 further supporting the route examined here.)



Scheme 7.1 Methanol activation on Pd surface via alkoxy and hydroxyalkyl pathways.

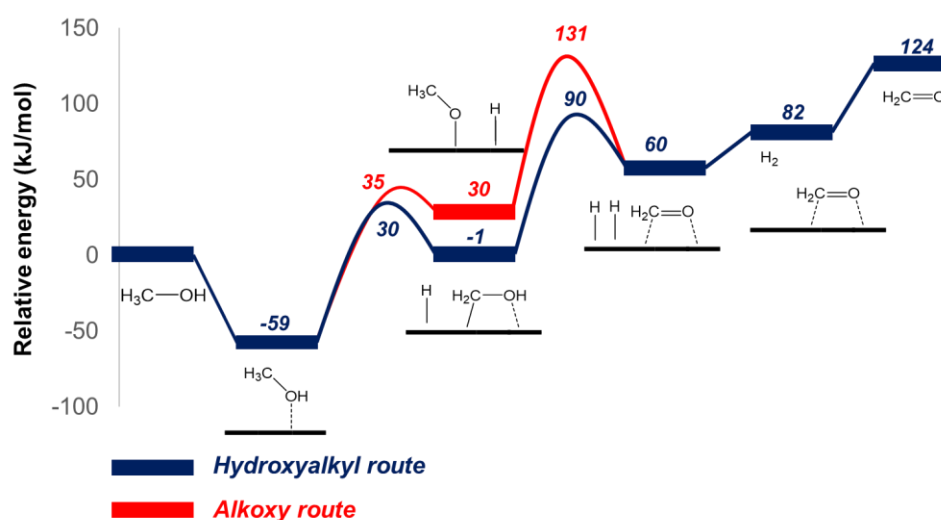


Figure 7.2 Reaction energy diagram for methanol activation in condensed phase over Pd-111 surface covered with 1/3 monolayer of atomic oxygen and 1/3 monolayer of sub-surface hydride.

A more detailed analysis suggests that the hydroxymethyl route seems to be the favored route for methanol activation consistent with previous reports,^{193,196,253,295,322} however, activation barriers obtained here appear to be higher than reported over pristine Pd-111 surfaces. Higher activation barriers and reaction energies are a result of high coverage of O^* that makes direct activation of methanol harder on the partially oxidized Pd surface. Energetics shown in Figure 7.2 suggest that methanol will likely not oxidize to form formaldehyde due to high activation barrier for hydroxymethyl activation (91 kJ/mol). However, experiments do show significant generation of formaldehyde (Figure S 7.4), suggesting that alternative mechanisms might exist for irreversible methanol activation.

Therefore, partially oxidized product of methanol- hydroxymethyl was tested as a hydrogen transfer agent, hydrogenating O_2^* and HOO^* to HOO^* and $HOOH^*$ respectively, concomitantly forming adsorbed formaldehyde in a Meerwein-Ponndorf-Verley mechanism³¹² (Scheme 7.2)

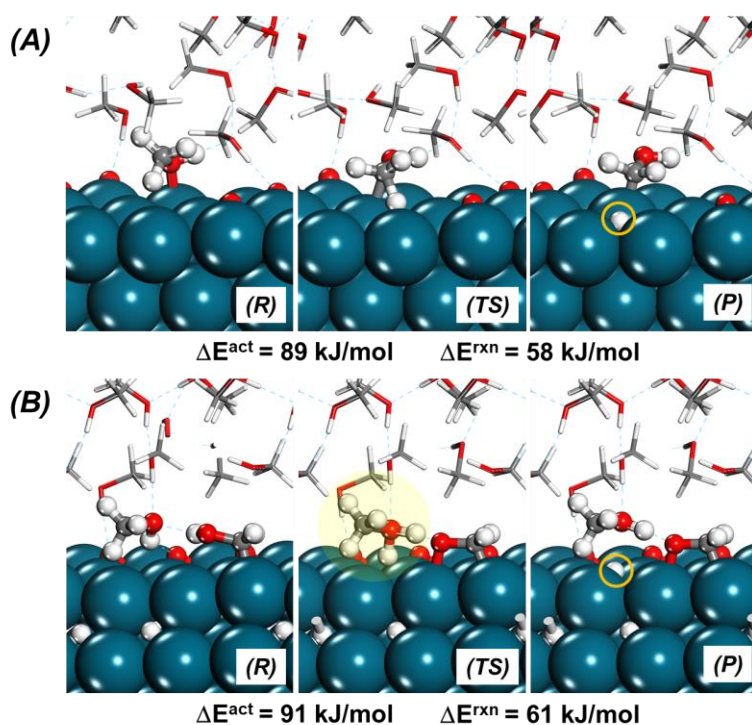
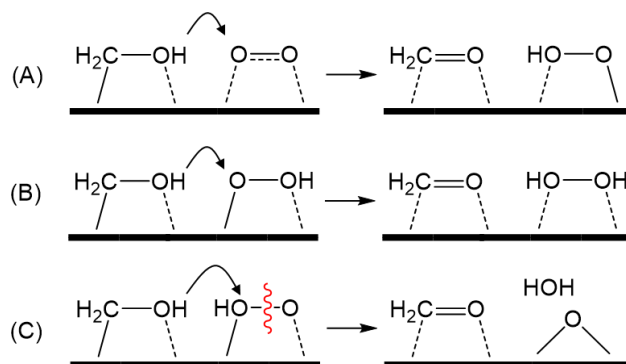


Figure 7.3 Methanol activation via the hydroxyalkyl pathway. (A) C-H activation on methanol to form the hydroxymethyl intermediate (B) O-H activation on the hydroxymethyl intermediate to form formaldehyde using the proton-coupled-electron transfer mechanism. The methoxonium ion ($CH_3OH_2^+$) is highlighted in yellow, and hydrogen atom on the surface is marked in orange.



Scheme 7.2 MPV type bimolecular routes leading to activation of hydroxymethyl (CH_2OH^*) to (A) CH_2O^* and HOO^* (B) CH_2O^* and HOOH^* (C) CH_2O^* , HOH and O^* . The arrow shows movement of hydrogen from CH_2OH^* to the reacting substrate.

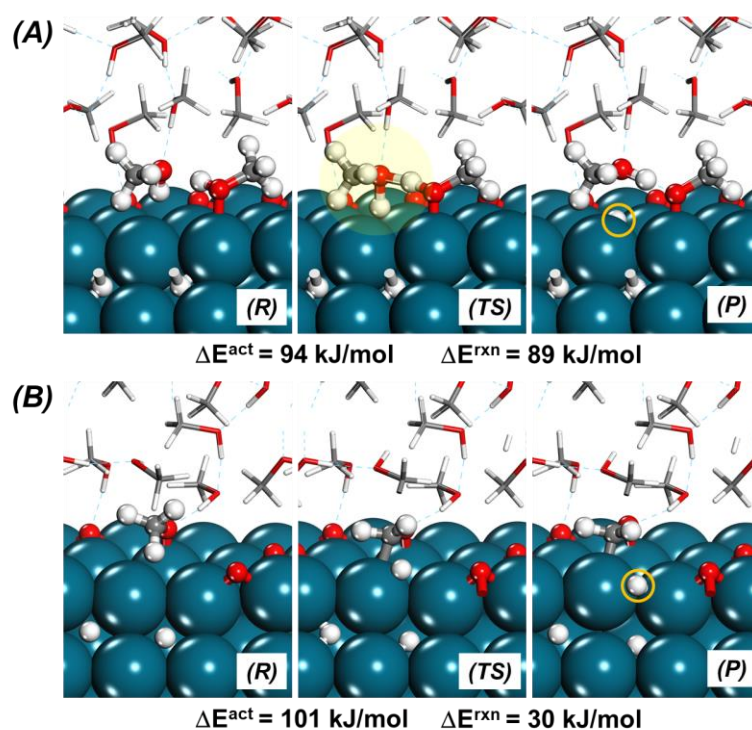


Figure 7.4 Methanol activation via the alkoxy pathway. (A) O-H activation on the methanol to form the methoxonium ion (CH_3OH_2^+) highlighted in yellow. (B) C-H activation on methoxy to form formaldehyde. Hydrogen atom on the surface is marked in orange.

DFT calculations show that proton on the CH_2OH^* intermediate can be readily transferred to O_2^* or HOO^* with low intrinsic activation barriers (Scheme 7.2 and Figure 7.5), forming HOO^* , HOOH^* or HOH^* and O^* along with formaldehyde (CH_2O^*). This intrinsic activation barrier is much lower than direct CH_2OH^* activation on the Pd surface to form CH_2O^* and H^* (91 kJ/mol, see Figure 7.3(B)) as well as hydrogenation of CH_2OH^* by H^* to form methanol (CH_3OH^*) (31 kJ/mol. See Figure 7.3(A)). This suggests that CH_2OH^* intermediates that form via methanol decomposition, can react faster with co-adsorbed O_2^* or HOO^* , instead of directly activating on the surface or reversibly forming methanol again. This would explain generation of formaldehyde seen experimentally, but, in an elementary step that simultaneously forms O-H bonds. Further, these formaldehyde molecules can undergo rapid hydrogenation by H^* regenerating CH_2OH^* intermediates,

which again transfer hydrogen atoms over to O_2^* or HOO^* instead of forming methanol. As such, methanol molecules that activate to form hydroxymethyl may not be able to reversibly form methanol due to low barriers for transfer hydrogenation steps consistent with irreversibility of methanol activation that is seen experimentally (Figure S 7.3). Therefore, the results show that by coupling methanol activation (oxidation) with dioxygen reduction, irreversible decomposition of methanol forming formaldehyde can be rationalized. In addition, very facile bimolecular oxygen reduction routes resulting in oxygen reduction are revealed, which are compared to mechanisms proposed in the literature.

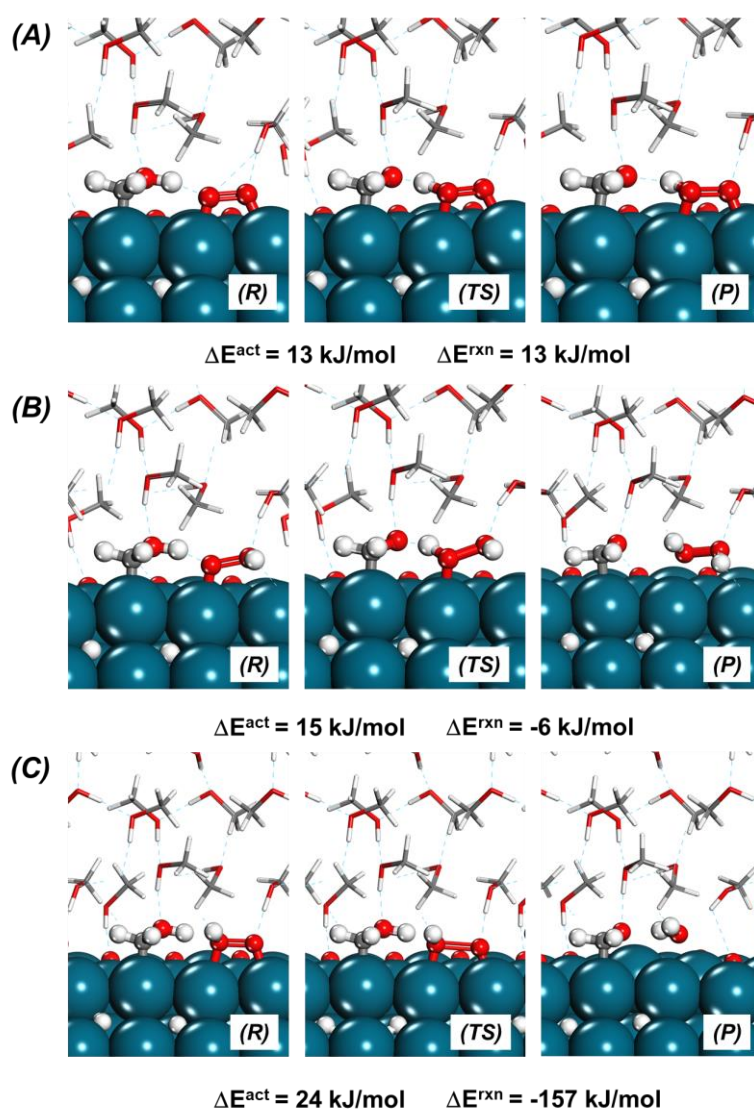


Figure 7.5 Optimized structures for CH_2OH^* catalyzed formation of (A) HOO^* and CH_2O^* , (B) $HOOH^*$ and CH_2O^* , (C) HOH^* , O^* and CH_2O^* .

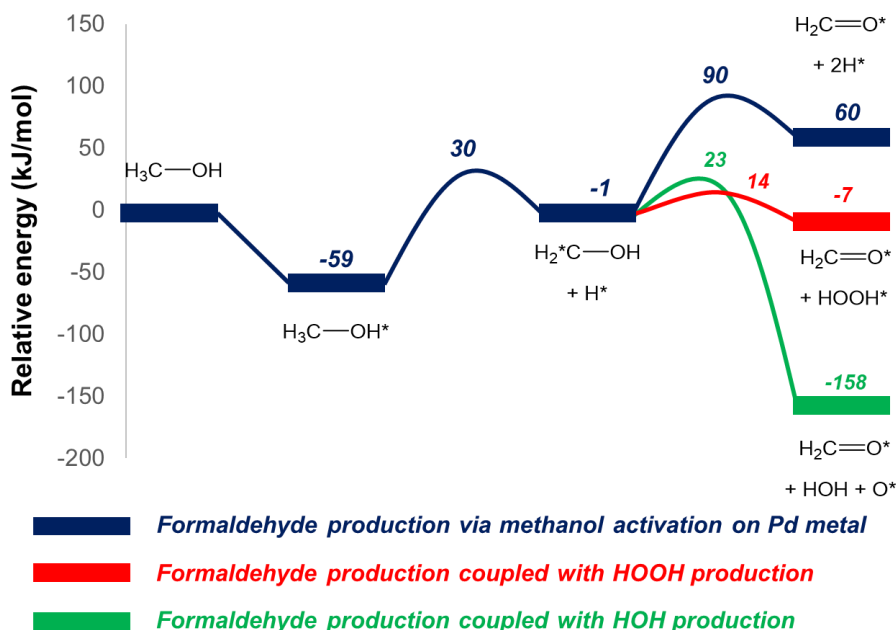


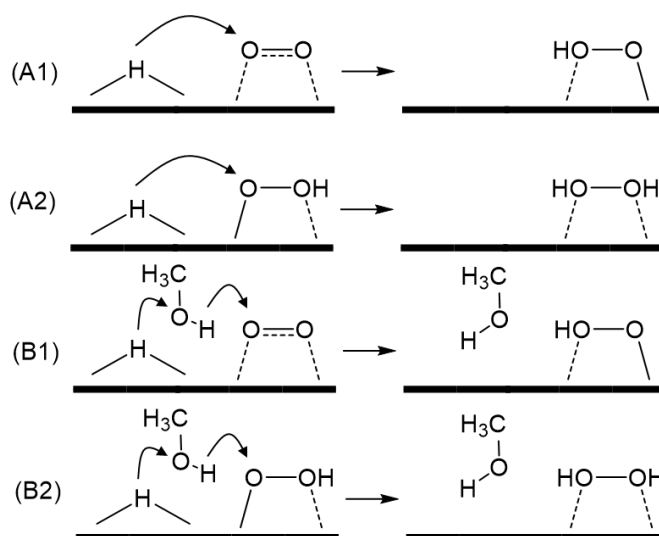
Figure 7.6 Energetics for formaldehyde formation using different routes. Shown in blue is the conventional route examined directly over Pd sites. Shown in red is the MPV mechanism forming HOOH^* and CH_2O^* (Scheme 7.2(B)). Shown in green is the MPV mechanism forming HOH^* , O^* and CH_2O^* (Scheme 7.2(C)).

7.2.2 Comparison of hydrogen peroxide production by different routes

Oxygen reduction appears to be very similar to C=O and C=C bond hydrogenation. Therefore, many studies have modeled oxygen reduction using the conventional Langmuir-Hinshelwood surface-mediated mechanism.^{305,325,326} In such a mechanism, hydrogen atoms are directly added from the catalyst surface to the double bond. In a recent study by Wilson and Flaherty, a proton coupled electron transfer pathway was proposed based on steady state rate measurements and the fact that O_2 reduction was active only in protic media. Both these routes are examined here and schematically shown in Scheme 7.3. The corresponding energetics is shown in Figure 7.7.

DFT simulations show that hydrogen peroxide production via the Langmuir-Hinshelwood surface mediated mechanism (Scheme 7.3(A1) and (A2), Figure 7.7(A1) and (A2)) involves activation barriers of ~50 kJ/mol. Lower activation barriers (~30 kJ/mol) are obtained if these reactions are instead carried out with the proton coupled electron-transfer mechanism (Scheme 7.3(B1) and (B2), Figure 7.7(B1) and (B2)) enabled by the formation of methoxonium cation (CH_3OH_2^+) seen experimentally by Masel.³²⁴ From Figure 7.5 (A)

and (B), we see that activation barriers are further lowered (by ~ 15 kJ/mol) when these reactions are mediated by surface-bound hydroxymethyl intermediates. DFT simulations, therefore, predict that among the examined routes the kinetically fastest involves reduction of oxygen via hydroxymethyl intermediates in a MPV fashion. Oxygen reduction appears to be kinetically coupled with methanol oxidation in a series of redox steps, also consistent with irreversible decomposition of methanol to formaldehyde.



Scheme 7.3 Formation of hydrogen peroxide via surface-mediated mechanism (A1 and A2) and via proton-coupled electron transfer (B1 and B2).

Bader charge analysis²⁸⁰ of the reaction co-ordinate involving hydrogen transfer from CH_2OH^* to O_2^* and HOO^* suggest that these reactions are also proton coupled electron transfer reactions (Figure 7.8). Charge analysis shows that the transferring hydrogen in both HOO^* and HOOH^* formation remains protonic in character (Bader charge = +0.6). In addition, as this proton is transferred from CH_2OH^* to O_2^* or HOO^* , there is an increase in the charge density of the CH_2O^- group on CH_2OH^* (by +0.3). Charge is simultaneously seen to transfer to the O_2^- and HO_2^- groups during HOO^* and HOOH^* formation respectively, since these groups become more negative. Therefore, the transfer of proton is found to be accompanied with electron transfer from CH_2OH^* group into the reacting group, suggesting CH_2OH^* group is functioning like a proton coupled electron transfer mediator.

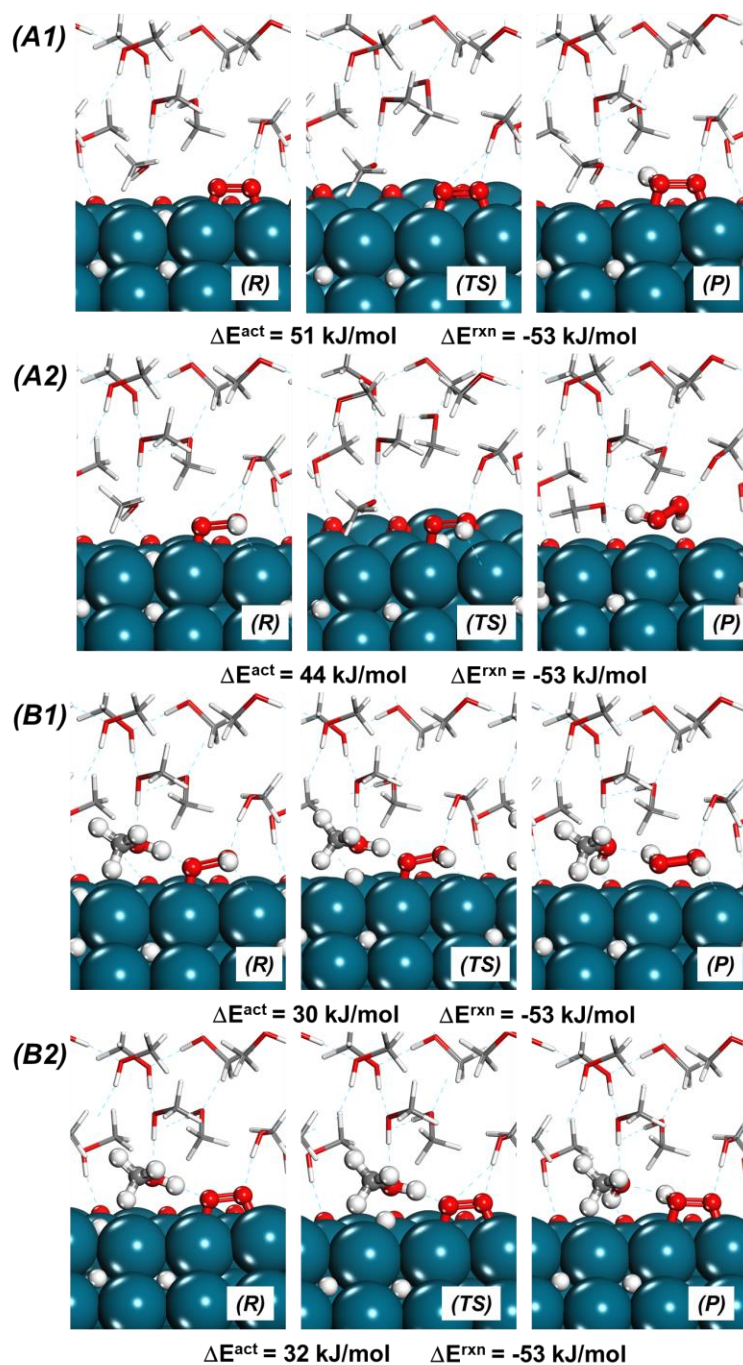


Figure 7.7 Structures for hydrogenation of oxygen to hydrogen peroxide with the Langmuir-Hinshelwood surface mediated mechanism (A1 and A2) and proton coupled electron transfer using a methanol molecule (B1 and B2).

Mediator-based proton and electron transfer chemistries are well-established in biological and organic transformations.^{58–61} The ability of CH_2OH^* group on Pd to donate e^- and H^+ was therefore compared to well-known mediators such as NADPH and TEMPOH. This

was captured by estimating dehydrogenation energies of these mediators as shown in Equations 7.1-7.2. Removal of one hydrogen radical accounts for concerted removal of one proton and one electron from the mediator. The calculated energies tabulated in Table 7.1 and the corresponding structures are shown in Figure 7.9. DFT calculations basically show that the hydroxymethyl intermediate on Pd has similar dehydrogenation energy as these well-known mediators.



$$\Delta E = E[\text{M} \cdot] + E[\text{H} \cdot] - E[\text{M-H}] \quad (7.2)$$

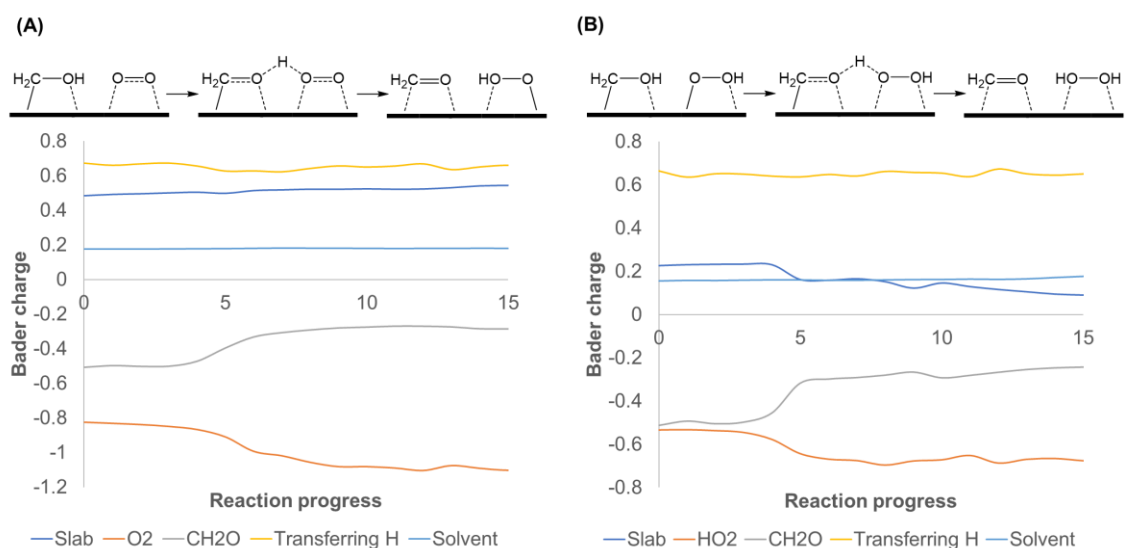


Figure 7.8 Bader charge analysis of the reaction coordinate for hydrogen transfer between (A) CH₂OH* and O₂* (B) CH₂OH* and HOO*.

Table 7.1 Dehydrogenation energies of different mediators.

Mediator	DHE (kJ/mol)
Hydroxymethyl on Pd	295
TEMPOH	285
NADPH	310

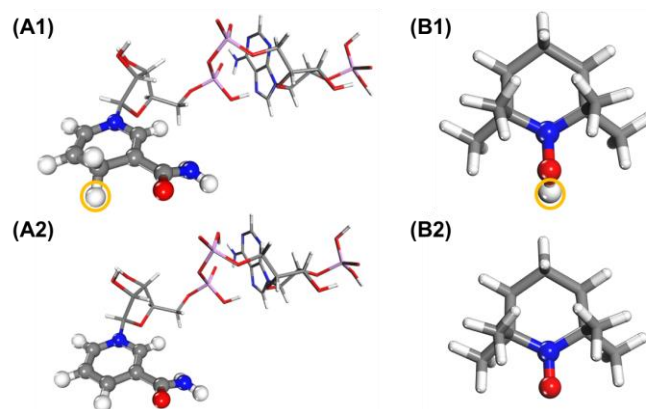


Figure 7.9 Structures of (A1) NADPH (A2) NADP (B1) TEMPOH (B2) TEMPO.

Previous in operando EXAFS measurements³²³ show existence of dissolved hydride in the Pd lattice during H_2O_2 synthesis in water. In methanol, similar features of PdH_x are seen (Figure 7.10(C)). Dehydrogenation energy of CH_2OH^* on the Pd surface was subsequently calculated for different concentrations of dissolved hydride to understand its role in altering reactivity as well as selectivity. Gas-phase dehydrogenation energies of CH_2OH^* for different concentrations of dissolved hydride is shown in Table 7.2. Dehydrogenation energy is seen to decrease slightly with an increase in hydride concentration, therefore, it seems that dissolved hydride may increase rate of PCET reaction.

Table 7.2 Influence of the dissolved hydride on dehydrogenation energy of CH_2OH^* intermediate on Pd. The surface coverage of O^* is kept constant at 1/3 monolayer.

% ML dissolved hydride	Calculated DHE (kJ/mol)
0	302
0.33	299
0.44	296
0.67	293

Detailed DFT calculations in the condensed phase were performed to simulation PCET reactions producing hydrogen peroxide for varying hydride concentrations (Table 7.3). The results show that the formation of HOOH^* becomes faster as activation barriers appear to decrease with increasing hydride concentration. Incorporation of subsurface hydride has been shown experimentally to decrease electron affinity of Pd.³²⁷ Therefore, by increasing

the concentration of dissolved hydride, electron transfer gets promoted, accelerating PCET reactions between CH_2OH^* and $\text{O}_2^*/\text{HOO}^*$.

Table 7.3 Influence of the dissolve hydrogen sublayer on the energetics of HOO^* and HOOH^* formation in methanol as solvent (surface coverage of O^* was constant at 1/3 ML),

Dissolved hydrogen concentration	HOO* formation		HOOH* formation	
	ΔE^{act} (kJ/mol)	ΔE^{rxn} (kJ/mol)	ΔE^{act} (kJ/mol)	ΔE^{rxn} (kJ/mol)
0	21	21	19	2
1/3 ML	13	13	15	-6
2/3 ML	10	10	8	-16

The influence of dissolved hydride was also examined on the selectivity of H_2O_2 production. Selectivity to H_2O_2 is reduced by irreversible O-O bond cleavage reactions that produce water. While detailed examination of different O-O cleavage pathways will be a part of future effort, here, we present energetics of HOO^* decomposition reaction only, mediated by CH_2OH^* at different concentrations of dissolved hydride (Scheme 7.2(C)). Table 7.4 shows that the decomposition reaction becomes harder as subsurface hydride concentration increases. Subsurface hydride seems to oxidize the Pd surface, thereby making further oxidation by O^* harder. Therefore, the subsurface hydrogen layer is found to play an important in increasing the activation barrier of the O-O cleavage reaction, while simultaneously reducing activation barrier for the selective hydrogen transfer reaction forming H_2O_2 .

Table 7.4 Activation barriers and reaction energies for HOO^* decomposition $\text{HOO}^* + \text{CH}_2\text{OH}^* \rightarrow \text{HOH}^* + \text{O}^*$ at different concentrations of the dissolved hydrogen sublayer.

Dissolved hydrogen	ΔE^{act} (kJ/mol)	ΔE^{rxn} (kJ/mol)
0	18	-157
1/3 ML	24	-157
2/3 ML	29	-146

Theoretical predictions suggest that dissolved hydride can improve selectivity towards H_2O_2 formation, consistent with experimental results in methanol and water (Figure 7.10). While in methanol, PdH_x is found to prevail in the range of examined concentrations, the selectivity is found to improve at higher pressures of H_2 , where higher hydride concentration is expected (Figure 7.10(A) and (C)). In water, the effect of PdH_x is more

evident. As seen, the rate as well as selectivity discontinuously increase to H₂O₂ with the formation of PdH_x. Detailed study of oxygen reduction in water as solvent is presented in subsequent sections.

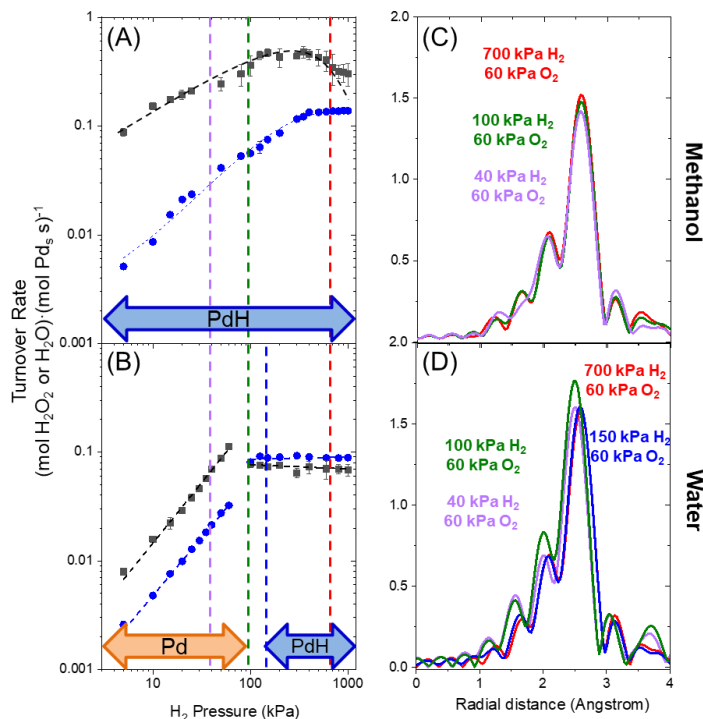


Figure 7.10 H₂O₂ (blue) and H₂O (black) formation rates as function of H₂ pressure (5-1000 kPa) in (a) methanol and (b) water at 60 kPa O₂. Complementary EXAFS spectra were conducted in operando at comparable H₂ and O₂ pressures in both (c) methanol and (d) water. All measurements were performed on silica-supported Pd catalysts (278 K, 35 cm³ min⁻¹ solvent).

7.2.3 More evidence for the proton-coupled-electron-transfer route in methanol

In previous sections, the experimental observation of irreversible methanol decomposition during H₂O₂ synthesis was probed using DFT to reveal an MPV-type bimolecular mechanism that may exist between hydroxymethyl intermediates and O₂^{*}/HOO^{*}. Analysis of other mechanisms that have been previously proposed suggested that the hydroxymethyl route would be kinetically faster. In this section, a series of experimental results are presented, which further support the hydroxymethyl-catalyzed mechanism.

H₂O₂ turnover rates are found to be different between CH₃OH and CH₃OD. The rate is 1.4 times higher in CH₃OH compared to CH₃OD, resulting in a primary kinetic isotope effect (KIE). Further, experiments done in CH₃OH with H₂ and D₂ also result in a primary KIE, here, the rate is higher in H₂ by a factor of 3.5. These results suggest that the proton on methanol as well as hydrogen on the Pd surface are involved in the rate-determining step.

The hydroxymethyl intermediate (CH₂OH*) that is generated by methanol activation irreversibly forms formaldehyde (CH₂O*) in a rate-limiting step by donating its proton (and electron) to O₂* or HOO*. The resulting formaldehyde molecule can be subsequently reduced by a surface hydrogen (H*), regenerating the hydroxymethyl intermediate as well as completing the catalytic cycle. The proton on hydroxymethyl, is therefore, in fact a hydrogen atom from the catalyst surface. Within the hydroxymethyl mechanism, the proton on hydroxymethyl, as well as surface hydrogen appear to participate in oxygen reduction consistent with the primary KIE observed with CH₃OH/CH₃OD and H₂/D₂. KIE estimations from DFT for the elementary steps CH₂OH* + O₂* → CH₂O* + HO₂* and CH₂OH* + HO₂* → CH₂O* + H₂O₂* result in values of 4.27 and 3.75 consistent with experiments.

The route involving the methoxonium ion (CH₃OH₂⁺) (Scheme 7.3(B1) and (B2) and Figure 7.7(B1) and (B2)), also seems to involve the proton on methanol as well as surface hydrogen. The transition state, in this case, shows formation of the methoxonium ion and an electron. The proton on methoxonium is transferred to O₂* or HO₂* after the transition state along the reaction coordinate, simultaneously with an electron from the metal. Estimations from DFT show that between H₂/D₂ in CH₃OH, KIE of 2.31 and 2.15 is obtained for the elementary steps H* + CH₃OH + O₂* → CH₃OH + * + HO₂* and H* + CH₃OH + HO₂* → CH₃OH + * + H₂O₂* respectively, consistent with experiments. However, between CH₃OH and CH₃OD with H₂ the same elementary steps demonstrate a secondary KIE of 1.22, inconsistent with experiments. Errors in KIE estimations from DFT under the quasi-harmonic approximation as well as experimental errors preclude a definitive conclusion regarding a specific proton coupled electron transfer mechanism for hydrogen peroxide synthesis, instead both these PCET reactions are supported by these observations.

Comparing theoretical activation barriers for both these routes, the hydroxymethyl route (Figure 7.5) seems to offer a kinetically faster route than the methoxonium ion route (Figure 7.7). Further, irreversible decomposition of methanol to formaldehyde can be

explained if hydroxymethyl is involved in a kinetically relevant step during oxygen reduction reaction. Formation of hydroxymethyl and its subsequent involvement in oxygen reduction is further supported by experiments done in DI water in the presence and absence of water (Figure 7.11), that show higher rates in the presence of formaldehyde. Water carries out oxygen reduction in a similar mechanism as the methoxonium ion mechanism by forming hydronium ions and electrons along the reaction coordinate. DFT results show that methanol and water (Figure 7.12(B1) and 7.13(B2)) have very similar activation barriers of ~ 30 kJ/mol and the enhancement in rates can be explained theoretically if hydroxymethyl catalyzed route is activated since involves lower activation barriers.

DFT results, along with multiple experimental observations, therefore, support the existence of a hydroxymethyl-catalyzed route during direct synthesis of hydrogen peroxide from H_2 and O_2 gases over supported Pd catalysts. The hydroxymethyl intermediate acts as a proton coupled electron transfer agent and mediates the formation of H_2O_2 in a series of redox reactions. Hydrogen atom on the Pd surface is oxidized to form protons and electrons on the hydroxymethyl intermediate during the reduction of formaldehyde. The hydroxymethyl intermediate then gets oxidized back to formaldehyde while reducing oxygen in an MPV-type mechanism (Scheme 7.4).

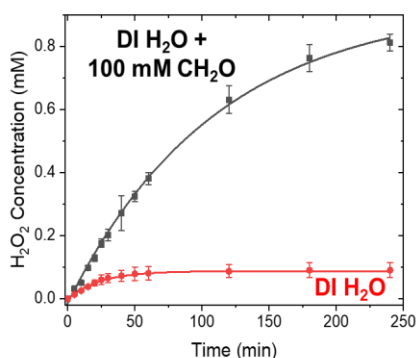
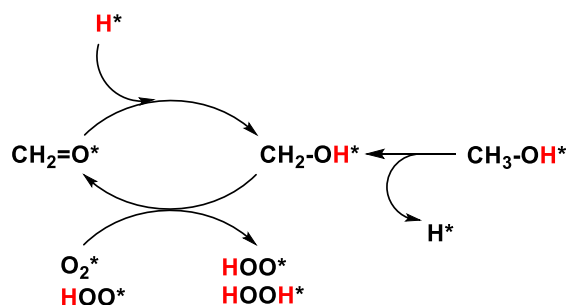


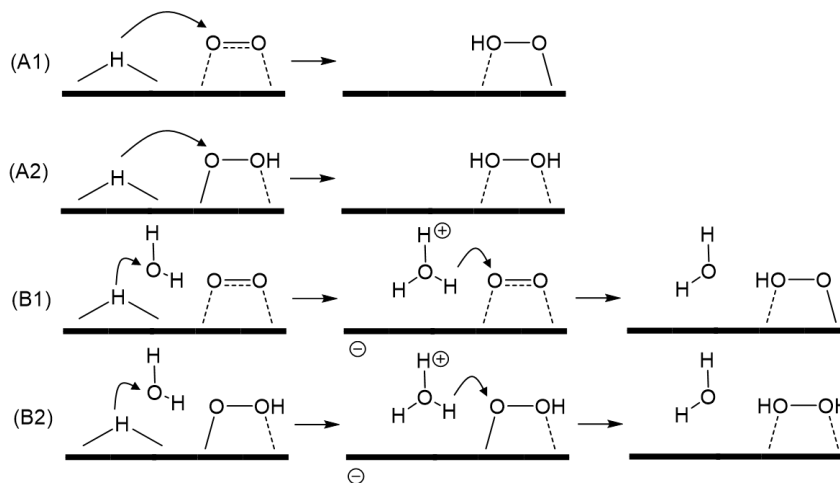
Figure 7.11 H_2O_2 concentration as a function of time in DI water in the presence and absence of formaldehyde.



Scheme 7.4 Proposed mechanism for oxygen reduction over Pd in methanol. Hydrogens shown in red are utilized in O-H formation reactions consistent with KIE measurements.

7.3 Oxygen reduction reactions in water

We examine two pathways for hydrogenation of dioxygen (Scheme 7.5). In the first pathway, we explore the conventional Langmuir-Hinshelwood surface-mediated pathway, wherein O_2^* and HOO^* intermediates are directly hydrogenated using a hydride (H^*) on the host Pd catalyst (Scheme 7.5(A1) and (A2)). In the second pathway, we explore the proton coupled electron transfer route, where, a surface hydride reacts with a co-adsorbed water molecule to form a proton in solution and an electron that resides in the host Pd catalyst. These protons and electrons are subsequently transferred to O_2^* and HOO^* catalyzing O-H formation reactions (Scheme 7.5(B1) and (B2)).



Scheme 7.5 Hydrogenation of dioxygen to hydrogen peroxide in water via Langmuir-Hinshelwood surface mediated mechanism (A1) and (A2) and via proton-coupled-electron-transfer mechanism (B1) and (B2).

Figures 7.12 and 7.13 report reactant, transition, and product state structures along with corresponding energetics for both the hydrogenation steps for both these routes on 111 Pd surfaces having oxygen coverage of 1/3 ML (O^*) and dissolved hydrogen of 1/3 ML (H^* s). The proton coupled electron transfer pathway appears to be the kinetically favored mechanism since the activation barrier is 10 kJ/mol lower than the surface-mediated pathway over examined surfaces. Within the proton coupled electron transfer route, two elementary steps are involved, first protons and electrons are generated (Figures 7.12(B1) and 7.13(B1)), that are subsequently delivered to the adsorbed surface intermediate (Figures 7.12(B2) and 7.13(B2)). Among the two elementary steps, the generation of proton and electrons appears to be much harder since the transfer of these involve negligible activation barriers.

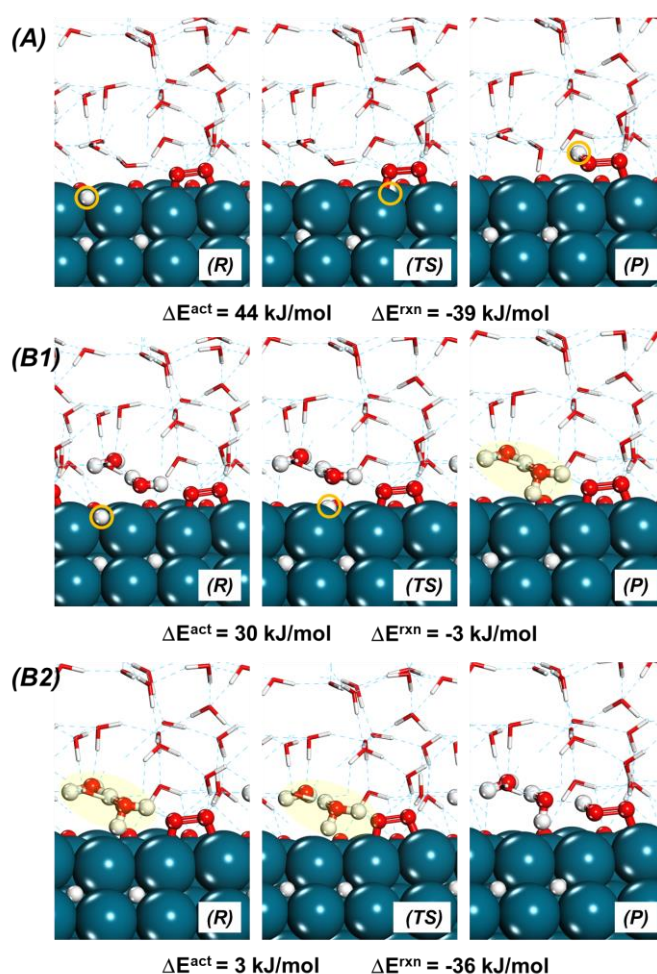


Figure 7.12 HOO^* formation pathway via (A) Surface-mediated route (B) Proton-coupled-electron-transfer route; B1 shows proton/electron generation, while B2 shows proton/electron transfer to O_2^* . Surface conditions of 1/3 O^* ML and 1/3 H^* s were simulated.

Surface hydrogen atom that is transferred is marked in orange. Hydronium ion is highlighted in yellow.

After identifying the kinetically faster mechanism, we explore the effects of dissolved surface hydrogen on the activation barriers and reaction energies of the individual hydrogenation steps. These effects are reported in Table 7.5. While activation barriers do not change significantly for HOO* formation, their values decrease with an increase in concentration of dissolved hydride for HOOH* formation, which is the harder hydrogenation step. Overall, the reaction energies become more exothermic for both hydrogenation steps consistent with increased electron transfer from the Pd surface with an increase in subsurface hydrogen concentration. Effect of the dissolved hydride was simulated next over the selectivity of oxygen reduction. Only HOO* decomposition reaction was simulated herein via the proton-coupled-electron-transfer mechanism. The results (Figure 7.14 and Table 7.6) show that dissolved hydride increases barrier for O-O cleavage reaction similar to results in methanol. Dissolved hydride in water as well, tends to oxidize the Pd surface and makes subsequent oxidation by O* harder. The results shown herein demonstrate the dual role of subsurface hydrogen- promoting the formation of HOOH* as well as hindering the formation of H₂O* consistent with experiments that show rates and selectivity discontinuously increase in water when PdH_x is formed (Figure 7.10).

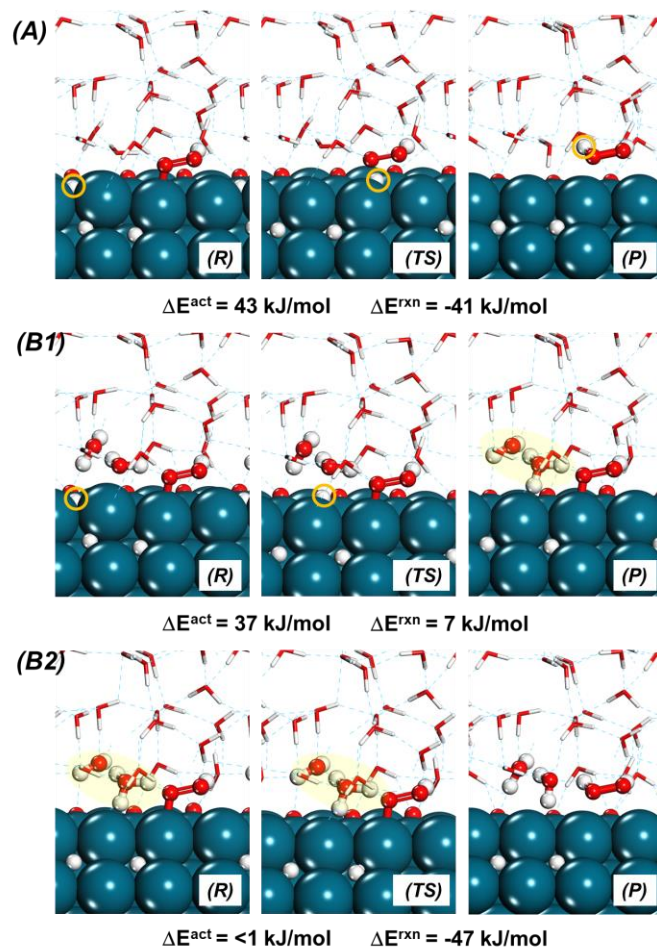


Figure 7.13 HOOH^* formation pathway via (A) Surface-mediated route (B) Proton-coupled-electron-transfer route; B1 shows proton/electron generation, while B2 shows proton/electron transfer to HO_2^* . Surface conditions of $1/3 \text{ O}^*$ ML and $1/3 \text{ H}^*$ s were simulated. Surface hydrogen atom that is transferred is marked in orange. Hydronium ion is highlighted in yellow.

Table 7.5 Influence of the dissolve hydrogen sublayer on the energetics of HOO^* and HOOH^* formation in water as solvent (surface coverage of O^* was constant at $1/3 \text{ ML}$).

Dissolved hydrogen concentration	HOO^* formation		HOOH^* formation	
	ΔE^{act} (kJ/mol)	ΔE^{rxn} (kJ/mol)	ΔE^{act} (kJ/mol)	ΔE^{rxn} (kJ/mol)
0	30	-35	39	-40
$1/3 \text{ ML}$	30	-39	37	-40
$2/3 \text{ ML}$	30	-48	33	-46

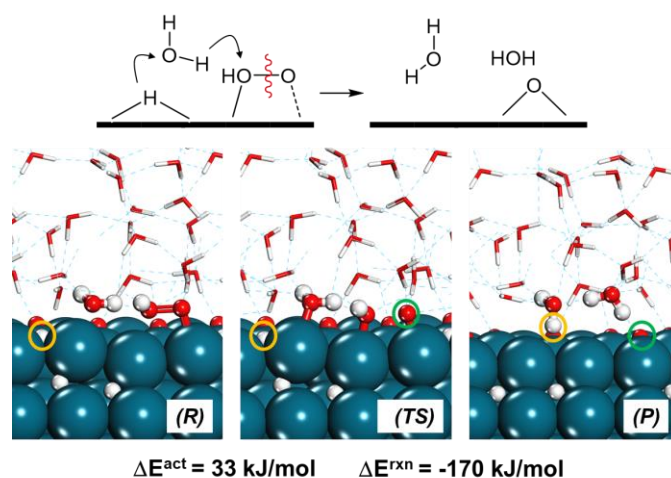


Figure 7.14 Structures and energies for the HOO^* decomposition pathway ($\text{H}^* + \text{HOO}^* \rightarrow \text{H}_2\text{O} + \text{O}^*$) using the proton couple electron transfer route at surface coverage of 1/3 ML O^* and 1/3 ML H^* s. The surface hydrogen is marked in orange. The surface O^* in the product state is marked in green.

Table 7.6 Influence of catalyst structure the decomposition of HOO^* in water as solvent via the proton-coupled-electron-transfer route

Dissolved hydrogen concentration	$\Delta E^{\text{act}}(\text{kJ/mol})$	$\Delta E^{\text{rxn}}(\text{kJ/mol})$
0	21	-209
1/3 ML	33	-170
2/3 ML	38	-170

7.4 Solvents control formation of PdH_x

Experiments (Figure 7.10) show that the PdH_x phase is prevalent in methanol in the entire range of H_2 pressure examined. However, in water, PdH_x phase is only detected after 100 kPa of H_2 pressure. The importance of PdH_x has been highlighted in the previous sections, therefore, it is crucial to understand the features that allow for the formation of PdH_x even at modest H_2 pressures. In methanol, high coverage of O^* as well as methanol decomposed products is detected. On the other hand, in water, high coverage of O^* is seen experimentally. The energetics of dissolved hydride formation ($0.5\text{H}_{2(\text{g})} + \text{*s} \rightarrow \text{H}^*\text{s}$, where *s is a subsurface Pd site) from H_2 gas were therefore studied at different surface coverage of atomic oxygen and hydroxymethyl group on Pd (Table 7.7). The corresponding structures are reported in Figure 7.15. As seen from Table 7.7, hydride formation is more favorable when the surface has high coverage of CH_2OH^* verses O^*

(entries 3-4 vs 1-2). When similar total surface coverage of species (5/9 ML) is maintained (entries 1 and 5), the results show that the presence of CH_2OH^* groups makes subsurface hydride formation easier. O^* , therefore, appears to be a stronger oxidant than CH_2OH^* preventing further oxidation of Pd via subsurface hydride formation. Consequently, in methanol, high coverage of CH_2OH^* species likely enables hydride formation in the entire range of pressure examined. In water, high coverage of O^* likely favors hydride formation at higher pressures.

Table 7.7 Subsurface hydrogen formation energy at different surface conditions

Entry	Surface conditions	Subsurface hydride formation energy with respect to H_2 in gas phase (kJ/mol)
1	5/9 ML O^*	-8
2	1/3 ML O^*	-14
3	4/9 ML CH_2OH^*	-16
4	1/3 ML CH_2OH^*	-22
5	1/3 O^* and 2/9 CH_2OH^*	-16

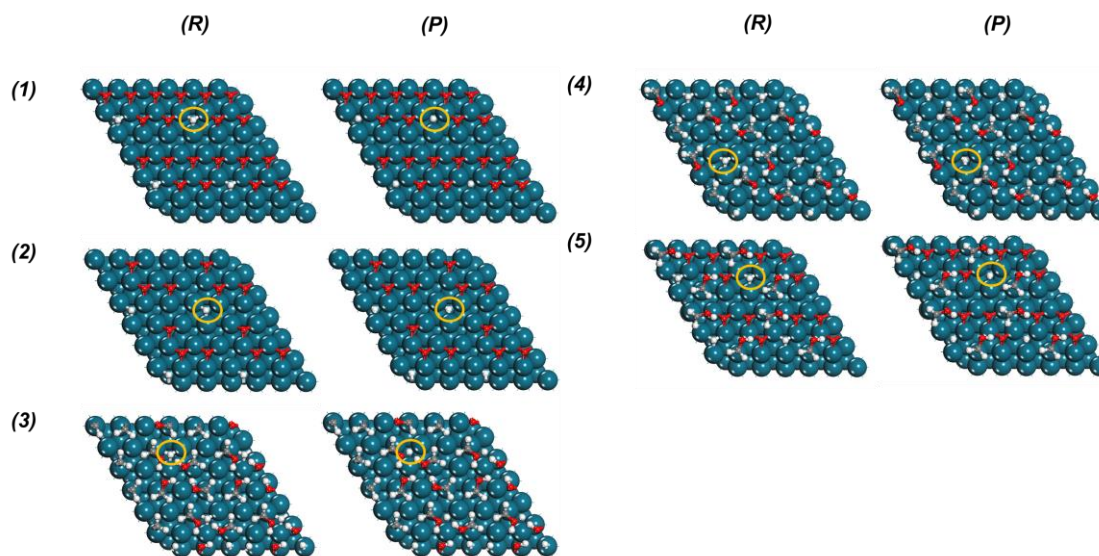


Figure 7.15 Hydride formation Reactant state (R) and Product state (P) structures for (1) 5/9 ML of O^* (2) 1/3 ML of O^* (3) 4/9 ML of CH_2OH^* (4) 1/3 ML of CH_2OH^* (5) 1/3 ML of O^* and 2/9 ML of CH_2OH^*

7.5 Hydrogen peroxide formation in methanol vs water

Kinetically fastest route producing hydrogen peroxide in methanol was found to involve a proton coupled electron transfer reaction between hydroxymethyl intermediates and dioxygen derived intermediates in an MPV-type mechanism. On the other hand, in water, hydrogen peroxide was produced in a proton coupled electron transfer reaction, where surface hydrogen directly reacted with water molecules to form protons and electrons. These protons and electrons were subsequently transferred to dioxygen derived intermediates catalyzing O-H formation reactions. The energetics of hydrogen peroxide formation in both these solvents (at 1/3 ML of O* and 2/3 ML of H*s) are shown in Figure 7.16 and 7.17. The energy diagrams simulate experimental conditions at high pressures of H₂ and O₂, where a zero-order dependence is observed.

In methanol, the energy diagram assumes that the exposed Pd sites are covered with hydroxymethyl intermediates and O₂*. An apparent activation barrier of 18 kJ/mol is obtained as result. In water, it is assumed that exposed metallic Pd sites have a high coverage of H* and O₂*. An activation barrier of 30 kJ/mol is predicted from Figure 7.17.

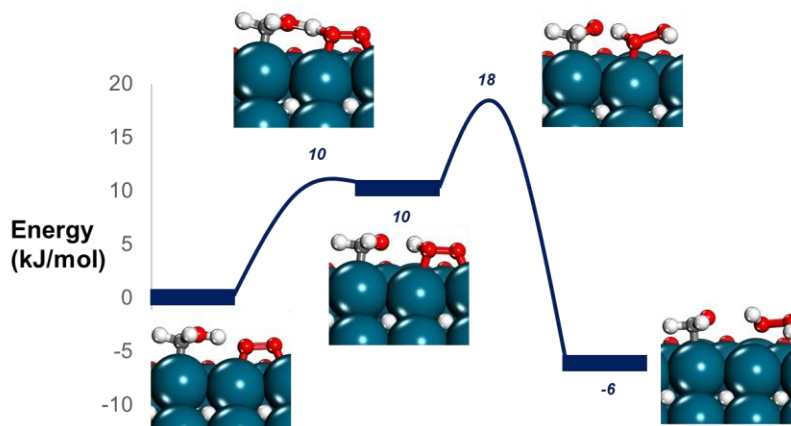


Figure 7.16 Reaction profile diagram for H₂O₂ formation in methanol over Pd at surface coverage of O* of 1/3 ML and H*s of 2/3 ML.

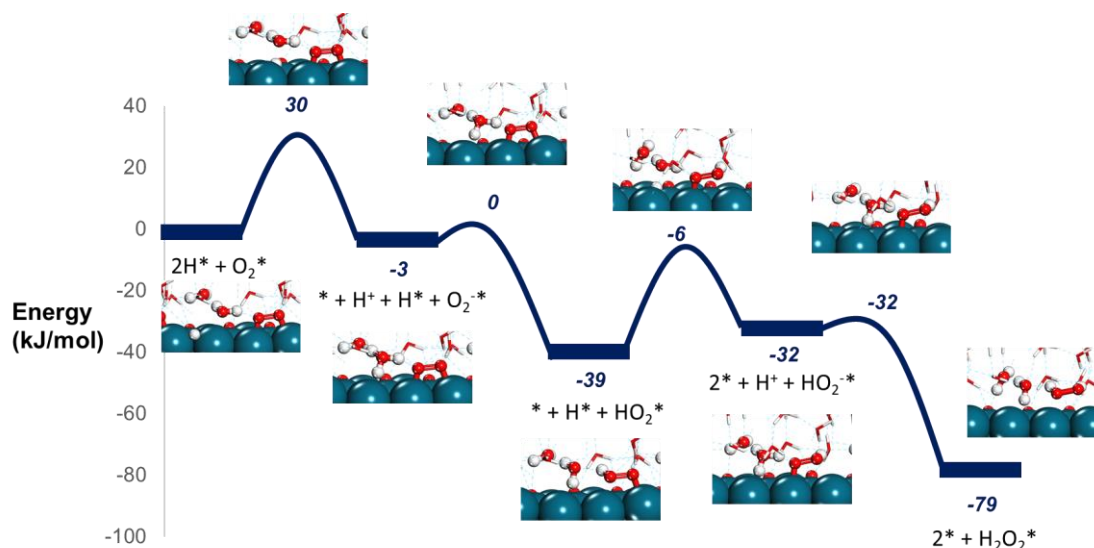


Figure 7.17 Reaction profile diagram for H_2O_2 formation in water over Pd at surface coverage of O^* of $1/3$ ML and H^* s of $2/3$ ML.

Theoretical analysis shows that hydrogen peroxide synthesis will be faster in methanol than in water since activation barrier in methanol is 12 kJ/mol lower. This explains higher rates in Figure 7.1 in the presence of methanol. Higher concentration of methanol, however, tends to deactivate the catalyst by blocking the active sites. In mixtures of methanol and water, the presence of methanol will enable activation of the hydroxymethyl route. In addition, lower concentration of methanol might alleviate site blocking caused by decomposition reactions. Mixtures of methanol and water were, therefore, examined. The results show a maximum rate and selectivity at 70 % wt. of methanol (Figure 7.18).

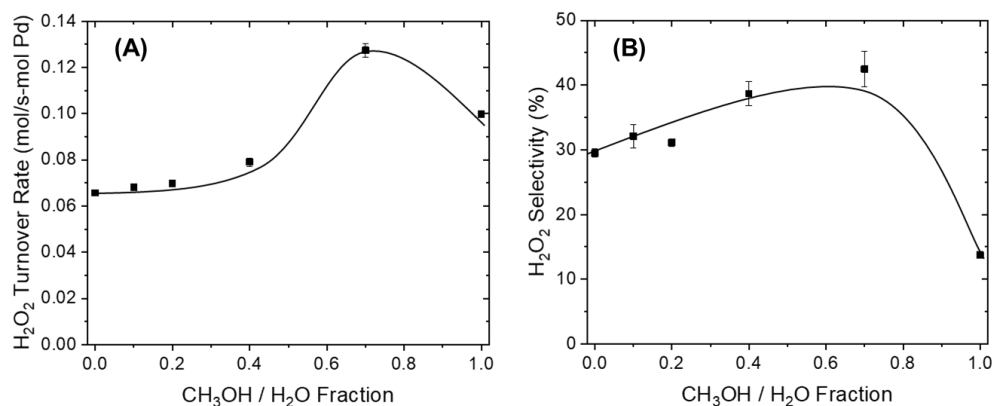


Figure 7.18 Rate and selectivity of hydrogen peroxide synthesis in mixtures of methanol and water.

7.6 Concluding remarks

Results presented herein highlight the complex involvement of commonly utilized solvents such as water and methanol in oxygen reduction chemistry. In addition to solvating reacting molecules, these solvents activate characteristically different mechanisms in which they directly participate as co-catalysts and co-reactants. The ability of these solvents to co-react and form protons and electrons sets up a sequence of oxidation/reduction cycles that drive oxygen reduction and possibly hydrogenation of other oxygenates over supported transition metals. Water directly reacts with co-adsorbed hydrogen atoms to generate protons and electrons that participate in O-H formation reactions, similar to elementary steps in electrochemical oxygen reduction.^{328–330} Methanol, on the other hand, tends to irreversibly reduce on Pd forming organometallic hydroxymethyl intermediates. These hydroxymethyl intermediates act as proton coupled electron transfer mediators and participate in O-H formation reactions, irreversibly forming formaldehyde in return. H₂ gas then acts as a source of electrons and protons regenerating hydroxymethyl from formaldehyde, thereby, sustaining catalytic activity. Methanol results in higher reactivity as well as selectivity to hydrogen peroxide, but, resulting formaldehyde condenses on the surface causing significant catalyst deactivation. A critical strategy in reaping the benefits of alcoholic solvents, therefore, involves using alcohol-water mixtures. Further, these solvents can also be used to induce subsurface hydride formation. Subsurface hydride can promote electron transfer while simultaneously hindering O-O cleavage and improving selectivity to hydrogen peroxide. These findings reveal unexplored, yet complex features of aqueous and alcoholic solvents in the direct synthesis of hydrogen peroxide, opening new opportunities in solvent selection and process optimization to economically manufacturing hydrogen peroxide as an alternative to non-green oxidants.

7.7 Computational methodology

Ab-initio density functional theory simulations were performed using methods implemented in the Vienna ab-initio simulation package (VASP).^{127–130} All calculations utilized a plane-wave cutoff of 396 eV. Exchange and correlation energies were described by the PBE¹³¹ form of generalized gradient approximation. In addition, dispersive interactions were modeled by Grimme's D3 correction.¹³²

All calculations were performed on periodic slabs consisting of 3 x 3 unit cells of 4 layers of the Pd-111 surface. Bottom two layers were held fixed at bulk positions of the Pd lattice, while top two layers were allowed to fully relax. Vacuum space of at least 18 Å was used in gas-phase calculations. In the condensed phase, a space of ~15 Å was utilized between the top and bottom layers to accommodate solvent and reacting molecules.

Structural optimizations were performed in two steps. In step one, wavefunctions were self-consistently optimized to within 10^{-4} eV on a 3 x 3 x 1 k-point¹³⁷ mesh. Atomic positions were iteratively optimized until maximum force was within 0.1 eV/Å. In step two, wavefunctions were optimized to within 10^{-6} eV on a 3 x 3 x 1 k-point mesh and maximum allowable force on each atom was less than 0.05 eV/Å. A single-point calculation on 5 x 5 x 1 k-point mesh and wavefunction convergence of 10^{-4} eV was used to determine energies of all structures used herein. Transition states were isolated using the nudged elastic band and dimer methods within VASP^{133–135} within the same optimization criteria.

Calculations in the condensed phase were performed at a density of ~1 g/cc for water and ~0.8 g/cc for methanol. Solvent molecules were allowed to relax around the reacting molecules using ab-initio molecular dynamics for a total of 5 ps. Low energy structures along the molecular dynamics trajectory were used to perform static DFT calculations using optimization procedure described above.

Kinetic isotope effect calculations were performed using the quasi-harmonic approach described by Iglesia et al.²⁵⁰

7.8 Supporting Information

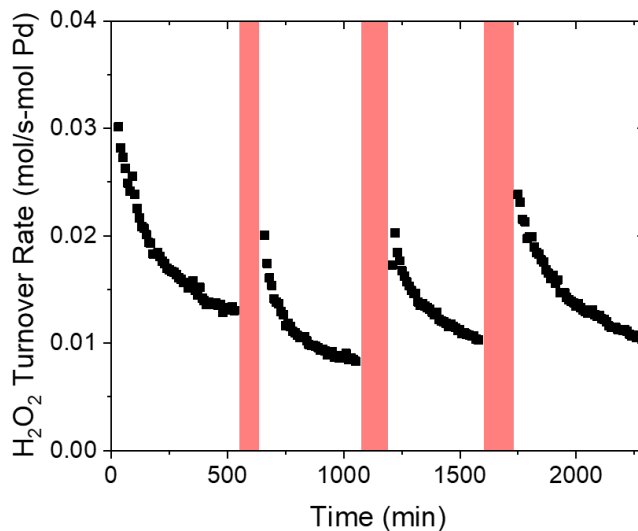


Figure S 7.1 Demonstration of regeneration of active sites by external addition of H_2O_2 -turnover rates as a function of time on 0.05 % wt. silica-supported Pd catalysts (800 kPa H_2 , 60 kPa O_2 , 278 K, $35 \text{ cm}^3 \text{ min}^{-1}$ CH_3OH). At time points denoted by a red shading, the condition is changed to 50 mM H_2O_2 in DI H_2O , 60 kPa H_2 , and 200 kPa O_2 to oxidize organic residues off of the Pd catalyst.

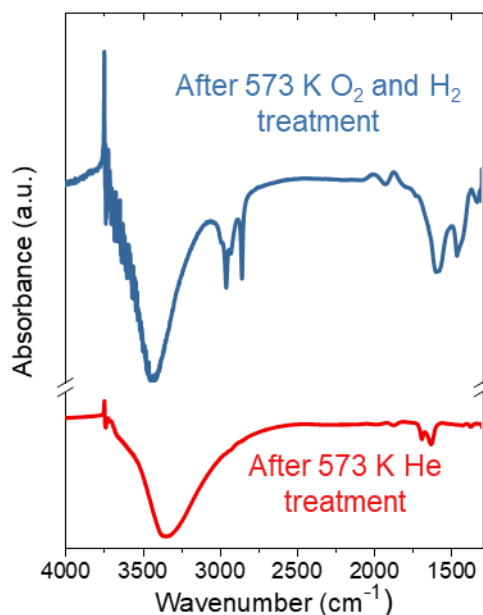


Figure S 7.2 FTIR showing the CH_2O and CH_3OH derived species that may accumulate on Pd/ SiO_2 while deactivating from methanol where these spectra was taken after a 573 K He (red) and 573 K O_2 treatment (blue). The sample was dried after 100 hours of reaction in

methanol and then heated in situ to 573 K (101 kPa He) to desorb weakly bound methanol and water, which are evident from the decreasing intensity between 3750 cm^{-1} and 2750 cm^{-1} caused by the loss of O-H stretches. The sample was then oxidized at 573 K (20 kPa O_2 , 80 kPa He) to remove persistent organic residues from the Pd nanoparticles. Subsequent infrared spectra reveal features at 3430, 2960, and 2855 cm^{-1} that correspond to $\nu(\text{OH})$, $\nu_{\text{as}}(\text{CH}_3)$, $\nu_{\text{s}}(\text{CH}_3)$ modes and at 1600 and 1460 cm^{-1} arising from C-O vibrations.^{331,332} These features are consistent with decomposed CH_3OH , CH_2O , and higher molecular weight organics that share similar vibrational modes with these species.

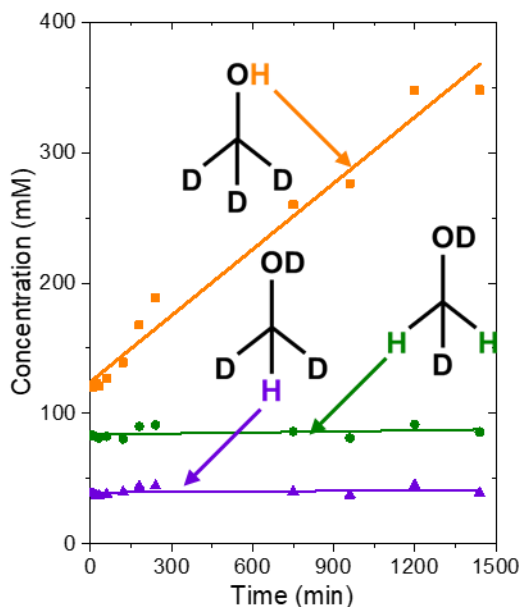


Figure S 7.3 ^1H NMR collected on CD_3OD tracks how H-atoms exchange with D-atoms on CD_3OD as a function of time

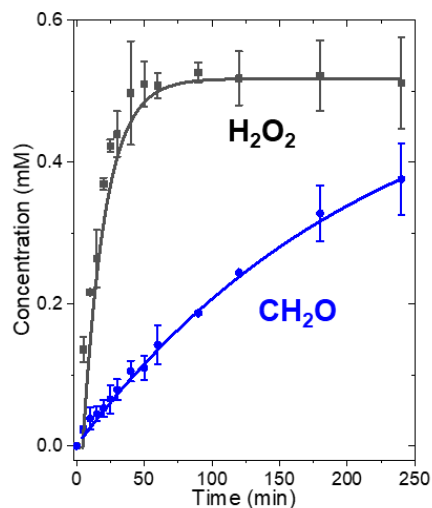


Figure S 7.4 An example of semi-batch data collected in methanol showing relative H_2O_2 and CH_2O formation over time. All measurements were performed on silica-supported Pd catalysts

8 Future Recommendations

Chapters 1-3 showed the chemical and structural flexibility of coumalic acid and esters in synthesizing variety of chemicals. Although the yield was high during synthesis of benzoic acid (Chapter 1) and toluic acid (Chapter 3), the yield is not necessarily high during synthesis of many other aromatics as shown by Krauss and co-workers.²⁶ Understanding the link between yield and electronics of the Diels-Alder reaction between coumalic acid and different dienophiles would be crucial in the synthesis of newer aromatics. Given that a large amount of experimental data for different dienophiles already exists, density functional theory simulations can be used to understand the features that lead to higher yields. Further, it would be useful to make Hammett-type linear relationships for a range of dienophiles; such relationship would aid in the synthesis of newer compounds as well as help in the design of dienophiles that result in high yields.

Chapter 4 showed the uniqueness of metallic Cu that allows for in-situ generation of basic alkoxide sites (RCH_2O^*). Such sites acquire basicity as well as nucleophilicity due to charge transfer from metallic Cu and catalyze both C-C and C-O bond formation reactions respectively. A possible future investigation could be improving the selectivity to C-C bond formation reactions, since these reactions are more important from biomass upgradation perspective. Cu could be supported on oxides such as MgO ³³³ and TiO_2 ,³³⁴ that are active for C-C coupling to understand how it impacts selectivity. Over such multifunctional catalysts, Cu would likely act towards oxidation of alcohols to aldehydes, and the oxide sites would be predominantly responsible for C-C bond formation. Further, it is worth exploring metallic Cu for other coupling reactions that require assistance from base such as Buchwald–Hartwig amination,³³⁵ where, a C-N bond is formed between an aromatic and an amine over homogeneous Cu or Pd complexes, and a base (typically tert-butoxide t-OBu^-) aids in the deprotonation of the amine. Such reaction could also be catalyzed by basic alkoxide sites over metallic copper.

C-O bond hydrogenolysis results presented in Chapter 5 over Pd-ReO_x in principle, can be applied to general bifunctional catalysts of the form $\text{M}_1\text{-M}_2\text{O}_x$, where M_1 can function as a reducible metal providing hydrides required for diol formation, and Brønsted acidic sites on M_2O_x provide protons for dehydration of the diol intermediate. The use of earth abundant elements instead of precious Pd and Re is desirable, consequently, using density functional theory other metals can be screened for their hydrogenolysis activity.

Earth abundant elements such as Ni and Cu can be potentially explored as reducible metals, while, more oxophilic abundant elements such as Fe, Co and Mo can be examined for their role in the formation of Brønsted acid sites.

The deceptively complex role of solvents has been presented in Chapters 6 and 7. The transition metal surface appears to be more active towards C-H bond formation due to the partial hydridic nature of surface hydrogens. However, protic solvents are shown to co-react with surface hydrides to form protons in the solution and electrons that reside in the host metal. These protons and electrons are more selective towards O-H bond formation. Further, alcoholic solvents can also irreversibly decompose on the Pd surface, generating hydroxymethyl intermediates that then participate in bimolecular MPV type transfer hydrogenation routes. These surface-bound hydroxymethyl intermediates appear to function like ancillary ligand that carry protons in homogeneous catalytic processes such as the Shvo catalyst^{336–338} and Noyori's Ru complexes.^{339,340} The ancillary ligands on homogeneous catalysts stay bound during catalysis, however, hydroxymethyl intermediates form aldehydes (after transferring protons and electrons) and can desorb from the surface. Higher coverage of O-H catalyzing functional groups on the surface would imply higher reactivity, therefore, future investigations could involve immobilizing mediators on heterogeneous transition metal surfaces. These mediators could be inspired from ancillary ligands used in the Shvo catalyst or Noyori's complexes such as cyclopentadienones and diamines. Other studies show the potential of imidazolium-based ionic liquids towards CO₂ reduction,^{341,342} that can be potentially examined for O-H formation reactions on other oxygenates. Further, heteropolyacids³⁴³ could also be deposited on the metal surface and tested towards oxygen reduction reactions. Mediators could also be designed to mimic well-understood nitroxyl-based compounds³¹¹ and enzymatic co-factors³⁴⁴ to carry out O-H formation reactions.

9 References

- (1) Chheda, J. N.; Huber, G. W.; Dumesic, J. A. Liquid-Phase Catalytic Processing of Biomass-Derived Oxygenated Hydrocarbons to Fuels and Chemicals. *Angew. Chem. Int. Ed.* **2007**, *46* (38), 7164–7183. <https://doi.org/10.1002/anie.200604274>.
- (2) Chheda, J. N.; Dumesic, J. A. An Overview of Dehydration, Aldol-Condensation and Hydrogenation Processes for Production of Liquid Alkanes from Biomass-Derived Carbohydrates. *Catal. Today* **2007**, *123* (1–4), 59–70. <https://doi.org/10.1016/j.cattod.2006.12.006>.
- (3) Kunkes, E. L.; Simonetti, D. A.; West, R. M.; Serrano-Ruiz, J. C.; Gartner, C. A.; Dumesic, J. A. Catalytic Conversion of Biomass to Monofunctional Hydrocarbons and Targeted Liquid-Fuel Classes. *Science* **2008**, *322* (5900), 417–421. <https://doi.org/10.1126/science.1159210>.
- (4) Huber, G. W. Production of Liquid Alkanes by Aqueous-Phase Processing of Biomass-Derived Carbohydrates. *Science* **2005**, *308* (5727), 1446–1450. <https://doi.org/10.1126/science.1111166>.
- (5) Serrano-Ruiz, J. C.; Luque, R.; Sepúlveda-Escribano, A. Transformations of Biomass-Derived Platform Molecules: From High Added-Value Chemicals to Fuels via Aqueous-Phase Processing. *Chem. Soc. Rev.* **2011**, *40* (11), 5266. <https://doi.org/10.1039/c1cs15131b>.
- (6) Bruijninx, P. C. A.; Weckhuysen, B. M. Shale Gas Revolution: An Opportunity for the Production of Biobased Chemicals? *Angew. Chem. Int. Ed.* **2013**, *52* (46), 11980–11987. <https://doi.org/10.1002/anie.201305058>.
- (7) Wagemann, K. Production of Basic Chemicals on the Basis of Renewable Resources as an Alternative to Petrochemistry? *ChemBioEng Rev.* **2015**, *2* (5), 315–334. <https://doi.org/10.1002/cben.201500005>.
- (8) de Jong, E.; Higson, A.; Walsh, P.; Wellisch, M. Product Developments in the Bio-Based Chemicals Arena. *Biofuels Bioprod. Biorefining* **2012**, *6* (6), 606–624. <https://doi.org/10.1002/bbb.1360>.
- (9) Huber, G. W.; O'Connor, P.; Corma, A. Processing Biomass in Conventional Oil Refineries: Production of High Quality Diesel by Hydrotreating Vegetable Oils in Heavy Vacuum Oil Mixtures. *Appl. Catal. Gen.* **2007**, *329*, 120–129. <https://doi.org/10.1016/j.apcata.2007.07.002>.
- (10) Mathers, R. T. How Well Can Renewable Resources Mimic Commodity Monomers and Polymers? *J. Polym. Sci. Part Polym. Chem.* **2012**, *50* (1), 1–15. <https://doi.org/10.1002/pola.24939>.
- (11) Ding, J.; Hua, W. Game Changers of the C3 Value Chain: Gas, Coal, and Biotechnologies. *Chem. Eng. Technol.* **2013**, *36* (1), 83–90. <https://doi.org/10.1002/ceat.201200297>.
- (12) Shiramizu, M.; Toste, F. D. Deoxygenation of Biomass-Derived Feedstocks: Oxorhenium-Catalyzed Deoxydehydration of Sugars and Sugar Alcohols. *Angew. Chem. Int. Ed.* **2012**, *51* (32), 8082–8086. <https://doi.org/10.1002/anie.201203877>.

- (13) Carlson, T. R.; Tompsett, G. A.; Conner, W. C.; Huber, G. W. Aromatic Production from Catalytic Fast Pyrolysis of Biomass-Derived Feedstocks. *Top. Catal.* **2009**, *52* (3), 241–252. <https://doi.org/10.1007/s11244-008-9160-6>.
- (14) Wang, K.; Kim, K. H.; Brown, R. C. Catalytic Pyrolysis of Individual Components of Lignocellulosic Biomass. *Green Chem* **2014**, *16* (2), 727–735. <https://doi.org/10.1039/C3GC41288A>.
- (15) Cheng, Y.-T.; Jae, J.; Shi, J.; Fan, W.; Huber, G. W. Production of Renewable Aromatic Compounds by Catalytic Fast Pyrolysis of Lignocellulosic Biomass with Bifunctional Ga/ZSM-5 Catalysts. *Angew. Chem.* **2012**, *124* (6), 1416–1419. <https://doi.org/10.1002/ange.201107390>.
- (16) Arceo, E.; Ellman, J. A.; Bergman, R. G. A Direct, Biomass-Based Synthesis of Benzoic Acid: Formic Acid-Mediated Deoxygenation of the Glucose-Derived Materials Quinic Acid and Shikimic Acid. *ChemSusChem* **2010**, *3* (7), 811–813. <https://doi.org/10.1002/cssc.201000111>.
- (17) Salavati-fard, T.; Caratzoulas, S.; Lobo, R. F.; Doren, D. J. Catalysis of the Diels–Alder Reaction of Furan and Methyl Acrylate in Lewis Acidic Zeolites. *ACS Catal.* **2017**, *7* (3), 2240–2246. <https://doi.org/10.1021/acscatal.6b02682>.
- (18) Cheng, Y.-T.; Huber, G. W. Production of Targeted Aromatics by Using Diels–Alder Classes of Reactions with Furans and Olefins over ZSM-5. *Green Chem.* **2012**, *14* (11), 3114. <https://doi.org/10.1039/c2gc35767d>.
- (19) Pacheco, J. J.; Davis, M. E. Synthesis of Terephthalic Acid via Diels–Alder Reactions with Ethylene and Oxidized Variants of 5-Hydroxymethylfurfural. *Proc. Natl. Acad. Sci.* **2014**, *111* (23), 8363–8367. <https://doi.org/10.1073/pnas.1408345111>.
- (20) Mahmoud, E.; Yu, J.; Gorte, R. J.; Lobo, R. F. Diels–Alder and Dehydration Reactions of Biomass-Derived Furan and Acrylic Acid for the Synthesis of Benzoic Acid. *ACS Catal.* **2015**, *5* (11), 6946–6955. <https://doi.org/10.1021/acscatal.5b01892>.
- (21) Green, S. K.; Patet, R. E.; Nikbin, N.; Williams, C. L.; Chang, C.-C.; Yu, J.; Gorte, R. J.; Caratzoulas, S.; Fan, W.; Vlachos, D. G.; et al. Diels–Alder Cycloaddition of 2-Methylfuran and Ethylene for Renewable Toluene. *Appl. Catal. B Environ.* **2016**, *180*, 487–496. <https://doi.org/10.1016/j.apcatb.2015.06.044>.
- (22) Shiramizu, M.; Toste, F. D. On the Diels–Alder Approach to Solely Biomass-Derived Polyethylene Terephthalate (PET): Conversion of 2,5-Dimethylfuran and Acrolein into p-Xylene. *Chem. - Eur. J.* **2011**, *17* (44), 12452–12457. <https://doi.org/10.1002/chem.201101580>.
- (23) Chang, C.-C.; Green, S. K.; Williams, C. L.; Dauenhauer, P. J.; Fan, W. Ultra-Selective Cycloaddition of Dimethylfuran for Renewable p-Xylene with H-BEA. *Green Chem* **2014**, *16* (2), 585–588. <https://doi.org/10.1039/C3GC40740C>.
- (24) van Putten, R.-J.; van der Waal, J. C.; de Jong, E.; Rasrendra, C. B.; Heeres, H. J.; de Vries, J. G. Hydroxymethylfurfural, A Versatile Platform Chemical Made from Renewable Resources. *Chem. Rev.* **2013**, *113* (3), 1499–1597. <https://doi.org/10.1021/cr300182k>.
- (25) Hu, L.; Zhao, G.; Hao, W.; Tang, X.; Sun, Y.; Lin, L.; Liu, S. Catalytic Conversion of Biomass-Derived Carbohydrates into Fuels and Chemicals via Furanic Aldehydes. *RSC Adv.* **2012**, *2* (30), 11184. <https://doi.org/10.1039/c2ra21811a>.

- (26) Lee, J. J.; Pollock III, G. R.; Mitchell, D.; Kasuga, L.; Kraus, G. A. Upgrading Malic Acid to Bio-Based Benzoates via a Diels–Alder-Initiated Sequence with the Methyl Coumalate Platform. *RSC Adv* **2014**, *4* (86), 45657–45664. <https://doi.org/10.1039/C4RA07105K>.
- (27) Lee, J. J.; Kraus, G. A. One-Pot Formal Synthesis of Biorenewable Terephthalic Acid from Methyl Coumalate and Methyl Pyruvate. *Green Chem* **2014**, *16* (4), 2111–2116. <https://doi.org/10.1039/C3GC42487A>.
- (28) Lee, J. J.; Kraus, G. A. Divergent Diels–Alder Methodology from Methyl Coumalate toward Functionalized Aromatics. *Tetrahedron Lett.* **2013**, *54* (19), 2366–2368. <https://doi.org/10.1016/j.tetlet.2013.02.083>.
- (29) Kraus, G. A.; Riley, S.; Cordes, T. Aromatics from Pyrones: Para-Substituted Alkyl Benzoates from Alkenes, Coumalic Acid and Methyl Coumalate. *Green Chem.* **2011**, *13* (10), 2734. <https://doi.org/10.1039/c1gc15650k>.
- (30) Kraus, G. A.; Pollock III, G. R.; Beck, C. L.; Palmer, K.; Winter, A. H. Aromatics from Pyrones: Esters of Terephthalic Acid and Isophthalic Acid from Methyl Coumalate. *RSC Adv.* **2013**, *3* (31), 12721. <https://doi.org/10.1039/c3ra42287a>.
- (31) Pfennig, T.; Johnson, R. L.; Shanks, B. H. The Formation of *p*-Toluic Acid from Coumalic Acid: A Reaction Network Analysis. *Green Chem.* **2017**, *19* (14), 3263–3271. <https://doi.org/10.1039/C7GC01290J>.
- (32) Wang, F.; Tong, Z. Dehydro-Aromatization of Cyclohexene-Carboxylic Acids by Sulfuric Acid: Critical Route for Bio-Based Terephthalic Acid Synthesis. *RSC Adv.* **2014**, *4* (12), 6314. <https://doi.org/10.1039/c3ra46670a>.
- (33) Miller, K. K.; Zhang, P.; Nishizawa-Brennen, Y.; Frost, J. W. Synthesis of Biobased Terephthalic Acid from Cycloaddition of Isoprene with Acrylic Acid. *ACS Sustain. Chem. Eng.* **2014**, *2* (8), 2053–2056. <https://doi.org/10.1021/sc5003038>.
- (34) Frost, J. W.; Miermont, A.; Schweitzer, D.; Bui, V. Preparation of Trans,Trans Muconic Acid and Trans,Trans Muconates. US20100314243A1, December 16, 2010.
- (35) Lu, R.; Lu, F.; Chen, J.; Yu, W.; Huang, Q.; Zhang, J.; Xu, J. Production of Diethyl Terephthalate from Biomass-Derived Muconic Acid. *Angew. Chem. Int. Ed.* **2016**, *55* (1), 249–253. <https://doi.org/10.1002/anie.201509149>.
- (36) Banella, M. B.; Gioia, C.; Vannini, M.; Colonna, M.; Celli, A.; Gandini, A. A Sustainable Route to a Terephthalic Acid Precursor. *ChemSusChem* **2016**, *9* (9), 942–945. <https://doi.org/10.1002/cssc.201600166>.
- (37) Bérard, S.; Vallée, C.; Delcroix, D. Sorbic Acid as a Renewable Resource for Atom-Economic and Selective Production of *p*-Toluic Acid and Alkyl-*p*-Toluates: Intermediates to Bioterephthalic Acid and Esters. *Ind. Eng. Chem. Res.* **2015**, *54* (28), 7164–7168. <https://doi.org/10.1021/acs.iecr.5b01972>.
- (38) Shanks, B. H.; Keeling, P. L. Bioprivileged Molecules: Creating Value from Biomass. *Green Chem.* **2017**, *19* (14), 3177–3185. <https://doi.org/10.1039/C7GC00296C>.
- (39) Eckermann, S.; Schröder, G.; Schmidt, J.; Strack, D.; Edrada, R. A.; Helariutta, Y.; Elomaa, P.; Kotilainen, M.; Kilpeläinen, I.; Proksch, P.; et al. New Pathway to Polyketides in Plants. *Nature* **1998**, *396* (6709), 387–390. <https://doi.org/10.1038/24652>.

- (40) Chia, M.; Schwartz, T. J.; Shanks, B. H.; Dumesic, J. A. Triacetic Acid Lactone as a Potential Biorenewable Platform Chemical. *Green Chem.* **2012**, *14* (7), 1850. <https://doi.org/10.1039/c2gc35343a>.
- (41) Kraus, G. A.; Wanninayake, U. K.; Bottoms, J. Triacetic Acid Lactone as a Common Intermediate for the Synthesis of 4-Hydroxy-2-Pyridones and 4-Amino-2-Pyrones. *Tetrahedron Lett.* **2016**, *57* (11), 1293–1295. <https://doi.org/10.1016/j.tetlet.2016.02.043>.
- (42) Yu, J.; Landberg, J.; Shavarebi, F.; Bilanchone, V.; Okerlund, A.; Wanninayake, U.; Zhao, L.; Kraus, G.; Sandmeyer, S. Bioengineering Triacetic Acid Lactone Production in *Yarrowia Lipolytica* for Pogostone Synthesis. *Biotechnol. Bioeng.* **2018**, *115* (9), 2383–2388. <https://doi.org/10.1002/bit.26733>.
- (43) Kraus, G. A.; Wanninayake, U. K. An Improved Aldol Protocol for the Preparation of 6-Styrenylpyrones. *Tetrahedron Lett.* **2015**, *56* (51), 7112–7114. <https://doi.org/10.1016/j.tetlet.2015.11.021>.
- (44) Guney, T.; Lee, J. J.; Kraus, G. A. First Inverse Electron-Demand Diels–Alder Methodology of 3-Chloroindoles and Methyl Coumalate to Carbazoles. *Org. Lett.* **2014**, *16* (4), 1124–1127. <https://doi.org/10.1021/ol403733n>.
- (45) Alonso, D. M.; Bond, J. Q.; Dumesic, J. A. Catalytic Conversion of Biomass to Biofuels. *Green Chem.* **2010**, *12* (9), 1493. <https://doi.org/10.1039/c004654j>.
- (46) Sad, M. E.; Neurock, M.; Iglesia, E. Formation of C–C and C–O Bonds and Oxygen Removal in Reactions of Alkanediols, Alkanols, and Alkanals on Copper Catalysts. *J. Am. Chem. Soc.* **2011**, *133* (50), 20384–20398. <https://doi.org/10.1021/ja207551f>.
- (47) Clark, S. J.; Wagner, L.; Schrock, M. D.; Piennaar, P. G. Methyl and Ethyl Soybean Esters as Renewable Fuels for Diesel Engines. *J. Am. Oil Chem. Soc.* **1984**, *61* (10), 1632–1638. <https://doi.org/10.1007/BF02541648>.
- (48) Prasad, L.; Das, L. M.; Naik, S. N. Effect of Castor Oil, Methyl and Ethyl Esters as Lubricity Enhancer for Low Lubricity Diesel Fuel (LLDF). *Energy Fuels* **2012**, *26* (8), 5307–5315. <https://doi.org/10.1021/ef300845v>.
- (49) Dabbagh, H. A.; Ghobadi, F.; Ehsani, M. R.; Moradmand, M. The Influence of Ester Additives on the Properties of Gasoline. *Fuel* **2013**, *104*, 216–223. <https://doi.org/10.1016/j.fuel.2012.09.056>.
- (50) Thakur, D. S.; Carrick, W. Copper Chromite Hydrogenation Catalysts for Production of Fatty Alcohols. WO2012074841A2, June 7, 2012.
- (51) Capello, C.; Fischer, U.; Hungerbühler, K. What Is a Green Solvent? A Comprehensive Framework for the Environmental Assessment of Solvents. *Green Chem.* **2007**, *9* (9), 927. <https://doi.org/10.1039/b617536h>.
- (52) Weinberg, D. R.; Gagliardi, C. J.; Hull, J. F.; Murphy, C. F.; Kent, C. A.; Westlake, B. C.; Paul, A.; Ess, D. H.; McCafferty, D. G.; Meyer, T. J. Proton-Coupled Electron Transfer. *Chem. Rev.* **2012**, *112* (7), 4016–4093. <https://doi.org/10.1021/cr200177j>.
- (53) Ksar, F.; Surendran, G.; Ramos, L.; Keita, B.; Nadjo, L.; Prouzet, E.; Beaunier, P.; Hagège, A.; Audonnet, F.; Remita, H. Palladium Nanowires Synthesized in Hexagonal Mesophases: Application in Ethanol Electrooxidation. *Chem. Mater.* **2009**, *21* (8), 1612–1617. <https://doi.org/10.1021/cm803492j>.

- (54) Tse, E. C. M.; Barile, C. J.; Kirchschrager, N. A.; Li, Y.; Gewargis, J. P.; Zimmerman, S. C.; Hosseini, A.; Gewirth, A. A. Proton Transfer Dynamics Control the Mechanism of O₂ Reduction by a Non-Precious Metal Electrocatalyst. *Nat. Mater.* **2016**, *15* (7), 754–759. <https://doi.org/10.1038/nmat4636>.
- (55) Chang, C.-P.; Wen-Chi, H.; Meng-Shin, K.; Chou, P.-T.; Clements, J. H. Acid Catalysis of Excited-State Double-Proton Transfer in 7-Azaindole. *J. Phys. Chem.* **1994**, *98* (35), 8801–8805. <https://doi.org/10.1021/j100086a034>.
- (56) Reece, S. Y.; Nocera, D. G. Proton-Coupled Electron Transfer in Biology: Results from Synergistic Studies in Natural and Model Systems. *Annu. Rev. Biochem.* **2009**, *78* (1), 673–699. <https://doi.org/10.1146/annurev.biochem.78.080207.092132>.
- (57) Chang, C. J.; Chang, M. C. Y.; Damrauer, N. H.; Nocera, D. G. Proton-Coupled Electron Transfer: A Unifying Mechanism for Biological Charge Transport, Amino Acid Radical Initiation and Propagation, and Bond Making/Breaking Reactions of Water and Oxygen. *Biochim. Biophys. Acta BBA - Bioenerg.* **2004**, *1655*, 13–28. <https://doi.org/10.1016/j.bbabi.2003.08.010>.
- (58) Ko, Y.; Park, H.; Kim, J.; Lim, H.-D.; Lee, B.; Kwon, G.; Lee, S.; Bae, Y.; Park, S. K.; Kang, K. Biological Redox Mediation in Electron Transport Chain of Bacteria for Oxygen Reduction Reaction Catalysts in Lithium-Oxygen Batteries. *Adv. Funct. Mater.* **2019**, *29* (5), 1805623. <https://doi.org/10.1002/adfm.201805623>.
- (59) Kracke, F.; Vassilev, I.; KrÄ¶mer, J. O. Microbial Electron Transport and Energy Conservation – the Foundation for Optimizing Bioelectrochemical Systems. *Front. Microbiol.* **2015**, *6*. <https://doi.org/10.3389/fmicb.2015.00575>.
- (60) Green, D. E.; Tzagoloff, A. The Mitochondrial Electron Transfer Chain. *Arch. Biochem. Biophys.* **1966**, *116*, 293–304. [https://doi.org/10.1016/0003-9861\(66\)90036-1](https://doi.org/10.1016/0003-9861(66)90036-1).
- (61) Ciriminna, R.; Pagliaro, M. Industrial Oxidations with Organocatalyst TEMPO and Its Derivatives. *Org. Process Res. Dev.* **2010**, *14* (1), 245–251. <https://doi.org/10.1021/op900059x>.
- (62) Francke, R.; Little, R. D. Redox Catalysis in Organic Electrosynthesis: Basic Principles and Recent Developments. *Chem. Soc. Rev.* **2014**, *43* (8), 2492. <https://doi.org/10.1039/c3cs60464k>.
- (63) D'Ecclesia, R. L.; Magrini, E.; Montalbano, P.; Triulzi, U. Understanding Recent Oil Price Dynamics: A Novel Empirical Approach. *Energy Econ.* **2014**, *46*, S11–S17. <https://doi.org/10.1016/j.eneco.2014.10.005>.
- (64) Christensen, C. H.; Rass-Hansen, J.; Marsden, C. C.; Taarning, E.; Egeblad, K. The Renewable Chemicals Industry. *ChemSusChem* **2008**, *1* (4), 283–289. <https://doi.org/10.1002/cssc.200700168>.
- (65) Fiorentino, G.; Ripa, M.; Ulgiati, S. Chemicals from Biomass: Technological versus Environmental Feasibility. A Review. *Biofuels Bioprod. Biorefining* **2017**, *11* (1), 195–214. <https://doi.org/10.1002/bbb.1729>.
- (66) Haveren, J. van; Scott, E. L.; Sanders, J. Bulk Chemicals from Biomass. *Biofuels Bioprod. Biorefining* **2008**, *2* (1), 41–57. <https://doi.org/10.1002/bbb.43>.

- (67) Wagemann, K. Production of Basic Chemicals on the Basis of Renewable Resources as an Alternative to Petrochemistry? *ChemBioEng Rev.* **2015**, 2 (5), 315–334. <https://doi.org/10.1002/cben.201500005>.
- (68) *Benzoic Acid and Sodium Benzoate*; Wibbertmann, A., Ed.; Concise international chemical assessment document; World Health Organization: Geneva, 2000.
- (69) Ghosh, S.; Chisti, Y.; Banerjee, U. C. Production of Shikimic Acid. *Biotechnol. Adv.* **2012**, 30 (6), 1425–1431. <https://doi.org/10.1016/j.biotechadv.2012.03.001>.
- (70) Draths, K. M.; Knop, D. R.; Frost, J. W. Shikimic Acid and Quinic Acid: Replacing Isolation from Plant Sources with Recombinant Microbial Biocatalysis. *J. Am. Chem. Soc.* **1999**, 121 (7), 1603–1604. <https://doi.org/10.1021/ja9830243>.
- (71) Brown, S. H.; Bashkirova, L.; Berka, R.; Chandler, T.; Doty, T.; McCall, K.; McCulloch, M.; McFarland, S.; Thompson, S.; Yaver, D.; et al. Metabolic Engineering of *Aspergillus Oryzae* NRRL 3488 for Increased Production of L-Malic Acid. *Appl. Microbiol. Biotechnol.* **2013**, 97 (20), 8903–8912. <https://doi.org/10.1007/s00253-013-5132-2>.
- (72) Zelle, R. M.; de Hulster, E.; van Winden, W. A.; de Waard, P.; Dijkema, C.; Winkler, A. A.; Geertman, J.-M. A.; van Dijken, J. P.; Pronk, J. T.; van Maris, A. J. A. Malic Acid Production by *Saccharomyces Cerevisiae*: Engineering of Pyruvate Carboxylation, Oxaloacetate Reduction, and Malate Export. *Appl. Environ. Microbiol.* **2008**, 74 (9), 2766–2777. <https://doi.org/10.1128/AEM.02591-07>.
- (73) Riley, S. J. Chemistry from Nature: From Natural Products to Biorenewables. Doctor of Philosophy, Iowa State University, Digital Repository: Ames, 2011. <https://doi.org/10.31274/etd-180810-630>.
- (74) Markó, I. E.; Evans, G. R.; Seres, P.; Chellé, I.; Janousek, Z. Catalytic, Enantioselective, Inverse Electron-Demand Diels-Alder Reactions of 2-Pyrone Derivatives. *Pure Appl. Chem.* **1996**, 68 (1), 113–122. <https://doi.org/10.1351/pac199668010113>.
- (75) Posner, G. H.; Ishihara, Y. Lewis Acid-Catalyzed, High Pressure, Stereospecific, Regiospecific, Diels-Alder Cycloaddition of Unsubstituted 2-Pyrone: Short Synthesis of a Racemic A-Ring Precursor to Physiologically Active 1-Hydroxyvitamin D₃ Steroids. *Tetrahedron Lett.* **1994**, 35 (41), 7545–7548. [https://doi.org/10.1016/S0040-4039\(00\)78339-0](https://doi.org/10.1016/S0040-4039(00)78339-0).
- (76) Shusherina, N. P. Diene Synthesis with 2-Pyrones and 2-Pyridones. *Russ. Chem. Rev.* **1974**, 43 (10), 851–861. <https://doi.org/10.1070/RC1974v043n10ABEH001867>.
- (77) Markó, I. E.; Evans, G. R. Diastereoselective, Lanthanide-Catalysed, Inverse Electron-Demand Diels-Alder (IEDDA) Reactions of 3-Carbomethoxy-2-Pyrone (3-CMP) Derivatives. *Tetrahedron Lett.* **1994**, 35 (17), 2767–2770. [https://doi.org/10.1016/S0040-4039\(00\)77028-6](https://doi.org/10.1016/S0040-4039(00)77028-6).
- (78) Markó, I. E.; Evans, G. R. Catalytic, Enantioselective, Inverse Electron-Demand Diels-Alder (IEDDA) Reactions of 3-Carbomethoxy-2-Pyrone (3-CMP). *Tetrahedron Lett.* **1994**, 35 (17), 2771–2774. [https://doi.org/10.1016/S0040-4039\(00\)77029-8](https://doi.org/10.1016/S0040-4039(00)77029-8).
- (79) Markó, I. E.; Evans, G. R.; Declercq, J.-P. Catalytic Asymmetric Diels-Alder Reactions of 2-Pyrone Derivatives. *Tetrahedron* **1994**, 50 (15), 4557–4574. [https://doi.org/10.1016/S0040-4020\(01\)89387-X](https://doi.org/10.1016/S0040-4020(01)89387-X).

- (80) Afarinkia, K.; Vinader, V.; Nelson, T. D.; Posner, G. H. Diels-Alder Cycloadditions of 2-Pyrones and 2-Pyridones. *Tetrahedron* **1992**, *48* (42), 9111–9171. [https://doi.org/10.1016/S0040-4020\(01\)85607-6](https://doi.org/10.1016/S0040-4020(01)85607-6).
- (81) Chia, M.; Haider, M. A.; Pollock, G.; Kraus, G. A.; Neurock, M.; Dumesic, J. A. Mechanistic Insights into Ring-Opening and Decarboxylation of 2-Pyrones in Liquid Water and Tetrahydrofuran. *J. Am. Chem. Soc.* **2013**, *135* (15), 5699–5708. <https://doi.org/10.1021/ja312075r>.
- (82) Alonso, D. M.; Wettstein, S. G.; Dumesic, J. A. Gamma-Valerolactone, a Sustainable Platform Molecule Derived from Lignocellulosic Biomass. *Green Chem.* **2013**, *15* (3), 584. <https://doi.org/10.1039/c3gc37065h>.
- (83) Strappaveccia, G.; Luciani, L.; Bartollini, E.; Marrocchi, A.; Pizzo, F.; Vaccaro, L. γ -Valerolactone as an Alternative Biomass-Derived Medium for the Sonogashira Reaction. *Green Chem.* **2015**, *17* (2), 1071–1076. <https://doi.org/10.1039/C4GC01728E>.
- (84) Fegyverneki, D.; Orha, L.; Láng, G.; Horváth, I. T. Gamma-Valerolactone-Based Solvents. *Tetrahedron* **2010**, *66* (5), 1078–1081. <https://doi.org/10.1016/j.tet.2009.11.013>.
- (85) Corma, A.; García, H. Lewis Acids: From Conventional Homogeneous to Green Homogeneous and Heterogeneous Catalysis. *Chem. Rev.* **2003**, *103* (11), 4307–4366. <https://doi.org/10.1021/cr030680z>.
- (86) Fringuelli, F.; Taticchi, A. *The Diels–Alder Reaction*; John Wiley & Sons, Ltd: Chichester, UK, 2001. <https://doi.org/10.1002/0470845813>.
- (87) Abdullahi, M. H.; Thompson, L. M.; Bearpark, M. J.; Vinader, V.; Afarinkia, K. The Role of Substituents in Retro Diels–Alder Extrusion of CO₂ from 2(H)-Pyrone Cycloadducts. *Tetrahedron* **2016**, *72* (40), 6021–6024. <https://doi.org/10.1016/j.tet.2016.07.066>.
- (88) Zhao, Y.; Truhlar, D. G. A New Local Density Functional for Main-Group Thermochemistry, Transition Metal Bonding, Thermochemical Kinetics, and Noncovalent Interactions. *J. Chem. Phys.* **2006**, *125* (19), 194101. <https://doi.org/10.1063/1.2370993>.
- (89) Zhao, Y.; Truhlar, D. G. Density Functionals with Broad Applicability in Chemistry. *Acc. Chem. Res.* **2008**, *41* (2), 157–167. <https://doi.org/10.1021/ar700111a>.
- (90) Frisch, M. J.; Trucks, G. W.; Schlegel, H. B.; Scuseria, G. E.; Robb, M. A.; Cheeseman, J. R.; Scalmani, G.; Barone, V.; Mennucci, B.; Petersson, G. A.; Nakatsuji, H.; Caricato, M.; Li, X.; Hratchian, P. H.; Izmaylov, A. F.; Bloino, J.; Zheng, G.; Sonnenberg, J. L.; Hada, M.; Ehara, M.; Toyota, K.; Fukuda, R.; Hasegawa, J.; Ishida, M.; Nakajima, T.; Honda, Y.; Kitao, O.; Nakai, H.; Vreven, T.; Montgomery, J. A., Jr.; Peralta, E. J.; Ogliaro, F.; Bearpark, M.; Heyd, J. J.; Brothers, E.; Kudin, K. N.; Staroverov, V. N.; Kobayashi, R.; Normand, J.; Raghavachari, K.; Rendell, A.; Burant, J. C.; Iyengar, S. S.; Tomasi, J.; Cossi, M.; Rega, N.; Millam, J. M.; Klene, M.; Knox, J. E.; Cross, J. B.; Bakken, V.; Adamo, C.; Jaramillo, J.; Gomperts, R.; Stratmann, R. E.; Yazyev, O.; Austin, A. J.; Cammi, R.; Pomelli, C.; Ochterski, J. W.; Martin, R. L.; Morokuma, K.; Zakrzewski, V. G.; Voth, G. A.; Salvador, P.; Dannenberg, J. J.; Dapprich, S.; Daniels, A. D.; Farkas, O.; Foresman, J. B.; Ortiz, J. V.; Cioslowski, J.; Fox, D. J. Gaussian 09, Revision A.02; Gaussian, Inc.: Wallingford, CT, 2016.
- (91) Frisch, M. J.; Pople, J. A.; Binkley, J. S. Self-consistent Molecular Orbital Methods 25. Supplementary Functions for Gaussian Basis Sets. *J. Chem. Phys.* **1984**, *80* (7), 3265–3269. <https://doi.org/10.1063/1.447079>.

- (92) Marenich, A. V.; Cramer, C. J.; Truhlar, D. G. Universal Solvation Model Based on Solute Electron Density and on a Continuum Model of the Solvent Defined by the Bulk Dielectric Constant and Atomic Surface Tensions. *J. Phys. Chem. B* **2009**, *113* (18), 6378–6396. <https://doi.org/10.1021/jp810292n>.
- (93) Zhang, X.; Wang, X.; Shanmugam, K. T.; Ingram, L. O. L-Malate Production by Metabolically Engineered *Escherichia Coli*. *Appl. Environ. Microbiol.* **2011**, *77* (2), 427–434. <https://doi.org/10.1128/AEM.01971-10>.
- (94) Werpy, T. A.; Holladay, J. E.; White, J. F. *Top Value Added Chemicals From Biomass: I. Results of Screening for Potential Candidates from Sugars and Synthesis Gas*; PNNL-14808, 926125; 2004; p PNNL-14808, 926125. <https://doi.org/10.2172/926125>.
- (95) Harmata, M. *Advances in Cycloaddition.*; Elsevier: Burlington, 1999.
- (96) Posner, G. H.; Carry, J.-C.; Kyoo Lee, J.; Bull, D. S.; Dai, H. Mild, Asymmetric Diels-Alder Cycloadditions of Electronically Matched 2-Pyrones and Vinyl Ethers. *Tetrahedron Lett.* **1994**, *35* (9), 1321–1324. [https://doi.org/10.1016/S0040-4039\(00\)76207-1](https://doi.org/10.1016/S0040-4039(00)76207-1).
- (97) Posner, G. H.; Dai, H.; Bull, D. S.; Lee, J.-K.; Eydoux, F.; Ishihara, Y.; Welsh, W.; Pryor, N.; Petr, S. Lewis Acid-Promoted, Stereocontrolled, Gram Scale, Diels-Alder Cycloadditions of Electronically Matched 2-Pyrones and Vinyl Ethers: The Critical Importance of Molecular Sieves and the Temperature of Titanium Coordination with the Pyrone. *J. Org. Chem.* **1996**, *61* (2), 671–676. <https://doi.org/10.1021/jo9515900>.
- (98) Cho, C.-G.; Kim, Y.-W.; Lim, Y.-K.; Park, J.-S.; Lee, H.; Koo, S. Diels-Alder Cycloadditions of 3,5-Dibromo-2-Pyrone: A New Ambident Diene. *J. Org. Chem.* **2002**, *67* (1), 290–293. <https://doi.org/10.1021/jo015804r>.
- (99) Imagawa, T.; Sueda, N.; Kawanisi, M. Diels-Alder Reaction of Methyl Coumalate with 1,3-Dienes. *Tetrahedron* **1974**, *30* (14), 2227–2231. [https://doi.org/10.1016/S0040-4020\(01\)97362-4](https://doi.org/10.1016/S0040-4020(01)97362-4).
- (100) Kranjc, K.; Kočevar, M. Diels-Alder Reaction of Highly Substituted 2H-Pyran-2-Ones with Alkynes: Reactivity and Regioselectivity. *New J. Chem.* **2005**, *29* (8), 1027. <https://doi.org/10.1039/b504852d>.
- (101) Imagawa, T.; Kawanisi, M.; Sisido, K. Double Diels-Alder Reactions of Coumalic Acid with Buta-1,3-Dienes: A Single-Step Synthesis of Tricyclo[3,2,1,0^{2,7}]Oct-3-Ene Derivatives. *J Chem Soc D* **1971**, *0* (20), 1292–1293. <https://doi.org/10.1039/C29710001292>.
- (102) Juranovič, A.; Kranjc, K.; Perdih, F.; Polanc, S.; Kočevar, M. Comparison of the Reaction Pathways and Intermediate Products of a Microwave-Assisted and High-Pressure-Promoted Cycloaddition of Vinyl-Moiety-Containing Dienophiles on 2H-Pyran-2-Ones. *Tetrahedron* **2011**, *67* (19), 3490–3500. <https://doi.org/10.1016/j.tet.2011.03.034>.
- (103) Reed, J. A.; Schilling, C. L.; Tarvin, R. F.; Rettig, T. A.; Stille, J. K. Diels-Alder Reactions of 2-Pyrones. Direction of the Addition Reaction with Acetylenes. *J. Org. Chem.* **1969**, *34* (7), 2188–2192. <https://doi.org/10.1021/jo01259a035>.
- (104) Pfennig, T.; Carraher, J. M.; Chemburkar, A.; Johnson, R. L.; Anderson, A. T.; Tessonnier, J.-P.; Neurock, M.; Shanks, B. H. A New Selective Route towards Benzoic Acid and Derivatives from Biomass-Derived Coumalic Acid. *Green Chem.* **2017**, *19* (20), 4879–4888. <https://doi.org/10.1039/C7GC02041D>.

- (105) Ipaktschi, J. Diels-Alder Reaction in the Presence of Zeolite. *Z. Für Naturforschung B* **1986**, *41* (4), 496–498. <https://doi.org/10.1515/znb-1986-0415>.
- (106) Narayana Murthy, Y. V. S.; Pillai, C. N. Diels-Alder Reactions Catalyzed by Zeolites. *Synth. Commun.* **1991**, *21* (6), 783–791. <https://doi.org/10.1080/00397919108019757>.
- (107) Otto, S.; Bertoncin, F.; Engberts, J. B. F. N. Lewis Acid Catalysis of a Diels–Alder Reaction in Water. *J. Am. Chem. Soc.* **1996**, *118* (33), 7702–7707. <https://doi.org/10.1021/ja960318k>.
- (108) Majors, P. D.; Raidy, T. E.; Ellis, P. D. A Multinuclear Solid-State NMR Investigation of the Chemisorption of Ammonia on γ -Alumina. *J. Am. Chem. Soc.* **1986**, *108* (26), 8123–8129. <https://doi.org/10.1021/ja00286a001>.
- (109) Wischert, R.; Laurent, P.; Copéret, C.; Delbecq, F.; Sautet, P. γ -Alumina: The Essential and Unexpected Role of Water for the Structure, Stability, and Reactivity of “Defect” Sites. *J. Am. Chem. Soc.* **2012**, *134* (35), 14430–14449. <https://doi.org/10.1021/ja3042383>.
- (110) Digne, M.; Sautet, P.; Raybaud, P.; Euzen, P.; Toulhoat, H. Hydroxyl Groups on γ -Alumina Surfaces: A DFT Study. *J. Catal.* **2002**, *211* (1), 1–5. <https://doi.org/10.1006/jcat.2002.3741>.
- (111) Bond, J. Q.; Wang, D.; Alonso, D. M.; Dumesic, J. A. Interconversion between γ -Valerolactone and Pentenoic Acid Combined with Decarboxylation to Form Butene over Silica/Alumina. *J. Catal.* **2011**, *281* (2), 290–299. <https://doi.org/10.1016/j.jcat.2011.05.011>.
- (112) Johnson, R. L.; Hanrahan, M. P.; Mellmer, M.; Dumesic, J. A.; Rossini, A. J.; Shanks, B. H. Solvent–Solid Interface of Acid Catalysts Studied by High Resolution MAS NMR. *J. Phys. Chem. C* **2017**, *121* (32), 17226–17234. <https://doi.org/10.1021/acs.jpcc.7b04102>.
- (113) Wiench, J. W.; Bronnimann, C. E.; Lin, V. S.-Y.; Pruski, M. Chemical Shift Correlation NMR Spectroscopy with Indirect Detection in Fast Rotating Solids: Studies of Organically Functionalized Mesoporous Silicas. *J. Am. Chem. Soc.* **2007**, *129* (40), 12076–12077. <https://doi.org/10.1021/ja074746+>.
- (114) Ishii, Y.; Tycko, R. Sensitivity Enhancement in Solid State ^{15}N NMR by Indirect Detection with High-Speed Magic Angle Spinning. *J. Magn. Reson.* **2000**, *142* (1), 199–204. <https://doi.org/10.1006/jmre.1999.1976>.
- (115) Amoureux, J. P.; Trebosc, J.; Wiench, J.; Pruski, M. HMQC and Refocused-INEPT Experiments Involving Half-Integer Quadrupolar Nuclei in Solids. *J. Magn. Reson.* **2007**, *184* (1), 1–14. <https://doi.org/10.1016/j.jmr.2006.09.009>.
- (116) Venkatesh, A.; Hanrahan, M. P.; Rossini, A. J. Proton Detection of MAS Solid-State NMR Spectra of Half-Integer Quadrupolar Nuclei. *Solid State Nucl. Magn. Reson.* **2017**, *84*, 171–181. <https://doi.org/10.1016/j.ssnmr.2017.03.005>.
- (117) Stanley, B. J.; Guiochon, G. Calculation of Adsorption Energy Distributions of Silica Samples Using Nonlinear Chromatography. *Langmuir* **1995**, *11* (5), 1735–1743. <https://doi.org/10.1021/la00005a051>.
- (118) Lunsford, J. H.; Rothwell, W. P.; Shen, W. Acid Sites in Zeolite Y: A Solid-State NMR and Infrared Study Using Trimethylphosphine as a Probe Molecule. *J. Am. Chem. Soc.* **1985**, *107* (6), 1540–1547. <https://doi.org/10.1021/ja00292a015>.

- (119) Wouters, B. H.; Chen, T.-H.; Grobet, P. J. Reversible Tetrahedral–Octahedral Framework Aluminum Transformation in Zeolite Y. *J. Am. Chem. Soc.* **1998**, *120* (44), 11419–11425. <https://doi.org/10.1021/ja982082l>.
- (120) Amberlyst™ 45 Resin High Temperature Strongly Acidic Catalyst; Form No. 177-02338-0315, Rev. 0 [Online]; The Dow Chemical Company: Midland, MI. http://msdssearch.dow.com/PublishedLiteratureDOWCOM/dh_092d/0901b8038092d737.pdf?filepath=liquidseps/pdfs/noreg/177-02338.pdf&fromPage=GetDoc
- (121) Gómez-Bombarelli, R.; Calle, E.; Casado, J. Mechanisms of Lactone Hydrolysis in Acidic Conditions. *J. Org. Chem.* **2013**, *78* (14), 6880–6889. <https://doi.org/10.1021/jo4002596>.
- (122) J. Sheehan, R. Terephthalic Acid, Dimethyl Terephthalate, and Isophthalic Acid. In *Ullmann's Encyclopedia of Industrial Chemistry*; Wiley-VCH Verlag GmbH & Co. KGaA, Ed.; Wiley-VCH Verlag GmbH & Co. KGaA: Weinheim, Germany, 2000; p a26_193. https://doi.org/10.1002/14356007.a26_193.
- (123) Chen, T.-H.; Wang, L.; Trueblood, J. V.; Grassian, V. H.; Cohen, S. M. Poly(Isophthalic Acid)(Ethylene Oxide) as a Macromolecular Modulator for Metal–Organic Polyhedra. *J. Am. Chem. Soc.* **2016**, *138* (30), 9646–9654. <https://doi.org/10.1021/jacs.6b04971>.
- (124) Brinkmann, A.; Kentgens, A. P. M. Proton-Selective ^{17}O – ^1H Distance Measurements in Fast Magic-Angle-Spinning Solid-State NMR Spectroscopy for the Determination of Hydrogen Bond Lengths. *J. Am. Chem. Soc.* **2006**, *128* (46), 14758–14759. <https://doi.org/10.1021/ja065415k>.
- (125) Metz, G.; Wu, X. L.; Smith, S. O. Ramped-Amplitude Cross Polarization in Magic-Angle-Spinning NMR. *J. Magn. Reson. A* **1994**, *110* (2), 219–227. <https://doi.org/10.1006/jmra.1994.1208>.
- (126) Fung, B. M.; Khitrin, A. K.; Ermolaev, K. An Improved Broadband Decoupling Sequence for Liquid Crystals and Solids. *J. Magn. Reson.* **2000**, *142* (1), 97–101. <https://doi.org/10.1006/jmre.1999.1896>.
- (127) Kresse, G.; Hafner, J. *Ab Initio* Molecular Dynamics for Liquid Metals. *Phys. Rev. B* **1993**, *47* (1), 558–561. <https://doi.org/10.1103/PhysRevB.47.558>.
- (128) Kresse, G.; Hafner, J. *Ab Initio* Molecular-Dynamics Simulation of the Liquid-Metal–Amorphous-Semiconductor Transition in Germanium. *Phys. Rev. B* **1994**, *49* (20), 14251–14269. <https://doi.org/10.1103/PhysRevB.49.14251>.
- (129) Kresse, G.; Furthmüller, J. Efficiency of *Ab-Initio* Total Energy Calculations for Metals and Semiconductors Using a Plane-Wave Basis Set. *Comput. Mater. Sci.* **1996**, *6* (1), 15–50. [https://doi.org/10.1016/0927-0256\(96\)00008-0](https://doi.org/10.1016/0927-0256(96)00008-0).
- (130) Kresse, G.; Furthmüller, J. Efficient Iterative Schemes for *Ab Initio* Total-Energy Calculations Using a Plane-Wave Basis Set. *Phys. Rev. B* **1996**, *54* (16), 11169–11186. <https://doi.org/10.1103/PhysRevB.54.11169>.
- (131) Perdew, J. P.; Ernzerhof, M.; Burke, K. Rationale for Mixing Exact Exchange with Density Functional Approximations. *J. Chem. Phys.* **1996**, *105* (22), 9982–9985. <https://doi.org/10.1063/1.472933>.

- (132) Grimme, S.; Antony, J.; Ehrlich, S.; Krieg, H. A Consistent and Accurate *Ab Initio* Parametrization of Density Functional Dispersion Correction (DFT-D) for the 94 Elements H-Pu. *J. Chem. Phys.* **2010**, *132* (15), 154104. <https://doi.org/10.1063/1.3382344>.
- (133) Henkelman, G.; Jónsson, H. Improved Tangent Estimate in the Nudged Elastic Band Method for Finding Minimum Energy Paths and Saddle Points. *J. Chem. Phys.* **2000**, *113* (22), 9978–9985. <https://doi.org/10.1063/1.1323224>.
- (134) Henkelman, G.; Uberuaga, B. P.; Jónsson, H. A Climbing Image Nudged Elastic Band Method for Finding Saddle Points and Minimum Energy Paths. *J. Chem. Phys.* **2000**, *113* (22), 9901–9904. <https://doi.org/10.1063/1.1329672>.
- (135) Henkelman, G.; Jónsson, H. A Dimer Method for Finding Saddle Points on High Dimensional Potential Surfaces Using Only First Derivatives. *J. Chem. Phys.* **1999**, *111* (15), 7010–7022. <https://doi.org/10.1063/1.480097>.
- (136) Wischert, R.; Copéret, C.; Delbecq, F.; Sautet, P. Optimal Water Coverage on Alumina: A Key to Generate Lewis Acid-Base Pairs That Are Reactive Towards the C–H Bond Activation of Methane. *Angew. Chem. Int. Ed.* **2011**, *50* (14), 3202–3205. <https://doi.org/10.1002/anie.201006794>.
- (137) Monkhorst, H. J.; Pack, J. D. Special Points for Brillouin-Zone Integrations. *Phys. Rev. B* **1976**, *13* (12), 5188–5192. <https://doi.org/10.1103/PhysRevB.13.5188>.
- (138) Campbell, C. T.; Sellers, J. R. V. The Entropies of Adsorbed Molecules. *J. Am. Chem. Soc.* **2012**, *134* (43), 18109–18115. <https://doi.org/10.1021/ja3080117>.
- (139) Davis, M. E.; Davis, R. J. *Fundamentals of Chemical Reaction Engineering*, International ed.; McGraw-Hill chemical engineering series; McGraw-Hill: Boston, 2003.
- (140) Fogler, H. S. *Elements of Chemical Reaction Engineering*, 4th ed.; Prentice Hall PTR international series in the physical and chemical engineering sciences; Prentice Hall PTR: Upper Saddle River, NJ, 2006.
- (141) Wilke, C. R.; Chang, P. Correlation of Diffusion Coefficients in Dilute Solutions. *AIChE J.* **1955**, *1* (2), 264–270. <https://doi.org/10.1002/aic.690010222>.
- (142) Lyons, T. W.; Guironnet, D.; Findlater, M.; Brookhart, M. Synthesis of *p*-Xylene from Ethylene. *J. Am. Chem. Soc.* **2012**, *134* (38), 15708–15711. <https://doi.org/10.1021/ja307612b>.
- (143) Wagemann, K. Production of Basic Chemicals on the Basis of Renewable Resources as an Alternative to Petrochemistry? *ChemBioEng Rev.* **2015**, *2* (5), 315–334. <https://doi.org/10.1002/cben.201500005>.
- (144) Settle, A. E.; Berstis, L.; Rorrer, N. A.; Roman-Leshkóv, Y.; Beckham, G. T.; Richards, R. M.; Vardon, D. R. Heterogeneous Diels–Alder Catalysis for Biomass-Derived Aromatic Compounds. *Green Chem.* **2017**, *19* (15), 3468–3492. <https://doi.org/10.1039/C7GC00992E>.
- (145) Nikbin, N.; Do, P. T.; Caratzoulas, S.; Lobo, R. F.; Dauenhauer, P. J.; Vlachos, D. G. A DFT Study of the Acid-Catalyzed Conversion of 2,5-Dimethylfuran and Ethylene to *p*-Xylene. *J. Catal.* **2013**, *297*, 35–43. <https://doi.org/10.1016/j.jcat.2012.09.017>.

- (146) Chang, C.-C.; Je Cho, H.; Yu, J.; Gorte, R. J.; Gulbinski, J.; Dauenhauer, P.; Fan, W. Lewis Acid Zeolites for Tandem Diels–Alder Cycloaddition and Dehydration of Biomass-Derived Dimethylfuran and Ethylene to Renewable *p*-Xylene. *Green Chem.* **2016**, *18* (5), 1368–1376. <https://doi.org/10.1039/C5GC02164B>.
- (147) Williams, C. L.; Chang, C.-C.; Do, P.; Nikbin, N.; Caratzoulas, S.; Vlachos, D. G.; Lobo, R. F.; Fan, W.; Dauenhauer, P. J. Cycloaddition of Biomass-Derived Furans for Catalytic Production of Renewable *p*-Xylene. *ACS Catal.* **2012**, *2* (6), 935–939. <https://doi.org/10.1021/cs300011a>.
- (148) Wang, B.; Gruter, G. J. M.; Dam, M. A.; Kriegel, R. M. Process for the Preparation of Benzene Derivatives from Furan Derivatives. US9637437B2, May 2, 2017.
- (149) Lu, R.; Lu, F.; Chen, J.; Yu, W.; Huang, Q.; Zhang, J.; Xu, J. Production of Diethyl Terephthalate from Biomass-Derived Muconic Acid. *Angew. Chem.* **2016**, *128* (1), 257–261. <https://doi.org/10.1002/ange.201509149>.
- (150) Carraher, J. M.; Pfennig, T.; Rao, R. G.; Shanks, B. H.; Tessonnier, J.-P. Cis,Cis-Muconic Acid Isomerization and Catalytic Conversion to Biobased Cyclic-C₆-1,4-Diacid Monomers. *Green Chem.* **2017**, *19* (13), 3042–3050. <https://doi.org/10.1039/C7GC00658F>.
- (151) Hoydonckx, H. E.; Van Rhijn, W. M.; Van Rhijn, W.; De Vos, D. E.; Jacobs, P. A. Furfural and Derivatives. In *Ullmann's Encyclopedia of Industrial Chemistry*; Wiley-VCH Verlag GmbH & Co. KGaA, Ed.; Wiley-VCH Verlag GmbH & Co. KGaA: Weinheim, Germany, 2007; p a12_119.pub2. https://doi.org/10.1002/14356007.a12_119.pub2.
- (152) Ozer, R. Vapor Phase Decarbonylation Process. WO2011026059A1, March 3, 2011.
- (153) Burnett, L. W.; Johns, I. B.; Holdren, R. F.; Hixon, R. M. Production of 2-Methylfuran by Vapor-Phase Hydrogenation of Furfural. *Ind. Eng. Chem.* **1948**, *40* (3), 502–505. <https://doi.org/10.1021/ie50459a034>.
- (154) Román-Leshkov, Y.; Barrett, C. J.; Liu, Z. Y.; Dumesic, J. A. Production of Dimethylfuran for Liquid Fuels from Biomass-Derived Carbohydrates. *Nature* **2007**, *447* (7147), 982–985. <https://doi.org/10.1038/nature05923>.
- (155) Nishimura, S.; Ikeda, N.; Ebitani, K. Selective Hydrogenation of Biomass-Derived 5-Hydroxymethylfurfural (HMF) to 2,5-Dimethylfuran (DMF) under Atmospheric Hydrogen Pressure over Carbon Supported PdAu Bimetallic Catalyst. *Catal. Today* **2014**, *232*, 89–98. <https://doi.org/10.1016/j.cattod.2013.10.012>.
- (156) Rosatella, A. A.; Simeonov, S. P.; Frade, R. F. M.; Afonso, C. A. M. 5-Hydroxymethylfurfural (HMF) as a Building Block Platform: Biological Properties, Synthesis and Synthetic Applications. *Green Chem.* **2011**, *13* (4), 754. <https://doi.org/10.1039/c0gc00401d>.
- (157) Casanova, O.; Iborra, S.; Corma, A. Biomass into Chemicals: Aerobic Oxidation of 5-Hydroxymethyl-2-Furfural into 2,5-Furandicarboxylic Acid with Gold Nanoparticle Catalysts. *ChemSusChem* **2009**, *2* (12), 1138–1144. <https://doi.org/10.1002/cssc.200900137>.
- (158) Gao, T.; Wong, Y.; Ng, C.; Ho, K. L-Lactic Acid Production by *Bacillus Subtilis* MUR1. *Bioresour. Technol.* **2012**, *121*, 105–110. <https://doi.org/10.1016/j.biortech.2012.06.108>.

- (159) US Patent for Synthesis of quinic acid from glucose Patent (Patent # 5,798,236 issued August 25, 1998) - Justia Patents Search <https://patents.justia.com/patent/5798236> (accessed May 14, 2019).
- (160) Averagesch, N. J. H.; Krömer, J. O. Tailoring Strain Construction Strategies for Muconic Acid Production in *S. Cerevisiae* and *E. Coli*. *Metab. Eng. Commun.* **2014**, *1*, 19–28. <https://doi.org/10.1016/j.meteno.2014.09.001>.
- (161) Frost, J. W.; Miermont, A.; Schweitzer, D.; Bui, V.; Wicks, D. A. Cyclohexane 1,4 Carboxylates. US8367859B2, February 5, 2013.
- (162) Bui, V.; Lau, M. K.; Macrae, D. Methods for Producing Isomers of Muconic Acid and Muconate Salts. WO2011085311A1, July 14, 2011.
- (163) Cho, H. J.; Ren, L.; Vattipalli, V.; Yeh, Y.-H.; Gould, N.; Xu, B.; Gorte, R. J.; Lobo, R.; Dauenhauer, P. J.; Tsapatsis, M.; et al. Renewable *p*-Xylene from 2,5-Dimethylfuran and Ethylene Using Phosphorus-Containing Zeolite Catalysts. *ChemCatChem* **2017**, *9* (3), 398–402. <https://doi.org/10.1002/cctc.201601294>.
- (164) Sheldon, R. A. Green and Sustainable Manufacture of Chemicals from Biomass: State of the Art. *Green Chem* **2014**, *16* (3), 950–963. <https://doi.org/10.1039/C3GC41935E>.
- (165) Werpy, T.; Petersen, G. *Top Value Added Chemicals from Biomass: Volume I -- Results of Screening for Potential Candidates from Sugars and Synthesis Gas*; DOE/GO-102004-1992, 15008859; 2004; p DOE/GO-102004-1992, 15008859. <https://doi.org/10.2172/15008859>.
- (166) Bozell, J. J.; Petersen, G. R. Technology Development for the Production of Biobased Products from Biorefinery Carbohydrates—the US Department of Energy's "Top 10" Revisited. *Green Chem.* **2010**, *12* (4), 539. <https://doi.org/10.1039/b922014c>.
- (167) Hamilton, C. A.; Jackson, S. D.; Kelly, G. J. Solid Base Catalysts and Combined Solid Base Hydrogenation Catalysts for the Aldol Condensation of Branched and Linear Aldehydes. *Appl. Catal. Gen.* **2004**, *263* (1), 63–70. <https://doi.org/10.1016/j.apcata.2003.12.009>.
- (168) West, R. M.; Liu, Z. Y.; Peter, M.; Gärtner, C. A.; Dumesic, J. A. Carbon–Carbon Bond Formation for Biomass-Derived Furfurals and Ketones by Aldol Condensation in a Biphasic System. *J. Mol. Catal. Chem.* **2008**, *296* (1–2), 18–27. <https://doi.org/10.1016/j.molcata.2008.09.001>.
- (169) Lowry, T. H.; Richardson, K. S. *Mechanism and Theory in Organic Chemistry*; Harper & Row: New York, 1976.
- (170) Henschel, H.; Prosenc, M. H.; Nicholls, I. A. A Density Functional Study on the Factors Governing Metal Catalysis of the Direct Aldol Reaction. *J. Mol. Catal. Chem.* **2011**, *351*, 76–80. <https://doi.org/10.1016/j.molcata.2011.09.019>.
- (171) Kumagai, N.; Matsunaga, S.; Yoshikawa, N.; Ohshima, T.; Shibasaki, M. Direct Catalytic Enantio- and Diastereoselective Aldol Reaction Using a Zn–Zn-Linked-BINOL Complex: A Practical Synthesis of *s* *Yn*-1,2-Diols. *Org. Lett.* **2001**, *3* (10), 1539–1542. <https://doi.org/10.1021/ol015878p>.
- (172) Kumagai, N.; Matsunaga, S.; Kinoshita, T.; Harada, S.; Okada, S.; Sakamoto, S.; Yamaguchi, K.; Shibasaki, M. Direct Catalytic Asymmetric Aldol Reaction of

- Hydroxyketones: Asymmetric Zn Catalysis with a Et₂Zn/Linked-BINOL Complex. *J. Am. Chem. Soc.* **2003**, *125* (8), 2169–2178. <https://doi.org/10.1021/ja028926p>.
- (173) Mahrwald, R.; Ziemer, B. Insight into the Mechanism of Direct Catalytic Aldol Addition Mediated by Ambifunctional Titanium Complexes. *Tetrahedron Lett.* **2002**, *43* (25), 4459–4461. [https://doi.org/10.1016/S0040-4039\(02\)00822-5](https://doi.org/10.1016/S0040-4039(02)00822-5).
- (174) Inoue, H.; Kikuchi, M.; Ito, J.; Nishiyama, H. Chiral Phebox–Rhodium Complexes as Catalysts for Asymmetric Direct Aldol Reaction. *Tetrahedron* **2008**, *64* (3), 493–499. <https://doi.org/10.1016/j.tet.2007.11.022>.
- (175) Di Cosimo, J. I.; Díez, V. K.; Apesteguía, C. R. Base Catalysis for the Synthesis of α,β -Unsaturated Ketones from the Vapor-Phase Aldol Condensation of Acetone. *Appl. Catal. Gen.* **1996**, *137* (1), 149–166. [https://doi.org/10.1016/0926-860X\(95\)00289-8](https://doi.org/10.1016/0926-860X(95)00289-8).
- (176) Wang, G.-W.; Zhang, Z.; Dong, Y.-W. Environmentally Friendly and Efficient Process for the Preparation of β -Hydroxyl Ketones. *Org. Process Res. Dev.* **2004**, *8* (1), 18–21. <https://doi.org/10.1021/op0341263>.
- (177) Shigemasa, Y.; Yokoyama, K.; Sashiwa, H.; Saimoto, H. Synthesis of Threo- and Erythro-3-Pentulose by Aldol Type Reaction in Water. *Tetrahedron Lett.* **1994**, *35* (8), 1263–1266. [https://doi.org/10.1016/0040-4039\(94\)88039-5](https://doi.org/10.1016/0040-4039(94)88039-5).
- (178) Palomares, A. E.; Eder-Mirth, G.; Rep, M.; Lercher, J. A. Alkylation of Toluene over Basic Catalysts—Key Requirements for Side Chain Alkylation. *J. Catal.* **1998**, *180* (1), 56–65. <https://doi.org/10.1006/jcat.1998.2253>.
- (179) Zeng, R.; Fu, X.; Gong, C.; Sui, Y.; Ma, X.; Yang, X. Preparation and Catalytic Property of the Solid Base Supported on the Mixed Zirconium Phosphate Phosphonate for Knoevenagel Condensation. *J. Mol. Catal. Chem.* **2005**, *229* (1–2), 1–5. <https://doi.org/10.1016/j.molcata.2004.11.002>.
- (180) Choudary, B. M.; Kantam, M. L.; Sreekanth, P.; Bandopadhyay, T.; Figueras, F.; Tuel, A. Knoevenagel and Aldol Condensations Catalysed by a New Diamino-Functionalised Mesoporous Material. *J. Mol. Catal. Chem.* **1999**, *142* (3), 361–365. [https://doi.org/10.1016/S1381-1169\(98\)00301-X](https://doi.org/10.1016/S1381-1169(98)00301-X).
- (181) Roelofs, J. C. A. A.; Lensveld, D. J.; van Dillen, A. J.; de Jong, K. P. On the Structure of Activated Hydrotalcites as Solid Base Catalysts for Liquid-Phase Aldol Condensation. *J. Catal.* **2001**, *203* (1), 184–191. <https://doi.org/10.1006/jcat.2001.3295>.
- (182) Climent, M. J.; Corma, A.; Iborra, S.; Velty, A. Activated Hydrotalcites as Catalysts for the Synthesis of Chalcones of Pharmaceutical Interest. *J. Catal.* **2004**, *221* (2), 474–482. <https://doi.org/10.1016/j.jcat.2003.09.012>.
- (183) Gines, M. J. L.; Iglesia, E. Bifunctional Condensation Reactions of Alcohols on Basic Oxides Modified by Copper and Potassium. *J. Catal.* **1998**, *176* (1), 155–172. <https://doi.org/10.1006/jcat.1998.2009>.
- (184) Swain, C. G.; Powell, A. L.; Sheppard, W. A.; Morgan, C. R. Mechanism of the Cannizzaro Reaction. *J. Am. Chem. Soc.* **1979**, *101* (13), 3576–3583. <https://doi.org/10.1021/ja00507a023>.
- (185) Berberich, H.; Roesky, P. W. Homoleptic Lanthanide Amides as Homogeneous Catalysts for the Tishchenko Reaction. *Angew. Chem. Int. Ed.* **1998**, *37* (11), 1569–1571.

[https://doi.org/10.1002/\(SICI\)1521-3773\(19980619\)37:11<1569::AID-ANIE1569>3.0.CO;2-C](https://doi.org/10.1002/(SICI)1521-3773(19980619)37:11<1569::AID-ANIE1569>3.0.CO;2-C).

- (186) Perdew, J. P.; Chevary, J. A.; Vosko, S. H.; Jackson, K. A.; Pederson, M. R.; Singh, D. J.; Fiolhais, C. Atoms, Molecules, Solids, and Surfaces: Applications of the Generalized Gradient Approximation for Exchange and Correlation. *Phys. Rev. B* **1992**, *46* (11), 6671–6687. <https://doi.org/10.1103/PhysRevB.46.6671>.
- (187) Vanderbilt, D. Soft Self-Consistent Pseudopotentials in a Generalized Eigenvalue Formalism. *Phys. Rev. B* **1990**, *41* (11), 7892–7895. <https://doi.org/10.1103/PhysRevB.41.7892>.
- (188) Qian, X.; Li, J.; Qi, L.; Wang, C.-Z.; Chan, T.-L.; Yao, Y.-X.; Ho, K.-M.; Yip, S. Quasiatomic Orbitals for *Ab Initio* Tight-Binding Analysis. *Phys. Rev. B* **2008**, *78* (24), 245112. <https://doi.org/10.1103/PhysRevB.78.245112>.
- (189) Johnston, S. M.; Mulligan, A.; Dhanak, V.; Kadodwala, M. The Bonding of Acetone on Cu(111). *Surf. Sci.* **2004**, *548* (1–3), 5–12. <https://doi.org/10.1016/j.susc.2003.11.028>.
- (190) Lamont, C. L. A.; Stenzel, W.; Conrad, H.; Bradshaw, A. M. The Oxidation of Acetaldehyde on Cu{111}: A High Resolution Electron Energy Loss Spectroscopy Study. *J. Electron Spectrosc. Relat. Phenom.* **1993**, *64–65*, 287–296. [https://doi.org/10.1016/0368-2048\(93\)80090-9](https://doi.org/10.1016/0368-2048(93)80090-9).
- (191) Ishikawa, Y.; Liao, M.-S.; Cabrera, C. R. Oxidation of Methanol on Platinum, Ruthenium and Mixed Pt–M Metals (M=Ru, Sn): A Theoretical Study. *Surf. Sci.* **2000**, *463* (1), 66–80. [https://doi.org/10.1016/S0039-6028\(00\)00600-2](https://doi.org/10.1016/S0039-6028(00)00600-2).
- (192) Gomes, J. R. B.; Gomes, J. A. N. F.; Illas, F. First-Principles Study of the Adsorption of Formaldehyde on the Clean and Atomic Oxygen Covered Cu(1 1 1) Surface. *J. Mol. Catal. Chem.* **2001**, *170* (1–2), 187–193. [https://doi.org/10.1016/S1381-1169\(01\)00059-0](https://doi.org/10.1016/S1381-1169(01)00059-0).
- (193) Desai, S. K.; Neurock, M.; Kourtakis, K. A Periodic Density Functional Theory Study of the Dehydrogenation of Methanol over Pt(111). *J. Phys. Chem. B* **2002**, *106* (10), 2559–2568. <https://doi.org/10.1021/jp0132984>.
- (194) Masel, R. I. *Principles of Adsorption and Reaction on Solid Surfaces*; Wiley series in chemical engineering; Wiley: New York, 1996.
- (195) Sinha, N. K.; Neurock, M. A First Principles Analysis of the Hydrogenation of C1C4 Aldehydes and Ketones over Ru(0001). *J. Catal.* **2012**, *295*, 31–44. <https://doi.org/10.1016/j.jcat.2012.07.018>.
- (196) Cao, D.; Lu, G.-Q.; Wieckowski, A.; Wasileski, S. A.; Neurock, M. Mechanisms of Methanol Decomposition on Platinum: A Combined Experimental and *Ab Initio* Approach. *J. Phys. Chem. B* **2005**, *109* (23), 11622–11633. <https://doi.org/10.1021/jp0501188>.
- (197) Desai, S. K.; Neurock, M. First-Principles Study of the Role of Solvent in the Dissociation of Water over a Pt-Ru Alloy. *Phys. Rev. B* **2003**, *68* (7), 075420. <https://doi.org/10.1103/PhysRevB.68.075420>.
- (198) Desai, S. K.; Pallasana, V.; Neurock, M. A Periodic Density Functional Theory Analysis of the Effect of Water Molecules on Deprotonation of Acetic Acid over Pd(111). *J. Phys. Chem. B* **2001**, *105* (38), 9171–9182. <https://doi.org/10.1021/jp002797m>.

- (199) Ammon, Ch.; Bayer, A.; Held, G.; Richter, B.; Schmidt, Th.; Steinrück, H.-P. Dissociation and Oxidation of Methanol on Cu(). *Surf. Sci.* **2002**, 507–510, 845–850. [https://doi.org/10.1016/S0039-6028\(02\)01361-4](https://doi.org/10.1016/S0039-6028(02)01361-4).
- (200) Bowker, M.; Madix, R. J. XPS, UPS and Thermal Desorption Studies of Alcohol Adsorption on Cu(110). *Surf. Sci.* **1980**, 95 (1), 190–206. [https://doi.org/10.1016/0039-6028\(80\)90135-1](https://doi.org/10.1016/0039-6028(80)90135-1).
- (201) Bowker, M.; Madix, R. J. XPS, UPS and Thermal Desorption Studies of Alcohol Adsorption on Cu(110). *Surf. Sci.* **1982**, 116 (3), 549–572. [https://doi.org/10.1016/0039-6028\(82\)90364-8](https://doi.org/10.1016/0039-6028(82)90364-8).
- (202) Pudney, P. A Molecular Beam Study of the Oxidative Dehydrogenation of Alcohols on Cu(110). *J. Catal.* **1991**, 131 (1), 104–114. [https://doi.org/10.1016/0021-9517\(91\)90327-Z](https://doi.org/10.1016/0021-9517(91)90327-Z).
- (203) Zope, B. N.; Hibbitts, D. D.; Neurock, M.; Davis, R. J. Reactivity of the Gold/Water Interface During Selective Oxidation Catalysis. *Science* **2010**, 330 (6000), 74–78. <https://doi.org/10.1126/science.1195055>.
- (204) Hibbitts, D.; Neurock, M. Promotional Effects of Chemisorbed Oxygen and Hydroxide in the Activation of C–H and O–H Bonds over Transition Metal Surfaces. *Surf. Sci.* **2016**, 650, 210–220. <https://doi.org/10.1016/j.susc.2016.01.012>.
- (205) Hibbitts, D. D.; Neurock, M. Influence of Oxygen and PH on the Selective Oxidation of Ethanol on Pd Catalysts. *J. Catal.* **2013**, 299, 261–271. <https://doi.org/10.1016/j.jcat.2012.11.016>.
- (206) Jensen, W. B. *The Lewis Acid-Base Concepts: An Overview*; Wiley: New York, 1980.
- (207) Calaza, F.; Stacchiola, D.; Neurock, M.; Tysoe, W. T. Coverage Effects on the Palladium-Catalyzed Synthesis of Vinyl Acetate: Comparison between Theory and Experiment. *J. Am. Chem. Soc.* **2010**, 132 (7), 2202–2207. <https://doi.org/10.1021/ja907061m>.
- (208) Stacchiola, D.; Calaza, F.; Burkholder, L.; Schwabacher, A. W.; Neurock, M.; Tysoe, W. T. Elucidation of the Reaction Mechanism for the Palladium-Catalyzed Synthesis of Vinyl Acetate. *Angew. Chem. Int. Ed.* **2005**, 44 (29), 4572–4574. <https://doi.org/10.1002/anie.200500782>.
- (209) *Surface Reactions*; Madix, R. J., Ed.; Ertl, G., Gomer, R., Mills, D. L., Lotsch, H. K. V., Series Eds.; Springer Series in Surface Sciences; Springer Berlin Heidelberg: Berlin, Heidelberg, 1994; Vol. 34. <https://doi.org/10.1007/978-3-642-78746-1>.
- (210) Xing, Q.; Pei, W. *Fundamental Organic Chemistry*; Higher Education Press.
- (211) Akashi, T.; Sato, S.; Takahashi, R.; Sodesawa, T.; Inui, K. Catalytic Vapor-Phase Cyclization of 1,6-Hexanediol into Cyclopentanone. *Catal. Commun.* **2003**, 4 (8), 411–416. [https://doi.org/10.1016/S1566-7367\(03\)00095-5](https://doi.org/10.1016/S1566-7367(03)00095-5).
- (212) Elliott, D. The Formation of Ketones in the Presence of Carbon Monoxide over CuO/ZnO/Al₂O₃. *J. Catal.* **1989**, 119 (2), 359–367. [https://doi.org/10.1016/0021-9517\(89\)90166-8](https://doi.org/10.1016/0021-9517(89)90166-8).
- (213) Liu, X.; Xu, B.; Haubrich, J.; Madix, R. J.; Friend, C. M. Surface-Mediated Self-Coupling of Ethanol on Gold. *J. Am. Chem. Soc.* **2009**, 131 (16), 5757–5759. <https://doi.org/10.1021/ja900822r>.

- (214) Xu, B.; Liu, X.; Haubrich, J.; Madix, R. J.; Friend, C. M. Selectivity Control in Gold-Mediated Esterification of Methanol. *Angew. Chem. Int. Ed.* **2009**, *48* (23), 4206–4209. <https://doi.org/10.1002/anie.200805404>.
- (215) Santen, R. A. van; Neurock, M. *Molecular Heterogeneous Catalysis: A Conceptual and Computational Approach*; Wiley-VCH: Weinheim, 2006.
- (216) Luo, S.; Falconer, J. L. Aldol Condensation of Acetaldehyde to Form High Molecular Weight Compounds on TiO₂. *Catal. Lett.* **1999**, *57* (3), 89–93. <https://doi.org/10.1023/A:1019003817314>.
- (217) Rekoske, J. E.; Barteau, M. A. Kinetics, Selectivity, and Deactivation in the Aldol Condensation of Acetaldehyde on Anatase Titanium Dioxide. *Ind. Eng. Chem. Res.* **2011**, *50* (1), 41–51. <https://doi.org/10.1021/ie100394v>.
- (218) Ordonsky, V. V.; Sushkevich, V. L.; Ivanova, I. I. Study of Acetaldehyde Condensation Chemistry over Magnesia and Zirconia Supported on Silica. *J. Mol. Catal. Chem.* **2010**, *333* (1–2), 85–93. <https://doi.org/10.1016/j.molcata.2010.10.001>.
- (219) Sun, J.; Zhu, K.; Gao, F.; Wang, C.; Liu, J.; Peden, C. H. F.; Wang, Y. Direct Conversion of Bio-Ethanol to Isobutene on Nanosized Zn_xZr_yO_z Mixed Oxides with Balanced Acid–Base Sites. *J. Am. Chem. Soc.* **2011**, *133* (29), 11096–11099. <https://doi.org/10.1021/ja204235v>.
- (220) Tanabe, K.; Yamaguchi, T. Acid-Base Bifunctional Catalysis by ZrO₂ and Its Mixed Oxides. *Catal. Today* **1994**, *20* (2), 185–197. [https://doi.org/10.1016/0920-5861\(94\)80002-2](https://doi.org/10.1016/0920-5861(94)80002-2).
- (221) Tanabe, K. Industrial Application of Solid Acid–Base Catalysts. *Appl. Catal. Gen.* **1999**, *181* (2), 399–434. [https://doi.org/10.1016/S0926-860X\(98\)00397-4](https://doi.org/10.1016/S0926-860X(98)00397-4).
- (222) Tanabe, K. The Future of Acid-Base Catalysis. *Appl. Catal. Gen.* **1994**, *113* (2), 147–152. [https://doi.org/10.1016/0926-860X\(94\)80023-5](https://doi.org/10.1016/0926-860X(94)80023-5).
- (223) Rozmysłowicz, B.; Kirilin, A.; Aho, A.; Manyar, H.; Hardacre, C.; Wärnå, J.; Salmi, T.; Murzin, D. Yu. Selective Hydrogenation of Fatty Acids to Alcohols over Highly Dispersed ReO_x/TiO₂ Catalyst. *J. Catal.* **2015**, *328*, 197–207. <https://doi.org/10.1016/j.jcat.2015.01.003>.
- (224) Takeda, Y.; Tamura, M.; Nakagawa, Y.; Okumura, K.; Tomishige, K. Characterization of Re–Pd/SiO₂ Catalysts for Hydrogenation of Stearic Acid. *ACS Catal.* **2015**, *5* (11), 7034–7047. <https://doi.org/10.1021/acscatal.5b01054>.
- (225) Takeda, Y.; Nakagawa, Y.; Tomishige, K. Selective Hydrogenation of Higher Saturated Carboxylic Acids to Alcohols Using a ReO_x–Pd/SiO₂ Catalyst. *Catal. Sci. Technol.* **2012**, *2* (11), 2221. <https://doi.org/10.1039/c2cy20302b>.
- (226) Pritchard, J.; Filonenko, G. A.; van Putten, R.; Hensen, E. J. M.; Pidko, E. A. Heterogeneous and Homogeneous Catalysis for the Hydrogenation of Carboxylic Acid Derivatives: History, Advances and Future Directions. *Chem. Soc. Rev.* **2015**, *44* (11), 3808–3833. <https://doi.org/10.1039/C5CS00038F>.
- (227) Steen, E. J.; Kang, Y.; Bokinsky, G.; Hu, Z.; Schirmer, A.; McClure, A.; del Cardayre, S. B.; Keasling, J. D. Microbial Production of Fatty-Acid-Derived Fuels and Chemicals from Plant Biomass. *Nature* **2010**, *463* (7280), 559–562. <https://doi.org/10.1038/nature08721>.

- (228) Baumann, I.; Westermann, P. Microbial Production of Short Chain Fatty Acids from Lignocellulosic Biomass: Current Processes and Market. *BioMed Res. Int.* **2016**, *2016*, 1–15. <https://doi.org/10.1155/2016/8469357>.
- (229) Adkins, Homer.; Folkers, Karl. THE CATALYTIC HYDROGENATION OF ESTERS TO ALCOHOLS. *J. Am. Chem. Soc.* **1931**, *53* (3), 1095–1097. <https://doi.org/10.1021/ja01354a042>.
- (230) Adkins, H.; Burgoyne, E. E.; Schneider, H. J. The Copper—Chromium Oxide Catalyst for Hydrogenation ¹. *J. Am. Chem. Soc.* **1950**, *72* (6), 2626–2629. <https://doi.org/10.1021/ja01162a079>.
- (231) Pallassana, V.; Neurock, M. Reaction Paths in the Hydrogenolysis of Acetic Acid to Ethanol over Pd(111), Re(0001), and PdRe Alloys. *J. Catal.* **2002**, *209* (2), 289–305. <https://doi.org/10.1006/jcat.2002.3585>.
- (232) Kammert, J. D.; Xie, J.; Godfrey, I. J.; Unocic, R. R.; Stavitski, E.; Attenkofer, K.; Sankar, G.; Davis, R. J. Reduction of Propionic Acid over a Pd-Promoted ReO_x/SiO₂ Catalyst Probed by X-Ray Absorption Spectroscopy and Transient Kinetic Analysis. *ACS Sustain. Chem. Eng.* **2018**, *6* (9), 12353–12366. <https://doi.org/10.1021/acssuschemeng.8b02820>.
- (233) Ly, B. K.; Tapin, B.; Aouine, M.; Delichere, P.; Epron, F.; Pinel, C.; Especel, C.; Besson, M. Insights into the Oxidation State and Location of Rhenium in Re-Pd/TiO₂ Catalysts for Aqueous-Phase Selective Hydrogenation of Succinic Acid to 1,4-Butanediol as a Function of Palladium and Rhenium Deposition Methods. *ChemCatChem* **2015**, *7* (14), 2161–2178. <https://doi.org/10.1002/cctc.201500197>.
- (234) Latusek, M. P.; Spigarelli, B. P.; Heimerl, R. M.; Holles, J. H. Correlation of H₂ Heat of Adsorption and Ethylene Hydrogenation Activity for Supported Re@Pd Overlayer Catalysts. *J. Catal.* **2009**, *263* (2), 306–314. <https://doi.org/10.1016/j.jcat.2009.02.022>.
- (235) Chądzyński, G. W.; Kubicka, H. Chemisorption of Hydrogen and Oxygen on γ -Alumina-Supported Rhenium. *Thermochim. Acta* **1990**, *158* (2), 353–367. [https://doi.org/10.1016/0040-6031\(90\)80083-B](https://doi.org/10.1016/0040-6031(90)80083-B).
- (236) Malinowski, A.; Juszczak, W.; Bonarowska, M.; Pielaszek, J.; Karpinski, Z. Pd-Re/Al₂O₃: Characterization and Catalytic Activity in Hydrodechlorination of CCl₂F₂. *J. Catal.* **1998**, *177* (2), 153–163. <https://doi.org/10.1006/jcat.1998.2062>.
- (237) Thompson, S. T.; Lamb, H. H. Palladium–Rhenium Catalysts for Selective Hydrogenation of Furfural: Evidence for an Optimum Surface Composition. *ACS Catal.* **2016**, *6* (11), 7438–7447. <https://doi.org/10.1021/acscatal.6b01398>.
- (238) Ferrin, P.; Kandoi, S.; Nilekar, A. U.; Mavrikakis, M. Hydrogen Adsorption, Absorption and Diffusion on and in Transition Metal Surfaces: A DFT Study. *Surf. Sci.* **2012**, *606* (7–8), 679–689. <https://doi.org/10.1016/j.susc.2011.12.017>.
- (239) Hammer, B.; Norskov, J. K. Why Gold Is the Noblest of All the Metals. *Nature* **1995**, *376* (6537), 238–240. <https://doi.org/10.1038/376238a0>.
- (240) Dong, W.; Hafner, J. H₂ Dissociative Adsorption on Pd(111). *Phys. Rev. B* **1997**, *56* (23), 15396–15403. <https://doi.org/10.1103/PhysRevB.56.15396>.

- (241) Faccin, F.; Guedes, F. F.; Benvenuti, E. V.; Moro, C. C. A FTIR Study of the Metal-Support Interactions and Hydrogen Spillover on Pd/TiO₂ and Ni/TiO₂. *Eclética Quím.* **2002**, *27* (0). <https://doi.org/10.1590/S0100-46702002000100008>.
- (242) Chen, H.-Y. T.; Tosoni, S.; Pacchioni, G. Hydrogen Adsorption, Dissociation, and Spillover on Ru₁₀ Clusters Supported on Anatase TiO₂ and Tetragonal ZrO₂ (101) Surfaces. *ACS Catal.* **2015**, *5* (9), 5486–5495. <https://doi.org/10.1021/acscatal.5b01093>.
- (243) Karim, W.; Spreafico, C.; Kleibert, A.; Gobrecht, J.; VandeVondele, J.; Ekinici, Y.; van Bokhoven, J. A. Catalyst Support Effects on Hydrogen Spillover. *Nature* **2017**, *541* (7635), 68–71. <https://doi.org/10.1038/nature20782>.
- (244) Solomons, T. W. G.; Fryhle, C. B.; Snyder, S. A. *Organic Chemistry*, 12e ed.; John Wiley & Sons, Inc: Hoboken, NJ, 2016.
- (245) Pallassana, V.; Neurock, M. Reaction Paths in the Hydrogenolysis of Acetic Acid to Ethanol over Pd(111), Re(0001), and PdRe Alloys. *J. Catal.* **2002**, *209* (2), 289–305. <https://doi.org/10.1006/jcat.2002.3585>.
- (246) Fernández-Torres, L. C.; Sykes, E. C. H.; Nanayakkara, S. U.; Weiss, P. S. Dynamics and Spectroscopy of Hydrogen Atoms on Pd{111}. *J. Phys. Chem. B* **2006**, *110* (14), 7380–7384. <https://doi.org/10.1021/jp055815e>.
- (247) Davis, J. L.; Barteau, M. A. Hydrogen Bonding in Carboxylic Acid Adlayers on Pd(111): Evidence for Catemer Formation. *Langmuir* **1989**, *5* (6), 1299–1309. <https://doi.org/10.1021/la00090a004>.
- (248) Xu, B.; Madix, R. J.; Friend, C. M. Predicting Gold-Mediated Catalytic Oxidative-Coupling Reactions from Single Crystal Studies. *Acc. Chem. Res.* **2014**, *47* (3), 761–772. <https://doi.org/10.1021/ar4002476>.
- (249) Neurock, M.; Tao, Z.; Chemburkar, A.; Hibbitts, D. D.; Iglesia, E. Theoretical Insights into the Sites and Mechanisms for Base Catalyzed Esterification and Aldol Condensation Reactions over Cu. *Faraday Discuss.* **2017**, *197*, 59–86. <https://doi.org/10.1039/C6FD00226A>.
- (250) Ojeda, M.; Li, A.; Nabar, R.; Nilekar, A. U.; Mavrikakis, M.; Iglesia, E. Kinetically Relevant Steps and H₂/D₂ Isotope Effects in Fischer–Tropsch Synthesis on Fe and Co Catalysts. *J. Phys. Chem. C* **2010**, *114* (46), 19761–19770. <https://doi.org/10.1021/jp1073076>.
- (251) Krishnamoorthy, S.; Tu, M.; Ojeda, M. P.; Pinna, D.; Iglesia, E. An Investigation of the Effects of Water on Rate and Selectivity for the Fischer–Tropsch Synthesis on Cobalt-Based Catalysts. *J. Catal.* **2002**, *211* (2), 422–433. <https://doi.org/10.1006/jcat.2002.3749>.
- (252) Mori, T.; Masuda, H.; Imai, H.; Miyamoto, A.; Hasebe, R.; Murakami, Y. Kinetics, Isotope Effects, and Mechanism of the Hydrogenation of Carbon Monoxide on a Supported Palladium Catalyst. *J. Phys. Chem.* **1983**, *87* (19), 3648–3652. <https://doi.org/10.1021/j100242a016>.
- (253) Greeley, J.; Mavrikakis, M. A First-Principles Study of Methanol Decomposition on Pt(111). *J. Am. Chem. Soc.* **2002**, *124* (24), 7193–7201. <https://doi.org/10.1021/ja017818k>.
- (254) Dudarev, S. L.; Botton, G. A.; Savrasov, S. Y.; Humphreys, C. J.; Sutton, A. P. Electron-Energy-Loss Spectra and the Structural Stability of Nickel Oxide: An LSDA+U Study. *Phys. Rev. B* **1998**, *57* (3), 1505–1509. <https://doi.org/10.1103/PhysRevB.57.1505>.

- (255) Hu, Z.; Metiu, H. Choice of U for DFT+ U Calculations for Titanium Oxides. *J. Phys. Chem. C* **2011**, *115* (13), 5841–5845. <https://doi.org/10.1021/jp111350u>.
- (256) Akpa, B. S.; D'Agostino, C.; Gladden, L. F.; Hindle, K.; Manyar, H.; McGregor, J.; Li, R.; Neurock, M.; Sinha, N.; Stitt, E. H.; et al. Solvent Effects in the Hydrogenation of 2-Butanone. *J. Catal.* **2012**, *289*, 30–41. <https://doi.org/10.1016/j.jcat.2012.01.011>.
- (257) Kusserow, B.; Schimpf, S.; Claus, P. Hydrogenation of Glucose to Sorbitol over Nickel and Ruthenium Catalysts. *Adv. Synth. Catal.* **2003**, *345* (12), 289–299. <https://doi.org/10.1002/adsc.200390024>.
- (258) Blaser, H.-U.; Malan, C.; Pugin, B.; Spindler, F.; Steiner, H.; Studer, M. Selective Hydrogenation for Fine Chemicals: Recent Trends and New Developments. *Adv. Synth. Catal.* **2003**, *345* (12), 103–151. <https://doi.org/10.1002/adsc.200390000>.
- (259) Vilar, M.; Oliveira, J. L.; Navarro, M. Investigation of the Hydrogenation Reactivity of Some Organic Substrates Using an Electrocatalytic Method. *Appl. Catal. Gen.* **2010**, *372* (1), 1–7. <https://doi.org/10.1016/j.apcata.2009.09.041>.
- (260) Horiuti, I.; Polanyi, M. Exchange Reactions of Hydrogen on Metallic Catalysts. *Trans. Faraday Soc.* **1934**, *30*, 1164. <https://doi.org/10.1039/TF9343001164>.
- (261) Mukherjee, S.; Vannice, M. Solvent Effects in Liquid-Phase Reactions. I. Activity and Selectivity during Citral Hydrogenation on Pt/SiO₂ and Evaluation of Mass Transfer Effects. *J. Catal.* **2006**, *243* (1), 108–130. <https://doi.org/10.1016/j.jcat.2006.06.021>.
- (262) Singh, U. K.; Vannice, M. A. Liquid-Phase Citral Hydrogenation over SiO₂-Supported Group VIII Metals. *J. Catal.* **2001**, *199* (1), 73–84. <https://doi.org/10.1006/jcat.2000.3157>.
- (263) Takagi, H.; Isoda, T.; Kusakabe, K.; Morooka, S. Effects of Solvents on the Hydrogenation of Mono-Aromatic Compounds Using Noble-Metal Catalysts. *Energy Fuels* **1999**, *13* (6), 1191–1196. <https://doi.org/10.1021/ef990061m>.
- (264) Mäki-Arvela, P.; Hájek, J.; Salmi, T.; Murzin, D. Yu. Chemoselective Hydrogenation of Carbonyl Compounds over Heterogeneous Catalysts. *Appl. Catal. Gen.* **2005**, *292*, 1–49. <https://doi.org/10.1016/j.apcata.2005.05.045>.
- (265) Rajadhyaksha, R. A.; Karwa, S. L. Solvent Effects in Catalytic Hydrogenation. *Chem. Eng. Sci.* **1986**, *41* (7), 1765–1770. [https://doi.org/10.1016/0009-2509\(86\)87055-5](https://doi.org/10.1016/0009-2509(86)87055-5).
- (266) Yamada, H.; Goto, S. The Effect of Solvents Polarity on Selective Hydrogenation of Unsaturated Aldehyde in Gas-Liquid-Solid Three Phase Reactor. *J. Chem. Eng. Jpn.* **2003**, *36* (5), 586–589. <https://doi.org/10.1252/jcej.36.586>.
- (267) Kun, I.; Szöllösi, G.; Bartók, M. Crotonaldehyde Hydrogenation over Clay-Supported Platinum Catalysts. *J. Mol. Catal. Chem.* **2001**, *169* (1–2), 235–246. [https://doi.org/10.1016/S1381-1169\(00\)00566-5](https://doi.org/10.1016/S1381-1169(00)00566-5).
- (268) Anderson, J. A.; Athawale, A.; Imrie, F. E.; McKenna, F.-M.; McCue, A.; Molyneux, D.; Power, K.; Shand, M.; Wells, R. P. K. Aqueous Phase Hydrogenation of Substituted Phenyls over Carbon Nanofibre and Activated Carbon Supported Pd. *J. Catal.* **2010**, *270* (1), 9–15. <https://doi.org/10.1016/j.jcat.2009.11.028>.
- (269) Hidalgo-Carrillo, J.; Aramendía, M. A.; Marinas, A.; Marinas, J. M.; Urbano, F. J. Support and Solvent Effects on the Liquid-Phase Chemoselective Hydrogenation of

- Crotonaldehyde over Pt Catalysts. *Appl. Catal. Gen.* **2010**, 385 (1–2), 190–200. <https://doi.org/10.1016/j.apcata.2010.07.012>.
- (270) Gallezot, P.; Richard, D. Selective Hydrogenation of α,β -Unsaturated Aldehydes. *Catal. Rev.* **1998**, 40 (1–2), 81–126. <https://doi.org/10.1080/01614949808007106>.
- (271) Murzin, D. Yu.; Backman, H. On Selectivity of Catalytic Reactions with Multi-Centered Adsorption. *React. Kinet. Catal. Lett.* **2007**, 91 (1), 141–147. <https://doi.org/10.1007/s11144-007-5095-3>.
- (272) Alcalá, R.; Greeley, J.; Mavrikakis, M.; Dumesic, J. A. Density-Functional Theory Studies of Acetone and Propanal Hydrogenation on Pt(111). *J. Chem. Phys.* **2002**, 116 (20), 8973–8980. <https://doi.org/10.1063/1.1471247>.
- (273) Delbecq, F.; Sautet, P. A Density Functional Study of Adsorption Structures of Unsaturated Aldehydes on Pt(111): A Key Factor for Hydrogenation Selectivity. *J. Catal.* **2002**, 211 (2), 398–406. <https://doi.org/10.1006/jcat.2002.3744>.
- (274) Laref, S.; Delbecq, F.; Loffreda, D. Theoretical Elucidation of the Selectivity Changes for the Hydrogenation of Unsaturated Aldehydes on Pt(111). *J. Catal.* **2009**, 265 (1), 35–42. <https://doi.org/10.1016/j.jcat.2009.04.010>.
- (275) Wellendorff, J.; Silbaugh, T. L.; Garcia-Pintos, D.; Nørskov, J. K.; Bligaard, T.; Studt, F.; Campbell, C. T. A Benchmark Database for Adsorption Bond Energies to Transition Metal Surfaces and Comparison to Selected DFT Functionals. *Surf. Sci.* **2015**, 640, 36–44. <https://doi.org/10.1016/j.susc.2015.03.023>.
- (276) van Druten, G. M. R.; Ponec, V. Hydrogenation of Carbonylic Compounds. *Appl. Catal. Gen.* **2000**, 191 (1–2), 163–176. [https://doi.org/10.1016/S0926-860X\(99\)00317-8](https://doi.org/10.1016/S0926-860X(99)00317-8).
- (277) Takeuchi, A.; Katzer, J. R. Mechanism of Methanol Formation. *J. Phys. Chem.* **1981**, 85 (8), 937–939. <https://doi.org/10.1021/j150608a002>.
- (278) Sen, B. Metal-Support Effects on Acetone Hydrogenation over Platinum Catalysts. *J. Catal.* **1988**, 113 (1), 52–71. [https://doi.org/10.1016/0021-9517\(88\)90237-0](https://doi.org/10.1016/0021-9517(88)90237-0).
- (279) Silverstein, K. A. T.; Haymet, A. D. J.; Dill, K. A. The Strength of Hydrogen Bonds in Liquid Water and Around Nonpolar Solutes. *J. Am. Chem. Soc.* **2000**, 122 (33), 8037–8041. <https://doi.org/10.1021/ja000459t>.
- (280) Tang, W.; Sanville, E.; Henkelman, G. A Grid-Based Bader Analysis Algorithm without Lattice Bias. *J. Phys. Condens. Matter* **2009**, 21 (8), 084204. <https://doi.org/10.1088/0953-8984/21/8/084204>.
- (281) Kizhakevariam, N.; Stuve, E. M. Coadsorption of Water and Hydrogen on Pt(100): Formation of Adsorbed Hydronium Ions. *Surf. Sci.* **1992**, 275 (3), 223–236. [https://doi.org/10.1016/0039-6028\(92\)90796-9](https://doi.org/10.1016/0039-6028(92)90796-9).
- (282) Desai, S. K.; Neurock, M. First-Principles Study of the Role of Solvent in the Dissociation of Water over a Pt-Ru Alloy. *Phys. Rev. B* **2003**, 68 (7), 075420. <https://doi.org/10.1103/PhysRevB.68.075420>.
- (283) Marx, D.; Tuckerman, M. E.; Hutter, J.; Parrinello, M. The Nature of the Hydrated Excess Proton in Water. *Nature* **1999**, 397 (6720), 601–604. <https://doi.org/10.1038/17579>.

- (284) Hasegawa, Y.; Jia, J. F.; Inoue, K.; Sakai, A.; Sakurai, T. Elemental Contrast of Local Work Function Studied by Scanning Tunneling Microscopy. *Surf. Sci.* **1997**, *386* (1–3), 328–334. [https://doi.org/10.1016/S0039-6028\(97\)00332-4](https://doi.org/10.1016/S0039-6028(97)00332-4).
- (285) Löber, R.; Hennig, D. Interaction of Hydrogen with Transition Metal Fcc(111) Surfaces. *Phys. Rev. B* **1997**, *55* (7), 4761–4765. <https://doi.org/10.1103/PhysRevB.55.4761>.
- (286) Goldmann, A.; Dose, V.; Borstel, G. Empty Electronic States at the (100), (110), and (111) Surfaces of Nickel, Copper, and Silver. *Phys. Rev. B* **1985**, *32* (4), 1971–1980. <https://doi.org/10.1103/PhysRevB.32.1971>.
- (287) Derry, G. N.; Ji-Zhong, Z. Work Function of Pt(111). *Phys. Rev. B* **1989**, *39* (3), 1940–1941. <https://doi.org/10.1103/PhysRevB.39.1940>.
- (288) Hansson, G. V.; Flodström, S. A. Photoemission Study of the Bulk and Surface Electronic Structure of Single Crystals of Gold. *Phys. Rev. B* **1978**, *18* (4), 1572–1585. <https://doi.org/10.1103/PhysRevB.18.1572>.
- (289) Zhu, Q.; Wang, S. Adsorption of Precious and Coinage Metals on Rh (111), Ru (0001) and W (110) Surfaces. *Appl. Surf. Sci.* **2017**, *410*, 282–290. <https://doi.org/10.1016/j.apsusc.2017.03.121>.
- (290) Kaack, M.; Fick, D. Determination of the Work Functions of Pt(111) and Ir(111) beyond 1100 K Surface Temperature. *Surf. Sci.* **1995**, *342* (1–3), 111–118. [https://doi.org/10.1016/0039-6028\(95\)00758-X](https://doi.org/10.1016/0039-6028(95)00758-X).
- (291) Kepp, K. P. A Quantitative Scale of Oxophilicity and Thiophilicity. *Inorg. Chem.* **2016**, *55* (18), 9461–9470. <https://doi.org/10.1021/acs.inorgchem.6b01702>.
- (292) Michaelides, A.; Alavi, A.; King, D. A. Different Surface Chemistries of Water on Ru{0001}: From Monomer Adsorption to Partially Dissociated Bilayers. *J. Am. Chem. Soc.* **2003**, *125* (9), 2746–2755. <https://doi.org/10.1021/ja028855u>.
- (293) Gao, X.; Heyden, A.; Abdelrahman, O. A.; Bond, J. Q. Microkinetic Analysis of Acetone Hydrogenation over Pt/SiO₂. *J. Catal.* **2019**, *374*, 183–198. <https://doi.org/10.1016/j.jcat.2019.04.033>.
- (294) Abdelrahman, O. A.; Heyden, A.; Bond, J. Q. Microkinetic Analysis of C₃–C₅ Ketone Hydrogenation over Supported Ru Catalysts. *J. Catal.* **2017**, *348*, 59–74. <https://doi.org/10.1016/j.jcat.2017.01.022>.
- (295) Franaszczuk, K.; Herrero, E.; Zelenay, P.; Wieckowski, A.; Wang, J.; Masel, R. I. A Comparison of Electrochemical and Gas-Phase Decomposition of Methanol on Platinum Surfaces. *J. Phys. Chem.* **1992**, *96* (21), 8509–8516. <https://doi.org/10.1021/j100200a056>.
- (296) Chia, M.; Pagán-Torres, Y. J.; Hibbitts, D.; Tan, Q.; Pham, H. N.; Datye, A. K.; Neurock, M.; Davis, R. J.; Dumesic, J. A. Selective Hydrogenolysis of Polyols and Cyclic Ethers over Bifunctional Surface Sites on Rhodium–Rhenium Catalysts. *J. Am. Chem. Soc.* **2011**, *133* (32), 12675–12689. <https://doi.org/10.1021/ja2038358>.
- (297) Mellmer, M. A.; Sanpitakseree, C.; Demir, B.; Bai, P.; Ma, K.; Neurock, M.; Dumesic, J. A. Solvent-Enabled Control of Reactivity for Liquid-Phase Reactions of Biomass-Derived Compounds. *Nat. Catal.* **2018**, *1* (3), 199–207. <https://doi.org/10.1038/s41929-018-0027-3>.

- (298) Gerceker, D.; Motagamwala, A. H.; Rivera-Dones, K. R.; Miller, J. B.; Huber, G. W.; Mavrikakis, M.; Dumesic, J. A. Methane Conversion to Ethylene and Aromatics on PtSn Catalysts. *ACS Catal.* **2017**, *7* (3), 2088–2100. <https://doi.org/10.1021/acscatal.6b02724>.
- (299) Flaherty, D. W. Direct Synthesis of H₂O₂ from H₂ and O₂ on Pd Catalysts: Current Understanding, Outstanding Questions, and Research Needs. *ACS Catal.* **2018**, *8* (2), 1520–1527. <https://doi.org/10.1021/acscatal.7b04107>.
- (300) Wilson, N. M.; Bregante, D. T.; Priyadarshini, P.; Flaherty, D. W. Production and Use of H₂O₂ for Atom-Efficient Functionalization of Hydrocarbons and Small Molecules. In *Catalysis*; Spivey, J., Han, Y.-F., Eds.; Royal Society of Chemistry: Cambridge, 2017; Vol. 29, pp 122–212. <https://doi.org/10.1039/9781788010634-00122>.
- (301) Goor, G.; Glenneberg, J.; Jacobi, S. Hydrogen Peroxide. In *Ullmann's Encyclopedia of Industrial Chemistry*; Wiley-VCH Verlag GmbH & Co. KGaA, Ed.; Wiley-VCH Verlag GmbH & Co. KGaA: Weinheim, Germany, 2007; p a13_443.pub2. https://doi.org/10.1002/14356007.a13_443.pub2.
- (302) Campos-Martin, J. M.; Blanco-Brieva, G.; Fierro, J. L. G. Hydrogen Peroxide Synthesis: An Outlook beyond the Anthraquinone Process. *Angew. Chem. Int. Ed.* **2006**, *45* (42), 6962–6984. <https://doi.org/10.1002/anie.200503779>.
- (303) Samanta, C. Direct Synthesis of Hydrogen Peroxide from Hydrogen and Oxygen: An Overview of Recent Developments in the Process. *Appl. Catal. Gen.* **2008**, *350* (2), 133–149. <https://doi.org/10.1016/j.apcata.2008.07.043>.
- (304) Wilson, N. M.; Flaherty, D. W. Mechanism for the Direct Synthesis of H₂O₂ on Pd Clusters: Heterolytic Reaction Pathways at the Liquid–Solid Interface. *J. Am. Chem. Soc.* **2016**, *138* (2), 574–586. <https://doi.org/10.1021/jacs.5b10669>.
- (305) Ford, D. C.; Nilekar, A. U.; Xu, Y.; Mavrikakis, M. Partial and Complete Reduction of O₂ by Hydrogen on Transition Metal Surfaces. *Surf. Sci.* **2010**, *604* (19–20), 1565–1575. <https://doi.org/10.1016/j.susc.2010.05.026>.
- (306) Edwards, J. K.; Hutchings, G. J. Palladium and Gold-Palladium Catalysts for the Direct Synthesis of Hydrogen Peroxide. *Angew. Chem. Int. Ed.* **2008**, *47* (48), 9192–9198. <https://doi.org/10.1002/anie.200802818>.
- (307) Liu, Q.; Bauer, J. C.; Schaak, R. E.; Lunsford, J. H. Direct Synthesis of H₂O₂ from H₂ and O₂ over Pd–Pt/SiO₂ Bimetallic Catalysts in a H₂SO₄/Ethanol System. *Appl. Catal. Gen.* **2008**, *339* (2), 130–136. <https://doi.org/10.1016/j.apcata.2008.01.026>.
- (308) Liu, Q.; Lunsford, J. H. Controlling Factors in the Direct Formation of H₂O₂ from H₂ and O₂ over a Pd/SiO₂ Catalyst in Ethanol. *Appl. Catal. Gen.* **2006**, *314* (1), 94–100. <https://doi.org/10.1016/j.apcata.2006.08.014>.
- (309) Chinta, S. A Mechanistic Study of H₂O₂ and H₂O Formation from H₂ and BO₂ Catalyzed by Palladium in an Aqueous Medium. *J. Catal.* **2004**, *225* (1), 249–255. <https://doi.org/10.1016/j.jcat.2004.04.014>.
- (310) Liu, Q.; Lunsford, J. The Roles of Chloride Ions in the Direct Formation of H₂O₂ from H₂ and O₂ over a Pd/SiO₂ Catalyst in a H₂SO₄/Ethanol System. *J. Catal.* **2006**, *239* (1), 237–243. <https://doi.org/10.1016/j.jcat.2006.02.003>.

- (311) Gerken, J. B.; Stahl, S. S. High-Potential Electrocatalytic O₂ Reduction with Nitroxyl/NO_x Mediators: Implications for Fuel Cells and Aerobic Oxidation Catalysis. *ACS Cent. Sci.* **2015**, *1* (5), 234–243. <https://doi.org/10.1021/acscentsci.5b00163>.
- (312) Wilds, A. L. Reduction with Aluminum Alkoxides: (The Meerwein-Ponndorf-Verley Reduction). In *Organic Reactions*; John Wiley & Sons, Inc., Ed.; John Wiley & Sons, Inc.: Hoboken, NJ, USA, 2011; pp 178–223. <https://doi.org/10.1002/0471264180.or002.05>.
- (313) Chia, M.; Dumesic, J. A. Liquid-Phase Catalytic Transfer Hydrogenation and Cyclization of Levulinic Acid and Its Esters to γ -Valerolactone over Metal Oxide Catalysts. *Chem. Commun.* **2011**, *47* (44), 12233. <https://doi.org/10.1039/c1cc14748j>.
- (314) Boronat, M.; Corma, A.; Renz, M. Mechanism of the Meerwein-Ponndorf-Verley-Oppenauer (MPVO) Redox Equilibrium on Sn- and Zr-Beta Zeolite Catalysts. *J. Phys. Chem. B* **2006**, *110* (42), 21168–21174. <https://doi.org/10.1021/jp063249x>.
- (315) Corma, A. Water-Resistant Solid Lewis Acid Catalysts: Meerwein-Ponndorf-Verley and Oppenauer Reactions Catalyzed by Tin-Beta Zeolite. *J. Catal.* **2003**, *215* (2), 294–304. [https://doi.org/10.1016/S0021-9517\(03\)00014-9](https://doi.org/10.1016/S0021-9517(03)00014-9).
- (316) Shylesh, S.; Gokhale, A. A.; Scown, C. D.; Kim, D.; Ho, C. R.; Bell, A. T. From Sugars to Wheels: The Conversion of Ethanol to 1,3-Butadiene over Metal-Promoted Magnesia-Silicate Catalysts. *ChemSusChem* **2016**, *9* (12), 1462–1472. <https://doi.org/10.1002/cssc.201600195>.
- (317) Kvisle, S.; Agüero, A.; Sneed, R. P. A. Transformation of Ethanol into 1,3-Butadiene over Magnesium Oxide/Silica Catalysts. *Appl. Catal.* **1988**, *43* (1), 117–131. [https://doi.org/10.1016/S0166-9834\(00\)80905-7](https://doi.org/10.1016/S0166-9834(00)80905-7).
- (318) Heidari, H.; Abedini, M.; Nemati, A.; Amini, M. M. Nanocrystalline Magnesium Oxide as a Versatile Heterogeneous Catalyst for the Meerwein-Ponndorf-Verley Reduction of Cyclohexanone into Cyclohexanol: Effect of Preparation Method of Magnesium Oxide on Yield. *Catal. Lett.* **2009**, *130* (1–2), 266–270. <https://doi.org/10.1007/s10562-009-9885-2>.
- (319) Chuah, G.; Jaenicke, S.; Zhu, Y.; Liu, S. Meerwein-Ponndorf-Verley Reduction over Heterogeneous Catalysts. *Curr. Org. Chem.* **2006**, *10* (13), 1639–1654. <https://doi.org/10.2174/138527206778249621>.
- (320) Manaviazar, S.; Frigerio, M.; Bhatia, G. S.; Hummersone, M. G.; Aliev, A. E.; Hale, K. J. Enantioselective Formal Total Synthesis of the Antitumor Macrolide Bryostatin 7. *Org. Lett.* **2006**, *8* (20), 4477–4480. <https://doi.org/10.1021/ol061626i>.
- (321) Haack, K.-J.; Hashiguchi, S.; Fujii, A.; Ikariya, T.; Noyori, R. The Catalyst Precursor, Catalyst, and Intermediate in the RuII-Promoted Asymmetric Hydrogen Transfer between Alcohols and Ketones. *Angew. Chem. Int. Ed. Engl.* **1997**, *36* (3), 285–288. <https://doi.org/10.1002/anie.199702851>.
- (322) Neurock, M.; Wasileski, S. A.; Mei, D. From First Principles to Catalytic Performance: Tracking Molecular Transformations. *Chem. Eng. Sci.* **2004**, *59* (22–23), 4703–4714. <https://doi.org/10.1016/j.ces.2004.08.048>.
- (323) Selinsek, M.; Deschner, B. J.; Doronkin, D. E.; Sheppard, T. L.; Grunwaldt, J.-D.; Dittmeyer, R. Revealing the Structure and Mechanism of Palladium during Direct

- Synthesis of Hydrogen Peroxide in Continuous Flow Using Operando Spectroscopy. *ACS Catal.* **2018**, *8* (3), 2546–2557. <https://doi.org/10.1021/acscatal.7b03514>.
- (324) Thomas, F.; Lu, C.; Lee, I. C.; Chen, N. S.; Masel, R. I. Evidence for a Cation Intermediate during Methanol Dehydration on Pt(110). *Catal. Lett.* **2001**, *72* (3), 167–175. <https://doi.org/10.1023/A:1009054006372>.
- (325) Voloshin, Y.; Halder, R.; Lawal, A. Kinetics of Hydrogen Peroxide Synthesis by Direct Combination of H₂ and O₂ in a Microreactor. *Catal. Today* **2007**, *125* (1–2), 40–47. <https://doi.org/10.1016/j.cattod.2007.01.043>.
- (326) Todorovic, R.; Meyer, R. J. A Comparative Density Functional Theory Study of the Direct Synthesis of H₂O₂ on Pd, Pt and Au Surfaces. *Catal. Today* **2011**, *160* (1), 242–248. <https://doi.org/10.1016/j.cattod.2010.07.011>.
- (327) Duś, R.; Nowakowski, R.; Nowicka, E. Chemical and Structural Components of Work Function Changes in the Process of Palladium Hydride Formation within Thin Pd Film. *J. Alloys Compd.* **2005**, *404–406*, 284–287. <https://doi.org/10.1016/j.jallcom.2004.12.165>.
- (328) Janik, M. J.; Taylor, C. D.; Neurock, M. First-Principles Analysis of the Initial Electroreduction Steps of Oxygen over Pt(111). *J. Electrochem. Soc.* **2009**, *156* (1), B126. <https://doi.org/10.1149/1.3008005>.
- (329) Stephens, I. E. L.; Bondarenko, A. S.; Grønbjerg, U.; Rossmeisl, J.; Chorkendorff, I. Understanding the Electrocatalysis of Oxygen Reduction on Platinum and Its Alloys. *Energy Environ. Sci.* **2012**, *5* (5), 6744. <https://doi.org/10.1039/c2ee03590a>.
- (330) Stephens, I. E. L.; Bondarenko, A. S.; Perez-Alonso, F. J.; Calle-Vallejo, F.; Bech, L.; Johansson, T. P.; Jepsen, A. K.; Frydendal, R.; Knudsen, B. P.; Rossmeisl, J.; et al. Tuning the Activity of Pt(111) for Oxygen Electroreduction by Subsurface Alloying. *J. Am. Chem. Soc.* **2011**, *133* (14), 5485–5491. <https://doi.org/10.1021/ja111690g>.
- (331) Paunovic, V.; Ordonsky, V. V.; Sushkevich, V. L.; Schouten, J. C.; Nijhuis, T. A. Direct Synthesis of Hydrogen Peroxide over Au-Pd Catalyst-The Effect of Co-Solvent Addition. *ChemCatChem* **2015**, *7* (7), 1161–1176. <https://doi.org/10.1002/cctc.201500050>.
- (332) Jerero, E.; Vohs, J. M. Zn Modification of the Reactivity of Pd(111) Toward Methanol and Formaldehyde. *J. Am. Chem. Soc.* **2008**, *130* (31), 10199–10207. <https://doi.org/10.1021/ja8001265>.
- (333) Young, Z. D.; Davis, R. J. Hydrogen Transfer Reactions Relevant to Guerbet Coupling of Alcohols over Hydroxyapatite and Magnesium Oxide Catalysts. *Catal. Sci. Technol.* **2018**, *8* (6), 1722–1729. <https://doi.org/10.1039/C7CY01393K>.
- (334) Singh, M.; Zhou, N.; Paul, D. K.; Klabunde, K. J. IR Spectral Evidence of Aldol Condensation: Acetaldehyde Adsorption over TiO₂ Surface. *J. Catal.* **2008**, *260* (2), 371–379. <https://doi.org/10.1016/j.jcat.2008.07.020>.
- (335) Sunesson, Y.; Limé, E.; Nilsson Lill, S. O.; Meadows, R. E.; Norrby, P.-O. Role of the Base in Buchwald–Hartwig Amination. *J. Org. Chem.* **2014**, *79* (24), 11961–11969. <https://doi.org/10.1021/jo501817m>.
- (336) Shvo, Y.; Goldberg, I.; Czerkie, D.; Reshef, D.; Stein, Z. New Ruthenium Complexes in the Catalytic Hydrogenation of Alkynes. Study of Structure and Mechanism. *Organometallics* **1997**, *16* (1), 133–138. <https://doi.org/10.1021/om960469w>.

- (337) Casey, C. P.; Singer, S. W.; Powell, D. R.; Hayashi, R. K.; Kavana, M. Hydrogen Transfer to Carbonyls and Imines from a Hydroxycyclopentadienyl Ruthenium Hydride: Evidence for Concerted Hydride and Proton Transfer. *J. Am. Chem. Soc.* **2001**, *123* (6), 1090–1100. <https://doi.org/10.1021/ja002177z>.
- (338) Comas-Vives, A.; Ujaque, G.; Lledós, A. Hydrogen Transfer to Ketones Catalyzed by Shvo's Ruthenium Hydride Complex: A Mechanistic Insight. *Organometallics* **2007**, *26* (17), 4135–4144. <https://doi.org/10.1021/om7004832>.
- (339) Kitamura, M.; Tsukamoto, M.; Bessho, Y.; Yoshimura, M.; Kobs, U.; Widhalm, M.; Noyori, R. Mechanism of Asymmetric Hydrogenation of α -(Acylamino)Acrylic Esters Catalyzed by BINAP–Ruthenium(II) Diacetate. *J. Am. Chem. Soc.* **2002**, *124* (23), 6649–6667. <https://doi.org/10.1021/ja010982n>.
- (340) Sandoval, C. A.; Ohkuma, T.; Muñiz, K.; Noyori, R. Mechanism of Asymmetric Hydrogenation of Ketones Catalyzed by BINAP/1,2-Diamine–Ruthenium(II) Complexes. *J. Am. Chem. Soc.* **2003**, *125* (44), 13490–13503. <https://doi.org/10.1021/ja030272c>.
- (341) Medina-Ramos, J.; DiMeglio, J. L.; Rosenthal, J. Efficient Reduction of CO₂ to CO with High Current Density Using in Situ or Ex Situ Prepared Bi-Based Materials. *J. Am. Chem. Soc.* **2014**, *136* (23), 8361–8367. <https://doi.org/10.1021/ja501923g>.
- (342) Sung, S.; Kumar, D.; Gil-Sepulcre, M.; Nippe, M. Electrocatalytic CO₂ Reduction by Imidazolium-Functionalized Molecular Catalysts. *J. Am. Chem. Soc.* **2017**, *139* (40), 13993–13996. <https://doi.org/10.1021/jacs.7b07709>.
- (343) Kozhevnikov, I. V. Catalysis by Heteropoly Acids and Multicomponent Polyoxometalates in Liquid-Phase Reactions. *Chem. Rev.* **1998**, *98* (1), 171–198. <https://doi.org/10.1021/cr960400y>.
- (344) Migliore, A.; Polizzi, N. F.; Therien, M. J.; Beratan, D. N. Biochemistry and Theory of Proton-Coupled Electron Transfer. *Chem. Rev.* **2014**, *114* (7), 3381–3465. <https://doi.org/10.1021/cr4006654>.